Development of Sustainable Processes *via* Novel Synthesis Methods and Environments

Thesis submitted for the degree of

Doctor of Philosophy

The University Of Sheffield.

Department of Chemical and Biological Engineering

Gareth Davies

Supervisor: Dr James McGregor

Second Supervisor: Dr Mark Ogden

December 2021

Abstract

Dwindling global resources necessitate the investigation, and development of more sustainable, optimised, and effective processes beyond conventional practices. Therefore, the present work explores novel synthesis methods and environments. The areas investigated are: hydrothermal carbonisation, alcohol/water mixtures, and aerosol-assisted sol-gel synthesis.

Hydrothermal carbonisation is an emerging thermochemical conversion process. Herein hydrothermal carbonisation processing is performed on two novel biomass waste feedstocks, bread waste and avocado seeds. Both of these feedstocks are unsuitable for animal feed or other thermochemical processes and therefore are generally sent to landfill. The valorisation of these waste streams would therefore produce value from a genuine waste product. Hydrothermal carbonisation of bread waste is investigated at a range of different processing temperatures (160-200 °C) and retention times (30-90 min), in addition to two different pressurising gases helium and carbon dioxide. Under carbon dioxide at 200 °C after 60 mins the hydrochar displayed exceptional energy density at 36 MJ Kg^{-1} and contained a large portion of volatile matter (58.8%). Thus, bread waste demonstrated high potential in producing a renewable solid fuel or activated carbon material. Hydrothermal carbonisation of avocado seeds examined the potential to perform a one-pot catalyst synthesis procedure. A mixture of magnetite and heamatite was supported on the hydrochar *in situ* to yield a magnetic carbon composite material. This catalyst showed full regioselectivity in an exemplary catalytic testing procedure as well as viable adsorption of indigo carmine (~49 mg g^{-1}). Therefore, the efficient production of catalytic materials is exhibited with potential application to a wide range of different lignocellulosic wastes and catalytic metals.

The molecular interactions within alcohol/water mixtures at both ambient and hydrothermal (sub-critical) conditions was analysed using Fourier-transform infrared spectroscopy. Mathematical analysis methods such as deconvolution, and perturbation induced 2D correlation analysis were performed to analyse the data. Using this methodology the molecular transition points discussed in literature for ambient alcohol/water mixtures were identified by trends in blueshifting and excess intensity of the crucial peaks O-H and C-O stretching. Following this, novel information about the molecular dynamics of alcohol/water mixtures under hydrothermal conditions was acquired. Further to this, the effect of ethanol/water mixtures on the hydrothermal carbonisation of bread waste and avocado seeds was

investigated. Whilst the properties of hydrochar were affected by varying ethanol concentration at lower processing temperatures these effects were reduced at higher processing temperatures.

Aerosol-assisted sol-gel synthesis mechanisms were investigated using optical trapping instrumentation at the Central Laser Facility. The initial stages of synthesis were imitated by trapping a single droplet of the precursor solutions using focussed light. This droplet was monitored using Raman spectroscopy and heated externally, therefore replacing the space domain in the aerosol flow tube with a time domain. From this investigation, evidence against the expected reactions based on bulk sol-gel synthesis was obtained. Furthermore, insight was gained into the effects of different compounds in the precursor solution on droplet stability and evaporation. Finally, an alternative reaction mechanism to that observed in bulk sol-gel synthesis was proposed based on the observed Raman spectroscopic data.

Thesis length (without references and appendix): 71,205 words.

Published Research

1) G. Davies, J. Driver, A. Ward, L. Negahdar, and J. McGregor, "Operando Studies of Aerosol-Assisted Sol–Gel Catalyst Synthesis *via* Combined Optical Trapping and Raman Spectroscopy ," *J. Phys. Chem. C*, vol. 125, no. 41, pp. 22591–22602, 2021, doi: 10.1021/acs.jpcc.1c07517.

2) G. Davies and J. McGregor, "Hydrothermal Synthesis of Biomass-Derived Magnetic Carbon Composites for Adsorption and Catalysis," *ACS Omega*, vol. 6, no. 48, pp. 33000–33009, 2021, doi: 10.1021/acsomega.1c05116.

3) G. Davies, A. El Sheikh, C. Collett, I. Yakub, and J. McGregor, "Chapter 5 - Catalytic carbon materials from biomass," in *Emerging Carbon Materials for Catalysis*, S. B. T.-E. C. M. for C. Sadjadi, Ed. Elsevier, 2021, pp. 161–195.

4) N. Atiqah Nasir, G. Davies, and J. McGregor, "Tailoring product characteristics in the carbonisation of brewers' spent grain through solvent selection," *Food Bioprod. Process.*, vol. 120, pp. 41–47, 2020, doi: 10.1016/j.fbp.2019.12.010.

Portions of publication 1 have been reused in Chapter 7 and have been reprinted with permission from the American Chemical Society, copyright © 2021. The article is available on public access *via* the link https://pubs.acs.org/doi/abs/10.1021/acs.jpcc.1c07517. Additionally the paper is attached at the end of the appendix.

Portions of publication 2 have been reused in Chapter 6 and have been reprinted with permission from the American Chemical Society, copyright © 2021. The article is available on public access *via* the link https://pubs.acs.org/doi/full/10.1021/acsomega.1c05116. Additionally the paper is attached at the end of the appendix.

Acknowledgments

Primarily I want to thank my supervisor, Dr James McGregor. He is, quite simply put, the best supervisor I could have ever had, and this research would not have been possible without his support. James always provided a keen scientific insight into any discussion I brought forward, he always supported my research interests and did not micromanage me. I always felt I was being treated as an equal and I appreciate that a great deal. Secondarily I want to express thanks to Dr Andrew Ward for generously welcoming our research group into his laboratory and teaching me several valuable lessons in both research and data analysis methods.

Additionally, I recognize that innumerable University of Sheffield associates have assisted me during my PhD. Therefore, I would like to generally thank all of the technical staff, academic staff, and administration staff in addition to the other PGR students at the University of Sheffield.

Personally speaking I am grateful for the support of my friends and family who have always been willing to help me in every way that they can. None more so than my best friend and partner, Beth Dickens, she is a bright light always shining during the darkest of hours. Additionally, special thanks goes out to Ana Casas Hidalgo and Edward Rackley for their welcoming friendship in my time of need. Finally, I would not be here without the support and guidance I received during my childhood from my loving mother and father.

Contents

Table of Figures

Table of Tables

Table of Equations

Nomenclature

Abbreviation	Meaning	Page
°C	Degrees Celsius	1
HTC	Hydrothermal carbonisation	2
AASG	Aerosol-assisted sol-gel	6
FT-IR	Fourier-transform infrared	7
2D	Two-dimensional	7
ATR	Attenuated total reflectance	7
XRD	X-ray diffraction	8
H_2O	Water	9
HTW	High temperature water	9
SCW	Supercritical water	9
nHB	Average number of hydrogen bonds	11
Kw	Ionic product	13
D_2O	Deuterated water	16
cm-1	Wavenumber	18
NMR	Nuclear magnetic resonance	21
ppm	Parts per million (mg L-1)	21
mol%	Molar concentration percentage	23
MeOH	Methanol	25
EtOH	Ethanol	25
IPA	Isopropanol	25
HTL	Hydrothermal liquefaction	35
HTG	Hydrothermal gasification	35
CO2	Carbon dioxide	35
5-HMF	5-(Hydroxymethyl)furfural	39
HHV	Higher heating value	40
FC	Fixed carbon	41
VM	Volatile matter	41
CHNS	Carbon, hydrogen, nitrogen, sulphur analyser	41
Wt.%	Weight concentration percentage	46
MB	Methylene blue	56
UV-Vis	Ultraviolet-visible	56
EDLC	Electric double layer capacitor	60
SEM	Scanning electron microscopy	61
EISA	Evaporation induced self-assembly	66
BET	Brunauer–Emmett–Teller	68
Pluronic P123	Poly(ethylene glycol)-block-poly(propylene glycol)-block-poly(ethylene glycol)	68
M	Concentration (mol dm-3)	72
DAS	Dried avocado seed	72
XRF	X-ray fluorescence	73
DBW	Dried bread waste	74
He	Helium	75
GC-MS	Gas chromatography mass spectroscopy	75
TGA	Thermogravimetric analysis	75
Ni/Al2O3	Nickel alumina catalyst	79
AAS	Atomic absorption spectroscopy	80
2B13D	2-benzyl-1,3,-dioxolane	81
XPS	X-ray photoelectron spectroscopy	85
νs	Symmetric stretching	90
νas	Asymmetric stretching	90
δ	Bending	90

ω	Wagging	90
ρ	Rocking	90
τ	Twisting	90
FWHM	Full width half maximum	99
PA	Palmitic acid	124
STDChar	Bread waste hydrochar synthesised at 180 °C, 60 minutes, under helium	142
IC	Indigo carmine	166
Al-iPr	aluminium isopropoxide	194
EP	aerosol comprising ethanol and P123	194
EPN	aerosol comprising ethanol, P123 and nitric acid	194
EPNA	aerosol comprising ethanol, P123, nitric acid and aluminium isopropoxide	194
EPNAN	aerosol comprising ethanol, P123, nitric acid, aluminium isopropoxide and nickel nitrate hexahydrate	194
HeEPNA	heated aerosol comprising ethanol, P123, nitric acid and aluminium isopropoxide	194
HeEPNAN	heated aerosol comprising ethanol, P123, nitric acid, aluminium isopropoxide and nickel nitrate hexahydrate	194
WGM	whispering gallery mode	194
CMC	Critical micelle concentration	195

Chapter 1 Introduction

1.1. Motivation

It is well known that human civilisation is reaching a tipping point on the scales of natural disaster, with some catastrophic predictions as soon as the year 2050 [1]. Just as Buckminster Fuller succinctly put it "whether it is to be Utopia or Oblivion will be a touch-and-go relay race right up to the final moment". There are various current global issues that need to be addressed to prevent future human suffering.

One key issue is that the global mean temperature has been increasing since the industrial revolution [2]. The effect that this has on the Earth is commonly known as global warming and can be attributed to the increasing concentration of greenhouse gasses (carbon dioxide, methane, nitrous oxide, *etc.*) [3]. Of the greenhouse gases, carbon dioxide is released in the largest quantities and is present in the highest concentration in the atmosphere. Global mean temperature has increased from pre-industrial levels to around 1 °C higher, whilst carbon dioxide concentration has increased from 280 up to ~400 parts per million. Global warming and therefore increasing carbon dioxide emissions are causing rising sea levels, destruction of ecosystems, extinction of many species, ocean acidification, reduction of crop yields and increasing starvation to name only a few of its serious implications [4]. This increase in carbon dioxide concentration is caused by our increased usage and dependence on fossil fuels (coal, natural gas, and oil). Currently, 21st century society relies wholly on fossil fuels for a myriad of essential industries and applications such as; transportation, heating, agriculture, manufacturing, plastics, fertilisers, chemicals, dyes, paints, building materials, cosmetics, and the list goes on [5]. Therefore, in order to limit the increase in mean global temperature from pre-industrial levels to 2 °C, in line with governmental targets, alternative sustainable replacements for fossil fuels must be investigated and developed [6]. Further to this, the reserves of coal, natural gas, and oil are predicted to run out in 95, 25, and 23 years respectively if the current rates of consumption do not change [7]. Because fossil fuels are necessary for such a wide variety of processes no one single source of renewable energy or manufactured goods will be suitable to fulfil all of these roles. Consequently, it is imperative to properly consider all potential sustainable processes to address this key global issue.

Another issue to overcome is the production and disposal of solid waste, currently around 11 billion tons of solid waste is produced globally every year [8]. This solid waste has adverse

environmental impacts polluting the air, water, and soil [9]. Further, the solid waste generated globally is predicted to double 2016 waste generation by the year 2050. Management of this solid waste is currently dominated by landfill or incineration practices which together dispose of over 80% of this solid waste. Landfilling causes a number of different environmental impacts and hazards to human health [10]. Leachate (complex liquid waste) often percolates through the disposed waste in landfill sites, this contaminates both the soil and groundwater and can continue for hundreds of years after the landfill site has been decommissioned. This infects both the soil and groundwater with a high concentration of dissolved organic matter, heavy metals and inorganic compounds [11]. Affected groundwater is thereafter unsuitable for aquatic life or human consumption because of toxic heavy metals and pathogens. Furthermore, landfill sites are a source of additional greenhouse gas emissions, typically methane in high concentrations. Besides this, landfill sites are breeding grounds for rats and insects which can act as vectors for transmission of a plethora of different diseases. Incineration of solid waste is also wreaked with problems; the process pollutes the air with greenhouse gas emissions (carbon dioxide) and noxious fumes which negatively affect the environment. Therefore alternative waste management applications need to be studied and developed which are able to process solid waste without causing a negative impact on the environment or human health. Currently ~1 billion tons of agricultural waste and 1.3 billion tons of food waste is produced globally every year [12], [13]. Together this waste accounts for over 20% of the solid waste produced annually. This organic waste can be valorised in a variety of different processes to produce energy, chemicals and materials, thus providing a basis for a sustainable circular economy which protects natural resources without sacrificing societal development [14]. A variety of different biochemical and thermochemical processes can be employed to achieve this such as anaerobic digestion, fermentation, pyrolysis, gasification, and biodiesel production.

This research aims to investigate innovative, sustainable synthesis methods and environments to combat the effects of global warming and waste generation. The areas investigated are as follows: hydrothermal carbonisation, alcohol/water mixtures, and aerosol-assisted sol-gel synthesis.

1.2. Introduction to Hydrothermal Carbonisation (HTC)

Friedrich Bergius is credited with pioneering the field of hydrothermal processes, with publications beginning in 1913. Bergius was initially attempting to produce hydrogen from

water with carbon acting as a reductant following Equation 1.1 [15]. The experimental set-up placed coal inside of a pressurised reaction vessel and heated to temperatures below 600 °C with pressures up to 200 bar. This reaction successfully produced hydrogen as postulated, however low reaction rates and high processing costs hindered commercial interest in the technique. Though, whilst studying this Bergius substituted peat for coal inside of the reaction vessel and produced an enriched carbonaceous product with properties comparable to natural coal, therefore mimicking natural coalification. This prompted Bergius to investigate treatment of plant-based materials in a high pressure vessel at milder temperatures (~200 °C). Following this, Bergius and his assistant Hugo Specht continued this research as classified by them as the hydrogenation of artificial coal [16]. For this, among other research, Bergius obtained the Nobel Prize in chemistry in 1931. This initial discovery was followed by a relative dark period within the field, with some notable research into the effect of process parameters on the decomposition of the feedstock by van Krevelen [17].

$$C + 2H_2O \rightarrow CO_2 + 2H_2$$

Equation 1.1 Bergius' proposed equation for the production of hydrogen from water using a carbon rich material as the reductant.

Resurgence into the field did not occur until 70 years after Bergius obtained his Nobel Prize at the turn of the millennium. Maria-Magdalena Titirici and her research associates are credited with pioneering this renaissance with initial publications starting in 2007 and the first book in the field "Sustainable Carbon Materials from Hydrothermal Processes" published in 2013 [18], [19]. Furthermore, the first international symposium on HTC was opened just 4 years ago in 2017 and now occurs every 2 years due to the increasing research attention that HTC is receiving. However, because HTC is still a developing research area the nomenclature of its scientific terminology and the necessary analysis procedures are still in dispute. HTC has also been referred to as the American "hydrothermal carbonization", hydrothermal pre-treatment, wet torrefaction, hot compressed water treatment, coalification and biomass hydrolysis [20]. The solid carbonaceous product was coined hydrochar by the European Biomass Industry Association to differentiate it from other biomass based carbonaceous products [21]. However, literature sources still refer to the product as bio-char, char, and bio-coal [22]. Herein, this document will exclusively use the term HTC (hydrothermal carbonisation) for the process and the product will be following the European Biomass Industry Associations guidance and be referred to as a hydrochar.

Currently the process parameters required for HTC are typically defined by the following; a high enough pressure to keep the water in the liquid phase (20-500 bar), all feedstock is submerged underwater during processing, temperatures between 180 to 250 °C, and at least 5 min retention time for significant carbonisation to occur (Figure 1.1) [23]. However, deviation from these conditions is not uncommon in the literature, therefore it is more valuable to consider any hydrothermal process aiming to yield a solid carbonaceous product (hydrochar). Hydrochar has a higher percentage of carbon compared to the raw feedstock, this is attributed to dehydration and decarboxylation reactions removing water and carbon dioxide from the feedstock [24]. A wide range of different feedstocks can be processed using HTC to produce hydrochar. Compared to biochar and charcoal produced from other thermochemical technologies hydrochar has significantly different chemical and physical properties such as increased aromatic surface structure and oxygenic functionality [25]. Besides hydrochar, the HTC of biomass also produces sugars, organic derivatives, organic acids, furanoids and phenolics in the aqueous liquid phase (bio-oil) [26], [27]. As well as carbon dioxide, methane, carbon monoxide, and trace hydrogen in the gaseous phase.

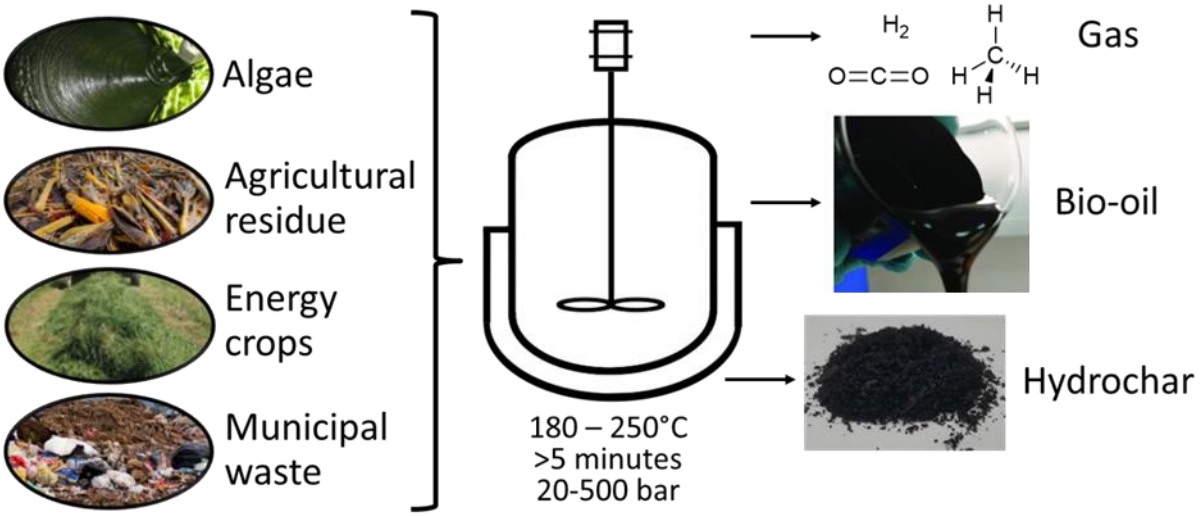

Figure 1.1 Typical processing parameters, feedstocks, and products in HTC processes.

1.3. Acknowledged Research Gaps

Considering HTC is a developing research area with renewed interest there are a significant number of gaps within the available literature. A research gap identified for further study and presented in this thesis is the addition of solvents during HTC and other hydrothermal processes [28]. Hydrothermal processes that utilise small chain alcohols (methanol, ethanol, *etc.*) can be referred to as “alcoholysis” or “alcohothermal” [29] [30]. Whilst the term “solvothermal”

involves the use of any organic solvent and is carried over from single crystal synthesis characterisation of hydrothermal technologies [31], [32]. Finally the use of the term "organosolv" is related to the pulping technique pioneered by the paper-making process [33]. This divided nomenclature obstructs a clear narrative of the effects that different solvent/water mixtures have on biomass during hydrothermal processes. Furthermore, there is no agreement on the use of pre-dried or wet biomass. The latter of which is recommended to lower processing steps and costs; therefore the moisture content of the biomass would affect the solvent/water ratio applied during HTC. Moreover, even small variations on the solvent/water ratio can have a dramatic effect on the molecular dynamics of the system and consequently alter the products formed. The most common solvent additives used during HTC in the literature are alcohols. This can be attributed to both parallels in chemical structure with water and because of the interesting non-ideal nature of alcohol/water mixtures. Therefore, one aim of this research is to initially characterise a novel HTC process and analyse the hydrochar product. Following this, the addition of alcohol during HTC at various molar percentages with water is to be investigated by its effect on the properties of the hydrochar formed. Then, this directs towards the second gap identified in the literature for further examination. Though many investigations study ambient alcohol/water mixtures there is minimal research into the molecular dynamics of alcohol/water mixtures under sub-critical conditions [34]. Consequently, an analysis of the molecular dynamics of alcohol/water mixtures using a cheap, facile and readily available analysis procedure will be established initially at ambient conditions. Following this an investigation of alcohol/water mixtures at sub-critical conditions using the same analysis procedure will be attempted to deliver insight into the change in the molecular dynamics of the alcohol/water mixtures.

Aerosol based catalyst synthesis techniques have several advantages over conventional wet and solid-phase production methods [35]. These include but are not limited to 1) no liquid by-products, 2) facile and cheap collection processes requiring no separation 3) high purity products with unique morphologies. For this reason aerosol processes are well-established and used to produce a variety of materials such as carbon black, fumed silica, and titania particles [36]. However, analysing the reactivity occurring within a flow tube during aerosol based processes is challenging with a myriad of different physical and experimental constraints. The concentration of the spray within a flow tube is low due to the low density of the spray and singular droplets cannot be studied along the flow tube. Furthermore, spray drying apparatuses are often large and unsuitable for attachment with external spectroscopic analysis instruments

such as cyclone collectors. Therefore, the mechanism of catalyst formation inside of aerosol processes are not fully understood and often considered a “black-box” this presents a gap within the literature [37]. To address this gap optical trapping is employed mirroring the early stages of aerosol processes, this technique traps a singular droplet within a beam of focussed light [38]. Therefore the space domain in a conventional flow tube is substituted for a time domain in the optical trapping cell. Aerosol-assisted sol-gel (AASG) synthesis techniques are the focus of this research [39]. However, the same methodology can be utilised to gain understating of other aerosol processes.

1.4. Research Aims and Objectives

The overall aim of this research is to investigate novel synthesis methods and environments with a foundation in innovative spectroscopic methods. It is hoped that the results of these investigations can consequently be used to inform on more sustainable synthesis processes for fuels, catalysts, and adsorbents. Additionally, the research is hoped to pave the way for further use of these spectroscopic analytical systems and mathematical methods. To achieve this several different objectives were identified based on gaps within the literature:

- Utilise simplistic ATR FT-IR analysis at ambient and sub-critical conditions on binary mixtures of water and methanol/ethanol/isopropanol at specified molar percentages. This is intended to yield information about the intermolecular bonding dynamics at sub-critical conditions. There is no similar investigation present in the literature.
- Perform mathematical analysis method such as deconvolution and perturbation induced 2D correlation analysis on the obtained FT-IR data to extract insights not readily available by conventional analysis methods. This would display the efficacy of using these complex analysis methods.
- Use a combined approach of optical trapping and *in situ* Raman analysis to observe the reaction dynamics of aerosol-assisted sol-gel synthesis. Currently reactions within the flow tube are unclear and assumptions are made. This would not only increase the understanding of AASG but also demonstrate the capability of combined optical trapping and Raman analysis as an innovative analysis technique for aerosol processes.
- Characterise the hydrothermal carbonisation of bread waste which is identified as a waste product from the food manufacturing industry. There are currently limited literature sources which investigate the hydrothermal carbonisation of bread waste despite its potential as a homogenous high value feedstock which is currently sent to

landfill. The hydrochar produced from this bread waste is theorised to have high potential as a sustainable solid biofuel.

- Investigate the effect of different pressurising gasses, alcohol/water systems, and particle sizes on the hydrothermal carbonisation of bread waste. These investigations could yield insightful conclusions on the potential turnability of hydrothermal carbonisation. In particular the effect of alcohol/water mixtures on hydrothermal carbonisation is not known and could greatly influence the hydrochars formed.
- Perform a hydrothermal carbonisation reaction on whole avocado seeds as an exemplary high lignocellulosic feedstock to produce high value carbon-based catalysts and adsorbents. This process will utilise cheap and abundant iron as the reactive catalytic material which is supported onto the hydrochar *in situ* using a 'one-pot' process. The successful demonstration of this would prove that hydrothermal carbonisation is a viable process for large scale production of carbonaceous adsorbents and catalysts from low value lignocellulosic waste.

1.5. Thesis Structure

Chapter 2 provides a study of the literature beginning with an explanation of the unique properties of high temperature water (sub-critical water), with attention on the experimental determination of those properties and its novel reactivity. Following this is the non-ideal properties of alcohol/water mixtures with a closing focus on the mixtures at sub-critical conditions. After, the potential of biomass to support a circular carbon based economy is detailed. This discusses the structure of lignocellulosic biomass and the potential biochemical and thermochemical conversion techniques providing a comparison to HTC. At which point HTC is comprehensively reviewed with an initial explanation of simplistic hydrochar formation reactions. Following this, hydrochar is assessed as a potential source of renewably sourced solid fuel with graphical analysis provided from a multitude of literature sources. This section is closed by sub-chapters focussed on the production of high value carbon based materials *via* HTC. Finally, a section on sol-gel synthesis with a focus on aerosol-assisted methods is presented.

Chapter 3 is a description of the analysis and experimental procedures employed to produce the wide variety of different solid products. as Additionally, the instrumentation used to perform the synthesis and analysis procedures is described in this subchapter. This section

closes with a brief overview of FT-IR and Raman spectroscopy which are the dominant analysis techniques employed within this thesis.

Chapter 4 constitutes the use of Fourier-transform infrared spectroscopy to study the properties of alcohol/water mixtures. Analysis methods are standardised by studying ambient alcohol/water mixtures with an attenuated total reflectance (ATR) plate. This allows for comparison to the abundant molecular and thermodynamic properties of alcohol/water mixtures at ambient conditions presented in the literature. The mathematical methods deconvolution and perturbation induced two-dimensional (2D) correlation analysis are employed to derive additional insights from the data. Following this, alcohol/water mixtures subjected to sub-critical conditions are then analysed using a specialised high temperature ATR reaction cell. This expands the understanding of the changes in molecular dynamics of alcohol/water mixtures under these conditions.

Chapter 5 presents, to the authors' knowledge, the first research into the HTC of bread waste which is a real waste stream from the Bradgate Bakery in Leicester. The bread waste produced is unsuitable for animal feed or for conventional biochemical and thermochemical conversion technologies. Therefore, the HTC of bread waste is characterised at a range of different processing conditions. Before HTC the bread waste is dried, and ground then separated into specific particle sizes. During HTC the processing temperature is varied from 160 to 200 °C, retention time is studied between 30 and 90 mins, two pressurising gases helium and carbon dioxide are investigated. Once the HTC of bread waste was characterised, the effect of ethanol on the properties of the hydrochar was investigated. The combustion characteristics of the bread waste hydrochars produced were analysed according to standard procedures displayed in the literature.

Chapter 6 develops a one-pot synthesis procedure to synthesise a high value carbon based magnetic material *via* HTC. An additional novel HTC feedstock, avocado seeds are processed to demonstrate the applicability of the synthesis procedure to a wide variety of lignocellulosic feedstocks. The process utilises relatively mild processing temperatures (230 °C) and the most abundant metal on Earth, iron to produce a magnetic carbon composite (Fe/C) material. This Fe/C exhibits selective adsorption behaviour of exemplar adsorbates in addition to acting as a regioselective catalyst. Furthermore, Fe/C has exceptional separation efficiency with facile magnetic removal. Therefore, a one-pot HTC technique is demonstrated to produce a

sustainable material which can be used in both wastewater treatment and catalytic processes instead of non-sustainable materials. Finally, the effect of ethanol during HTC on the properties and function of the Fe/C is examined.

Chapter 7 presents an additional research opportunity made possible due to collaboration with Dr Andrew Ward and the Central Laser Facility in Harwell. The basis of the research was to utilise optical trapping to investigate the mechanisms involved in aerosol-assisted sol-gel (AASG) synthesis. This impactful research contains overlapping analysis methods (Raman spectroscopy) with the content of Chapter 4 and catalyst synthesis procedures further to that presented in Chapter 6. To achieve this goal prior to work at the Central Laser Facility, bulk sol-gel synthesis of 12 different catalyst systems was accomplished. Catalysts were characterised using Raman spectroscopy and XRD to confirm successful synthesis. Of these catalytic precursor solutions only one was suitable for optical trapping due to limitations in the trapping procedure.

Chapter 8 is a summary for the conclusions presented in Chapters 4, 5, 6, and 7, these are put into context with the objectives outlined in this introduction (Section 1.4). Following this a description of the recommended avenues for future work towards achieving these objectives is outlined. The accomplishment of which would expand the boundaries of HTC and provide inspiration for further development of the research area.

References provides a complete list of the literature cited in this thesis in order of citation and in IEEE style. Appendix includes both literature and thesis data/figures not included within the thesis. At the end of the appendix first author papers are attached.

Chapter 2 Literature Review

2.1. High Temperature Water (HTW)

The importance of water (H_2O) should not be understated, it is one of the most important substances to our society in existence [40]. Water is used to produce electricity in steam turbines, is the most common solvent used in chemistry and chemical engineering, and of course is essential for all living organisms. The physical and chemical properties of water change dramatically based on the temperature and pressure exerted upon it. Of interest in this research are the distinct properties of high temperature water (HTW) also referred to as superheated water or sub-critical water. HTW is broadly defined as water above 180 °C and below 374 °C under sufficient pressure to avoid the phase change to steam and hold it in the liquid phase (Figure 2.1) [41]. Above 374 °C and 220 bar water becomes a supercritical fluid which has significantly different properties to that of both ambient water and HTW. In practice HTW has the properties of a polar organic solvent, whilst supercritical water (SCW) has properties similar to a non-polar organic solvent [42]. Consequently, HTW and SCW present different challenges and opportunities, this difference has been highlighted to eliminate confusion, only HTW is the considered in this research.

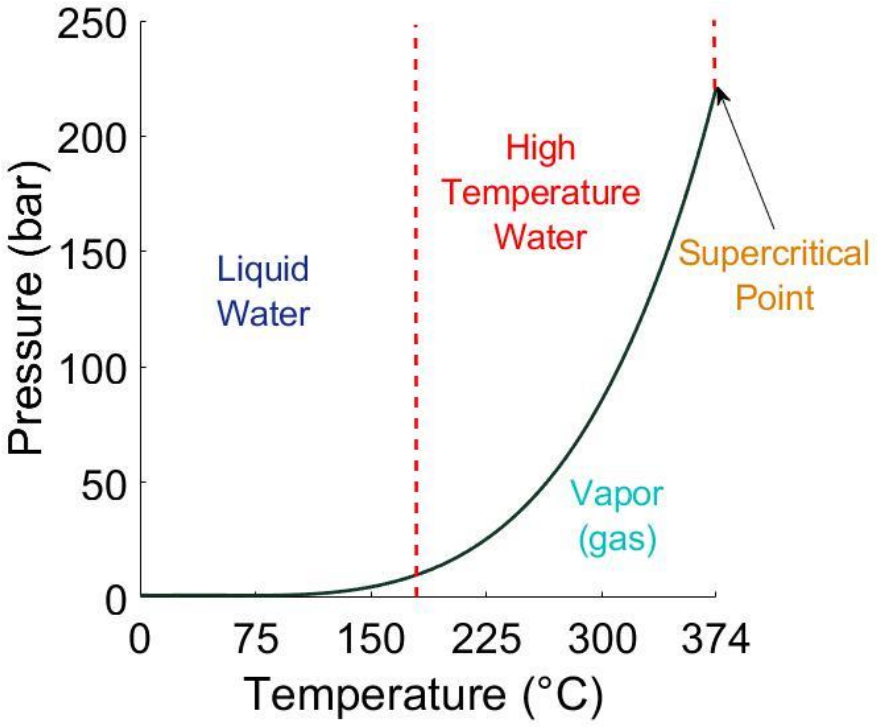

Figure 2.1 Phase diagram for water displaying high temperature water, supercritical point, as well as steam (vapor) and liquid (ambient) conditions.

2.1.1. HTW Properties

The physical and chemical properties of HTW are more like organic solvents (*e.g.* acetone, ethanol) than ambient water, because of this many organic compounds have a high solubility in HTW [43]. Water is non-toxic, cheap, highly abundant, and renewable. Therefore, HTW has the potential to replace organic solvents as a reaction medium for more "green" processes with reduced environmental impact. Moreover, the properties of HTW can be tuned towards different processes by varying the pressure and temperature used. This allows for a more precise control over products using HTW processing conditions. Additionally, HTW is a very versatile reaction medium, it can act as a solvent, reactant, catalyst, and an acid or base. Among the physical properties which differ significantly between ambient water and HTW are density, hydrogen bonding, dielectric constant, and ionic product. The surface tension, viscosity, and thermal conductivity of HTW are also different to that of ambient water [44]. These are all important properties for solvent selection in a wide variety of industrial processes [45].

2.1.1.1. Density

The density of the reaction medium can have a strong influence on the chemical reaction rates through concentration effects increasing the number of successful collisions [46]. In most cases, the density of a solvent will decrease as temperature is increased but will remain stable with changes in pressure [47]. As is expected the density of HTW decreases as temperature is increased, the density is between 0.9 g cm^{-3} and 0.74 g cm^{-3} from 180 to 300 °C. This density range is relatively small compared to other solvents used industrially; chloroform is at the upper range used and has a density of 1.48 g cm^{-3}, whilst diethyl ether has one of the lowest densities at 0.71 g cm^{-3}. Density is important in most HTW processes because individual water molecules participate in initial reaction steps as reactants, products, and catalysts in hydrolysis, hydration, hydrogen exchange, and free-radical oxidation, therefore concentration effects have more ramifications in HTW systems [41]. This suggests that some compromise could be necessary in process design between enough temperature to initiate desired reactions whilst limiting it to keep density high allowing for more successful collisions and thus a faster reaction rate.

2.1.1.2. Hydrogen Bonding

Hydrogen bonding is a type of dipole-dipole interaction between molecules, it occurs when a compound has a hydrogen atom covalently bonded to a highly electron withdrawing group

such as nitrogen, oxygen, and fluorine [48]. The dipole-dipole interaction then occurs between the electropositive hydrogen and a neighbouring lone pair. Hydrogen bonding influences many important characteristics of a solvent (structure, dielectric constant) and is responsible for many of the unique properties of water. This is because it has the single strongest hydrogen bonding effect of all molecules [41]. Water contains a highly electronegative oxygen (3.44 on the Pauling scale, second only to fluorine) with two lone pairs and two covalent bonds to hydrogen, this allows each water molecule to form two hydrogen bonds with other water molecules to create a lattice type structure in solution (Figure 2.2) [49]. This is in stark contrast to most organic solvents used industrially which have little to no hydrogen bonding [50].

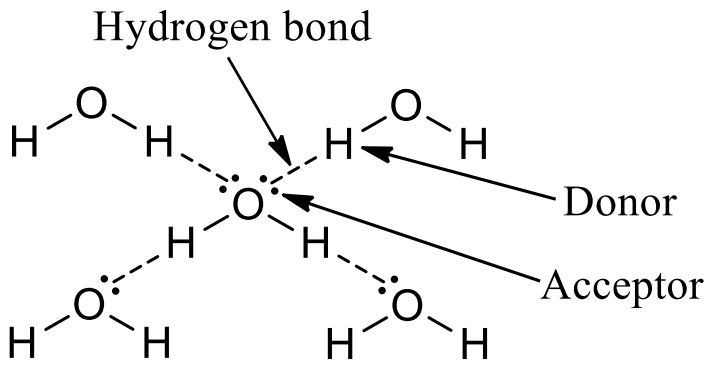

Figure 2.2 Hydrogen bonded tetrahedral water structure showing both hydrogen donor and acceptor.

Hydrogen bonding within water becomes weaker and less obstinate as temperature and pressure is increased [51]. Hydrogen bonding can be reported as an average number of hydrogen bonds per molecule (nHB). Molecular dynamics simulations have been used to determine nHB for subcritical water and SCW at four different temperatures 100, 200, 300, and 400 °C [52], [53]. The nHB decreases from 3.89 at ambient conditions linearly down to 1.73 at 300 °C, however there is a sharper decrease in hydrogen bonding once supercritical conditions have been reached at 400 °C (Figure 2.3).

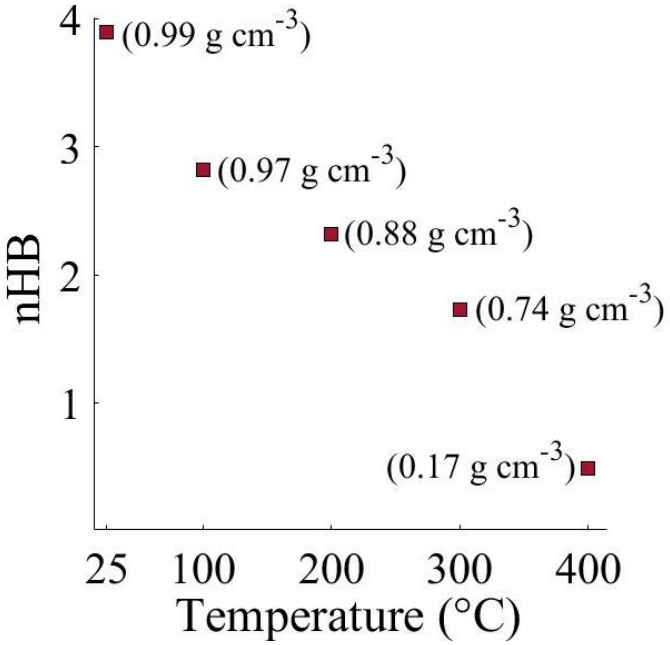

Figure 2.3 Molecular simulation data for the average number of hydrogen bonds (nHB) as a function of temperature with density shown in brackets [52], [53].

The reduction in hydrogen bonding lowers the energy required for translational and rotational motions because there are fewer hydrogen bonds holding the water molecule in a structured orientation [41]. This effect increases the rate of self-diffusion in the water molecules in HTW as the number and strength of hydrogen bonds decreases. Hydrogen bonding still has a large effect on the properties of HTW despite this reduction in the number of hydrogen bonds per water molecule. In HTW the hydrogen bond network is often considered to exist as small hydrogen bonded clusters of water molecules, where every pair of molecules in the group is connected by at least one hydrogen bond. These hydrogen bonded clusters of water can act as a "solvent cage" which surrounds reactants and/or products during chemical reactions, therefore the formation of these has large implications on reactivity in the HTW [54]. Solvent cages are present in other organic solvents; however, this effect is more prevalent in HTW than organic solvents because of the increased persistence of hydrogen bonds meaning longer lived solvent cages. Notably, this solvent cage effect is nearly absent once supercritical conditions are reached. Diffusion can be hindered by the formation of "solvent cages" around molecules, preventing initiation and decomposition reactions because of reactant reformation reactions. The influence that this effect has on reactivity is lower when the reaction is not diffusion limited.

2.1.1.3. Dielectric Constant

Dielectric constant is the ratio between the permittivity of the solvent and permittivity of free space; hence it is also called relative permittivity [55]. The dielectric constant is a measure of the polarity of a molecule and is denoted as ε, the higher ε the more polar the solvent is. The dielectric constant of ambient water is relatively high at 78 ε compared to organic solvents which are typically between 2 to 40 ε, with notable exceptions such as formamide which has a dielectric constant of 109 [56]. The dielectric constant of water decreases linearly as temperature is increased under constant pressure up until the critical point after which the dielectric constant is stable at 1.5 (Figure 2.4) [46]. These dielectric constant measurements show that HTW has polarity comparable to many different polar organic solvents and can be easily adjusted using temperature. This lowered dielectric constant is a large contributor towards the increased solubility of small organic compounds in HTW, as well as their complete miscibility with supercritical water. However, inorganic salts show inverse solubility, as the dielectric constant is reduced their solubility is also reduced in HTW.

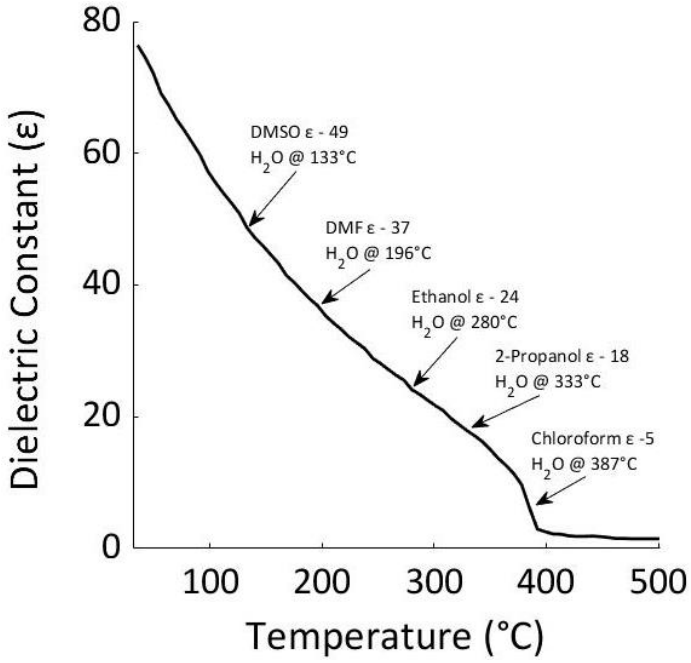

Figure 2.4 Dielectric (ε) constant of water at 250 bar as a function of temperature. Dielectric constants (ε) of the organic solvents dimethyl sulfoxide (DMSO), dimethylformamide (DMF), ethanol, 2-propanol, and chloroform measured at 25 °C and 1 bar [46], [56].

2.1.1.4. Ionic Product

Water has the potential to be used as a hydrogen source in chemical reactions because of its ability to dissociate into hydronium and hydroxide ions. This dissociation is described by the ionic product of water and is reported as K_w. The ionic product of ambient water is 1.00 ×

10^{-14} mol^2 dm^{-6} (Equation 2.1) [57]. The ionic product of water can be estimated using an equation proposed by Marshall *et al.* (Equation 2.2) [58].

$$2H_2O \rightarrow H_3O + OH^-$$

Equation 2.1 Dissociation of water into hydroxide and hydronium ions.

$$logK_W \rightarrow A + \frac{B}{T} + \frac{C}{T_2} + \frac{D}{T_3} + \left(E + \frac{F}{T} + \frac{G}{T_2}\right) \times log\rho$$

Equation 2.2 Estimation for the ionic product of water (T is temperature in Kelvin (K), ρ is density in g cm^{-3}, and Kw is in mol^2 dm^{-6}, the remaining letters are the fitting parameters).

As temperature in increased under constant pressure the ionic product of water increases by a factor of 2, at 180 °C $K_w = 3 \times 10^{-12}$ mol^2 dm^{-6} this stays relatively consistent until 320 °C, after which the ionic product of water rapidly decreases upon approaching the supercritical point of water (Figure 2.5) [41]. This increased ionic product under HTW conditions means that there are more hydroxonium and hydroxide ions present which can participate in and facilitate reactions. In principle this shows HTW has more Brønsted–Lowry acid/base character, enhancing the amphoteric nature of water. Thereby HTW is better than ambient water at facilitating acid/base catalysed reactions and can also catalyse hydrolysis reactions by reducing the activation energy of the reaction and stabilising the transition state by making it less energy strained.

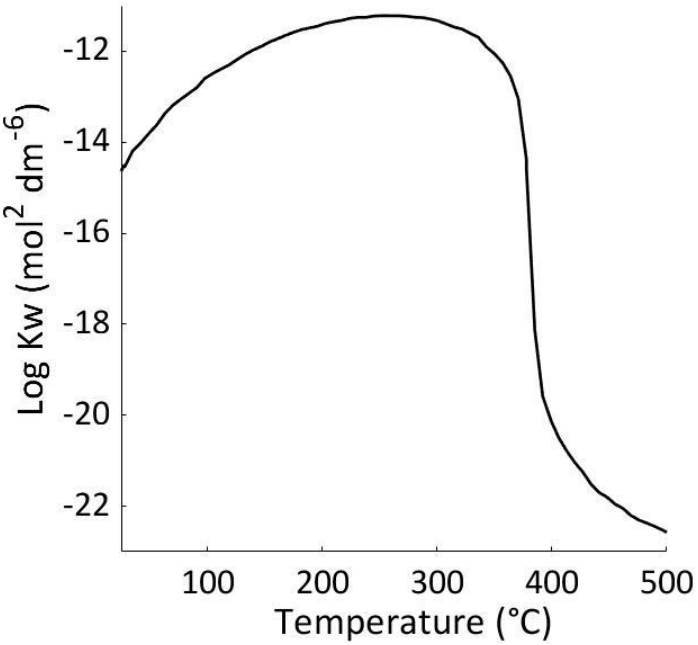

Figure 2.5 Ionic product (Kw) of water as a function of temperature under 250 bar [41].

2.1.1.5. Viscosity

Viscosity is an important transport property which influences the rate of diffusion controlled processes and reactions [41]. Viscosity is a measure of how resistant a liquid is to deformation, related to the concept of "thickness" in fluids. Ambient water has a viscosity of 0.89 mPa·s as temperature is increased under constant pressure its viscosity decreases until it becomes a supercritical fluid (Figure 2.6). Under HTW conditions (250 bar, 180-374 °C) the viscosity of the water is between 0.15 and 0.05 mPa·s. This is a low viscosity compared to other ambient organic solvents such as acetone (0.3 mPa·s), dimethyl ether (0.122 mPa·s), and ethanol (1.08 mPa·s).

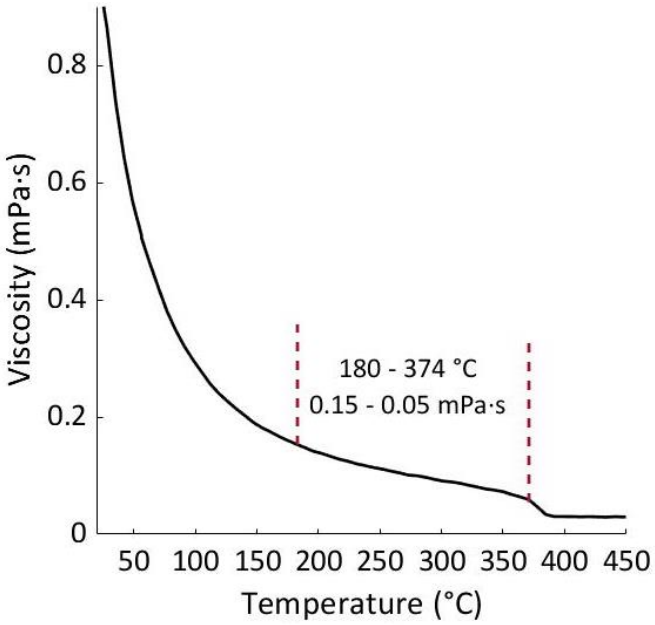

Figure 2.6 Viscosity (mPa·s) of water as a function of temperature under 250 bar [41].

2.1.2. Experimental Analysis and Characterisation of HTW

The intramolecular and intermolecular bonding dynamics of water under sub-critical conditions can be investigated with various analytical techniques, including Raman spectroscopy, X-ray diffraction, neutron diffraction, Fourier-transform infrared (FT-IR) spectroscopy, and NMR spectroscopy [59], [60].

2.1.2.1. X-ray and Neutron Scattering

X-ray and neutron scattering are complementary analysis techniques which have been used to analyse water under a large variety of conditions [60]. Both techniques measure the differential scanning cross section produced by incident X-rays or neutrons. In analysis of water these techniques can give intermolecular atomic correlation distances or radial distribution functions, denoted as $g_{OO(r)}$, $g_{OH(r)}$, and $g_{HH(r)}$ for the distance between the oxygen to oxygen, oxygen to hydrogen, and hydrogen to hydrogen atoms respectively (Figure 2.7). Additionally, the average coordination number for each of these interactions can be calculated (N_{OO}, N_{OH}, N_{HH}). This information can be used to further understand the intermolecular bonding present in water and how it changes under different conditions. There are limitations to each type of scattering: X-ray diffraction gives very little information from water because of the low electron density through a very small cross section, especially hydrogen because it only has one electron; neutron diffraction has large incoherent scattering and attenuation effects. Diffraction

measurements are preferably performed on H_2O/D_2O mixtures with less than 50% H_2O. This is done to reduce incoherent scattering and attenuation effects and yield clearer more accurate data. However, this presents issues because heavy water has different physical properties to that of ordinary water.

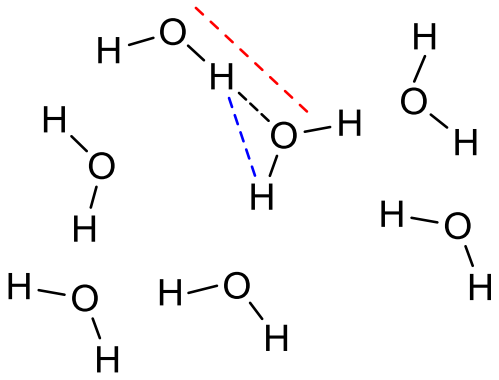

Figure 2.7 Hydrogen bonding clusters present in water, intermolecular interactions as follows; red dotted line (oxygen-oxygen), black dotted line (hydrogen-oxygen), and blue dotted line (hydrogen-hydrogen).

X-ray diffraction has been used to analyse sub-critical water to obtain the oxygen-oxygen distance between both hydrogen bonded water, neighbouring water molecules and non-hydrogen bonded water [59]. However, the hydrogen-oxygen and hydrogen-hydrogen distances are challenging to obtain with X-ray diffraction as stated. Therefore, neutron diffraction can be used to obtain this information in sub-critical water systems. It can be observed that the distance between neighbouring water molecules remains mostly unchanged with temperature and pressure (Figure 2.8).

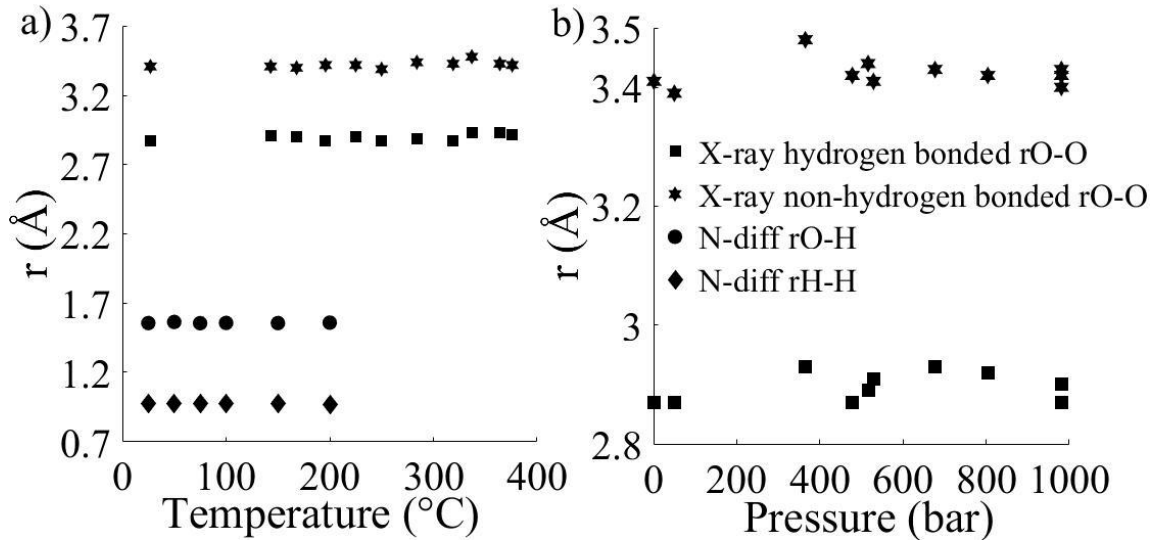

Figure 2.8 Atomic distances in angstroms (Å) between water molecules (displayed in Figure 2.7) as a function of (a) temperature and (b) pressure [59], [61].

The coordination number for the oxygen-oxygen interactions for both hydrogen bonded, and non-hydrogen bonded water molecules does change with varying temperature (Figure 2.9) [59]. As the temperature of sub-critical water is increased the number of hydrogen bonded water molecules with oxygen-oxygen coordination interactions decreases linearly (Figure 2.9, a, squares). Initially averaging 3.1 oxygen-oxygen interactions from hydrogen bonded water molecules and reducing to 1.6 at the supercritical point. Therefore, X-ray diffraction data provides additional evidence of the reducing number of average hydrogen bonds present in sub-critical water. This is further supported by the increasing coordination number of non-hydrogen bonded oxygen-oxygen interactions measured with temperature. No such relationship can be given for increasing pressure in the sub-critical water system.

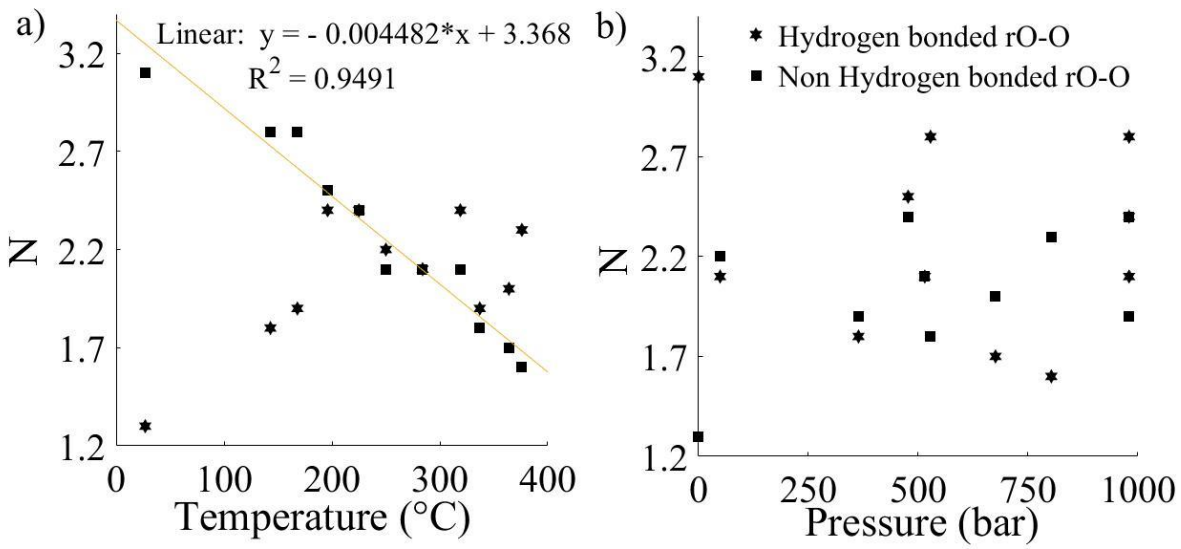

Figure 2.9 Coordination number (N) for the amount of oxygen-oxygen interactions in water plotted against (a) temperature and (b) pressure [59], [61].

2.1.2.2. Raman and FT-IR Spectroscopy

Raman and FT-IR spectroscopies are two of the most important analytical techniques for obtaining information about the intra and inter molecular vibrational modes of water molecules under HTW conditions [62]. These techniques are complementary and analyse the absorbance of different wavelengths of light which correspond to vibrational absorbances from intermolecular and intramolecular bonds. There are three foremost modes of molecular vibration in water which are most frequently investigated; O-H bending, O-H symmetric stretching, and O-H asymmetric stretching; in gaseous water these are well defined at 1595 cm^{-1}, 3657 cm^{-1}, and 3756 cm^{-1} respectively (Figure 2.10) [63]. However, also present in water are liberational and translational vibration modes within the fingerprint region. In total 7 intramolecular vibrations, and 9 intermolecular vibrations can be observed [64]. These additional absorbances arise due to variations in bond lengths and angles occurring in both intermolecular and intramolecular bonding structures. In liquid water the wavelengths of absorption are broadened and redshifted down which makes peak assignment more problematic. Gaussian deconvolution can be performed on these broadened peaks to extract each vibrational absorbance band.

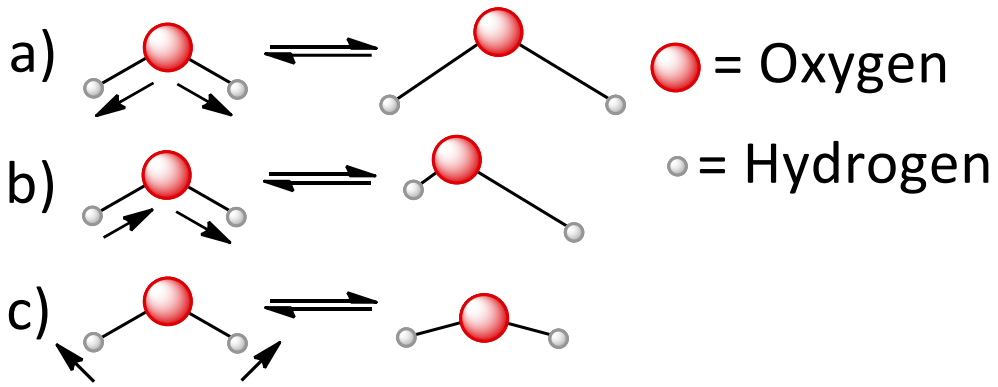

Figure 2.10 Characteristic absorbance modes of water in Raman and FT-IR spectroscopy, (a) symmetric O-H stretching, (b) asymmetric O-H stretching, (c) O-H bending (c).

Raman spectroscopy investigations have shown that as temperature is increased at constant pressure the O-H stretching band intensity decreases and the peak maximum wavelength increases until the supercritical point is reached [65]. Once the supercritical point is reached the O-H stretching band is sharp (3580 cm^{-1}) and less intense than ambient water. This change is attributed to a reduction in the number and strength of hydrogen bonds in the water. Furthermore, the O-H stretching region can be deconvolved into five contributing absorbance vibrations based on the hydrogen bonding present in the water (Figure 2.11) [66].

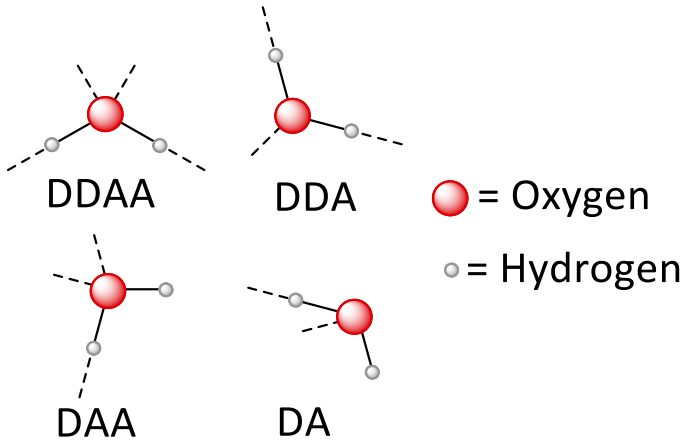

Figure 2.11 Different hydrogen bond environments of individual water molecules present in liquid water [36].

These are referred to by the number of lone pairs of electrons they are donating and accepting as hydrogen bonds, for example fully hydrogen bonded water has four hydrogen bonds and a tetrahedral structure this is referred to as double donor – double acceptor (DDAA) [35]. These bonding configurations identified in the Raman spectra are ν_{DAA-OH}, $\nu_{DDAA-OH}$, ν_{DA-OH}, ν_{DDA-OH} as well as the free non-hydrogen bonded O-H stretching. Further, the deconvoluted bands are

attributed to peaks at 3041, 3220, 3430, 3572, and 3636 cm^{-1} respectively. The elimination of these bands at supercritical conditions shows a change in the water structure from three-dimensional to string-like hydrogen bonding based on the Raman spectra of water under supercritical conditions. However, under HTW conditions at 200 °C and 15 bar there is still a broad O-H peak present, reduced in intensity at the lower wavelengths even at 300 °C and 15 bar there is still presence of hydrogen bonded O-H stretching peaks. This provides further evidence that although the number and strength of hydrogen bonds is reduced under HTW conditions they are still present in spread out three-dimensional clusters.

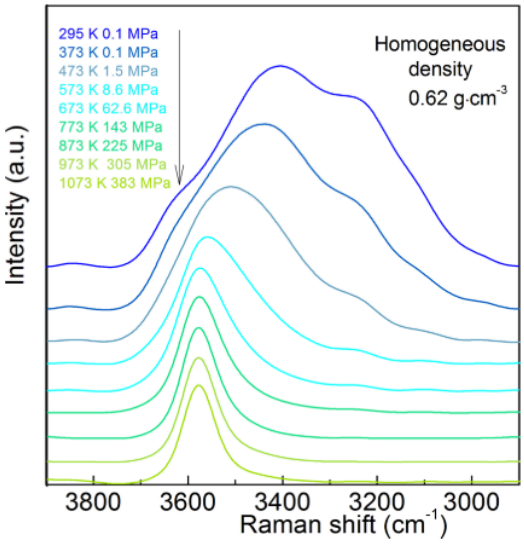

Figure 2.12 Raman O-H stretching bands of water up to 1073 K and 383 MPa presented by Sun *et al.* [65].

A comprehensive FT-IR spectroscopy study analysed changes in the structure of water from 25 to 380 °C and 1 to 250 bar [67]. This study showed a similar relationship to Raman spectra, whereby as the temperature was increased from 25 °C up to 340 °C under constant pressure of 250 bar the broad O-H stretching band reduced in intensity and the peak maximum position was shifted to a higher wavenumber. From 160 °C to 340 °C the intensity decreased by over one third and the peak maximum shifted by over 200 cm^{-1} higher. Additionally, the broad O-H peak began to split into a more obvious doublet at 340 °C representing symmetric and asymmetric stretching more clearly as is shown in gaseous water FT-IR spectra. Since a portion of the signal from the O-H adsorption comes from intermolecular hydrogen bonding the reduction and change in shape of this broad O-H peak shows a change in the extended hydrogen bond network of the water molecules as temperature is increased. Therefore, temperature can be used to control the number of tetrahedral, trimer, dimer, and singular water molecules present in the system.

2.1.2.3. Nuclear Magnetic Resonance (NMR) Spectroscopy

^{1}H nuclear magnetic resonance (NMR) spectroscopy has been used to study the self-diffusion coefficients of water as well as hydrogen bonding dynamics under raised pressure and temperature [62]. Proton NMR measures the magnetic relaxation time of hydrogen atoms which varies based on their local environment and bonding, yielding different chemical shift (δ ppm) values. The abundance of the hydrogen atom environments relative to one another is also gained by intensity of the peaks. Generally, the chemical shift values increase as the proton is less shielded by local electron withdrawing groups. For example, carboxylic acids occupy the highest chemical shifts from 10-12 δ ppm and alkanes occupy the lowest chemical shifts from 0-2 δ ppm.

The chemical shift of protons is known to be susceptible to hydrogen bonding [68]. At room temperature there is one chemical shift for proton NMR of water at 4.2 δ ppm, this decreases linearly until 300 °C down to 2 δ ppm. After which the rate of decrease changes based on the volume of water (density) within the analysis chamber to be somewhere between 1.6-1.1 δ ppm at the supercritical point. Small peaks for gaseous water molecules can also be seen in the proton NMR spectra between 200 and 370 °C. The chemical shifts for water in nonpolar organic solvents is less than 1.1 δ ppm, in this analysis mixture only small clusters of water hydrogen bonded together can exist in the system. Therefore, the hydrogen bonding in supercritical water can be equated to that of a small amount of water in a non-polar organic solvent. However, the hydrogen bonding in HTW is somewhere in between the two and can be controlled by temperature. Researchers have also used pulsed-field-gradient spin echo measurements to calculate the self-diffusion coefficients of water under elevated temperature and pressure [69]. This method was able to calculate the diffusion coefficient of HTW at all temperatures and pressures with high accuracy when compared to literature data. This proved that the self-diffusion coefficient increases with increasing temperature and reducing density of HTW.

2.1.3. HTW Reactivity and Products

Unlike most organic solvents HTW can participate in reactions as a reactant/product, catalyst, and an acid/base. Under HTW conditions water molecules have been observed as reactants and products in hydrolysis, hydration, hydrogen exchange, and free-radical oxidation reactions [41]. The strict definition of hydrolysis is a bond cleavage reaction involving water, it is often

enhanced by acids or bases. The primary application of hydrolysis reactions in HTW is the processing of biomass (organic waste), this is discussed in detail in Section 2.3. In short, this is widely studied as a method to produce renewable chemicals and fuels from waste materials. There are however many investigations into the hydrolysis of model organic compounds ethers, esters, amides, amines, alkyl halides, and nitroalkanes [70]–[77]. The expected reaction products from these investigations are highlighted in Figure 2.13. The main advantage that HTW offers for hydrolysis reactions is that no additional catalysts, acids, or bases are required to perform them, therefore hydrolysis reactions using HTW are greener than currently used hydrolysis reactions

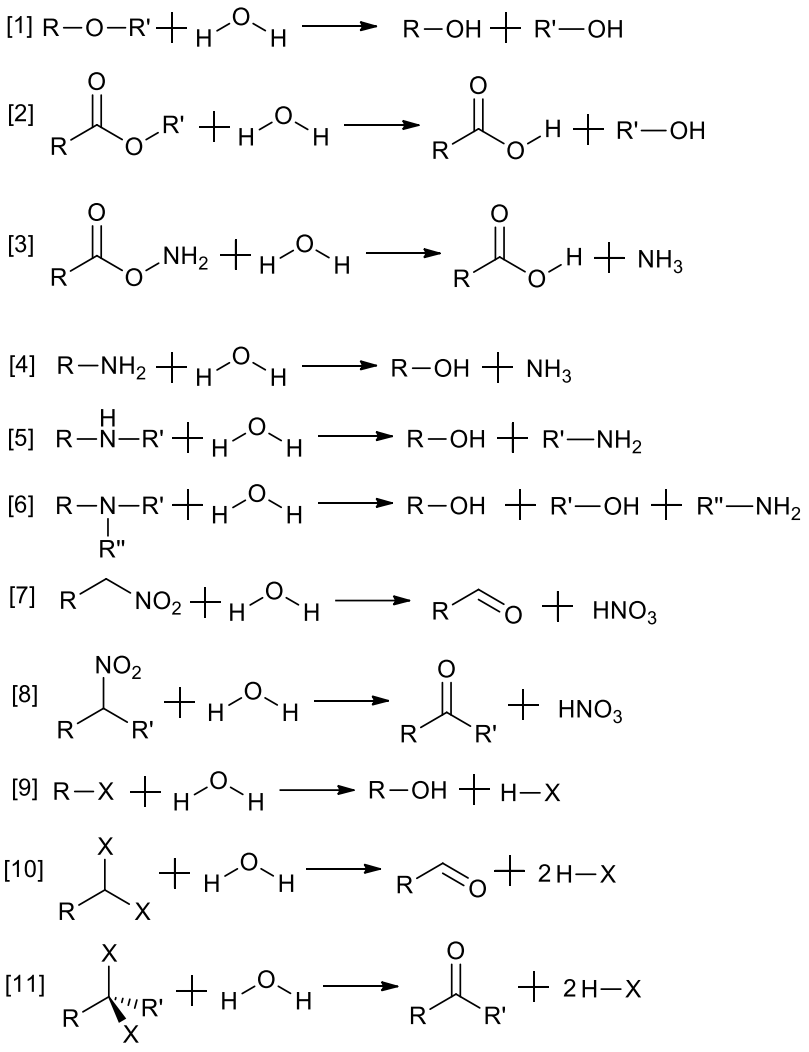

Figure 2.13 Hydrolysis conversion reactions for different types of compound in HTW (1 - ethers, 2 - esters, 3 - amides, 4 - primary amines, 5 - secondary amines, 6 - tertiary amines, 7 - primary nitroalkanes, 8 - secondary nitroalkanes, 9 - alkyl halides, 10 - primary dihalides, 11 - secondary dihalides) [70]–[77].

In these HTW reactions the water is disproportionately higher in equivalents, because of this it is difficult to stop reactions at a desired product. Additionally, some reactions are enhanced

through autocatalysis, *e.g.* this is true for nitroalkanes producing nitric acid which then further propagates the hydrolysis reactions [41]. This autocatalysis also occurs for esters, aldehydes, amines, and halides [70]–[77]. The hydrolysis of these functional groups is effective in HTW because of the electron withdrawing substituents which promote the attack of the neighbouring carbon by water molecules.

2.1.4. Influence of Binary Alcohol/Water Mixtures in HTW

Binary mixtures of alcohol and water are used as solvents in a variety of different biological and chemical processes [78]. These include but are not limited to; separation and purification of biopharmaceuticals, organic synthesis in heterogeneous catalysis, and chemical energy storage in fuel cells [79], [80]. Using alcohol/water mixtures as solvents offers the same advantage that HTW does, the properties of the solvent mixture can be easily tuned to fit the requirements of the process [81]. This is done by varying the alcohol/water ratio and the structure of the alcohol used. The physicochemical properties of alcohol/water mixtures are unique and exhibit many anomalies at different compositions [82].

2.1.4.1. Unique Properties of Alcohol/Water Mixtures

The importance of alcohol/water mixtures on many industrial processes and therefore their properties have been widely investigated over the past eight decades. Many thermodynamic properties have been shown to deviate from the ideal solution, such as; diffusion coefficient, viscosity, thermal conductivity, compressibility, excess enthalpy of mixing *etc.* [83]–[85]. When analysing data for these properties in alcohol/water mixtures it is beneficial to look at the mixtures in terms of the molar percentage or molar fraction of the alcohol in water, thus this is the standard in the literature [83], [86]. The excess enthalpy of mixing in alcohol/water mixtures follows a non-ideal relationship (Figure 2.14). Non-ideal mixtures are any that have positive (endothermic) or negative (exothermic) excess enthalpies of mixing [87]. If a mixture has a negative enthalpy of mixing this means that there are more positive interactions between the solvents in the mixture and thus the energy required to mix them is reduced and their mixing is exothermic, the opposite is true for a positive deviation. Each alcohol/water mixture has a peak maximum at a certain molar alcohol percentage for the negative excess enthalpy of mixing (Figure 2.14). Peak negative maximums occur around 35, 15, and 11 mol% for methanol, ethanol, and isopropanol respectively [87].

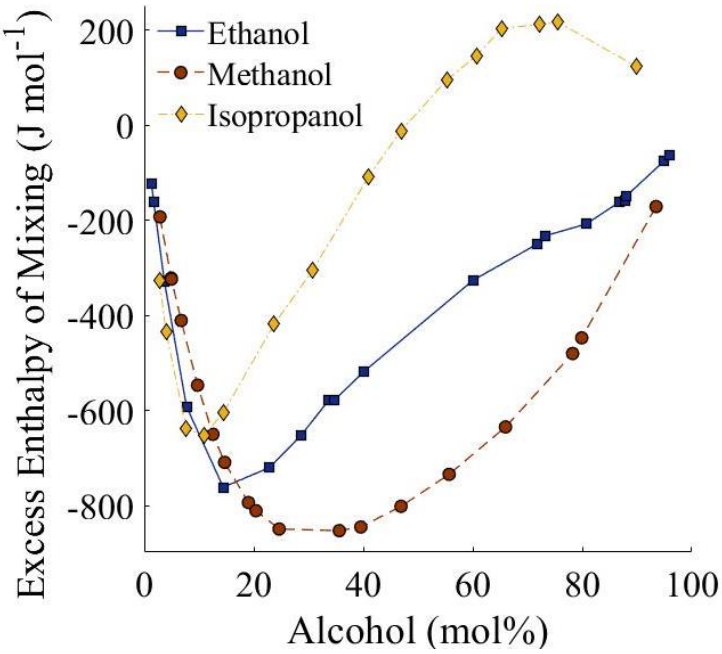

Figure 2.14 Excess enthalpy of mixing across different molar percentages of aqueous ethanol (EtOH), methanol (MeOH) , and isopropanol (IPA) at 25 °C [87].

The dielectric constant of alcohol/water mixtures shows a monotonic relationship which is indicative of an ideal mixture (Figure 2.15, a) [88]. However, as the chain length of the alcohol increases the non-linear relationship between the molar percentage of alcohol and the dielectric constant can be clearly observed. The dielectric constant measured is consistently lower than would be expected in alcohol/water mixtures. Another important property, viscosity, also shows a non-ideal behaviour (Figure 2.15, b). In this case a peak maximum can be observed for all alcohol/water mixtures examined. This peak maximum occurs between 31-38, 27-32, and 23-31 mol% alcohol for 1-propanol, ethanol, and methanol respectively. This increased viscosity can be attributed to the increased intermolecular interactions between the alcohol and water which contribute to the unique molecular structure, this is discussed in Section 2.1.4.2.

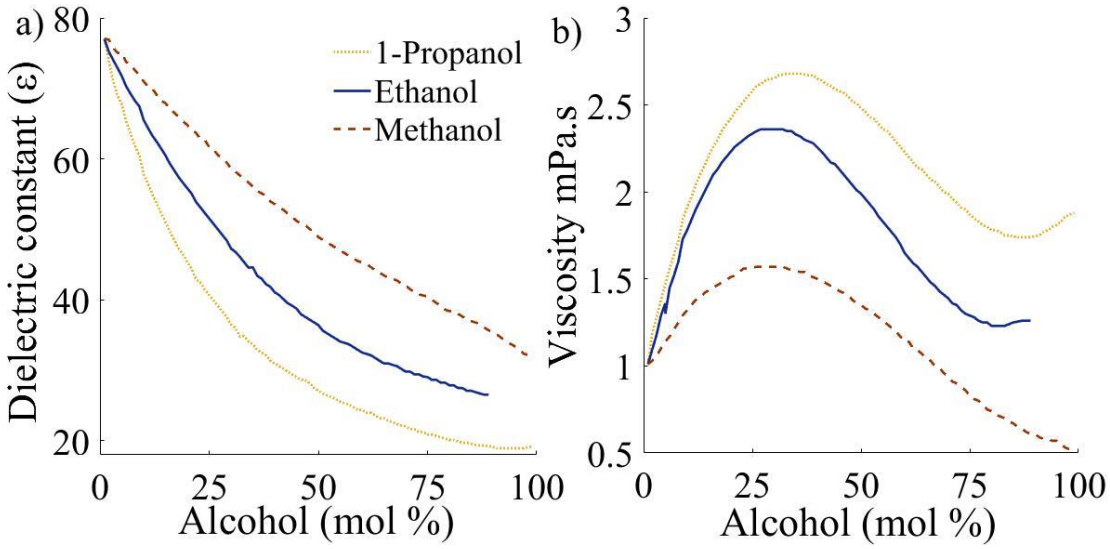

Figure 2.15 (a) dielectric constant (ε) and (b) viscosity (mPa·s) across different molar percentages of aqueous ethanol, methanol, and 1-propanol at 25 °C [88].

2.1.4.2. Proposed Theories for the Molecular Structure of Alcohol/Water Mixtures

The molecular structure and intermolecular bonding in alcohol/water mixtures is a highly contested area, the complete details of which are not yet fully understood. There are two main theories proposed in literature for the molecular structure present in alcohol/water mixtures to explain their anomalous thermodynamic properties (Figure 2.16) [89]. One is that the alcohol/water mixtures exhibit their non-ideal behaviour because of incomplete mixing whereby the water within alcohol/water mixtures has identical structure to its pure form [90], [91]. The alternative is that water in alcohol/water mixtures exhibits an enhanced or destroyed structure and forms various clathrate-like structures because of the presence of hydrophobic ends of the alcohols [92]–[95]. Therefore, the arguments and evidence for both theories needs to be understood to gain a full understanding of this complex system.

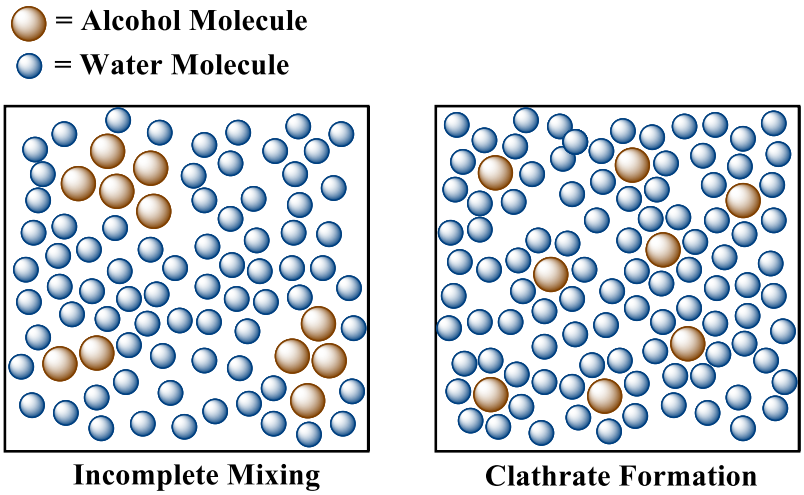

Figure 2.16 Two-dimensional (2D) diagram representation of the two dominant theories for non-ideal behaviour of alcohol/water mixtures in a low alcohol concentration mixture.

The theory of inhomogeneous mixing of alcohol and water is supported by neutron diffraction measurements performed on methanol/water mixtures by Dixit *et al.* [90]. They calculated the number of hydrogen bonds present in pure methanol and water in addition to methanol and water in ratios of 7:3 and 3:7. They found that for pure methanol and water there were 1.8 and 3.6 hydrogen bonds per molecule respectively; this would predict 2.3 hydrogen bonds per molecule in a 7:3 mixture of methanol/water if mixed. The analysis of said mixture contained on average 2.3 hydrogen bonds, this means that the hydrogen bonds from methanol/water mixing exactly compensates for lost bonds of the pure liquid. Furthermore, cluster analysis of water molecules in this 7:3 methanol/water mixture showed that 87% of the water molecules occurred in clusters of strings. This indicates that incomplete mixing is present in the system with no evidence of clathrates and supports the existence of alcohol-rich and water-rich clusters within any alcohol/water mixture. Another study analysed alcohol/water mixtures using mass spectrometry to observe cluster structures [96]. Between 10-20 vol.% ethanol in water it was found that the hydrogen bond network was identical to that of pure water with ethanol clusters contained therein. Further evidencing the theory that the anomalous properties of alcohol/water mixtures come from incomplete mixing and the formation of separate clusters within the solution.

Researchers have also used different analytical techniques as evidence to support the theory for clathrate-like structures in binary alcohol/water mixtures. Li *et al.* used terahertz time-domain spectroscopy and pulsed field gradient nuclear magnetic resonance spectroscopy on water mixtures with methanol, ethanol, 1-propanol, and isopropanol [92]. They found that

extended hydrogen bond networks which exhibit an enhanced hydrogen bonded network and structure can be observed at two specific molar compositions. These were presented as self-organised aggregates of either alcohol in water or water in alcohol, for ethanol these occurred at 15 and 60 mol%. Investigation of low molar percentage ethanol in water (3 mol%) using FT-IR spectroscopy, mass spectrometry, and X-ray diffraction confirmed a hydrophobic core surrounded by a hydrogen bonded clathrate like structure [97]. FT-IR spectroscopic analysis of these ≤3 mol% alcohol/water mixtures showed a reduction in the "free" water molecules from reduced intensity of the broad O-H stretching band at 3600 cm^{-1} presenting a more structured "icy hydrogen bond" structure.

2.1.4.3. Changes in Alcohol/Water Mixtures Properties Under Hydrothermal Conditions

Whilst it is important to understand the molecular structure of alcohol/water mixtures much of the research has been performed at ambient conditions, in which little if no processes are performed. Therefore, investigations into the properties and molecular structure of alcohol/water mixtures at raised temperature and pressure is imperative to justify and indicate their use in chemical and biological processes [98]. This is the basis of investigation for Chapter 4. With further motivation for this research based on literature discussed in Section 2.3.5. Additionally, thermochemical and physical properties of alcohol/water mixtures at raised temperatures and pressures are not well presented in the literature. Some examination of the change in density of ethanol/water mixtures is presented (Figure 2.17).

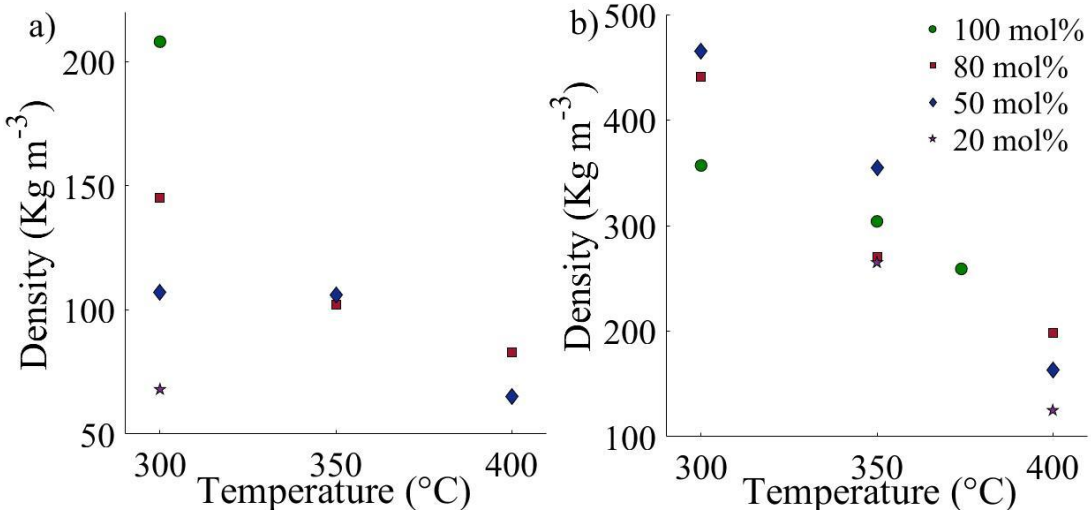

Figure 2.17 Change in density (Kg m^{-3}) of different molar percentages of EtOH in water at (a) 100 bar and (b) 200 bar [98]–[100].

At the lower pressure (Figure 2.17, a) the addition of more water lowers the density at 300 °C whilst at the higher pressure (Figure 2.17, b) the opposite correlation is shown. At the higher

pressure (Figure 2.17, b) this higher density in lower mol% ethanol at 300 °C decreases significantly when raised to 350 °C where the density is now lower than the pure ethanol. This alludes to the unique properties which are brought out in alcohol/water mixtures when subjected to raised temperatures and pressures.

2.2. Sustainability from a Biomass-Based Economy

Biomass is the general name for all organic matter from both plants and animals, it is often a term used when discussing energy generation [101]. Principally biomass can be considered a solar storage material which exploits biological pathways to store energy. Before the discovery of fossil fuels our society met its energy requirements using plant biomass and made a substantial number of products from sustainable biomass resources [102]. In the 19th century more than 90% of the energy used in the U.S. came from plant biomass [103]. Biomass has no net carbon dioxide emissions because it is part of the carbon cycle, no new carbon is being put into the atmosphere, additionally the use of biomass reduces harmful nitrogen oxide and sulphur oxide gas emissions [104]. A turning point was the mining of coal for use in steam engines instead of charcoal because the fossil fuel coal was cheaper and had a higher energy density which made transportation more efficient. Then, early 20th century research and development was heavily focussed on exploiting fossil fuel resources [105]. This research meant that fossil fuels were utilised to produce a huge number of products such as fuels, plastics, detergents, fertilizers, lubricants, activated carbon, pharmaceuticals, waxes, *etc.* Consequently, fossil fuel-based resources vastly increased the quality of human life worldwide during the industrial revolution [106].

Global population is estimated to increase to 8 billion by 2024-2030 and more countries are becoming industrialised thus the demand for fossil fuels such as crude oil, coal, and natural gas are increasing whilst resources are dwindling [105]. In 2008, 11705.1 million tonnes of oil equivalent energy was consumed globally, this increased to 13864.9 million tonnes by 2018 [107]. At the end of 2018 global reserves of oil were down to 244,100 million tonnes, this means if the energy demands were met by only oil reserves, the planet would run out of crude oil in just 18 years. Additionally, the widespread use of fossil fuels has contributed towards global warming and caused irreparable damage to the planet. In short, fossil fuels are a limited resource, the use of which risks the end of humanity on Earth. Therefore, alternative sustainable replacements for fossil fuels need to be implemented. Many other sustainable energy sources

are intermittent and weather dependent (solar, wind, *etc.*) [108]. Bioenergy can be used to supplement these energy sources, because bioenergy is a consistent and reliable source of renewable energy [109]. Additionally, biomass can be used to produce biochemicals to ensure the sustainable production of many products which currently rely on fossil fuels [103]. There is currently no other feasible source for the required chemicals to produce many such products. Therefore, companies such as Shell, and UOP are preparing to work just as their 19th century ancestors did, utilising biomass resources to replace existing fossil fuel processes by producing sustainable biofuels and biochemicals [103].

2.2.1. Categorisation, Structure and Composition of Biomass

All biomass is derived initially from the photosynthesis reaction performed by plants to produce carbohydrates from carbon dioxide, oxygen, water, and sunlight. Consequently 75% of the 170 billion metric tons of biomass produced by nature each year are carbohydrate based [101], [110]. Biomass can be broken down into the three main categories: wastes; standing forests; and energy crops [111]. The biochemicals and biofuels produced from these biomasses are categorised into primary, and secondary first (1st), second (2nd), third (3rd) and fourth (4th) generation based on the category of biomass used as well as how/if they are processed [112]. These categories are essential to understand if a biomass and biofuel/biochemical is an effective replacement to fossil fuels based on how sustainable, consistent, and reliable they are [112].

2.2.1.1. Primary Biofuels

Primary biofuels are the longest and oldest fuels used by society. The term is applied whenever natural unprocessed biomass is directly combusted; these are typically forestry or energy crops [112]. Secondary biofuels and biochemicals are produced from processing biomass into either solids (charcoal), liquids (biodiesel), or gases (syn-gas) [113]. These secondary biofuels and biochemicals are the reason biomass has potential to replace fossil fuels in industrial processes. Secondary biofuels and biochemicals are further separated into first, second, and third generation biofuels and biochemicals.

2.2.1.2. First Generation Biofuels

First generation biofuels and biochemicals are synthesised directly from sugars and oils which are extracted or refined from energy crops [105]. Sugars are short chain soluble carbohydrates, glucose (d-glucopyranose) is the most widely used sugar in this process because of its

simplicity and naturally high abundance [112]. Sugar cane and corn grain is widely utilised to produce a renewable source of bioethanol [114]. In the United States alone over 4 billion gallons of bioethanol is produced annually from these crops. Vegetable oils are mostly triglycerides which are made up from a hydrophilic glycerol "head" and a lipophilic hydrocarbon "tail" joined by an ester bond (Figure 2.18). These triglycerides are used to produce alkyl esters *via* acid correction and then transesterification reactions under catalysts such as KOH [115]. The alkyl esters produced are commonly referred to as biodiesel, recent interest around soybeans to produce high yields of biodiesel has been developing in this area.

However, because first generation biofuels are mainly produced from energy crops which are high in sugar and oil content this creates unwanted competition for the small amount of arable farmland available. This has obvious moral questions with an estimated 10.8% of the global population considered undernourished (have a caloric intake below minimum energy requirements) in 2018 [116]. Despite this over 50 billion litres are still produced annually because the production of first generation biofuels is both effective and renewable.

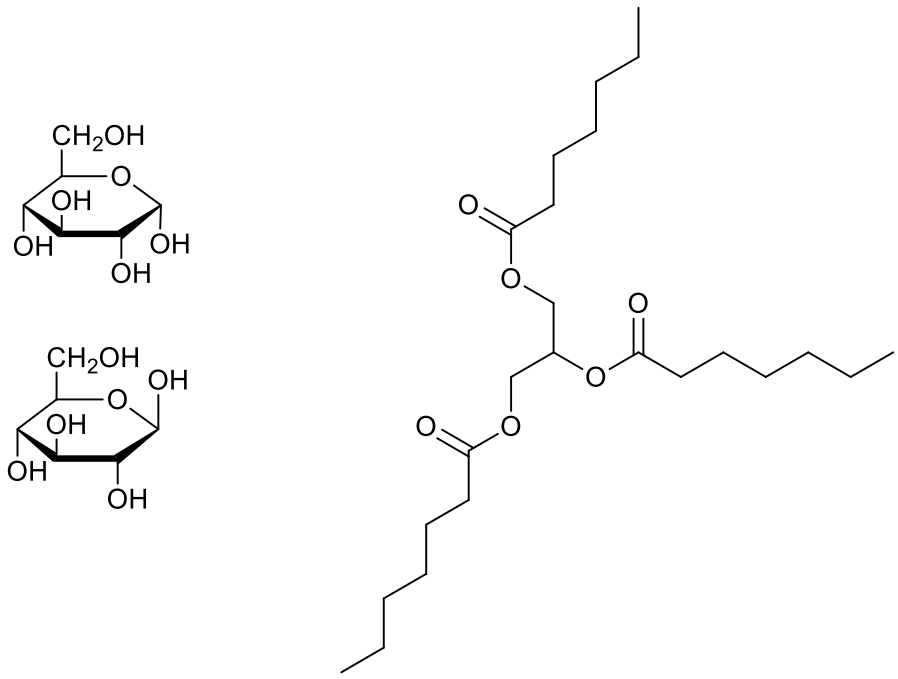

Figure 2.18 α-d-glucopyranose and β-d-glucopyranose displayed as a Haworth projection as well as an example triglyceride with caprylic acid fatty chains.

2.2.1.3. Second Generation Biofuels

Second generation biofuels are produced from forest or waste biomass which is lignocellulosic in nature (agricultural wastes, crop residues, urban organic wastes, woody biomasses) [111],

[112]. This has the significant advantage of utilising unwanted by-products which would otherwise be sent to landfill or incinerated. Lignocellulose is a mixture of cellulose, hemicellulose, lignin and various other extractives [117]. Cellulose is the most abundant natural polysaccharide with the general formula $(C_6H_{10}O_5)_n$. It typically has around 10,000 monomeric d-glucopyranose (glucose) units joined by glycosidic bonds [117]. Hemicellulose is a short chain polysaccharide comprised of 100-200 monomeric units from a multitude of different monosaccharides (sugars) which are joined by glycosidic bonds [117]. Lignin is a natural polymer where phenolic and aromatic compounds are joined by ether bonds between the hydroxyl and methoxy groups (Figure 2.19). The various extractives which are also present in lignocellulose feedstocks encompass a wide range of organic and inorganic compounds in much lower concentrations; proteins, lipids, polyphenolics, resins, trace metals, and ionic salts.

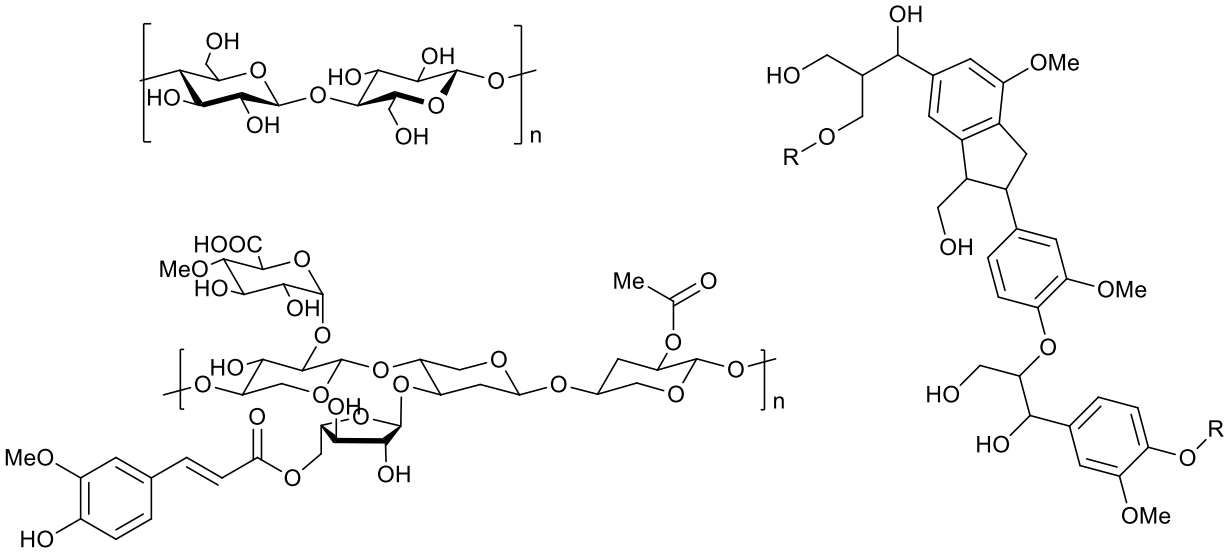

Figure 2.19 Chemical structure of cellulose, xylan a natural hemicellulose, and a small branch chain of lignin.

There is potential to produce bioethanol from the cellulose, this is commonly referred to as cellulosic ethanol [118]. However, the cost of converting lignocellulosic material into bioethanol is more costly than from pure cellulose despite the lower price of lignocellulose. Hence, innovation is needed to increase the efficiency of converting the lignocellulose to fermentable carbohydrates. For this reason, research into the conversion of lignocellulose has accelerated in recent years by examining the potential thermochemical and biochemical pre-treatment technologies.

2.2.1.4. Third Generation Biofuels

Third generation biofuels use biomasses that require no arable terrestrial land to produce, such

as aquatic plants [113]. Aquatic plants generally have very low lignin and cellulose content because they need to be more flexible under ocean currents [119]. On average all seaweeds contain 50% carbohydrates on a dry weight basis, however these carbohydrates are mostly not digestible by mammalian enzymes. This means that although aquatic plants have low calorific value as a food source there is potential to unlock a large amount of energy through biochemical and thermochemical processing [112]. However, the second most abundant component in seaweeds is minerals (~30%). The high content of these in biofuels and biochemicals leads to issues such as ashing and fouling. The remaining content of seaweeds and other aquatic plants is made up of proteins and lipids, both of which can be used to produce biofuels and biochemicals.

2.2.1.5. Fourth Generation Biofuels

Finally, fourth generation biofuels are produced solely from genetically modified microalgae [120]. Functionally these microorganisms perform the same as more traditional crops, converting carbon dioxide into stored energy *via* photosynthesis. However, they are genetically modified to increase growth rate and grow in nutrient poor conditions. Fourth generation biofuels are still in the early stages of development and most of the literature around them is focussed on the effects of different genetic adjustments [121]. The aim of these alterations is to produce the lowest environmental impact biofuels.

2.2.2. Biochemical Conversion of Biomass

Biological conversion processes are performed using microbic digestion and/or fermentation [111]. Biochemical technologies are commonly used on high moisture herbaceous plants, aquatic plants, and manures because it does not require costly pre-drying steps.

2.2.2.1. Fermentation

Ethanol production from sugars using yeast is known as alcoholic fermentation [111]. Farmers have cultivated crops for the production of alcoholic beverages for over 7000 years [122]. Before commercial fermentation for fuel production sugars must be extracted from sugar crops by crushing and mixing with water, yeast is added to this slurry in a temperature controlled tank called a fermenter. Starchy biomasses can be used in alcoholic fermentation; however, additional processing is required to obtain glucose. Lignocellulosic biomass can be pre-treated to extract and convert cellulose to glucose for fermentation [123]. Once the sugars have been

converted into alcohol, distillation is typically used to remove the water and other impurities. This extraction and processing of the biomass leaves a large amount of residue as a waste by-product.

2.2.2.2. Anaerobic Digestion

Anaerobic digestion is the biochemical conversion of complex organic matter in absence of oxygen into biogas using anaerobic bacteria [123]. This is fundamentally a different type of fermentation process because it is using anaerobic microorganisms to chemically breakdown the biomass [111]. Biogas is a combustible gas which mainly consists of methane and carbon dioxide with some amount of other gases and trace elements [124]. In many counties biogas is used for combined heat and power generation, it can also be used as vehicle fuel or in fuel cells. The yield of methane is affected by several factors such as; feedstock, bacteria species, growth stage, and bedding material. Anaerobic digestion is a suitable technology to treat both solid waste and wastewater. The process is performed inside a sealed vessel, referred to as a digester. Digesters can be built for household use which are as small as 1 m^3 whilst commercial units can be as large as 2000 m^3. Anaerobic digestion has the advantage of limiting the carbon dioxide released to the environment and there is a substantial amount of viable feedstock material which can be processed. However, the recalcitrant nature of these feedstocks often make them challenging to digest *via* microbial hydrolysis.

The most common feedstocks used in European Biogas production are animal manures/slurries and agricultural residues [124]. However, the scope of potential feedstocks is increasing through the use of pre-treatment technologies on hard to digest materials [125]. The pre-treatment methods currently being investigated are; organosolv, ionic liquid, alkaline, hydrogen peroxide, biological, comminution, steam explosion, and acid. Each of these pre-treatment techniques has different advantages and disadvantages. For example, ionic liquid pre-treatment offers high potential recyclability which could be beneficial for large scale industrial operations. Therefore, it is essential to choose the ideal pre-treatment technology based on the feedstock, desired product, and digestor setup.

2.2.3. Thermochemical Conversion of Biomass

Thermochemical conversion processes encompass the use of heat, catalysts, and chemicals to convert biomass into more energy dense, homogeneous fuels and useful substances [126]. The

thermochemical conversion technologies examined herein are; combustion, gasification, pyrolysis, hydrothermal processing, and transesterification.

2.2.3.1. Direct Combustion

Direct combustion of biomass, whilst workable, is far from ideal. This process burns the biomass in air at temperatures of around 800-1000 °C to produce heat energy [111], [123]. Low moisture content biomass (<50%) is required for combustion to be feasible. The conversion efficiency of combustion is very low from 20 to 40 percent. The higher efficiencies are achieved when biomass is co-fired with coal in large-scale power plants. However, direct combustion of compressed wood pellets without co-firing is presented as a sustainable source of renewable energy and it is utilised by the Drax Group PLC in power stations in the UK. Compressed wood pellets are produced by a series of drying, milling, pelletizing, cooling, and separating stages [127]. Therefore specialised and expensive processing equipment is required to produce compressed wood pellets efficiently.

2.2.3.2. Charcoal Production

The oldest thermochemical conversion method is carbonisation which is the production of charcoal from wood [128]. The conversion efficiency of this technique is poor, taking approximately 6-12 equivalents of wood to produce 1 equivalent of charcoal on a per weight basis. There are three methods for carbonisation: 1) internal heating also known as controlled combustion; 2) external heating; 3) hot recirculating gas. Internally heated carbonisation is the most widely used production method, despite the losses of carbon dioxide and carbon monoxide to the atmosphere. Externally heated reactors allow the use of a closed system which eliminates these loses and gives the highest yields of charcoal.

2.2.3.3. Biodiesel Production

Biodiesel can be produced from vegetable oils by a combination of transesterification, pyrolysis, and emulsification often with the assistance of catalysts [129]. Therefore, in order to produce biodiesel from vegetable oils they need to be extracted and separated from a fatty biomass. Transesterification is the substitution of an ester from an alcohol group, in practice this is the combination of triglycerides and long chain fatty acids [130]. Thus, biodiesel is made up of monoalkyl esters of long chain fatty acids, is non-toxic, and has a low emission profile compared to fossil fuels. However, there have been a variety of different issues when using biodiesel directly in diesel combustion engines, including; heavy coking which blocks fuel

atomization, gelling of engine lubricants, and oil ring sticking allowing unburned gases into lower parts of the engine.

2.2.3.4. Pyrolysis

Pyrolysis is a thermochemical process in which lignocellulosic biomass is heated in the absence of air/oxygen [128]. This method produces solid (charcoal), liquid (tar and more liquid organics), and gas (H_2, CO_2, CO) products [131]. The basic process for this is as follows: 1) biomass is heated under an inert atmosphere, this causes pyrolysis reactions, the release of volatiles and formation of solid char; 2) the volatiles released increase the heat transfer to unpyrolysed biomass whilst some volatiles condense to form tar; 3) autocatalytic secondary pyrolysis reactions continue until the reaction is quenched. Whilst pyrolysis can be used as an independent process to produce these biofuels it is also the initial step in many commercial gasification and combustion processes. Pyrolysis is further subdivided into conventional, fast, and flash pyrolysis based on the processing conditions used [131]. Conventional pyrolysis is performed under slow heating and yields solid, liquid, and gaseous products in equal proportions and large volumes. Whereas fast pyrolysis is performed at higher temperatures with a higher heating rate and yields mainly liquid products (up to 80% yield) [123]. Finally, flash pyrolysis produces mostly gaseous products (up to 80% yield) by utilising a rapid heating rate, high maximum temperature, and small biomass particle size. Pyrolysis is predominantly performed on lignocellulosic biomasses which have low moisture content this often requires pre-drying and grinding in the case of fast and flash pyrolysis.

2.2.3.5. Gasification

Gasification is performed by heating lignocellulosic biomass under oxygen to temperatures of 800-900 °C which produces a synthesis gas (mixture of hydrogen, carbon dioxide, and carbon monoxide) [123], [128]. The synthesis gas produced is more versatile than the biomass used to produce it and can be burned directly as a fuel in which case only carbon dioxide and water are produced which gives the fuel a relatively low environmental impact [111]. Economic studies of gasifiers have shown it can be as effective as coal fired power plants. Syn-gas can also be used to produce high value chemicals or biofuels [123]. Fischer-Tropsch is a good example of this whereby syn-gas is used to produce alkanes with the help of copper, iron, and ruthenium based catalysts [132]. This process was developed early in the 20th century and is still in use today to produce diesel and gasoline fuels. The overall basic reaction for Fischer-Tropsch is carbon monoxide and hydrogen are converted into hydrocarbons and water (Equation 2.3).

$$CO + 2H_2 \rightarrow C_nH_n + H_2O$$

Equation 2.3 Fundamental chemical reaction pathway for Fischer-Tropsch.

2.2.3.6. Hydrothermal Processing

Hydrothermal processing is the conversion of biomass using sub-critical or supercritical water also known as high temperature water which is described in detail in Section 2.1 [133]. An advantage of this process is that it does not require costly biomass pre-drying steps and the biomass can be processed directly with any moisture content [134]. Hydrothermal processing is broken down into the subcategories; hydrothermal carbonisation, liquefaction, and gasification based on the state of matter that the target product is in solid, liquid, and gas respectively [27], [135]. The yield of these three phases is controlled mainly by processing temperature, retention time, and the properties of biomass used. Hydrothermal carbonisation requires the mildest processing conditions and is discussed in detail in Section 2.3 because it is a large focus of this research. Hydrothermal liquefaction requires higher temperatures between 250-374 °C and is usually performed for shorter residence times of less than 5 h. The bio-oil produced has higher oxygen and water content, high corrosiveness, high viscosity, and low heating values when compared to crude oil. Therefore, hydrothermal liquefaction bio-oils are inadequate for direct use in traditional combustion processes and need to be further processed using similar techniques to crude oil processing. It is possible to use steam reformation, hydrodeoxygenation, or catalytic cracking procedures to reduce the oxygen and water content within the bio-oil. Additionally, the bio-oil can be esterified to convert acid/aldehydes to esters/acetals and then separated using distillation [136]. Hydrothermal gasification can be performed at sub-critical conditions (>300 °C) with the assistance of catalysts or under supercritical conditions to yield gaseous products in significant volumes. The main products are hydrogen, carbon dioxide, and methane, also known as syn-gas [137]. When performing supercritical hydrothermal gasification compared to traditional gasification the heating of the large volumes of water in hydrothermal gasification significantly increases the energy required.

2.3. Hydrothermal Carbonisation/Hydrochar Synthesis

Hydrothermal carbonisation (HTC) is the formation of a solid carbonaceous material using water held under pressure at raised temperatures, this process is introduced in Section 1.2 and the unique properties of the reaction medium HTW are detailed in Section 2.1. HTC has some

significant advantages over the previously described thermochemical and biochemical conversion technologies. Direct processing of wet feedstocks is not only possible but beneficial when performing HTC, whereby if the feedstock has a high enough moisture content it can be processed without additional water [138]. This eliminates the need for energetically expensive drying steps and means that previously untenable waste streams *e.g.* sewage sludge can be processed using HTC [139]. HTC is a versatile processing technique which has been used on a wide range of different feedstocks such as; purified carbohydrates [140], agricultural residues [20], food waste (vegetables, fruits, meats, and staple foodstuffs) [141], faecal waste [142], sewage sludge [143], algae [144], and discarded plastics [145]. Additionally, HTC also requires lower processing temperatures than other thermochemical conversion technologies and meaningfully shorter residence times than biochemical conversion technologies [146]. Finally, the properties of the hydrochar can be tuned by selection of feedstock, retention time, pH, catalysts, processing temperature, templating agents, solvents, and post-treatment procedures [147], [148]. This means HTC can be used to produce hydrochar with applications in a multitude of fields. The main areas highlighted in this review are; solid biofuels [149] (Section 2.3.2), adsorbents [150], catalysts [151], soil amendment, energy storage, fuel cells, photocatalysis, drug delivery, gas storage, and bioimaging [148] (Section 2.3.4)

2.3.1. Synthesis Mechanism of Hydrochar Carbons

When HTC is performed on a biomass based feedstock it undergoes a complex series of hydrolysis, dehydration, decarboxylation, polymerisation, poly-condensation, and aromatisation reactions [152], [153]. These reactions yield a highly functionalised carbonaceous material which is unique to HTC and referred to as hydrochar or hydrothermal carbon. There are a multitude of different potential side reactions depending on feedstock properties and processing conditions. This occurs alongside solid-solid charring reactions similar to low temperature pyrolysis reactions under inert gases which form the familiar char carbonaceous material [154]. The combination of these two reaction mechanisms proceeding concurrently produces a functionalised carbon product with reduced mass and increased energy density (Figure 2.20). Since the reactivity during HTC of biomass is very complex, many authors have studied basic carbohydrate systems in depth to understand the formation of hydrochar carbons more fully [140], [155], [156].

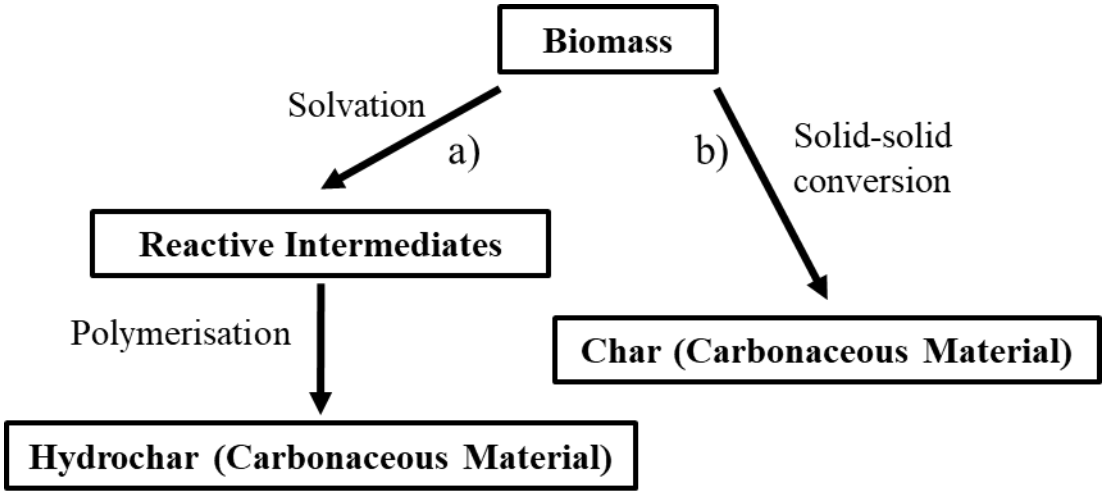

Figure 2.20 Conversion of biomass into carbonaceous material by the two routes during HTC; (a) the liquid phase polymerisation of dissolved reactants, (b) the pyrolysis like carbonaceous reactions.

Herein, the basic mechanism for the conversion of sucrose to carbon microspheres using HTC is explained based on what is presented in the literature. The sucrose (β-d-fructofuranosyl α-d-glucopyranoside) is initially hydrolysed by the water to yield glucose (α-d-glucopyranose and β-d-glucopyranose) and fructose (α-d-fructofuranose and β-d-fructofuranose) [157]. The ether bond between both monomers is protonated by hydronium ions which makes it more electron withdrawing, this allows for hydroxide ions to attack the carbon attached to either side of this newly protonated ether bond. Two isomers of glucose and fructose are produced because the hydroxide ions can attack the carbon from above or below and bond cleavage can occur from either side of the ether bond (Figure 2.21) [157].

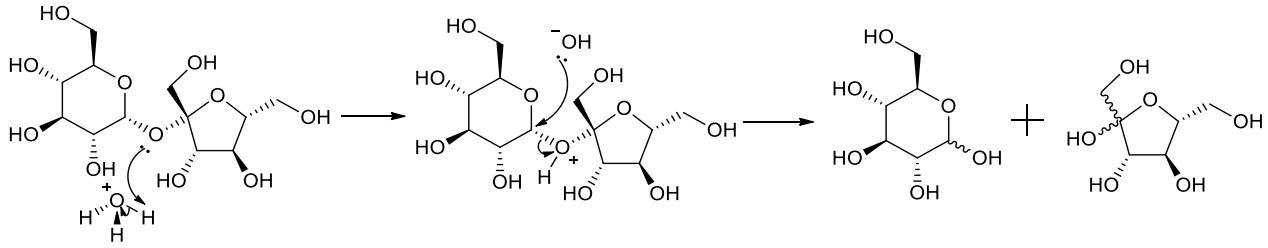

Figure 2.21 Initial hydrolysis of sucrose to form a mixture of α-d-glucopyranose and β-d-glucopyranose as well as α-d-fructofuranose and β-d-fructofuranose [157]**.**

Glucose is converted into fructopyranose (α-d-fructopyranose and β-d-fructopyranose) then fructose (α-d-fructofuranose and β-d-fructofuranose) by a series of tautomerization reactions. Then the fructose monomers follow a series of dehydration reactions to form 5-(hydroxymethyl)furfural (5-HMF) [155]. The initial reaction is propagated by protonation of a hydroxide group at position 5, this forms a good leaving group for the formation of a double bond, after which the double bond is pushed by formation of a carbonyl group, this reaction

occurs at the same time as displayed by the brackets [157]. Finally, the last hydroxide group is cleaved by the same dehydration reaction as occurred initially to form 5-HMF (Figure 2.22) [158].

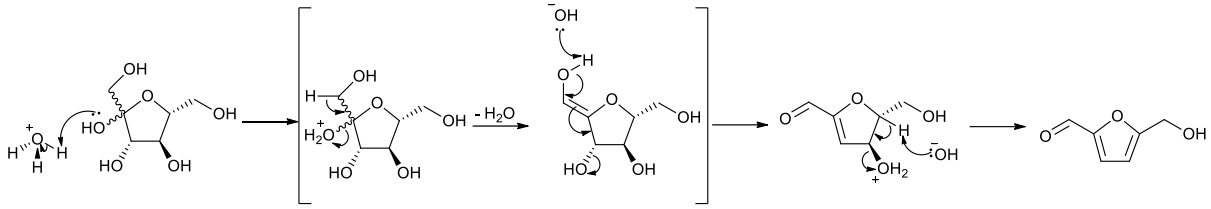

Figure 2.22 Dehydration reactions for the conversion of fructose to 5-HMF during HTC [157]**.**

Aldol polycondensation reactions then occur between 5-HMF molecules which form an extended polymeric structure of primary spherical particles which can then aggregate to generate larger carbonaceous spheres (Figure 2.23) [156], [157]. Initially an enolate forms from the 5-HMF, this attacks the carbonyl on a different 5-HMF molecule [140]. From this water is removed by condensation reaction to leave a stable carbon double bond, this reaction proceeds to form an extended structure of bonded 5-HMF molecules, which when large enough appear as carbonaceous spheres. The carbon microspheres formed during HTC have oxygen (and other heteroatom) functionality built into their structure because of these polycondensation reactions between dissolved organic compounds which contain oxygen (and other heteroatoms) [148].

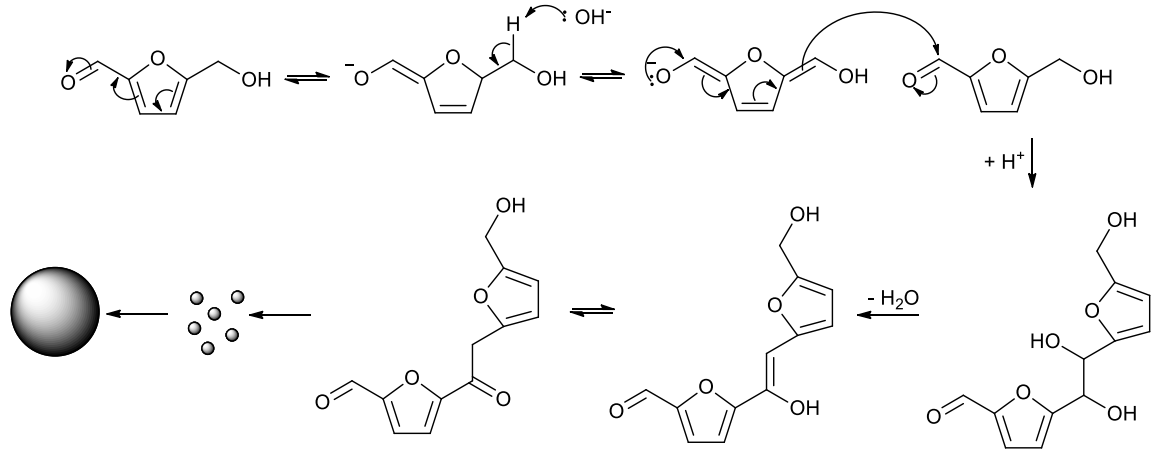

Figure 2.23 Aldol polycondensation of 5-HMF to form carbonaceous spheres during HTC [157]**.**

Whilst this is a limited view into the reactivity present in HTC, it is useful for understanding some of the driving mechanisms when more complex feedstocks are processed. It should also be noted that many other reactions occur during the HTC of sucrose which produces; formic, levulinic, and acetic acid in substantial quantities in addition to many other organics in lower

concentrations [157].

2.3.2. HTC of Biomass to Produce Renewable Solid Fuels

There are innumerable sources of waste biomass which if appropriately managed can be a huge reserve of renewable energy [153]. However, biomass has unfavourable properties for direct combustion such as high moisture content which lowers combustion temperature and increases carbon monoxide emissions, therefore biomass requires further processing to use in energy production as explained in Section 2.2. HTC has competitive potential in the pre-treatment of waste biomass avoiding costly pre-drying steps, and as previously stated, HTC can be used on a wide variety of different feedstocks [159], [160]. Comparative technoeconomic assessment of the processing of rice husk further cements these theorised advantages [161]. HTC showed a calculated cost of 0.013 \$ MJ^{-1} significantly lower than direct combustion, pyrolysis, or anaerobic digestion at 0.021, 0.043, and 0.055 \$ MJ^{-1} respectively. Additionally, the HTC process produced lower greenhouse gas emissions at 0.125 kg of carbon dioxide equivalent per MJ of energy produced, again lower than direct combustion, pyrolysis, or anaerobic digestion at 0.795, 0.426, and 0.522 respectively. Therefore HTC can be used to improve the combustion properties of the biomass waste showing higher carbon content, lower oxygen content, increased higher heating value (HHV), higher density, and lower emissions of greenhouse gases [162]. For this reason, HTC has been heavily investigated for bioenergy production.

2.3.2.1. Analysis of Hydrochar as a Renewable Solid Biofuel

It is possible to approximate how hydrochars will perform as solid fuels by obtaining the higher heating value (HHV), proximate analysis, and ultimate/elemental analysis [163]–[165]. Ultimate/elemental analysis is used to determine the percentage of the carbon, nitrogen, hydrogen, and oxygen in the hydrochar, from these atomic H/C and O/C ratios are determined so that the degree of polyaromatisation which has occurred can be shown, this is often displayed graphically with the use of van Krevelen diagrams which plot O/C (x-axis) against H/C (y-axis) (Figure 2.24) [166]. Ultimate/elemental analysis is determined by burning the sample in oxygen with an oxidising agent to enable complete combustion which forms carbon dioxide (carbon), water (hydrogen), gaseous nitrogen (nitrogen), and sulphur dioxide (sulphur). These gases are then passed through a column which separates them and are detected by a thermal conductivity detector [167]. From this data the percentage of carbon, hydrogen, nitrogen, and

sulphur can be determined, whilst oxygen is typically calculated by subtracting these and the ash content from 100 (Equation 2.4).

$$\boldsymbol{O}(\%) = \mathbf{100} - (\boldsymbol{C}(\%) + \boldsymbol{H}(\%) + \boldsymbol{N}(\%) + \boldsymbol{S}(\%) + \boldsymbol{Ash}(\%)$$

Equation 2.4. Calculation of oxygen content from CHNS elemental analyser data.

HHV is also referred to as calorific content which is how much energy is given out when the fuel is completely combusted, herein reported in MJ Kg^{-1} [168]. HHV can be experimentally determined by controlled combustion in a bomb calorimeter. This hydrochar is ignited with an electrical impulse in pure oxygen inside of the sealed bomb. This is placed inside of a large vat of water in which the temperature is measured, the change in temperature shows how much energy is given from the combustion and HHV can be calculated. HHV can also be estimated mathematically for which there are numerous linear equations based on the percentage of elements in the sample; these are often termed "Dulong-type" because Dulong *et al.* developed the first of these [169]. Herein HHV has been calculated when required using the formula presented by Friedl *et al.* (Equation 2.5) [170].

$$\boldsymbol{HHV} = \mathbf{0.0355}\boldsymbol{C}^{\mathbf{2}} - \mathbf{0.232}\boldsymbol{C} - \mathbf{2.23}\boldsymbol{H} + \mathbf{0.0512}\boldsymbol{CH} + \mathbf{1.31}\boldsymbol{N} + \mathbf{20.6}$$

Equation 2.5. Equation to calculate the HHV from carbon (C), hydrogen (H), oxygen (O), and nitrogen (N) content.

Proximate analysis is performed on a solid material (hydrochar) by controlled heating under different atmospheres whilst monitoring the weight of the solid. In a laboratory setting this is often performed using thermogravimetric analysis, this gives key information about the behaviour of the fuel (hydrochar) during utilisation [171]. The analysis is performed by initial heating in an inert atmosphere or vacuum at 110±5 °C for an hour, the weight loss during this time is the moisture content of the solid material (hydrochar) [172]. The higher the moisture content of the fuel the more energy it will take to dry it before combustion. Following this an increase to 900±20 °C under the same inert atmosphere yields a second weight loss. This raised temperature expels various gaseous species both inorganic and organic. This material is not analysed, and the sum of the losses are combined and defined as volatile matter (VM). The remaining material is held at temperature and exposed to in air, this burns off the remaining organic material which was not volatile, and this is known as the fixed carbon (FC). To accurately obtain the weight of all inorganics (ash) it is vital that these are not volatilised off and therefore the solid material must be combusted in an oxygen rich environment at a lower temperature (<300 °C) [173]. If the inorganic volatile matter is a desirable characteristic to

determine, a lower secondary temperature must be used after drying below 500°C to prevent volatilisation of inorganic species.

Fuels (hydrochars) with high VM are easy to ignite and burn quickly, whilst fuels (hydrochars) with high FC contents are difficult to ignite and burn more slowly. The ratio of VM to FC is known as the fuel ratio which gives an indication of how hard the fuel is to ignite, how long it will burn, and the quality of the flame produced. The ash content of the fuel (hydrochar) needs to be low enough so that it does not cause issues during combustion in the reactor. Whilst research has shown that ash contents up to 55% can be used in some power plants and even up to 75% when co-fired with oil, it is desirable to have an ash content below 20% [174].

2.3.2.2. Different Processing Conditions of Hydrochars and Severity Factor Calculation

Hydrochar properties are directly dependant on a multitude of different factors, processing temperature, temperature ramp rate, compositions of the biomass (lignin, hemicellulose, cellulose, protein, inorganics), moisture content of feedstock, water/feedstock ratio, application of stirrer, rate of stirring, and the use of catalysts (homogeneous and heterogeneous) [23]. It is suggested in the literature that the most important factor of HTC is processing temperature followed by retention time. To examine the effect of different temperatures, retention times, and biomass in HTC, literature data was collected and compiled. The respective values for the HHV, proximate, and ultimate/elemental analysis are compared with fossil fuel coals, and other types of solid bio fuels as discussed in Section 2.2.3 (Appendix 1, Appendix 2, Appendix 3). To add additional value to the discussion where relevant a severity factor was calculated from the temperature and retention time of the reaction following Equation 2.6. This concept was originally developed by Chornet and Ralph Overend to unify data of complex systems which were processed at different operating conditions, experimental equipment, and even laboratories [175].

$$\boldsymbol{R_0 = t \times e^{\left[\frac{T-100}{14.75}\right]}} \qquad \boldsymbol{SF = Log(R_0)}$$

Equation 2.6. Equation for the calculation of severity factor in a reaction. R_0 = reaction ordinate (min), t = retention time (min), T = processing temperature (°C).

2.3.2.3. van Krevelen Diagrams Based on Literature Data for Hydrochars

van Krevelen diagrams are used to assess the viability of a carbonaceous material in fuel applications. There are, as previously discussed in Section 2.3.1 many different reaction

mechanisms which change the oxygen, carbon, and hydrogen content during HTC. Two of the most important in HTC for fuel applications are dehydration, and decarboxylation which remove H_2O, and CO_2 from the raw material respectively [176]. The van Krevelen diagram of the hydrochars shows that at HTC any temperature and time decreased both the oxygen and hydrogen content of the raw material (black markers) more than its carbon content (Figure 2.24). This is displayed by the reduction in both O/C and H/C ratios in all hydrochars. This means – among other things – that the hydrochars are a more viable carbonaceous material for fuel applications than their raw biomasses when produced at any processing temperature or time.

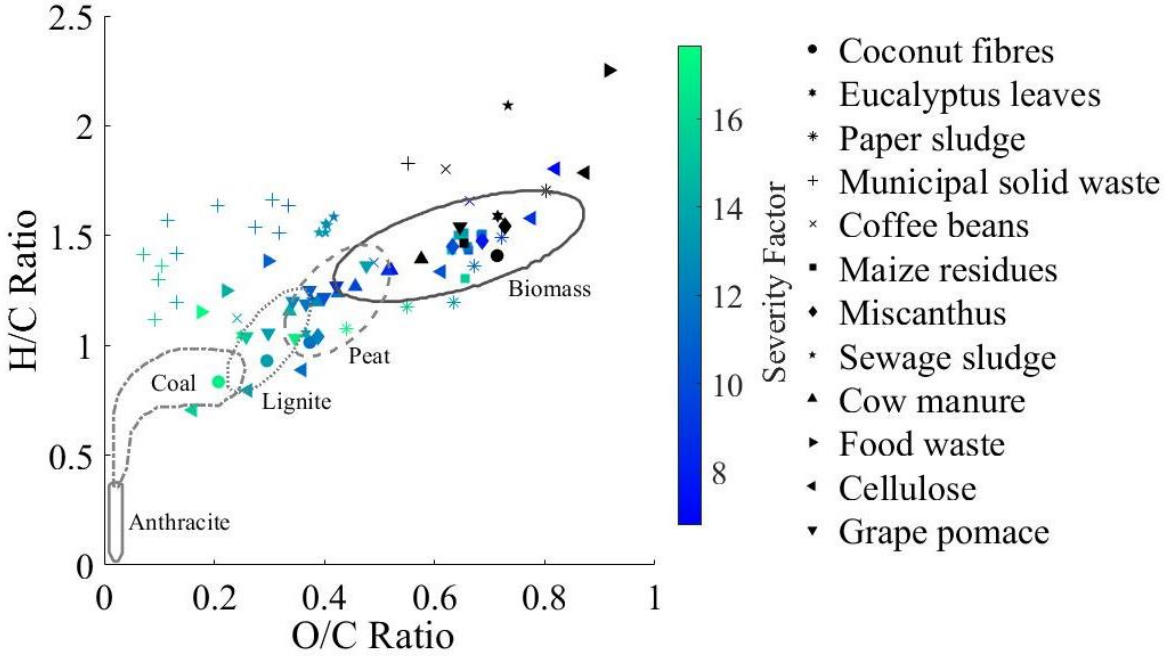

Figure 2.24 van Krevelen diagram displaying hydrochars produced from 12 different biomass sources. Severity factor for the HTC process was calculated using Equation 2.6 and is displayed by coloured datapoints from 7 (dark blue) to 17 (bright green). Extracted literature data is available in Appendix 1 [163]–[165], [177]–[184]**.**

Furthermore, the hydrochar produced by coconut fibres and cellulose had a similar O/C and H/C ratio to industrially used coals under certain conditions [176]. Whilst grape pomace, eucalyptus leaves, miscanthus and coffee beans produced a hydrochar with, at best, properties similar to those of lignite. Maize residues, paper sludge, municipal solid waste, sewage sludge, cow manure, and food waste (mixed vegetables, fruits, meats, and staple foodstuffs) did not produce a carbonaceous material with properties applicable to fuel application judging only by the van Krevelen diagram. This shows that the properties of biomass used in HTC exerts significant control over the properties of the hydrochar. However, potential alternative applications of these hydrochars still remain, see Section 2.3.4.

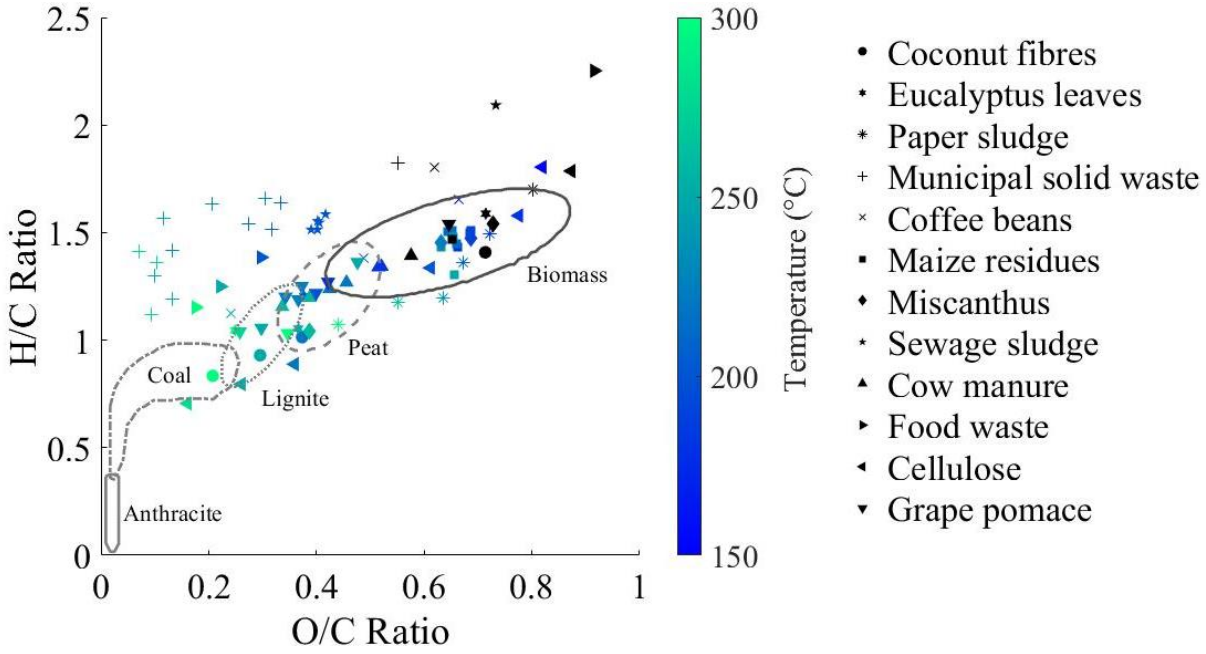

Figure 2.25 van Krevelen diagram displaying hydrochars produced from 12 different biomass sources. Processing temperature is displayed with coloured datapoints from 150 °C (dark blue) to 300 °C (bright green). Extracted literature data is available in Appendix 1 [163]–[165], [177]–[184]**.**

From these data the hydrochar with lowest O/C and H/C ratio is always produced by the highest processing temperature which is in line with the literary discussion [185] (Figure 2.25). This is further compounded by the evidence that the retention time of the HTC has little to no effect on the O/C and H/C ratios of the hydrochar (Figure 2.26). The reaction only requires 5 min at the specified retention time to undergo enough conversion based on the van Krevelen diagrams produced from literature data. However, there are many other important parameters for solid fuels which are not observable in a van Krevelen diagram.

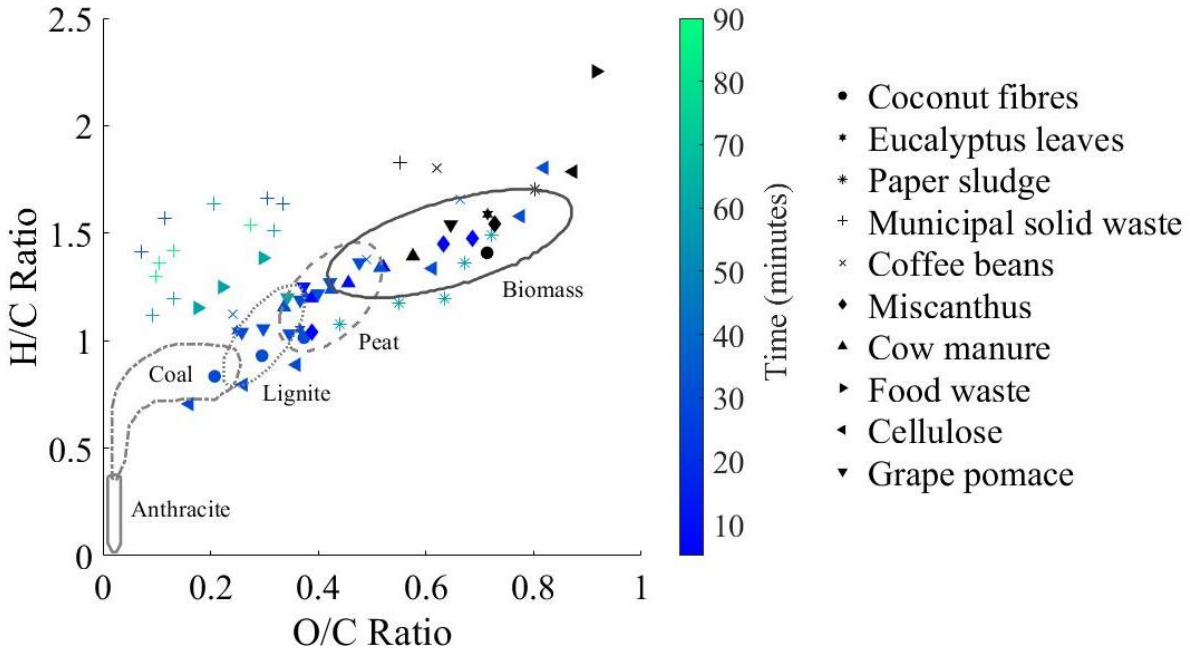

Figure 2.26 van Krevelen diagram displaying hydrochars produced from 10 different biomass sources. Retention time is displayed with coloured datapoints from 0 min (dark blue) to 90 min (bright green). Extracted literature data is available in Appendix 1 [163]–[165], [177]–[184]**.**

2.3.2.4. Proximate Analysis of Hydrochars in the Literature

As previously stated, the proximate analysis (volatile matter (VM), fixed carbon (FC), and ash content) yields vital information about the combustion properties of the hydrochar (fuel). The change in these properties from the raw material to the hydrochar and at the designated temperature and retention times is shown visually (Figure 2.27, Figure 2.28, Figure 2.29, Figure 2.30). For comparison, some of the highest ranked coals for combustion are anthracite and bituminous. Anthracite has a volatile matter content between 2-12%, FC content between 75-85%, whilst bituminous has between 15-45% and 50-70% for VM and FC respectively [186]. Lower rank coals sub-bituminous and lignite have 28-45% and 24-32% VM and for FC 30-57% and 25-30% both respectively. For all biomasses reported their VM (%) content was reduced, and FC (%) content increased under any HTC processing condition. Furthermore, there is a clear trend that a higher processing temperature yields a hydrochar with higher FC (%) and lower VM (%) compared with the lower processing temperature. The same relationship could not be determined from retention time of the HTC process. This is identified to be connected to the dissolution of volatile organics and their subsequent reaction and final self-polymerisation into carbonaceous material as previously outlined in Section 2.3.1 [152], [153]. This results in a hydrochar with an increased fuel ratio (FC to VM ratio). In practice this

means that the hydrochar will burn longer and cleaner due to the increased FC content (%) although it will be harder to ignite due to the decreased VM content (%). Thus the desired fuel ratio can be acquired based on the proximate analysis of the raw biomass and the processing temperature of the HTC process, allowing for control over the combustion properties of the fuel to suit the furnace and boiler system.

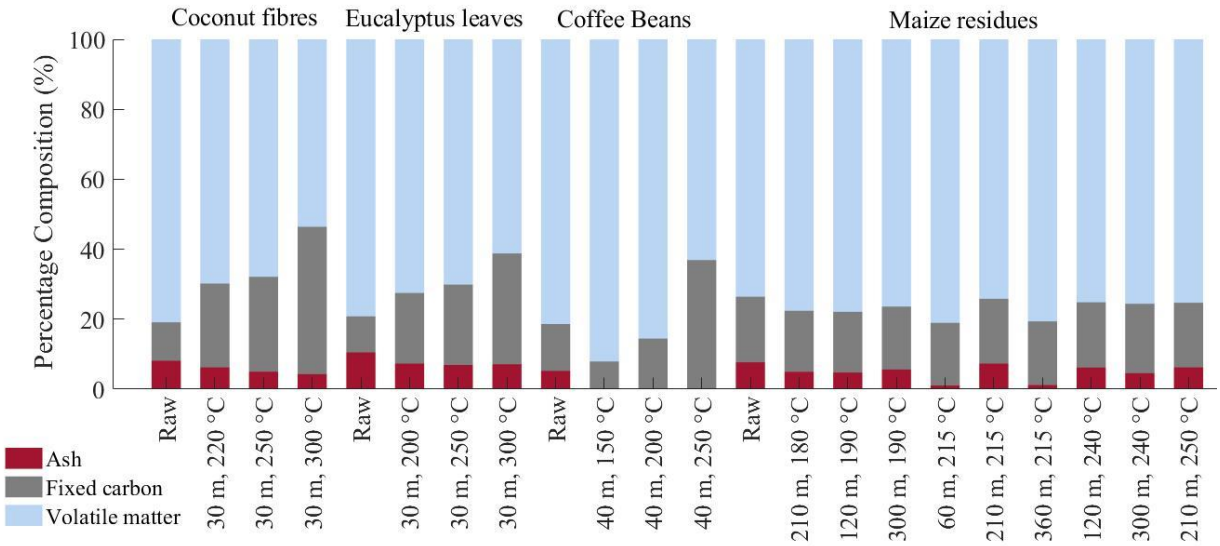

Figure 2.27 Stacked bar chart showing the percentage composition of the unprocessed biomasses (Raw), and the hydrochar produced from HTC of the biomass for a specified retention time in mins (m) and processing temperature in °C. Composition is given on a dry basis as the ash, fixed carbon (FC), and volatile matter (VM) given in wt.% [163]–[165], [177]–[184]**.**

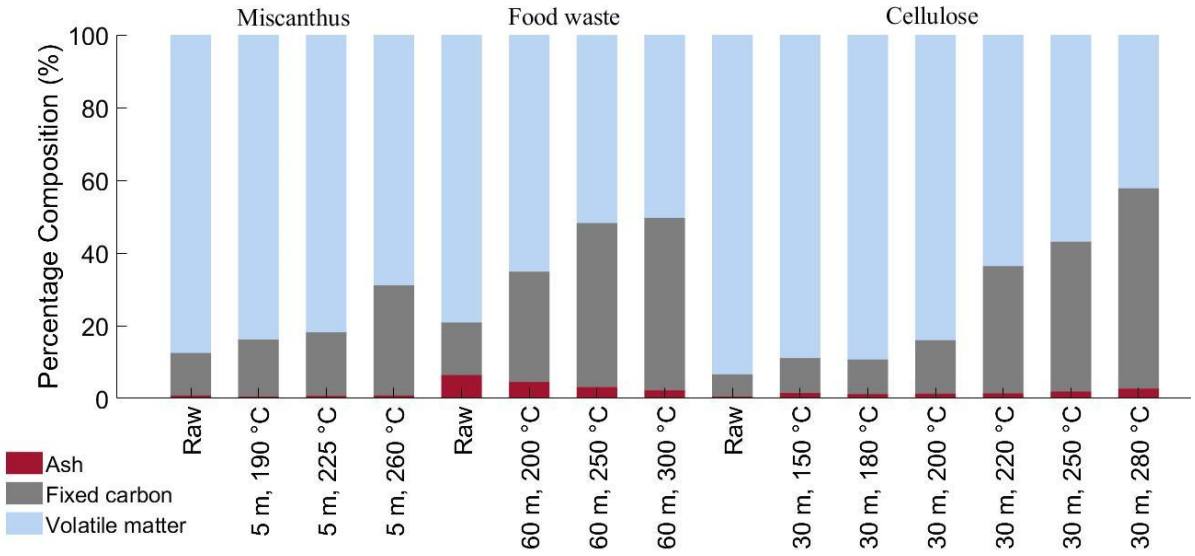

Figure 2.28 Stacked bar chart showing the percentage composition of the unprocessed biomasses (Raw), and the hydrochar produced from HTC of the biomass for a specified retention time in mins (m) and processing temperature in °C. Composition is given on a dry basis as the ash, fixed carbon (FC), volatile matter (VM) given in wt.% [163]–[165], [177]–[184]**.**

The proximate analysis of hydrochar from coconut fibres, eucalyptus leaves, coffee beans, maize residues, miscanthus, food waste, and cellulose are in the same category because of their similar raw biomass composition and the trends seen upon HTC processing (Figure 2.27, Figure 2.28). In nearly all these biomasses their ash content was reduced under HTC at any

temperature and retention time (cellulose being the exception). Additionally, all these hydrochars contained less than 10% ash which is the lower maximum accepted industrially for coals. This means that based on ash content alone all these hydrochars are viable for use as a solid fuel in place of coals. Comparing the FC and VM contents to the coals previously stated, only the cellulose processed at 280 °C for 30 min has both a VM and FC content in range of the values for coal. Specifically, in this case bituminous coal at 42% VM and 55% FC. This hydrochar would be a more than adequate replacement for fossil fuel coals however, it has the caveat that this is the only hydrochar listed which is produced from a pure processed material and not a waste biomass. The other hydrochars listed often suffer from a high VM content, even whilst their FC content is comparable to sub-bituminous coals in many examples (coconut fibres 300 °C and 30 min, eucalyptus leaves 300 °C and 30 min, coffee beans 250 °C and min, miscanthus 260 °C and 5 min, food waste >200 °C and 60 min, cellulose >220 °C and 30 min). In practice this would mean that the hydrochar would burn much faster than fossil fuel coals and would likely not burn as cleanly (producing smoke), however adaptations in the combustion process could overcome these issues. Finally, it is important to note that often higher temperatures of >250 °C were required to produce a viable hydrochar fuel, the exceptions being cellulose, and food waste. This may posit a focus on the processing of food wastes in the HTC process.

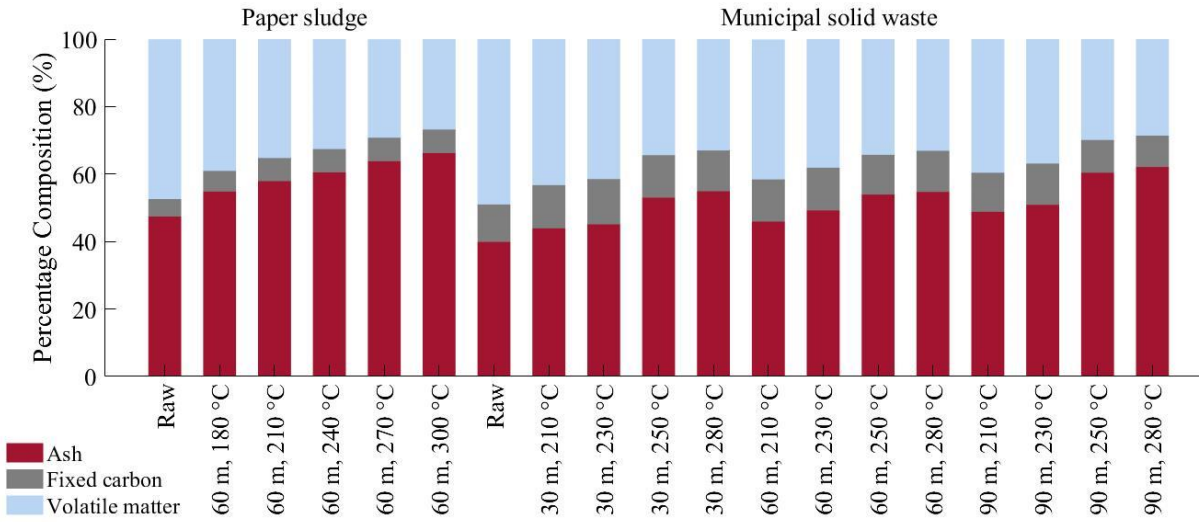

Figure 2.29 Stacked bar chart showing the percentage composition of the unprocessed biomasses (Raw), and the hydrochar produced from HTC of the biomass for a specified retention time in mins (m) and processing temperature in °C. Composition is given on a dry basis as the ash, fixed carbon (FC), and volatile matter (VM) given in wt.% [163]–[165], [177]–[184]**.**

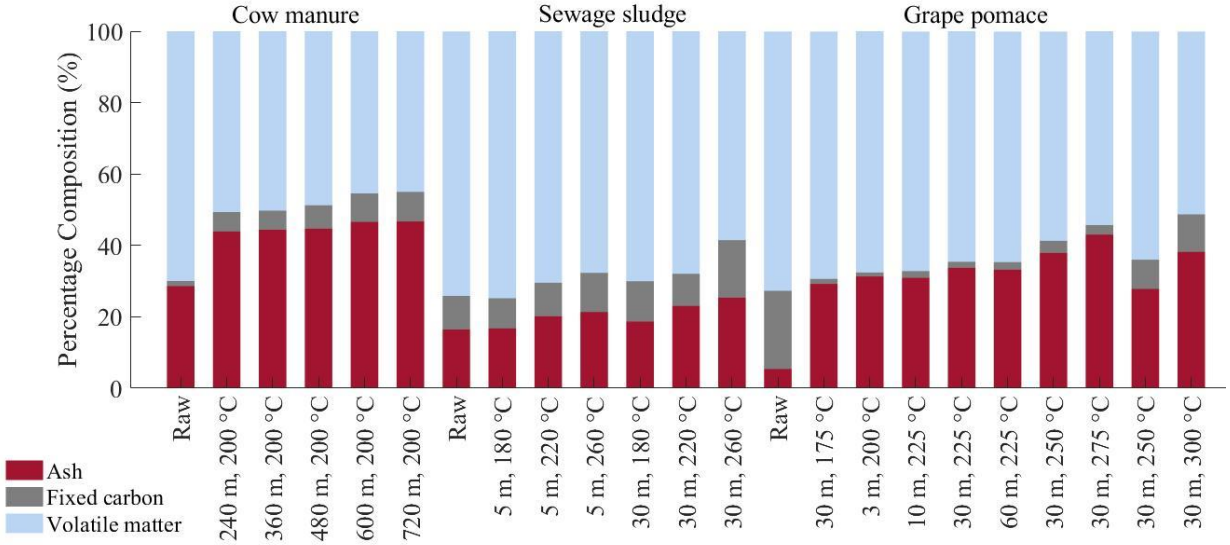

Figure 2.30 Stacked bar chart showing the percentage composition of the unprocessed biomasses (Raw), and the hydrochar produced from HTC of the biomass for a specified retention time in mins (m) and processing temperature in °C. Composition is given on a dry basis as the ash, fixed carbon (FC), and volatile matter (VM) given in wt.% [163]–[165], [177]–[184]**.**

Another category of biomasses are high ash content and sludge type waste biomasses; paper sludge, municipal solid waste, cow manure, sewage sludge, and grape pomace (Figure 2.29 and Figure 2.30). These biomasses show the opposite behaviour for ash content, where HTC processing under any conditions increased the ash content of the solid material. Smith *et al.* proposed that the feedstocks with high ash contents due to silicon and iron yield higher ash

hydrochars [187]. It is hypothesised that the HTW does not solubilise these inorganic materials thus they cannot be removed from the feedstock using HTC. They additionally noted that potassium, sodium, magnesium, and phosphorus were more readily removed from the feedstocks using HTC. Another potential cause is the formation of surface functionalities which reabsorb metals from the process water; it has been shown that carboxylic groups on the hydrochar surface can cause a high cation exchange capacity [188]. The same increase in FC content and reduction in VM content is shown for these high ash content sludge type wastes as previously observed in the lignocellulosic wastes. However, the ash content is too high for these to be suitable for use in combustion processes, in addition to their low FC and VM contents. These types of biomass therefore have little to no potential in replacement of fossil fuels, however the HTC processes may still be useful to generate hydrochars for alternative applications, see Section 2.3.4 for more details on this.

2.3.2.5. Energy Density Increase in Hydrochars Presented in the Literature

Finally the energy content of the hydrochar is essential to evaluating how successful it would be in replacing fossil fuel coals. The increase in HHV of the biomasses based upon processing temperature and severity factor used in HTC is shown to evaluate effectiveness of the HTC process (Figure 2.31, Figure 2.32). There is a clear overall trend that an increase in processing temperature and/or severity factor causes a larger increase in the HHV of the hydrochar formed. Furthermore, temperature is a better indicator of this, and the addition of retention time (for severity factor) confuses the expected HHV increase. Solidifying the point cited in literature that processing temperature is the most important parameter in the HTC of biomass and only a minimum retention time is required for the organic reactions to take place and convert the biomass. A good example of this is miscanthus (purple star) which is operated at the same processing temperature but different processing times. The increase in severity factor does not cause a larger increase in HHV.

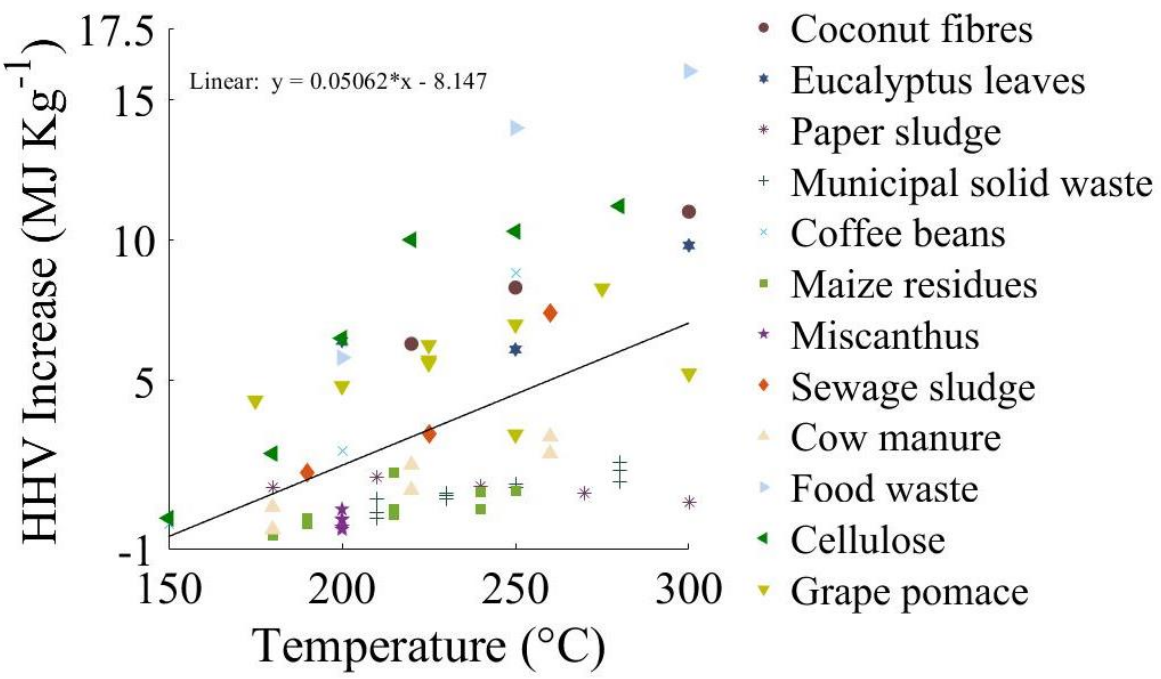

Figure 2.31 Increase in higher heating value (HHV) of 12 from raw feedstock plotted against the processing temperature of the HTC reaction [163]–[165], [177]–[184]**.**

Additional examination of the HHV increase with temperature (Figure 2.31) shows that the same biomass hydrochars with lower ash and higher FC content e also have larger increases in HHV (coconut fibres, eucalyptus leaves, coffee beans, maize residues, miscanthus, food waste, and cellulose). The hydrochars from all these biomasses have HHV comparable to sub-bituminous coals >17.4 MJ Kg^{-1} when produced at any HTC processing temperature, whilst they can yield a hydrochar with high HHV values comparable to anthracite >27.9 MJ Kg^{-1} in many cases (coconut fibres 300 °C and 30 min, eucalyptus leaves 300 °C and 30 min, coffee beans 250 °C and 40 min, food waste >250 °C and 60 min) [186]. The remaining biomasses which are high ash and sludge based show little to no increase in HHV further compounding evidence that they are ill suited for use in fossil fuel replacement.

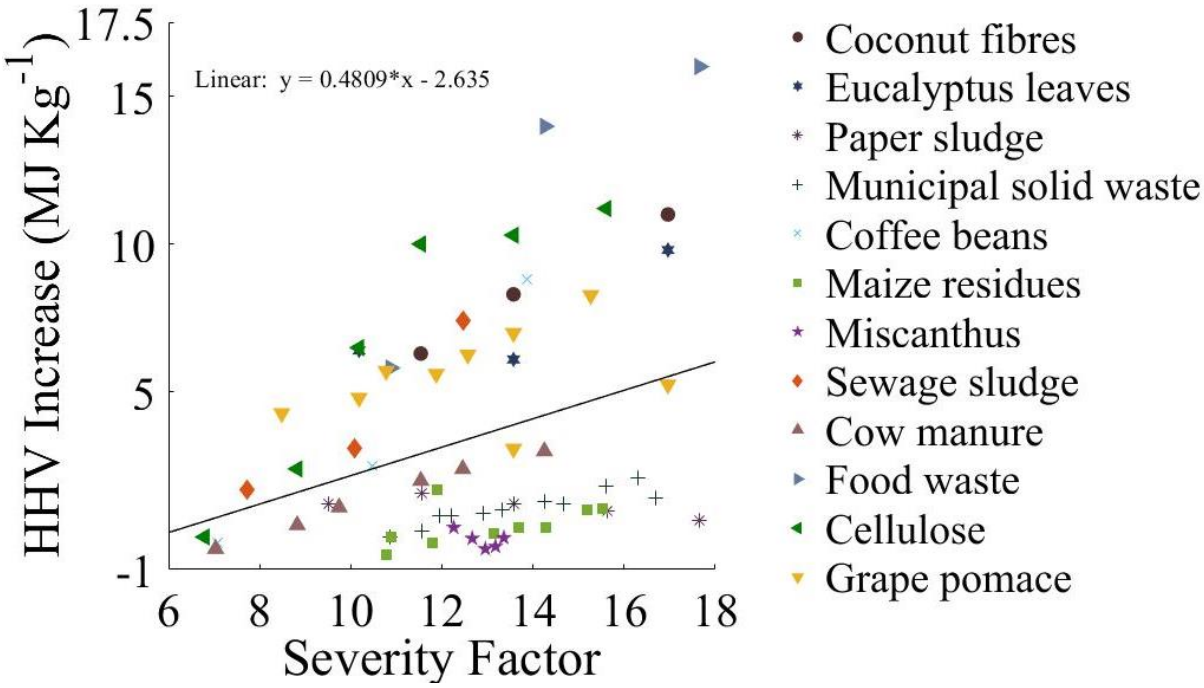

Figure 2.32 Increase in higher heating value (HHV) of 12 biomasses from raw feedstock plotted against the severity factor of the HTC reaction. Calculated from temperature and retention time (Equation 2.6) [163]–[165], [177]–[184]**.**

In summary, an analysis of the fuel properties of hydrochar presented in the literature shows three key findings. 1) biomasses with a high ash content (>20%) cannot be upgraded enough using HTC to replace fossil fuels, therefore some biomass streams are ill suited to this application. 2) processing temperature is the key metric in determining the carbonisation degree of the biomass to hydrochar, with only a minimal retention time required. 3) hydrochars which have very favourable HHV, and proximate analysis (comparable to anthracite) can be produced at low temperature (<250 °C) if the biomass processed is carefully selected (*e.g.* food waste).

2.3.3. Additional Processing Methods to Control the Properties of Hydrochars

Hydrochar is also used to produce high value specialised carbon based materials, these have applications in many different areas such as adsorbents [150], catalysts [151], soil amendment, energy storage, fuel cells, photocatalysis, drug delivery, gas storage, and bioimaging [148]. This is discussed in Section 2.3.4. There are several methods employed both pre- post- and during HTC to change the properties of hydrochar synthesised in order to specialise and control the hydrochar properties for applications in these different areas.

2.3.3.1. Post-Treatment of Hydrochar to Induce Porosity

Hydrochar generally has a low surface area and almost no porosity [189]. The most direct

industrially used comparison to hydrochar is activated carbon which is a highly carbonaceous material with many small pores and a large surface area. Activated carbon is commonly produced from non-porous carbonaceous materials with low surface areas *via* several different methods [190]. However, only a small number of resources are currently used industrially for production of activated carbon; coal, peat, wood, shells, and some synthetic organic polymers. Activated carbon is heavily applied in separation, removal, retrieval, and modification of various compounds in the liquid and gas phase. A similar processing method used to synthesise activated carbon can be applied to hydrochars [191]. One method uses physical activation in a two-step process starting with initial thermal treatment (>700 °C) under an inert atmosphere (pyrolysis) followed by activation under oxidising gases (steam, CO_2, CO, N_2, and air) between 800-1100 °C [192]. The second step using activation with oxidising gases at high temperatures >800 °C can be applied directly to hydrochars. The temperature, gas, and processing time all have significant effects on the morphology, structure, and functionality of the hydrochar after thermal treatment [193]. Compared to the pyrolysis step, HTC has mild and simplistic processing conditions and can be used on a more diverse range of feedstocks without pre-treatment [194]. Chemical activation is another post-processing method that has also been investigated to induce porosity. This is typically performed with the addition of dehydrating groups such as potassium hydroxide, zinc chloride, phosphoric acid, and sodium hydroxide, removing oxygen and hydrogen in the form of water [19]. Fortunately, hydrochar has a high concentration of oxygen functional groups which react readily with the activation chemicals to leave a highly porous aromatic carbon shell [195].

2.3.3.2. Using Hydrochar as a Catalyst Support Material

Metals and inorganics can also be supported onto hydrochar in place of other catalyst support materials [196]. Carbon has a few significant advantages over traditional support materials, it is cheap, abundant, and can be sourced from environmentally friendly processes, carbon is resistant to degradation in acidic and basic solutions, stable at high temperature, offers higher control over pore and macro structure, has modifiable surface properties, and a recoverable active phase through destruction of the carbon support [197]. Metals can be supported onto hydrochar from biomass wastes by wet impregnation to transfer the metals onto the hydrochar [198]. Another method used to support metals onto carbon is the addition of powder or nanoparticles during HTC which embeds these materials onto the hydrochar produced. This has been shown to support metals onto specialised carbon materials such as activated carbon, carbon nanotubes, graphene sheets, *etc.* [199]. A few studies have also investigated a one-pot

approach combining these two methods, whereby biomass wastes are hydrothermally carbonised and metal oxides are precipitated onto the produced hydrochar *in situ* [200].

2.3.3.3. Soft and Hard Templating in the Synthesis of Hydrochars

Porous hydrochar with well-defined structure has also been synthesised by both hard and soft templating methods [148]. Nanoporous carbon synthesised using nanostructured silica as sacrificial templating materials was first presented by Knox *et al.* [201]. This founded the basis of hard templating procedures in which a carbon precursor (phenol) is infiltrated into a sacrificial (silica) template and is coked onto the sacrificial template at temperatures above 700 °C, the template is then removed (using HF or NaOH) to leave the inverse of the sacrificial template (Figure 2.33) [202]. Another method often referred to as soft templating involves the use of sol-gel chemistry; sol-gel procedures are discussed in depth in Section 2.4. This method uses block copolymers and aromatic precursors to form ordered porous carbon *via* evaporation induced self-assembly, followed by polymerisation to bind the aromatic precursors together and then finally carbonisation to produce a highly ordered porous carbon material (Figure 2.33) [203].

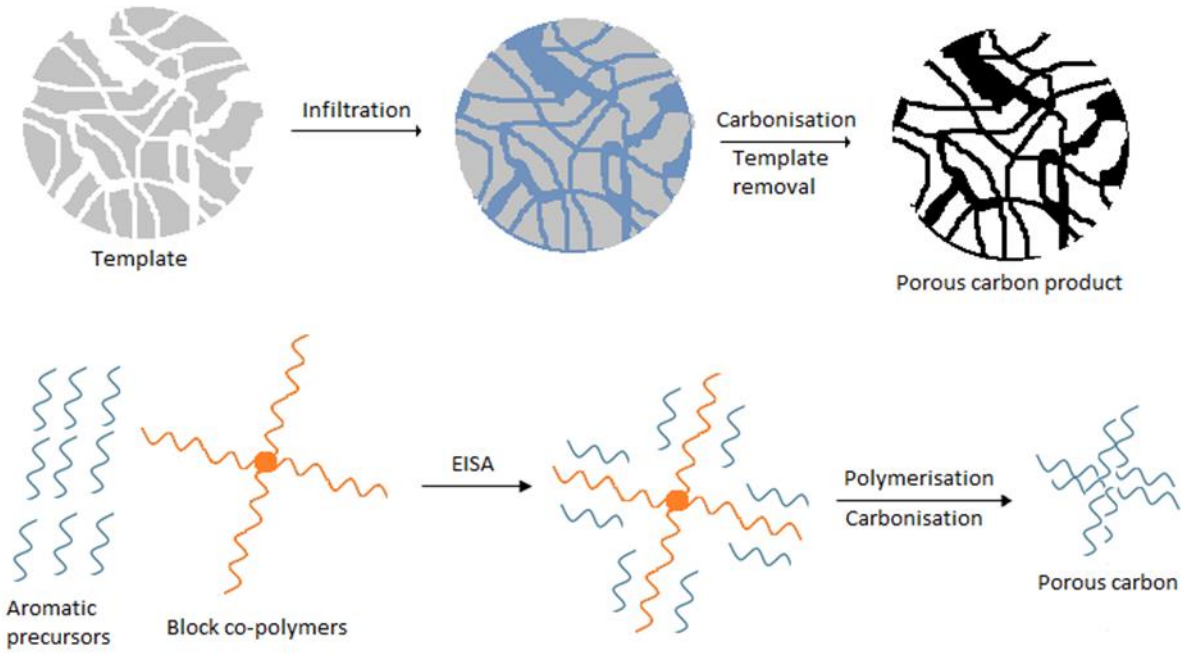

Figure 2.33 (top) Hard and (bottom) soft templating procedures used in HTC for production of porous carbon materials.

HTC has been used to produce porous carbon *via* both hard and soft templating procedures [148]. Since HTC takes place in the aqueous phase, incorporation into existing templating

procedures is simple. Furthermore the functionalised hydrochar synthesised by HTC allows for further modification; a more facile process than when starting from highly aromatic or graphitic carbons [204]. Hard templating procedures are easily replicated under HTC conditions whereby infiltration and carbonisation are performed in a single step [205]. A carbon precursor which dissolves in the solvent is selected (glucose), this is heated under pressure with a nanostructured sacrificial template (silica) which causes polycondensation of carbon precursor onto the sacrificial template, the sacrificial template can then be dissolved (HF, NaOH) to leave only a nanostructured porous carbon. Soft templating procedures can be employed using a similar technique [206]. Block copolymers (polystyrene latexes) are dispersed into aqueous solutions with water soluble precursors (glucose), the polymers form a macro structure *via* self-assembly then hydrothermal carbons form by polycondensation onto the surface of the polymers, after which the polymers can be decomposed to leave only porous carbon spheres.

2.3.4. Applications of Different Specialised Hydrochars

Using the methods discussed in the previous sub-chapter and varying the processing conditions specialised hydrochars can be produced for use in a large variety of different applications. The use of these specialised carbon materials produced by HTC in adsorption and catalysis applications is investigated more in depth because of its relevance to research performed in Chapter 6.

2.3.4.1. Hydrochars in Adsorption

Using hydrochar made from waste biomass in adsorption is a relatively new topic within the literature. "Web of Science" search terms "hydrochar AND adsor*" show an increasing number of publications every year with the first reported in 2011 (Figure 2.34). Currently activated carbon is used in the tertiary treatment phases industrially (food, textiles, petroleum refineries, dyes, explosives) to remove a wide range of organics (pesticides, phenolics, alcohols, surfactants, soluble dyes, *etc*.) and inorganics (ammonia, nitrate, heavy metals) [207]. Therefore, there is a clear demand for carbonaceous adsorbents industrially.

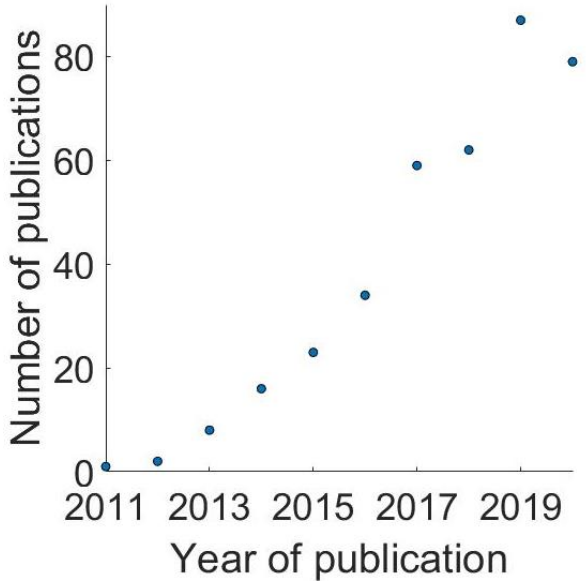

Figure 2.34 Number of publications by year for search term "hydrochar AND adsor*" on "Web of Science".

As discussed in the Section 2.3.4 hydrochar has tuneable physical morphology, surface area, and modifiable surface chemistry (oxygen functionality, metal impregnation, nitrogen doping) [198], [204], [208]. HTC can produce sustainably sourced high-quality adsorbents from low quality waste materials as an alternative to activated carbon, which is mostly sourced from non-renewables [148]. A high quality adsorbent needs to have a high adsorption capacity (the amount of adsorbate that can adhere to the adsorbent) and a fast adsorption rate (the speed at which the adsorbate adheres to the adsorbent) [209]. What is considered a high adsorption capacity and a fast adsorption rate varies based on the type of adsorbate which is being adsorbed. The two factors that are the most important for having a high adsorption capacity and a fast adsorption rate are that the hydrochar has a high surface area (>1200 m^2 g^{-1}) and a large pore network [210]. On top of this the adsorbent needs to be inclined to one or more of the four types of adsorption; ion exchange, physical, chemical or specific [211]. Ion exchange involves the displacement of ionic species attached to the adsorbent, physical adsorption is primarily caused by Van der Waals forces, chemical adsorption occurs due to a reaction between the adsorbate and adsorbent, and specific adsorption requires the use of specific functional groups which are "fitted" to the adsorbate.

There are a few useful analysis methods to estimate a materials efficiency for adsorption such as measuring the surface area (BET), and surface functionality (FT-IR). Actual adsorption capacities and kinetics can be determined by performing kinetic and isothermal adsorption

studies with ideal organic compounds (methylene blue, tetracycline) or inorganic compounds (heavy metals, nitrates) [212]. Adsorption studies are performed by soaking the adsorbent in a representative contaminant solution for a measured period then measuring the concentration of the contaminant after adsorption [213]. Isothermal tests vary the concentration of the contaminant solution for the same amount of time. To these data adsorption isotherms are fitted (Langmuir, Freundlich) to determine the maximum adsorption capacity. Kinetic adsorption analysis varies the time the adsorbent is soaking, to this pseudo-first and pseudo-second order fitting is performed, yielding gives information about the speed and mechanism of adsorption.

Examples of hydrochar being used to adsorb methylene blue have been selected from the literature for comparison with industrial activated carbon and other adsorbents (Table 2.1). Methylene blue (MB) is often used in adsorption studies because it is widely used as a dye in textiles, printing, and food production [214]. MB is a known environmental pollutant from these industries and because of its strong colour is easily quantifiable by ultraviolet–visible (UV-Vis) spectroscopic analysis, these combined make MB an ideal testing contaminant for laboratory analysis of adsorption efficiency. The hydrochars synthesised from coffee husk, acerola pulp, and wastewater sludge have the lowest adsorption capacities of 35, 109, and 63 mg g^{-1} respectively which is significantly less than the highest performing commercial adsorbents at 980 mg g^{-1} [215]–[217]. This lower adsorption capacity is because these hydrochars have no post-treatment after HTC, so their porosity, surface area, and surface functionality are only controlled by the parameters used during HTC (temperature, retention time, pH) and the feedstock processed. This, as stated previously, leads to a hydrochar with less than ideal properties. The synthesis of composite based materials such as heamatite and silicate porous carbon from starch and walnut shell gave much higher adsorption capacities of 370.2 and 434.78 mg g^{-1}. This is a large improvement in adsorption capacity showing at least four times as much capacity for methylene blue, with the added boon of efficient removal and separation provided by the magnetic material [218], [219]. Physical and/or chemical activation of the hydrochar also greatly increased the adsorption capacity shown by camellia oleifera shell and sycamore sawdust at 493.02 and 644 mg g^{-1}; the main reason for this is in increase in surface area [220], [221]. Finally, a hydrochar with better adsorption capacity for methylene blue than some commercial activated carbons is presented by Li *et al.* The synthesis of a polyaminocarboxylate modified hydrochar using etherification, amination, and carboxylation reactions is described to yield a hydrochar with MB adsorption of 1238.66 mg g^{-1} [222]. This research shows the potential to use HTC based methods to produce adsorbents from waste

biomass which can replace existing commercial activated carbon industrially.

Table 2.1 Example adsorption capacities for methylene blue (MB) on hydrochar and other commercially used adsorbents.

Hydrochar precursor (composite)	Adsorption capacity (mg g^{-1})	Reference	Commercial adsorbent	Adsorption capacity (mg g^{-1})	Reference
Coffee husk	34.85	[216]	Commercial activated carbon	980.3	[223]
Acerola pulp	108.88	[215]	New Zealand coal activated carbon	588	[223]
Wastewater sludge	63.3	[217]	Peat	324	[223]
Starch (heamatite)	370.2	[218]	Charcoal	62.7	[223]
Walnut shell (silicate)	434.78	[219]	Straw activated carbon	472.1	[223]
Camellia oleifera shell	493.02	[221]	Groundnut shell activated carbon	164.9	[223]
Sycamore sawdust	644	[220]	Rosa canina seeds activated carbon	47.2	[223]
Bamboo powder	1238.66	[222]	Almond shell activated carbon	1.33	[223]

2.3.4.2. Hydrochars in Catalysis

Historically the primary application of carbonaceous material in catalysis has been as a support material for metals and metal oxides [24]. They can however also act directly as catalysts, called “carbocatalysts” in a variety of different industrial reactions. Carbon based materials offer a more environmentally friendly cheaper alternative to expensive and non-renewable catalysts. Acidified carbonaceous material is widely used in a variety of acid-catalysed reactions such as hydrolysis, dehydration, and esterification [224]. Hydrochar has significant potential both as a carbocatalyst and as a catalyst support material because of the tuneable properties, as discussed in Section 2.3.3 [197], [225].

The main properties which influence the performance of hydrochars in catalysis are surface area, porosity, surface functionality, electron conductivity, hydrophilicity, and elemental composition [24]. Hydrochars exhibit a high amount of heteroatom functionality because of the polymerisation reactions which produce the coke (Section 2.3.1). This functionality is beneficial in a few different ways; they prove as anchoring sites for metals during catalyst synthesis which can enhance dispersion, they increase the hydrophilicity of the surface, and they can interact catalytically to increase the catalyst efficiency [226], [227]. As discussed in Section 2.3.4.1 it is possible to synthesise highly porous carbon materials with large surface areas (>1200 m^2 g^{-1}), adding to the efficiency of the hydrochar as catalysts because there are

more sites for reactions to occur [228]. Finally, the main advantage that HTC offers for catalyst production is the highly tuneable properties of the hydrochar and that it can support a wide range of different metals and metal oxides. The hydrochar catalysts can be designed and optimised for use in specific reactions by varying the processing conditions (feedstock, retention time, processing temperature) and utilising different additives and post-treatment procedures.

In depth examples of different catalytic applications using hydrochar are also described in the following text. Porous hydrochar encapsulated iron nanoparticles have been used to decompose phenol under mild reaction conditions (600 °C, 1 h) in a fixed bed reactor, the highest conversion observed was 98.4% [199]. In this case the phenol is acting as a model compound for the proposed use, the decomposition of biomass tar, which is mainly composed of phenolics, alkylated aromatics, and polycyclic aromatics. The catalytic dehydration of fructose into 5-HMF was also performed using carbon microspheres synthesised directly from glucose *via* HTC with no further processing [229]. This was performed in an ionic liquid at 100 °C using 20% of the weight of fructose in synthesised carbon microspheres after 2 h 5-HMF yield was 79.9%, without any catalyst 5-HMF yield was 10% after 4 h, showing an 8-fold increase in yield with the hydrochar catalyst. This investigation is one of few which uses the hydrochar directly without further modification through addition of inorganics and/or physical/chemical activation after producing the hydrochar. Metal supported onto hydrochar are also developed for catalytic uses, utilising the carbon in lieu of existing supports such as silica or alumina. Palladium nanoparticles have been impregnated onto hydrochar particles. These were used successfully in a Suzuki-Miyaura coupling reaction between 4-iodoanisole and phenylboronic acid to yield 4-methoxybiphenyl at 93% [21]. The Pd/hydrochar showed better catalytic activity for Suzuki-Miyaura coupling reactions between a variety of different aryl halides and boronic acids than commercial Pd (10 wt.%) on charcoal. There are many more examples of hydrochar being used in catalysis in the literature some examples of which are summarised in Table 2.2. These show that hydrochar is a versatile catalyst support material and carbocatalyst which can be effective in numerous different catalytic reactions.

Photocatalysts have also been prepared using HTC for use in renewable solar energy applications [230], [231]. Photocatalysts increase the efficiency for the conversion of solar energy into chemical energy, typically by offering a lower energy reaction pathway. The hydrochar photocatalysts require the addition of photoactive metallics and it cannot be used

simply as a “carbocatalyst”

Table 2.2 Example catalytic applications for hydrochars compared to other commercially used catalysts [199], [232]–[235]**.**

HTC feedstock	Catalyst	Reaction	Yield or conversion (%)	Ref
Iron(III) nitrate nonahydrate($Fe(NO_3)3{\cdot}9H_2O$) catalysts and pinewood sawdust	Iron nanoparticles supported on hydrochar (Fe_2O_3/C)	Thermal decomposition of phenol	90.7 – 98.4	[199]
N/A	No catalyst		48.7	
Straw	Hydrochar	Oxidation of benzylamine by oxygen	95.3	[232]
N/A	No catalyst		16.1	
$CuSO_4{\cdot}5H_2O$, F127, chitosan, and maleic acid	Copper nanoparticles supported on hydrochar	Ullmann C-N coupling	98	[233]
N/A	$CuSO_4$ supported on chitosan		70	
Macroalgae	Sulfonated hydrochar	Esterification of oleic acid and methanol	96.6	[234]
N/A	Amberlyst-15		86.7	
Defatted rice bran	Sulfonated hydrochar	Cellulose hydrolysis	49.6	[235]
N/A	Sulfonated activated carbon		48.9	

2.3.4.3. Further Applications of Hydrochars

Chars and carbonaceous material produced by other methods are often used for soil amendment purposes, hydrochar has potential to be used in the same area [236]. Carbon sequestration (removal of carbon dioxide from the atmosphere) is often used to reduce greenhouse gas emissions, hydrochar has been found to be less effective in this area than other chars because they have a more facile degradation compared to other chars, this has been measured by NH_3, CO_2, and CH_4 emissions from soil which was amended with hydrochar [237]. Hydrochar can also be used to improve the soil properties for agricultural applications, and has potential to increase the nutrient content, water retention, soil pH, cation exchange capacity, and bulk density of the soil [238], [239]. When hydrochar has been added to soil in addition to fertilizers it has been found to increase the yield of various crops, *e.g.* barley, but decrease the yield for others *e.g.* leek [240].

Another emerging application of hydrochars is as sustainable energy storage devices, hydrochars can be used as a type of supercapacitor called an electric double layer

capacitor (EDLC) [241]. EDLCs store energy through the adsorption of ions in the electric double layer, they are reported to have high power density, high coulombic reversibility, long cycle lifetimes, and a wide operational temperature range, because of this they have the potential to replace traditional batteries [242]. Hydrochars can be adapted to have many of the properties required for sustainable EDLCs such as high surface area, chemical stability, cheap production, conductivity, and low density [243]. In the same vein as the production of adsorbents the surface area of hydrochars has to be increased for them to be effective as EDLCs, this can be done as previously stated using physical or chemical activation [148], [244].

Hydrochar can also be used as a support material for anodes and cathodes in different types of types of fuel cells [148]. Polymer electrolyte membrane fuel cells are the most heavily researched application of hydrochar and other carbonaceous materials for use as anodes and cathodes in fuel cell applications [245]. Polymer electrolyte membrane fuel cells consist of an anode, cathode, and an electrolyte. The fuel is oxidised to produce electrons at the anode, these travel to the cathode which combines with protons to form water and energy as products. Hydrochar and other carbonaceous materials are valuable in this application not only because of the same catalytic reasons in the previous sub-chapter but also because carbon is naturally conductive. Hydrochar which has been doped with nitrogen has shown high potential in this field [246].

Nanocomposites synthesised using HTC by encapsulating nanoparticles and arranging them in superstructures have been reported as showing high potential in drug delivery and bioimaging [230]. One example is the synthesis of green-luminescent silver core shell spheres which gave off strong emission under excitation at 340 nm [247]. These particles (and similar materials) can be inserted into human lung cancer cells with no cytotoxic effects, thereby allowing for the identification of cancerous tissue or drug delivery by modifying the surface of the sphere's to more strongly uptake into them.

2.3.5. Synthesis of Hydrochar Type Materials through Solvothermal Methods

As previously discussed in Section 2.1.4, when a different organic solvent is used to process the biomass the method is usually described as solvothermal or alcohothermal [29], [248]–[250]. The application of different solvent/water mixtures under hydrothermal conditions on

biomass is an underdeveloped area in the literature. The use of different solvent/water mixtures drastically changes the properties of the aqueous system which as discussed in Section 2.1.4 this allows for a swath of different reactions to take place and hence the formation of novel products, permitting optimisation of the solvent/water mixture to give highest solid yield, desired surface functionality, highest HHV, *etc.* [28], [251]. Herein all solvent/water mixtures are reported on an organic solvent percentage molarity basis (mol%) to allow for clear comparison between investigations. A variety of organic solvents including acids, esters, phenols, alcohols, ketones, and amines have been applied in the solvothermal processing of biomass [252]. It is important when selecting a solvent to identify low boiling point, low toxicity chemicals which are soluble in water [253].

Of the available organic solvents, simple alcohol water mixtures have been studied the most in solvothermal processing of biomass. This is likely to be because simple alcohols (methanol, ethanol, isopropanol) are cheap, abundant and have relatively low toxicity [250]. Feng *et al.* treated cellulose, lignin, and a 50/50 wt.% mix of cellulose and lignin at 300 °C for 15 min in pure water, ethanol/water (28.5 mol%), and pure ethanol [254]. The solid yield was significantly lower in the ethanol/water mixture reaction and the bio-oil yield was the highest for all feedstocks examined. For cellulose, hydrochar yields were 23%, 6.9%, and 27.9% for the pure water, ethanol/water (28.5 mol%), and pure ethanol respectively and bio-oil yields of 30.25%, 40.3%, and 30.1% were obtained. Under these conditions the water is degrading the biomass through the typical hydrolysis reactions as discussed in Section 2.3.1. However, the ethanol is inhibiting the usual condensation reactions which cause hydrochar formation, and thus is beneficial for achieving a larger yield of bio-oil. Also observed was enhanced solvent permeation into the biomass through SEM analysis of the hydrochar. Yuan *et al.* hydrothermally treated rice straw at 260 °C holding for 3 min in pure water, 3, 11.1, and 23.5 mol% ethanol/water mixtures and pure ethanol [252]. This had a similar effect on the hydrochar yield which was lower in the ethanol/water mixtures at ~38% than in the pure water at ~46%. The inhibition of condensation reactions can also be observed, however, under these milder reaction conditions there is still significant yield of hydrochar. Porous carbon materials have also been produced in ethanol/water mixtures at 8.8, 23.5, 49.4 mol% comparing to pure water and ethanol under the same mild conditions 180 °C for 20 min. The highest surface area porous carbon was obtained from the 8.8 mol% ethanol/water mixture, FT-IR spectroscopy analysis revealed this was due to the selective removal of cellulose from the biomass [249].

2.4. Aerosol-Assisted Sol-Gel (AASG) Synthesis of Catalysts

2.4.1. Bulk Sol-Gel Synthesis

Sol-gel processes are defined by their transition between a sol and gel state by gelation [39]. A sol is a colloidal suspension of amorphous or crystalline solid particles in a liquid, it can have a dense, porous, or polymeric substructure depending on the aggregation behaviour of the solid particles [255]. A gel is a porous covalently bonded solid network with three-dimensional structure surrounded by a liquid phase. The gelation is caused by irreversible reactions forming covalent bonds between the solid particles; because of this the shape and size of the solid particles determines the structure of the gelated network. After a gel has been formed the liquid phase is removed – often by calcination – to produce a stable solid material. If drying of the gel by evaporation causes shrinkage of the gel network by a factor of 5–10 times as a result of capillary forces collapsing the gel network, then the product is referred to as a xerogel. When the gel is dried at a controlled temperature and relative humidity the structural integrity of the network is maintained in the dried product, when this is performed the product is known as an aerogel [256]. When temperature and relative humidity are not controlled carefully the drying stress causes partial destruction of the porous structure and a disordered porous solid is obtained (xerogel) (Figure 2.35).

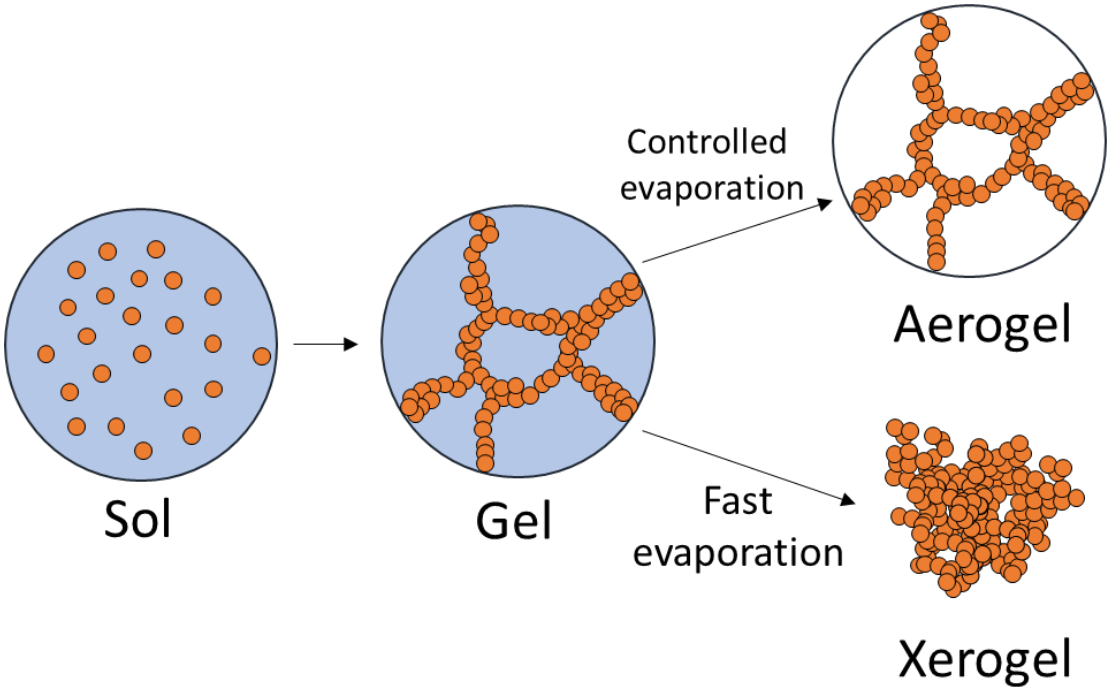

Figure 2.35 Sol-gel synthesis diagram showing the structure of two potential products; aerogels and xerogels.

Research into sol-gel synthesis surged in the 1950s & 1960s because of the potential to produce

heterogeneous silica-based materials with high homogeneity [257]. This proved invaluable as sol-gel processing is used currently to synthesise silica-based materials and mixed metal oxides in a large range of applications such as adsorption [258], catalysis [259], drug delivery [260], and energy storage [261]. The distinction between silica-based and mixed metal oxides is important because they have different chemical reactivity and form structurally distinct gel networks.

2.4.1.1. Mechanisms and Reactions Involved in Traditional Sol-Gel Synthesis

Silica-based processes involve the hydrolysis of Si-OR into silicone hydroxide groups which then, through polycondensation reactions, form a highly structured siloxane network [255]. The precursors for this reaction are typically silicates (stabilised with metal salts *e.g.* Na, K) and silicon alkoxides (*e.g.* tetramethoxysilane & tetraethoxysilane). Silicates are unreactive between pH 1.5 and 4.5 in water, above or below this pH the surface silicates becomes charged because it is no longer stable as Si-OH and therefore sol-gel reactions can be initiated [262]. This means that silicate based processes can be initiated by simple addition of acid or base. In contrast, silicone alkoxides need to be hydrolysed to produce the Si-OH reactive groups before polycondensation reactions can occur; this is achieved through the addition of alcohol/water mixtures for dissolution and acids to increase rate of reaction. This is notably very different to most other polymerisation reactions. The reaction mechanism is the same for silicates and silicon alkoxides, however, it is different in acidic and basic conditions (Figure 2.36). In acidic conditions the reaction is initiated by protonation of the oxygen atom on the silicon creating a alcohol/water leaving group rendering the silicon atom susceptible to nucleophilic attack by water (hydrolysis) or silanol (condensation). In basic conditions the reaction is initiated by nucleophilic attack from a hydroxide (hydrolysis) or siloxide (condensation) which are produced by deprotonation of water and silanol respectively. These two different mechanisms produce more chain-like networks in acidic conditions and more branched networks in basic conditions.

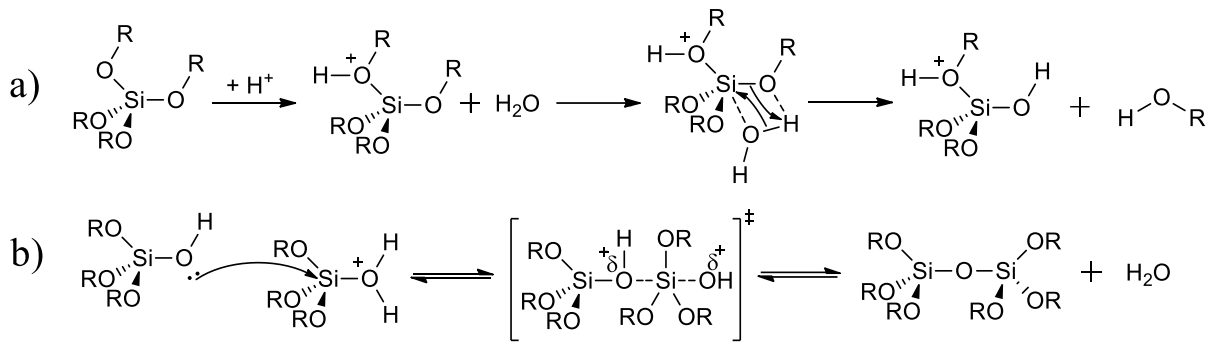

Figure 2.36 General reaction mechanism for (a) acidic hydrolysis and (b) condensation reactions in silicon alkoxides.

Metal oxide based synthesis of sol-gel materials differs because metals have stronger Lewis acid activity (ability to accept a lone pair of electrons) and they can have a wide variety of co-ordination numbers potentially ranging from 2 to 9; silicon always has a co-ordination number of 4 [263]. This increased bonding potential allows for the gel networks in metal oxide based materials to have structurally different bonding geometry based on the metals used, whereas silicon-based sol-gel materials always have tetrahedral geometry. The chemical reactivity of metal oxide sol-gel processes is the same as silica-based, following hydrolysis and condensation mechanisms. However, because of the increased Lewis acid activity of metal alkoxides the hydrolysis and condensation reactions occur over much shorter time-scales compared to silica-based processes. This can be problematic when the addition of water causes spontaneous precipitation, these reaction rates need to be moderated to produce gels instead of precipitates [264]. The reaction rates of metal alkoxides can be controlled by replacing alkoxo ligands with -OR groups that are more difficult to hydrolyse such as carboxylate or bidentate ligands.

Initial condensation reactions form three-dimensional particles which aggregate. This increases the viscosity of the solution up until the gelation point in which a solid structured three-dimensional network is formed (wet gel) [265]. After this gel point has been reached there are still unbound/unreacted species present and chemical reactions are not complete. Therefore, to obtain a more strongly structured three-dimensional network controlled aging can be employed. This increases the strength of the three-dimensional network which is advantageous when aiming to synthesise a porous monolith *e.g.* aerogels. When producing coatings or powder catalysts ageing is a dispensable step in the sol-gel process. Once a gel has been produced the organic compounds used during synthesis are usually removed by heating in an air or inert atmosphere. This is done at low temperatures to yield an amorphous material

but can be done at higher temperatures to yield crystalline materials, however the latter is not typical for sol-gel processes.

2.4.2. Aerosol-Assisted Sol-Gel (AASG) Synthesis

Aerosol/spray drying techniques have no liquid by-products, offer facile and cheap collection processes with no separation, and yields high purity products with unique morphologies requiring only a few preparation steps [35]. A vast array of manmade materials are produced using aerosol-based techniques. A few examples are carbon black particles in tyres, fumed silica in cosmetics and pharmaceuticals, and titania particles used in paints [266], [267]. Aerosol processes simplistically comprise atomising a solution/dispersion into droplets into a carrier gas, these atomised droplets are then heated to induce evaporation of the solvent and condensation of the non-volatile molecules into solid particles (Figure 2.37).

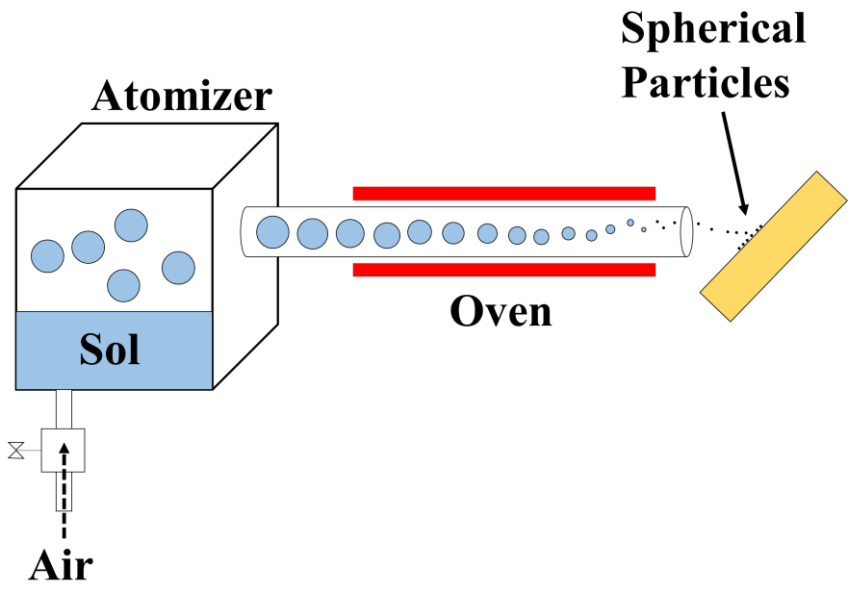

Figure 2.37 Diagram showing the general set-up of aerosol based processes.

Recently aerosol techniques have been applied using sol-gel precursors to establish aerosol-assisted sol-gel (AASG) synthesis as a new innovative sol-gel processing technique [37]. To perform this technique, it is necessary to have a sol which is stable over a reasonable timescale to allow for processing of a full batch (>1 h). The sol needs to contain the same metal precursors to form the structured gel network. Additionally, additives such as solid polymers and surfactants can be used to influence the structure of the extended gel network. When the atomised droplets are heated, hydrolysis and condensation reactions occur in the same vein as bulk synthesis, whilst the additives control the formation of the networks.

2.4.2.1. Additives Used in AASG Processes

There are three main additive types and methods used to control this formation in AASG synthesis (Figure 2.38). One is using micrometre sized particles such as polymer beads and inorganic powders which act as templating agents which the gel network forms around [268]. After synthesising the gel/catalyst these micrometre sized particles are removed to produce a material with pores of a controllable size and shape. Another method uses surfactants or block copolymers to form micelles in the droplet which the gel network is then produced around. This controlled formation in AASG synthesis is often referred to as evaporation induced self-assembly (EISA). A further modification to this process combines both micrometre sized particles and surfactants to produce a very complex precursor sol which can yield a wide variety of multifunctional materials [269].

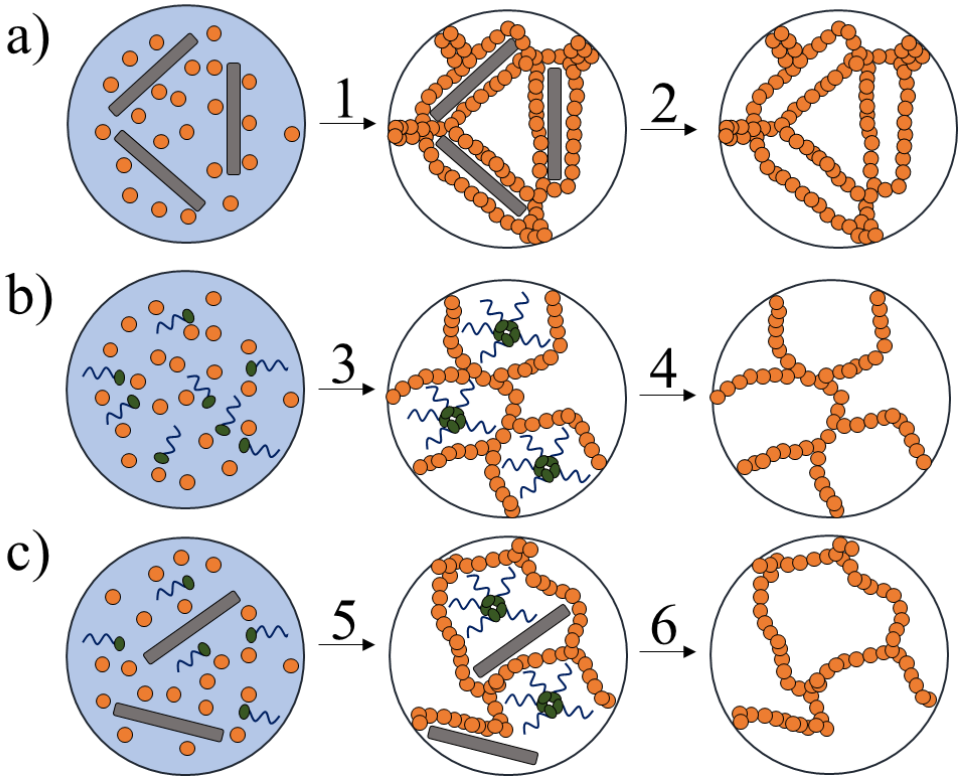

Figure 2.38 AASG synthesis diagram with three different additives to direct structure; (a) solid polymers, (b) surfactants (EISA), (c) a combination of both solid polymers and surfactants. Step 1, 3, and 5 all occur during drying and steps 2, 4, and 6 involve removal of the surfactants and/or solid polymers.

2.4.2.2. Advantages of Evaporation Induced Self-Assembly (EISA) AASG Synthesis

EISA-AASG synthesis (Figure 2.38, b) is the type of sol-gel processing studied in Chapter 7.

This method can be used to produce mesoporous & nonporous spherical materials with consistent and reliable structural morphology [270]. There are a few advantages of EISA-AASG synthesis which makes it excel in the production of these specialised spherical materials. One is because using a surfactant as a templating agent means that the micellisation can be controlled simply with operating conditions [266]. Therefore, micelles can be formed before, after, or during the inorganic polycondensation reactions in the sol-gel. These micelles are trapped within the inorganic material and can be readily removed to release the structured porosity. The control of the micelle formation consequently allows for control of the final catalyst porosity and structure with changes in operating conditions.

EISA-AASG synthesis also has the general advantage of most AASG synthesis type processes where the starting solution(s) are dilute and therefore are metastable during atomisation and storage [266]. Therefore, no gelation or precipitates are synthesised at these points and the solution remains homogeneous. This is a key point to the homogeneity of the final spherical material and allows again for precise control of the final composition of the product based on the reactants used. Finally, high metastability is also displayed in the solid spherical gel particles produced [271]. The main cause of this is "kinetic quenching" which is the trapping of non-reactive species within the inorganic network.

2.4.2.3. Examples of EISA-AASG Synthesis in the Literature

Smeets *et al.* described the application of AASG synthesis with tetrapropylammonium hydroxide as a surfactant structure directing compound to synthesise titanium silicates [272]. The TiO_2-SiO_2 structured catalysts were evaluated using the epoxidation reaction of cyclohexane with cumene hydroperoxide and compared to titanium silicates synthesised *via* hydrothermal methods. The TiO_2-SiO_2 AASG catalysts gave yields up to 62% compared to the 20% yielded from the hydrothermally synthesised catalysts. Structural analysis of the TiO_2-SiO_2 AASG synthesised catalysts showed that many different pore sizes and structures can be produced and controlled, as well as varying the distribution, morphology and homogeneity of the titanium species. They proposed that this process has high potential for application in future industrial applications. Kim *et al.* utilised table salt (NaCl) as a templating agent in the synthesis of silica particles using AASG processing [273]. The process involved a long aging period (<50 h) to create initial three-dimensional gel networks around the solubilised NaCl. During spray drying the droplets formed strong three-dimensional gel networks with NaCl precipitating out and incorporating into the gel structure. Both the silica

and NaCl survived a low temperature calcination procedure (400 °C) after which the salt was easily removed by dissolution in water. The silica catalyst that was synthesised by this method had large surface areas ranging from 200 to 1200 m^2 g^{-1}.

Maksasithorn *et al.* synthesised a silica supported tungsten catalyst (WO_3-SiO_2) using polyethylene glycol monocetyl ether as a surfactant for templating and a typical AASG process for synthesis [274]. This produced a catalyst with a high specific surface area with a small range from 500 to 600 m^2 g^{-1}. This surface area was caused by pores which are all around 2 nm predicted using BET and a Barrett, Joyner, and Halenda model. These pores are produced when the inorganic network forms around the micelles which are then removed after gelation. Additionally, they found that temperatures beyond 650 °C collapsed the porous structure of the catalysts and produced aggregated WO_3 crystals. Another study produced an alumina and silica supported tungsten catalyst by AASG synthesis using pluronic P123, which is a block copolymer, as a surfactant templating agent [275]. This also had a large surface area 525 m^2 g^{-1} with an average pore diameter of around 5 nm. The catalysts were evaluated catalytically based on cross-metathesis of ethene and 2-butene to propene. It was found to be highly selective for propene with high yields (39%). It was theorised that this reactivity was because of the matrix acidity of the tungsten-oxo species. The key finding to extract from these studies and others presented in the literature is that EISA-AASG synthesis is an important option to consider when the aim is to synthesise a consistent homogeneous spherical porous material. This is because the process allows for precise control of the final structure of the material by tuning the reactants, operating conditions, and calcination temperature. The final product can have a defined pore size, surface area, and metallic loading within a small range if the process is correctly designed. This is advantageous to industrial catalytic processes which require consistent homogeneous catalysts.

Chapter 3 Experimental Methods

3.1. Equipment and Materials

3.1.1. Materials

Iron(III) nitrate nonahydrate ACS reagent ≥98%, iron(II) sulfate heptahydrate ACS reagent, ≥99.0%, n-hexane anhydrous 95%, nitric acid puriss p.a. ≥65%, methanol anhydrous 99.8%, ethanol absolute EMPLURA®, isopropyl alcohol ≥99.7% FCC FG, hydrochloric acid fuming ≥37%, iron ≥99% reduced powder (fine), aluminum chloride hexahydrate, cobalt(II) nitrate hexahydrate, molybdenum(V) chloride 95%, nickel(II) nitrate hexahydrate 99.999%, poly(ethylene glycol)-block-poly(propylene glycol)-block-poly(ethylene glycol) average Mn ~5,800 (pluronic P123), tetraethyl orthosilicate ≥99.0% (GC), vanadium(IV) oxide sulfate hydrate 97%, aluminum isopropoxide ≥98%, 5-(hydroxymethyl)furfural ≥99% FG, ammonium molybdate 99.98% trace metals basis, iron(III) chloride reagent grade 97%, ammonium hydroxide 28-30 wt.% solution of NH_3 in water p.a, iodobenzene 98%, phenylacetylene 98%, ethylene glycol anhydrous 99.8%, potassium carbonate anhydrous free-flowing Redi-Dri™ ACS reagent ≥99%, and diphenylacetylene 98% were all purchased from Sigma Aldrich (Dorset, UK). Deionized water was obtained from a Suez L300130 (>1M Ω cm). Carbon dioxide and helium was supplied by a BOC cylinder. Iron (II, III) oxide 97% (metals basis), sodium hydroxide pellets 98%, and L11860 carbon powder activated Norit GSX steam activated acid washed, were all purchased from Alfa Aesar. Methylene blue chloride trihydrate purchased from Bio Basic. Acetone >95% technical, phosphoric acid pure ACROS Organics™ was purchased from Fisher Scientific. Avocado seeds were collected from fresh avocados supplied by Marks and Spencer Group plc. Bread waste was supplied by Bradgate Bakery in Leicester UK, part of the Samworth Brothers food manufacturing company.

3.1.2. Instrumentation Diagrams for Pressurised Reaction Vessels

Instrumentation diagrams for the pressurised reaction vessels used in this research are shown below in addition to a picture of the reactor setup. Nomenclature is as follows; B is a BOC gas cylinder fitted with a Harris regulator, TIC indicates a thermocouple which measures and controls the temperature, TI is a thermocouple which only measures the temperature, PG is a pressure gauge, PI is an electronic pressure indicator, and V is a valve.

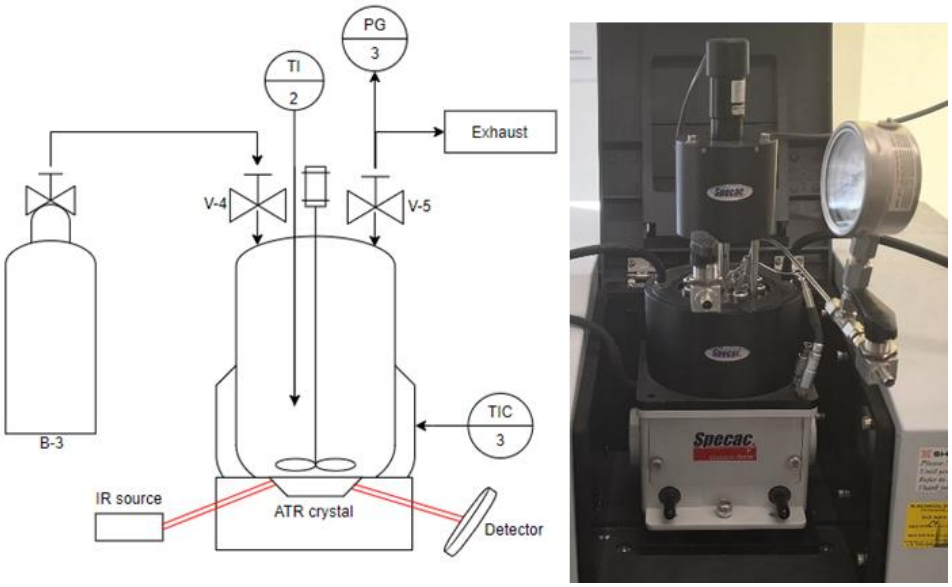

Figure 3.1 Instrumentation diagram and photograph for 22 mL Reaction Cell Top Plate for Golden Gate™ ATR FT-IR (Specac, Orpington, UK) used for research presented in Chapter 4.

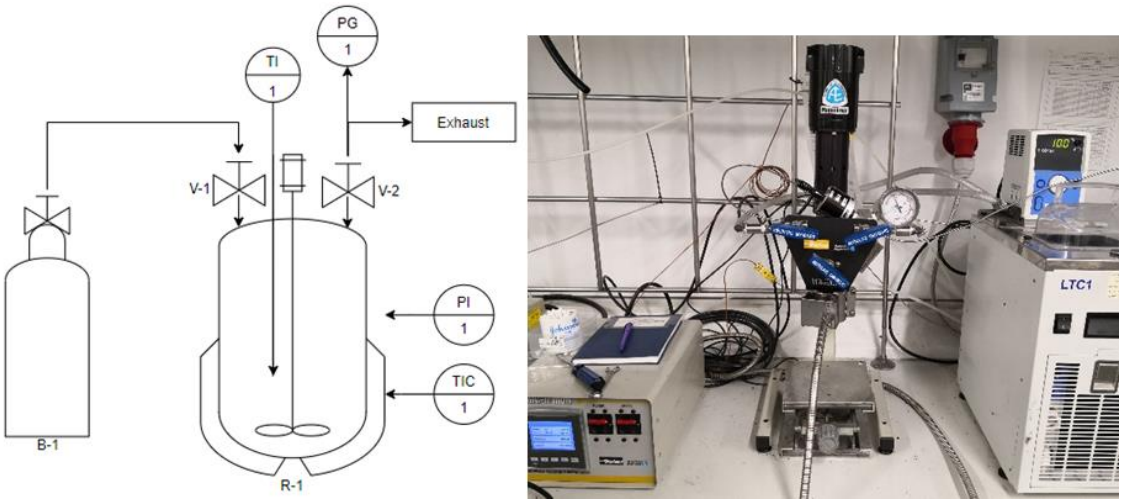

Figure 3.2 Instrumentation diagram and photograph for 50 mL E-Z Seal Autoclave Engineers pressurised reaction vessel (Parker, Huntsville, USA) used for research presented in Chapter 5.

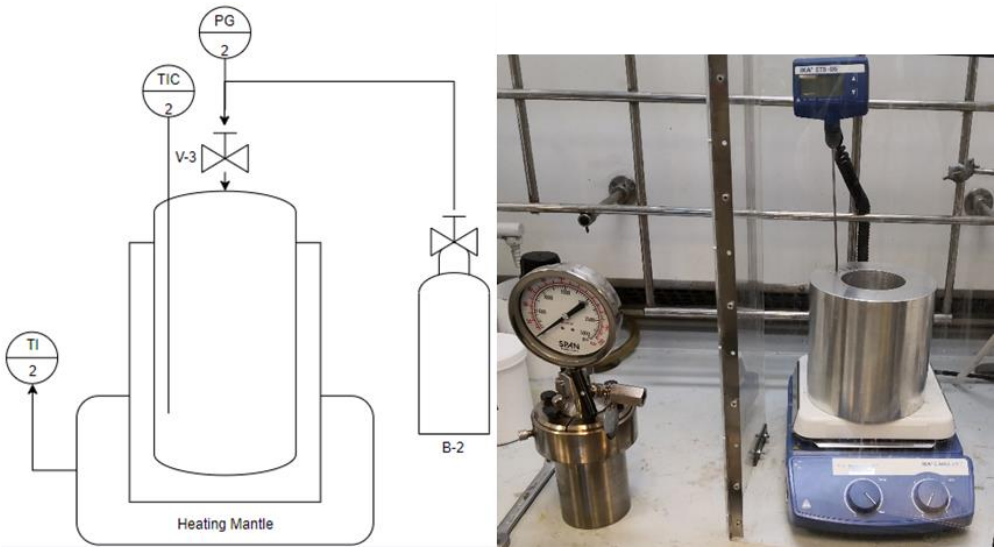

Figure 3.3 Instrumentation diagram and photograph for 300 mL Parr autoclave Series 3050, (Parr instrument company, Illinois USA) used for research presented in Chapter 6.

3.1.3. Optical Trapping Configuration

Liquid droplets were delivered to a small trapping cell, of aluminium construction, with approximate dimensions 10 × 2 × 1 cm. Windows made from borosilicate cover-slips allowed the passage of the laser beams through the cell. Droplets were generated using an ultrasonic nebuliser (aerosonic, combineb model 3019) to generate a mist which flowed into the cell through ¼" PTFE tubing. A right angle turn in the tubing is achieved using a Portex PVC connector tube.

Droplets were trapped using counter-propagating Nd:Yag laser beams operating at 1064 nm. The typical laser beam powers required for stable trapping were 15 mW through the top objective and 10 mW through the lower objective. The objective lenses were Mitutoyo x50 NA 0.42 long working distance objectives. The asymmetric power balance was required to force the particle into the optical focus plane of the lower objective, thereby allowing focused images to be acquired. The Nd:Yag beam is passed through a beam splitter (Oz Optics) to obtain two separate fibre-coupled beams. Both beams are then expanded and collimated so that they slightly overfill the back apertures of the objective lenses. Dichroic mirrors (CVI Melles Griot) reflect the laser beams but allow transmission of illumination light and the Raman signals. The LED illumination (Comar Optics) is filtered to prevent interference with the Raman signal.

Raman spectra were acquired by probing the droplet using a 514.5 nm laser. The laser was

directed through the lower objective lens and focussed onto the droplet. The backscattered Raman signal was collected using the same lens and focussed into a spectrometer (Acton SP2500i and Princeton Instruments Spec 10 CCD). A 600 grooves/mm grating was calibrated using spectrophotometric grade toluene as a reference. Typical laser power was 2 mW, acquisition time was 30 s, and the 514.5 nm laser was shuttered such that the droplet was only illuminated during collection of spectra.

3.2. Procedures and Methods

3.2.1. Synthesis of Magnetic Carbon Composites (Fe/C) from Avocado Seeds (AS) Using HTC

All avocado seeds (AS) processed were between 10 and 15 grams. AS are composed of carbohydrates (~49%), proteins (~15-16%), lipids (~18%), moisture (~15%), and ash (~2%) [276]. AS were dried in an oven (Memmert, Schwabach, Germany Model) at 100 °C for 24 h and subsequently stored in a cold room at 5 °C. Dried avocado seeds (DAS) were pre-treated by refluxing in sodium hydroxide (0.1 M, 50 mL) at 70 °C for 2 h to remove tannins and dyes [277] prior to separation by filtration and washing with deionized water (3 × 50 mL). The DAS were then dried in an oven (100 °C, 24 h). The DAS were soaked in a solution of 1:2 mol ratio Fe^{2+}/Fe^{3+} (0.5 M $FeSO_4 \cdot 7H_2O$, 1 M $Fe(NO_3)_3 \cdot 9H_2O$, 50 mL) for ≥3 days. Subsequently the soaked DAS and iron solution was transferred into a 300 mL Parr autoclave (Figure 3.3) along with sodium hydroxide solution (1 M, 50 mL). The vessel pressurised with carbon dioxide (30 bar) and transferred to an aluminium block preheated to 230 °C using a heating mantle (C-MAG HS7, IKA®, Oxford UK). The temperature was monitored using a thermocouple. The internal temperature reached 230 °C after 45 min and this temperature was maintained for 3 h. The reaction was then quenched in a water bath for 30 min. Solid Fe/C was collected by vacuum filtration and soaked in acetone (50 mL) for 24 h. It was then subject to a further vacuum filtration and then washed with deionized water (50 mL × 3) and dried in an oven (100 °C, 24 h). The Fe/C was then heated in a tube furnace to 400 °C (ramp rate 6.5 °C min^{-1}) under constant nitrogen gas flow and held at that temperature for 1 h before cooling to room temperature. The resultant product was ground using a pestle and mortar and sieved to a size fraction of 38-212 μm using mesh Retsch steel sieve (test sieve ISO 3310-1 body 316 mesh s-steel/RF body 200 mm × 50 mm). Particles < 38 μm were also retained in order to compare to the larger grains in order to investigate any particle size effects. The larger particles will herein be denoted as Fe/C particles (38-212 μm) and the smaller as Fe/C powder (< 38 μm).

For clarity a flow chart displaying the synthesis steps as a flow diagram is given in Figure 3.4

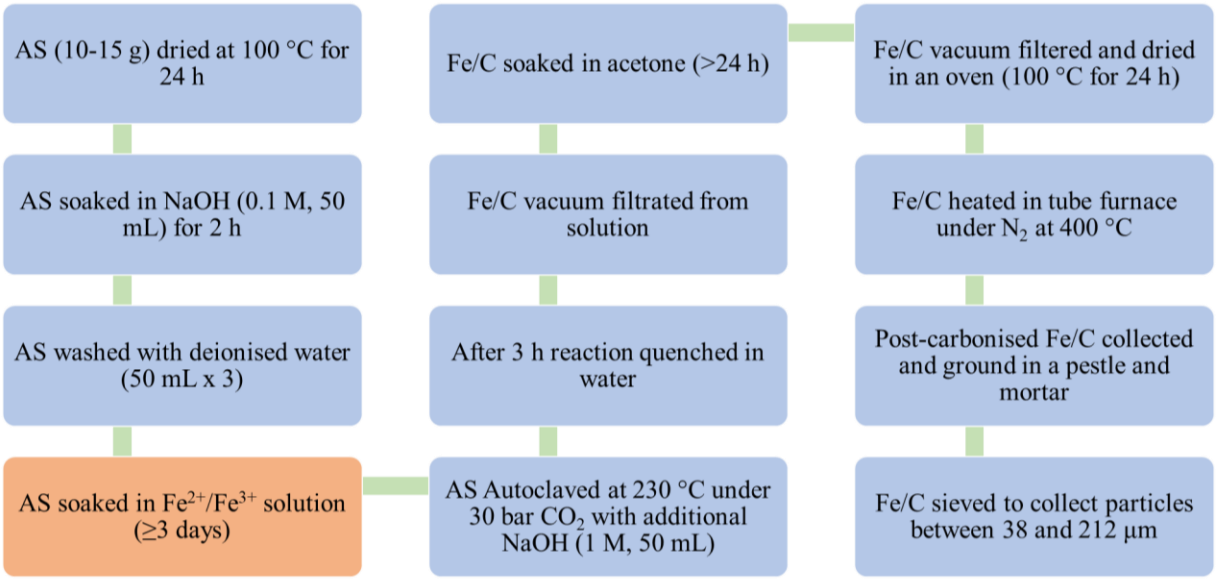

Figure 3.4 Flow chart describing the Fe/C synthesis process in full, essential iron soaking step highlighted in orange.

Hydrochar without iron supported on it was also synthesised by this method by removing the iron soaking step (displayed in orange in Figure 3.4) and adding additional deionized water (50 mL) in the reaction vessel during HTC in lieu of this solution. This was also separated into hydrochar particles (38-212 µm) and the smaller hydrochar powder (< 38 µm).

Following this synthesis, the amount of ethanol in the solvent was varied during HTC to examine the effect on the Fe/C synthesised. This was done by varying the amount of ethanol in the Fe^{2+}/Fe^{3+} soaking solution and sodium hydroxide processing solution (1 M, 50 mL) Table 3.1.

Table 3.1 Ethanol/water mixture molar and volumetric concentrations used in synthesis of Fe/C.

Ethanol mol%	Ethanol vol%	Ethanol in Fe^{2+}/Fe^{3+} soaking solution (mL)	Ethanol in sodium hydroxide processing solution (mL)
3.0	10	5	5
6.7	20	10	10
11.1	30	15	15
16.6	40	20	20
23.5	50	25	25
32.0	60	30	30
42.9	70	35	35
56.9	80	40	40
75.3	90	40	50

Fe/C and hydrochar synthesised by this method were characterised by: AAS, catalytic testing, XRF, FT-IR, SEM, XRD, adsorption testing, and BET surface area analysis the details are presented in sections: 3.3.1, **Error! Reference source not found.**, 3.3.3, 3.3.4, 3.3.8, 3.3.9, REF _Ref80884212 \r \h 3.3.12, 3.3.13.

3.2.2. Synthesis of Magnetite Nanoparticles

Iron chloride hexahydrate (6.1 g) and iron sulphate heptahydrate (4.2 g) were dissolved in deionized water (100 mL) and heated to 90 °C. When the desired temperature was reached, ammonium hydroxide (25%, 10 mL) was added, and the solution was stirred for another 30 min at 90 °C. The reaction mixture was cooled to room temperature and the solid magnetite nanoparticles were collected by vacuum filtration and washed with deionized water (3 × 25 mL).

3.2.3. HTC of Dried Bread Waste (DBW)

Bread waste was stored in a cold room at 5 °C prior to drying in an oven (100 °C, 24 h). The weight of dry and wet bread waste was measured and noted (Thermo Fisher Scientific MH-214 model analytical balance). The dried bread waste was ground using a pestle and mortar then separated by particle size using 4 mesh sieves (Sigma Aldrich). This separated the dried bread waste (DBW) into five different particle sizes; < 63 μm, 63-125 μm, 125-250 μm, 250-500 μm, and >500 μm. DBW (5 g) with particle size 63-125 μm was made up into a 20 wt.% slurry in deionized water (20 g). This slurry was transferred to a 50 mL EZ seal autoclave (Figure 3.2). The reaction vessel was pressurised with either helium (He) or carbon dioxide (CO_2). Slurry was processed at three different temperatures (160, 180 or 200 °C) and three different retention times (30, 60 or 90 min) under constant agitation with an impeller (500 RPM). After the retention time the vessel was quenched in an ice bath. The solid (hydrochar) and aqueous fraction were separated by vacuum filtration. Aqueous fraction was syringe filtered (0.2 μm) and stored in a cold room at 5 °C. Hydrochar was collected, dried in an oven (100 °C, 24 h), and stored in a cool dry place (Table 3.2). The resulting hydrochar was weighed to calculated yield (Equation 3.1).

Table 3.2 Different HTC processing conditions investigated on DBW.

Temperature (°C)	Retention time (Min)	Pressurising gas
160	30	He
160	60	He
160	90	He
180	30	He
180	60	He
180	90	He
200	30	He
200	60	He
200	90	He
160	30	CO_2
160	60	CO_2
160	90	CO_2
180	30	CO_2
180	60	CO_2
180	90	CO_2
200	30	CO_2
200	60	CO_2
200	90	CO_2

$$Hydrochar\ Yield\ (\%) = \frac{Weight\ of\ Dried\ Hydrochar}{Weight\ of\ Dried\ Ground\ Bread\ Waste\ Used} \times 100$$

Equation 3.1 Calculation of bread waste hydrochar yield. Weight of dried bread waste was 5 g ± 0.01 g in all experiments.

Additional reactions were performed using central reaction conditions, 180 °C and 60 min, pressurised with carbon dioxide (CO_2). These were performed on the four other particle sizes of DBW 63 μm, 125-250 μm, 250-500 μm, and >500 μm. Ethanol/water mixtures detailed in Table 3.3 were evaluated using the same 63-125 μm DBW pressurised with helium (He). Finally, a reaction using palmitic acid (PA) (3.4 g) instead of carbon dioxide (CO_2) or He on 63-125 μm DBW was also performed.

Table 3.3 Ethanol/water mixtures used in HTC of DBW at 180 °C and 60 min under CO_2.

Ethanol (mL)	Water (mL)	Ethanol (wt.%)	Ethanol (mol%)
2	18	8.1	3.0
4	16	16.5	6.7
6	14	25.3	11.1
8	12	34.5	16.6
10	10	44.1	23.5
12	8	54.2	32.0
14	6	64.8	42.9
16	4	75.9	56.9
18	2	87.7	75.3

All bread waste hydrochar was characterised by: FT-IR, TGA, Bomb calorimetry, SEM, and CHNS analysis presented in sections: 3.3.4, 3.3.6, 3.3.7, 3.3.8, 3.3.11. The aqueous fraction was analysed by GC-MS presented in section 3.3.5.

3.2.4. FT-IR of Different Alcohol/Water Mixtures

Alcohol/water mixtures were made up to a volume of 10 mL, measured by weight with a Fischer Scientific MH-214 model analytical balance. Methanol, ethanol, and isopropanol water mixtures were produced at 5 vol% intervals for analysis at room temperature and 10 vol% intervals for analysis in the hydrothermal cell shown in Figure 3.1 (Table 3.4).

Table 3.4 Methanol/water mixtures analysed using FT-IR.

Methanol (g)	Water (g)	Methanol (vol%)	Methanol (wt.%)	Methanol (mol%)
0.40	9.5	5	4.0	2.1
0.79	9	10	8.1	4.3
1.19	8.5	15	12.3	6.7
1.58	8	20	16.5	9.4
1.98	7.5	25	20.9	12.2
2.38	7	30	25.3	15.3
2.77	6.5	35	29.9	18.7
3.17	6	40	34.6	22.3
3.56	5.5	45	39.3	26.3
3.96	5	50	44.2	30.6
4.36	4.5	55	49.2	35.3
4.75	4	60	54.3	40.4
5.15	3.5	65	59.5	45.9
5.54	3	70	64.9	51.9
5.94	2.5	75	70.4	58.4
6.34	2	80	76.0	65.5
6.73	1.5	85	81.8	73.1
7.13	1	90	87.7	81.4
7.52	0.5	95	93.8	90.4

Table 3.5 Ethanol/water mixtures analysed using FT-IR.

Ethanol (g)	Water (g)	Ethanol (vol%)	Ethanol (wt.%)	Ethanol (mol%)
0.39	9.5	5	4.0	1.4
0.79	9	10	8.1	3.0
1.18	8.5	15	12.2	4.8
1.58	8	20	16.5	6.7
1.97	7.5	25	20.8	8.8
2.37	7	30	25.3	11.1
2.76	6.5	35	29.8	13.7
3.16	6	40	34.5	16.6
3.55	5.5	45	39.2	19.9
3.95	5	50	44.1	23.5
4.34	4.5	55	49.1	27.5
4.74	4	60	54.2	32.0
5.13	3.5	65	59.4	37.1
5.53	3	70	64.8	42.9
5.92	2.5	75	70.3	49.4
6.31	2	80	75.9	56.9
6.71	1.5	85	81.7	65.4
7.10	1	90	87.7	75.3
7.50	0.5	95	93.7	86.7

Table 3.6 Isopropanol/water mixtures analysed using FT-IR.

Isopropanol (g)	Water (g)	Isopropanol (vol%)	Isopropanol (wt.%)	Isopropanol (mol%)
0.39	9.5	5	4.0	1.1
0.79	9	10	8.0	2.3
1.18	8.5	15	12.2	3.7
1.57	8	20	16.4	5.2
1.96	7.5	25	20.7	6.9
2.36	7	30	25.2	8.7
2.75	6.5	35	29.7	10.9
3.14	6	40	34.4	13.2
3.53	5.5	45	39.1	15.9
3.93	5	50	44.0	19.0
4.32	4.5	55	49.0	22.5
4.71	4	60	54.1	26.5
5.10	3.5	65	59.3	31.1
5.50	3	70	64.7	36.5
5.89	2.5	75	70.2	42.8
6.28	2	80	75.8	50.3
6.67	1.5	85	81.6	59.2
7.07	1	90	87.6	70.0
7.46	0.5	95	93.7	83.3

Ambient temperature analysis was performed using a Specac Quest ATR. Disposable glass pipettes were used to transfer the solutions onto the ATR crystal. FT-IR spectroscopy measurements were performed with resolution of 4 cm^{-1} and 100 scans on a Shimadzu IRAffinity-1S (Shimadzu, Kyoto, Japan) with a range of 400-4000 cm^{-1} (Section 3.3.4). High temperature and high pressure analysis was performed using the 22 mL Specac reaction cell top plate for golden gate™ ATR (Section 3.1.2, Figure 3.1). For high temperature analysis the alcohol/water mixtures were sealed in the reaction vessel which was pressurised with helium (30 bar), and heated to 25, 50, 100, 150, 175, and 200 °C being held at temperature for analysis using FT-IR. Analysis conditions were; resolution of 4 cm^{-1}, 250 scans, and a range of 400-4000 cm^{-1}. Data produced were analysed by methods presented in Section 3.3.16.

3.2.5. Benchtop Sol-Gel Synthesis Procedures

For the metal salts precursors, a stock solution of 0.05 M hydrochloric acid was prepared from concentrated HCl (32%, 1.23 mL, 1.43 g) in a volumetric flask (250 mL) up to the mark with deionized water. Pluronic P123 (4.64 g) was dissolved in 0.05 M HCl (30 mL) and ethanol (10 mL) to make a 0.02 M “organic” solution. Then the support metal, either aluminium chloride hexahydrate (4.83 g) or tetraethyl orthosilicate (4.17 g) was dissolved in 0.05 M HCl

(30 mL) and ethanol (10 mL) to make a 0.8 M “inorganic” solution. The catalytic metal salt was dissolved in the inorganic solution and made to a concentration of 0.016 M in the solution. The catalytic metal salts used were cobalt (II) nitrate hexahydrate, molybdenum (V) chloride, vanadium (IV) oxide sulfate hydrate, and nickel (II) nitrate hexahydrate. The inorganic solution was heated to 80 °C under reflux, to this solution the organic solution was added dropwise. This solution was then heated under reflux to 160 °C for and held for 1 h. The solution was aged at room temperature for an extended period to form a gel (>2 weeks). The gel was dried in an oven (200 °C, 24 h), this dried gel was calcined in a furnace by ramping to 600 °C holding for an hour, then further ramping to 800 °C and holding for an additional two hours. After this the xerogel was collected, ground and stored in a cool dry place. The nomenclature for these catalysts is the metal followed by support material with an affix for the state the material is in *e.g.* nickel alumina as a catalyst is NiAl-Cat.

For the alkoxide precursors, pluronic P123 (3.48 g) was dissolved in ethanol (40 mL) to make a concentration of 0.015 M. To this the catalytic metal salt was added and made to a concentration of 0.012 M. The catalytic metals salts used were cobalt (II) nitrate hexahydrate, molybdenum (V) chloride, vanadium (IV) oxide sulfate hydrate, and nickel (II) nitrate hexahydrate. Aluminium isopropoxide (4.90 g) was dissolved in ethanol (10 mL) and concentrated nitric acid (68%, 10 mL) to make a concentration of 1.2 M solution. This alkoxide solution was added dropwise under stirring to the pluronic P123 and catalytic metal solution. This solution was used in Section 6.5. The solution was aged at room temperature for an extended period to form a gel (>2 weeks). The gel was dried in an oven (200 °C, 24 h), and then calcined in a furnace by ramping to 600 °C holding for an hour then further ramping to 800 °C and holding for an additional two hours. After this the xerogel was collected, ground and stored in a cool dry place. Alkoxide synthesised catalysts have the prefix Alk, a table for all the reference names is displayed (Table 3.7).

Table 3.7 Reference nomenclature for the sol-gel catalysts synthesised with the additional affixes Sol, Gel, Cat, colours are shown in Appendix 5.

Reference	Metal	Support	Synthesis Conditions	Colour of Catalyst
NiAl	Nickel	Alumina	Salt	Light blue
CoAl	Cobalt	Alumina	Salt	Black
MoAl	Molybdenum	Alumina	Salt	White
VAl	Vanadium	Alumina	Salt	Dirty Green
NiSi	Nickel	Silica	Salt	Grey
CoSi	Cobalt	Silica	Salt	Dark grey
MoSi	Molybdenum	Silica	Salt	Mint green
VSi	Vanadium	Silica	Salt	Orange
AlkNiAl	Nickel	Alumina	Alkoxide	Light blue
AlkCoAl	Cobalt	Alumina	Alkoxide	Bright blue
AlkMoAl	Molybdenum	Alumina	Alkoxide	White
AlkVAl	Vanadium	Alumina	Alkoxide	Yellow

3.2.6. Aerosol Analysis (*operando* Raman)

For AASG syntheses, the freshly mixed solution was transferred into a nebuliser (aerosonic, combineb model 3019) that delivered a mist of aerosol droplets into a trapping cell, the precise configuration of which is described in Section 3.1.3. From this aerosol, a single droplet could be trapped and lowered into the centre of an annular ceramic heater, with the applied power then increased incrementally (0-14 W) to raise the internal temperature of the cell (≤ 200 °C). Direct temperature measurements were not possible since the positioning of thermocouples sufficiently close to the trapped droplet would disrupt the trapping beams. Instead, the cell temperature was inferred from calibration measurements performed on an empty cell, where a thermocouple could be positioned directly in the centre of the annular heater to measure the temperature over a range of powers (Figure 3.5). The elevated temperature in the cell initiated EISA and the incipient formation of the Ni/Al_2O_3 catalyst, which was spectroscopically analysed by *operando* Raman. Measurements were typically taken at the onset of trapping, and subsequently at intervals of 10 or 30 s over the spectral range 500-3100 cm^{-1} until the droplet was lost from the optical trap. In this way, the catalyst formation could be spectroscopically interrogated under conditions representative of the AASG process.

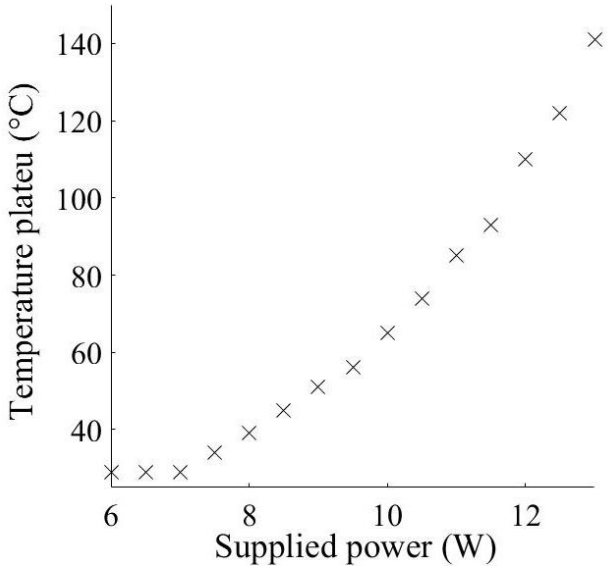

Figure 3.5 Temperature calibration used for heated cell in Section 7.2.3.

3.3. Characterisation and Analysis Techniques

3.3.1. Acid Digestion of Fe/C and Production of Iron Standards for Analysis by AAS

A stock solution of 1:3 nitric: hydrochloric acid (aqua regia) was made by mixing concentrated nitric acid (30 mL) with concentrated hydrochloric acid (90 mL). A stock solution of 1% nitric acid was prepared by transferring concentrated nitric acid (15 mL, 64-66%) to a 1 litre volumetric flask and making it to the mark with deionized water. Iron standards were produced to provide a calibration curve for the absorbance in the Perkin Elmer AAS AAnalyst 400 (Perkin Elmer, Massachusetts, USA). Iron powder (0.1 g) was dissolved in aqua regia (10 mL) under gentle heating (80 °C) for 4 h. This solution was transferred to a 100 mL volumetric flask and made to the mark with 1% nitric acid. This solution was diluted by transferring 30 mL into a 100 mL volumetric flask and made to the mark with 1% nitric acid to produce a 1000 ppm Fe standard. This was further diluted by transferring 5 mL of the 1000 ppm Fe standard into a 50 mL volumetric flask and making to the mark with 1% nitric acid to make a 100 ppm Fe standard. Dilutions were performed from this 100 ppm Fe standard to make the final calibration standards in 50 mL volumetric flasks following (Table 3.8).

Table 3.8 Dilutions from 100 ppm Fe stock used to produce the iron standards for AAS analysis.

Standard (ppm)	Volume of 100 ppm Fe Stock (mL)	Volume of Deionized Water (mL)
2	1	49
4	2	48
6	3	47
8	4	46
10	5	45
12	6	44

For the Fe/C produced by 3.2.1. Fe/C (0.02 g) was weighed out and carbonised (400 °C, 2 h). The remaining material was then dissolved in aqua regia (10 mL) under gentle heating (80 °C) for 4 h. This solution was cooled and decanted into a 100 mL volumetric flask and made to the mark with 1% nitric acid. This solution was diluted by transferring 10 mL into a 100 mL volumetric flask and making to the mark with 1% nitric acid [278]. All samples were analysed on Perkin Elmer AAS AAnalyst 400 (Perkin Elmer, Massachusetts, USA).

3.3.2. Catalytic Testing - Hydroalkoxylation of Phenylacetylene with Ethylene Glycol

The catalytic performance of Fe/C was evaluated in the hydroalkoxylation of phenylacetylene with ethylene glycol, yielding 2-benzyl-1,3-dioxolane (2B13D) as the desired product (Figure 3.6) [272], [273]. Iodobenzene (1 mmol, 0.20 g/0.11 mL), phenylacetylene (2 mmol, 0.20 g/0.22 mL), potassium carbonate (2 mmol, 0.276 g), and catalyst (0.25 mmol iron oxide, magnetite nanoparticles 0.058 g, Fe/C and hydrochar 0.116 g) were dissolved in ethylene glycol (3.34 g / 3 mL) and stirred for 48 h under reflux. The solid material was then separated using an external magnet. Deionized water (5 mL) and hexane (5 mL) were then added to the remaining solution and the hexane layer separated. The hexane extract was analysed by GC-MS method presented in Section 3.3.5 with 2-benzyl-1,3-dioxolane (2B13D) calibration curve and dibenzofuran internal standard $R^2 = 0.991$.

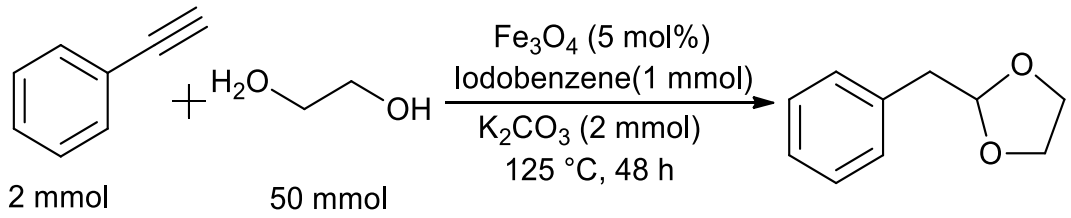

Figure 3.6 Schematic of the hydroalkoxylation of phenylacetylene with ethylene glycol to yield 2-benzyl-1,3-dioxolane (2B13D).

3.3.3. X-ray Fluorescence (XRF)

XRF analysis of the Fe/C produced by 3.2.1 was performed on an Olympus delta DP-2000-C (GP Technical Equipment, Savannah, USA) using a titanium filter, tube voltage of 15 kV and a current of 55 μA. These conditions are selected because they provide the ideal analysis of light elements Fe and below. Fe/C particles and powder samples were transferred to into transparent polymer containers which the X-rays could penetrate without providing interference signals in the XRF results. This analysis measures iron content accurately at the depth that the X-ray laser penetrates the solid material. Quantification was performed with calibration standards produced from magnetite (iron(II,III) oxide) and activated carbon following Table 3.9.

Table 3.9 Weights used for production of the standards for XRF analysis.

Wt.% Fe	Fe_3O_4 (g)	Activated carbon (g)
0	0.000	0.500
5	0.052	0.448
10	0.104	0.396
15	0.155	0.345
20	0.207	0.293
25	0.259	0.241
30	0.311	0.189
35	0.363	0.138
40	0.414	0.086
45	0.466	0.034

3.3.4. Fourier-Transform Infrared (FT-IR) Spectroscopy

FT-IR measurements were performed with a Shimadzu IRAffinity-1S. Resolution used was always 4 cm^{-1}, with a scanning range between 4000-400 cm^{-1}, average scans varied between 100 and 4000. A Specac Quest ATR Diamond Accessory (Specac, Orpington, UK) was used for ambient condition measurements. A Specac Golden Gate™ ATR Reaction Cell used for

high temperature/pressure analysis Section 3.1.2. Stirrer used at 10 V/50 RPM; external cooling provided by 5 mm diameter tubing with constant running water. Internal heating was controlled using a Golden Gate High Temperature Top-Plate + Controller (Specac, Orpington, UK).

3.3.5. Gas Chromatography-Mass Spectrometry (GC-MS)

Analysis of volatiles within the aqueous fractions produced during HTC was performed on a Shimadzu gas chromatograph mass spectrometer QP2010 SE (Buckinghamshire UK). Prior to analysis samples were syringe filtered using Fisherbrand nylon syringe filter (25 mm diameter 0.2 µm pore size) to remove small particles. Analysis was carried out using a DB5-MS column (24.5 m, 0.25 mm, 0.25 µm) 1 µL of aqueous phase was injected at 250 °C with an initial oven temperature of 40 °C which was raised to 240 °C at 10 °C min^{-1}. High purity helium (A Grade, 99.996%, BOC) was used as a carrier gas at a flow rate of 1 mL min^{-1}.

3.3.6. Thermogravimetric Analysis (TGA)

Thermogravimetric analysis was performed on Perkin Elmer TGA 4000 (Perkin Elmer, Massachusetts, USA). This provided proximate analysis of the hydrochars (moisture, fixed carbon (FC), volatile matter (VM), and ash). The program method used was as follows: initial holding temperature 40 °C for 5 minutes under N_2 atmosphere (100 mL min^{-1}), after initial holding period temperature ramped at 10 °C min^{-1} until 800°C. Finally, the flow gas was changed to oxygen (50 mL min^{-1}).

3.3.7. Bomb Calorimetry

Calorific analysis of energy content was performed by bomb calorimetry using a Parr 6100 Calorimeter (Parr, Illinois, USA) analysis conditions used were: 30 bar oxygen, 10 cm ignition wire. The calorimeter was calibrated using benzoic acid of a known calorific value. The samples analysed were produced by method following Section 3.2.3. Analysis was performed on samples of mass between 0.3 and 0.5 g. In the case of a misfire the analysis was repeated.

3.3.8. Scanning Electron Microscopy (SEM)

SEM was performed to analyse the surface structure and morphology of solid materials. The analysis was performed on a JEOL JSM 1010LA SEM (Jeol, Tokyo, Japan). Sample preparation involved dispersion of solid (0.01 g) into hexane (5 mL) and pipetting a single

droplet onto the surface of carbon tape attached to a 10 mm cylinder SEM stub. Non-conductive samples were sputter coated in a 10 nm layer of gold using an Emscope Sputter Coater (Emazer, Barcelona, Spain) to improve SEM imaging resolution.

3.3.9. X-ray Diffraction (XRD)

Bruker D2 Phaser XRD (Bruker, Massachusetts, USA) was used to analyse the crystal structure of the solid materials. Standard analysis was performed using a Cu tube with 1.54184 Å, scanning for 1 second at increments of 0.02° between 24 and 65°. Following this, data acquisition analysis was performed using PDF4+ as well as MATCH! XRD analysis software.

3.3.10. Raman Spectroscopy

Bulk Raman spectroscopy was performed on a Renishaw inVia Raman microscope (Renishaw, Gloucestershire, UK) fitted with a green laser (514 nm). Solid samples were analysed on a glass microscope slide using a 50× objective lens and optimised Raman laser focussing. Analysis settings were: 60 seconds exposure time, 20 acquisitions averaged, with cosmic ray removal, full analysis range 50-4000 cm^{-1}. Liquid samples were analysed in glass vials using a 5× objective lens and matching analysis settings.

3.3.11. CHNS (Carbon, Hydrogen, Nitrogen, Sulphur) Elemental Analyser

Carbon, hydrogen, nitrogen, sulphur analysis was performed on Thermo Fisher Flash 2000 EA (ThermoFisher, Massachusetts, USA). Hydrochar samples produced using 3.2.3 were prepared for analysis by weighing out 2-5 mg into a silver capsule, in addition to this 3-5 mg of vanadium pentoxide was added to ensure complete combustion. The instrument was calibrated using 2,5-bis(5-tert-butyl-2-benzo-oxazol-2-yl) thiophene (BBOT) which has known carbon, hydrogen, nitrogen, sulphur, and oxygen percentages.

3.3.12. Adsorption Studies with Ultraviolet-Visible Spectroscopy Analysis

Adsorption capacity and rate of adsorption was investigated using kinetic and isothermal adsorption experiments. These were performed with 0.01 g of adsorbent in 25 mL of methylene blue solutions at 4-40 ppm (isothermal) and retention times from 0.25 to 24 h (kinetic) in an Infors HT multitron shaker at 30 °C and 180 RPM. Fe/C was subsequently magnetically separated while hydrochar was separated by filtration and the remaining solutions analysed using a Genesys 150 UV-Vis spectrophotometer (ThermoFisher, Massachusetts, USA) λ =

634 nm. The amount of methylene blue adsorbed, q_e (mg g^{-1}) and q_t (mg g^{-1}) were calculated as shown in Equation 3.2.

$$q_e = (C_0 - C_e) \times \frac{V}{W} \qquad q_t = (C_0 - C_t) \times \frac{V}{W}$$

Equation 3.2 Calculation of methylene blue adsorption where C_0 and C_e are initial and equilibrium concentrations of the methylene blue (mg L^{-1}), V is the volume of solution (L), and W is the weight of the adsorbent used (g).

3.3.13. Brunauer-Emmett-Teller (BET) Surface Area Analysis

BET surface area analysis was performed on Quadrasorb Surface Area Analyzer and Degasser (Quantachrome, Florida, USA). Analysis performed by Dr Leila Negahdar at the Central Laser Facility, Rutherford Appleton Laboratory, Harwell, UK.

3.3.14. X-ray Photoelectron Spectroscopy (XPS)

Surface composition was examined using X-ray photoelectron spectroscopy (XPS), performed on Kratos Supra (Kratos Analytical Ltd, Manchester UK) instrument with a monochromated aluminium source two analyses per sample, each of area 700 µm by 300 µm. Survey scans were collected between 1200 to 0 eV binding energy, at 160 eV pass energy, 1 eV intervals, and 300 seconds/sweep with one sweep being collected. High-resolution Fe 2p, O 1s, C 1s, N 1s, and In 3d were also collected. Data was analysed using CasaXPS software. Analysis performed by Dr Debbie Hammond at the Sheffield Surface Analysis Centre.

3.3.15. Magnetisation Superconducting Quantum Interference Device (SQUID)

Magnetisation was measured using a Quantum Design (London, UK) SQUID Vibrating Sample Magnetometer MPMS3. Analysis performed by Dr Richard Rowan-Robinson the Department of Material Science and Engineering at the University of Sheffield.

3.3.16. Perturbation Induced 2-D Correlation Analysis and Deconvolution of FT-IR Alcohol/Water Mixture Data

Computational analysis was performed on the FT-IR data obtained in Section 3.2.4, this is discussed in Chapter 4. The data was analysed and plotted using Microsoft Excel, Matlab, and Origin Pro. The deconvolution of peaks was performed in Origin Pro using the "peak analyser". This modelled the peaks under a Gaussian curve by selecting two points and fitting for the best fit.

Synchronous and asynchronous 2D correlation spectroscopy contour plots were obtained following the tutorial presented by Noda [279]. Initially a dynamic spectrum Ã must be calculated (Equation 3.3). Therefore, the average intensity at each wavenumber (j) is obtained to produce the average spectrum ($\bar{A}(\nu_j)$). At which point the dynamic spectra $\tilde{A}(\nu_j,t_i)$ for each perturbation (t_i) is obtained by subtracting the average spectrum ($\bar{A}(\nu_j)$) from the obtained spectrum $A(\nu_j,t_j)$ at that perturbation.

$$\tilde{A}(\nu_j, t_i) = A(\nu_j, t_i) - \bar{A}(\nu_j)$$

$$\bar{A}(\nu_j) = \frac{1}{m}\sum_{i=1}^{m} A(\nu_j, t_i)$$

Equation 3.3 Calculation of dynamic spectrum (Ã) from reference spectrum (Ā) and obtained spectrum (A).

The synchronous correlation data is then obtained following Equation 3.4. This equation measures the similarity among spectral intensity variations along the perturbation variable (t_i). The simplified matrix representation of this inserts the reference spectra (Ã) and the transposed reference spectra ($\tilde{A}^T$) to produce the synchronous output (ϕ). This is then plotted using a contour plot to obtain the synchronous 2D correlation spectrum.

$$\phi(\nu_1, \nu_2) = \frac{1}{m-1}\sum_{i=1}^{m} \tilde{A}(\nu_1, t_i) \cdot \tilde{A}(\nu_2, t_i)$$

$$\phi = \frac{1}{m-1} \cdot \tilde{A} \cdot \tilde{A}^T$$

Equation 3.4 Calculation of synchronous correlation variable (ϕ).

The asynchronous correlation data is obtained through application of the Hilbert–Noda transformation (N_{ik}) [280]. Which is given by the matrix displayed in Equation 3.5. This matrix is then applied to the dynamic spectra previously obtained to produce the asynchronous correlation variable (Ψ) which can be plotted in a contour plot.

$$N = \frac{1}{\pi}\begin{bmatrix} 0 & 1 & \frac{1}{2} & \frac{1}{3} \\ -1 & 0 & 1 & \frac{1}{2} \\ -\frac{1}{2} & -1 & 0 & 1 \\ -\frac{1}{3} & -\frac{1}{2} & -1 & 0 \end{bmatrix}$$

Equation 3.5 Calculation of Hilbert–Noda transformation matrix.

$$\Psi = \frac{1}{m-1} \cdot N \cdot \tilde{A} \cdot \tilde{A}^T$$

Equation 3.6 Matrix calculation of asynchronous correlation variable (Ψ).

The 2D spectra were plotted on contour maps with the x and y axis as the wavenumber and the synchronous and asynchronous spectrums as the z axes. This was performed with two different perturbations composition and temperature from ambient and raised temperature experiments, respectively. For transparency and clarity the full matlab code used for 2D correlation analysis and plotting is shown below:

```
D={INSERT COMPILED DATA HERE}; %Compile spectra data as wavenumber variables (vertically) in different columns and perturbation variables (horizontally) in different rows
W=Wavenumber; %Values displayed in different columns (horizontally)
m ={INSERT NUBER OF PERTUBATIONS HERE); % Number of perturbations is given by rows (horizontal) in the data
R = mean(D); %This averages the data displayed in the columns and produces the reference spectra
A = D - R; %This produces the dynamic spectra
Syn = (1/(m-1)).*(A')*A;
Syn(Syn<0.001 & Syn>-0.01) = NaN; %Noise in data is eliminated for plot
[C,h]=contourf(W,W,Syn); %Synchronous data is then plotted into a filled contour plot
axis square
xlabel('Wavenumber (cm^-^1)');
ylabel('Wavenumber (cm^-^1)');
box off
set(gca,'FontSize',24)
set(gca, 'FontName', 'Times New Roman')
```

```
c.LineWidth = 1;
clabel(C,h)

n = m; %Following this Asynchronous data is calculated
Z = zeros(m,n);
for j = 1:m
for k = 1:n
if (j == k)
Z(j,k)=0;
else
Z(j,k)=1/(k-j);
end
end
end
N = Z*(1/pi);
ASyn = (1/(m-1)).*(A')*N*A;
ASyn(ASyn<0.001 & ASyn>-0.01) = NaN; %Noise in data is eliminated for plot
contourf(W,W,ASyn) %Asynchronous data is then plotted into a filled contour plot
axis square
xlabel('Wavenumber (cm^-^1)');
ylabel('Wavenumber (cm^-^1)');
box off
set(gca,'FontSize',24)
set(gca, 'FontName', 'Times New Roman')
c.LineWidth = 1;
```

3.4. Fundamentals of FT-IR and Raman Spectroscopy

FT-IR or Raman spectroscopy (which are complementary techniques) permeate each results and discussion chapter within this thesis. Chapter 4 involves the in depth analysis and deconvolution of FT-IR data of alcohol/water mixtures. Both Chapter 5 and Chapter 6 use FT-IR to analyse the surface functionality of hydrochar and catalyst samples. Finally Chapter 7 uses Raman spectroscopy as its primary analytical tool in examining the early changes within trapped aerosolised droplets and bulk equivalents. Therefore the function of this subchapter is

to demonstrate a basic understanding of FT-IR and Raman techniques to allow for unperturbed discussion of the data in the results and discussion chapters. The information laid out here is not exhaustive and gives only a broad simplistic explanation of the fundamental science without insight into specific instrumentation variations and advances.

Spectroscopy is the study of the interaction of electromagnetic waves with matter. Electromagnetic waves are categorised by their wavenumber/wavelength into the electromagnetic spectrum Figure 3.7 [281]. Electromagnetic radiation is a combination of periodically oscillating electric and magnetic fields, these oscillate at the same frequency but at perpendicular orientation [251]. Spectroscopy as an analytical tool has been instrumental in the development of many different industrial and research areas including biology, medicine, chemistry, and physics.

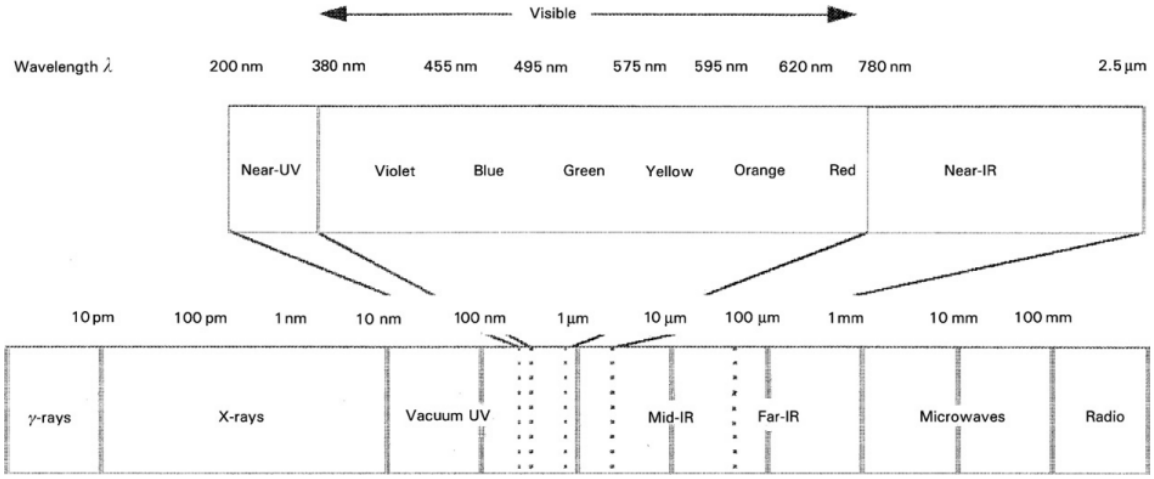

Figure 3.7 The full electromagnetic spectrum displaying all frequencies with respect to their wavelength ranges [282]**.**

3.4.1. FT-IR Spectroscopy

Infrared (IR) and Raman spectroscopy are often coupled together because they yield complementary information which can be combined together for in depth structural analysis [283]. Infrared spectroscopy looks at the vibrational absorption of infrared radiation whilst Raman spectroscopy analyses the inelastic Raman scattered light produced by UV-visible radiation [284], [285].

The IR region of the electromagnetic spectrum is between 14000-10 cm^{-1}, in IR spectroscopy this is further subdivided into near (14000-4000 cm^{-1}), mid (4000-400 cm^{-1}), and far

(400-10 cm^{-1}) [284], [286]. Near is used to study overtone and harmonic or combinational vibrations, mid is used to study fundamental vibrations, and far is used to study the low heavy atom vibrations (*e.g.* metal ligands). In this research mid-IR spectroscopy is used exclusively. IR absorption occurs because the electromagnetic radiation interacts with the polarity of chemical bonds in the molecules. The polarity is due to dipole moments, thus if no dipole moment is present in a chemical bond there is no infrared interaction (no signal). The frequency of the absorbed IR is the same as the molecular vibration in the dipole moment. The number of vibrational modes in a molecule can be calculated using the equation 3N-6 for non-linear molecules and 3N-5 for linear molecules where N is the number of atoms. When two vibrational modes have the same frequency (and thus wavenumber) they are said to be degenerate. Vibration-rotation spectra are observed for gaseous samples, whereas liquid and solid spectra are purely vibrational.

Vibrations involve either a change in bond length (stretch) or bond angle (bend). The stretching vibrations are further subdivided if they are in phase known as symmetrical (s) whilst out of phase is asymmetrical (as) [284], [287], [288]. Bending vibrations are further complicated by the division of in-plane and out-of-plane bending known as deformation (or bend), rock, wag, and twist. These vibrations are displayed visually in Figure 3.8 along with the Greek letter assignments for each type of vibration. Characteristic or group vibrations occur at approximate wavenumbers, these provide clues for identifying compounds and their substructures using IR. For example, C=O symmetric stretch (ν_s) occurs at roughly 1706 cm^{-1} with a strong sharp peak, this characteristic peak allows for quick identification of carbonyl groups.

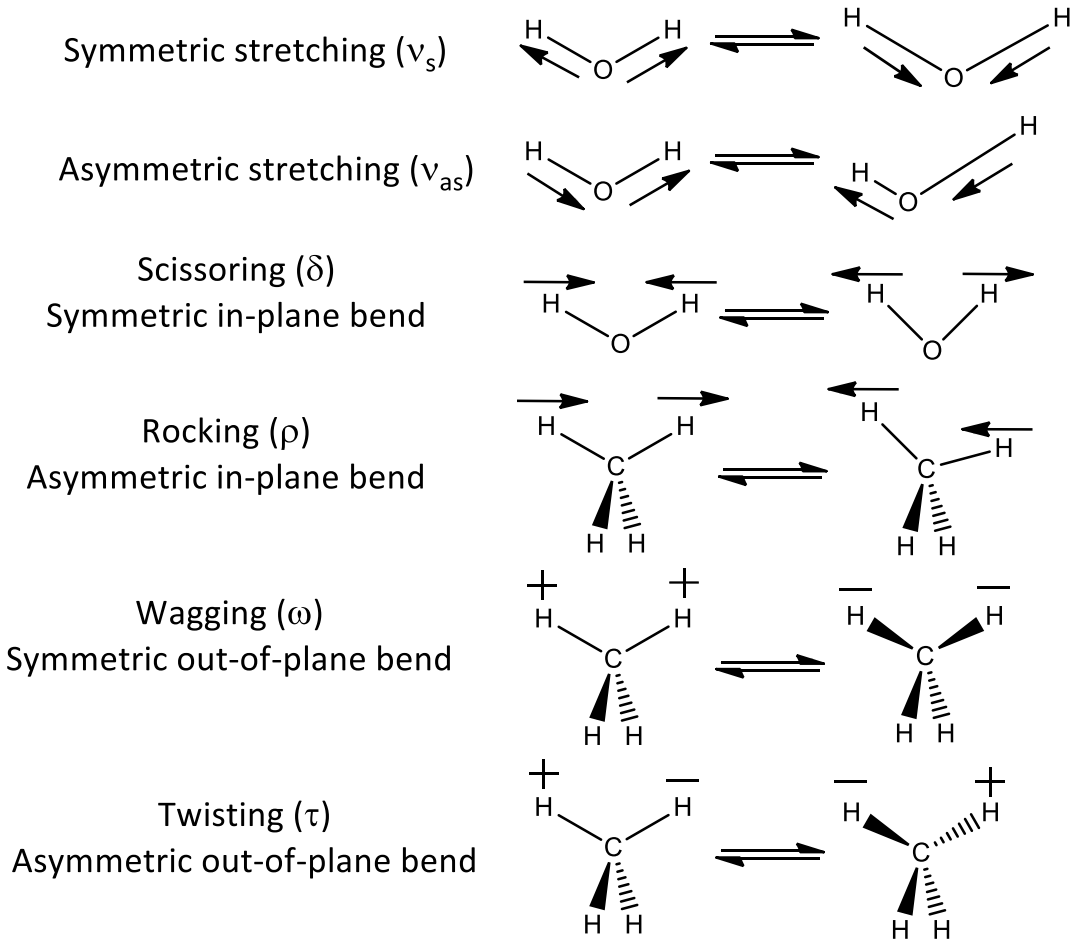

Figure 3.8 Classifications of fundamental vibrational absorbances which are observed in IR spectroscopy.

These IR absorbances are further complicated by overtones and combination bands, fermi resonance, and coupling [284], [287]. First overtone bands occur when vibrational energy transitions from the base level to two levels above, this can be applied further and yield second, third, fourth, *etc.* overtone bands. Functionally the overtone bands occur at twice that of the initial fundamental vibrations. Combination bands occur when two fundamental bands absorb energy simultaneously; the wavenumber is the combination of both their respective fundamental absorption bands. Fermi resonance is a phenomenon whereby an overtone or combinational band has the same wavenumber position as a fundamental vibration, this causes them to both be shifted in opposite directions and form a doublet. Vibrations in the skeletal structure of molecules can become coupled, this means that vibrations are not limited to one or two bonds causing shifts in the bond absorption positions.

IR spectrometers have been commercially available since 1940, these spectrophotometers relied on prisms as their dispersive element to select the wavelength to be analysed and detected

[284], [286]. A significant improvement on these spectrometers came with the invention and implementation of Fourier-transform infrared spectrometers (FT-IR) which allowed for concurrent analysis of all wavelengths of IR radiation. This required the combination of the Michelson interferometer which merged two light sources together to create an interference pattern and the mathematical process of Fourier transforming the obtained data. Additionally there are different sampling handling techniques each of which are better suited for different phases and sample structures. The main four sample handling techniques are attenuated total reflection (ATR), diffuse reflectance (DRIFTS), true specular reflectance/reflexion (absorption), and transmission.

3.4.2. Raman Spectroscopy

Raman spectroscopy analyses the signal from Raman scattering when an intense monochromatic beam of electromagnetic radiation is exposed to a sample [289]. When the energy hits the sample, it is absorbed, transmitted, and scattered. This scattering can be thought of as a two-photon process, where one photon of energy from the beam of energy excites a photon in the sample to a higher virtual state. This then relaxes down and emits a photon which is the scattered energy observed. Ninety nine percent of this scattered energy is Rayleigh scattering which has the same frequency (energy) as the incident radiation. The remaining 1% of the scattered energy is Raman scattering, which has a different frequency to the incident radiation [285]. This Raman scattering can be further broken down into Stokes which has a lower energy than the incident radiation and anti-Stokes which has a higher energy than the incident radiation. This occurs when the photon either relaxes down to a higher energy state or is evolved from a higher energy state for Stokes and anti-Stokes, respectively. The energy level diagram displaying these changes is shown in Figure 3.9.

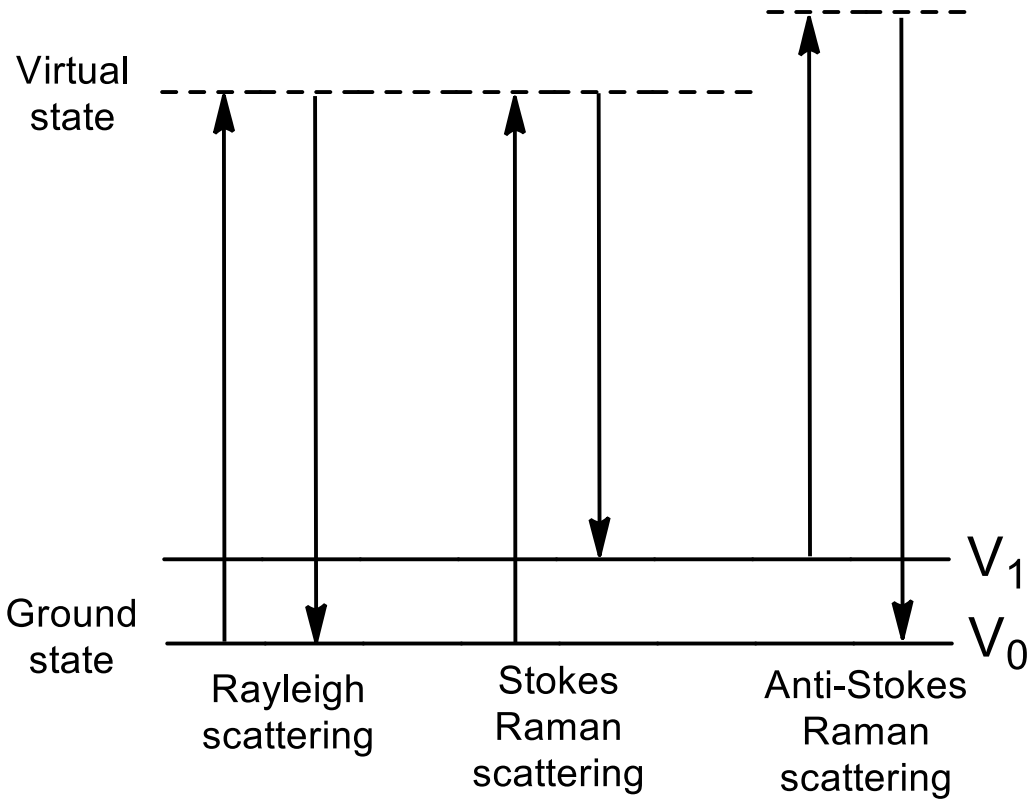

Figure 3.9 Energy level diagram depicting Rayleigh and Raman scattering.

The sample is distorted on a molecular level when it is subjected to the electromagnetic radiation. This distortion is caused by the electrons being attracted to the positive pole and nuclei being attracted to the negatively charged pole of the electromagnetic field, this produces a dipole moment within the molecule [285]. This distortion is caused by polarizability of the electron cloud within the perturbed molecule; therefore Raman scattering is only observed when a molecule is polarisable [290]. To put it more succinctly a bond vibration is Raman active when the dipole moment of the molecule is changed, this is known as a polarisable bond. The Raman scattering signal is usually plotted in intensity (counts) as a function of the Raman shift (cm^{-1}) which is the difference in frequency between the incident radiation and the scattered radiation [289]. This means that the symmetry of a molecule defines what vibrations are Raman and IR active, therefore symmetric vibrations are studied by Raman spectroscopy and asymmetric vibrations using IR spectroscopy. Raman spectroscopy provides complementary information to that of IR spectroscopy, thus using them in tandem unlocks the potential for full molecular dynamic analysis.

A Raman instrument consists of four parts; an excitation source, collection optics, wavelength selector, and a detector [289]. Whilst Rayleigh and Raman scattering are produced in all

directions from the sample the most common instrumental configurations are at 90 and 180 degrees to the incident beam [285]. The main challenge in Raman analysis is the elimination of the large amount of Rayleigh scattering and selection of the relatively weak Raman scattering. Older Raman spectrometers used single grating-based monochromators whilst newer models are fitted with Rayleigh line filters which offer increased optical throughput.

Chapter 4 Vibrational Analysis of Alcohol/Water Mixtures Under Hydrothermal Conditions using FT-IR

As previously discussed in Section 2.1.4, binary alcohol/water mixtures are unique and have long intrigued physical chemists [94]. They are a low cost useful industrial solvent medium for a variety of chemical reactions and separation processes [291]. The unique properties of binary alcohol/water mixtures are likely attributed to both direct alcohol-water hydrogen bonding and hydrophobic hydration interactions. Vibrational spectroscopy is a critical tool for probing and understanding the structure and dynamics of water and other aqueous systems [292]. However, theoretical modelling of the fundamental vibration transitions in water is difficult and cannot reach agreement with experimental data. Therefore, the further complication provided by the addition of alcohol interactions necessitates the use of experimental vibrational spectroscopy. Mid-infrared spectroscopy is considered to be one of the most promising methods for identifying the formation of alcohol hydrates by examining the hydrogen bonding dynamics between different O-H groups [293]. This chapter focuses on the analysis of alcohol/water mixtures using Fourier transform infrared (FT-IR) spectroscopy.

The data for the spectra are analysed in three different stages, firstly peak assignment and qualitative analysis is performed on whole spectra, this is followed by peak deconvolution of the overlapping peaks in O-H stretching region, and finally 2-dimensional (2D) correlation analysis is performed using both temperature and alcohol molar concentration as perturbations. The alcohols investigated in this section were methanol, ethanol, and isopropanol, the compositional mixtures which were studied are displayed in Section 3.2.4. The aim of this research is to utilise FT-IR to gain further insight into the structure of alcohol/water systems at raised temperatures and pressures.

4.1. Analysis and Assignment of Alcohol/Water Mixture FT-IR Spectra

4.1.1. Full FT-IR Assignment for Ambient Water, MeOH, EtOH, and IPA

To understand more effectively the intermolecular and intramolecular bonding variations which are being observed in the FT-IR spectra it is imperative that a full analysis and peak assignment is performed for water, methanol (MeOH), ethanol (EtOH), and isopropanol (IPA). This analysis allows any observed peak shifting, broadening, and changes in intensity to then be attributed to changes within the physical structure of the alcohol/water system which are related to the non-ideal behaviour of the mixtures which is discussed previously and well

reported. The full FT-IR spectra for pure ambient liquid water, methanol, ethanol, and isopropanol are displayed in Figure 4.1 and the tabulated peak assignments are shown in Table 4.1, Table 4.2, Table 4.3, & Table 4.4.

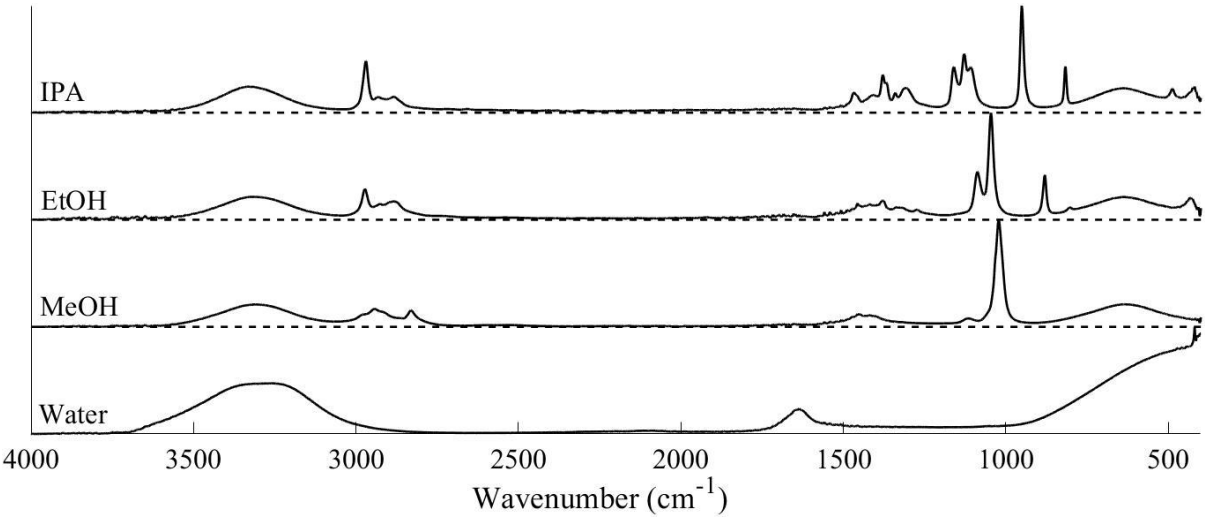

Figure 4.1 FT-IR spectra full range for ambient water, MeOH, EtOH, and IPA analysed using a Shimadzu IRAffinity-1S spectrometer fitted with a Specac ATR plate. Analysis conditions: scans 100, resolution 4 cm^{-1}, absorbance mode.

Water is a non-linear molecule which contains only three atoms. Following the equation 3N-6 there are 3 different characteristic absorbances for a single water molecule. These are O-H scissoring, and O-H stretching, both symmetric and asymmetric. The assignments for these in the most common isotopologue of water ($^{1}H_2{}^{16}O$) are 1594.7, 3653.1 and 3755.9 cm^{-1} respectively [294]. In practice, the analysis of gas-phase, liquid phase, or frozen water do not show only these simplistic absorbances as single sharp peaks (Figure 4.2). There are a multitude of different peaks present in the FT-IR of gaseous water, these occur because water has a very small moment of inertia on rotation causing a rich tapestry of vibrational-rotational bands. In liquid and solid (frozen) water the stretching vibrations are redshifted and broadened [63]. This is predominantly caused by the multitude of different hydrogen bond environments which absorb at different wavenumbers. The effect of hydrogen bonding is to increase the IR intensity and lower the O-H stretching frequency, thus lower the wavenumber the more intermolecular bonding is present between the water molecules.

Both symmetric and asymmetric OH stretching modes are also present and overlapping, further complicating the spectra. Additionally, in liquid water, OH scissoring overtones are observed at approximately 3250 cm^{-1} which overlaps with these mixed and broadened OH stretching modes. It can be observed that frozen water has a sharp peak which is at lower wavenumbers

compared to the liquid water. This is because the water molecules are locked into a heavily ordered hydrogen bonded environment, therefore most water molecules have the same amount of hydrogen bonding which is more than that of liquid water. Researchers have used infrared and Raman spectroscopic techniques to analyse this OH stretching region and provide insightful information in the microscopic hydrogen-bond network of water in aqueous solutions. It is common to use deconvolution to separate out some of the different hydrogen bonding environments which are then assigned to clusters [293], [295], [296]. Deconvolution of the obtained data in this research is presented in Section 4.2. The structure and dynamics of the hydrogen bonding network in water also depends on local molecular structure, concentration, and co-solvents, as well as already explained temperature effects [296]. Therefore investigation into the OH stretching region of alcohol/water mixtures using FT-IR can provide an understanding of the molecular dynamics and structure, expanding upon the research into the cause and implications of their non-ideal behaviour.

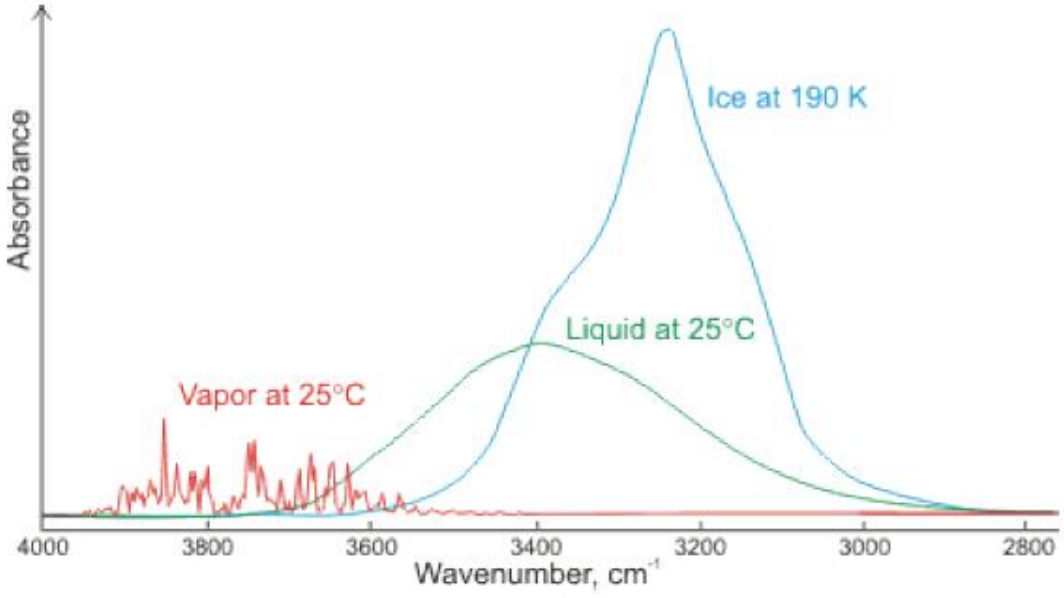

Figure 4.2 FT-IR spectra for water vapor, liquid, and ice between 4000-2800 cm^{-1} [294]**.**

FT-IR spectra for alcohols have additional vibrational absorbances stemming from the C-H and C-O bonds. In alcohols the C-H bond typically has stretching modes between 2700-2975 cm^{-1} and bending modes located from 1300-1500 cm^{-1}. C-O has stretching modes between 1050-1205 cm^{-1}, the wavenumber is higher the more structurally hindered the alcohol. So primary alcohols have C-O stretching at lower wavenumbers and tertiary alcohols at the higher wavenumbers. Methanol, the most simplistic primary alcohol, has twelve normal modes of vibration. There is only one O-H stretching vibration because there is only a single bond

thus no symmetry to allow for symmetric or asymmetric stretching variations. However this O-H stretching region is broadened by the coexistence of many different hydrogen bond environments just as is observed with water O-H stretching, therefore a broad peak is observed around 3308 cm^{-1}. There are three C-H stretching modes observed next to the O-H stretching between 2800-3000 cm^{-1}. A particularly complicated region of the methanol spectra is found between 1600-1300 cm^{-1}, here there are three different C-H bending modes and one O-H bending mode. However there are also many different combinational bands and coupled peaks from fermi-resonance making this section difficult to interpret. Moving down the spectra there are weak absorbances from the rocking of the methyl groups at 1120 and 1153 cm^{-1}. There is a very sharp peak coming from the C-O stretching vibrations at 1022 cm^{-1}. Finally the broad absorbance centred at 636 cm^{-1} comes from O-H···O torsion. The FT-IR spectra for ethanol and isopropanol have more different local environments of these fundamental vibrations with no new fundamental vibrations. Therefore the spectra for ethanol and isopropanol contain more peaks within the same ranges explained for methanol. New skeletal absorbances are present in these though because of the larger backbone. A full breakdown of the assigned absorbances for water, methanol, ethanol, and isopropanol is displayed for reference in Table 4.1, Table 4.2, Table 4.3, Table 4.4, respectively.

Table 4.1 The assignment of identified absorbance bands in ambient water from the spectra in Figure 4.1 with intensity (vw = very weak, w = weak, m = medium, s = strong, vs = very strong, sh= shoulder br = broad).

Wavenumber (cm^{-1})	Intensity	Assignment
925-400	br	Librations (hindered rotations)
1636	s, br	δ O-H_2 scissoring (symmetric in-plane bend)
3090	s, br	2δ O-H_2 scissoring overtone (symmetric in-plane bend)
3280	s, br	ν_s O-H_2 symmetric stretching
3490	s, br	ν_{as} O-H_2 asymmetric stretching

Table 4.2 The assignment of identified absorbance bands in MeOH from the spectra in Figure 4.1 with intensity (vw = very weak, w = weak, m = medium, s = strong, vs = very strong, sh= shoulder br = broad).

Wavenumber (cm^{-1})	Intensity	Assignment
636	s, br	δ O-H···O torsion
1022	vs	ν C-O stretching
1120	w	ρ -CH_3 rocking (asymmetric in-plane bend)
1153	vw	ρ -CH_3 rocking (asymmetric in-plane bend)
1418	w, sh	δ O-H bending (in-plane bend)
1449	m, sh	δ C-H_3 scissoring (symmetric in-plane bend)
1472	m, sh	ω C-H_3 wagging (symmetric out-of-plane bend)
1506	m, sh	τ C-H_3 twisting (asymmetric out-of-plane bend)
2830	m	ν_s C-H_3 symmetric stretching
2943	m	ν_{as} C-H_3 asymmetric stretching
2980	w, sh	ν_{as} C-H_3 asymmetric stretching
3308	s, br	ν O-H stretching

Table 4.3 The assignment of identified absorbance bands in EtOH from the spectra in Figure 4.1 with intensity (vw = very weak, w = weak, m = medium, s = strong, vs = very strong, sh= shoulder br = broad).

Wavenumber (cm^{-1})	Intensity	Assignment
434	m	δ C-C-O bending
637	s, br	δ O-H···O torsion
804	w, sh	ρ C-H_2 rocking (asymmetric in-plane bend)
880	s	ν C-C-O skeleton stretching
1045	vs	ν C-O stretching gauche
1088	s	ν C-O stretching eclipsed
1149	vw	ρ -CH_3 rocking (asymmetric in-plane bend)
1273	m, sh	τ C-H_2 twisting (asymmetric out-of-plane bend)
1325	m	δ O-H bending (in-plane bend)
1379	s	δ C-H_3 scissoring (symmetric in-plane bend)
1418	m, sh	ω C-H_2 wagging (symmetric out-of-plane bend)
1456	m	ρ C-H_2 rocking (asymmetric in-plane bend)
1489	w, sh	δ C-H_3 scissoring (symmetric in-plane bend)
2876	m, sh	ν_s C-H_2 symmetric stretching
2889	m, sh	ν_s C-H_3 symmetric stretching
2928	m, sh	ν_{as} C-H_2 asymmetric stretching
2972	s	ν_{as} C-H_3 asymmetric stretching
3312	s, br	ν O-H stretching

Table 4.4 The assignment of identified absorbance bands in IPA from the spectra in Figure 4.1 with intensity (vw = very weak, w = weak, m = medium, s = strong, vs = very strong, sh= shoulder br = broad).

Wavenumber (cm^{-1})	Intensity	Assignment
419	m	δ C-C-O bending
488	w	δ C-C-O bending
637	s, br	δ O-H···O torsion
816	s	ν C-C-O skeleton stretching
951	vs	ν C-C stretching
1107	s, sh	ρ -CH_3 scissoring (symmetric in-plane bend)
1128	s	ν C-O stretching
1159	s	ρ -CH_3 rocking (asymmetric in-plane bend)
1306	m, br	δ O-H bending (in-plane bend)
1341	w	δ C-H bending
1368	m, sh	δ C-H_3 scissoring (symmetric in-plane bend)
1406	w	ω C-H_2 wagging (symmetric out-of-plane bend)
1458	w, sh	ρ C-H_2 rocking (asymmetric in-plane bend)
1466	m	δ C-H_3 scissoring (symmetric in-plane bend)
2884	m	ν_s C-H_1 stretching
2930	m	ν_s C-H_3 symmetric stretching
2970	s	ν_{as} C-H_3 asymmetric stretching
2980	w, sh	ν_{as} C-H_3 asymmetric stretching
3327	s, br	ν O-H stretching

4.1.2. Peak Analysis of Ambient Alcohol/Water Mixtures as a Function of Mol%

Vibrational frequencies in the FT-IR spectra are very sensitive to the local molecular environment, including intermolecular interactions such as hydrogen bonding [297]. Therefore, the FT-IR spectra can be related to the structure of the liquid. Herein, O-H stretching, and C-O stretching, vibrational bands of the alcohol/water systems have been analysed for broadening, shifting, and intensity changes. These are given as full width half maxima (FWHM), peak maxima position, and peak maxima intensity in absorbance. These vibrational bands are among the largest in the FT-IR spectra, they are also corresponding to some of the functionalities participating in hydrogen bonding in water and methanol for O-H and C-O respectively. Additionally O-H stretching is present in both pure water and alcohol systems, C-O stretching is present in only alcohols, allowing for the changes in the hydrogen bond dynamics of the alcohol to be singled out.

Blueshifting (an increase in wavenumber) of a vibrational band corresponds to a reduction in hydrogen bonding (and related intermolecular interactions) in the aqueous system [298]. Breadth (FWHM) of a vibrational absorbance can be related to the number of different hydrogen bonding systems attached to the functionality [299]. Finally as demonstrated by the Beer-Lambert law absorbance in the FT-IR spectra is proportional to concentration [300]. This

relationship has been used to successfully determine the concentration of a dissolved solute. However, this becomes problematic when strong intermolecular interactions alter dipole moments creating non-linear intensities. Therefore, the non-linear changes in intensity in the binary alcohol/water mixtures are identified by determining the excess peak maxima intensity following Equation 4.1. Calculated excess intensity (ExI) shows if the intensity of the peak is higher (positive) or lower (negative) than would be expected for a binary mixture of the alcohol/water mixture based on the peak intensities of pure substances.

$$\boldsymbol{PreI} = \left(\frac{(\boldsymbol{ActIPWater} - \boldsymbol{ActIPOH})}{\mathbf{100}} \times \boldsymbol{WaterMol}\right) + \boldsymbol{ActIOH}$$

$$\boldsymbol{ExI} = \boldsymbol{ActI} - \boldsymbol{PreI}$$

Equation 4.1 Calculation of the excess peak maxima intensity (ExI) of the O-H stretching peak as well as the C-O stretching. Variables are: predicted peak maxima intensity at given molar percentage alcohol/water mixture (PreI), actual peak maxima intensity of pure water (ActIPWater), actual peak maxima intensity of pure alcohol (ActIPOH), molar percentage water (WaterMol), actual peak maxima intensity at given molar percentage of alcohol/water mixture (ActI).

Excess intensity of the O-H stretching band in methanol/water mixtures is negative at all molar percentages (Figure 4.3), suggesting that there is reduced intermolecular O-H interactions in methanol/water mixtures, with a minima at 45.9 mol% methanol. However, further inspection of the peak maxima position reveals tiered blueshifting from initially ~3263 cm^{-1} up to 22.3 mol% methanol, the peak position then shifting up to ~3282 cm^{-1} until 45.9 mol%, then finally the position shifts to ~3312 cm^{-1} above 51.9 mol%. Within the O-H stretching vibrational band in water there are many different types of hydrogen bonded clusters, the deconvolution of which is presented in Section 4.2. Blueshifting of the O-H stretching peak can be related to a reduction in the presence of tetrahedrally bonded clusters in methanol/water mixtures at higher molar percentages [301]. The transition point at which the hydrogen bonding between water molecules is heavily disrupted by methanol molecules is cited at 40 mol%, closely aligning with the increase in wavenumber. Therefore, the negative excess intensity is caused by a shifting in the major peak location. A methanol molar percentage of 45.9 mol% therefore represents a transition point from dominance of tetrahedral structures. FWHM is generally difficult to obtain for the O-H stretching peak because of the aliphatic C-H stretching obscuring it, however the breadth of the peak is relatively stable up until 22.3 mol% at around 393 cm^{-1}. At 58.4 mol%, the breadth of the peak is 362 cm^{-1} after which it rapidly reduces and at 90.3 mol% methanol it is 290 cm^{-1}. This change is associated the reduction of tetrahedrally bonded water molecules.

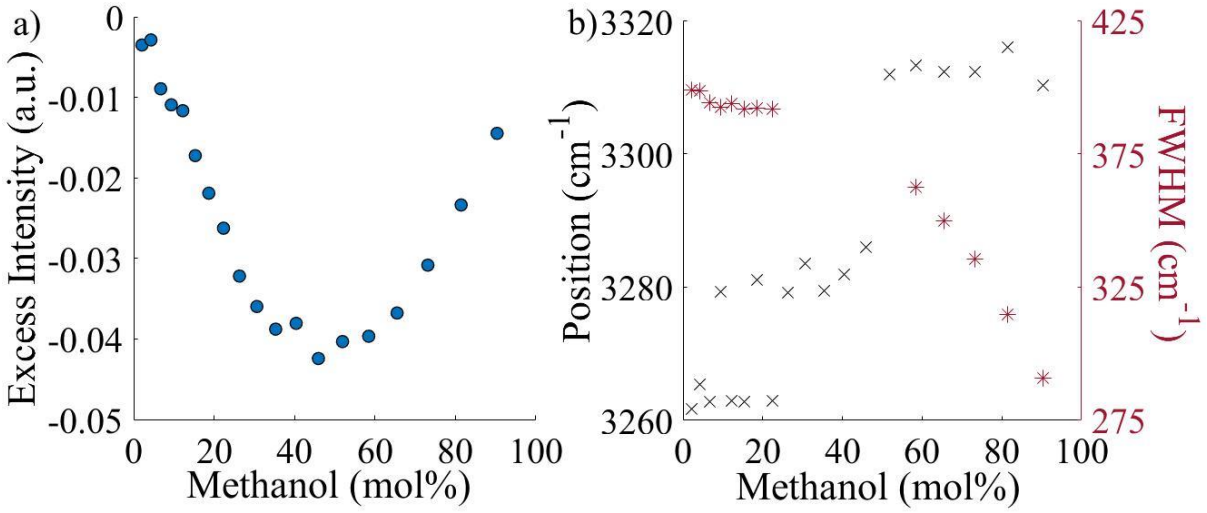

Figure 4.3 O-H stretching (3280 cm^{-1}) band in MeOH, (a) excess peak maxima intensity (a.u.) marked with circles (o), (b) peak maxima position (cm^{-1}) marked with cross (x) and full width of peak at half maximum height (cm^{-1}) marked with an asterisk (*).

Matching trends can be observed in the O-H stretching profile for both ethanol and isopropanol (Figure 4.4). The largest contributors to the broad O-H stretching are related to higher wavenumber peaks at 3320 cm^{-1} and 3345 cm^{-1} for the highest molar percentages of ethanol and isopropanol respectively. The peak maximum position is higher with increasing chain length of alcohols and also increases at lower molar percentages 23.5 and 15.9 mol% for ethanol and isopropanol. For ethanol/water mixtures this shift in position can be attributed to the structural transition from tetrahedral-like networks to a zigzag chain network [302]. Isopropanol/water mixtures observe this transition at a lower molar percentage because the aliphatic tail is bulkier and more sterically hindering. Identical reduction in FWHM observed in methanol/water mixtures is shown, rapid descent beginning at 56.9 and 42.8 mol% for ethanol and isopropanol respectively. Therefore, increasing alcohol chain length also relates to narrowing of the O-H stretch at higher molar percentages, because of the reduction in tetrahedrally bonded clusters. Finally, excess intensity is negative in all alcohol/water systems, linked again to this shift in the main contributor to the O-H stretching absorbance. Minima are located at 56.9 and 42.8 mol% for ethanol, and isopropanol.

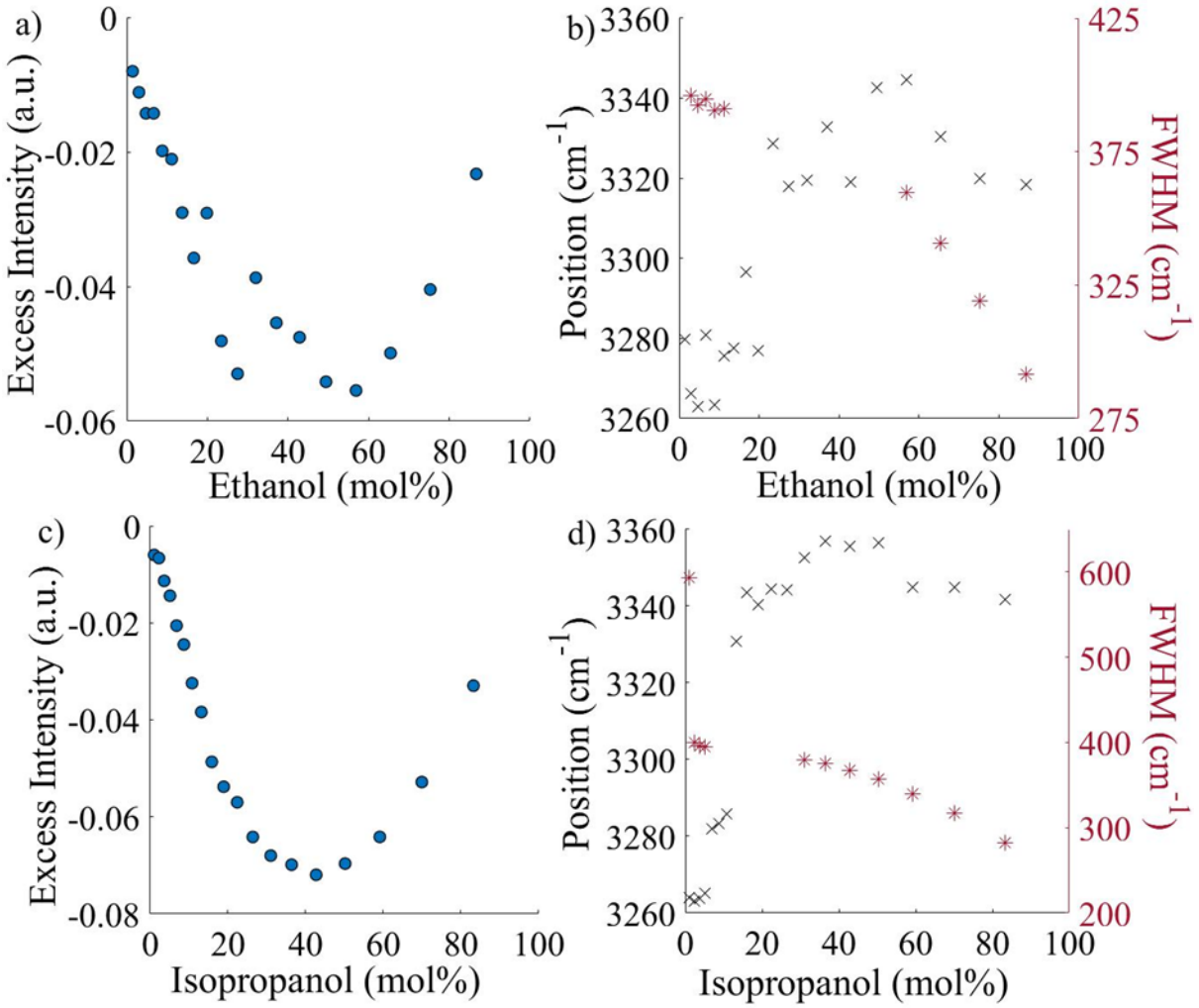

Figure 4.4 O-H stretching (3280 cm^{-1}) band in EtOH, and IPA, (a, c) excess peak maxima intensity (a.u.) marked with circles (o), (b, d) peak maxima position (cm^{-1}) marked with cross (x) and full width of peak at half maximum height (cm^{-1}) marked with an asterisk (*).

C-O stretching for methanol provides many interesting observations (Figure 4.5). Peak maxima position is initially redshifted down to 1013 cm^{-1} at both 26.3 and 30.6 mol%, after which it is blueshifted up to 1021 cm^{-1} at 90.4 mol%, demonstrating that there is increased intermolecular interactions associated with the C-O stretch, the largest increase is between 26.3 and 30.6 mol%. Position distribution present has similar structure to the excess enthalpy of mixing discussed in Section 2.1.4 and displayed in Figure 2.14. Minima for excess enthalpy of mixing for methanol are between 24.6 and 35.6 mol%. Furthermore, the excess intensity follows the same profile, however the positive values represent an increase in intermolecular interactions with the highest extent of interaction at 30.6 mol%. Ahmed *et al.* discussed the contributions of four different hydrogen bonding environments causing the shifting in peak maxima position [303]. First a weak vibration at 1000 cm^{-1} is attributed to the methanol oxygen acting as the

hydrogen acceptor to either a methanol or water molecules hydrogen. Next at 1010 cm^{-1} a strong absorbance at 1010 cm^{-1} designated to methanol hydrogen bonded to water by both the oxygen and hydrogen groups concurrently. Another strong contributor was at 1023 cm^{-1} coming from trimer hydrogen bonded clusters of methanol. Finally, a weak component at 1060 cm^{-1} when the methanol was a hydrogen donor to either a water or methanol molecule. Therefore, this minimum in the peak position represents a maximum amount of fully hydrogen bonded methanol-water or methanol-methanol environments. Moreover, this highly structured methanol/water mixture is responsible for many of the non-ideal thermodynamic properties (such as excess enthalpy of mixing), hence the overlap with peak maxima position. FWHM below 12.2 mol% is unreliable due to small peak height, however after this point there is a noticeable linear increase until 45.9 mol% after which the peak becomes narrower. This indicates that after 45.9 mol% methanol the relative concentration of the stronger methanol-water hydrogen bonds is reducing, and the weaker methanol-methanol hydrogen bonds are increasing in relative concentration [301].

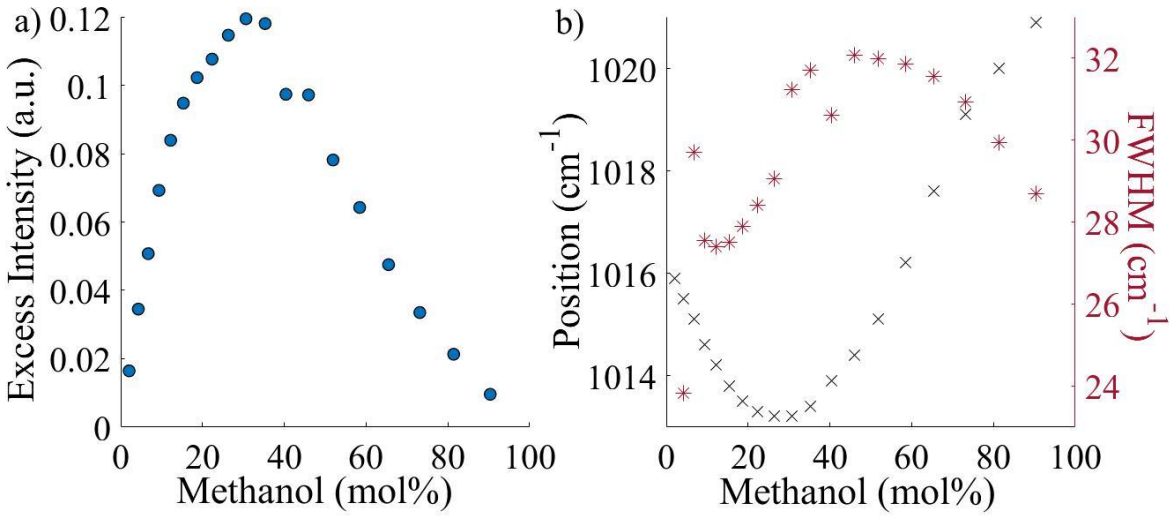

Figure 4.5 C-O stretching (1022 cm^{-1}) band in MeOH, (a) excess peak maxima intensity (a.u.) marked with circles (o), (b) peak maxima position (cm^{-1}) marked with cross (x) and full width of peak at half maximum height (cm^{-1}) marked with an asterisk (*).

Peak maxima position for the C-O stretching in both ethanol and isopropanol have the same initial redshifting (lowering of position in cm^{-1}) followed by blueshifting (increasing of position in cm^{-1}) as alcohol mol% is increased (Figure 4.6). However, they are less closely aligned with excess enthalpy (Figure 2.14) compared to methanol. Ethanol presents its lowest C-O stretching peak position between 16.6 and 23.5 mol%, with the largest excess enthalpy of ethanol at 14.4 mol%. For isopropanol the lowest C-O stretching position is between 3.7 and 6.9 mol%, and the largest excess enthalpy is positioned at 10.9 mol%. However, the C-O

stretching position for both ethanol and isopropanol follow the same shaped curve as excess enthalpy of mixing. As previously discussed for methanol/water mixtures this is related to different hydrogen bonding environments [303]. Shifting to lower peak position is attributed to increased density of intermolecular hydrogen bonds between the alcohol hydroxide group and water molecules. The reduced shifting observed in isopropanol can be attributed to the bulkier aliphatic tail which sterically hinders the formation of isopropanol-water hydrogen bonding. Both ethanol and isopropanol have roughly Gaussian excess intensities with maxima at 49.4 mol% and 31.1 mol%, respectively (Figure 4.6, a, c). This increase in excess intensity for ethanol/water mixture can be attributed to the formation of ethanol-water clathrates which exhibits a maximum at 50 mol%. Above 50 mol% formation of ethanol-ethanol clusters is increased and below it the formation of water-water clusters is favoured. Isopropanol/water mixtures can be accepted to follow the same trend with a maximum in isopropanol-water clathrates at a lower molar percentage somewhere around 31 mol%. FWHM shows little variation in isopropanol. C-O stretching FWHM peak jumps to narrower at 37.1 mol% ethanol compared to 42.9 mol% ethanol, again indicating a transition to more ethanol/water hydrogen bond systems [301].

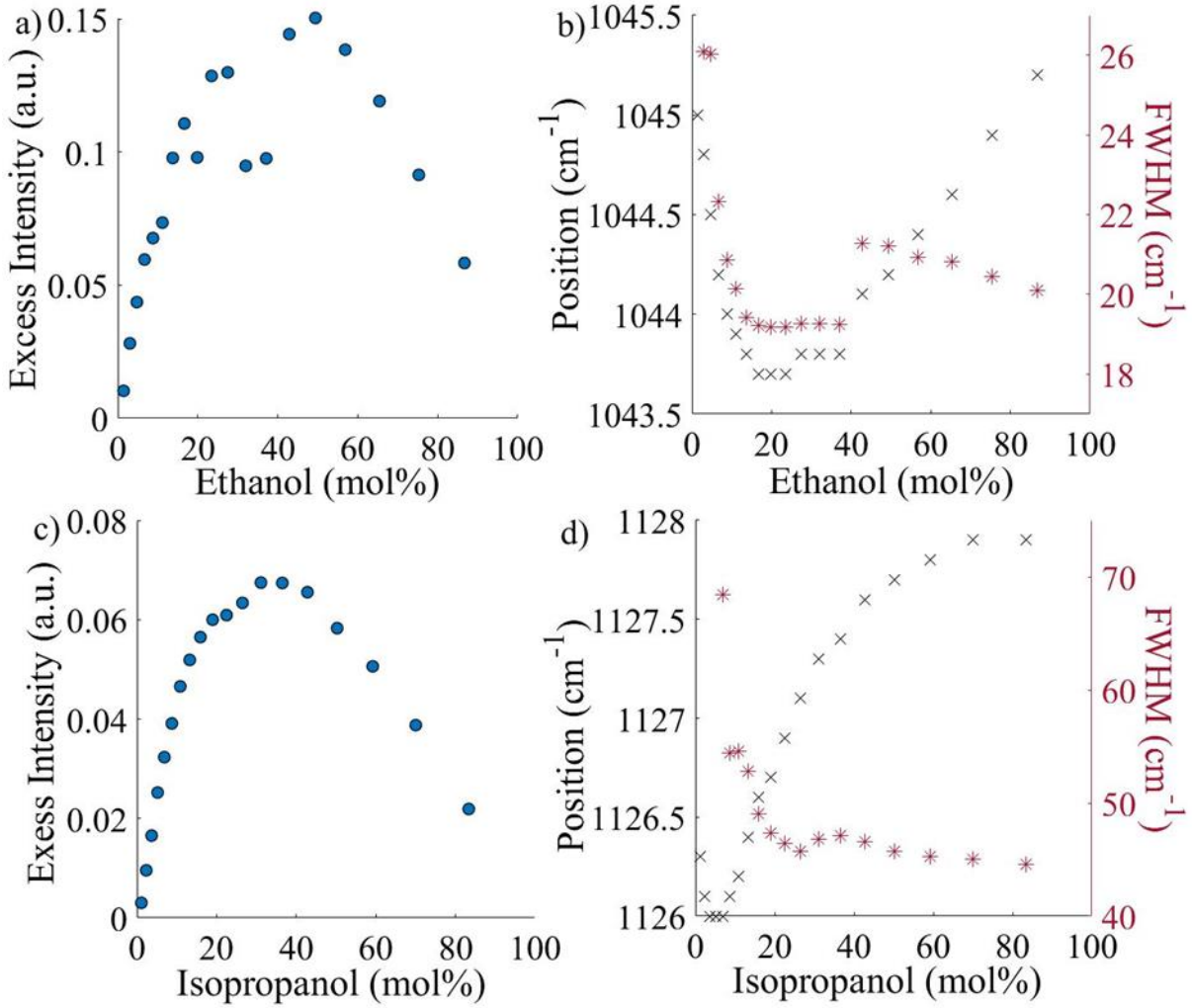

Figure 4.6 C-O stretching (1045 cm^{-1}, 1128 cm^{-1}) band in EtOH, and IPA, (a, c) excess peak maxima intensity (a.u.) marked with circles (o), (b, d) peak maxima position (cm^{-1}) marked with cross (x) and full width of peak at half maximum height (cm^{-1}) marked with an asterisk (*).

4.1.3. FT-IR Spectra for Sub-Critical Alcohol/Water Mixtures

FT-IR spectroscopy data obtained at raised temperatures and pressures in the Specac reaction cell (Figure 3.1) created particular challenges. At higher temperatures the background absorbance of the cell changed in a repeatable pattern based on the temperature alone. Additionally, the signal output was ~50x lower than for the ATR plate. To overcome these challenges and produce reliable data for analysis the background spectra at each temperature was subtracted from the obtained spectra (with an ambient background). This data was then further processed using Spectragryph (http://spectroscopy.ninja) to perform adaptive baseline removal with 100% coarseness. Full spectra for pure water, methanol, ethanol, and isopropanol are presented at each temperature point in Figure 4.7. Blueshifting and a reduction in intensity

for O-H stretching is observed in all systems as temperature is increased. This has been shown for water in literature and is attributed to a reduction in hydrogen bonded hydroxyl (OH) groups, as evidenced by the reduction in the average number of hydrogen bonds as temperature and pressure is increased [51], [304]. Alcohols also exhibit a clear reduction in the C-O stretching intensity as temperature is increased. This can also be attributed to a reduction in the hydrogen bonding for the C-O groups of the alcohols.

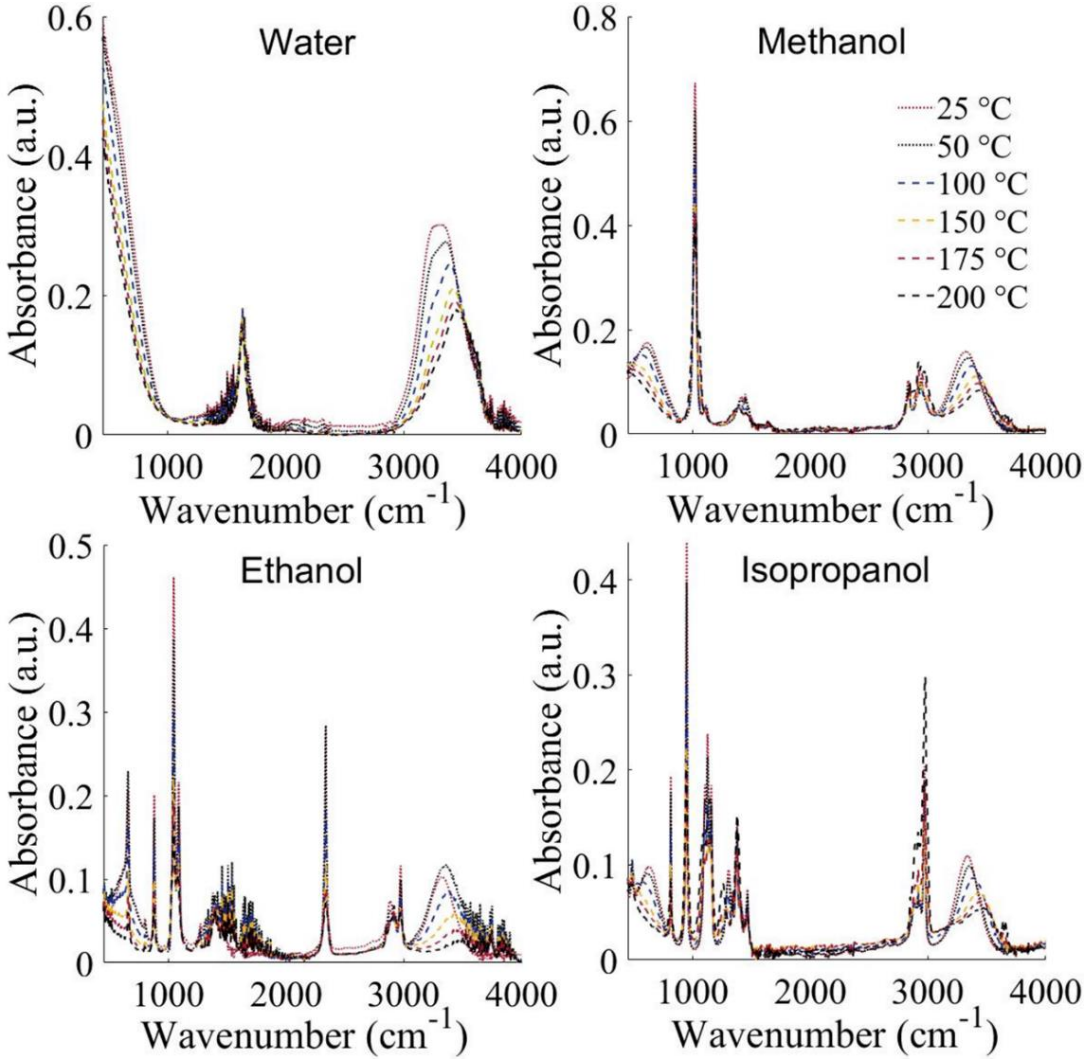

Figure 4.7 FT-IR spectra full range for water, methanol, ethanol, and isopropanol at 200 °C analysed using a Shimadzu IRAffinity-1S spectrometer fitted with a 22 mL Specac reaction cell top plate for golden gate™. Analysis conditions: scans 250, resolution 4 cm^{-1}, absorbance mode.

None of the same trends for peak position, excess intensity, or FWHM are observed with methanol, ethanol, and isopropanol/water mixtures (Section 4.1.2) when studied at 200 °C under pressure. However, the excess intensity in the C-O stretching peak for the alcohol/water mixtures remains positive, showing that the peak intensity for C-O stretching is higher than expected for that alcohol/water mixture. This suggests that there is still some enhanced

intermolecular hydrogen bonding occurring between the alcohol and water molecules under these conditions. Observing trends by analysing the peak positions and intensity becomes increasingly difficult and unintuitive as more variables are added in the sub-critical system. 2D correlation analysis presented in Section 4.3 provides a basis for complex multivariate analysis of this complex system, allowing for more insightful investigation into the sub-critical alcohol/water mixtures.

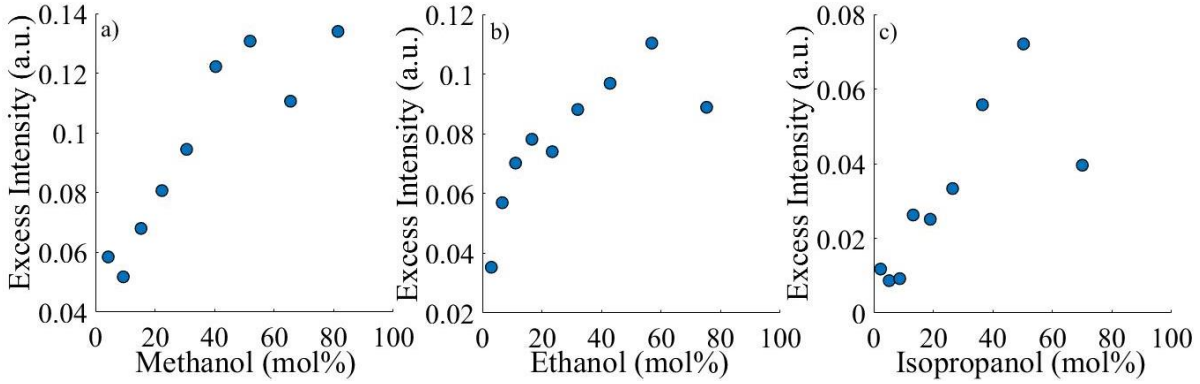

Figure 4.8 C-O stretching (1022 cm^{-1}, 1045 cm^{-1}, 1128 cm^{-1}) band in methanol, ethanol, and isopropanol, (a, b, c) excess peak maxima intensity (a.u.) marked with circles (o) at 200 °C in 22 mL Specac reaction cell top plate for golden gate™.

4.2. Deconvolution of Peaks Within FT-IR of Alcohol/Water Mixtures

Observed peaks within an FT-IR spectra may be further complicated by overlapping absorbance bands convoluted into a singular peak. The deconvolution of these peaks in the FT-IR spectra into the absorbance bands of their respective species is a widely practiced procedure with many examples, such as the deconvolution of non-apatitic, A-type, and B-type carbonate bands (920-800 cm^{-1}), secondary structure determination of proteins using the amide bands (1900-1400 cm^{-1}), and alkoxy groups bound to silica (1250-1000 cm^{-1}) [305]–[307]. The deconvolution of these bands allows for a more accurate understanding of the species and bonding environment present. Therefore, deconvolution of the O-H and C-O stretching bands of alcohol/water mixtures is attempted to elucidate more information about the bonding structure and environment in Sections 4.2.1 and 4.2.2.

4.2.1. Deconvolution of O-H Vibrational Stretching Band

Water OH stretching (3800-2800 cm^{-1}) vibrations are delocalised over 10 or more molecules as a result of hydrogen bonding and the associated dipolar (and polarisation) interactions [308]. Intermolecular fermi resonance coupling to the HOH bending overtone makes it harder to

quantify the influence of O-H stretching intermolecular interactions. Whilst hydrogen bonding in simple alcohols such as methanol, ethanol, and isopropanol does not have the HOH bending they can still be deconvoluted into di-hydrogen bonded alcohol molecules, monomerically bonded alcohol molecules and non-hydrogen bonded molecules [309]. Therefore, alcohol/water mixtures contain too many different hydrogen bond environments to allow for straightforward deconvolution into every category.

This challenge is tackled in this research by breaking down the broad O-H stretching into four Gaussian distributions as representative bands using OriginPro multiple peak fit software. The HOH bending overtone (D1) is ascribed to a fixed band at 3090 cm^{-1}. Strongly hydrogen bonded alcohol/water (D2) molecules (*e.g.* tetrahedrally hydrogen bonded water molecules) are assigned to a fixed position at 3220 cm^{-1}. Non-hydrogen bonded alcohol/water (D4) molecules are given the fixed position at 3540 cm^{-1}. And finally the moderately bonded alcohol/water (D3) molecules (*e.g.* dimer/trimer hydrogen bonded water) are given a flexible position at 3390 cm^{-1}. For the reader a table with the reference name to the deconvoluted band is presented in Table 4.5, in addition to a figure depicting each bonding environment for water molecules (Figure 4.9).

Table 4.5 Reference shorthand for the deconvoluted bands in the O-H stretching of alcohol/water mixtures and a description of the bonding environment.

Reference	Wavenumber (cm^{-1})	Description
D1	3090	HOH bending overtone (fixed position)
D2	3220	Strongly hydrogen bonded O-H groups (fixed position)
D3	3390	Moderately hydrogen bonded O-H groups (flexible position)
D4	3540	Non-hydrogen bonded O-H groups (fixed position)

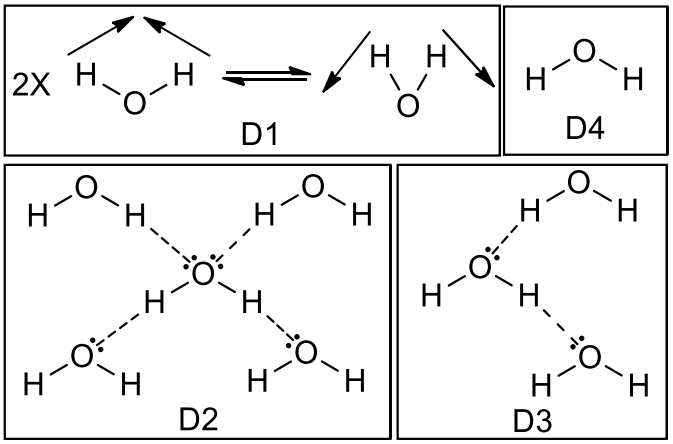

Figure 4.9 Hydrogen bonding environments of water in deconvoluted peaks from the O-H stretching band of alcohol/water mixtures.

The deconvoluted O-H stretching spectra for pure water, methanol, ethanol, and isopropanol are presented in Figure 4.10. Aliphatic (C-H) stretching bands in the alcohols and alcohol/water mixtures additionally had to be fitted to eliminate their influence on the deconvoluted O-H stretching bands. These aliphatic bands had to be fitted for the alcohol/water mixtures at 9.4, 16.6, and 6.9 mol% for methanol, ethanol, and isopropanol, respectively. Additionally, the HOH bending overtone (D1) became non-existent at alcohol/water mixtures of 90, 65, and 59 mol% for methanol, ethanol, and isopropanol, respectively. The expected trend for D1 is therefore a linear decrease with increasing alcohol concentration. For the other peaks D2, D3, and D4 the peak area is also expected to decrease with increasing alcohol concentration because the water has a higher absorbance O-H stretching peak than the alcohols. It can also be observed that the ratio of D2 to D3 in water is significantly higher than the ratio observed in the pure alcohol/water mixtures. This is because water is able to easily coordinate 4 hydrogen bonds with other water molecules in a tetrahedral structure and therefore exhibits a larger proportion of strongly hydrogen bonded molecules than the alcohols.

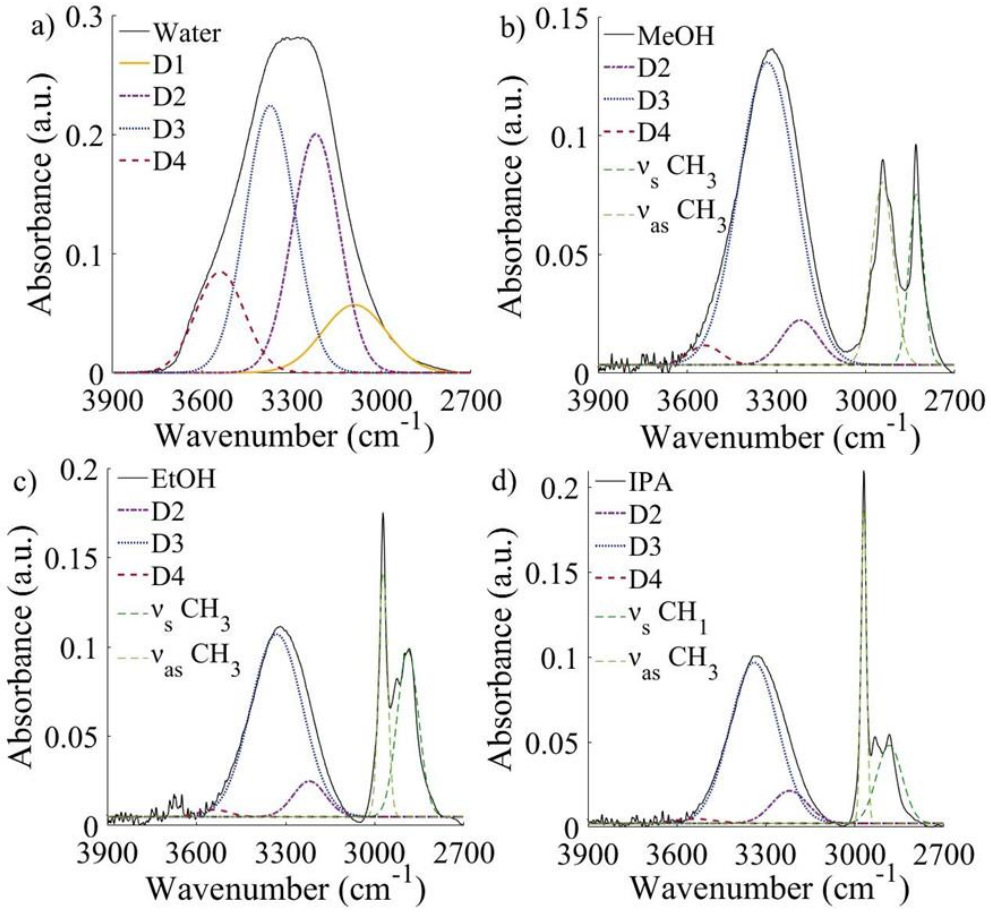

Figure 4.10 FT-IR spectra deconvolution of O-H stretching vibrations for water, MeOH, EtOH, and IPA between 3800-2800 cm^{-1} using a Shimadzu IRAffinity-1S spectrometer fitted with a Specac ATR plate. Analysis conditions: scans 100, resolution 4 cm^{-1}, absorbance mode.

The peak area for each deconvolved Gaussian distribution at varying alcohol molar percentages for methanol, ethanol, and isopropanol under ambient conditions is displayed in Figure 4.13. A jump in D1 and D2 is observed at 9.4, 16.6, and 6.9 mol% for methanol, ethanol, and isopropanol, respectively. This is attributed to the inclusion of aliphatic fitting at these molar percentages. A sharp reduction in peak area for D1 is observed for all alcohols, the position is at a lower molar percentage as chain length increases. This is observed at 65.5, 56.9, and 50.3 mol% for methanol, ethanol, and isopropanol respectively. After these molar percentages a transition point is considered to occur where the water exists as small clusters surrounded by alcohol molecules [92]. This transition point is identified as 70, 60, and 50 mol% for methanol, ethanol, and isopropanol. The large reduction in D1 peak area is because the intensity of the OH bending overtone of water is dependent on fermi-resonance with tetrahedrally hydrogen bonded water, which at this molar percentage is diminished [293]. The majority of the strongly hydrogen bonded O-H stretching (D2) can be attributed to hydrogen bonding between alcohol

molecules and not water.

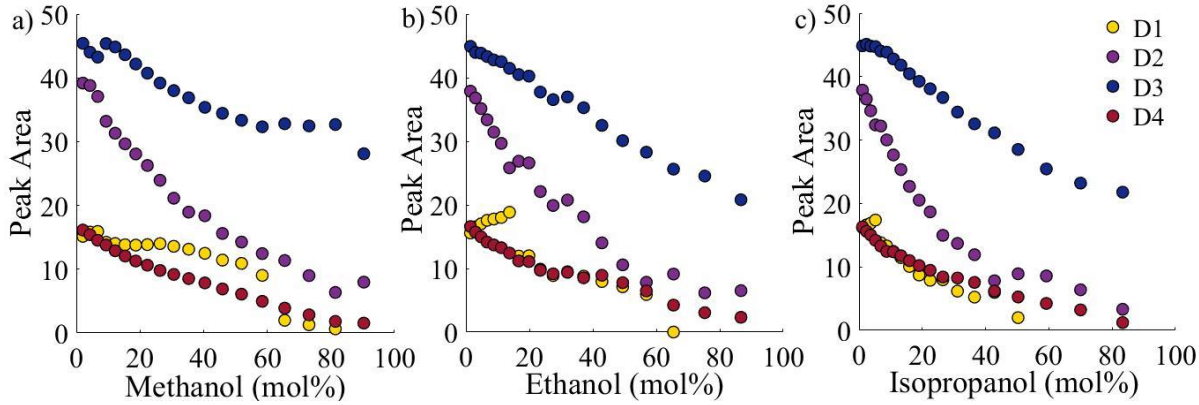

Figure 4.11 Peak area of deconvoluted O-H stretching bands in (a) MeOH, (b) EtOH, and (c) IPA at ambient conditions.

From the peak area of D2 a transition point is observed where the rate the peak is decreasing is reduced. This transition point occurs at 35.3, 32, and 26.5 mol% for methanol, ethanol, and isopropanol, respectively. Therefore, the strongly hydrogen bonded clusters of water are being distributed until they are all linked with alcohols at these molar percentages. The transition point occurs at lower molar percentages with increasing alcohol chain length because of the larger hydrophobic aliphatic tails causing increased disruption to the hydrogen bonding structure of water. D2 also stabilises and remains at a relatively stable peak area at 81.4, 56.9, and 42.8 mol% for methanol, ethanol and isopropanol, respectively. After these molar percentages the strongly hydrogen bonded structures remain the same as more alcohol molecules are present. D3 shows gradual reduction with increase in alcohol molar percentage for all alcohol/water mixtures. Indicating that this peak changes only based on a reduction in the number of hydroxide groups present in the system and not hydrogen bonding. D4 has a transition point of reducing the rate of decrease at 26.3, 16.6, and 8.7 mol% for methanol, ethanol, and isopropanol, respectively, aligning well with the maximum structured environments of the alcohol/water mixtures [92]. This can be attributed to the transition point where the minimum number of both alcohol and water molecules are orphaned in solution and do not have any hydrogen bonding.

Deconvolution of the OH stretching band at 200 °C and 60 bar is shown in Figure 4.12. D1 could not be deconvolved because of a reduction in the tetrahedrally bonded water structures (D2) which cause the increased intensity of the OH bending overtone (D1) *via* fermi-resonance [293]. Additionally, because of the reduced overall signal provided by the high temperature reaction cell it was problematic to follow trends in the deconvolved OH stretching peaks. The

reduced signal to noise ratio leads to inaccurate analysis of deconvolved peak areas. Issues associated with overall low signal and low signal to noise are overcome by multivariate analysis techniques such as 2D-correlation spectroscopy presented Section 4.3.

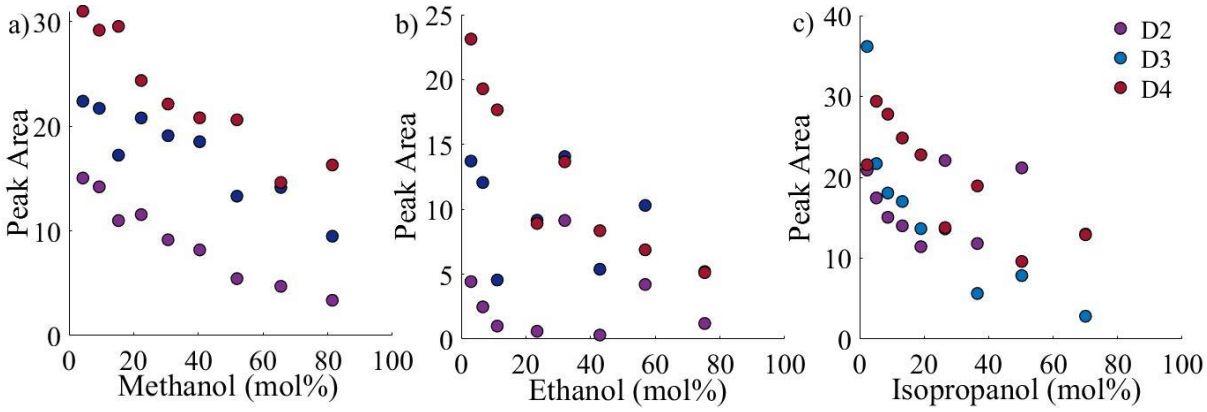

Figure 4.12 Peak area of deconvoluted O-H stretching bands in (a) MeOH, (b) EtOH, and (c) IPA at 200 °C, 30 bar He.

4.2.2. Deconvolution of C-O Vibrational Stretching Band

Ahmed *et al.* presented deconvolution of the C-O stretching band in alcohol/water mixtures to avoid the issues associated with the overlapping alcohol and water bands observed in the O-H stretching band [303]. In this instance the C-O stretching band for methanol/water mixtures was observed to consist of four different Gaussian distributions. The first was an absorbance for the methanol acting as a hydrogen acceptor at the hydroxide site (1000 cm^{-1}) labelled as D5. Next an absorbance for methanol hydroxide with hydrogen bonds on both the oxygen and hydrogen to two water molecules (1010 cm^{-1}) categorised as D6. Then an absorbance at 1023 cm^{-1} is ascribed to methanol hydroxide with hydrogen bonds on both oxygen and hydrogen to two methanol molecules (D7). Finally, a weak absorbance at 1060 cm^{-1} arises from methanol acting as a hydrogen donor at the hydroxide site (D8). A reference table is provided for clarity (Table 4.6) in addition to a figure depicting each system (Figure 4.13).

Table 4.6 Reference shorthand for the deconvoluted peaks in the C-O stretching of MeOH/water mixtures and a description of the bonding environment.

Reference	Wavenumber (cm^{-1})	Description
D5	1000	Methanol hydrogen acceptor with either water or methanol in hydrogen bond
D6	1010	Methanol hydrogen donor and acceptor in hydrogen bond with two water molecules
D7	1023	Methanol hydrogen donor and acceptor in hydrogen bond with two methanol molecules
D8	1060	Methanol hydrogen donor with either water or methanol in hydrogen bond

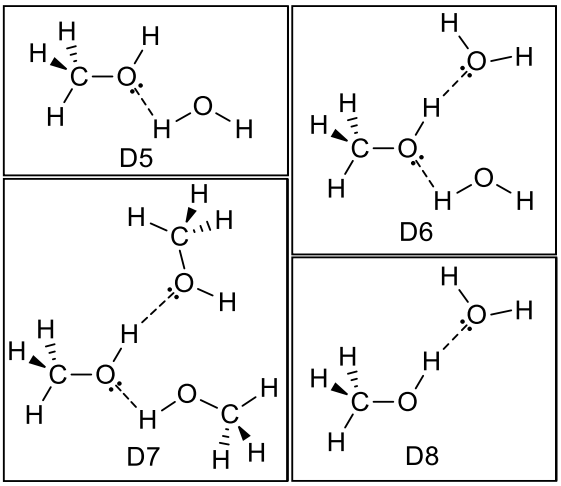

Figure 4.13 Different hydrogen bonding environments of deconvoluted peaks in C-O stretching vibrational band of MeOH/water mixtures.

Dawes *et al*. simplified the fitting when deconvoluting the C-O stretching band in methanol/water mixtures deposited as ice (30 K) into only three observed bands [310]. They observed a shift in the dominant deconvolved peak at 50 mol% methanol, indicating that a larger majority of methanol below 50 mol% was hydrogen bonded to two water molecules. Additionally evidence was found in blueshifting of C-H stretching positions that at low methanol concentrations the methyl group was participating in hydrogen bonding. This supports the theory that at low alcohol molar percentage in alcohol/water mixtures the individual alcohol molecules are surrounded by water as hydration shells [92]. Therefore, the application of this deconvolution in both ambient and sub-critical methanol/water mixtures should provide further insights into the hydrogen bonding environment.

Ambient methanol/water mixtures were deconvolved into the two stronger absorbances D7 and D8. The ratio of the peak area for each of these deconvolved peaks is then plotted against the molar percentage of methanol (Figure 4.14). This can be used to assess the number of methanol

molecules forming hydrogen bonds with methanol molecules vs water molecules and therefore give an indication of the hydrogen bonding environment. From 2 mol% methanol to 12.2 mol% there is only a minor decrease in the D6/D7 ratio from 3.77 to 3.47. After this the next point at 15.3 mol% there is a large decrease in D6/D7 ratio down to 2.20. This is attributed to a transition point in structure of the methanol/water mixture from methanol mostly surrounded by water hydration shells to clusters of methanol forming part of the hydrogen bond network in the mixture [301]. After this point the rate of decrease in D6/D7 ratio reduces until linearity is observed from 30.6 mol% methanol. This indicates that after this molar concentration methanol molecules are mostly formed into aggregates hence hydrogen bonding of methanol with water is obstructed and reduced [311]. The linear decrease in D6/D7 ratio is observed up until the highest mol% of 90.4 mol%, representative only of a reduced number of water molecules available to form hydrogen bonds with methanol. No further structural observations for the methanol/water mixture can be surmised from this deconvolution.

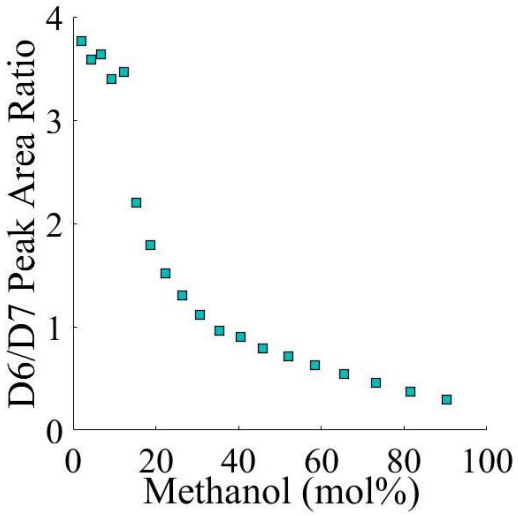

Figure 4.14 Peak area ratio of D6 over D7 for the deconvoluted peaks in C-O stretching of MeOH/water mixtures at ambient conditions.

Deconvolution of the C-O stretching region for methanol/water mixtures at sub-critical conditions is complicated by the appearance of gaseous methanol bands at 40.4 methanol mol% Figure 4.15 [312]. The methanol/water mixture is at 200 °C and 60 bar, whilst 30 bar of He was used at room temperature, the ideal gas law provides an estimate of 48 bar attributed to the He at 200 °C. Therefore, an additional 12 bar is provided by the methanol/water mixture, with an estimated maximum liquid volume of 0.43 mL entering the gaseous phase compared to 10 mL used as filling volume. However, whilst the majority of the methanol is present in solution the gaseous phase methanol obscures the C-O stretching region sufficiently to make deconvolution unfeasible. Therefore, alternative data analysis techniques are required to gain

insight into the structure of methanol/water mixtures (and other alcohol/water mixtures) at sub-critical conditions.

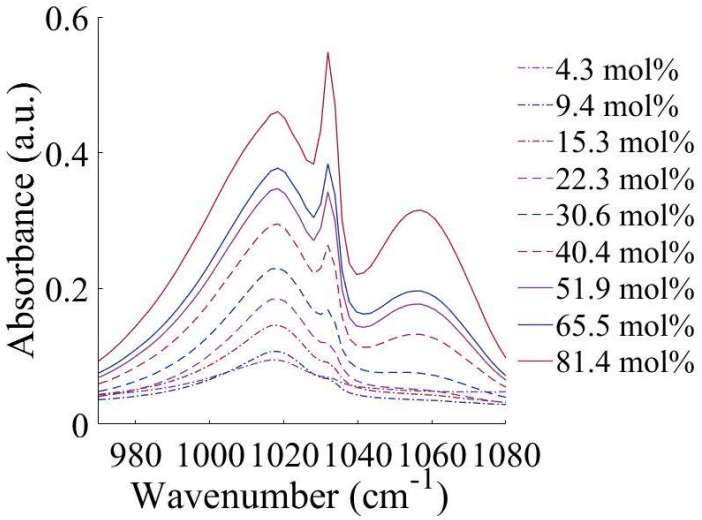

Figure 4.15 FT-IR spectral range for C-O stretching in methanol water using a Shimadzu IRAffinity-1S spectrometer fitted with a 22 mL Specac reaction cell top plate for golden gate™. Analysis conditions: scans 250, resolution 4 cm^{-1}, absorbance mode.

4.3. 2D FT-IR Correlation Analysis of Alcohol/Water Mixtures

In 1971 the concept of multidimensional NMR spectroscopy to aid in identification of organic compounds was proposed by Jean Jeener [313]. Fundamentally 2D NMR spectroscopy is achieved by multiple radio frequency pulses being applied to the sample with a wait (t_1) between them and the time for relaxation (t_2). These time domains are then converted into frequency domains and can be plotted against one another to create a contour (3D) plot which yields information about interactions between the different chemical shifts absorbances. Whilst resonance based spectroscopic techniques such as this dominate the field there is a different form of 2D correlation spectroscopy which can be applied to a broad range of analytical techniques [314]. This is known as perturbation-based 2D correlation spectroscopy and involves the analysis of perturbation-induced spectral vibrations. This is achieved by performing standard analysis of samples with unmodified instrumentation and adding a single external perturbation to the sample such as temperature, concentration, pressure, *etc.* Herein, this multivariate analysis technique is applied to the obtained spectra for alcohol/water mixtures with the separate perturbations of both concentration and temperature. The equations and mathematical conversions performed on the obtained data to produce 2D contour plots is detailed in Section 3.3.16. 2D correlation analysis provides a method of simplifying complex spectra with overlapping peaks and increasing the spectral resolution. Furthermore the

assignment of correlation is unambiguous and precise because the correlations are related to exact x and y variables (*e.g.* wavenumber). The product of 2D correlation analysis is a synchronous and asynchronous contour plot, this is shown schematically by Harrington *et al.* in Figure 4.16 [315]. In the synchronous contour plot the peaks along the X=Y line (orange) are autopeaks as they originate from a correlation of a peak with itself and therefore they are ignored in the contour plot. A positive peak in the synchronous plot as observed at (C, D) is caused by peaks that are correlated with one another and therefore as one peak increases with the perturbation it causes the other peak to increase as well. The opposite occurs in negatively correlated peaks in the synchronous contour plot as in (A, B) the increase of one peak across the perturbation causes a decrease in the other peak. Absence of any peak (flat) portions of the contour plot occur because the peaks have no correlation with one another. Moving over to the asynchronous contour plot there are no autopeaks present and datapoints are asymmetric across the line X=Y. The sequential order of peak intensity change can be determined from the asynchronous 2D correlation contour plot. For a peak position (x,y) if the asynchronous spectral peak is positive then the change in the x value occurs first followed by the change in the y variable. For negative asynchronous peaks the opposite is true. If no peak is observed in the asynchronous spectrum the peaks are fully correlated and can be attributed to the same cause.

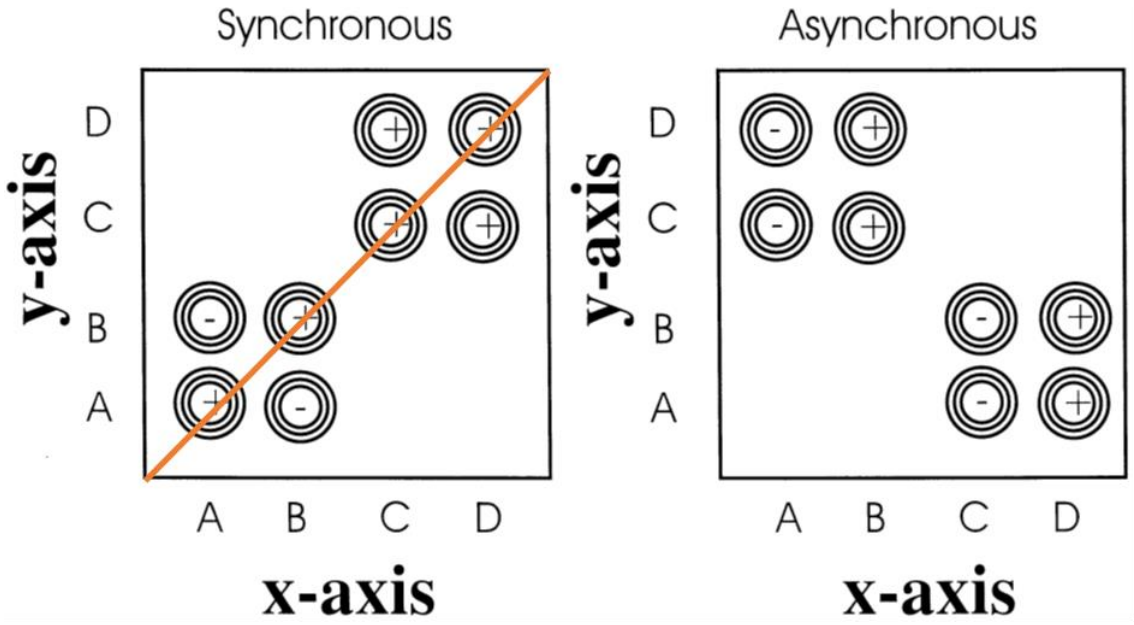

Figure 4.16 Examples of synchronous and asynchronous 2D correlation contour plots presented by Harrington *et al.* [315]**.**

4.3.1. Concentration Perturbation at Ambient Temperature

Contour plots (synchronous and asynchronous) for the 2D correlation analysis of methanol/water mixtures with the perturbation of methanol concentration (at 5 v/v%) is displayed in Figure 4.17. The analysed range was reduced to 3700-925 cm^{-1} to reduce noise in the correlation spectra without removing the observable trends thus, producing an improved correlation spectra for analysis. In the synchronous plot (Figure 4.17,a) a strong negative correlation between the O-H stretching (3270 cm^{-1}) and the C-O stretching (1018 cm^{-1}) band is observed at an intensity of -0.013, this is assigned the descriptor OH_s-CO_s. Negative correlation is expected as the methanol has a lower intensity O-H stretching band and the water has no C-O stretching band. Therefore, as methanol concentration increases the size of the C-O stretching band increases and the size of the O-H vibrational band decreases. An additional correlation observed and expected is between the O-H bending (1633 cm^{-1}) and the C-O stretching vibrations with an intensity of -0.008 (OH_δ-CO_s). Finally, examining the correlation between C-H asymmetric stretching (2980 cm^{-1}) and C-O stretching as both arise from the increased concentration of methanol, this has a reduced correlation intensity of 0.006 (CH_{as}-CO_s). The synchronous and asynchronous contour plots for ethanol/water and isopropanol water mixtures under ambient condition with concentration perturbation are displayed in Appendix 9 & Appendix 10.

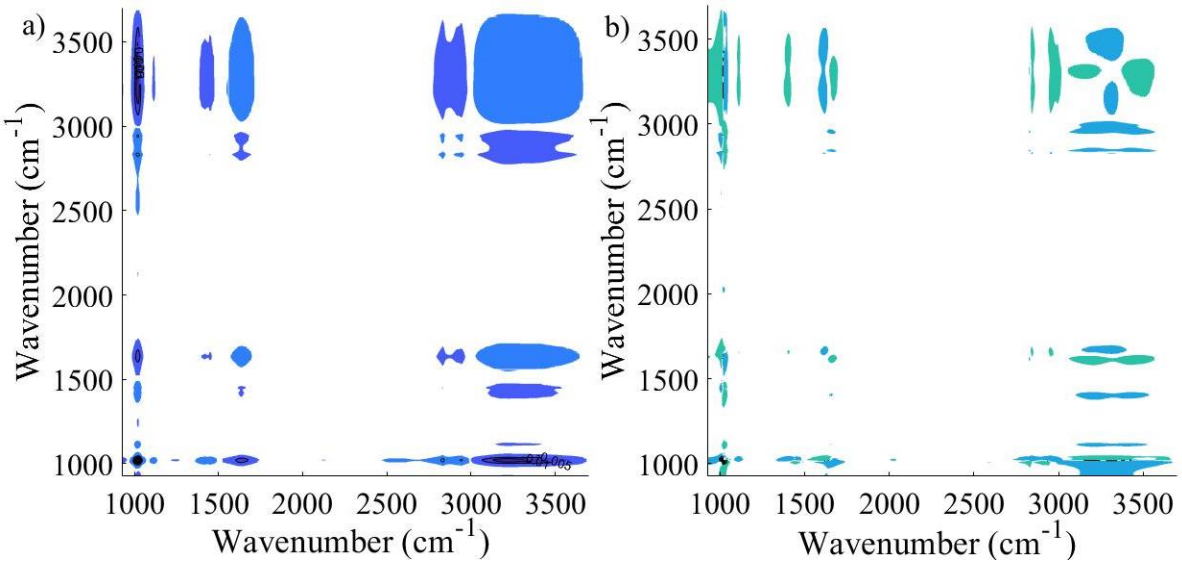

Figure 4.17 (a) Synchronous and (b) asynchronous 2D correlation contour plots for ambient MeOH/water mixtures with MeOH concentration as the perturbation.

Broad autopeaks are observed for O-H stretching (3270 cm^{-1}) because it is a broad peak. There is potential to extract further information from close examination of this autopeak due to the different hydrogen bonding environments present within the O-H stretching. Hence, a close up

synchronous and asynchronous plot is displayed in Figure 4.18. Positive correlation is observed as the concentration of methanol decreases the peak intensity decreases; the correlation maximum point is along the y=x line as expected for autopeaks. Deviation from this would suggest correlation between different hydrogen bonding environments within the broad O-H stretching peak. Analysis of the asymmetric contour plot (Figure 4.18, b) shows two asymmetric peaks at (3310, 3177) and (3464, 3310) which are negative and positive respectively. Therefore both the 3177 cm^{-1} and 3464 cm^{-1} peak decrease in intensity after the 3310 cm^{-1} peak decreases in intensity. This is related to a reduction in strongly tetrahedrally bonded water clusters (D2, 3220 cm^{-1}) in addition to a reduction in the breadth of the O-H stretching peak which is only observed at the higher methanol molar percentages.

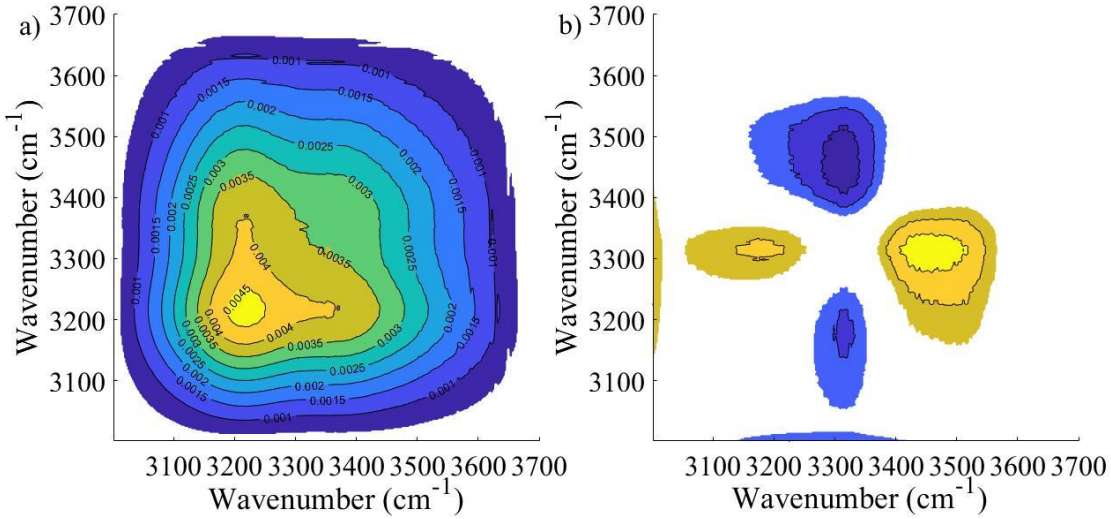

Figure 4.18 (a) Synchronous and (b) asynchronous 2D correlation contour plots for O-H stretching region in ambient MeOH/water mixtures with MeOH concentration as the perturbation.

4.3.2. Concentration Perturbation at 200 °C

The 2D correlation analysis of alcohol/water mixtures with concentration perturbation at 200 °C as investigated (Figure 4.19). The asynchronous spectra in this 2D correlation analysis were flat indicating that all of the correlations are occurring at the same time (in-phase). Examination of the synchronous 2D correlation contour plot of the alcohol/water mixtures provides evidence of the reduced hydrogen bonding network at sub-critical conditions. This is shown by reduced correlation intensities for OH_s-CO_s, OH_δ-CO_s, and CH_{as}-CO_s at -0.006, 0.0016, and 0.0013. These lower intensities are attributed to a lack of hydrogen bonding environment affecting the size and shape of the O-H stretching and C-O stretching vibrations. The observed correlations from these contour plots are attributed to only the change in alcohol

or water concentration.

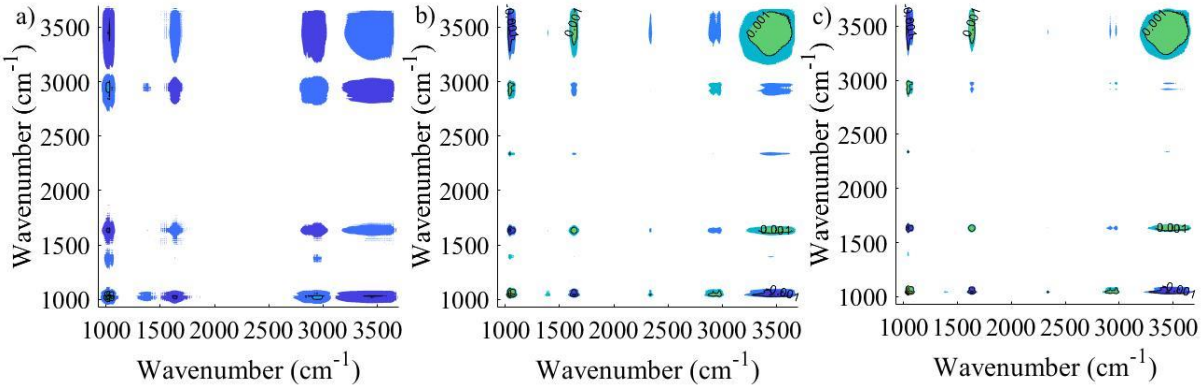

Figure 4.19 Synchronous 2D correlation spectra contour plots for (a) MeOH/water (b) EtOH/water, and (c) IPA/water mixtures at 200 °C concentration as the perturbation.

4.3.3. at Specific Molar Concentrations with Temperature Perturbation

Finally, 2D correlation analysis of different alcohol/water mixtures at a specified concentration (10 v/v%) using temperature as a perturbation was attempted. The synchronous and asynchronous contour plots for 30 mol% methanol/water mixtures is shown in Figure 4.20. No OH_{δ}-CO_s correlation is observed when using temperature as the perturbation because O-H bending does not reduce in intensity as temperature is increased (Figure 4.7), this is because the O-H bending vibration is unaffected by the hydrogen bonding environment. Furthermore, the correlation intensity of OH_s-CO_s is positive and can be related to the reduction in the hydrogen bonding environment in the alcohol/water mixtures. As observed in the 200 °C alcohol/water spectra there is minimal hydrogen bonding present. Therefore, the C-O stretching and O-H stretching peaks are reduced in intensity through the reduction in the extended hydrogen bonding network. Analysis of the asynchronous spectra reveals a positive peak centered at (3394, 3217), this shows that the 3220 cm^{-1} peak decreases in intensity first followed by 3394 cm^{-1} by the peak. This is attributed to an initial reduction in the strongly hydrogen bonded molecular clusters (D2) followed by a reduction in the remaining O-H stretching peak as discussed in Section 4.2. This shows that initial disruption occurs within the strongly hydrogen bonded clusters as temperature is increased followed by reduction in the overall O-H intensity of the stretching peak.

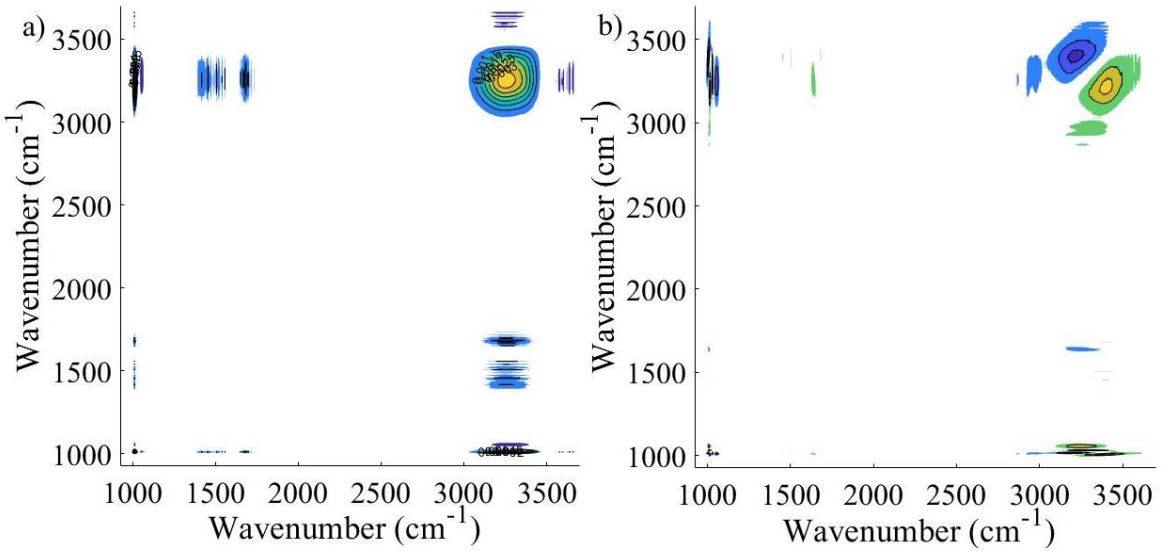

Figure 4.20 (a) Synchronous and (b) asynchronous 2D correlation contour plots for MeOH/water mixtures at 30 mol% MeOH with temperature as the perturbation.

Correlation intensity for the OH_s-CO_s at each methanol molar percentage with temperature perturbation is calculated and displayed in Figure 4.21. The maximum of this plot aligns well with the negative excess enthalpy of mixing in methanol/water mixtures (Figure 2.14) and it follows a comparable shape. The cause of this correlation with excess enthalpy of mixing is attributed to the positive OH_s-CO_s intermolecular interactions between methanol and water forming the extended hydrogen bonding network. This provides a direct analogue to the amount of hydrogen bonding in the system and how the hydrogen bonding network changes over time by measuring the OH_s-CO_s at each methanol molar percentage with temperature perturbation. A maximum correlation intensity is observed at 30 mol% and therefore at this molar percentage there is the most strongly hydrogen bonded methanol/water environment. This aligns with previous investigation the literature showing maximum methanol/water structuring at 30 mol% [316]. The same relationship can be determined from analysing the ethanol/water and isopropanol/water mixtures.

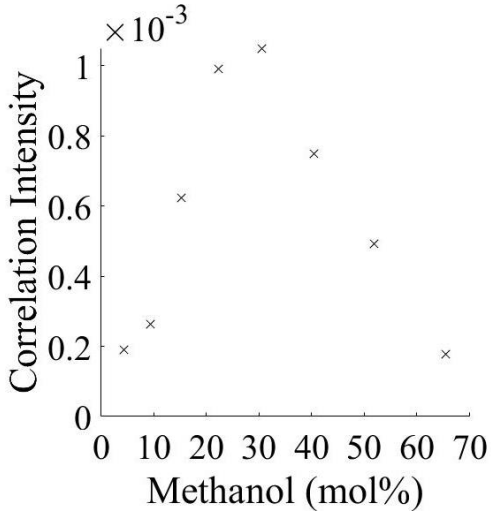

Figure 4.21 Synchronous correlation intensity of O-H stretching to C-O stretching peak against the molar concentration of MeOH. 2D correlation used with temperature as the perturbation at specific concentrations.

4.4. Conclusions

This research chapter exemplifies the use of FT-IR as a facile, cheap, and non-destructive technique to analyse the molecular dynamics of alcohol/water systems. To aid this a full FT-IR spectral assignment is presented for methanol, ethanol, and isopropanol. This is challenging to obtain in the literature and suitable for reference by future researchers. Three different analytical approaches are exemplified which can provide information about molecular and hydrogen bonding within the alcohol/water mixture. These techniques can be transferred to other solvents systems in addition to different techniques such as Raman spectroscopy. The effect that hydrogen bonding dynamics have on the spectroscopic information is explained and demonstrated in the FT-IR data.

Firstly wavenumber position and intensity analysis is presented as the typical technique used in FT-IR analysis. Wavenumber position (blueshifting and redshifting) is widely used, whereby an increase in position is related to a reduction in intermolecular interactions. However, the calculation of excess intensity presented gave further evidence of hydrogen bonding dynamics and agreed with the structural changes measured by other techniques. Excess intensity has been demonstrated to be a valuable and easily obtainable dataset which is underutilised in the research area. Secondly deconvolution which is often used in the literature to separate different hydrogen bonding environments has been demonstrated and provides well resolved peaks. However, the main challenge with this application is determining the appropriate number of

peaks for deconvolution and the correct assignment of those peaks once extracted. Finally, to the authors knowledge this research represents the first attempt at using perturbation based 2D correlation spectroscopy on sub-critical alcohol/water mixtures. Moreover, the analysis of temperature effects on specified concentration methanol/water mixtures provided data in agreement with the maximum structured environment of methanol/water at 30 mol%. This was achieved because the minimal hydrogen bonding environment in sub-critical conditions allowed for assessment of the ambient hydrogen bonding through the reduction in spectroscopic interactions. This demonstrates the effectiveness of perturbation based 2D correlation analysis techniques.

Subsequently, it is important to consider how these changes in the structure of the liquid phase will effect its properties and thus how this will influence the reactions in other processes such as hydrothermal carbonisation. This is investigated experimentally, in Chapter 5 (Section 5.7) the effect of ethanol/water mixtures on properties of the hydrochar produced from bread waste is investigated at a full range of different molar compositions. The increase in intermolecular bonding which is observed clearly in the FT-IR data and discussed in the literature is theorised to encourage different reaction pathways to those observed in only water sub-critical conditions. Some potential interactions are as follows. Increased intermolecular bonding, particularly at the critical molar percentage (23.5 mol% in ethanol), increases the number and strength of solvent cages on the dissolved molecules which reduces the polycondensation reactions and limits the amount of hydrochar formed. The intermolecular interactions between the alcohol and water mean that the more permeative alcohol (given by self-diffusion coefficients) ‘drags’ the water further into the biomass and therefore hydrolyses and increased percentage of the biomass into the aqueous phase. If the addition of alcohol during hydrothermal carbonisation can produce these effects on the process it could be utilised as a valuable tool to allow tunability of the reaction towards the desired product characteristics.

Chapter 5 HTC of Bread Waste

In this chapter the HTC of dried bread waste (DBW) is assessed by characterising the hydrochar produced under various reaction conditions. Temperatures between 160-200 °C, retention times between 30-90 min, and pressurising gases helium (He) and carbon dioxide (CO_2) are examined. In addition, pressurising gases are substituted for palmitic acid (PA) and the effect of varying the DBW particle size is investigated. The full outline for experimental procedures and parameters can be found in Section 3.2.3. HTC of bread waste was investigated for several reasons; An estimated 10% of all food waste produced in the United Kingdom can be attributed to bread waste [317]. Due to a propensity for microbial spoilage, bread waste is problematic when used as animal feed[318]. Furthermore, sources of pure bread waste can be obtained from food manufacturers as "bread ends" are not used in production and as unsold products from supermarkets. Bread waste is a relatively simplistic feedstock when compared to complex municipal solid waste mixtures, consisting of water (~39%), carbohydrate (~43%), protein (~10.3%), fibre (~5%), lipid (~2.2%) and salt (~0.5%) [319]. Finally there are only a few investigations into the hydrothermal treatment of unmixed bread waste with no analysis of varying processing conditions [320], [321]. After characterising the HTC of DBW the effect of different alcohol/water mixtures is investigated in Section 5.7.

5.1. Energy Density and Yield of DBW Hydrochar

Combustion characteristics of the hydrochar are evaluated in full as described in Section 2.3.2. Bomb calorimetry was used to determine higher heating values (HHV) - energy densities - of all hydrochars and the DBW. Yield was also analysed on a dry weight basis. HHV and yield are displayed with both the processing temperature, retention time, and pressurising gas in Figure 5.1. DBW feedstock has a HHV of 17.69 MJ Kg^{-1} comparable to approximate values of hemicellulose and cellulose at 14.7-18.2 MJ Kg^{-1} and 16.1-19 MJ Kg^{-1}, respectively [182]. HHV of the DBW feedstock was subtracted from that of the hydrochars to quantify the energy densification during HTC. The general trend observed is that HHV and yield of the hydrochar both increase with higher processing temperatures and longer retention times. This is expected as increased retention time allows for the reactions occurring during HTC to proceed to completion. Increased processing temperature provides additional activation energy, allowing for a larger number of hydrothermal carbon producing reactions to occur. However, at 160 °C as retention time increases there is a reduction in yield, at 30 min under CO_2 hydrochar yield is 18.3% lowering down to 10.1% at 90 min, the same is trend is seen under He. This is because

at 160 °C there is sufficient heat to allow the dissolution and hydrolysis of organic compounds into the aqueous phase however there is insufficient activation energy for carbonisation reactions to occur [322]. Therefore the increase in HHV, with respect to the DBW, is because the compounds which are resistant to hydrolysis and dissolution at 160 °C have a larger HHV. Increasing retention time from 30-60 min for HTC at 180 and 200 °C has a notable increase on both yield and energy density, however, there is negligible effect on increasing from 60 to 90 min. Thus, 60 min is sufficient retention time for carbonisation reaction to proceed to completion during HTC and additional time provides minimal benefit. Increases to processing temperature have a more significant effect on yield than HHV. Under CO_2 after 60 min, increasing the temperature from 180 °C to 200 °C raises the HHV of the hydrochar by 2.4% but increases the yield by 70.4%. With a hydrochar yield of 30.0%at 200 °C and 17.7% at 180 °C. This demonstrates that higher activation energy is required for some of the carbonisation reactions to occur within the dissolved organics and form the hydrothermal carbons.

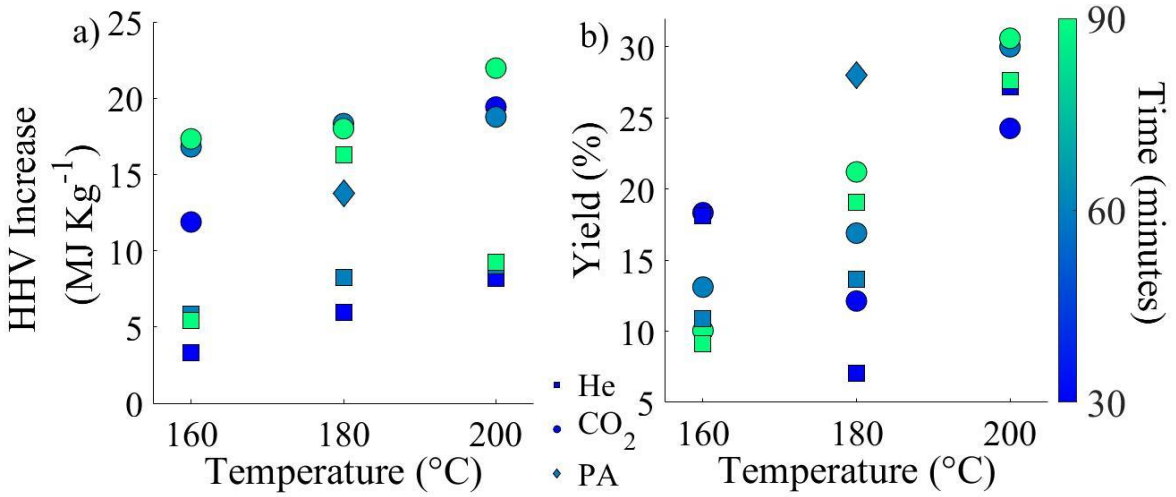

Figure 5.1 (a) HHV increase (MJ Kg^{-1}) from DBW feedstock of hydrochars analysed with bomb calorimeter (3.3.7), (b) yield (%) from HTC of DBW both of which plotted against processing temperature. Datapoints are coloured for retention time from 30 mins (dark blue) to 90 mins (bright green). He (squares), CO_2 (circles), and PA (diamonds).

HHV of the hydrochar formed after 60 min at 180 °C and 200 °C in CO_2 is 36.02 and 36.46 MJ Kg^{-1} respectively. Whilst this is by no means the most important or only indication of the quality of solid fuel, this HHV is significantly high, above the most energy dense types of anthracite (31.4 MJ Kg^{-1}) and bituminous (33.7 MJ Kg^{-1}) coals [186]. Compared to the HHV of hydrochars analysed from literature (Section 2.3.2.5) this DBW hydrochar synthesised in presence of CO_2 has the highest HHV and is processed at comparatively low operating

temperatures. For example, mixed food waste hydrochar processed at 200 °C and 300 °C for 60 min produced hydrochar with HHVs of 20.8 and 31 MJ Kg^{-1}, respectively [183]. HHV of hydrochar formed under He is significantly lower at 25.91 and 26.71 MJ Kg^{-1} for 180 °C and 200 °C respectively at 60 min, just slightly below that of the least energy dense anthracite (27.9 MJ Kg^{-1}) and bituminous (27.9 MJ Kg^{-1}) coals. Therefore, using CO_2 as the pressuring gas instead of He produces a hydrochar with between 8.5 and 12.5 MJ Kg^{-1} larger HHV. This increased HHV when using CO_2 as the pressurisation gas is attributed to carbonic acid formation which acts as a homogeneous acid catalyst for carbonisation reactions of the organics in the aqueous phase [323]. Therefore, the carbonic acid is catalysing a different reaction pathway for either the aqueous organics or further carbonisation of the solid material to produce a hydrochar with an increased HHV. This opposes previous investigations into using CO_2 in the HTC of lignocellulosic wastes which did not show a significant difference in the HHV of the hydrochar when CO_2 was used instead of N_2 [324]. It is speculated that the large increase to HHV observed on DBW using CO_2 is because of its different composition. DBW contains a large percentage of short chain saccharides (43%), which are more readily dissolved into the aqueous phase and consequently carbonised compared to the more resistant cellulose and lignin present in lignocellulosic wastes. Though, yield of hydrochar remained similar between CO_2 and He under the same processing conditions. A potential reaction causing this is the acid catalysed dehydration of the alcohol present on the surface of the hydrochar (Figure 5.2). Conversion of surface hydroxides to alkenes would increase the HHV of the hydrochar.

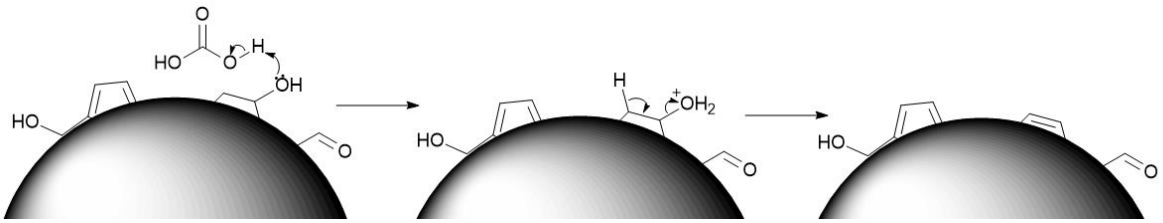

Figure 5.2 Schematic representation for the dehydration of hydrochar surface hydroxide (OH) functionality catalysed by carbonic acid during HTC.

PA is the most common saturated fatty acid in flora and fauna [325]. Therefore, it is a common component in many feedstocks used in HTC and understanding how it impacts the hydrochar formed is useful for future processes. However, to the authors knowledge the effect of PA as an additive during HTC has not been investigated. Whilst strong acids such as nitric, hydrochloric, and sulfuric have been shown to change the structure of the hydrochars and potentially offer different reaction pathways as well as transferring heteroatoms into the hydrochar structure [326]. The addition of PA instead of a pressurisation gas at 180 °C for

60 min was found to yield 28.0% hydrochar which is higher than that of both CO_2 and He at 16.9% and 21.9% respectively. The increased yield is hypothesized to come for carbonisation of the PA during HTC and not from it acting as a homogeneous catalyst. HHV increase for the PA synthesised hydrochar was 13. MJ Kg^{-1} higher than that of the He synthesised at 8.2 MJ Kg^{-1} respectively. Pure PA has a HHV of 38.8 MJ Kg^{-1}, therefore the increased HHV of the hydrochar compared to the He synthesised hydrochar can be attributed to PA incorporation [327].

Severity factor is a useful tool to combine both processing temperature and retention time into one parameter [328]. The calculation of severity factor is shown in Section 2.3.2.2. HHV and yield of hydrochar has been compared against the calculated severity factor and displayed in Figure 5.3. HHV is shown to increase relatively linearly with an increase in severity factor. Demonstrating the utility of severity factor where the processing conditions can be approximated based upon the required HHV of the hydrochar. Yield shows an initial decrease for lowest severity factors at 7.46, 8.16, 8.57, these correspond to the lowest processing temperature of 160 °C. Following this there is a linear increase in yield correlated with severity factor. This is attributed to the previously discussed, 160 °C does not provide substantial heat for carbonisation reactions to occur [322]. Therefore, a severity factor above 9 is recommended for substantial yield of hydrochar from DBW with a processing temperature at or above 180 °C to provide sufficient activation energy for carbonisation reactions.

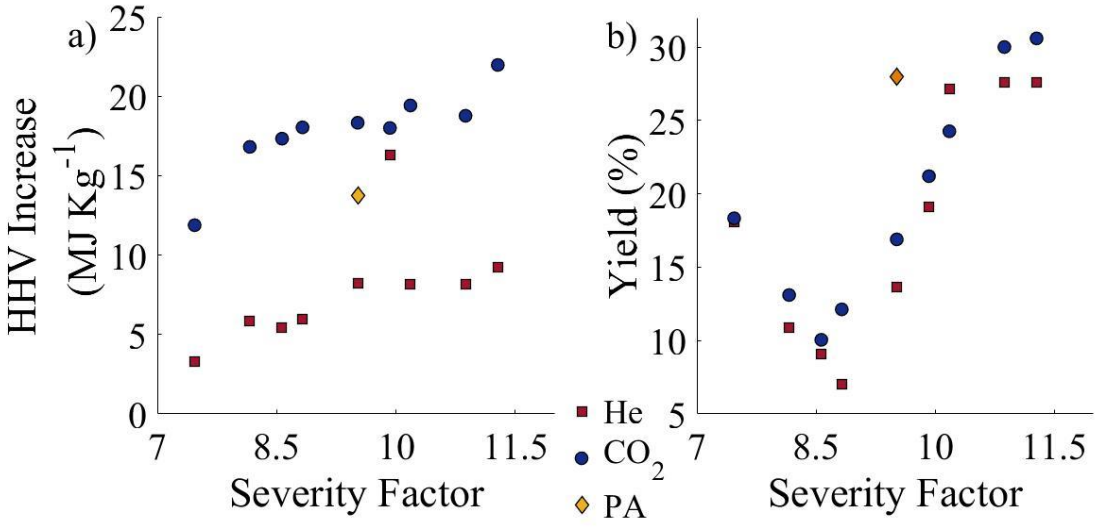

Figure 5.3 (a) HHV increase (MJ Kg^{-1}) from DBW feedstock of hydrochar analysed with bomb calorimeter (3.3.7), (b) yield (%) from HTC of DBW both of which plotted against severity factor [328]**.**

5.2. H/C and O/C Ratios of DBW Hydrochar

van Krevelen diagrams have been produced from CHNS elemental analysis of the hydrochars from DBW (Figure 5.4). As was discussed in Section 2.3.2.3 van Krevelen diagrams are used to estimate the viability of a solid material for fuel applications. Lower H/C and O/C ratios are typically associated with higher energy densities because C-C bonds contain more energy than C-H or C-O bonds [101]. Additionally there is a range of expected H/C and O/C ratios for coals and biomasses, therefore these ratios allow approximation of the combustion behaviour of hydrochars. Reduction in H/C and O/C ratio is also indicative of dehydration and decarboxylation of the feedstock. Higher H/C ratio and lower O/C ratio is evidence of higher aromaticity and lower polarity, respectively [329].

The retention time in the HTC process has little to no impact on the O/C and H/C ratios of the hydrochar with no correlation visible (Figure 5.4, a). Whilst increased processing temperature is shown to correlate strongly with a reduction in both O/C and H/C ratios (Figure 5.4, b). Further cementing the conclusion drawn in literature that processing temperature is the more important variable for HTC reactions [23]. At 200 °C the hydrochar has comparable H/C and O/C ratios to that of lignite with no clear difference between the He and CO_2 synthesised hydrochars. The hydrochars produced at 180 °C for 60 min and 90 min showed slightly higher H/C and O/C ratios mostly comparable to that of peat. Moreover it is clearly shown that 180 °C

and 60 min is the minimum requirement for the hydrochar to have superior qualities than untreated biomass. Hydrochar synthesised in the presence of PA has a low O/C ratio but a large H/C ratio, this is further evidence of the incorporation of PA into the hydrochar as the empirical formula for PA is $C_{16}H_{32}O_2$. Thus PA or carbonised products of PA have been integrated within the hydrochar and it is not acting as a homogeneous catalyst. However, this reveals PA and similar long chain fatty acids can be used as doping agents during HTC to manipulate the hydrogen, carbon, and oxygen content of hydrochars. Following the concept of tailoring the properties of the hydrochar for application, comparable to nitrogen doping using organics such as urea or melamine [330], [331]

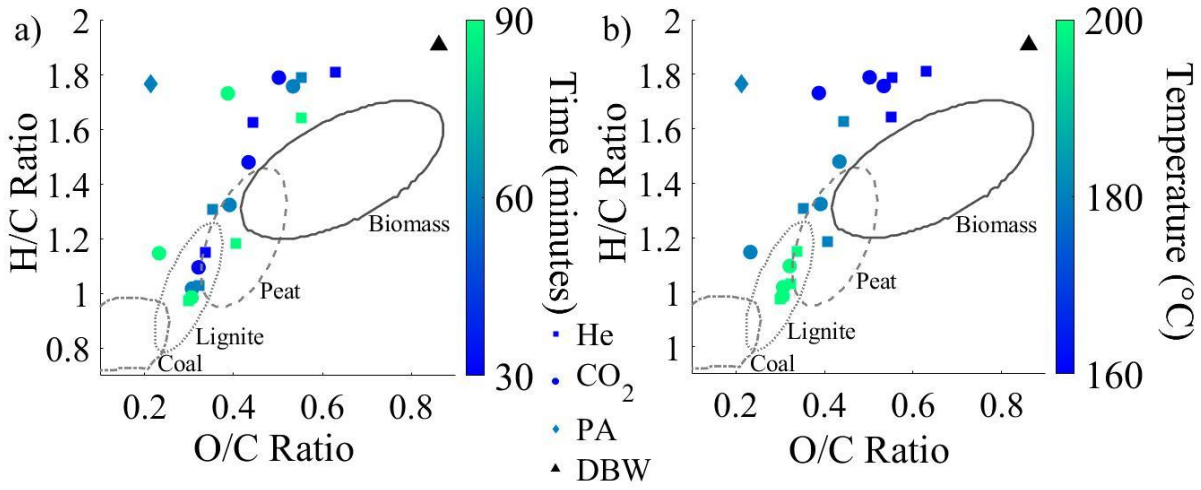

Figure 5.4 van Krevelen diagrams for hydrochars produced with pressurised gasses He (square), CO_2 (circle), additive PA (diamond), unprocessed DBW (triangle). (a) Retention time is displayed with coloured datapoints from 30 mins (dark blue) to 90 mins (bright green). (b) Processing temperature is displayed with coloured datapoints from 160 °C (dark blue) to 200 °C (bright green).

The van Krevelen plot with severity factor again shows the effectiveness of this combined processing parameter for use in HTC (Figure 5.5). A direct correlation between increasing severity factor and a reduction in both H/C and O/C ratios is observed. Further demonstrating that severity factor can be used as an effective tool to predict the degree of carbonisation that a feedstock will undergo during HTC at varying processing temperatures and retention times.

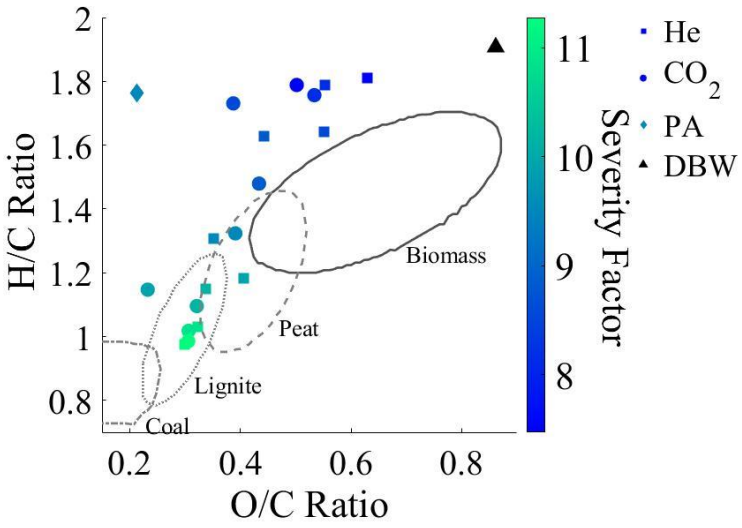

Figure 5.5 van Krevelen diagrams for hydrochars produced with pressurised gasses He (square), CO_2 (circle), additive PA (diamond), and unprocessed DBW (triangle). Severity factor for the HTC process was calculated using Equation 2.6 and is displayed by coloured datapoints from 7 (dark blue) to 12 (bright green) [328]**.**

5.3. Proximate Analysis of DBW Hydrochar

Proximate analysis of the hydrochars was performed using a TGA following the procedure outlined in Section 3.3.6. Percentage (wt.%) volatile matter (VM), fixed carbon (FC), and ash of the hydrochars synthesised is shown in Figure 5.6. The ash content in the DBW feedstock is partially attributed to the salt (NaCl) that is added during bread production to control fermentation, strengthen gluten, and modify the flavour [332]. Additional ash content in the DBW is from the additive's calcium carbonate, and iron. As well as this the main naturally occurring minerals in wheat flour are calcium, copper, iron, potassium, manganese, magnesium, phosphorus and zinc. However, they are present at less than 0.1 wt.% concentration [333]. Ash is a significant industrial waste from the combustion of coal which can pollute the environment, however ash also represents a valuable raw material which can be used in many different applications based on the chemical composition [334]. The ash content of the hydrochars was larger than the DBW for all processes at 160 °C. As previously discussed, this is because 160 °C is insufficient heating to allow for reactions and formation of hydrothermal carbons during HTC. Therefore, no hydrothermal carbons are being deposited but a large portion of the DBW has been hydrolysed/dissolved into the aqueous phase. Whilst some inorganics are dissolved in the aqueous phase it is proportionally a smaller amount. The ash content of the hydrochars at all higher temperatures is generally the same or slightly lower than the DBW feedstock. It is speculated that the NaCl readily dissolves during HTC to the

aqueous phase, whilst the calcium carbonate and iron remain to make up the ash content in the hydrochar. Previous studies on the fate of inorganics during HTC displayed calcium as having limited removal during HTC and feedstocks containing iron correlated with a higher ash content [187].

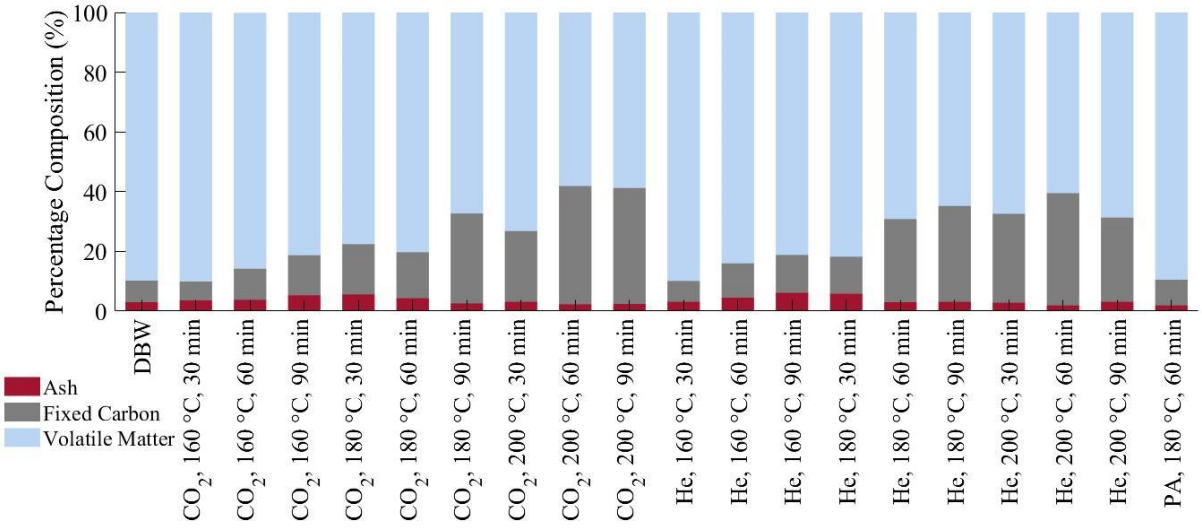

Figure 5.6 Stacked bar chart showing the percentage composition of the DBW, and the hydrochar produced from HTC of the DBW for a specified retention time in mins and processing temperature in °C. Composition of the ash, fixed carbon (FC), volatile matter (VM) is given on a dry basis in wt.%.

FC content is a good indicator for the performance of a fuel, whereby the higher the FC content the hotter and more energy efficient it is to burn. The FC of the hydrochars is almost always higher than that of the DBW feedstock. The 160 °C reactions show the lowest increase where it is likely the hydrolysis and dissolution resistant material is the FC in the DBW therefore no new FC is being produced, simply that is the remaining material. Retention time has no obvious impact on the amount of FC in the 180 and 200 °C reactions. At 180 and 200 °C after 60 min the FC present is 15.4% and 39.6% for CO_2 whilst it is 32.1% and 37.6% for He. At 180 °C, He is the slightly advantaged pressurisation gas to CO_2 by FC content alone, though there is no difference at 200 °C. This is in contrast with the energy density which was significantly higher for the CO_2 produced hydrochars. The high energy density of the CO_2 synthesised hydrochars must therefore be attributed to the structure and composition of the VM. The difference in VM composition between the CO_2 and He synthesised hydrochars can be characterised using evolved gas analysis which is typically TGA fitted with FTIR, MS, or GC-MS detector [335].

VM is an indicator for how easy the material will be to ignite, the higher the VM content the easier to ignite. VM accounts for the rest of the percentage composition in the hydrochar and

is reduced compared to the DBW feedstock under all conditions. Our observations match that in the literature HTC data (Section 2.3.2.4) an increase in processing temperature decreases the VM content of the hydrochar. This reduction in VM with increasing processing temperature is because the compounds making up the VM are soluble at lower temperatures. After dissolution they undergo carbonisation and reform carbonaceous material in the hydrochar during HTC. The VM remaining in the hydrochar at higher temperatures is attributed to a mix of hydrothermal carbons which are volatile and some unreacted volatile compounds within the DBW.

5.4. Varying the Particle Size of DBW Used for HTC

An additional factor examined was the selection of different particle size ranges of DBW. Particle sizes investigated are >500, 250-500, 125-250, 63-125, and <63 μm all processed at 180 °C for 60 min pressurised with He. Particle size is an important consideration for the industrial application of HTC because it contributes to the required energy for shredding and pumping of the feedstock. Particle size effects during HTC have been investigated previously in the literature, with the conclusion that smaller particle sizes undergo higher conversion because of increased surface area for heat and mass transfer [336]. Combustion characteristics of the hydrochars synthesised from different particle sizes of DBW are compiled in Table 5.1. For comparison the combustion characteristics of the DBW before HTC is displayed in Table 5.2.

The most striking observation is that the HHV increase is very minimal at only 3.7 MJ Kg^{-1} when the largest particle size above 500 μm was used. This suggests that under these processing conditions there is insufficient energy to break up these larger particles and allow for HTC reactions to take place. This conclusion is backed up by the proximate analysis which showed only a minor increase in FC relative to DBW of 2.5% and a minor decrease in VM relative to DBW of 3% which is significantly different to observations of hydrochar from smaller particle sizes. There is further evidence in the H/C and O/C ratios which only have a small decrease of 0.2 and 0.1 respectively.

Table 5.1 Compiled combustion characteristics for hydrochar produced from different particle sizes of DBW (20 wt.% slurry) processed by HTC at 180 °C for 60 min pressurised with He. VM (volatile matter), FC (fixed carbon), H/C and O/C are ratios between the atomic abundance of hydrogen/carbon and oxygen/carbon, respectively.

Particle Size Range (μm)	Yield (%)	HHV Increase (MJ Kg^{-1})	VM (%)	FC (%)	Ash (%)	H/C	O/C
>500	20	3.7	86.4	10.5	3.1	1.8	0.6
250-500	20	20.2	80.8	15.1	4.2	1.3	0.4
125-250	16	19.7	76.8	19.8	3.5	1.3	0.4
63-125	14	18.0	69.2	27.8	3.0	1.3	0.4
<63	14	11.9	85.4	9.6	5.0	1.3	0.3

The DBW between 250-500 μm has the largest yield (20%) and HHV increase (20.2 MJ Kg^{-1}), this then decreases with the decrease in particle size. A sharp drop in the HHV increase is observed when particles smaller than 63 μm were processed down to 11.9 MJ Kg^{-1} which is 6.1 MJ Kg^{-1} lower than 63-125 μm. The VM decreases and FC increases as the particle size is decreased from 250-500 μm, again this trend follows up until particles smaller than 63 μm were processed. For particles smaller than 63 μm a large amount of VM and small FC remains at 85.4% and 9.6% respectively. H/C and O/C ratios for all DBW particle sizes smaller than 500 μm were relatively similar with no significant trend. When considered together this suggests that the initial composition of the different particle size DBW below 500 μm are intrinsically different. This is caused by different compounds such as fibre being more resistant to milling and so comprise less of the smaller particle sizes. However, it is clear that milling the DBW below 500 μm allows for better energy and mass transfer. This is significant because controlling the maximum particle size for HTC reactions is considered an important factor for efficient processing.

Table 5.2 Compiled combustion characteristics for different particle sizes of unprocessed DBW. VM (volatile matter), FC (fixed carbon), H/C and O/C are ratios between the atomic abundance of hydrogen/carbon and oxygen/carbon respectively.

Particle Size Range (μm)	HHV (MJ Kg^{-1})	VM (%)	FC (%)	Ash (%)	H/C	O/C
>500	18.1	89.4	8.0	2.6	2.0	0.7
250 – 500	18.2	89.9	6.9	3.3	1.9	0.8
125 – 250	17.6	86.7	10.1	3.2	2	0.8
63-125	17.7	89.8	7.2	3.0	1.9	0.9
<63	17.3	84.5	12.5	3.0	1.9	0.8

5.5. Surface Characterisation of DBW Hydrochar

Surface functionality of the hydrochar and DBW was analysed using FT-IR spectroscopy and

surface morphology was probed using SEM as described in Sections 3.3.4 and 3.3.8, respectively.

5.5.1. Surface Functionality by FT-IR

To appropriately determine the changes to the DBW during HTC under different processing conditions the DBW FT-IR spectra needs to be fully interpreted and assigned (Figure 5.7). A broad absorbance band is attributed to O-H stretching (**1**, 3650-3050 cm^{-1}) vibrations [191]. Two aliphatic bands for asymmetric (**2**, 2922 cm^{-1}) and symmetric (**3**, 2857 cm^{-1}) C-H stretching. Both these aliphatic and hydroxide absorbances are present in all compounds within DBW. Conjugated (**4**, 1744 cm^{-1}) and unconjugated (**5**, 1649 cm^{-1}) carbonyl (C=O) stretching absorbances owe their presence to the acidic carbonyl in the proteins (gluten) and lipids (long chain fatty acids) present in the DBW. Amide bonds within the proteins are also responsible for the N-H bending (**6**, 1537 cm^{-1}) vibration [337]. The C-O modes (1150-900 cm^{-1}) are often related to saccharide (carbohydrates and fibre) presence within the DBW [338]. These are more accurately assigned to C-O-C stretching (**7**, 1150 cm^{-1}), C-C-O asymmetric stretching (**8**, 1076 cm^{-1}), C-O stretching (**9**, 997 cm^{-1}), and C-C-O symmetric stretching (**10**, 933 cm^{-1}) [339]. Finally further aliphatic presence can be determined by C-H out of plane bending (**11**, 855 cm^{-1}) [329].

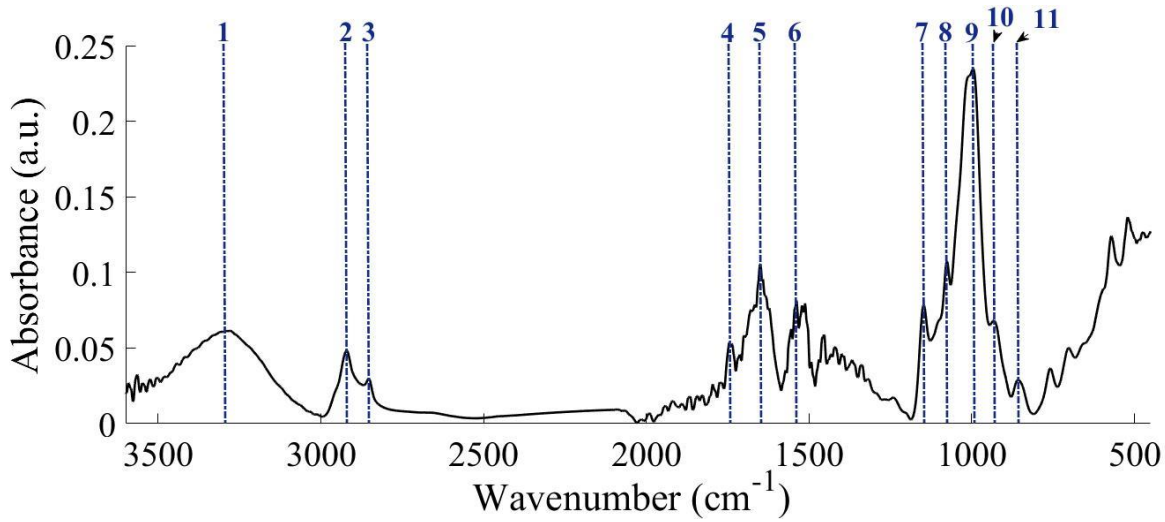

Figure 5.7 FT-IR spectra obtained for DBW using a Shimadzu IRAffinity-1S spectrometer fitted with a Specac ATR plate. Analysis conditions: scans 4000, resolution 4 cm^{-1}, absorbance mode. 1: νO-H,; 2: ν_{as}C-H; 3: ν_{s}C-H; 4 and 5: νC=O; 6: δN-H; 7: νC-O-C; 8: ν_{as}C-C-C; 9: νC-O; 10: ν_{s}C-C-O; 11: δC-H.

Hydrochars produced at 160 °C displayed have the same peak structure in the FT-IR spectra at 30 and 60 min (Figure 5.8). After 90 min severe reduction in the peak intensity throughout the

spectrum is observed. Backing up previous conclusions in Section 5.1, 160 °C is insufficient processing temperature to allow carbonisation reactions to occur during HTC. The process is only dissolving/hydrolysing the DBW compounds into the aqueous phase. No evidence for carbon formation can be found in the FT-IR spectra of hydrochars processed at 160 °C. The same is observed in the FT-IR spectra for hydrochars synthesised with CO_2 as the pressurising gas.

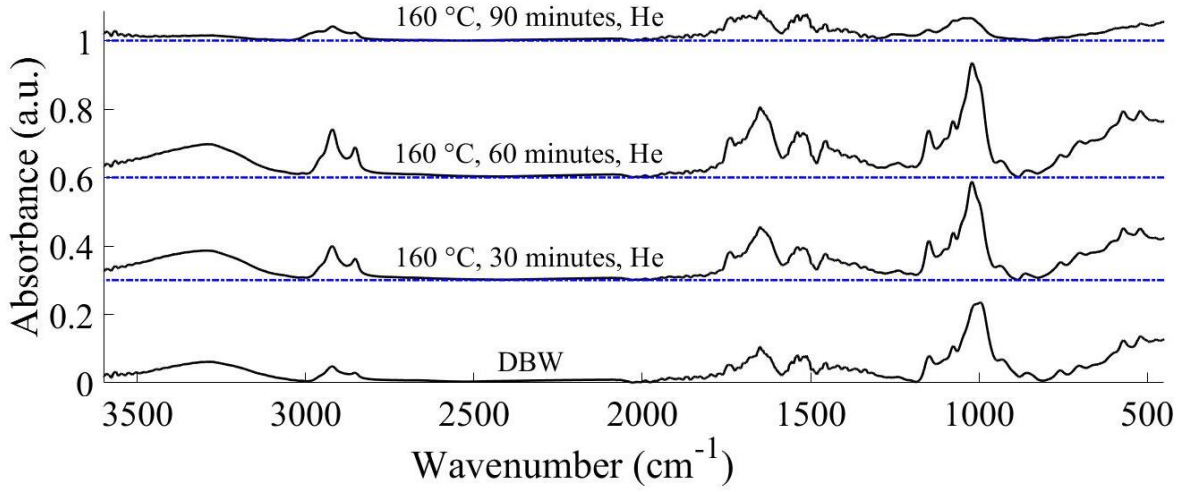

Figure 5.8 FT-IR spectra obtained for hydrochars produced at 160 °C under He compared to DBW using a Shimadzu IRAffinity-1S spectrometer fitted with a Specac ATR plate. Analysis conditions: scans 4000, resolution 4 cm^{-1}, absorbance mode.

Hydrochars produced at 180 °C show significant changes in the FT-IR spectra compared to DBW (Figure 5.9). There are significant differences between the 30 min and 60 min hydrochars, because 30 min is not sufficient time for HTC reactions to proceed to completion and after 60 min no further changes are observed. The same trend is seen for 180 °C using CO_2 and 200 °C with both He and CO_2. Therefore backing up the established conclusion in Section 5.1. that retention time of 60 min is required for the majority of HTC reactions to occur. Consequently, further comparisons between retention times are disregarded and only 60 min retention times analysed.

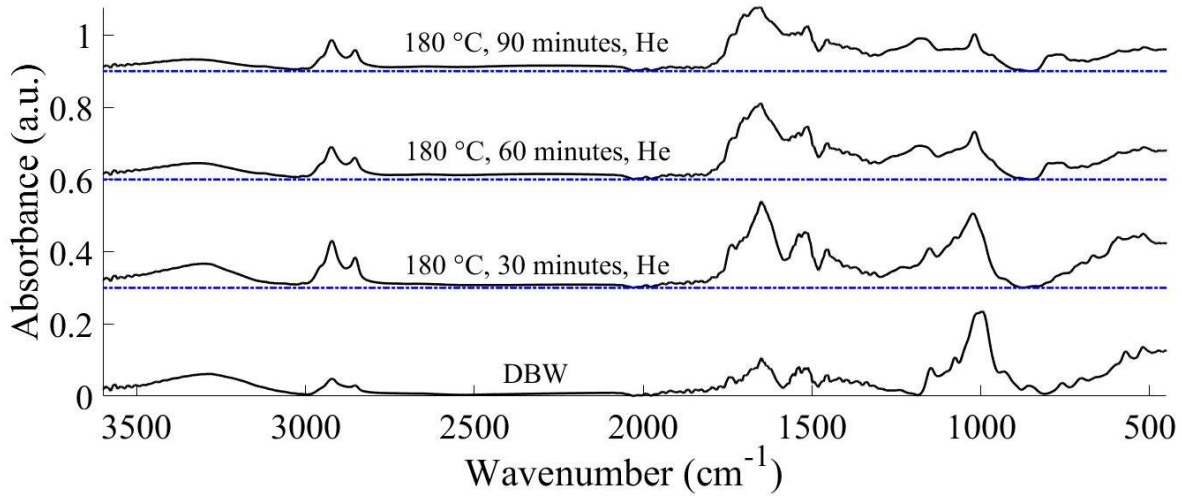

Figure 5.9 FT-IR spectra obtained for hydrochars produced at 180 °C under He compared to DBW using a Shimadzu IRAffinity-1S spectrometer fitted with a Specac ATR plate. Analysis conditions: scans 4000, resolution 4 cm^{-1}, absorbance mode.

Comparison between the FT-IR spectra of hydrochars synthesised in different reaction environments He, CO_2, and PA at 180 °C for 60 min (Figure 5.10). The PA synthesised spectra has significant differences compared to He and CO_2 following the same trend established in Section 5.1. There is a large increase in the asymmetric (2914 cm^{-1}) and symmetric (2914 cm^{-1}) C-H stretching, as well as the appearance of a sharp peak for C=O stretching (1699 cm^{-1}) [340]. The C-O stretching (1018 cm^{-1}) is slightly lower than in the CO_2 and He produced hydrochars. New peaks appear related to the CH_2 groups and the long hydrocarbon chain in the PA these are: CH_2 scissoring (1470 cm^{-1} & 1429 cm^{-1}), a variety of skeletal C-C-C stretching (1298- cm^{-1}), C-C stretching (941 cm^{-1}), and H-C-C stretching (723 cm^{-1}). The structure of the long hydrocarbon chain in PA and the carbonyl bond has been retained whilst the C-O and O-H functionality has been removed. This suggests that the PA is participating in reactions during HTC which is selectively removing the hydroxide group. The PA is possibly participating in the polycondensation reactions with molecules such as 5-HMF as presented in Section 2.3.1.

Both He and CO_2 reduced the hydroxide functionality of the material shown by a lower O-H stretching (3650-3050 cm^{-1}) band. This is attributed to dehydration reactions during HTC and causes the hydrochar to have higher hydrophobicity which is a desirable characteristic for fuels [163], [341]. Aliphatic asymmetric (2922 cm^{-1}) and symmetric (2857 cm^{-1}) C-H stretching increases in absorbance for both hydrochars compared to DBW. Following the expected reduction in aliphatic C-H stretching observed for wastewater sludge which is opposed by HTC of pure cellulose, lignin, and xylose in the literature [217], [342]. Based on these studies and

observations from Saha *et al.* the intensity of C-H stretching peaks is related to both processing temperature and feedstock composition [343]. Therefore 180 °C is insufficient for DBW to remove aliphatic groups in the hydrochar but the hydrothermal carbons deposited from aromatisation and polycondensation reactions contain C-H bonds that increase the relative presence of them within the hydrochar surface. Furthermore, the C-H stretching band is smaller in the CO_2 synthesised hydrochar indicating that CO_2 increases the removal of surface aliphatics.

There is a drastic reduction in C-O linkages which are mostly saccharide (carbohydrate and fibre) related [279]. The saccharides are mostly dissolved/hydrolysed at 180 °C in both He and CO_2. The new broad band between 1196-1153 cm^{-1} however is assigned to C-O ester linkages which are likely produced by polycondensation reactions during HTC. Additional evidence of HTC reactions is given by appearance of C=C aromatics (1512, 1454 cm^{-1}) stretches and hence aromatisation reactions. Finally the increase in C=O stretching (1649 cm^{-1}) presenting as a broad peak is designated to the amide groups within the hydrochar and the N-H stretching (1540 cm^{-1}) peak for amides is shouldered by neighbouring peaks [344]. Demonstrating that the amino acid (proteins) within the DBW are resistant to dissolution/hydrolysis at 180 °C.

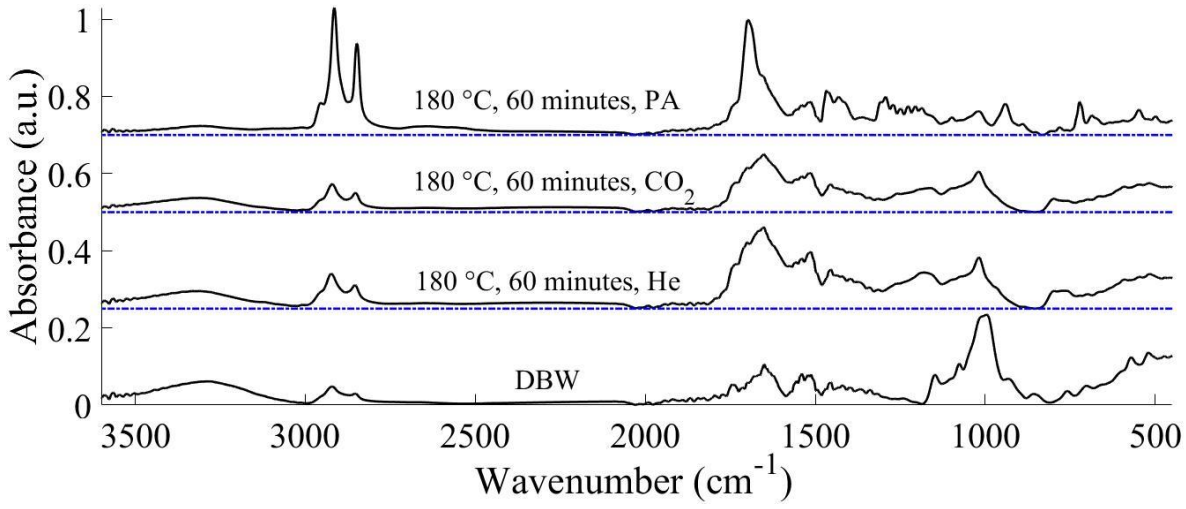

Figure 5.10 FT-IR spectra obtained for hydrochars produced at 180 °C under He, CO_2, and with additive PA compared to DBW using a Shimadzu IRAffinity-1S spectrometer fitted with a Specac ATR plate. Analysis conditions: scans 4000, resolution 4 cm^{-1}, absorbance mode.

FT-IR spectra for hydrochars produced at 200 °C for 60 min in both He and CO_2 (Figure 5.11). A large reduction in all surface functionality is displayed in these hydrochars. CO_2 produced hydrochar has a lower surface functionality than the He produced hydrochar. As established

previously in Section 5.1. the CO_2 acts as a homogeneous acidic catalyst during HTC increasing the conversion of DBW to hydrothermal carbons [323]. The largest remaining peaks in the hydrochars between 1750-1490 cm^{-1} come from a combination of C=C aromatics, C=O, and N-H stretches which are the main functionalities observed on the hydrochar surface [163], [345]. Therefore 200 °C is sufficient to carbonise the DBW almost completely with no DBW associated surface functionality intact.

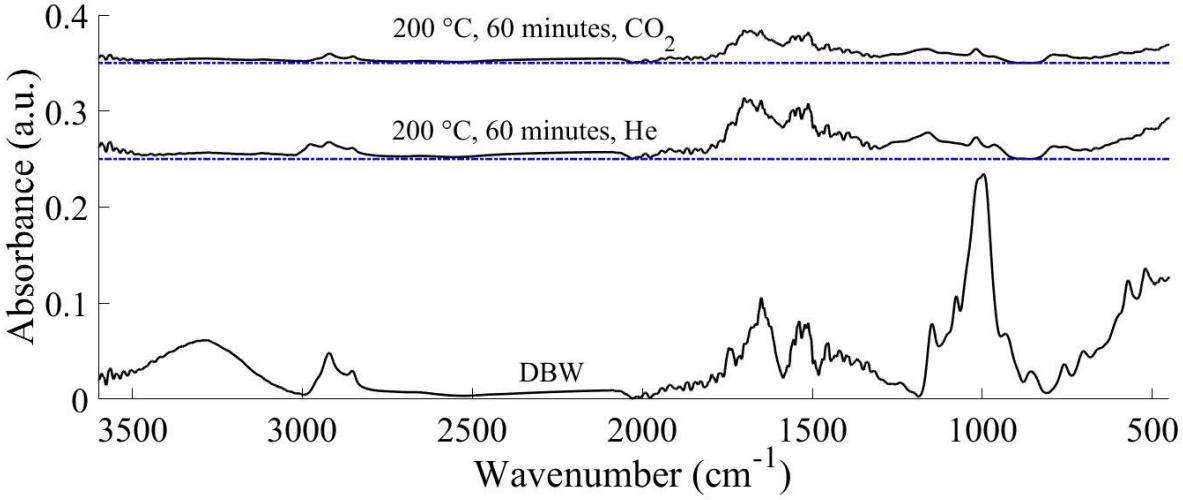

Figure 5.11 FT-IR spectra obtained for hydrochars produced at 200 °C under He and CO_2 compared to DBW using a Shimadzu IRAffinity-1S spectrometer fitted with a Specac ATR plate. Analysis conditions: scans 4000, resolution 4 cm^{-1}, absorbance mode.

5.5.2. Surface Morphology by SEM

Surface morphology of the hydrochar compared to the initial morphology of DBW (63-125 μm) was assessed using SEM. Raw DBW appeared as unstructured, flat chunks of biomass (Figure 5.12, b). Irrespective of processing conditions the hydrochar was visibly distinct to DBW and displayed increased signal and hence conductivity, this is attributed to increased relative carbon content. Hydrochars presented a generally amorphous structure and retention time had negligible effect on the structure compared to processing temperature. Hydrochars produced at 160 °C had a more structured rough surface, often with visible holes and cracks from the hydrolysis of the compounds in DBW (Figure 5.12, a) [346]. Hydrochars synthesised under 180 °C had the formation of discernible microspheres on the surface often fused together, not completely covering the material. Microspheres are the product HTC polycondensation reactions as described in Section 2.3.1 [347]. At 200 °C the microspheres are larger and completely cover the surface of the hydrochar showing that considerably more hydrothermal carbons have been formed. The use of CO_2 did not change the morphology of

the hydrochars under any given processing conditions (Figure 5.12, c). PA synthesised hydrochar was structurally distinct from all other hydrochars with no evidence of microsphere formation and therefore expected polycondensation reactions. The surface was however structured and rough with no holes or cracks from hydrolysis of DBW. Building upon previous conclusions this is attributed to the PA taking part in condensation reactions and being deposited onto the surface of the material.

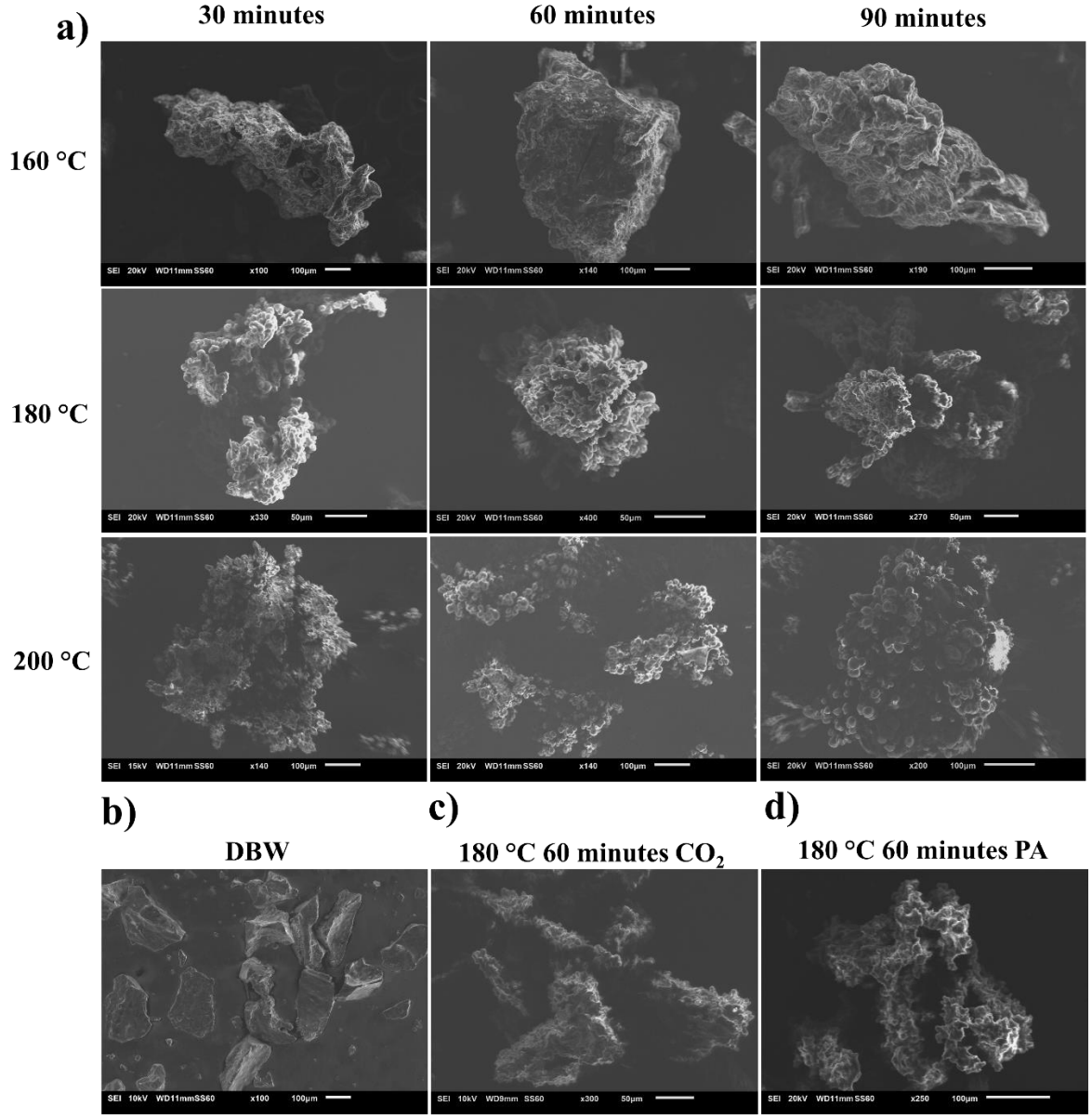

Figure 5.12 SEM images of (a) hydrochar synthesised under He with varying processing temperatures and retention times, (b) DBW feedstock 63-125 µm, (c) hydrochar produced at 180 °C under CO_2, (d) hydrochar produced at 180 °C with no pressurising gas and PA additive. SEM performed on instrument in Section 3.3.8.

5.6. Qualitative Analysis of Aqueous Phase

Volatile organics within the aqueous phase were analysed by GC-MS to give complementary analysis on the hydrochar formation reactions which occur within the aqueous phase. Instrumental analysis settings for GC-MS are outlined in Section 3.3.5. Chromatograms were often dominated by a peak eluted at 12.5 minutes, this has been attributed to only 5-HMF (Figure 5.13) in this research, 5-HMF is previously discussed is a common product in HTC from carbohydrates, which constitute ~60 wt.% DBW (Section 2.3.1). Whilst the authors are aware that the peak is not separated and other organics with similar structures are being eluted at the same time it was not possible to resolve this issue in the given timeframe. Consequently 5-HMF was the only product quantified by GC-MS in this convoluted peak, the peak area is used to qualitatively determine the relative abundance of other products (Appendix 8). The calculated HMF concentration of the aqueous phase under each condition is displayed in Table 5.3.

Table 5.3 5-HMF concentration of the aqueous phases produced at different processing conditions obtained by GC-MS (Section 3.3.5).

Temperature (°C)	Retention Time (Min)	Pressurising Gas	HMF Concentration (ppm)
180	30	He	1499
180	60	He	9748
180	90	He	2892
160	30	CO_2	10
160	60	CO_2	488
160	90	CO_2	218
180	30	CO_2	1207
180	60	CO_2	5935
180	90	CO_2	8873
200	30	CO_2	10259
200	60	CO_2	6695
200	90	CO_2	2904

HTC at 160 °C produced a sweet smelling yellow liquid which was likely high in dissolved sugars which are not detectable by GC-MS. Low overall signal was present in the GC-MS chromatogram. 5-HMF was present at a relatively low concentration (488 mg L^{-1}), giving further evidence that this processing temperature is insufficient for HTC reactions. d-allose was the only detectable sugar by GC-MS, non-volatile sugars are expected from the dissolution/hydrolysis of the DBW. Processing at 180 °C yielded a brown liquid which was found to have significant concentration of 5-HMF which increased with the retention time.

Beginning at 1207 mg L^{-1} after 30 min and increasing to 5935 then 8873 mg L^{-1} for 60 and 90 min, respectively. Indicating that more of the carbohydrates are being converted into 5-HMF as the retention time increases however they are not all undergoing polycondensation to form hydrothermal carbons, a large proportion are left in the aqueous phase even after a long retention time. An increase in long chain fatty acids *e.g.* dodecanoic acid is also observed with this increase in temperature, attributed to the dissolution of lipids in the DBW. At 200 °C the highest concentration of 5-HMF is observed at 30 min with 10259 mg L^{-1} this decreases with time to 6695 and 2904 mg L^{-1} for 60 and 90 min respectively. Demonstrating that the hydrolysis and dissolution occurs rapidly at 200 °C which is followed by polycondensation reactions of the 5-HMF into hydrothermal carbons. Further carbonisation reactions are occurring shown by the presence of 2-furaldehyde and 3-methyl-1,2-cyclopentanedione which are ascribed to different conversion reactions of carbohydrates and 5-HMF. The observed highest 5-HMF concentration equates to 0.2 g from 5 g of DBW, therefore for every 25 tons of DBW processed 1 ton of 5-HMF would be produced that could be extracted. 5-HMF has a retail price of approximately \$1100 ton^{-1} [348].

Aqueous phases of He pressurised reactions were quantified only at 180 °C because of experimental limitations. Though no difference between the products in these chromatograms was found, hence no insight gained. PA reaction chromatogram at 180 °C for 60 min showed a large reduction in 5-HMF to 5869 mg L^{-1}. Two possible reasons for this are speculated. The PA is retarding HTC reaction mechanisms and preventing the formation of 5-HMF. PA is reacting with 5-HMF by condensation reactions to produce a different form of carbonaceous material. Based on previous observations showing differences in the hydrochar when PA is used the later speculation is more probable.

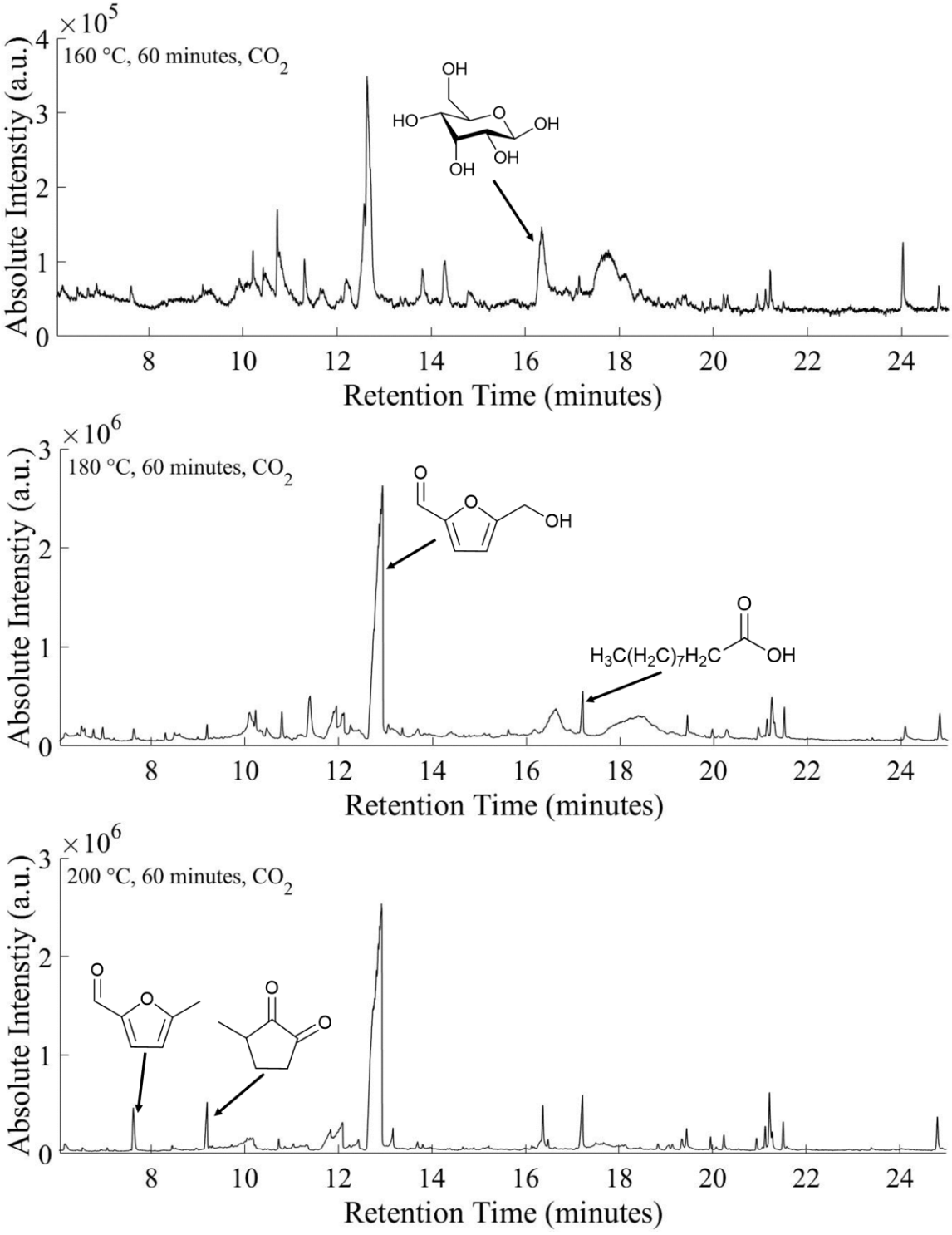

Figure 5.13 GC-MS chromatograms for the aqueous phase produced at 160, 180, and 200 °C processing temperature with 60 min retention time and carbon dioxide pressurisation gas.

5.7. Effect of EtOH/Water Mixtures on HTC of DBW

The impact of solvent additives such as ethanol during hydrothermal processes is a neglected

area within the literature. Solvent additives have the potential to tailor the characteristics of hydrochar and bio-oil to required applications by changing the reaction dynamics during HTC [28]. The objective of this research was to investigate the effect that ethanol had on the HTC of DBW at a full range of different molar percentages. With full characterisation of the physical and chemical characteristics of the hydrochar, this information can be correlated to the physicochemical properties of the solvent mixture. Therefore, a deeper understanding of the effect that ethanol (and other short chain alcohols) has on the HTC process can be acquired and applied to future processes.

Used herein are molar ethanol/water mixtures at 3.0, 6.7, 11.1, 16.6, 23.5, 32.0, 42.9, 56.9, 75.3, and 100 mol% ethanol, the calculation of which is shown in Section 3.2.3. The processing conditions used were 180 °C for 60 min under He (30 bar). When compared with results presented in the previous section without ethanol additives the hydrochar will be referred to as STDChar. The non-ideal nature of alcohol/water mixtures is discussed in Section 2.1.4.1. It is suggested that there are three critical molar percentages for ethanol/water mixtures at 7, 15, and 60 mol% [92]. At mixtures below 7 mol% the ethanol molecules exist independent of one another surrounded by water in a "hydration shell". Between 7 and 60 mol% ethanol there is significant hydrogen bonding interaction between the ethanol and water molecules. There is a maximum for this interaction at the point of greatest nonideality, occurring at 15 mol% ethanol.

5.7.1. Energy Density and Yield in EtOH/Water Mixture Hydrochar

Clear differences in the physical appearance and form of the product were shown compared to STDChar. At 3, 6.7, 11.1, 16.6, 23.5 mol% the hydrochar was a comprised of more finely dispersed and smaller particles. At 32, 42.9, and 56.9 mol% a single large oily lump was produced. Finally at 75.3 and 100 mol% a very fine powder material which was brown in colour was produced. In all instances at 6.7 mol% and above there was prevention of carbon formation on the wall and impeller of the autoclave which required removal after STDChar HTC. HHV shows the largest increase at 6.7 mol% at 18.12 MJ Kg^{-1} higher than the DBW feedstock (Figure 5.14). This is observed maxima where either side at 3 and 11.1 mol% yielded lower HHV hydrochars with 5.91 and 16.03 MJ Kg^{-1} increases respectively. STDChar had a lower HHV increase of 8.22 MJ Kg^{-1}. Providing evidence that when ethanol molecules are present at significant quantities independently in solution (below 7 mol%) they facilitate different reaction mechanisms for carbon formation. However, it could also be due to the hydrothermal

conversion of the ethanol molecules into carbon during HTC, with the HHV of pure ethanol at 29.7 MJ Kg^{-1} which is 12 MJ Kg^{-1} higher than the DBW feedstock at 17.69 MJ Kg^{-1}. Evidence against the latter theory is that the yield of each of hydrochar at 3, 6.7 and 11.1 mol% is lower between 12-13% compared to STDChar at 16.9%. The yield of hydrochar would be anticipated to be higher if ethanol was being carbonised into the hydrochar during HTC.

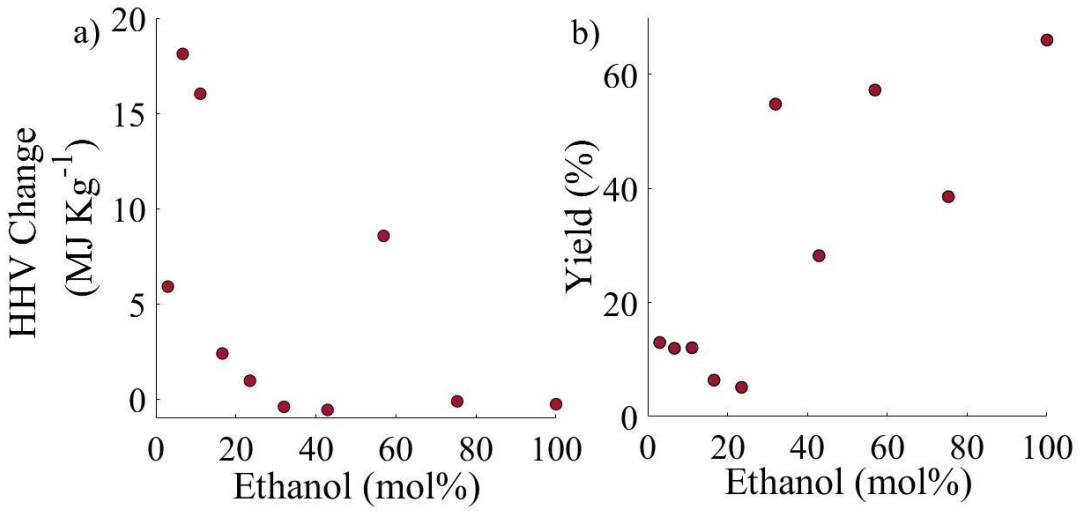

Figure 5.14 (a) HHV (MJ Kg^{-1}) of DBW, hydrochar analysed with bomb calorimeter (3.3.7), (b) yield (%) from HTC of DBW both of which plotted against the ethanol (mol%) present in the reaction mixture (Table 3.3). (Reaction conditions 180 °C, 60 min, 30 bar He).

HHV shows a gradual decrease after 6.7 mol% which reaches the same HHV as the DBW feedstock at 32 mol% (Figure 5.14). The excess enthalpy of mixing for ethanol/water mixtures at these conditions has a Gaussian distribution with maximum ~45 mol% (Figure 5.15). Therefore, the rapid decrease in the HHV of the hydrochar after 6.7 mol% can be correlated to this increasingly positive excess enthalpy of mixing. Further evidenced by flattening of HHV at 32 mol% correlating to the levelling off point in the excess enthalpy of mixing for ethanol/water mixtures at these conditions. Because this represents the ethanol and water have negative interactions with each other at these conditions. Hence it is proposed that the HHV of the hydrochar is the same as from DBW since the structure of the solid material is the same and no carbonaceous material is being deposited. Indicating that above 32 mol% ethanol polycondensation reactions observed in HTC are inhibited and the process is acting only to dissolve or extract the organics into the aqueous phase. Qualitative analysis of the aqueous phase is presented in Section 5.7.6. Maximum extraction into the aqueous phase is displayed at 23.5 mol% yielding only 5.1% hydrochar with no HHV change. At 56.9 mol% ethanol HHV change is relatively high at 8.57 MJ Kg^{-1} this is considered an erroneous data point which

would not be repeatable if HTC was performed again under these conditions and is therefore eliminated. Though higher molarities of alcohol/water mixtures may be applicable to hydrothermal liquefaction applications. There is a large variation in the yield of hydrochar for all between 32 and 100 mol% with no observable trend.

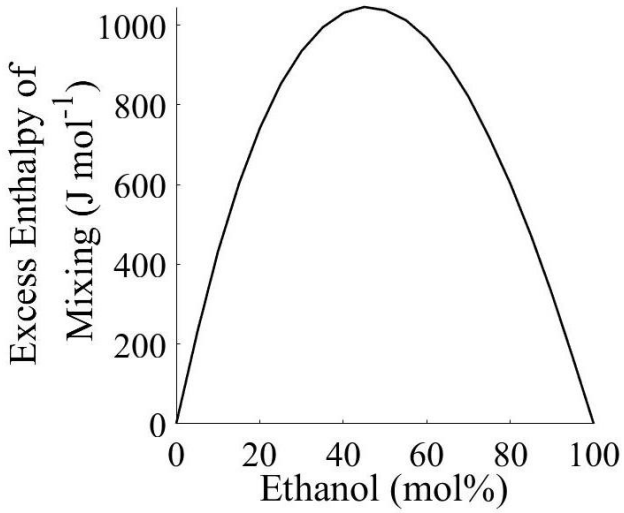

Figure 5.15 Excess enthalpy of mixing for EtOH/water mixtures at 175 °C under 50 bar external pressure [349]**.**

5.7.2. H/C and O/C Ratios in EtOH/Water Mixture Hydrochar

H/C and O/C ratios can give further evidence for the degree of carbonisation at each molar percentage of ethanol investigated and are displayed in Figure 5.16. A general trend observed is that as the ethanol mol% increases the H/C and O/C ratios also increase. As observed in the yield of each hydrochar there is a jump at 32 mol% ethanol where the H/C and O/C ratios group up around the DBW. Placing all of these hydrochars within what is expected of cellulose, indicating that insignificant carbonisation has occurred under these conditions [350]. The exception to this is at 56.9 mol%, going back down again in H/C and O/C ratio. This sample also exhibited an increased HHV. Both of these considered together points towards some carbonisation type reactions occurring at this molar ratio of ethanol. The H/C and O/C ratios for water synthesised hydrochar are 1.31 and 0.35 placing it well within the range of peat. Hydrochar from 3 mol% showed slightly less carbonisation with higher H/C and O/C ratios of 1.41 and 0.42. However the previously observed high HHV hydrochar synthesised with 6.7 mol% hydrochar had a lower O/C ratio but a higher H/C ratio at 0.32 and 1.56. Thus ethanol may be acting as a hydrogen donor during HTC, acting as a deoxygenation agent further depolymerising the DBW [351].

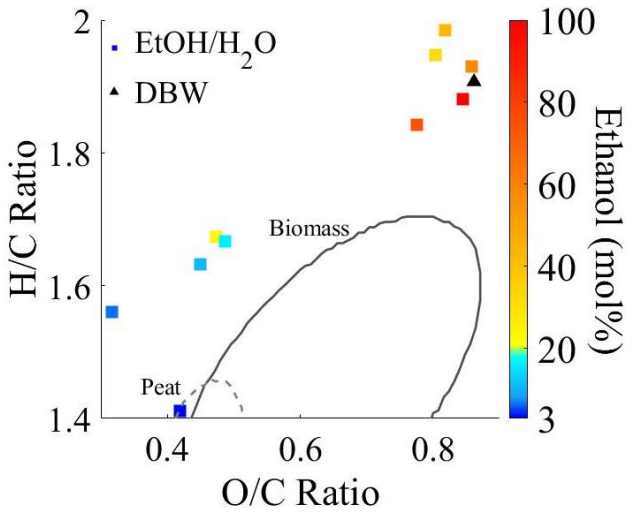

Figure 5.16 van Krevelen diagram for hydrochars produced in EtOH/water mixtures (squares) compared to DBW (triangle). Datapoints are coloured for EtOH molar concentration from 3 mol% (dark blue) to 100 mol% (red).

5.7.3. Proximate Analysis of EtOH/Water Mixture Hydrochar

Ash content of the hydrochar is increased compared to the DBW for all hydrochars from 6.7 mol% up to 32 mol%. A maximum in the ash content occurs at 23.5 mol% containing 9.3% ash. The hydrochar at 23.5 mol% contains 6.3% higher ash content than raw DBW and the STDChar. This is caused by a reduction in the solubility of NaCl in the ethanol/water mixture without an enhancement of solubility of either calcium carbonate or iron. Solubility of NaCl at 25 °C in ethanol is 0.65 g kg^{-1} compared to solubility in water at ~360 g kg^{-1} and solubility increases in both as temperature is increased [352], [353]. The reduction in solubility of the ethanol/water even at low molar presence of ethanol is a noteworthy finding, demonstrating that the single ethanol molecules surrounded by hydration shells noticeably change its thermodynamic properties. Ash content increase is likely further compounded at 23.5 mol% by a low final yield of hydrochar with a majority of the DBW transferring into the aqueous phase, as previously established. Hydrochar ash content then lowers down to similar levels of DBW at 42.9 mol% and higher. This is attributed to matching dissolution of inorganics and organics at the higher ethanol molar percentages with little to no carbonisation of dissolved organics. This causes the overall percentage of ash present to remain unchanged.

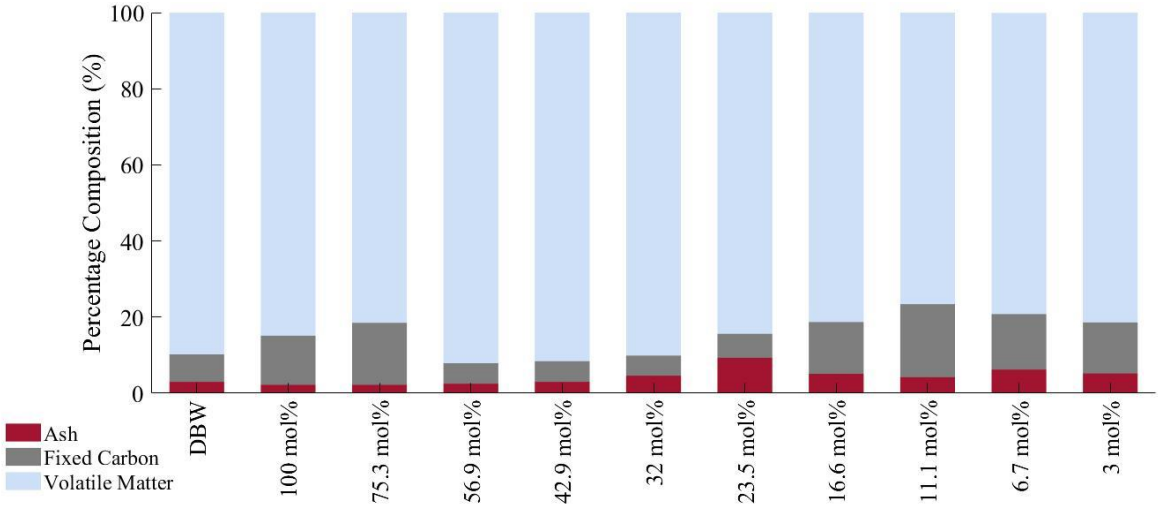

Figure 5.17 Stacked bar chart showing the percentage composition of the DBW, and the hydrochar produced at different EtOH molar percentages. Composition of the ash, fixed carbon (FC), volatile matter (VM) is given on a dry basis in wt.%.

At 3, 6.7, 11.1, and 16.6 mol% ethanol molar percentages a reduction in VM and an increase in FC was observed. This is attributed to dissolution of less resistant material which encompasses a higher percentage VM and then carbonisation of the dissolved organics into a mixture containing a higher amount of FC than VM into the hydrochar. As observed in the literature for hydrochar synthesised under typical HTC conditions. Peak FC is displayed at 11.1 mol% with 19.2% FC. It can therefore be surmised that reactivity at these lower molar percentages up to 16.6 mol% is similar to that in STDChar formation. Then with 23.5, 32, 42.9, and 56.9 mol% there is a shift observed, FC content decreases and VM increases. This effect has been observed previously from addition of ethanol to lignocellulosic wastes during HTC [28]. The range observed here of 16.6 mol% to 56.9 mol% is significant because it roughly aligns with the range in which ethanol/water mixtures exhibit an extended hydrogen bond network [92]. Compounds constituting the FC require nucleophilic species to disrupt the chemical bonds and the fragments need to be dissolved. The extended ethanol/water network links the water which can disrupt the structure of the FC to the ethanol which can then dissolve the fragments. In this way the ethanol and water complement each other to cause maximum dissolution of the FC into the aqueous phase. Furthermore, this is backed up by maximum delignification of wood chips occurring at 50 mol% ethanol, where lignin is a highly resistant constituent of lignocellulosic feedstocks [354]. With 56.9, 42.9, and 32 mol% having a lesser effect on the DBW overall and particularly the VM content. At both 100 and 75.4 mol% there is increased FC content which is likely due to selective dissolution of VM within the DBW instead of any carbonisation.

5.7.4. Surface Functionality of EtOH/Water Mixture Hydrochar

To further understand the effect of different ethanol/water mixtures FT-IR analysis was performed on all hydrochars produced using different molar percentages of ethanol (Figure 5.18). The hydrochar produced under 3 mol% ethanol showed the same functionality as observed in STDChar (Figure 5.9). This amount of ethanol therefore has a negligible effect on surface functionality during HTC. However, at 6.7 mol% there is significant decrease in the O-H stretching (3650-3050 cm^{-1}), and C=O stretching (1649 cm^{-1}) bands. As well as an increase in the aliphatic asymmetric (2922 cm^{-1}), and symmetric (2857 cm^{-1}) C-H stretching. This 6.7 mol% hydrochar represents an observed tipping point for these absorption bands. C-H functionality then decreases with increase molarity up to 42.9 mol% where it is then consistent with the DBW feedstock. O-H stretching increases up to the same 42.9 mol% returning to DBW absorbances. Carbonyl (C=O) stretching returns to DBW levels at 32 mol%. Hydrochar synthesised with 6.7 mol% ethanol was previously observed to have a higher H/C ratio than the water synthesised equivalent this increase in aliphatic functionality is consistent with that observation. Leading credence to the hypothesis that the ethanol is acting as a hydrogen donor during HTC, thereby facilitating deoxygenation and depolymerising reactions [351]. It is an important molar percentage, just before the critical molar percentage, the mixture is considered as individual ethanol molecules surrounded by water as hydrates [92]. Consequently, whilst ethanol is free moving in the ethanol/water system it is able to act as a hydrogen donor and increase aliphatic functionality in the hydrochar. At higher molar percentages of ethanol there is a change in liquid structure after this critical concentration into an extended hydrogen bond network between ethanol and water molecules. Because the hydroxide in the ethanol is hydrogen bonded to water more strongly, the hydrogen is more strongly bound into the meso-structure limiting its capacity for hydrogen donation.

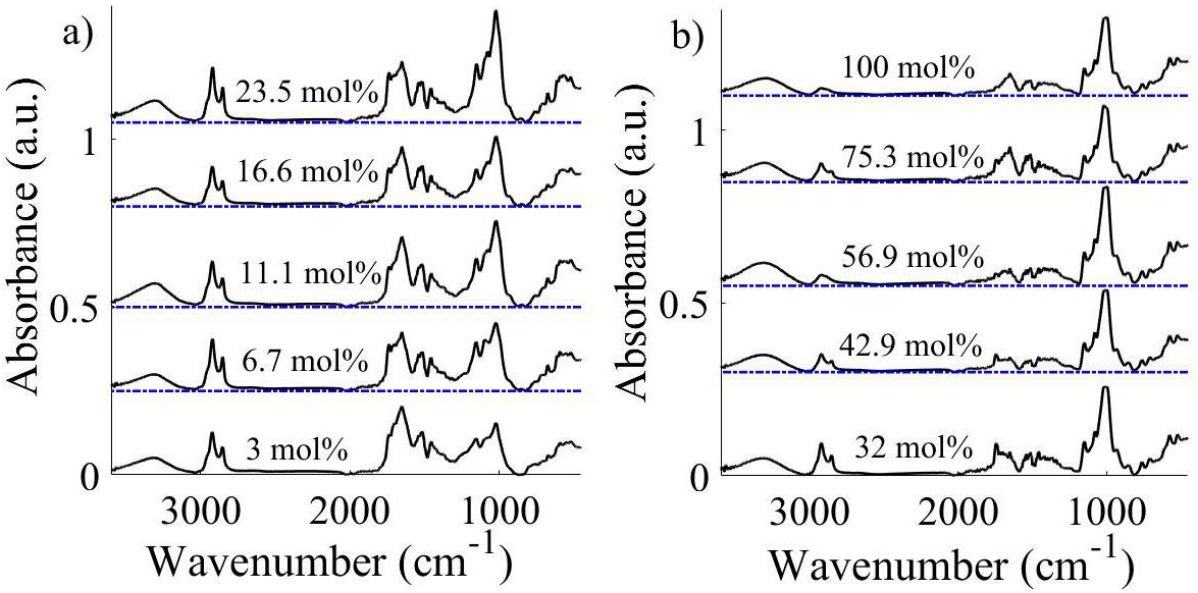

Figure 5.18 FT-IR spectra obtained for hydrochars obtained in different ethanol/water mixture molarities using a Shimadzu IRAffinity-1S spectrometer fitted with a Specac ATR plate. Analysis conditions: scans 4000, resolution 4 cm^{-1}, absorbance mode.

The gradual increase in the intensity of the C-O functionality (1150-900 cm^{-1}) attributed to saccharides is displayed up until 32 mol% at which point it matches DBW (Figure 5.9) [338]. At 42.9 mol% the FT-IR spectra of the hydrochar is near that of the DBW feedstock showing only a reduction in the N-H bending (1537 cm^{-1}). Moving further to 75.9 mol% the spectra exactly matches that of the DBW. At 100 mol% ethanol a large increase in O-H stretching is observed, it is concluded that the ethanol protonates the surface of the hydrochar and therefore increases the intensity of the O-H stretching band.

5.7.5. Surface Morphology of EtOH/Water Mixture Hydrochar

At the lower molar percentages of ethanol, 3 and 6.7 mol% the hydrochar had a similar form to the STDChar with a noticeable reduction in the microsphere concentration on the surface (Figure 5.19). Further evidence that HTC proceeds by similar mechanisms below the critical ethanol molar concentration of 7 mol% where ethanol molecules exist in isolation of one another [92]. Looking at the morphology of the 11.1, 16.6, and 23.5 mol% hydrochars there was no visible microsphere formation but a heavily structured amorphous surface with a number of holes and cracks. This indicates that the DBW structure is being broken up and potentially solid-solid conversions during HTC are agglomerating the remaining material. At 32 mol% the hydrochar is a large unstructured lump of carbon, the solid product at these molar percentages was a large oily lump and once dried was broken up into smaller pieces. The same was observed for 42.9 and 56.9 mol%. For 75.3 and 100 mol% the structure of the hydrochar

was comparable to that of the DBW, a small number of cracks and holes was evidence from minor hydrolysis/dissolution.

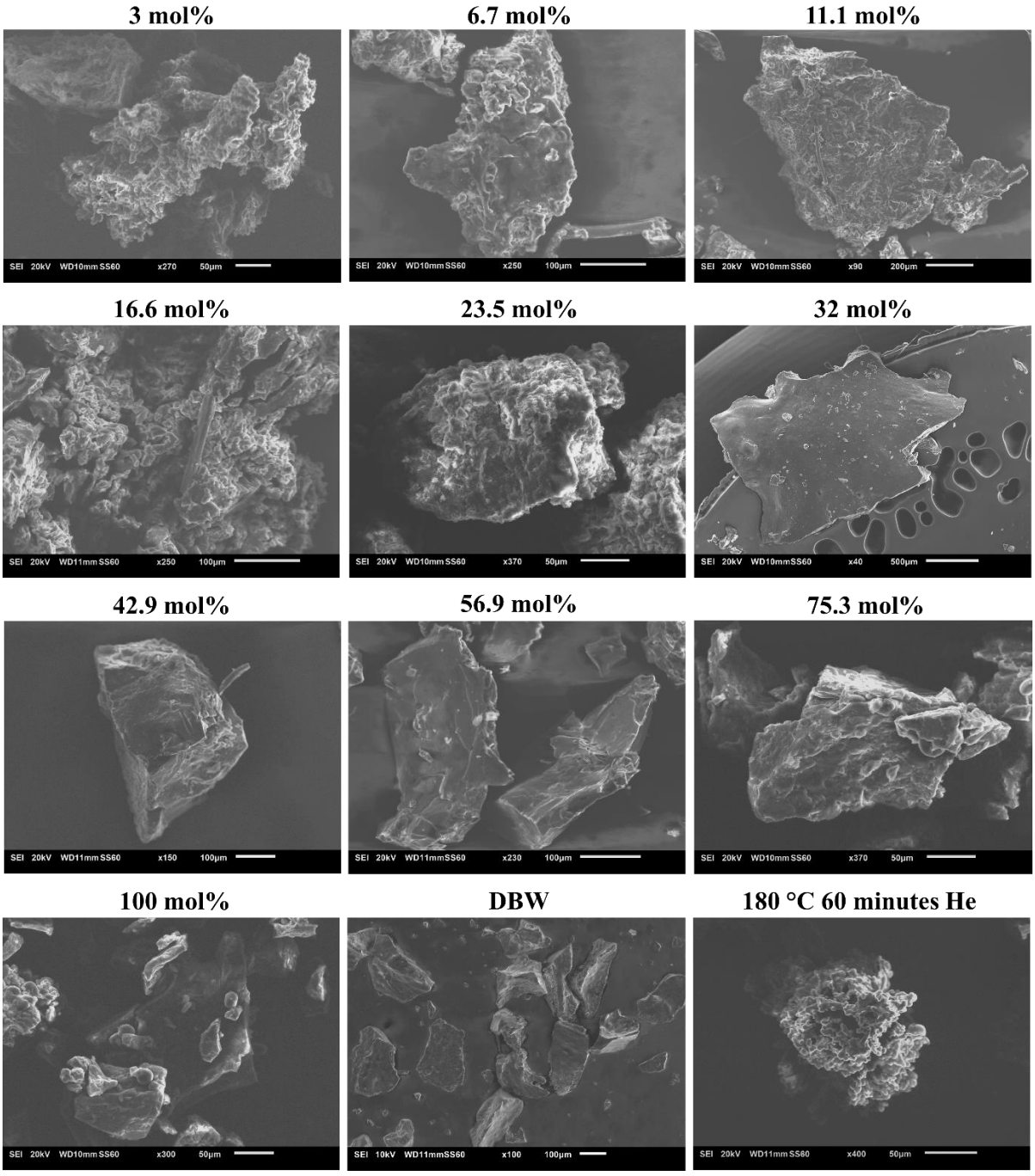

Figure 5.19 SEM images of hydrochar synthesised 180 °C under He with varying EtOH/water molar percentages. SEM performed on instrument in Section 3.3.8.

5.7.6. Qualitative Analysis of Aqueous Phase from EtOH/Water Mixture HTC

GC-MS analysis provides complementary information, allowing for speculation of the reactions occurring in the aqueous phase. All ethanol/water mixtures yielded a lower

concentration of 5-HMF compared to 5935 mg L^{-1} without ethanol (Table 5.4). A slow decrease in 5-HMF concentration initially occurred up to 11.1 mol%. This is followed by a relative increase in 5-HMF concentration for both 16.6 and 23.5 mol%. This can be attributed to the large dissolution/hydrolysis of the DBW at these temperatures as shown by the low yield in Section 5.7.1. Following this the 5-HMF concentration for the ethanol/water mixtures from 32 to 75.3 mol% remains between 1000-2200 mg L^{-1} this can be ascribed to the low dissolution/hydrolysis of the DBW under these conditions. Finally pure ethanol yields a very low concentration at 400 mg L^{-1}, providing further evidence that water is the more reactive nucleophile during HTC and causes the majority of the bond cleavage reactions to the feedstock.

Table 5.4 5-HMF concentration of the aqueous phases produced at each EtOH/water molar percentage calculated from GC-MS data.

Ethanol (mol%)	5-HMF (ppm)	Ethanol (mol%)	5-HMF (ppm)
3	5467	32	1103
6.7	4823	42.9	1946
11.1	3559	56.9	2165
16.6	4452	75.3	1050
23.5	3977	100	400

Chromatograms contained a myriad of different products in these ethanol/water mixtures compared to the pure HTC, some of which are displayed in Figure 5.20. 3,4-altrosan was produced with similar peak area to 5-HMF in 3 and 6.7 mol% ethanol/water mixtures. This is reported to be an early product from the dehydration of glucose units during HTC [355]. However, it is not observed as a product conversion of DBW without ethanol under these conditions. For 11.1 mol% and all higher molar concentration of ethanol it is observed that ethyl alpha-d-glucopyranoside becomes the dominant peak for the rest of the ethanol/water mixtures. Ethyl alpha-d-glucopyranoside is a simple sugar with one modified hydroxyl group. Observing both of these together it is evident that the ethanol is hindering the expected HTC conversion reactions typically imposed upon the dissolved sugars. Another unique product created is hydrazinecarboxamide, 2-(2-methylcyclohexylidene) formed in 3, 6.7, and 11.1 mol% mixtures. Peak area is highest under 3 mol% then decreases with increasing ethanol concentration. Reactions of dissolved proteins from the DBW facilitated by the ethanol are attributed to the formation of this product. Pyroglutamic acid, which is a product of glutamine when heated in water, is observed only in 16.6 and 23.5 mol% mixtures. Above that at 32, 42.9, 56.9, and 75.3 mol% glutamine appears as a peak instead. Although there is generally low signal and few peaks in all chromatograms at 32 mol% ethanol and higher. Further evidence

that HTC reactions are retarded at molar percentage ethanol/water mixtures above 32 mol%. Oleoyl chloride was a significant product from 23.5 mol% ethanol HTC of DBW. Likely produced from a novel reaction between the dissolved sodium chloride and long chain fatty acids (lipids). This reaction is facilitated by the dissolution of long chain fatty acids in the ethanol rich part of solution whilst the NaCl is dissolved by the water rich part of solution. The free interaction between these two then allows for the formation reaction to take place.

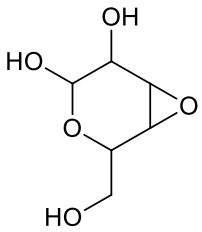

3,4-Altrosan

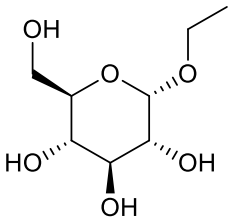

Ethyl alpha-d-glucopyranoside

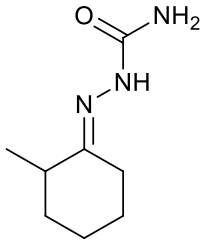

Hydrazinecarboxamide, 2-(2-methylcyclohexylidene)

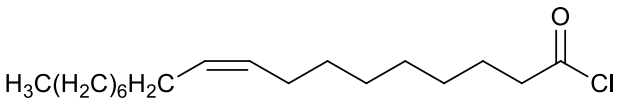

Oleoyl chloride

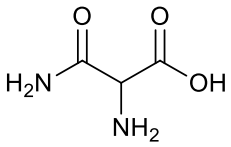

L-glutamine

Figure 5.20 Chemical structures of different products discovered in the aqueous phase from HTC of DBW under different ethanol/water mixtures.

5.8. Conclusions

HTC of a real waste stream (DBW) has successfully been assessed at a range of different processing temperatures and retention times. Hydrochar was thoroughly characterised by composition and morphology. Following this the effect of ethanol as a solvent additive during HTC is profitably investigated at specific molar percentages. At 200 °C and after 90 min under CO_2 the hydrochar had a large HHV at 39.66 MJ Kg^{-1} with reasonable yield at 1.53 g from 5 g of DBW (30% yield). CO_2 acting as a homogeneous catalyst during HTC is attributed to the large HHV. Moreover, hydrochar had O/C and H/C ratios within the expected lignite and proximate analysis gave favourable FC, VM, and ash content for fuel application. Demonstrating the feasibility of performing HTC on DBW to produce a high value renewable solid fuel. Potential issues identified are that large particle size material (> 500 μm) undergo reduced conversion during HTC and calcium carbonate/iron is retained in the hydrochar.

As described in literature processing temperature was a more important factor for the qualities of the hydrochar produced from HTC. After 60 min additional retention time had little effect on the hydrochar produced, therefore most reactions have proceeded to completion at 60 min. However, the combination of processing temperature and retention time into one variable (severity factor) gave good correlation with HHV, yield, as well as O/C and H/C ratios. Giving credence to using severity factor in modelling and designing HTC reactions of biomass. 160 °C was insufficient for the formation of hydrothermal carbons but dissolved/hydrolysed a large amount of the DBW. Representing potential for pre-treatment to yield the carbohydrate rich liquid product for use in anaerobic digestion or fermentation. 180 °C was shown to yield unreacted of 5-HMF in solution but the hydrochar had microsphere formation attributable to the polycondensation of 5-HMF. Consequently 180 °C was a conflicted processing temperature not completely favouring hydrochar formation or the production of a high value liquid phase. Compared to 200 °C many larger agglomerated microspheres were formed and 5-HMF was minimal in solution, thereby favouring the formation of hydrochar. When PA was used as an additive it underwent carbonisation reactions being incorporated into the structure of the hydrochar. Yielding a significantly different carbonaceous product, this displays potential to use PA and other derivatives to produce a doped hydrochar product for adsorption/catalysis applications.

Looking at ethanol as a solvent additive a couple of critical molar percentages were observed. For both 3 and 6.7 mol% the DBW is dissolved/hydrolysed to produce a recognisable hydrochar (microspheres, increased HHV, reduced O/C and H/C ratios). Moreover, the hydrochar was a finer powder and had higher miscibility, therefore the reactor required less cleaning. However, it is clear that ethanol is acting as a hydrogen donor and facilitating different reaction mechanisms. A product with increased HHV is produced compared to STDChar and a higher H/C ratio but lower O/C ratio. This is because the ethanol exists as singular molecules in the mostly water solution, consequently water can react as expected for HTC with ethanol available to facilitate additional reactivity not otherwise observed. After these molar percentages the formation of hydrothermal carbons is inhibited until 23.5 mol% where minimal carbon is formed. This is important as above 7 mol% the ethanol/water mixture exists as a non-ideal solvent with an extended hydrogen bond network. Therefore as the water molecules become entangled in the extended ethanol/water mixture they are prevented from interacting with the dissolved organics for long enough to enable HTC reactions. This is true at 180 °C but might only require a higher processing temperature to enable these reactions. A

large amount of the DBW is however dissolved/hydrolysed into the aqueous phase up to 23.5 mol% ethanol. After this point there is a huge reduction in the interaction between the ethanol/water mixture and the DBW. Low dissolution/hydrolysis and minor carbonisation evidence can be found.

In future research it is recommended that evolved gas analysis is used to further analyse the composition of the hydrochar formed. Additionally analysing the effect of ethanol during HTC at higher processing conditions is essential towards fully characterising its influence of reactivity. It is possible there is insufficient activation energy for different carbonisation reactions at the higher ethanol molar percentages.

Chapter 6 Magnetic Carbon Composites from Avocado Seeds *via* HTC and the Effect of Ethanol/Water Mixtures

This research chapter discusses the synthesis and characterisation of iron oxide supported/encapsulated in hydrothermal carbonaceous material, classified as magnetic iron-carbon composites (Fe/C). Avocado seeds (AS) have been processed in high temperature water (230 °C) at elevated pressure (30 bar at room temperature) in the presence of iron nitrate and iron sulfate. Fe/C was separated into two particle sizes: 32-232 μm (particles) and <32 μm (powder) these have been characterised using analytical techniques: XRD, AAS, XRF, XPS, FT-IR, ICP-OES, BET, this is presented in Section 6.1. The adsorption of methylene blue and indigo carmine is presented in Section 6.2. A hydroalkoxylation reaction was used to evaluate catalytic efficiency in Section 6.3. Where appropriate, Fe/C has been compared to raw AS, hydrochar produced from AS without iron salts, and magnetite nanoparticles. The effect of ethanol as a solvent additive on the Fe/C produced has been evaluated in Section 6.4.

AS were chosen as the waste feedstock for a number of reasons. They are a rapidly growing source of waste with global production of avocados forecast to triple by 2030 as compared to 2010 values [356]. The AS and avocado peel are produced in high quantities from industrial production of guacamole, sauces, oils, and frozen avocado products [357]–[359]. An estimated 12 Mt of avocados are processed every year producing ~2 Mt of waste AS. Furthermore, the AS are rarely used in animal feed because of their unpleasant taste and low nutrient content, therefore a large amount of AS waste is sent to landfill.

Iron oxide was studied as the supported material because it has a wide variety of different applications including adsorption, heterogeneous catalysis, photocatalysis, immobilisation, and bio-pharmaceuticals [360], [361]. Moreover, the surface functionality can be controlled by employing different synthesis conditions. Some of the procedures for preparing iron oxide nanomaterials are: sol-gel, oxidation, co-precipitation, hydrothermal, aerosol, supercritical, and microbial syntheses. These synthesised iron oxide nanomaterials can exhibit ferrimagnetism, high biodegradability, and low toxicity.

Previous research into hydrothermal synthesis of iron materials has demonstrated potential to produce functional iron oxide materials supported on, or encapsulated within, hydrochar. One example, produced carbon encapsulated nanoparticles using glucose as the feedstock [362],

[363]. For example, Rattanachueskul et al. demonstrated a 24 hour one-pot synthesis approach to magnetic carbon composites using sugarcane bagasse as a feedstock [200]. Most other research has focussed on the synthesis of hydrochar followed by wet impregnation of iron and pyrolysis under an inert atmosphere [364]–[366]. This approach requires pyrolysis at temperatures above 600 °C in order to oxidise the carbon and produce porous a carbonaceous structure.

6.1. Physical and Chemical Characteristics of Fe/C

Analysis of Fe content was performed by AAS, and XRF on 5 different Fe/C samples, the results of which were corroborated with one sample externally analysed by ICP-OES (Table 6.1). Each of these analyses were in good agreement with each other (within the standard error from 5 different samples). Based upon the final weight of the Fe/C, the metallic loading of the samples and the moles of iron used in the precursor iron nitrate, iron sulfate solution it was calculated that losses of iron during the process are negligible because they are less than the standard error associated with analysis. Therefore, the majority of the iron precursor solution is incorporated into the final Fe/C and the metallic loading can be adjusted by altering the weight of AS (or other lignocellulosic) feedstock used in HTC. This allows for the metallic loading of the Fe/C to be tuned for the desired process. Whilst Fenton-like processes for wastewater treatment requires low metallic loadings down to 3 wt.%, higher iron content (~20 wt.%) is required for electrocatalysis applications [367], [368].

Table 6.1 Iron (Fe) content in Fe/C analysed by AAS, XRF, and ICP-OES.

Sample	AAS (wt.% Fe)	XRF (wt.% Fe)	ICP-OES (wt.% Fe)
Fe/C particles	36.6 ± 5.4	37.5 ± 9.1	34.5
Fe/C powder	31.1 ± 4.6	34.2 ± 6.8	-

XRD analysis of the Fe/C showed the crystal structure was dominated by the characteristic peaks for magnetite (Fe_3O_4) at 30.2, 35.6, 43.3, 57.2, and 62.8°; additionally, a smaller contribution from haematite (Fe_2O_3) is observed (Figure 6.1, a). The percentage composition of magnetite and heamatite was quantitatively determined using MATCH! Software. Fe/C particles comprised 73 ± 5.6% magnetite (Index# 96-151-3305) and 27 ± 5.6% haematite (Index# 96-154-6384), while Fe/C powder comprised 72.4 ± 8.9% magnetite and 27.6 ± 8.9 % haematite. Magnetite is widely shown as the product of iron nitrate, iron sulfate and sodium hydroxide [369]. However, Li *et al.* demonstrated that magnetite is oxidised to heamatite under hydrothermal conditions [370]. At 275 °C under autogenously generated pressures 41% of the

magnetite was oxidised to heamatite. Therefore, it is determined that the heamatite in the Fe/C is attributed to oxidation during HTC. Furthermore, the presence of heamatite is likely preferred at the exposed surface iron oxide particles whilst the carbon encapsulated iron oxide remains as magnetite because it is shielded during HTC.

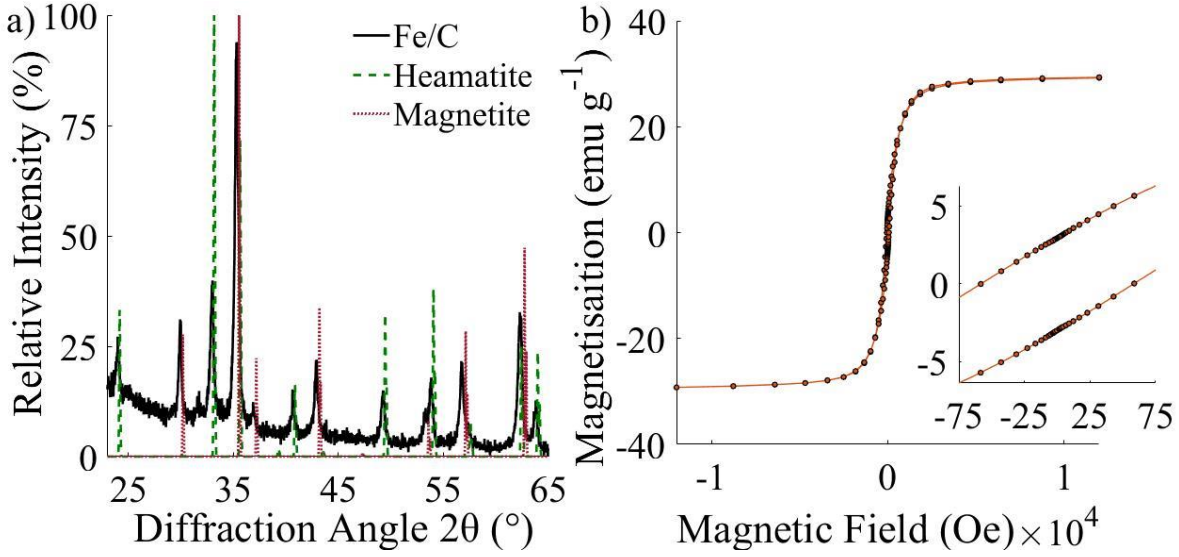

Figure 6.1 (a) X-ray diffractogram patterns for Fe/C particles compared to RRUFF spectroscopic references for magnetite and haematite between 17 – 65° obtained using a Cu tube with 1.54184 Å, scanning for 1 second at increments of 0.02° [371], [372]**. (b) Magnetisation hysteresis loop for Fe/C particles, inset shows small remnant of magnetisation at zero field (~10% of total moment), measured using a Quantum Design SQUID-VSM Magnetometer MPMS3.**

XPS analysis of surface composition was performed externally on one sample of Fe/C particles (Table 6.1). This analysis revealed a reduced presence of iron on the surface with an iron content of 23.9 wt.%, 4.5 wt.% below the low limit of the standard error and 13 wt.% below the average. Therefore, more of the iron oxide is encapsulated within the carbonaceous hydrochar than on the surface. A minor presence of sodium, nitrogen, and sulphur was detected in the Fe/C. Sodium can be attributed to sodium hydroxide used during synthesis and can be eliminated with longer washing steps. The nitrogen and sulphur can be attributed to lignin and proteins within the AS feedstock. Additionally, detection of indium through the pores in a pressed Fe/C sample via XPS was possible, suggesting a heavily porous, and hence high surface area material.

Table 6.2 Surface composition (wt.%) of Fe/C particles determined by quantifying XPS survey scans performed on Kratos Supra instrument with a monochromated aluminium source.

Analysis Number	Na (wt.%)	Fe (wt.%)	O (wt.%)	In (wt.%)	N (wt.%)	C (wt.%)	S (wt.%)
Position 1 (20eV pass)	1.1	22.8	21.9	3.4	2.9	47.1	0.8
Position 2 (20 eV pass)	0.9	22.0	22.1	0.7	3.0	50.7	0.6
Position 3 indium (20 eV pass)	-	-	17.1	67.7	0.5	14.7	-
Position 3 (10 eV pass)	1.2	27.3	22.6	-	2.8	45.4	0.8
Position 4	1.3	21.0	22.2	-	2.9	52.1	0.4
Position 5 (10 eV pass)	1.1	26.3	22.2	-	3.1	46.7	0.6

C 1s analysis by XPS (Figure 6.2, b) showed a majority of sp3 hybridized carbon (285.35 eV, 50.31%), some of which is oxygen functionalised (287.59 eV, 23.76%), there is also evidence of graphitic carbon (284.38 eV, 15.19%). Fe 2p analysis (Figure 6.2, a) is difficult due to multiplets and satellites. However, the major peak for Fe $2P_{3/2}$ is likely attributed to a mix of heamatite Fe^{3+} (711.0 eV) and magnetite Fe^{2+} (709.6 eV) contributors. Iron carbide presence was not detected.

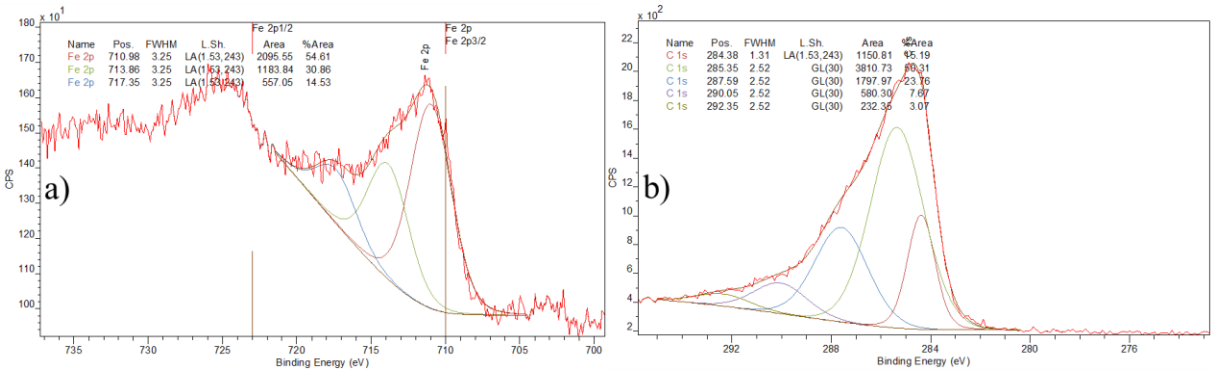

Figure 6.2 high resolution XPS from position 1, collected at 20 eV pass energy, after curve fitting to determine main peak position (a) Fe 2p (b) C 1s.

BET analysis reveals surface areas of 546 and 1454 $m^2\ g^{-1}$ for Fe/C particles and powder respectively, whilst hydrochar has a reduced surface area at 45 and 194 $m^2\ g^{-1}$ for particles and powder respectively. The increased surface area in the Fe/C is attributed to the iron oxide acting as a Lewis acid to facilitate the aromatic condensation and emission of volatiles, hence increasing porosity compared to hydrochar post-carbonised without iron oxide [373]. Furthermore, increased surface area of powder samples (~3-4× larger) is recognised to be because of increased surface area to volume ratio of the smaller size. The surface areas obtained for Fe/C are comparatively large compared to lignin synthesised hydrochar with wet impregnation of iron before post carbonisation (1100 °C) at 272 $m^2\ g^{-1}$ [374]. In order to achieve a high surface area (>1000 $m^2\ g^{-1}$) sacrificial templating materials such as silica is often

used during HTC to deposit the hydrothermal carbons onto as discussed in Section 2.2.3.3. Procedures using sacrificial templates require several more preparation steps, higher processing temperatures (800 °C), and the utilisation of more costly and less environmentally friendly reactants [375].

Both the Fe/C and hydrochar have a heterogeneous surface, comprised of carbonaceous material with hydroxide, carbonyl, and iron functionalities unevenly dispersed across the surface. Nitrogen adsorption isotherms for both Fe/C and hydrochar are between Type II and V (Figure 6.3), suggesting that the material has weak interaction with the nitrogen leading to minor adsorption at low p/p_0 [376]. However, at high p/p_0 molecular clustering and unrestricted monolayer-multilayer adsorption of nitrogen onto the micro-mesoporous carbonaceous material produces high adsorption volumes [377]. The obtained nitrogen adsorption isotherms are comparable to that of catalysed graphitised hydrothermal carbon presented in the literature [374], [375].

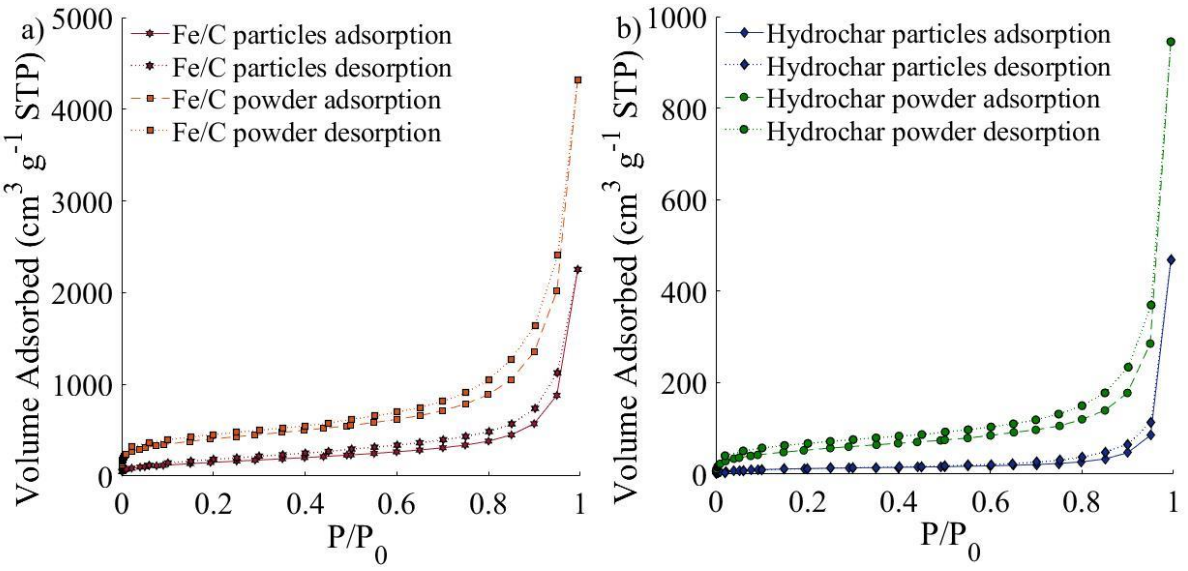

Figure 6.3 N_2 adsorption-desorption isotherm for (a) magnetic carbon composites (Fe/C) particle and powder, and (b) hydrochar particles and powder.

Further evidence of microporosity is shown in Figure 6.4, the majority of the pores present are below 2 nm [377]. Microporosity is a desirable characteristic of adsorbents and catalysts because it often yields high surface area as well as a high pore density [378]. For this reason microporous carbons (as observed in Fe/C and hydrochar) can be used widely for gas and liquid phase adsorption processes [379].

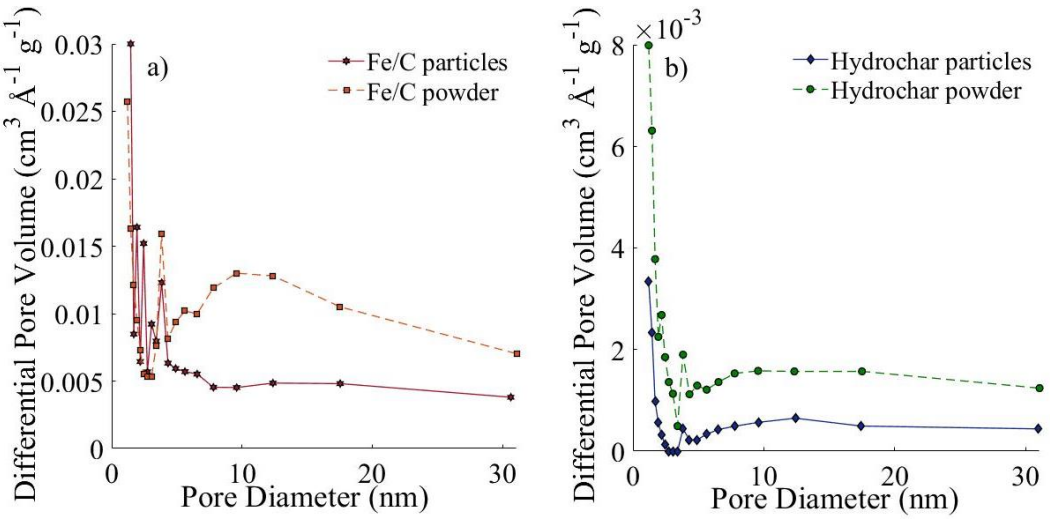

Figure 6.4 Pore size distribution for (a) magnetic carbon composites (Fe/C) particle and powder, and (b) hydrochar particles and powder.

The surface functionality of Fe/C, hydrochar, and dried avocado seed (DAS) has been characterised by FT-IR spectroscopy (Figure 6.5). DAS exhibits strong absorbance in the O-H stretching region (**1**, 3650-3050 cm^{-1}), however this is significantly reduced in the hydrochar and fully eliminated in Fe/C. A similar trend is observed in the aliphatic region for asymmetric (**2**, 2919 cm^{-1}) and symmetric (**3**, 2858 cm^{-1}) C-H stretching which is linked to the presence of methyl and methylene groups. The loss of these aliphatic and hydroxide bonds can be attributed to condensation reactions occurring during HTC [342]. Aldol polycondensation reactions are the final reactions within HTC that result in the formation of the extended polymeric structure of the synthesised carbonaceous material [156]. That these are further reduced in Fe/C as compared to the hydrochar may indicate that the reaction has proceeded to a greater extent and that it may therefore be catalysed by the presence of iron. It has been previously demonstrated that iron chloride acted as a Lewis acid during HTC and increased the carbonisation, hence reducing the oxygen functionality of the hydrochar [380]. However, it should also be noted that the presence of iron oxide means that a lower fraction of the surface is hydrocarbonaceous, when compared to hydrochar. C=O functionalities are also more apparent in DAS, as indicated by the presence of peaks associated with conjugated (**4**, 1737 cm^{-1}) and unconjugated (**6**, 1619 cm^{-1}) C=O stretching. The large C=O stretching band (**5**, 1690 cm^{-1}) present for hydrochar is attributed to conjugated aldehydes formed during HTC. Further evidence of carbonisation is observed in the samples through the appearance of an aromatic C=C stretching band (**7**, 1575 cm^{-1}) in the spectrum of Fe/C and hydrochar, in addition to C-C aromatic stretching (**8**, 1397 cm^{-1}) [149], [381]. This is

supported by the loss of C-O-C (**9**, 1149 cm^{-1}), C-O (**10**, 1005 cm^{-1}) and C-C-O (**11**, 938 cm^{-1}) stretches present in the DAS spectrum. These peaks are associated with ether C-O linkages from cellulose, lignin and hemicelluloses and elimination of this is indicative of the carbonisation of these compounds during HTC [342]. The broad absorbance between 1475-1211 cm^{-1} present in the spectrum of DAS is attributed to a mixture of C-C aromatic, C-N and C-O stretching vibrations. This is notably reduced in intensity for both hydrochar and Fe/C. Some surface C-O functionality does remain after HTC as indicated by the peaks between 1250 to 1050 cm^{-1}. Notably, hydrochar has relatively greater absorbance in this region than Fe/C. This is attributed both to the increased carbonisation noted by the reduction in aliphatic C-H, *vide supra*, but also to the likely displacement of these functionalities by supported iron particles.

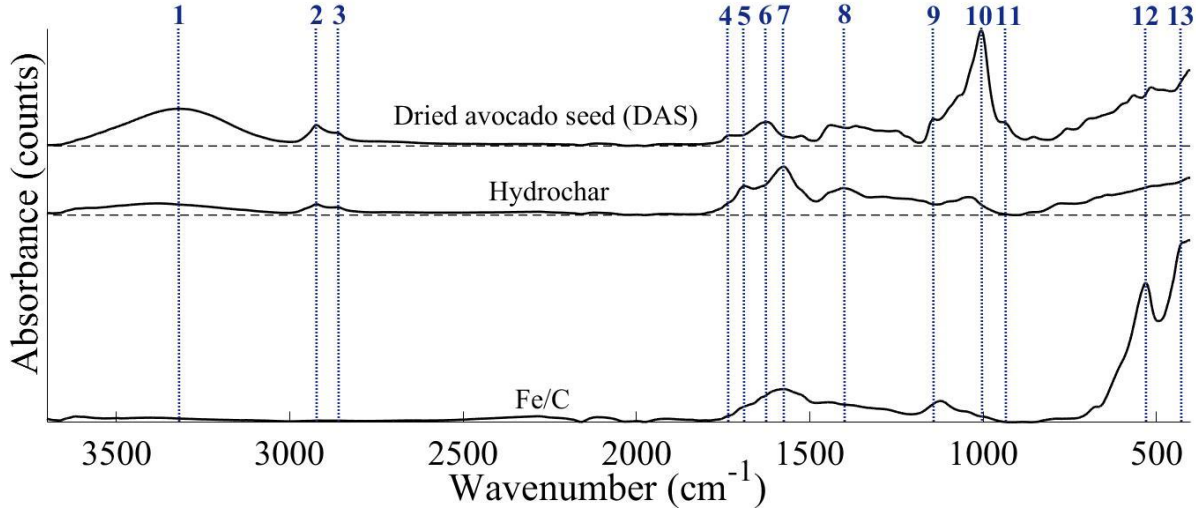

Figure 6.5 FT-IR spectra obtained for dried avocado seed (DAS), hydrochar, and Fe/C using a Shimadzu IRAffinity-1S spectrometer fitted with a Specac ATR plate. Analysis conditions: scans 4000, resolution 4 cm^{-1}, absorbance mode. The numbered peaks are assigned as follows: 1: νO-H,; 2: ν_{as}C-H; 3: ν_{s}C-H; 4, 5 and 6: νC=O; 7: νC=C; 8: νC-C; 9: νC-O-C; 10: νC-O; 11: νC-C-O; 12 and 13: νFe-O.

The FT-IR spectrum of Fe/C is dominated by Fe-O stretching associated with heamatite (**12**, 532 cm^{-1}, **13**, 440 cm^{-1}) [382], [383]. Magnetite typically exhibits a peak at 588 cm^{-1}; if present this is obscured in this work by the broad haematite peak. Bulk characterisation (XRD, *vide supra*) indicated that magnetite was the dominant iron oxide phase present. ATR is a surface sensitive technique and therefore the identification of haematite is indicative of the oxidation of the surface iron oxide.

Material stability in solution was qualitatively examined by leaving in deionised water for 24 h. Previous investigations showed iron-carbon composites discoloured the water

after soaking for 24 h [200]. However, the synthesised Fe/C showed no discolouration in solution during or after the soaking period. All of the Fe/C was easily collected with an external magnet. Analysis of the metallic content of the recovered Fe/C revealed an iron loading of 35.6% by AAS and 36% by XRF, consistent with characterisation of the as-synthesised material, and hence showing no evidence of iron leaching during the soaking period. Furthermore, XRD analysis confirmed the phase of the iron oxide remained unchanged with magnetite and haematite contents of 79.2% and 20.8% respectively, indicating that negligible oxidation or reduction of the oxide occurred. In contrast, hydrochar visibly discoloured the solution to light grey immediately upon addition and then to dark brown after 24 h. The material leaching from the hydrochar is most likely unconverted hydrocarbonaceous material, with the brown colouration of the hydrochar indicative of the presence of tannins. Ultimately, the increased stability of the Fe/C is related to its increased carbonisation and therefore higher resistance to leaching which is a desirable characteristic for liquid phase adsorption and catalysis processes.

SEM was used to investigate the physical surface morphology of the DAS, Fe/C, and hydrochar (Figure 6.6). Analysis of the DAS shows an irregular mesoporous surface, the structure of raw AS has a non-porous surface [384]. The porosity observed is attributed to removal of tannins and water in the AS producing the empty cavities observed. The Fe/C particles appeared as large separate graphitic grains with no evidence of iron oxide clumping. Additionally, there is no evidence of microsphere formation typically associated with hydrochar and observed in Section 5.5.2 for HTC of DBW. This suggests that the microspheres formed during HTC are converted into graphitic carbon during post-carbonisation as microspheres are not observed in other post-carbonised hydrochar samples [385]. SEM analysis exposes the drawbacks of Fe/C powder samples; they contain separate clusters of iron oxide and carbonaceous material. Hydrochar particles also have a graphitic surface however they have more mesoporosity and more structured surface than Fe/C particles, this can be related to the FT-IR showing an increased surface functionality and therefore more remnants of microspheres formed during HTC.

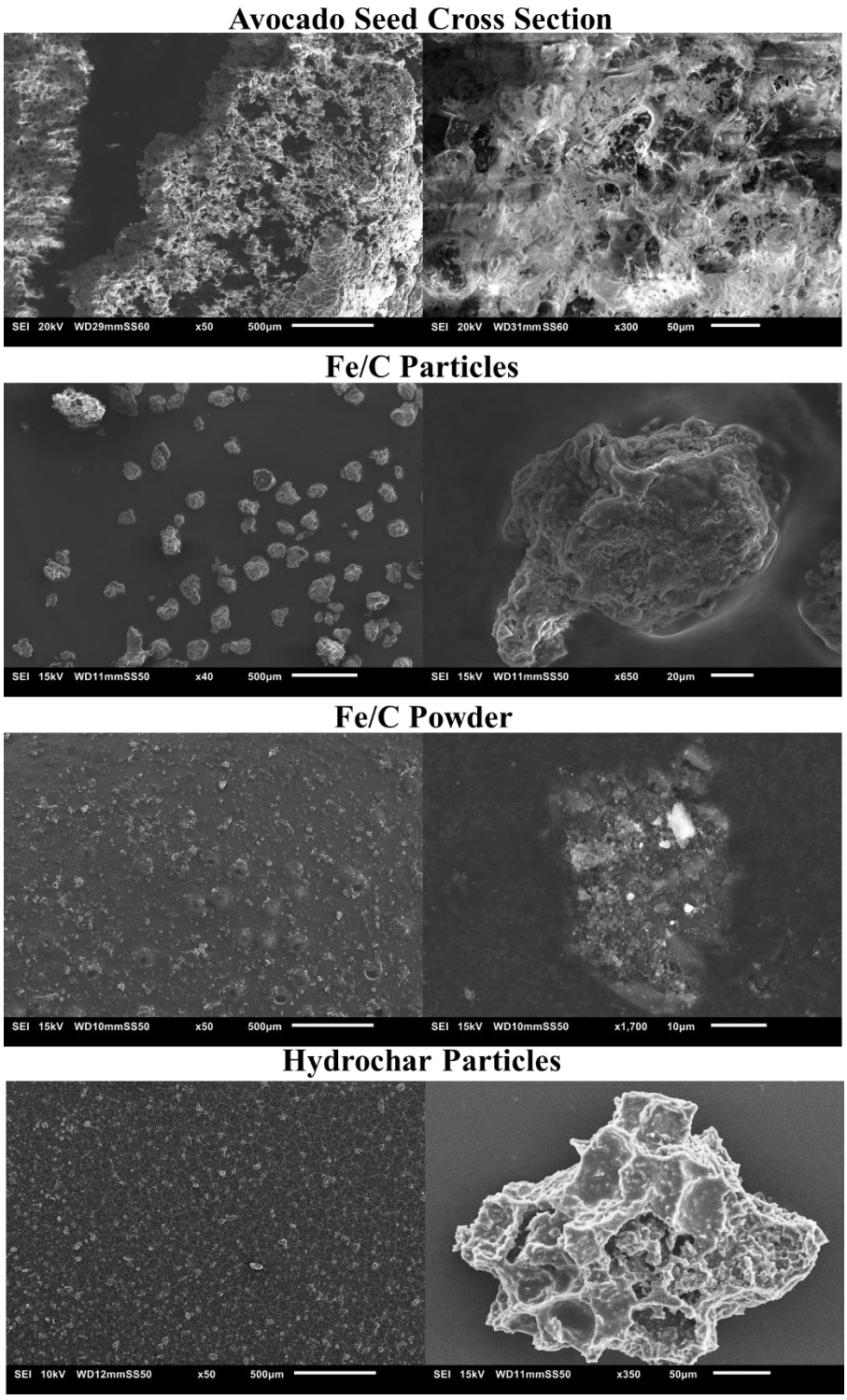

Figure 6.6 SEM images of DAS, Fe/C particles, Fe/C powder, and hydrochar particles SEM performed on instrument in Section 3.3.8.

6.2. Adsorption Testing of Fe/C

The adsorption of methylene blue (MB) and indigo carmine (IC) onto Fe/C and hydrochar has been examined to model their liquid-phase adsorption behaviour. Adsorption is an important

material characteristic for many different applications such as wastewater treatment, heterogeneous catalysis, metal leaching, gas storage, molecular separation, and molecular gas sensing [386]–[391]. The main areas of application for the synthesised Fe/C and other HTC produced materials are low-cost environmentally friendly heterogeneous catalysis and wastewater adsorbents. A reactant must be adsorbed to the surface of a heterogeneous catalyst for a significant period of time to allow for catalytic reactions to occur, therefore it is an important characteristic to understand. Non-biodegradable, toxic, and carcinogenic synthetic dyes are leached into waste streams from the textile, paint and printing industries [359], [360]. Often these dyes have adverse effects on both the environment and human health. Therefore, it is necessary to remove them from wastewater. Magnetic adsorbents such as Fe/C are increasingly proposed as a solution because of their simple operation, high separation, removal efficiency and wide applicability [361], [392]. Isothermal adsorption data are fitted using the Langmuir isotherm model for its applicability in both chemisorption and physical adsorption processes [393].

Isothermal adsorption of MB on Fe/C showed a maximum adsorption capacity of 24.8 ± 1.3 mg g^{-1} and 34.6 ± 2.6 mg g^{-1} for particles and powder, respectively (Figure 6.7,a). Hydrochar had a significantly higher maximum adsorption capacity at 246 ± 21 mg g^{-1} and 267 ± 26 mg g^{-1} for particles and powder, respectively. Thus, an increase in maximum adsorption capacity is seen with smaller particle sizes, 40% and 9% for Fe/C and hydrochar respectively. However, the surface area increase from the particles to the powder was significantly higher at 166% and 331% increased surface area in the powder samples for Fe/C and hydrochar respectively. This demonstrates that a higher majority of the surface sites in the powder samples are unfeasible for adsorption (and hence catalytic) applications. Moreover, the particles were easier to handle, more quickly collected and separated, with no volatilisation into breathable dust. Consequently, it is recommended that the smallest particles (powder) are separated and discarded.

The maximum, adsorption capacity of MB on Fe/C is consistent with previously studied iron carbon materials. For example a graphene/magnetite material synthesised from high-value activated carbon exhibited a maximum adsorption capacity of 43.82 mg g^{-1} [394]. Thus Fe/C which is produced from low-value waste materials exhibits similar adsorption performance to high-cost materials. Hydrochar is clearly observed to be a

more effective adsorbent than Fe/C despite its lower surface area demonstrating an adsorption capacity of 246 ± 21 mg g^{-1}. This increased surface area is ascribed to hydrochar having more surface functional groups as shown by FT-IR. Since MB has been shown to bind to surface hydroxide and carbonyl groups on the carbon surface *via* hydrogen-bond interactions [395].

Compared to other biomass produced carbon the hydrochar obtained from AS herein displays a comparatively high surface area. For instance, adsorbents produced from olive stones, hazelnut shells, apricot stones, and walnut shells have been shown to have adsorption capacities of 22.1, 8.82, 4.11, 3.53 mg g^{-1} respectively for MB [223]. However, the previously described leaching of organic components such as tannins into the aqueous phase is undesirable where discolouration of the solution is unwanted. Moreover adsorbents are typically used in the tertiary stage of water treatment to remove any discolouration. In summary whilst Fe/C shows a reduced adsorption capacity it is more resistant against leaching and therefore may be better suited to wastewater treatment. Furthermore, removal of Fe/C from the solution after adsorption is extremely facile as this can be accomplished by magnetic separation.

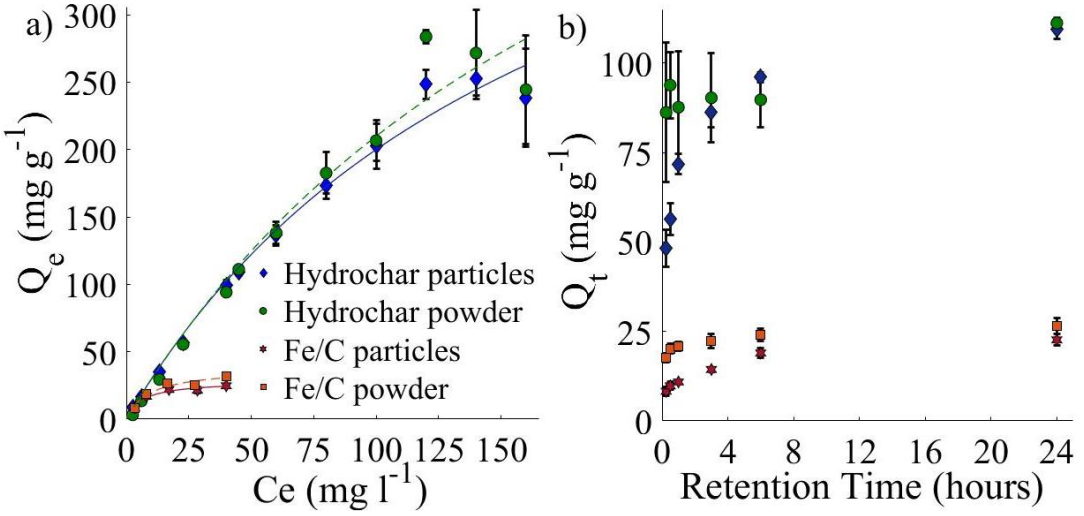

Figure 6.7 Isothermal adsorption of MB on Fe/C and hydrochar over 24 h at 30 °C, 180 RPM, using 0.01 g in 25 mL of solution fitted with Langmuir adsorption isotherms (a). Kinetic adsorption of MB on Fe/C and hydrochar 16 mg L^{-1} and 45 mg L^{-1} respectively, for 0.5, 1, 3, 6, and 24 h at 30 °C, 180 RPM, using 0.01 g in 25 mL solution (b).

The results of kinetic adsorption of MB on both Fe/C and hydrochar are shown in (Figure 6.7, b). After 6 h both materials reach >80% of maximum adsorption. The rate of adsorption for Fe/C is comparable to literature reported iron carbon composite materials

by conventional methods, *e.g.* 54% of maximum adsorption is achieved after 2.5 h [200]. To gain further insight into the adsorption mechanism the kinetic data were fitted to Lagergren pseudo-first order and pseudo-second order rate equations (Equation 6.1 and Equation 6.2) [396], [397].

$$ln(q_e - q_t) = ln\ q_e - \frac{k_1 t}{2.303}$$

Equation 6.1 Lagergren pseudo-first order, qt (mg g^{-1}) is the amount of adsorbed MB on hydrochar at time t (min), k1 (min^{-1}) is the pseudo-first order adsorption rate constant.

$$\frac{t}{q_t} = \frac{1}{k_2 q_e^2} + \frac{1}{q_e t}$$

Equation 6.2 Lagergren pseudo-second order, qt (mg g^{-1}) is the amount of adsorbed MB on hydrochar at time t (min), k_2 (mg g^{-1} min^{-1}) is the pseudo-second order adsorption rate constant.

The Lagergren pseudo-first and second order fitted data are shown in Figure 6.8 and the extracted adsorption capacity at equilibrium and rate constant are shown in Table 6.3 alongside R^2 values. It is apparent that pseudo-second order rate equations describe the adsorption process well, and significantly better than pseudo-first order kinetics in the case of hydrochar, which does not fit for the hydrochar powder. Thus, adsorption of MB on Fe/C and hydrochar is considered to follow second order kinetics. Mechanistically this is indicative of MB being chemisorbed onto the material surface (rather than physisorbed) [398]. The main advantage of chemisorption is the improved retention of MB. As previously discussed the chemisorption occurs due to hydrogen bonding between surface hydroxide and carbonyl groups to the MB [395].

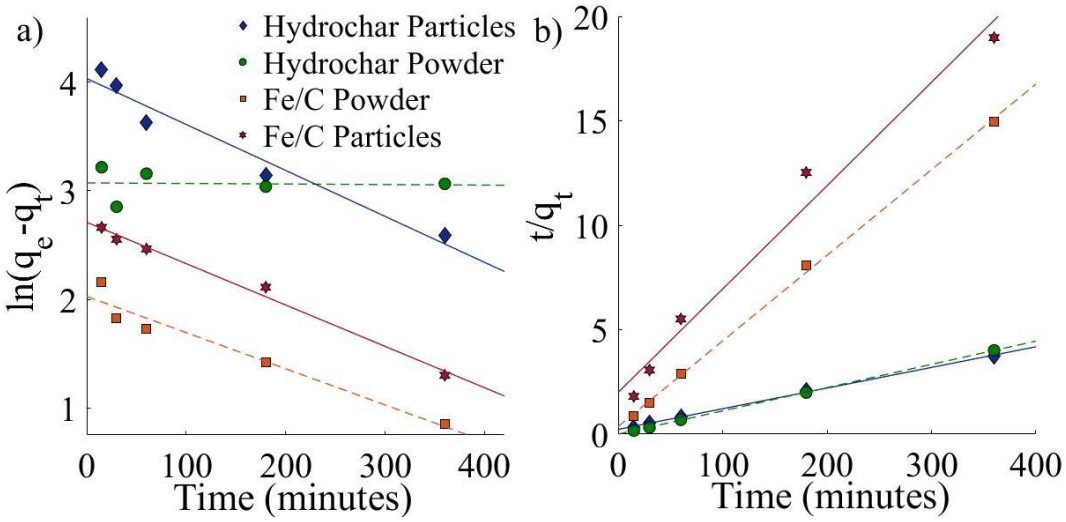

Figure 6.8 (a) Pseudo first and (b) second order fitting graphs made from kinetic methylene blue adsorption data.

Table 6.3 Extracted data from first and second order pseudo fitting of kinetic adsorption experiment.

		Pseudo-first order			Pseudo-second order		
Sample	Exp q_e (mg g^{-1})	q_e cal (mg g^{-1})	k_1 (min^{-1})	R^2	q_e cal (mg g^{-1})	K_2 (mg g^{-1} min^{-1})	R^2
Fe/C Particles	24.8 ± 1.3	14.9	0.0088	0.9907	20.4	0.0012	0.9777
Fe/C Powder	34.6 ± 2.6	7.39	0.0076	0.9453	24.4	0.0047	0.9988
Hydrochar Particles	246 ± 21	54.6	0.0097	0.9553	101	0.00043	0.9985
Hydrochar Powder	267 ± 26	22.2	0.00015	0.0027	90.9	0.014	0.9999

Electronic interactions play a key role in adsorption processes: an increase in adsorption is expected if the adsorbate and adsorbent have opposing charges causing positive interactions [399]. Considering this it is speculated that the surface charge of Fe/C is positive, thereby lowering its adsorption capacity for the positively charged cationic dye MB relative to that of hydrochar [400]. Consequently, the adsorption of indigo carmine (IC) which is an anionic dye (negatively charged) was investigated [401]. Furthermore, the adsorption analysis of powder samples was removed because the small increase to adsorption capacity is negligible compared to the challenges involved in using the powder samples. The isothermal adsorption of IC on Fe/C and hydrochar particles is displayed in Figure 6.9. The maximum adsorption capacity of indigo carmine on Fe/C and hydrochar particles was determined to be 49.0 ± 3.7 and 50.9 ± 2.9 mg g^{-1} respectively. Therefore, both the hydrochar and Fe/C therefore show the same adsorption properties for IC. Suggesting that the iron oxide is not participating in the adsorption mechanism, however the Fe/C have the advantage of facile magnetic separation from solution.

However, this also suggests that the iron oxide is not causing electronic repulsion with the IC which would limit its adsorption. In literature π-interactions are suggested as the main cause of chemisorption of IC [402]. This is backed up by evidence of graphitic carbon given by XPS analysis. The IC is therefore adsorbed *via* π- π interactions between the benzene on IC and the delocalised electrons present in the graphitic part of the Fe/C and hydrochar. Finally, it should also be noted that, typically, the maximum adsorption capacity for IC is generally lower than MB *e.g.* a commercial activated carbon has exhibited a maximum adsorption capacity seven-times lower for IC (135 mg g^{-1}) than for MB [403].

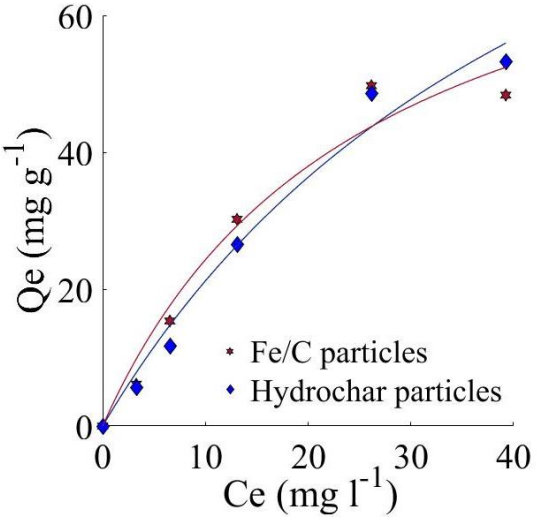

Figure 6.9 Isothermal adsorption of indigo carmine on Fe/C and hydrochar particles over 24 h at 30 °C, 180 RPM, using 0.01 g in 25 mL of solution fitted with Langmuir adsorption isotherms.

6.3. Catalytic Testing of Fe/C

To evaluate the catalytic application of the Fe/C its effect on the hydroalkoxylation of phenylacetylene with ethylene glycol was evaluated and compared to both hydrochar and unsupported magnetite nanoparticles. Hydroalkoxylation reactions offer an atom-economical method of creating a carbonyl bond using an alkene or alkyne and an alcohol [404]. The reaction was first demonstrated in 1936 using a mercuric oxide catalyst with boron trifluoride based co-catalysts [405] Since then, systems based on Hg, Os, Ru, Pt, Ag, and Au within organic complexes and as oxides have been widely reported [406]. However, many of these materials suffer from challenges around high toxicity or high cost. Therefore, alternative catalysts such as iron salts are investigated to overcome these challenges [407]–[409]. The first studies on heterogeneous iron catalysts were presented in 2015 by Antoniotti *et al* [410]. These employed

montmorillonite-supported iron, achieving yields of up to 86% for the hydroalkoxylation of 5-methyl-2,2-diphenyl-4-hexen-1-ol to 2,2-dimethyl-5,5-diphenyltetrahydro-2H-pyran in dimethyl carbonate (DMC) as a solvent. The further development of low-cost, active, heterogeneous catalysts based on Earth-abundant materials remains a desirable objective.

The results for catalytic hydroalkoxylation are displayed in Table 6.4. Each catalytic test was performed in triplicate and results averaged. Particle samples produced consistently higher yields than powder samples, providing another reason to remove the smaller particle sizes of produced samples. Unsupported magnetite nanoparticles were found to successfully yield 2B13D with a yield of 22.7%, whilst hydrochar particles produced a lower yield at 11.2%. These two serve as benchmarks with which to compare the catalytic efficiency of the Fe/C. Fe/C showed a greater yield than both of them combined at 45%. It should be noted that the same quantity of iron oxide is present as the magnetite nanoparticles, displaying that this difference is reflective of a truly higher activity in the Fe/C compared to the sum activity of magnetite nanoparticles and hydrochar. It is thus speculated that a synergistic interaction between iron oxide and carbon is occurring, whereby the hydrochar facilitates hydroalkoxylation through stabilising the hydroxide group, resulting in the formation of the stabilised enol transition state [197], [411]. Previously, the hydroalkoxylation of phenylacetylene with ethylene glycol has been studied utilising a homogeneous Au(I)/$AgBF_4$ catalyst [412]. In contrast to the present work, Au(I)/$AgBF_4$ demonstrated high selectivity for the alternative regioisomer, producing 2-methyl-2-phenyl-1,3-dioxolane (2P13D) with a yield of 87% (corresponding to a selectivity of 75%). No 2P13D is observed over Fe/C, hydrochar, or magnetite. This exceptional regioselectivity for 2B13D is attributed to the conformation adopted by the transition state, with bonding to heterogeneous iron active site taking place *via* the enol functionality [413]. The high selectivity, and the ability to produce exclusively one isomer, is a key objective in catalyst development, and one successfully demonstrated by the material synthesised in this work. These catalytic studies demonstrate the potential to synthesise active and selective catalytic materials from low value waste and co-product streams *via* HTC.

Table 6.4 Percentage yield of 2-benzyl-1,3-dioxolane from hydroalkoxylation reaction (Table 3.4) between ethylene glycol and phenylacetylene based on the theoretical yield from the amount of phenylacetylene used.

Catalyst	Yield 2-benzyl-1,3-dioxolane (%)
Magnetite Nanoparticles	22.7
Hydrochar Particles	11.2
Hydrochar Powder	7.0
Fe/C Particles	45.0

6.4. Changes in Fe/C from Addition of Ethanol During HTC

The effect of ethanol as an additive during HTC on the properties of the Fe/C was investigated at 9 different ethanol/water mixture concentrations in triplicate. Iron loading of the Fe/C was analysed using AAS and XRF (Figure 6.10, a). In all experiments iron was fully incorporated into the final Fe/C, verified by analysis of the HTC filtrate liquid by AAS which contained iron below the limit of detection (1 ppm, 100 ml). This means that changes in the iron loading of the Fe/C are related to the yield of hydrochar from the AS. There is some variation that can be attributed to differing AS weight (10-15 g) the effect of this is minimised by samples being prepared in triplicate. In Section 5.7.1 the yield of hydrochar from HTC was raised above 32 mol% ethanol related to a reduced/eliminated carbonisation of the DBW. This trend is not observed in HTC of AS, the majority of the Fe/C has an iron loading between 30 and 40 wt.% with no correlation related to ethanol concentration. Therefore, under these conditions' ethanol concentration has little to no effect on yield of hydrochar which can be used as a proxy for degree of carbonisation. Whilst different reaction mechanisms may proceed from ethanol addition during HTC if harsher processing conditions are used a fully carbonaceous product can be produced. Investigating the HTC of lignocellulose at higher ethanol concentrations over a range of processing conditions would elicit valuable information not properly conveyed in the literature. The most obvious outlier occurs at 32 mol% ethanol where synthesised Fe/C contains between 47.4 and 50.3 wt.% iron by XRF and AAS respectively. This represents a reduced yield of hydrochar which is attributed to a reduced polycondensation of dissolved organics. Furthermore, 32 mol% ethanol at these conditions has potential for investigation of hydrothermal liquefaction processes.

The percentage phase distribution between heamatite and magnetite was determined by XRD using MATCH! Software (Figure 6.10, b). As previously discussed the heamatite presence is attributed to oxidation of magnetite during HTC [370]. XRD analysis showed a lack of maghemite in the Fe/C therefore the oxidation is occurring through the mechanism observed

at 275 °C. In this mechanism the surface magnetite is dissolved and then oxidised to heamatite which is precipitated onto the surface. The oxidation is therefore limited to the penetration depth of the liquid phase and its ability to dissolve the magnetite. Examination of the phase composition shows the Fe/C synthesised at 11.1 and 16.6 mol% has a significantly higher proportion of magnetite at 94.5% and 91.5%, respectively. Consequently, at these molar percentages either there is low penetration depth for the ethanol/water mixture, or it has low capacity for magnetite dissolution. On the opposite side a large oxidation of magnetite is shown at 56.9 mol% with the magnetite phase only consisting of 47.9%, and thus smaller than the heamatite phase. This provides evidence that at this concentration the ethanol/water mixture is either highly penetrative or has a high capacity to dissolve the magnetite. This is ascribed to a maximum structured hydrogen bonding environment within the ethanol/water mixture at 56.9 mol% as observed from C-O bond absorption in Section 4.1.3 (Figure 4.8), providing evidence that the hydrogen bonding structure of the ethanol/water mixture has a different maximum structuring under different temperatures in hydrothermal conditions compared to the established molecular dynamics at ambient conditions. At 11.1 and 16.6 mol% there is the least interaction between ethanol and water which causes a reduction in the oxidation of magnetite.

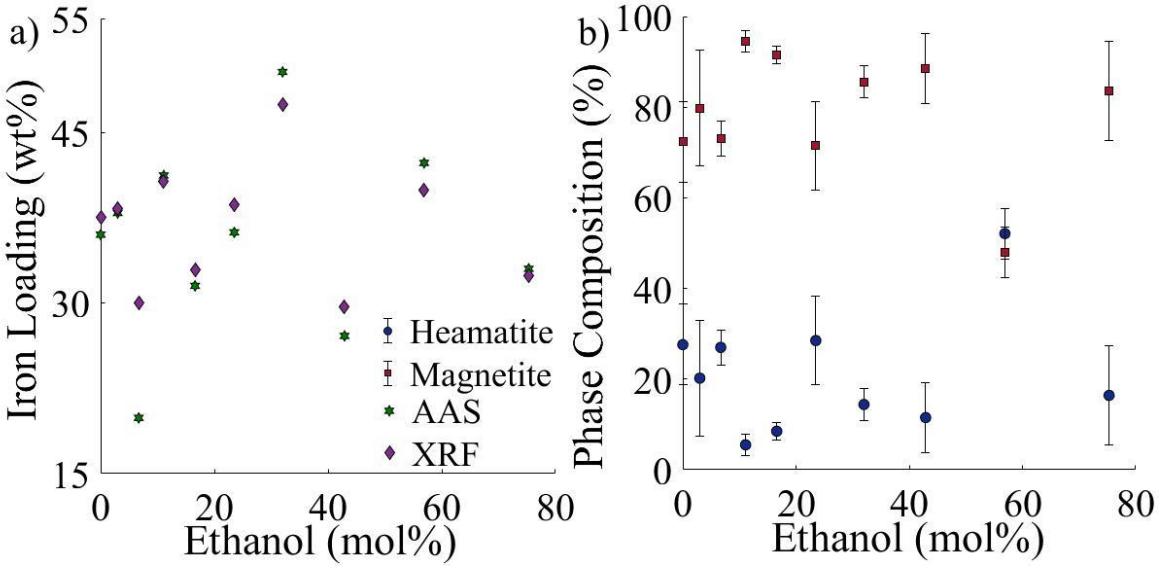

Figure 6.10 (a) Iron loading for Fe/C under different ethanol/water mixtures measured using AAS (green hexagram) and XRF (purple diamond). (b) Phase composition of Fe/C broken into heamatite (blue circle), and magnetite (red square) measured using XRD.

FT-IR analysis was performed to assess changes in the surface functionality of the Fe/C with changing ethanol concentration during synthesis. Above 600 cm^{-1} the FT-IR spectra of all Fe/C had excellent overlap hence the surface organic functionality is not affected by the addition of ethanol during HTC at any concentration. This is in contrast with HTC of DBW observed in

Section 5.7.4 where above 32 mol% the FT-IR spectra paralleled that of the raw DBW. The uniformity in the Fe/C surface functionality in different ethanol/water mixtures is attributed to the higher processing temperature causing increased carbonisation of the lignocellulosic feedstock. In addition to this any minor effect that ethanol has on the surface functionality is converted into graphitic type carbon during post-carbonisation which is facilitated by the iron oxide acting as a Lewis acid to produce char. However, changes were observed between 600-400 cm^{-1} which are related to the iron oxide (Fe-O) vibrational absorbances (Figure 6.11). The absorbance is considered to be proportional to the amount of iron oxide present on the surface of the Fe/C. Following this, Fe/C synthesised under 32 mol% has the highest Fe-O FT-IR absorbance, this aligns with iron loading observations by AAS and XRF (Figure 6.10, a). Furthermore, 42.9 and 75.3 mol% have the lowest observed iron oxide Fe-O FT-IR absorbances and they both have the joint lowest iron loading. Consequently FT-IR is presenting high potential in fast non-destructive screening of iron content in synthesised Fe/C. Moreover, this can be applied to any metal with absorbances in the FT-IR spectra that has been supported onto hydrochar/carbonaceous material.

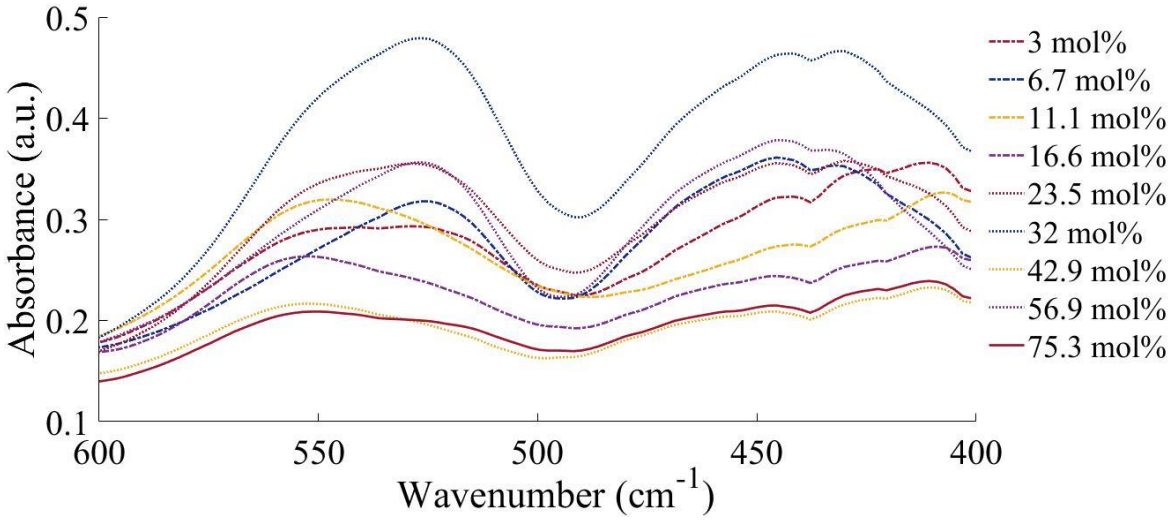

Figure 6.11 FT-IR absorbance for Fe/C synthesised in different EtOH/water mixtures between 600-400 cm^{-1} using a Shimadzu IRAffinity-1S spectrometer fitted with a Specac ATR plate. Analysis conditions: scans 100, resolution 4 cm^{-1}, absorbance mode.

Surface morphology by SEM of the Fe/C synthesised in different ethanol/water mixtures (Figure 6.12) revealed they have comparable structure to previously observed Fe/C particles in Figure 6.6. Once again opposing the results in Section 5.7.5 which can be attributed to the higher processing temperature, post-carbonisation, and presence of iron oxide.

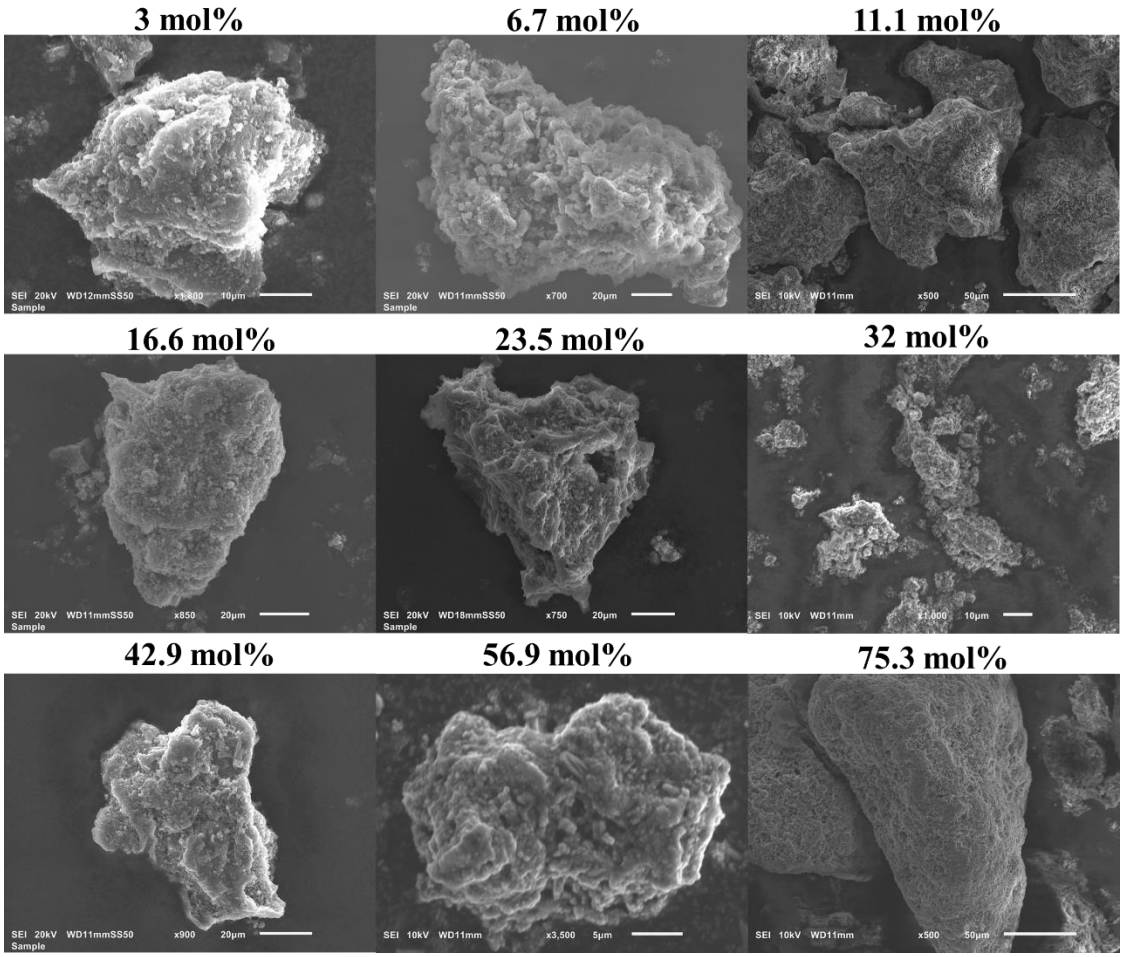

Figure 6.12 SEM images of Fe/C synthesised under different EtOH/water mixtures SEM performed on instrument in Section 3.3.8.

Isothermal adsorption of IC onto the Fe/C produced in different ethanol/water mixture is displayed in Figure 6.13. The maximum adsorption capacity is between 46.4 and 51.2 mg g^{-1} for 9 of the 10 Fe/C samples. However, significantly higher maximum adsorption capacity is observed for Fe/C synthesised in 56.9 mol% ethanol at 65.2 mg g^{-1}. This increased adsorption is attributed to the higher percentage phase distribution of heamatite in this Fe/C. Therefore, heamatite is preferential to magnetite for IC adsorption. Furthermore, this demonstrates the potential to utilise different ethanol/water mixtures to manipulate the structure of the iron oxide to suit different applications. In addition to the potential in applying ethanol additives to the hydrothermal synthesis of different supported metal oxides.

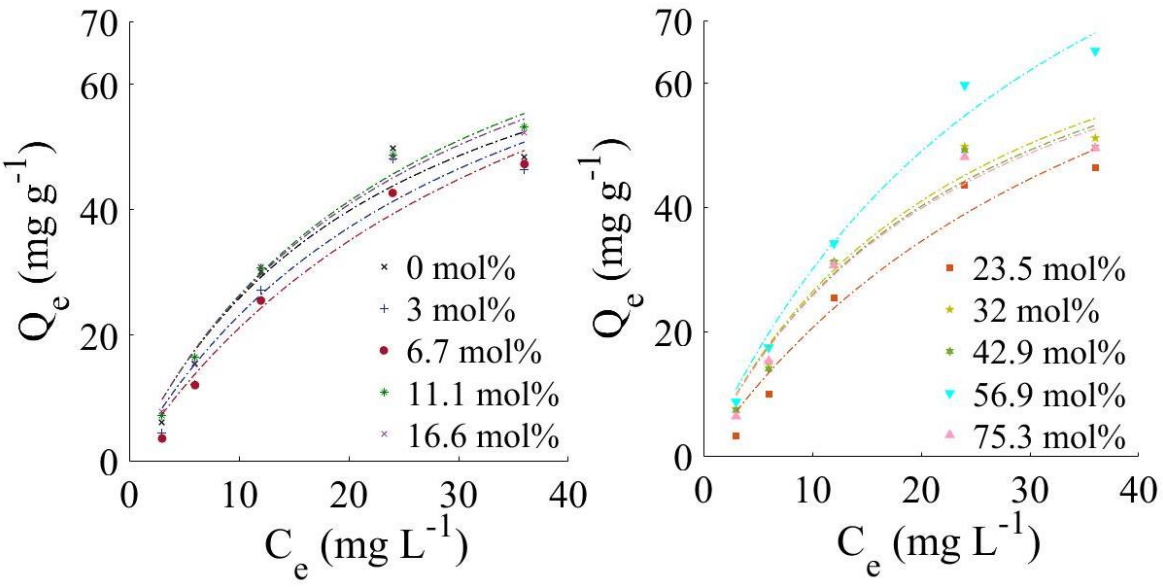

Figure 6.13 Isothermal indigo carmine (IC) adsorption onto Fe/C synthesised in different concentration EtOH/water mixtures.

The catalytic hydroalkoxylation of ethylene glycol and phenylacetylene to yield 2-benzyl-1,3-dioxolane (2B13D) is attempted for Fe/C synthesised in all ethanol/water mixtures (Table 6.5). These 2B13D yields must not be compared to previously obtained yields in Section 6.3 due to experimental limitations specified in the Covid-19 impact form. The results are accordingly compared to one another as an isolated experiment. Some of the highest 2B13D yields are observed with Fe/C synthesised in 11.1, 42.9, and 75.3 mol% ethanol which also produced the alternative regioisomer (Figure 6.14) 2-methyl-2-phenyl-1,3-dioxolane (2P13D). Each of these Fe/C samples contained some of the highest magnetite phase percentages at 94.5%, 88.5%, and 83.6%. The lack of 2P13D in 16.6 mol% synthesised Fe/C (which contains a large magnetite phase) is attributed to its low overall yield from the hydroalkoxylation. Supporting this conclusion, the high heamatite phase Fe/C produced at 56.9 mol% ethanol gave a relatively high yield of 2B13D at 9.3% and produced no 2P13D. Therefore, the heamatite produced during HTC is essential in the selectivity of the catalytic hydroalkoxylation reaction.

Table 6.5 Percentage yield of 2-benzyl-1,3-dioxolane (2B13D) from hydroalkoxylation reaction (Figure 3.6) between ethylene glycol and phenylacetylene based on the theoretical yield from the amount of phenylacetylene used.

Ethanol (mol%)	Yield 2-benzyl-1,3-dioxolane (%)	Peak area 2P13D
3	1.4	-
6.7	3.1	-
11.1	13.9	15347679
16.6	3	-
23.5	1.4	-
32	2.5	-
42.9	5.1	4845457
56.9	9.3	-
75.3	5	4995822

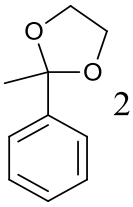

2-methyl-2-phenyl-1,3-dioxolane

Figure 6.14 Chemical structure of alternative regioisomer from hydroalkoxylation reaction 2-methyl-2-phenyl-1,3-dioxolane.

6.5. Conclusions

To the authors knowledge avocado seeds have been used for the first time in hydrothermal carbonisation to produce an enriched carbonaceous material. Iron oxide was deposited onto this hydrochar *in situ* to produce a magnetic carbon composite (Fe/C) material. The synthesis process used is a facile, rapid (3h) and relatively low temperature (230 °C) one-pot HTC process. The synthesised Fe/C has been evaluated using an exemplar catalytic hydroalkoxylation reaction and wastewater adsorbates methylene blue (MB) and indigo carmine (IC). This has demonstrated the potential that HTC has in the production of high value carbon materials from low value waste lignocellulose. Furthermore, the metal-hydrochar produced can be used in environmental and industrial applications following synthesis principles that are rooted within creating a circular carbon based economy. Additionally, the effect of ethanol as an additive during HTC on the properties of the Fe/C has been evaluated.

The synthesised Fe/C were mostly composed of magnetite (73 ± 5.6%) with a smaller quantity of heamatite (27 ± 5.6%). They displayed ferromagnetic behaviour which allows for facile collection with an external magnet after catalytic and adsorption testing. Evidence suggests that varying ethanol/water mixtures used in HTC can control the amount of oxidation of

magnetite to heamatite during the reaction. In adsorption testing Fe/C showed preferential adsorption of the anionic adsorbate IC with a maximum adsorption capacity of ~49 mg g^{-1} which is comparable to iron-carbon based materials produced through more costly, and less environmentally friendly processes. This adsorption capacity can be improved (~65.2 mg g^{-1}) by increasing the percentage of heamatite in the iron oxide as demonstrated by the use of ethanol/water mixtures during HTC. In addition Fe/C showed enhanced catalytic efficiency when compared to magnetite nanoparticles, exhibiting a 2B13D yield in the hydroalkoxylation of phenylacetylene of ~45%, versus ~23% for the nanoparticles. The Fe/C showed exceptional regioselectivity towards 2B13D, the yield of which is enhanced by an increase in surface heamatite functionality. Increased surface magnetite functionality in ethanol/water synthesised Fe/C resulted in the production of the alternative regioisomer 2P13D.

Chapter 7 Optical Trapping of Sol-Gel Catalysts with *in-situ* Raman Analysis of Gelation Mechanism

This chapter is focused on analysis of the molecular and reaction dynamics present in the early stages of aerosol-assisted sol-gel (AASG) synthesis processes. To achieve this in Section 7.1 twelve bulk catalysts have been synthesised by sol-gel method (Section 3.2.5) on a laboratory scale. The sol, gel, and solid catalyst have been analysed using Raman spectroscopy (Section 3.3.10). The data presented in this section also provides characterisation of the solid catalysts for using in future processes with crystal structure verified using XRD. This has been done to guide the selection of these different precursor solutions for use in AASG synthesis. Furthermore, these bulk sample observations provided a basis of knowledge for peak assignment to use when evaluating the spectra obtained from optically trapped droplets which replicated the conditions of AASG synthesis (Section 7.2).

Currently AASG synthesis (Section 2.4.2) can be considered as a black box, the reactions occurring within single droplets in the flow tube are highly challenging to study using conventional techniques. Whilst analysis can be performed on post-synthesised catalysts to characterise particle size, molecular mass, structure, and composition this provides no insight into the reactivity within the flow tube [414]. Mechanistic insights into AASG synthesis are typically inferred from bulk sol-gel synthesis. The use of optical trapping is implemented to investigate the mechanisms occurring to droplets in a flow tube during AASG synthesises. Therefore in Section 7.2 a single droplet of the precursor solution is trapped in place with the time domain acting as an analogue for the space domain in the flow tube. Raman spectroscopy is used to probe the structural and bonding dynamics within the trapped droplet. Furthermore, the aspect of external heating is explored to emulate the conditions of AASG synthesis more accurately. This investigation can hence be considered an *operando* investigation of the AASG synthesis process.

7.1. Raman and XRD Analysis of Bulk Sol-Gel Catalysts

For reference, the Raman spectrum of bulk ethanol and water with dissolved pluronic P123 solution made with same concentrations as the metal salt solution is analysed and assigned Figure 7.1. The peaks in this spectrum are expected to be present in both the sol and gel. Broad O-H stretching bands (**11**, 3262 cm^{-1}) and (**12**, 3420 cm^{-1}) for water are readily allocated, there is notable exclusion of O-H bending which should appear around 1630 cm^{-1}. The lack of this

peak is attributed to low water concentration, which is noted to disappear below 65 w/w% water [296]. All other peaks are attributed to the pluronic P123 and/or the ethanol since they contain the same covalent bonds within different local environments. Large peaks associated with C-H symmetric and asymmetric stretching of either methyl or methylene groups (**8**, **9**, **10**).

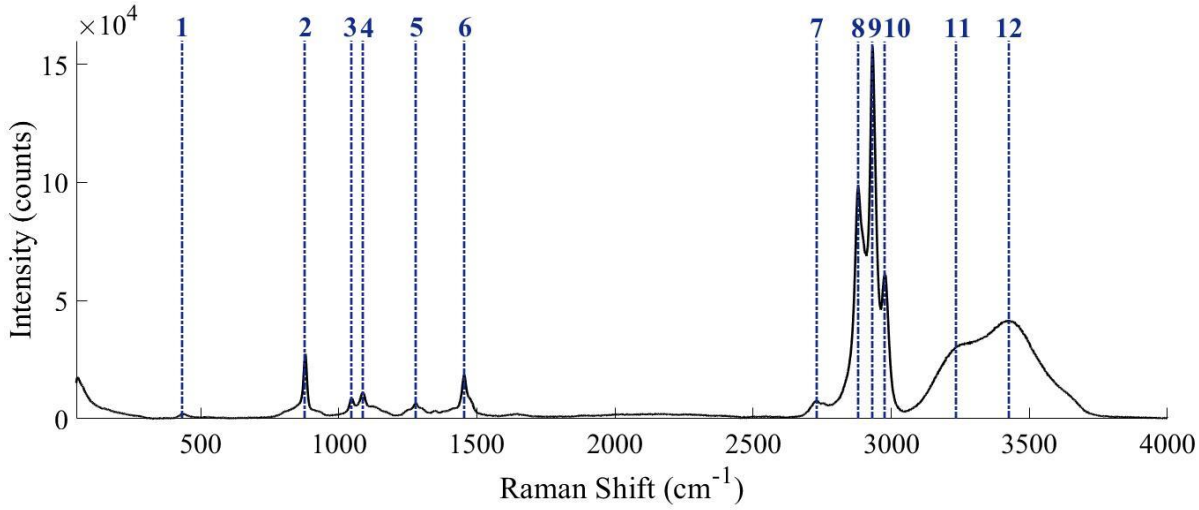

Figure 7.1 Raman spectrum for ethanol, pluronic P123, and water system used in metal salt synthesis of sol-gel catalysts between 50-4000 cm^{-1}.

In the Raman spectrum of the sol-gel catalysts the main changes between sol, gel, and catalyst above 1600 cm^{-1} is a decrease in the C-H stretching and O-H stretching peaks. This is associated simply with evaporation of the solvents ethanol and water. There is additionally baseline curvature of increasing intensity in the higher wavenumbers displayed in all solid catalyst data. This is typical for Raman spectra and the effect of it can be diminished by advanced baseline correction [415]. However the high intensity of this baseline shifting obscures the peaks of interest displayed at the lower Raman shift values. Therefore, only the lower spectral range between 50-1600 cm^{-1} is studied herein.

Table 7.1 Raman assignment for the three components present in all of the sol-gel samples based on the spectra shown in Figure 7.1 [296]**.**

Number	Raman Shift (cm^{-1})	Intensity	Assignment
1	436		δ C-C-O bending
2	879		ν C-C stretching
3	1045		ν_s C-O stretching
4	1097		ν_s C-O stretching
5	1280		τ C-H_2 twisting (asymmetric out-of-plane bend)
6	1454		δ CH_3 + CH_2 bending
7	2729		Combinational frequencies
8	2880	vs	ν_{as} C-H_2 asymmetric stretching
9	2932	vs	ν_s C-H_3 symmetric stretching
10	2977	vs	ν_{as} C-H_3 asymmetric stretching
11	3262	br, s	ν O-H stretching (strongly hydrogen bonded)
12	3420	br, s	ν O-H (weakly hydrogen bonded)

7.1.1. Cobalt Sol-Gel Catalysts

The CoAl-Sol Raman spectra is mostly attributed to ethanol and water related peaks which is expected because they have the largest relative abundance and therefore engulf the Raman spectra (Figure 7.2). Peak **11** is much broader than observed in the Raman spectrum of ethanol, pluronic P123, and water. Furthermore, there is an additional broad peak **4** both of these variations can be attributed to the absorbance of cobalt chloride produced from the reaction of cobalt ions and the hydrochloric acid [416]. The relative height of these peaks matches that observed in bulk solution without aluminium chloride hexahydrate and cobalt nitrate hexahydrate (Figure 7.1). The CoAl-Gel Raman spectra exhibit new peak **7**, **9**, **12**, **13**, **14** and an increase in peaks **15** all of which can be attributed to the presence of pluronic P123 (Appendix 6). The absorbances are broad due to the large number of different bonding environments present in the pluronic P123. The presence of peaks at **12**, **13**, **15** is attributed to C-O-C asymmetric stretching. the dominance of these peaks in the Raman data for sol and gel of catalysts is often only attributable to the expected alcohol/water and pluronic P123 peaks. In future Raman spectra only deviations from this expectation will be highlighted.

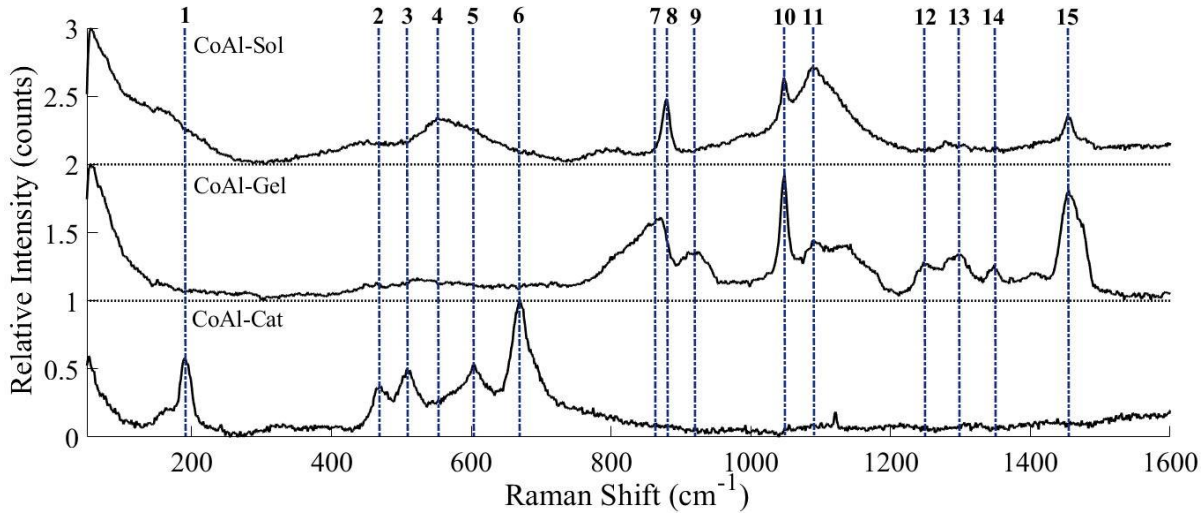

Figure 7.2 Raman spectra for CoAl sol, gel and catalyst, Raman shift 50-1600 cm^{-1}, acquired using Renishaw inVia Raman microscope 514 nm (green), Ar laser, 12 mW.

Notably there is an increased peak height for **10** in both CoAl-Sol and CoAl-Gel compared to pure alcohol/water and pluronic P123 respectively. This increased peak height is attributed to the nitrate ions present in the cobalt nitrate hexahydrate. The symmetric stretching band of free nitrate ($-NO_3$) occurs at 1047 cm^{-1} [417]. This band is shifted to 1050 cm^{-1} when bound to cobalt to however the peaks overlap to form one convoluted peak. This peak can be deconvoluted to give the relative proportion of free and cobalt bound nitrate. Raman spectra for CoAl-Cat had features typical for cobalt oxide (Co_3O_4) [418]. The spectra lacked any other visible peaks, this suggests that the solid catalyst is only Co_3O_4. All five of the Raman active modes (A_{1g}, E_g, and three F_{2g}) can be assigned (Table 7.2) [419]. The presence of alumina (Al_2O_3) is verified with SEM/EDX analysis (Appendix 7). The lack of signal for Al_2O_3 in the Raman spectra has been observed in literature synthesised Co_3O_4/Al_2O_3 catalysts [420]. This is ascribed to the low Raman signal produced by Al_2O_3.

Table 7.2 Raman assignment the three states of CoAl shown in Figure 7.2 [418]**.**

CoAl-Sol		
Reference	Raman Shift (cm^{-1})	Assignment
4	551	$^4T_1$ $CoCl_2$
8	880	ν C-C stretching
10	1048	ν_s C-O stretching
11	1096	ν_s C-O stretching
15	1453	δ CH_3 + CH_2 bending
CoAl-Gel		
Reference	Raman Shift (cm^{-1})	Assignment
7	872	ν_s C-O-C stretching
9	921	ν_s C-O-C stretching
10	1048	ν_s C-O stretching
11	1096	ν_s C-O stretching
12	1248	ν_{as} C-O-C stretching
13	1297	ν_{as} C-O-C stretching
14	1348	ν_{as} C-O-C stretching
15	1455	δ CH_3 + CH_2 bending
CoAl-Cat		
Reference	Raman Shift (cm^{-1})	Assignment
1	190	F_{2g} Co_3O_4
2	470	E_g Co_3O_4
3	508	F_{2g} Co_3O_4
5	604	F_{2g} Co_3O_4
6	668	A_{1g} Co_3O_4

Co_3O_4 phase crystal for the solid catalyst is confirmed with XRD analysis Figure 7.3 [421].The XRD analysis displays no peaks that can be attributed to alumina which indicates that the alumina is in an amorphous form [422].

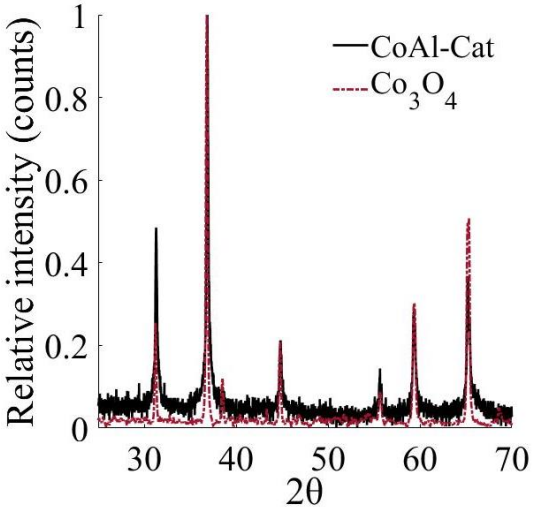

Figure 7.3 X-ray diffractogram pattern for CoAl to RRUFF spectroscopic references for Co_3O_4 between 25– 70° obtained using a Cu tube with 1.54184 Å, scanning for 1 second at increments of 0.02°.

The cobalt alumina catalyst was also synthesised using aluminium alkoxide method instead

termed AlkCoAl. AlkCoAl-Sol contained the same alcohol/water associated peaks in addition to a new peak at 816.4 cm^{-1} this can be assigned to the symmetric stretching of C-C-C because of the presence of the isopropoxide group [423]. There is also an increase to 881 cm^{-1} C-C symmetric stretching peak due to the increased abundance of C-C bonds. In both AlkCoAl-Sol and AlkCoAl-Gel the 1050 cm^{-1} is significantly higher than expected; this is attributed to the previously discussed presence of -NO_3 symmetric stretching [417]. AlkCoAl-Cat also shows the same peaks for Co_3O_4 displayed in CoAl-Cat.

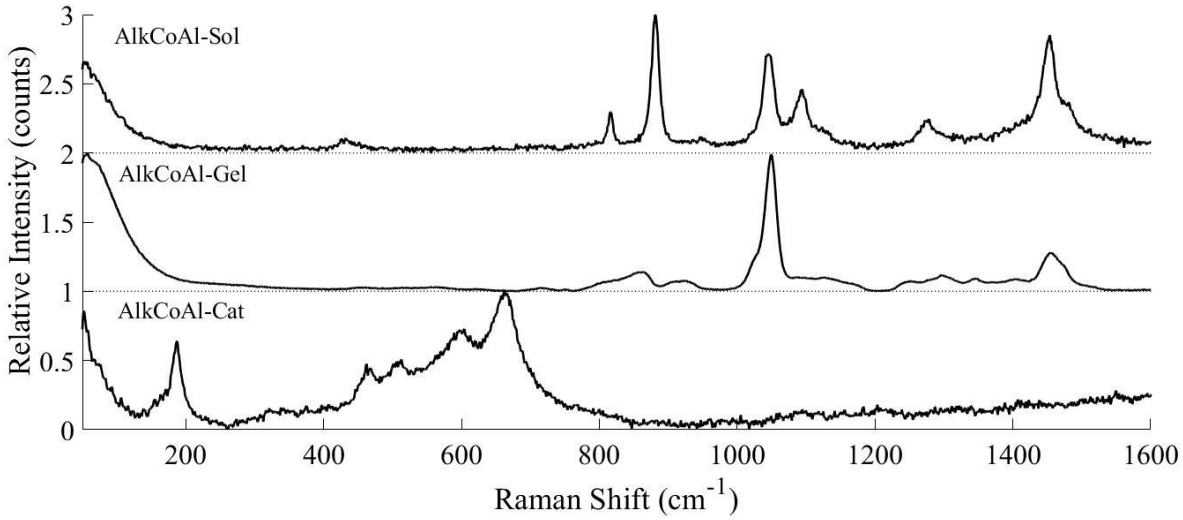

Figure 7.4 Raman spectra for AlkCoAl sol, gel and catalyst, Raman shift 50-1600 cm^{-1}, acquired using Renishaw inVia Raman microscope 514 nm (green), Ar laser, 12 mW.

Co_3O_4 is again confirmed for the AlkCoAl-Cat with XRD analysis Figure 7.5 [421]. Therefore alumina is in an amorphous state again in this solid catalyst.

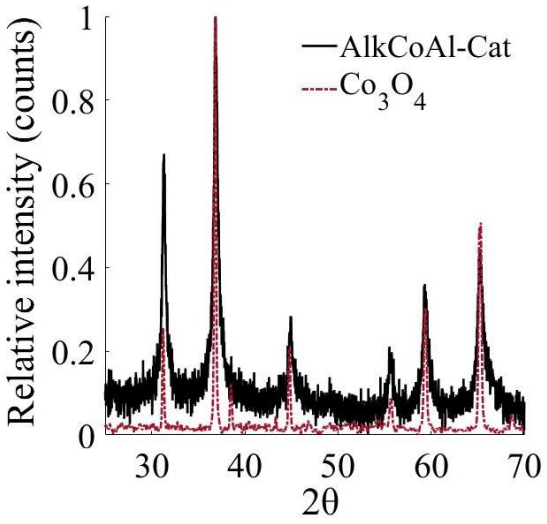

Figure 7.5 X-ray diffractogram pattern for AlkCoAl to RRUFF spectroscopic references for Co_3O_4 between 25– 70° obtained using a Cu tube with 1.54184 Å, scanning for 1 second at increments of 0.02°.

The CoSi catalyst was synthesised using tetra ethyl ortho silicate (TEOS) to produce the silica (SiO_2) support material. There is little of interest in both the CoSi-Sol and CoSi-Gel Raman spectra, the same -NO_3 symmetric stretching vibrations is observed but is significantly lower than in the CoAl Raman data (Figure 7.6). CoSi-Cat shows no peaks for any oxidation states of cobalt oxide. All observed peaks are related to the Raman of silica [424]. The 400 cm^{-1} peak is due to bond-rocking Si-O-Si. The band at 495 cm^{-1} is due to D_0 symmetric oxygen stretch. 975 cm^{-1} is due to symmetric stretch vibration of silanols in SiO_2. Finally the band at 800 cm^{-1} is characteristic of fused SiO_2 due to bond-bending vibration parallel to the bisector.

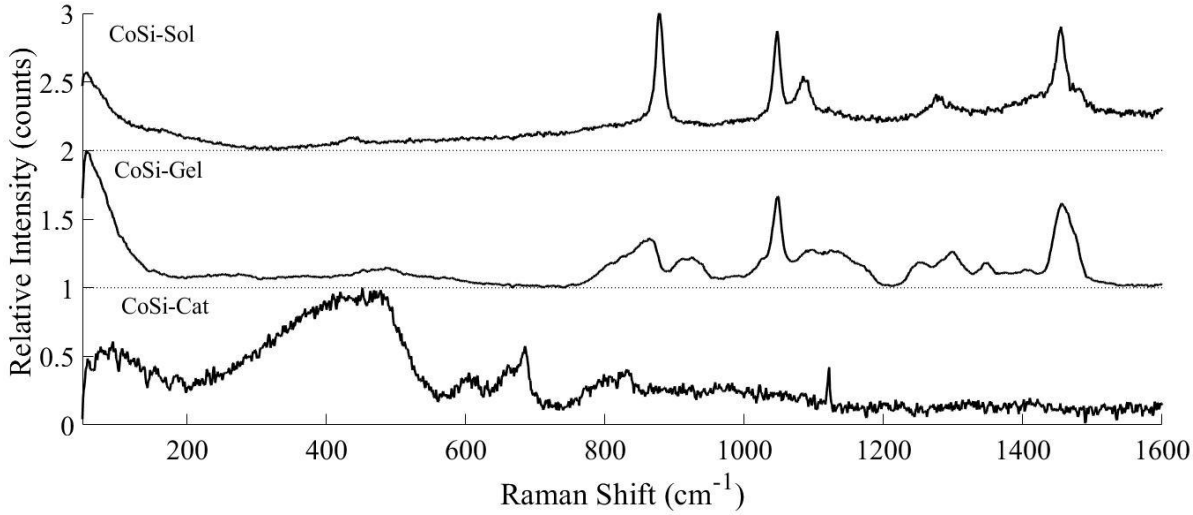

Figure 7.6 Raman spectra for CoSi sol, gel and catalyst, Raman shift 50-1600 cm^{-1}, acquired using Renishaw inVia Raman microscope 514 nm (green), Ar laser, 12 mW.

In contrast, XRD analysis clearly displays the presence of Co_3O_4 (Figure 7.7). SiO_2 is also

displayed by the sloping curve in the lower edge of 2θ, this is because SiO_2 has a broad peak at around 22° [425]. SiO_2 verified using SEM/EDS analysis (Appendix 7).

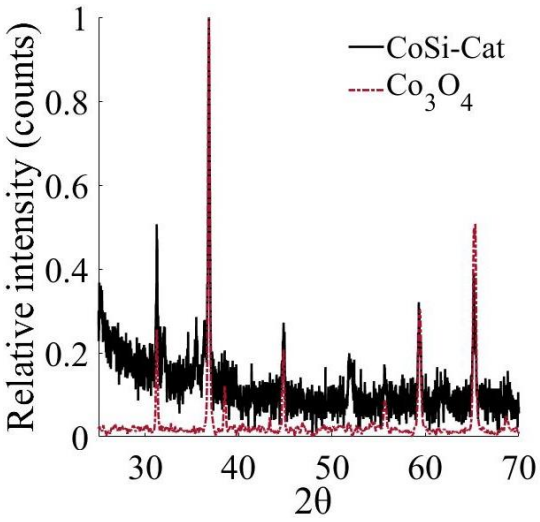

Figure 7.7 X-ray diffractogram pattern for CoSi to RRUFF spectroscopic references for Co_3O_4 between 25– 70° obtained using a Cu tube with 1.54184 Å, scanning for 1 second at increments of 0.02°.

7.1.2. Nickel Sol-Gel Catalysts

NiAl-Sol and NiAl-Gel only deviation from bulk is the -NO_3 stretch band at 1050 cm^{-1} (Figure 7.8) [417]. NiAl-Cat shows Raman vibrational bands for NiO [426]. The vibrational band at 570 cm^{-1} corresponds to one-phonon TO and LO modes, whilst the peak at 1090 cm^{-1} is attributed to the two-phonon 2LO mode of absorbance. The two phonon 2TO (730 cm^{-1}) and TO + LO (906 cm^{-1}) modes in addition to two-magnon band (1550 cm^{-1}) are not observed. This suggests that the crystallite size of the NiO particles is larger than 100 nm causing these bands to be broadened and disappear as shown by Mironova-Ulmane *et al*. No Al_2O_3 bands are again attributed to its low Raman signal. Presence of Al_2O_3 was confirmed with SEM/EDS analysis (Appendix 7).

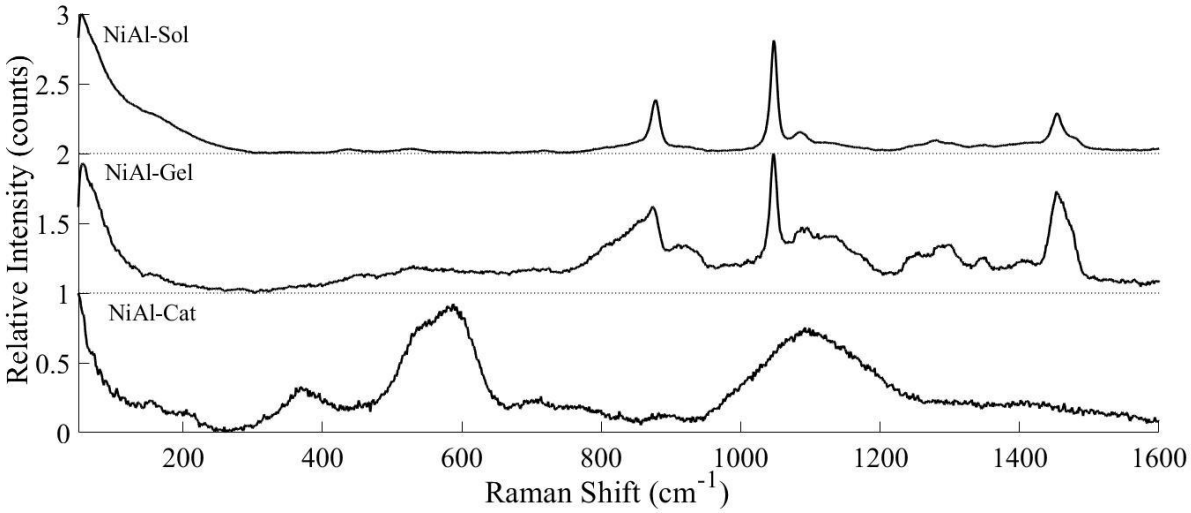

Figure 7.8 Raman spectra for NiAl sol, gel and catalyst, Raman shift 50-1600 cm^{-1}, acquired using Renishaw inVia Raman microscope 514 nm (green), Ar laser, 12 mW.

XRD analysis of NiAl also shows the presence of NiO (Figure 7.9) [427]. The two other peaks at 45° & 66° may be attributed to the presence of aluminum metal within the catalyst [428].

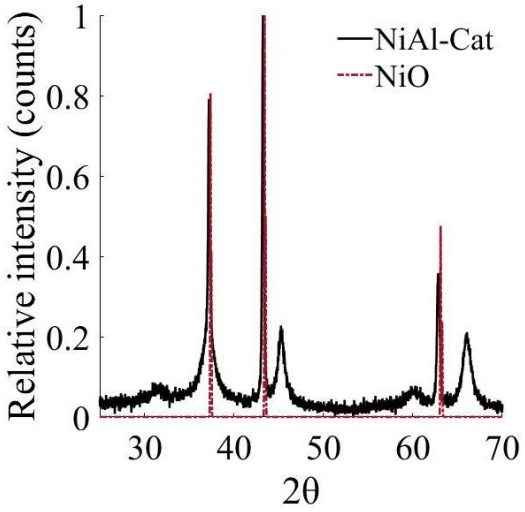

Figure 7.9 X-ray diffractogram pattern for NiAl to RRUFF spectroscopic references for NiO between 25– 70° obtained using a Cu tube with 1.54184 Å, scanning for 1 second at increments of 0.02°.

AlkNiAl showed the same peaks in the Raman spectra for the sol and gel as NiAl with the additional peaks for alkoxide groups as previously discussed (Section 7.1.1) (Figure 7.10). The AlkNiAl-Cat Raman spectra contained very little to no signal therefore the phase of the catalyst cannot be determined using Raman spectroscopy.

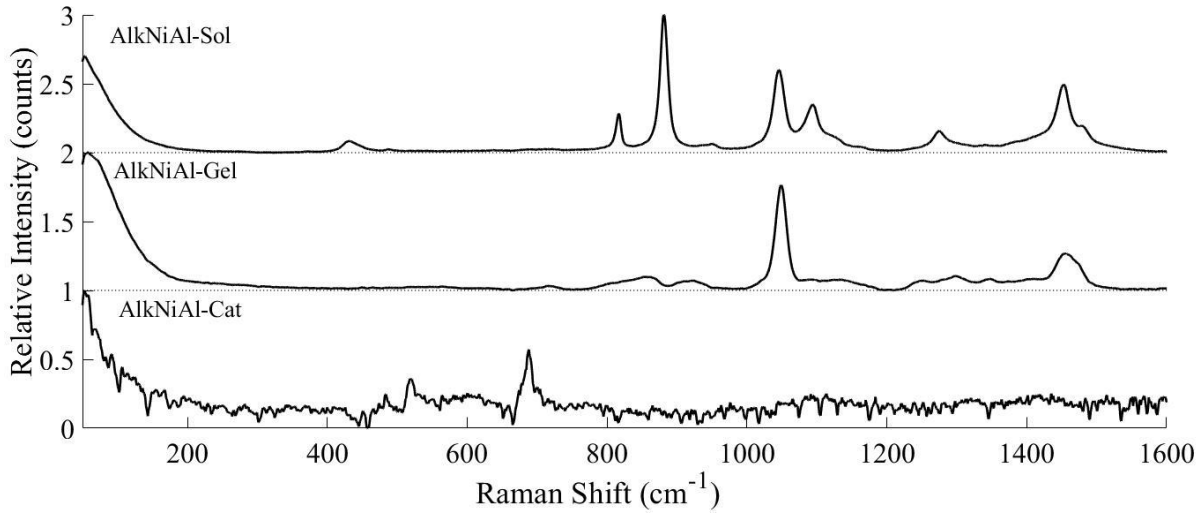

Figure 7.10 Raman spectra for AlkNiAl sol, gel and catalyst, Raman shift 50-1600 cm^{-1}, acquired using Renishaw inVia Raman microscope 514 nm (green), Ar laser, 12 mW.

XRD analysis of AlkNiAl-Cat allowed the presence of the spinel dialuminium nickel tetraoxide ($NiAl_2O_4$) to be determined (Figure 7.11) [429]. Literature synthesised $NiAl_2O_4$ spinel is shown to bear little to no yield no information for the solid catalyst in the Raman spectra [430]. Therefore this structural assignment for AlkNiAl-Cat based on the X-ray diffractogram is convincing.

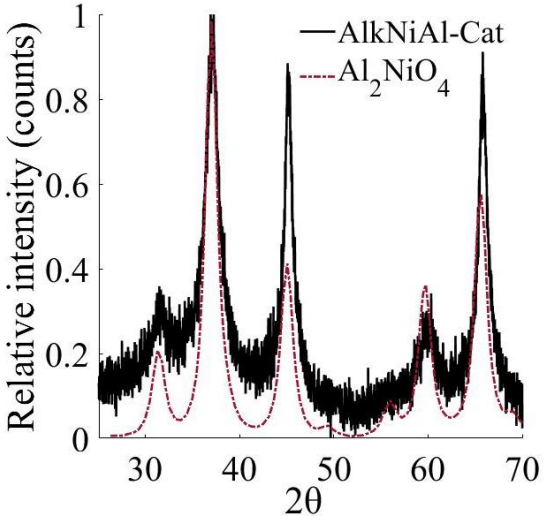

Figure 7.11 X-ray diffractogram pattern for AlkNiAl compared to Al_2NiO_4 between 25–70° obtained using a Cu tube with 1.54184 Å, scanning for 1 second at increments of 0.02°.

NiSi did not successfully form a stable gel and the solution was calcined directly to yield the final catalyst. The NiSi-Sol is as expected alcohol/water with no additional peaks (Figure 7.12) The NiSi-Cat can be assigned to NiO as was discussed previously for NiAl [426].

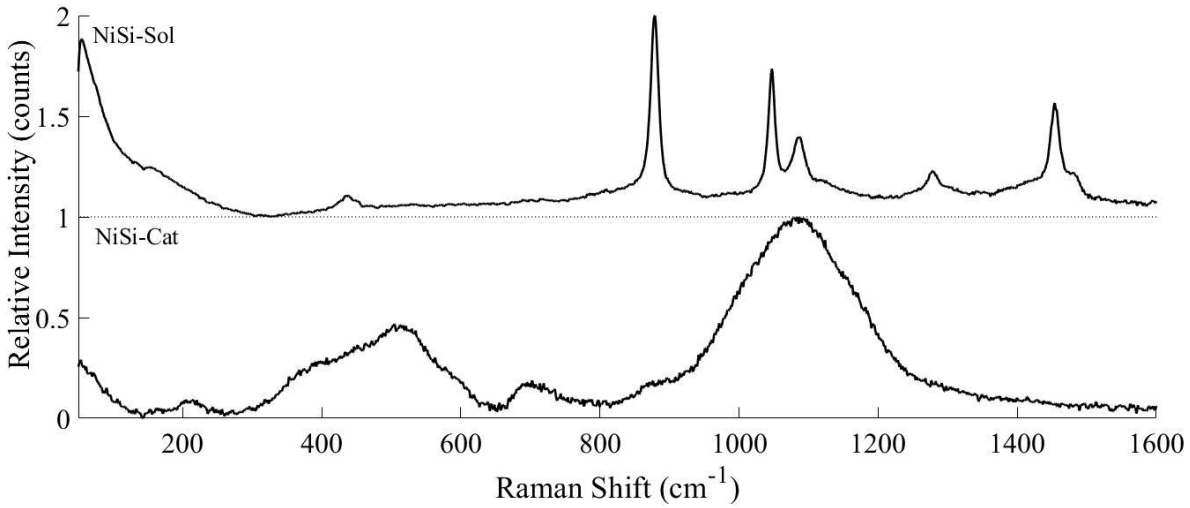

Figure 7.12 Raman spectra for NiSi sol, gel and catalyst, Raman shift 50-1600 cm^{-1}, acquired using Renishaw inVia Raman microscope 514 nm (green), Ar laser, 12 mW.

XRD confirms that NiO is the dominant crystalline phase present (Figure 7.13) [427]. Silica presence in the X-ray diffractogram is hinted at with the rising slope towards the lower end of the 2θ, this would lead up to the broad peak at 22° for SiO_2 [425]. SiO_2 is confirmed by SEM/EDS analysis (Appendix 7).

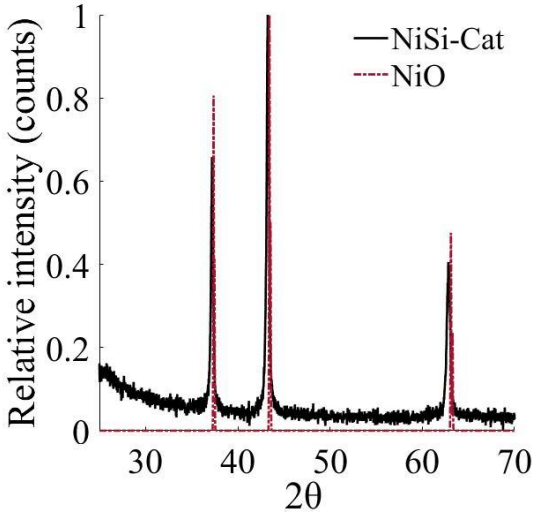

Figure 7.13 X-ray diffractogram pattern for NiSi to RRUFF spectroscopic references for NiO between 25– 70° obtained using a Cu tube with 1.54184 Å, scanning for 1 second at increments of 0.02°.

7.1.3. Vanadium Sol-Gel Catalysts

ViAl-Sol and gel both contain a significant amount of baseline drift at the lower wavenumbers, this is attributed to fluorescence within the sample (Figure 7.14) [431]. Every peak in the VAl-Cat Raman spectra corresponds to V_2O_5 [432]. VAl-Gel & VAl-Sol both contain a peak

at 984 cm^{-1} which corresponds to sulphate (SO_4^{2-}) stretching [433].

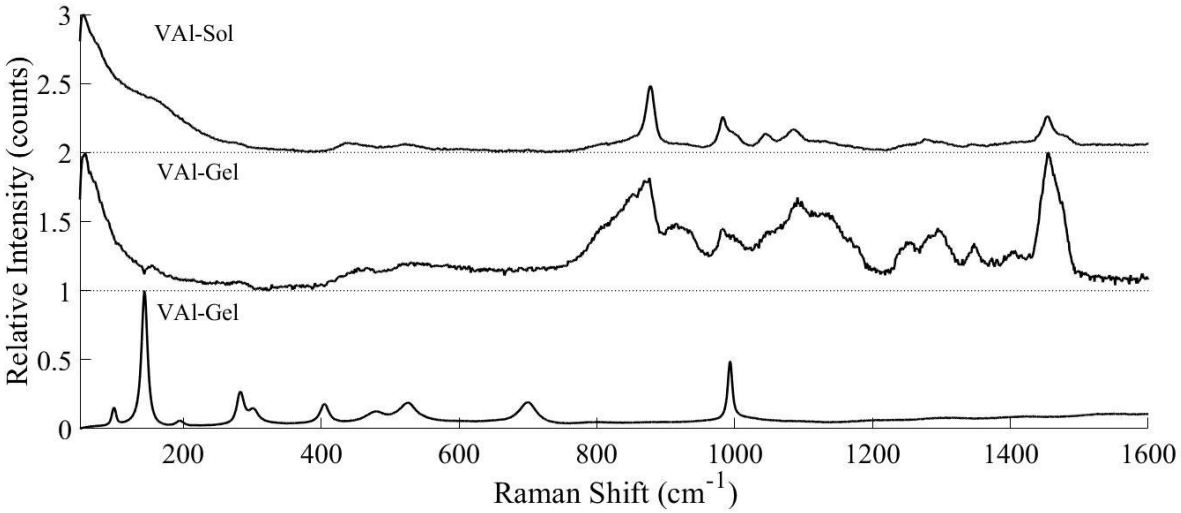

Figure 7.14 Raman spectra for VAl sol, gel and catalyst, Raman shift 50-1600 cm^{-1}, acquired using Renishaw inVia Raman microscope 514 nm (green), Ar laser, 12 mW.

The X-ray diffractogram of the VAl-Cat contains a myriad of different peaks and is not easily assigned to any oxidation state (Figure 7.15). This is likely because the vanadium-oxygen system has a large number of non-stoichiometric mixed-valence phases [434]. These different polymorphic structures produce different crystal structures and therefore complicate analysis with XRD.

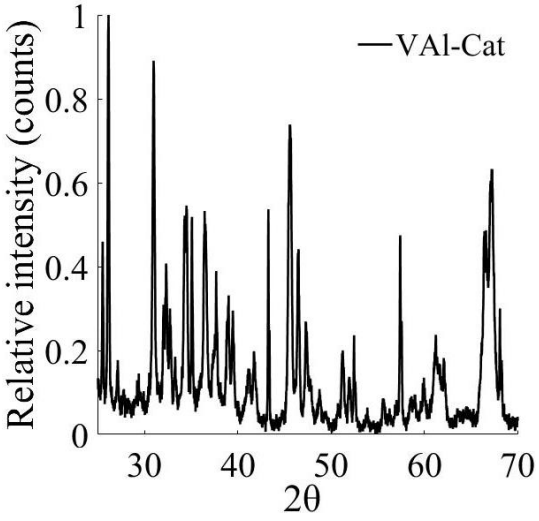

Figure 7.15 X-ray diffractogram pattern for VAl between 25– 70° obtained using a Cu tube with 1.54184 Å, scanning for 1 second at increments of 0.02°.

AlkVAl-Sol Raman spectra are as expected based on previous alkoxide solution data, showing no new peaks. AlkVAl-Gel displays a wavy baseline with raised intensity. This is attributed to fluorescence within the sample. AlkVAl-Cat contains broad peaks which cannot be defined as vanadium or alumina providing no useful characterisation of the catalyst. The diffractogram of

VAl-Cat was highly complex due to the presence of multiple oxidation states of and hence XRD analysis reveals minimum insights for this material. Therefore, it is recommended to find alternatives to XRD analysis to characterise the vanadium supported on alumina catalyst produced using this method. VSi-Sol, shows only peaks for ethanol and water in addition to those previously assigned to SO_4^{2-} stretching [280]. The VSi-Gel spectra are again disrupted by fluorescence within the sample which completely obscures the organic peaks for pluronic P123. VSi-Cat shows all of the bands associated with V_2O_5 as was seen with Val-Cat [432].

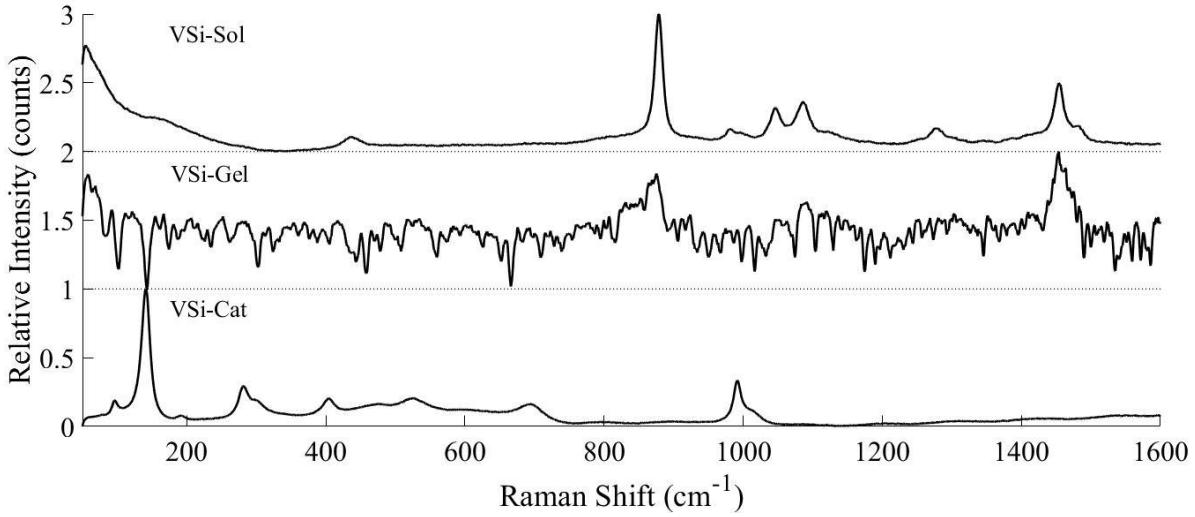

Figure 7.16 Raman spectra for VSi sol, gel and catalyst, Raman shift 50-1600 cm^{-1}, acquired using Renishaw inVia Raman microscope 514 nm (green), Ar laser, 12 mW.

XRD analysis of VSi-Cat shows evidence of both silica and V_2O_5 [435]. A broader range and longer scanning time would likely be adequate to analyse the structure of this solid catalyst.

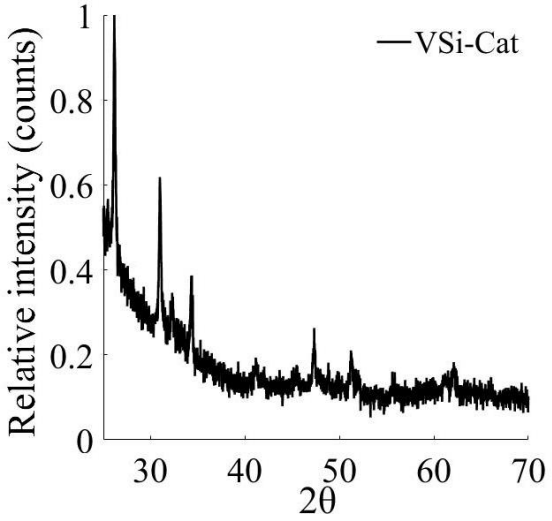

Figure 7.17 X-ray diffractogram pattern for VSi 25– 70° obtained using a Cu tube with 1.54184 Å, scanning for 1 second at increments of 0.02°.

7.1.4. Molybdenum Sol-Gel Catalysts

MoAl-Sol is a dark solution, because of this most of the signal is absorbed and optical efficiency is greatly reduced (Figure 7.18). The Raman analysis of dark samples is also problematic because of the large heating that the Raman laser provides to these samples. MoAl-Gel contains only peaks associated with pluronic P123. MoAl-Cat has peaks attributed to the presence of MoO_3 bands at 1000 cm^{-1} and 820 cm^{-1} which are assigned to Mo=O and Mo-O-Mo stretching respectively [436].

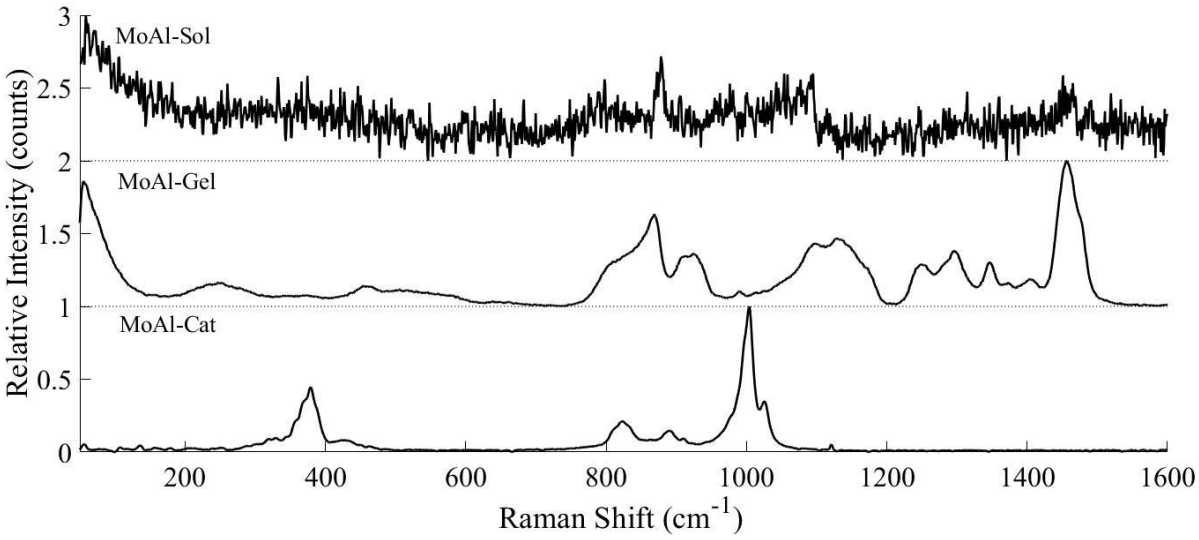

Figure 7.18 Raman spectra for MoAl sol, gel and catalyst, Raman shift 50-1600 cm^{-1}, acquired using Renishaw inVia Raman microscope 514 nm (green), Ar laser, 12 mW.

XRD analysis of the solid catalyst can attribute some of the peaks to MoO_3 however many other peaks remain unassigned, this is seen within the literature for MoO_3 [437] (Figure 7.19).

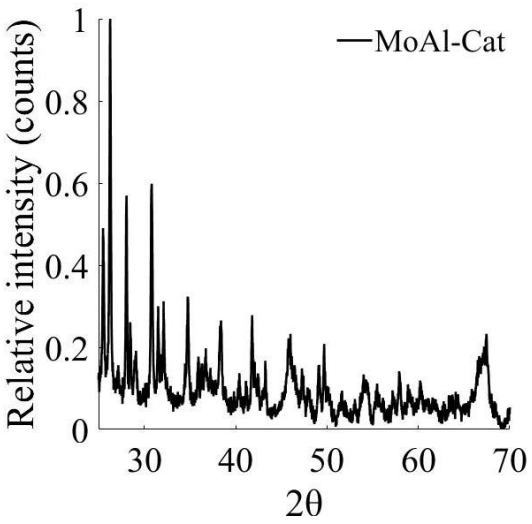

Figure 7.19 X-ray diffractogram pattern for MoAl to RRUFF spectroscopic references for MoO_3 between 25– 70° obtained using a Cu tube with 1.54184 Å, scanning for 1 second at increments of 0.02°.

AlkMoAl-Sol, looks as expected for alkoxide solution Raman spectra (Figure 7.20). AlkMoAl-Gel has additional peaks at 960 and 984 cm^{-1}, these are attributed to Mo=O stretching in $Mo^{VI}O_2Cl_2$ and $MoOCl_5$ respectively [438]. Arising from the use of molybdenum chloride in the precursor solution. AlkMoAl-Cat has a raised baseline absorbance with a few broad peaks which cannot be attributed to either molybdenum or aluminium oxide presence. The X-ray diffractogram did not aid identification of the solid catalyst showing a similar myriad of peaks as was displayed in MoAl.

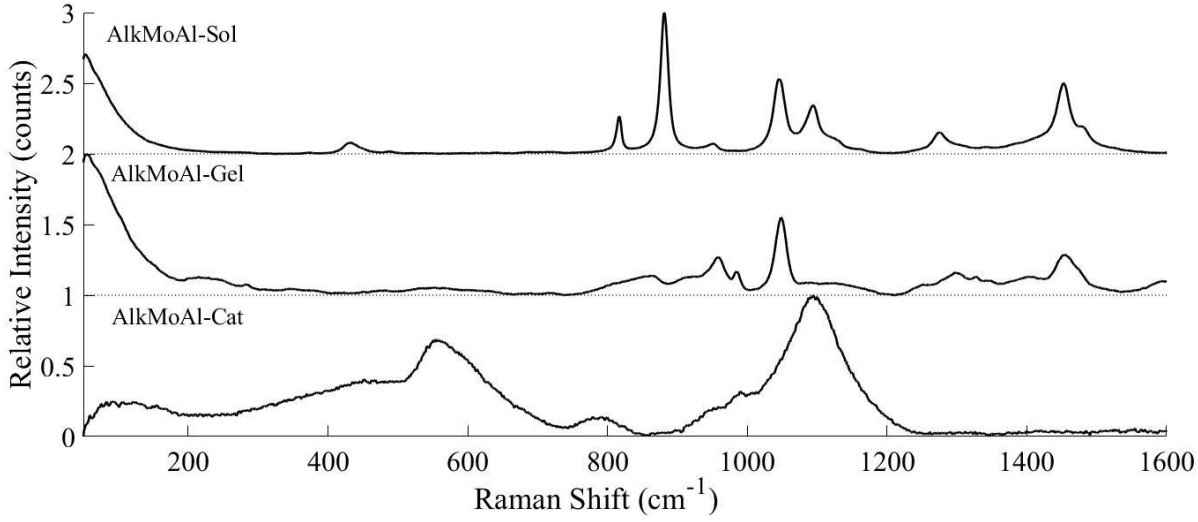

Figure 7.20 Raman spectra for AlkMoAl sol, gel and catalyst, Raman shift 50-1600 cm^{-1}, acquired using Renishaw inVia Raman microscope 514 nm (green), Ar laser, 12 mW.

MoSi-Sol displays the same issue as MoAl-Sol, the dark solution is absorbing too much of the Raman laser which is lowering the optical efficiency (Figure 7.21). Despite the noise the

MoSi-Gel can still be identified as only pluronic P123. MoSi-Cat is dominated by a sharp peak at 818 cm^{-1} which can be assigned to Mo-O-Mo in MoO_3. The increase in this peak has been observed previously in MoSi catalysts and is attributed to an increase in more "free" MoO_3 [439]. This shows there is low interaction between the silica support and MoO_3. XRD analysis showed only peaks for MoO_3 with no evidence of SiO_2 (Figure 7.22) [437].

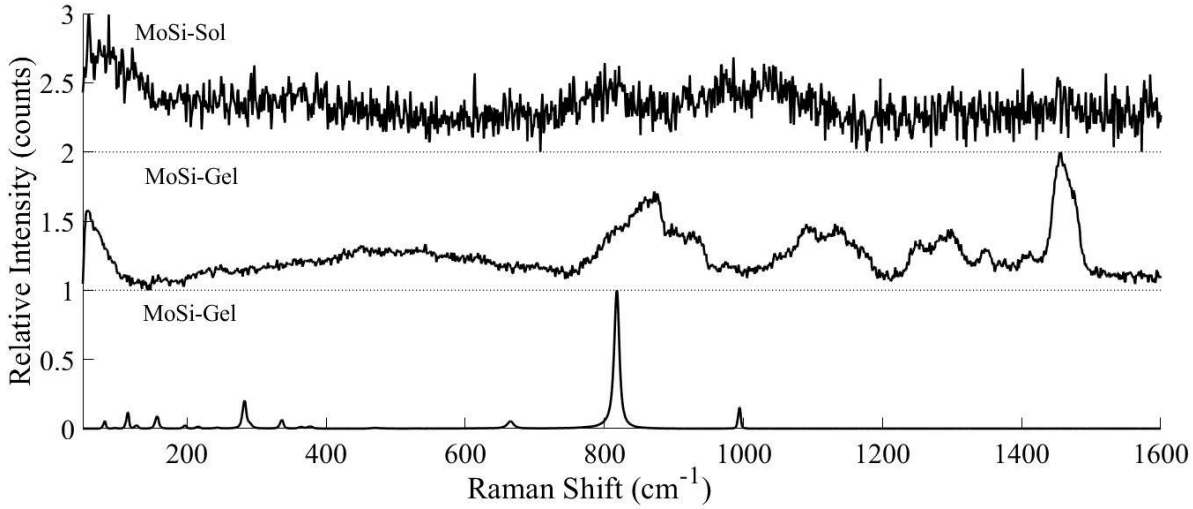

Figure 7.21 Raman spectra for MoSi sol, gel and catalyst, Raman shift 50-1600 cm^{-1}, acquired using Renishaw inVia Raman microscope 514 nm (green), Ar laser, 12 mW.

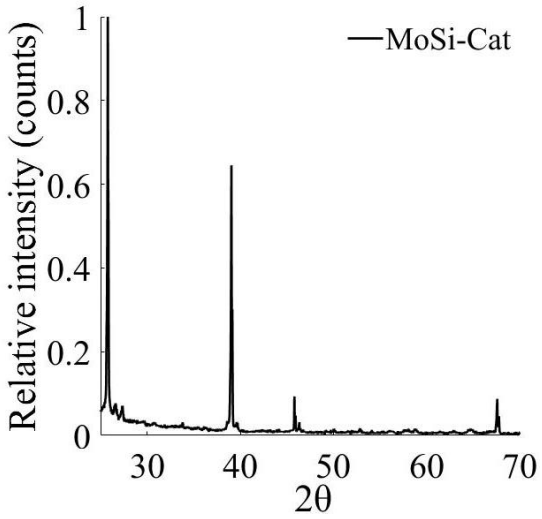

Figure 7.22 X-ray diffractogram pattern for MoSi between 25– 70° obtained using a Cu tube with 1.54184 Å, scanning for 1 second at increments of 0.02°.

7.2. Optical Trapping of Sol-Gel Droplets Combined with Raman Spectroscopy

Optical trapping is a technique invented and developed by Dr Arthur Ashkin in 1986 [440]. The objective of optical trapping is to constrain liquid or solid particles in place with the use

of focussed light (lasers). The laser is controlled by various focussing lenses and mirrors, lenses are used to concentrate the light into a focal point which can trap sizes between 10 nm and 10s of µm [38]. Laser position and intensity is measured during trapping, for example with a quadrant photodetector, a basic optical trapping set-up is shown in Figure 7.23. The physical trapping of the droplet is achieved by balancing the radiation pressure imparted by the two opposing lasers, effectively levitating the droplet. Radiation pressure is caused by the transfer of momentum from photons scattered on the droplet surface. There are a number of conditions that must be met to achieve optical trapping; (1) the droplet has a larger refractive index than the surrounding gas, (2) the scattered light is evenly distributed, (3) gravitational force acting upon the droplet is low enough to be offset by the radiation pressure. Optical trapping has proven to be an exceptionally valuable technique to probe reaction dynamics in many different fields. It has been used to study molecular motors, the physics of colloidal systems, and biopolymers [441]. A description of the optical trapping set-up used for the following experiments is given in Sections 3.1.3 & 3.2.6.

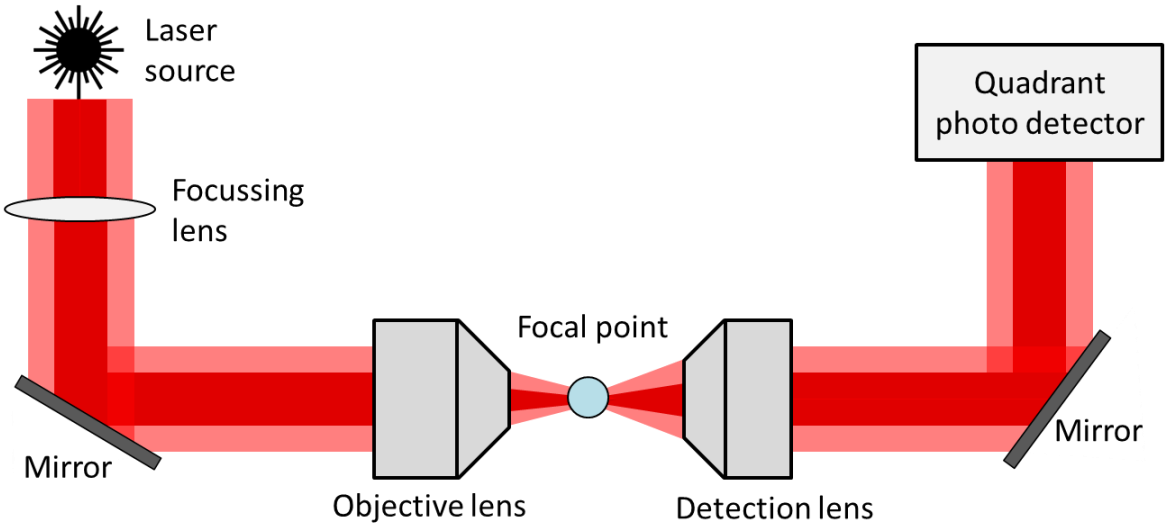

Figure 7.23 Rudimentary schematic for an optical trapping system.

7.2.1. Optical Trapping Screening Experiments

Initial screening experiments were required to observe which of the catalyst precursor solutions synthesised in Section 7.1 (1) could be trapped in the optical tweezers for a meaningful period of time, (2) had large enough peaks in the Raman spectra to observe organic transformations. Of all precursor solutions investigated the AlkNiAl system was the most stable and had the richest Raman spectra, therefore this system was fully investigated (Sections 7.2.2 & 7.2.3 & 7.2.4). The initial trapping periods without optimisation, observations in the Raman spectra

and challenges associated with the other precursor solutions is given in Table 7.3. Aluminum chloride based precursor solutions were the most unstable in the trap and could not be held for long enough to study with Raman spectroscopy. Silica based precursor solutions were not stable after exposure to the Raman laser, associated with fluorescence and the precipitation of metals. Of the alkoxide based precursor solutions only the nickel contained enough peaks in the Raman spectra to allow for investigation.

Table 7.3 Initial trapping period and Raman spectra observations for the precursor catalyst solutions demonstrated in Section 7.1.

Reference	Initial Trapping Period (min)	Raman Spectra	Other Challenges
NiAl	2	N/A	
CoAl	2	N/A	
MoAl	0.5	N/A	
VAl	N/A	N/A	
NiSi	5	NiO related peaks	Suggested precipitation of metal oxides
CoSi	N/A	N/A	
MoSi	9	Not stable under Raman laser	
VSi	8	Not stable under Raman laser	
ALK-NiAl	6	Ethanol/P123 and Ni-NO_3/Al-NO_3 associated peaks	
ALK-CoAl	2	Minimal/no peaks	
ALK-MoAl	7	Weak fluorescence	Acted as a cavity
ALK-VAl	N/A	N/A	Trapped out of plane

7.2.2. Isothermal Aerosols

The effect of each component within the AlkNiAl precursor solution on the trapping period and Raman spectra was interrogated individually. In total four different precursor solutions were trapped for investigation in the isothermal optical trapping cell; ethanol and pluronic P123 (EP), ethanol, pluronic P123, and nitric acid (EPN), ethanol, pluronic P123, nitric acid, and aluminium isopropoxide (EPNA), and the full precursor solution with nickel nitrate hexahydrate (EPNAN). For reference see Table 7.4. In this table water (H_2O) is not added as a separate component but is present in both nitric acid (HNO_3) and nickel nitrate hexahydrate ($Ni(NO_3)_2 \cdot 6H_2O$) solutions. However, the H_2O content in all droplet systems is sufficiently low that no spectral bands associated with it are observed. The estimated water content (v/v%) of the precursor solutions for EP, EPN, EPNA, EPNAN are 2%, 3.4%, 3.2%, and 3.9%, respectively. Raman investigations of ethanol/water mixtures show that the O-H bending vibration (~1630 cm^{-1}) is at insignificant intensity in H_2O concentrations below ~60% v/v [442]. As discussed in Chapter 4 water can influence the local structure and vibrational bands of other molecules *via* hydrogen bonding.

Table 7.4 Composition of the droplets investigated in the isothermal and investigated with Raman spectroscopy. EP (ethanol, pluronic P123), EPN (ethanol, pluronic P123, nitric acid), EPNA (ethanol, pluronic P123, nitric acid, aluminium alkoxide), EPNAN (ethanol, pluronic P123, nitric acid, aluminium alkoxide, nickel nitrate).

Reference	Component					
	Ethanol (C_2H_5OH)	Water (H_2O)	Triblock Pluronic (P123)	Nitric Acid (HNO_3)	Aluminium Isopropoxide (Al-iPr)	Nickel Nitrate ($Ni(NO_3)_2$)
EP	Y		Y			
EPN	Y	Y	Y	Y		
EPNA	Y	Y	Y	Y	Y	
EPNAN	Y	Y	Y	Y	Y	Y

In all trapped droplets Raman spectra whispering gallery modes (WGMs) were observed, this is indicative of sphere formation (Figure 7.24) [443]. WGMs are caused by inelastic scattering of light in the optical cavity of the spherical droplets and can be understood by Mie scattering theory [444]. Adaptive baseline removal with data processing tool Spectragryph (http://spectroscopy.ninja) was used to minimise the effect that WGMs had on the Raman spectra. The advantage of WGMs is that they allow for estimation of the size and refractive index of the trapped droplets, this is explored in Section 7.2.2.3.

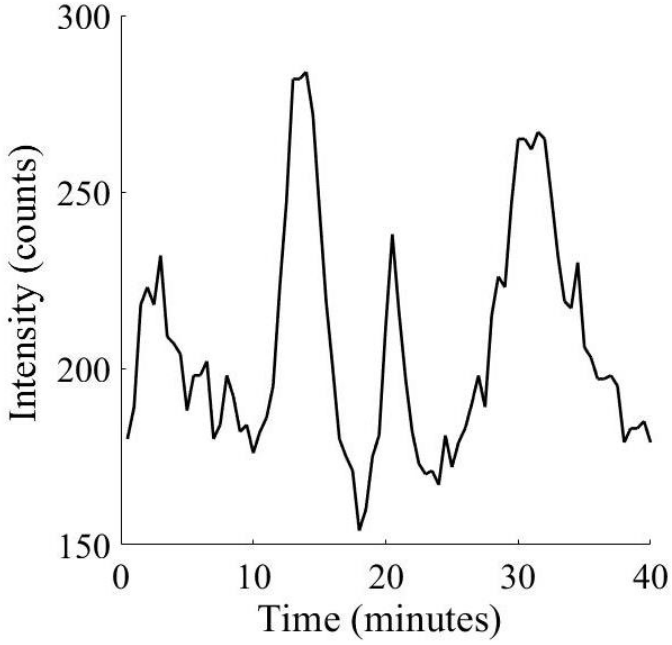

Figure 7.24 Variation in baseline (2500 cm^{-1}) intensity over time demonstrating the presence of whispering gallery modes (WGM) in the acquired experimental spectra. (600g, centered at 1900 rel cm^{-1}, 30 secs, 2 mW.)

7.2.2.1. Transformations in Metal-Free Droplets

Raman spectra for EP and EPN are shown in Figure 7.25. The peaks present can be ascribed to C-H bending (1454 cm^{-1}) and stretching (2877, 2928 and 2974 cm^{-1}) vibrations assigned from bulk studies in Figure 7.1 & Table 7.1. A reduction in these vibrational bands is observed as the droplet is trapped over time, this is attributed to ethanol evaporation.

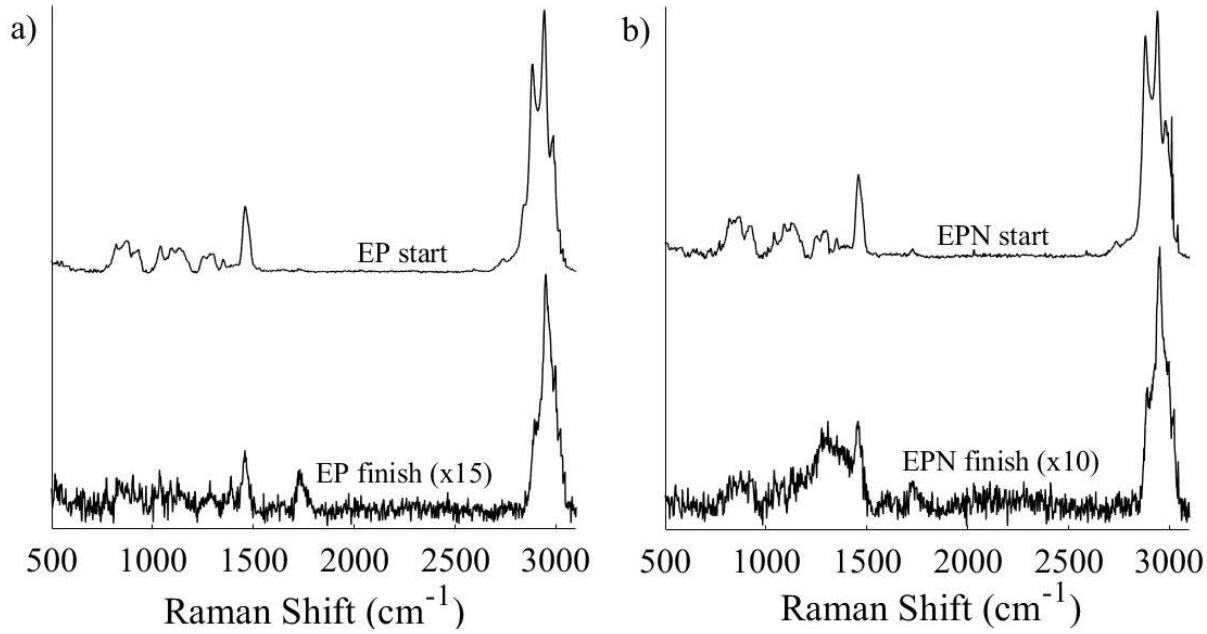

Figure 7.25 Offset Raman spectra for (a) EP and (b) EPN droplets. Top curves show the averaged first 10 scans, bottom curves show the averaged final 10 scans. Time between initial and final scans was ~250 min for EP and ~50 minutes for EPN. Note that to ease comparison the intensity of the final scans has been expanded 15-fold for EP and 10-fold for EPN. (600 groove, centred at 1900 cm^{-1}, 30 secs, 2 mW).

After optimising the optical trapping set-up for the precursor solution the EP droplet was held and monitored for changes in the Raman spectra over 4 hours after which point it was manually ejected. It should also be noted that after 4 hours the EP droplet had excellent stability and could be held with only the Raman lasers; whereas aerosolised ethanol can only be constrained in the optical trap for less than a few seconds. This can be increased to a few minutes by creating a high ethanol vapour concentration within the optical trap but measurement with Raman laser is impractical. Additionally, the presence of ethanol in the EP droplet is visible after being held for over 1 hour. This reduction in evaporation is ascribed to pluronic P123 both micelle formation and a decreased vapour pressure following Raoult's law. Micelle formation in the pluronic P123 is expected at the given concentration which is 40 times larger (10 mM) than the reported critical micelle concentration (CMC) at 25 °C [445]. Evidence of micelle formation is given by the deconvolution of the C-H stretching vibration (2800-3025 cm^{-1}) displayed in Table 7.5. The Raman band for each C-H stretch is blueshifted as a function time, this is

attributed to micelle formation in the pluronic P123 and the formation of ethanol/water mixtures and discussed in Section 4.1 [446], [447]. The decreased vapour pressure can be effectively described using Köhler theory which combines Raoult's Law with the Kelvin effect [448]. Herein, the pluronic P123 is acting as a solute to restrict the evaporation of ethanol through intermolecular interactions thereby reducing the vapour pressure of the ethanol.

Table 7.5 Spectral parameters obtained from deconvolution of the C-H stretching region (2800-3025 cm^{-1}) shown in Figure 4 and Figure 6. Indicated are: peak intensity and wavenumber for the asymmetric CH_2, symmetric CH_3, and asymmetric CH_3 stretches; and the ratio of the intensities of the symmetric CH_3: asymmetric CH_2 (I_2/I_1) and asymmetric CH_3: asymmetric CH_2 (I_3/I_1) peaks. *Data is from spectrum acquired after 120 min as the low peak intensity in the final scan prevented accurate deconvolution from that spectrum.

Reference	ν_{as} CH_2 intensity (counts)	ν_s CH_3 intensity (counts)	ν_{as} CH_3 intensity (counts)	I_2/I_1 ratio	I_3/I_1 ratio	ν_{as} CH_2 position (cm^{-1})	ν_s CH_3 position (cm^{-1})	ν_{as} CH_3 position (cm^{-1})
EP Start	2241	2744	1350	1.22	0.60	2874	2927	2971
EP Finish	65	171	97	2.62	1.48	2884	2936	2982
EPN Start	1478	1530	882	1.03	0.60	2872	2924	2972
EPN Finish	83	165	101	1.99	1.22	2881	2933	2978
EPNA Start	2754	3437	2151	1.25	0.78	2876	2925	2968
EPNA Finish*	337	544	367	1.61	1.09	2877	2928	2969
EPNAN Start	1345	1601	903	1.19	0.67	2875	2926	2969
EPNAN Finish	179	239	148	1.34	0.83	2879	2929	2970

The relative stability of EP and EPN were investigated by monitoring changes in the relative intensity of the Raman peaks with time. The reduction in peak height over time is shown for both the C-H bending (1454 cm^{-1}) and C-H stretching (2877, 2928, and 2974 cm^{-1}) vibrations (Figure 7.26). There is an initial induction period of increasing rate of decrease for all vibrations, then a maximum rate of decreasing peak height which follows exponential decay behaviour. The exact transition time for this can be identified by taking the first derivatives of the curves. At which point exponential decay analysis can be performed after the transition point following Equation 7.1 which provides the rate of decay ($1/t_1$) to allow for comparison between different droplets. The most representative data for each droplet system is aggregated and provided in Table 7.6.

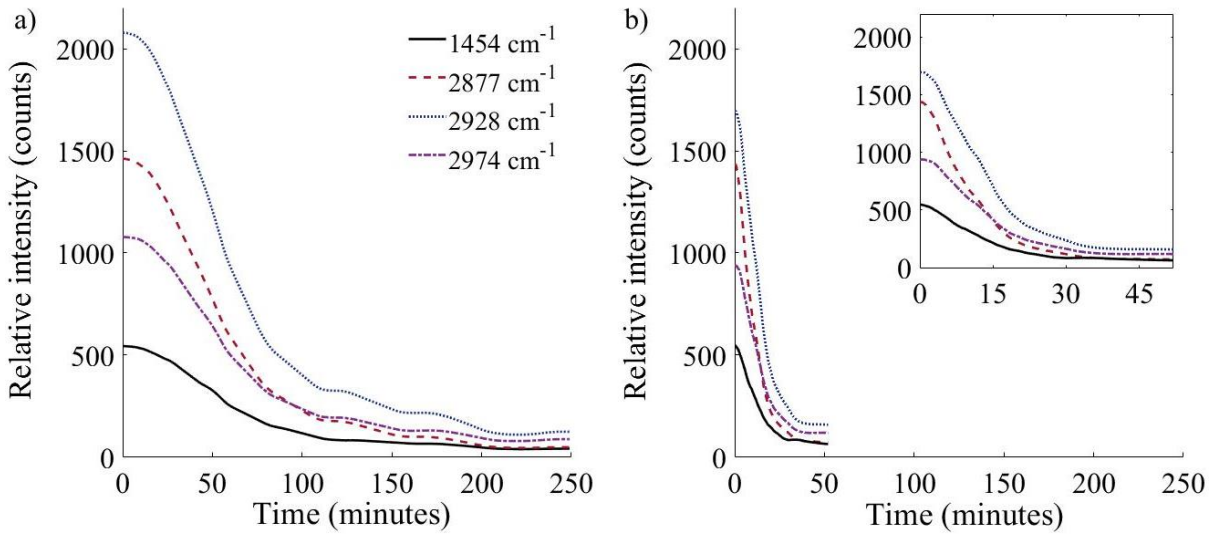

Figure 7.26 Change in Raman spectral intensity of C-H stretching and -$CH_{2/3}$ bending peak for (a) EP and (b) EPN droplets with time (600 groove, centred at 1900 cm^{-1}, 30 secs, 2 mW).

$$y = A_1 \times e^{\frac{-x}{t_1}} + y_0$$

Equation 7.1 y_0 = offset, A_1 = amplitude, t_1 = time constant, y = absorbance (counts), x = time (minutes). From this, the rates of decay ($1/t_1$) can be determined.

Table 7.6 Values for exponential decay rate in min^{-1} calculated for each peak under different compositions.

Raman shift (cm^{-1})	EP Exp Dec (min^{-1})	EPN Exp Dec (min^{-1})	EPNA Exp Dec (min^{-1})	EPNAN Exp Dec (min^{-1})	HeEPNA Exp Dec (min^{-1})	HeEPNAN Exp Dec (min^{-1})
1048	-	-	-0.019	0.027	-0.037	0.040
1454	0.027	0.11	0.0082	0.048	-0.14	0.21
2877	0.026	0.086	0.014	0.048	-0.51	0.057
2928	0.025	0.083	0.012	0.048	-0.0074	0.083
2974	0.023	0.096	0.0087	0.048	-0.3065	0.10

EPN was less stable than EP during optical trapping and was lost due to evaporation after ~1 hour in the optical trap. Exponential decay periods are displayed for EP and EPN in Figure 7.27. EPN displayed a significantly faster rate of evaporation for ethanol compared to EP. EPN contained roughly 5 times higher (faster) rates of decay compared to EP. Specifically, C-H bending decayed at 0.11 min^{-1} for EPN and at 0.027 min^{-1} for EP and CH_3 symmetric stretching (2928 cm^{-1}) decayed at 0.086 min^{-1} and 0.025 min^{-1} for EPN and EP respectively. Therefore, the addition of nitric acid (HNO_3) is correlated with an increase in the evaporation and decrease in the droplet stability. A potential cause is that the HNO_3 is destabilising the formation of micelles by pluronic P123 which is causing an increase in isolated ethanol which can freely

evaporate. This is backed up by bulk observations of pluronic P123 and hydrochloric acid (HCl), which provides evidence that the HCl impedes micellisation [449]. This micelle retardation is caused by increased hydrogen-bonding between the ethanol and pluronic P123 because of the higher concentration of free protons in solution. Further evidence of this is shown by the reduced blueshifting observed in EPN (Table 7.5). Moreover, this observation agrees with previous assumptions that the micelle formation restricts ethanol evaporation and increases droplet stability.

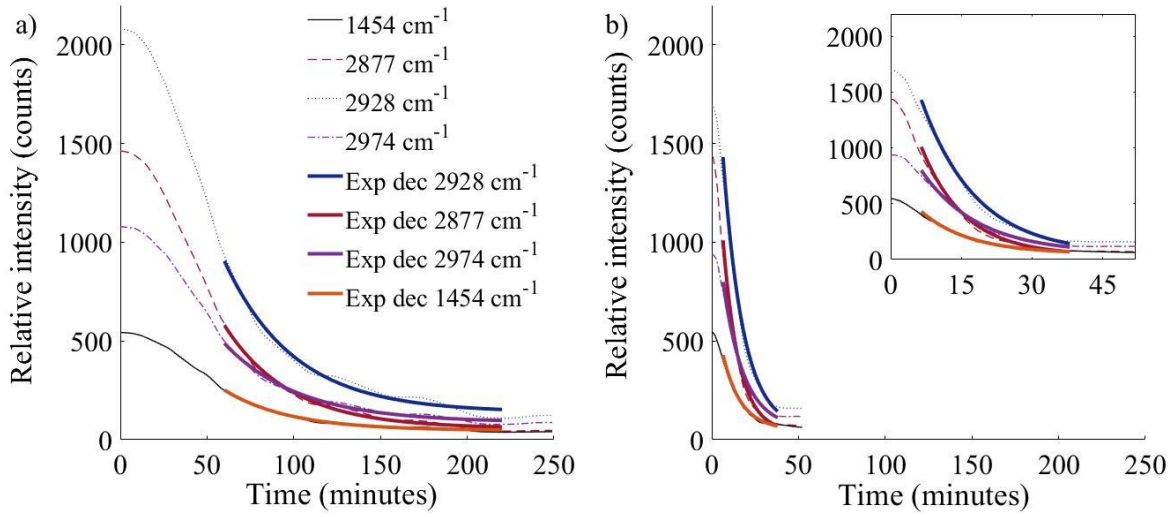

Figure 7.27 Exponential decay fittings for the change in Raman spectral intensity of C-H stretching and -$CH_{2/3}$ bending peak for (a) EP and (b) EPN droplets with time (600g, centered at 1900 rel cm^{-1}, 30 secs, 2 mW).

7.2.2.2. Transformations in Metal-Containing Droplets

The inclusion of aluminum isopropoxide (Al-iPr) and nickel nitrate ($Ni(NO_3)_2$) into the precursor solution produced a new peak in the Raman spectra at 1048 cm^{-1} (Figure 7.28). This peak is observed in bulk AlkNiAl gel and sol in Section 7.1.2 (Figure 7.10) and is attributed to Al-NO_3 and Ni-NO_3 stretching vibrations [450]. EPNA demonstrated high stability in the optical trap, it was trapped for over 4 hours and had to be manually removed due to experimental time constraints, additionally trapping with the Raman laser was possible as discussed with the EP droplet. Whilst EPNAN had reduced stability in the optical trap and could only be constrained for between 50-70 minutes, in both of the successfully trapped droplets with the second in Figure 7.29. As discussed in the previous section the C-H bending (1454 cm^{-1}) and C-H stretching (2877, 2928, and 2974 cm^{-1}) peaks are attributed to ethanol and therefore can be used to measure the amount of evaporation within the trapped droplet. While the -NO_3 stretching peak is used to investigate the bonding and reactivity of the aluminium and

nickel ions in the droplet which occur during sol-gel processes.

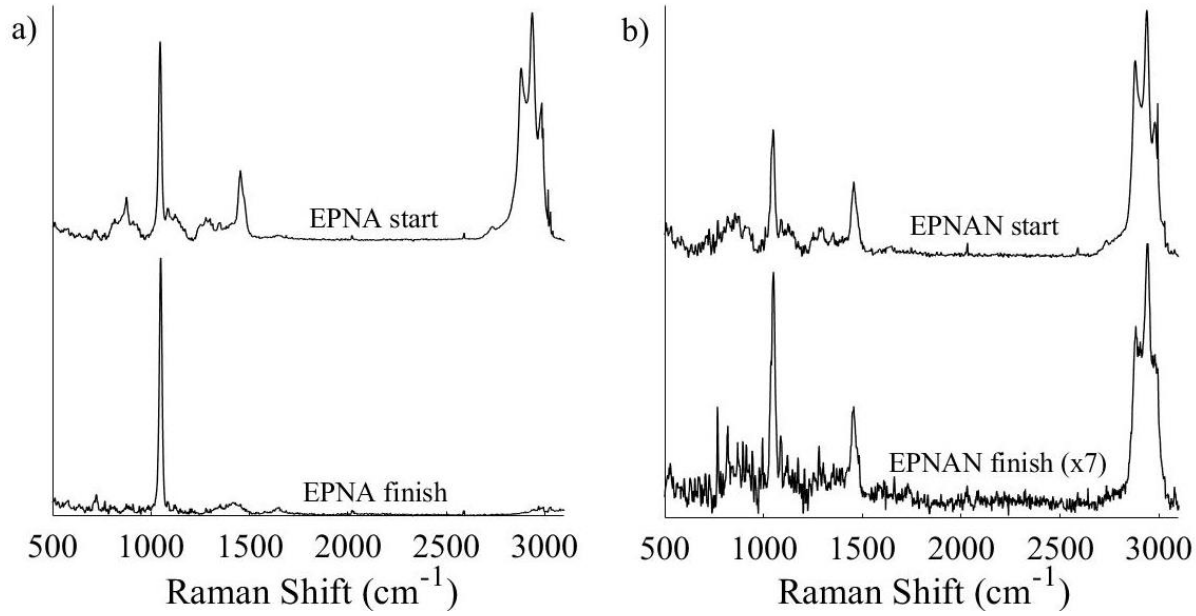

Figure 7.28 Offset Raman spectra for (a) EPNA and (b) EPNAN. Top curves show the averaged first 10 scans, bottom curves show the averaged final 10 scans. Time between initial and final scans was ~240 min for EPNA and ~50 minutes for EPNAN. Note that to ease comparison the intensity of the final scans for EPNAN (only) has been expanded 7-fold. (600 groove, centred at 1900 cm^{-1}, 30 secs, 2 mW).

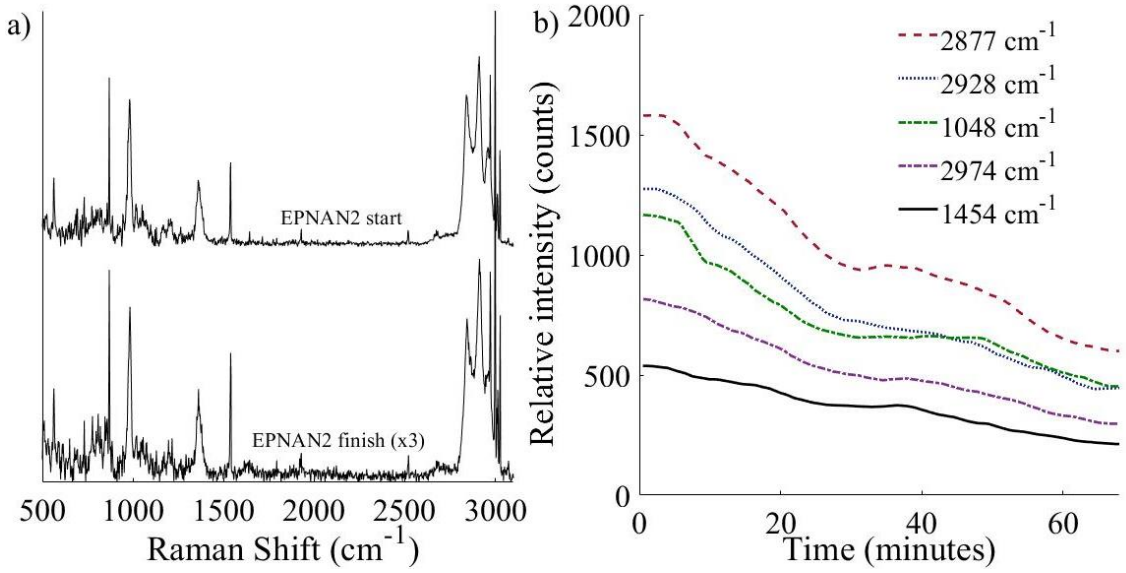

Figure 7.29 (a) Offset Raman spectra for second EPNAN droplet. Top curves show the first scan, bottom curves show the final 10 scans. Time between initial and final scans was ~65 minutes. Note that to ease comparison the intensity of the final scans for EPNAN has been expanded 3-fold. (b) Raman absorbance of significant peaks for EPNAN fitted against time (600 groove, centred at 1900 cm^{-1}, 30 secs, 2 mW).

A slow reduction in the ethanol related bands is observed for EPNA and a faster decrease is observed for EPNAN (Figure 7.30). Therefore, ethanol evaporation is faster for EPNAN and

slower for EPNA. This can be quantified by calculating the rates of decay as discussed for EP and EPN (Section 7.2.2.1), the data for EPNA and EPNAN is visualised in Figure 7.31. Decay rates for ethanol related peaks in EPNA are 0.0082 (1454 cm^{-1}), 0.014 (2877 cm^{-1}), 0.012 (2928 cm^{-1}), and 0.0087 min^{-1} (2974 cm^{-1}). This is 3-6 times slower than the rate of decay for ethanol related peaks in EPNAN which is 0.048 min^{-1} for all C-H related peaks and 2-3 times faster than for EP. Furthermore, there is a larger discrepancy in EPNA in the rate of decay for the different C-H bending and stretching peaks than for EP or EPNAN. This enhanced stability and the varied decay rates observed in EPNA is attributed to the formation of Al-iPr stabilised micelle structures which limit evaporation and change the bonding environment in the trapped droplet. It is suggested that the Al-iPr is intermolecularly bonded to the hydrophilic head of the pluronic P123 to create a macro-structured solution; this phenomenon has been demonstrated by ethylammonium nitrate promoted micellisation in pluronic P123 [445]. Showing that the intensity of C-H bending a C-H stretching peaks is influenced by this intermolecular interaction with Al-iPr creating the observed variation in decay rates. Additionally, there is an increase in the Al-NO_3 (1048 cm^{-1}) stretching peak in the first 2 hours of trapping, the source of this is explained in Section 7.2.4.

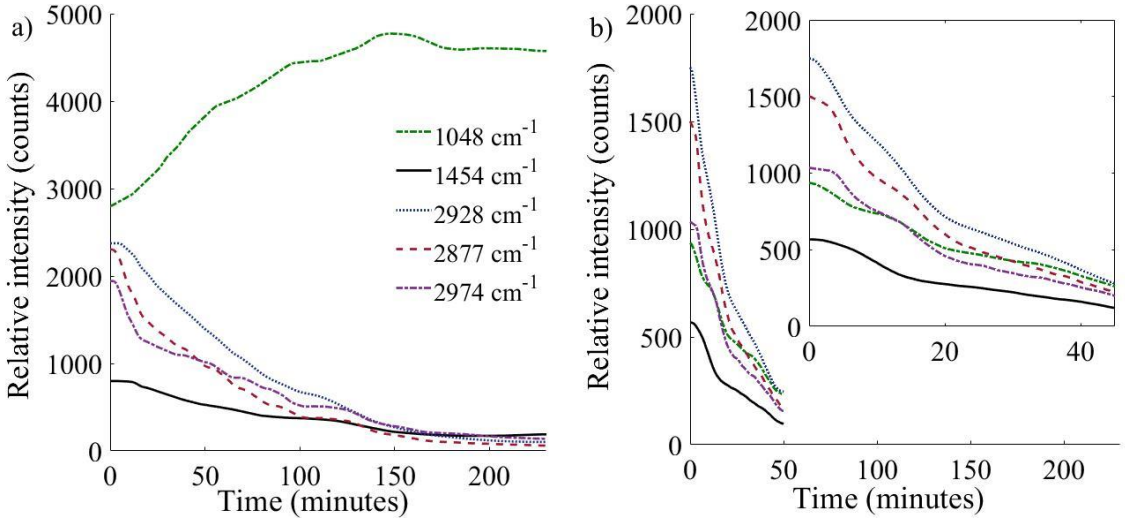

Figure 7.30 Raman absorbance of significant peaks for (a) EPNA and (b) EPNAN fitted against time (600 groove, centred at 1900 cm^{-1}, 30 secs, 2 mW).

The evaporation rate of ethanol in EPNAN is relatively fast, with ethanol related decay rates 2× slower than EPN (the fastest evaporation droplet) and 2× faster than EP. Additionally, the -NO_3 stretching peak shows decay at 0.027 min^{-1} which is slower than evaporation of ethanol in EPNAN but has the opposite behaviour observed in EPNA. The reduction in the -NO_3 stretching peak observed is attributed to chemical transformations and cross linking (gelation) reactions within the droplet that are established to occur in bulk solutions. Therefore,

addition of $Ni(NO_3)_2$ to the precursor solution produces visible cross-linking reactions over the trapping period. Further mechanistic insights are discussed in Section 7.2.4. In addition to this, bulk synthesis of AlkNiAl presented in Section 7.1.2 presents more evidence that $Ni(NO_3)_2$ has a significant effect on sol-gel reactivity. When the precursor solutions for EPNA and EPNAN were stored in a sealed container at room temperature they did not undergo significant gelation reactions. However when exposed to air and allowed passive evaporation the EPNA took over a week to produce a more viscous solution whilst the EPNAN formed an immobile gel after only 30 minutes. This follows literature synthesis procedures for EPNA solutions which involve aging the solution for long timescales (>1 week) in air at 40 °C [451]–[453]. This confirms the increased reactivity observed in the trapped EPNAN compared to EPNA and suggests an alternative reaction pathway.

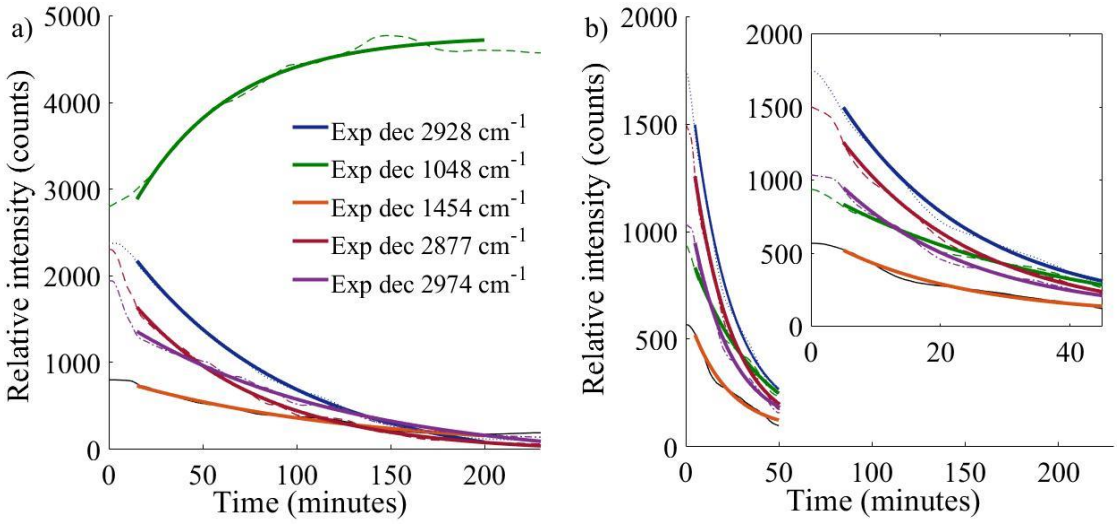

Figure 7.31 Exponential decay fittings for the Raman absorbance of significant peaks for (a) EPNA and (b) EPNAN fitted against time (600g, centered at 1900 rel cm^{-1}, 30 secs, 2 mW).

7.2.2.3. Droplet Size

The presence of WGMs (Section 7.2.2) allows for an estimation of trapped droplet size over time using Mie theory. This is important as aerosol droplet size is directly correlated with catalyst particle size for AASG processes and catalyst particle size can affect the activity, selectivity, and stability of the catalyst [454], [455]. Furthermore, Mie theory presents the most suitable calculation of droplet size during optical trapping because the size range typically 0.01-10 μm renders them unsuitable for size determination using imaging optics (for which they are too small) or using Rayleigh scattering calculations (for which they are too large) [456]. Droplet size analysis with Mie Theory was performed on the EPNA as the ideal

candidate due to its high stability. This was done by extracting Mie scattering peak positions across the spectral range and comparing this to a theoretical model for Mie scattering assuming a homogeneous sphere and an initial refractive index approximating to the original components (n = 1.430). Initially the diameter of the droplet was 2.64 μm this reduced at a rate of 0.3 μm h^{-1} down to 1.92 μm after 200 minutes. After this point the EPNA droplet is assumed to consist of only pluronic P123 and Al-NO_3 in an extended meso-structured droplet.

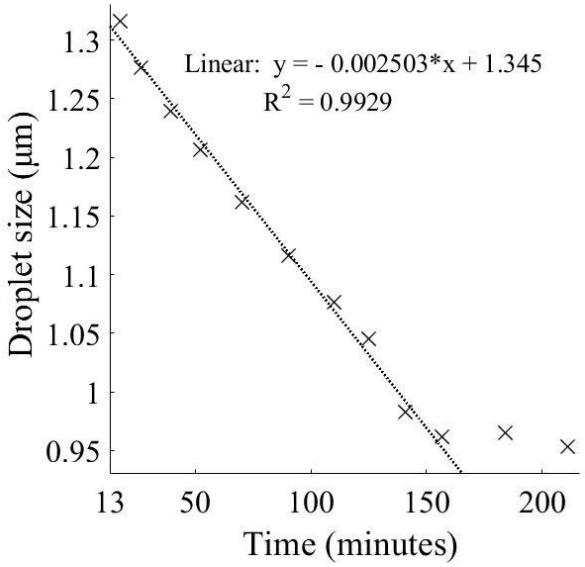

Figure 7.32 Droplet size (radius) in microns for EPNA against time in minutes.

7.2.3. Heated Aerosols

The heated optical trapping cell allowed for comparison to the early stages of AASG processes and was focussed on the EPNA and EPNAN solutions as they can be used to produce catalytic materials. These are denoted by the He- prefix indicating it is the heated droplet system as HeEPNA and HeEPNAN. The limitation of this system was the reduced trapping capacity and low maximum heating temperature at ~140 °C. Whilst some AASG synthesises apply temperatures of 100s °C, this low temperature maximum limits observations to the initial gel forming reactions in AASG synthesis. Furthermore, optical trapping becomes more difficult as liquid to gel cross-linking reactions occur due to external heating and cause morphological changes in the droplet. Therefore, studying the higher temperature gel-solid transitions in AASG processes would be highly problematic using optical tweezers due to the changes in the droplet density, shape, and size. Initial and final spectra for HeEPNA and HeEPNAN are displayed in Figure 7.33.

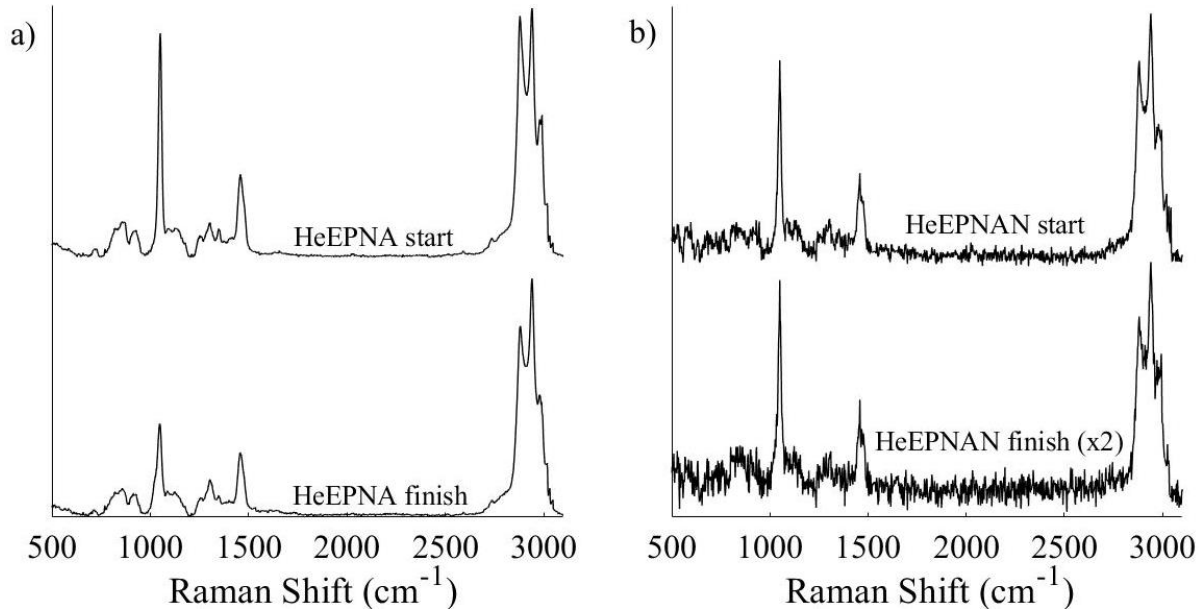

Figure 7.33 Offset Raman spectra for (a) HeEPNA and (b) HeEPNAN. Top curves show the averaged first 10 scans, bottom curves show the averaged final 10 scans. Time between initial and final scans was ~30 min for HeEPNA and ~15 minutes for HeEPNAN. Note that to ease comparison the intensity of the final scan for HeEPNAN been expanded 2-fold. (600 groove, centred at 1900 cm^{-1}, HeEPNA 30 sec, HeEPNAN 10 secs, 2 mW).

HeEPNA was heated to a maximum of 120 °C at a rate of 4 °C min^{-1} (Figure 7.34). Heating beyond this temperature caused the droplet to become unstable and was lost. Despite the elevated temperature there is only minor reduction observed in the ethanol related C-H bending and stretching peaks. This establishes that only limited evaporation is observed in the HeEPNA. However, a large decrease in the Al-NO_3 (1048 cm^{-1}) stretching was observed. Showing the opposite behaviour observed in EPNA which had an increase in the Al-NO_3 peak. The Al-NO_3 decrease in HeEPNA is observed to start after heating to 56 °C and is correlated with the retardation of ethanol evaporation. Suggesting that at this temperature there is sufficient activation energy to initiate cross-linking gelation reactions and that these reactions form a stabilised droplet that inhibits evaporation despite the raised temperature. This is considered in the mechanistic insights Section 7.2.4. The implied reactivity without evaporation of ethanol is opposite to the demonstrated evaporation driven reactivity in the bulk solutions. However, there are a few alternative reasons to explain the retarded evaporation observed in the HeEPNA. The CMC of pluronic P123 decreases at increasing temperature and therefore even a modest rise in temperature increases the strength and interconnectivity of the micelles in the EPNA droplet, hence preventing evaporation [457]. At 25 °C the CMC of pluronic P123 is 0.03 w/v%; this decreases to 0.001 w/v% at 35 °C [458]. Another potential contributor to reduced evaporation is an enhancement of the previously described meso-structured intermolecular

system between Al-iPr and pluronic P123 which prevents evaporation by an encapsulation-type mechanism [459].

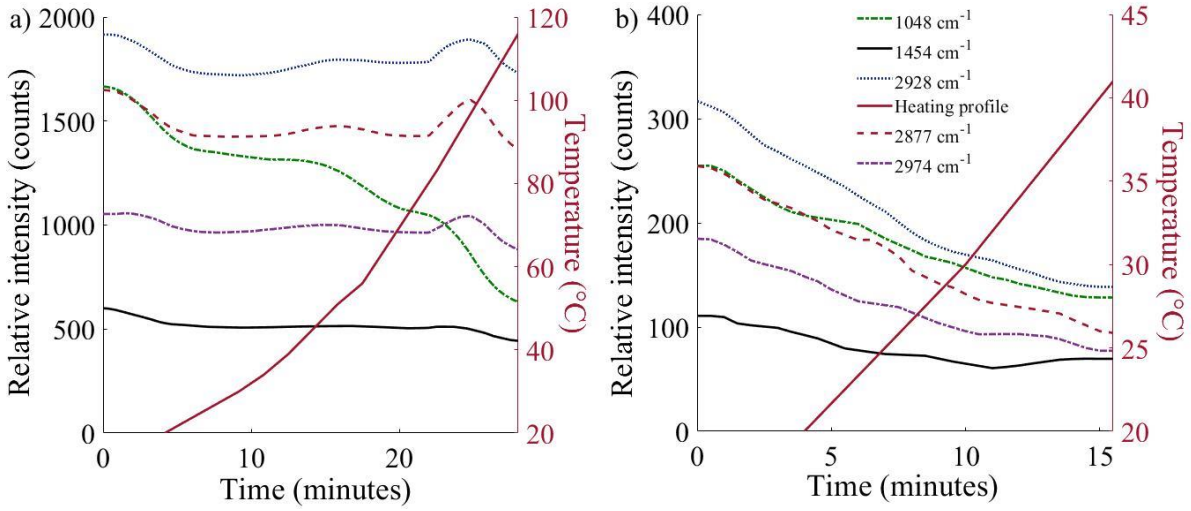

Figure 7.34 Raman spectral intensity of significant peaks for (a) HeEPNA and (b) HeEPNAN fitted against time with an additional temperature axis to display the temperature of the heated cell at that given point in time (600 groove, centred at 1900 cm^{-1}, HeEPNA 10 sec, HeEPNAN 30 sec, 2 mW). Temperature at the trapping time was determined *via* calibration of input voltage (Figure 3.5).

HeEPNAN had reduced stability compared to EPNAN and could only be held to a maximum temperature of 40 °C at a rate of 1.5 °C min^{-1}. Rates of decay for ethanol related and nitrate stretching peaks decreased at different speeds relative to one another. There is relatively a faster rate of decrease for C-H bending (1454 cm^{-1}) at 0.21 min^{-1} from 0.048 cm^{-1} for EPNAN (4× increase). Whilst the -NO_3 (1048 cm^{-1}) stretching peak has a decay rate of 0.040 min^{-1} up from 0.027 min^{-1} (~2× increase). Therefore, ethanol evaporation is increased more in HeEPNAN compared to the cross-linking gelation reaction of Al-NO_3 and Ni-NO_3. Furthermore, the retardation of evaporation at raised temperature in HeEPNA is not shown at all in HeEPNAN.

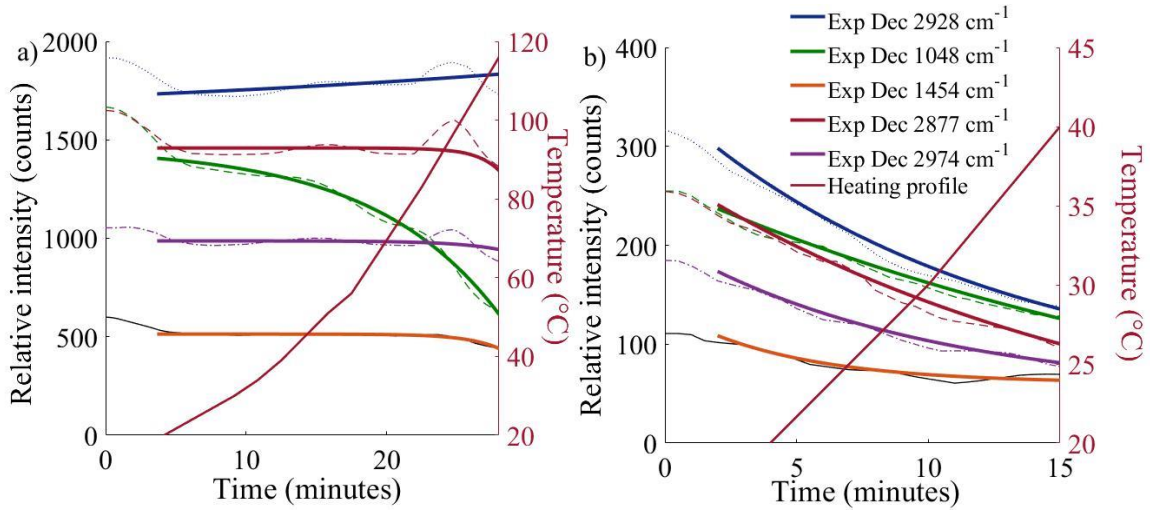

Figure 7.35 Exponential decay fitting for the Raman spectral intensity of significant peaks for (a) HeEPNA and (b) HeEPNAN fitted against time with an additional temperature axis to display the temperature of the heated cell at that given point in time 600g, centered at 1900 rel cm^{-1}, HeEPNA 10 sec, HeEPNAN 30 secs, 2 mW). Temperature at the trapping time was determined *via* calibration of input voltage (Figure 3.5)

7.2.4. Mechanistic Insights

The reaction mechanism causing gelation in AASG synthesis is assumed based on bulk synthesis observed hydrolysis and condensation reactions [307], [460], [461]. The balanced chemical equation for this in the EPNA droplet is displayed in Equation 7.2. This droplet system required heat in HeEPNA to observe evidence of gelation reactions over the trapping period. Whilst the slow reactivity in EPNA is consistent with bulk samples where gelation requires longer than a week to occur the HeEPNA suggests chemical reactivity at relatively low temperatures ~56 °C without being caused by evaporation. For hydrolysis reactions to proceed a minimum amount of water is required to initiate the reaction, as previously discussed the water content is each droplet is below detection in the Raman spectra (<4 v/v%). Hydrolysis reactions require an Al:P123:solvent:water molar ratio of 1:0.015:40.5:0.8 [451]. Still, the corresponding ratio in present work is 0.47:0.012:19:1 therefore hydrolysis reactions would be able to proceed in EPNA. However, after 2 hours in the optical trap a majority of the ethanol had evaporated in the droplet and a similar evaporation of water can be assumed. Moreover, the AASG synthesis set-up is not operated over those long timescales. Therefore, based on the reactivity observed in HeEPNA it is suggested that an alternative to the hydrolysis-polycondensation reaction is occurring. Particularly because of the presence of the Al-NO_3 band which is not accounted for in this reaction mechanism.

$$\boldsymbol{a)\ Al(OCH(CH_3)_2)_3 + 3H_2O \rightarrow Al(OH)_3 + 3HO - CH(CH_3)_2}$$

$$\boldsymbol{b)\ Al(OH)_3 + Al(OH)_3 \rightarrow (OH)_2AlOAl(OH)_2 + H_2O}$$

$$\boldsymbol{\rightarrow Al - (OAl(OH)_2)_3 + 2H_2O}$$

Equation 7.2 Balanced sol-gel reaction observed to occur in bulk aluminium alkoxide (a) hydrolysis (b) condensation reactions.

The addition of $Ni(NO_3)_2$ in EPNAN is shown to generate different chemical reactivity in the droplet by reduction in the Al-NO_3 and Ni-NO_3 associated stretch (1048 cm^{-1}). A moderate increase is observed in water content (57%) and therefore it is possible that this higher water content allows for hydrolysis reactions to occur, and reactivity follows that of bulk solutions. Herein, it is postulated that an alternative reaction mechanism is occurring within both EPNA and EPNAN. A mechanism is proposed for this in Figure 7.36. In this an initial hydrolysis reaction (a) occurs which forms aluminium hydroxide (Al-OH) following the first step observed in bulk sol-gel reactions. Al-OH then reacts with HNO_3 (b) to from Al-NO_3 in solution. This produces the peak observed for Al-NO_3 and explains its increase in EPNA. Elsewhere, this process is known from the dissolution of gibbsite ($Al(OH)_3$) in HNO_3 [462]. Further, this reaction would regenerate previously consumed water molecules, thereby facilitating further sequential (a) hydrolysis and (b) neutralisation reactions. The EPNA droplet is therefore theorised to be "stuck" at this stage with a majority of the aluminum ions converted to Al-NO_3. When activation energy is provided in HeEPNA this causes condensation reactions that are observed in bulk solutions. However, in EPNAN heat is not required to cause a decrease in the Al-NO_3 stretching and therefore initial cross linking gelation reactions. It is speculated that the presence of Ni^{2+} ions permits the disruption of the Al-NO_3 complex and the formation of a continuous Al-O-Ni-NO_3 structure *via* a rearrangement type reaction (c). Further evidence for this reactivity is given by the reduced stability of EPNAN which is ascribed to morphological changes in the droplet. Moreover, this reaction is supported by previous studies of bulk phase sol-gel synthesis of nickel aluminide (Ni_3Al) from Al-iPr, $Ni(NO_3)_2$, and HNO_3 in ethanol by Madon *et al.* [463]. The actual reaction mechanism can be determined by performing full structural analysis of the final nanostructured catalyst using electron microscopy and X-ray/neutron diffraction would elicit if the catalyst were highly ordered as Ni-Al-Ni-Al or exhibited structural and compositional heterogeneity, suggesting either the nickel induced reaction pathway, or the condensation reaction observed in bulk solutions respectively [464].

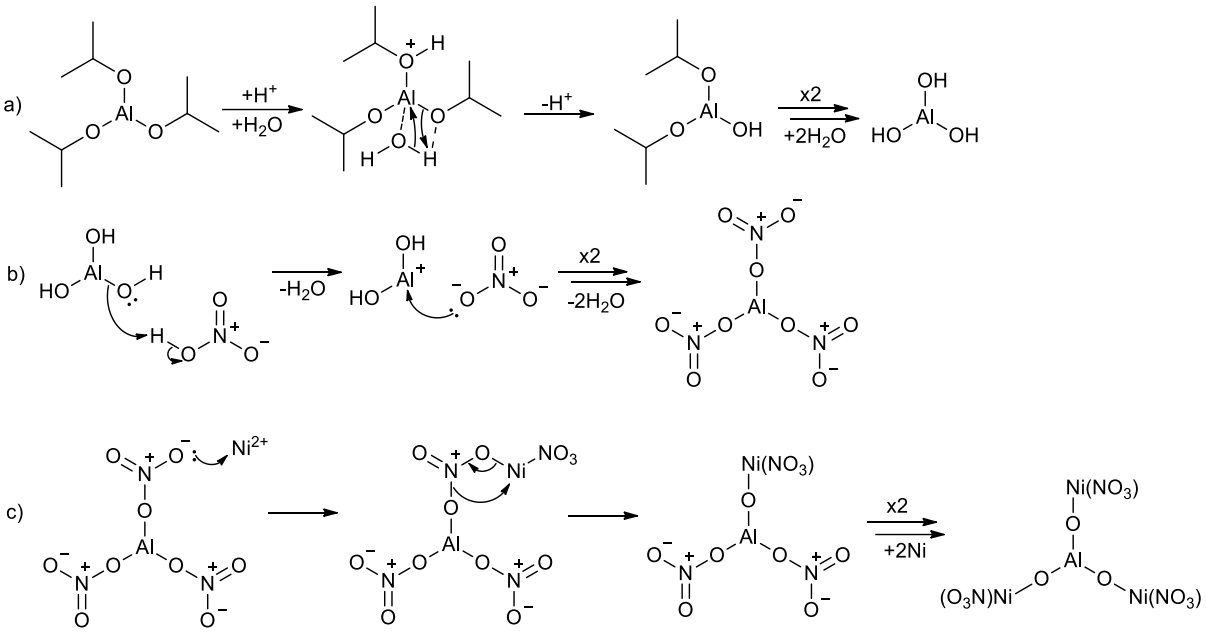

Figure 7.36 Postulated mechanism for the initial reactions in the AASG synthesis of Ni/Al_2O_3 based upon the Raman spectroscopy observations. Initial hydrolysis reaction of Al-iPr (a), followed by neutralisation reaction between HNO_3 and Al-OH (b), and a final proposed cross-linking (gelation) reaction caused by presence of the Ni^{2+} (c). Balanced chemical equation displayed in Equation 7.3.

$$\boldsymbol{a)\ Al(OCH(CH_3)_2)_3 + 3H_2O \rightarrow Al(OH)_3 + 3HO - CH(CH_3)_2}$$

$$\boldsymbol{b)\ Al(OH)_3 + 3HNO_3 \rightarrow Al(NO_3)_3 + 3H_2O}$$

$$\boldsymbol{c)\ Al(NO_3)_3 + 3Ni(NO_3)_2 6H_2O \rightarrow Al(ONiNO_3)_3 + 3NO_2}$$

Equation 7.3 Balanced chemical equation for the postulated mechanism in the EPNA and EPNAN droplets (a) hydrolysis of Al-iPr, (b) neutralisation of HNO_3, and (c) cross-linking.

7.3. Conclusions

Three different sol-gel support materials and four different metal catalysts have been investigated on a lab scale to synthesise 12 different sol-gel catalyst systems. Each of these 12 different catalysts were characterised by Raman and XRD analysis. Optical trapping combined with Raman spectroscopy has been attempted on each of these catalytic precursor solutions. Of these only 1 catalyst precursor solution was viable for Raman interrogation during optical trapping to understand reactivity during AASG synthesis. Investigation of the AlkNiAl system provided evidence that reactions within AASG synthesis do not follow those observed in bulk sol-gel synthesis. Furthermore, alternative reaction mechanisms have been proposed for the

cross-linking reactions which are supported by Raman spectroscopy as well as reactions in the literature. Additionally, the effect of each component in the AlkNiAl precursor solution has been investigated. It was found that the pluronic P123 stabilises the aerosol against ethanol evaporation postulated to be a consequence of micelle formation, while HNO_3 acts to destabilise the formed micelles. Whilst the addition of Al-iPr produces a stabilised macro structure in solution by intermolecular interactions to the hydrophilic head groups of the pluronic P123. No transitions such as gelation were observed for EPNA, however the addition of $Ni(NO_3)_2$ triggered cross-linking reactions and reduced stability in the EPNAN. Gelation reactions could be triggered within EPNA in the heated cell with sufficient activation energy supplied (~56 °C). This ability to successfully interrogate AASG syntheses and other flow tube based processes spectroscopically during reaction can therefore bring further understanding. This can in turn support the design of improved processes and the synthesis of materials with specific targeted properties such as structure or morphology.

Chapter 8 Summary and Future Directions

8.1. Summary

As discussed in the abstract the objective of this research was to investigate novel synthesis methods and environments. This is broken down into three different areas: hydrothermal carbonisation, alcohol/water mixtures, and aerosol-assisted sol-gel synthesis. The thesis addresses important gaps within the literature in these areas. This was achieved through utilising specialised analytical instrumentation for *operando* measurements; optical trapping equipment and an attenuated total reflectance high temperature reaction cell. Following acquisition, data analysis methods were used to understand and interpret spectroscopic data. Finally, these observations were compared to and corroborated with exemplary laboratory based bulk synthesis and hydrothermal processing procedures. Including the hydrothermal carbonisation of two novel biomasses and the synthesis of twelve sol-gel catalysts. Therefore, this research has demonstrated the viability of hydrothermal carbonisation as a more sustainable synthesis method to produce carbonaceous material. Furthermore, the importance of understanding the synthesis mechanisms and conditions using analytical techniques such as FT-IR has been demonstrated. Through understanding how different components affect the reactivity a more tuneable product can be produced; this allow for more efficient and therefore less environmentally damaging processes to be designed.

8.1.1. A Case Study on the HTC of Dried Bread Waste and Avocado Seeds

To the authors knowledge the HTC of both bread waste (BW) and avocado seeds (AS) is reported for the first time. Both feedstocks are a source of waste which is currently sent to landfill, hence sustainable valorisation of them must be accomplished to reduce landfilling practices and provide sustainably sourced materials to replace those produced by non-renewable processes. In this vein HTC has shown promise for both of these waste feedstocks to produce renewable solid fuel or high value carbon materials from BW and AS respectively. The hydrochar synthesised from BW displayed lower HHV, higher volatile matter, lower fixed carbon content, and more surface functionality when helium was used as the pressurising gas compared to carbon dioxide. This demonstrates that carbon dioxide, when used to pressurise the HTC reaction, acts as a homogeneous acid during processing. The effect of this is more pronounced at lower operating temperatures because higher temperatures reduce the need for catalysts during HTC. The use of carbon dioxide is beneficial in HTC-based synthesis of renewable solid fuel because it reduces the thermal requirements of HTC and

yields a more valuable product. This finding would add value to carbon dioxide if implemented in commercial HTC processes which would encourage the capture and storage of carbon dioxide present in the environment. Thus, improving the economics of carbon capture by providing a valuable application of the trapped carbon dioxide.

The hydrochar produced from BW under carbon dioxide showed potential as a sustainable alternative to fossil fuel coals. Relatively mild HTC processing conditions (200 °C, 1 h) were used compared to literature (Appendix 1). Hydrochar had a HHV of 36 MJ Kg^{-1} which is 2.3 MJ Kg^{-1} higher than the most energy dense fossil fuel coals and exceptionally high compared to other hydrochars presented in the literature [186]. Further to this a low ash content of 2.3% was determined which is just below the general range of fossil fuel coals (3-15%). This low ash content would decrease the reactor fouling/slagging after combustion compared to fossil fuel coals. Notably the BW hydrochar contained a high volatile matter content at 58.8%, which is 13.8% above the most volatile types of bituminous and sub-bituminous coals. This volatile matter is mostly composed of aromatic hydrocarbons which form in hydrothermal conditions. Compared to fossil fuel coals, the BW hydrochar could be efficiently combusted at lower temperatures because of the increased oxygen content [465]. Fixed carbon (41.2%) in the hydrochar is comparable with sub-bituminous coals.

Based on surface functionality analysis by FT-IR of BW and AS hydrochar, AS was the more lignin rich biomass, the hydrochar of which showed increased surface functionality, containing more oxygenic surface groups despite the higher processing conditions. This is because lignin is more thermally resistant than the largely saccharide based BW feedstock. Therefore more lignin rich biomass feedstocks are suited towards adsorption and catalysis applications of high value sustainably produced carbonaceous material. In that vein, AS were demonstrated as the feedstock for a HTC based synthesis procedure to produce magnetic carbon composite (Fe/C) materials. The synthesised Fe/C was composed of mostly magnetite on graphitic hydrochar with an outer heamatite layer. Fe/C displayed selective adsorption of indigo carmine over methylene blue at a competitive adsorption capacity of ~49 mg g^{-1}. In addition to this, excellent regioselectivity was demonstrated using Fe/C in a catalytic testing hydroalkoxylation reaction. A further advantage was the facile magnetic separation which can be employed in both catalytic and adsorption applications. This facile, non-toxic, one-pot synthesis procedure exhibited the potential that HTC has in utilising typically low value high lignin feedstocks to produce sustainably sourced catalysts. The process has high tuneability, metallic loading can be

manipulated by changing the biomass to iron precursor ratio and the metal oxide formation can be selected from the wide range of inorganic hydrothermal synthesis procedures discussed in literature.

8.1.2. Insights Gained into Sub-critical Alcohol/Water Mixtures, their Effect on Hydrochar Properties and the Molecular Dynamics Present at Those Conditions

Direct connections between the sub-critical FT-IR ethanol/water data and the effect of ethanol/water mixtures on the hydrochar composition have been identified. Firstly, monitoring the excess intensity of the C-O stretching band at ambient conditions aligned with the negative excess enthalpy for all alcohol/water mixtures. This is attributed to hydrogen bond formation to the C-O group which is most prevalent when the alcohol/water mixture is in a highly structured state. Therefore, by examining the excess intensity of the C-O stretching band at sub-critical conditions, this gives an idea for the most structured ethanol/water environment. A notable peak was measured at 56.9 mol% for ethanol/water mixtures, indicating at this point maximum structuring around the exposed C-O bond is occurring. At this same molar percentage it is observed that there is a change in the main oxide formed on the Fe/C from AS during HTC. Fe/C synthesis under 56.9 mol% ethanol yielded a 47.9% magnetite phase and 52.1% heamatite phase. Initially the iron oxide is formed as magnetite and a portion of the exposed iron oxide is converted into heamatite during processing. Therefore, at this molar percentage ethanol there is either increased reactivity to convert the oxides or higher penetration of the iron oxide during HTC. Varying oxidation states based on processing temperature and retention time for hydrothermal synthesis of inorganics is well reported. However, the potential to utilise varying solvent/water mixture ratios to afford different oxidation state catalysts is an underinvestigated area in the literature.

In deconvolution analysis of the O-H stretching peak the D2 peak area is attributed to tetrahedrally bonded water molecules which are disrupted with the addition of alcohol molecules. Under ambient conditions D2 shows gradual decrease with increasing alcohol concentration with a clear transition point where alcohol becomes the dominant molecule in the meso-structure which aligns with values of this transition point stated in the literature. At sub-critical conditions for ethanol/water mixtures D2 completely disappears above 11.1 mol% ethanol. This is ascribed to a lower concentration of alcohol required before it overtakes the intermolecular bonding dynamics and prevents any tetrahedrally bonded water complexes

forming. Moving over to HTC of bread waste above 11.1 mol% ethanol no evidence of typical polycondensation reactions was found and the hydrochar yield was heavily decreased for both 16.6 and 23.5 mol%. At 32 mol% ethanol and above for HTC of bread waste the dissolution of the feedstock was greatly impeded which provided a falsely high yield. These two shifts are further evidenced by the HHV, proximate, and ultimate analysis. The initial change above 11.1 mol% ethanol where no tetrahedral water complexes are formed in solution which prevents polycondensation reactions during HTC. Following this another shift occurs where the hydrolysis of lignocellulose is limited in capacity at 32 mol% and above.

Finally, the hydrochar produced from AS with iron precursor salts demonstrated similar carbonaceous properties no matter the ethanol molar concentration added, whereas the hydrochar from BW was heavily affected. This is attributed to the higher processing temperature and longer retention time in the AS HTC.

8.1.3. Novel Observations of Aerosol-Assisted Sol-Gel Catalyst Synthesis under *Operando* Conditions

Optical trapping permitted the novel investigation of the initial reactions within a single droplet using Raman spectroscopy. Novel observations in reactivity and evaporation were made which controvert the expected based upon bulk sol-gel synthesis. Ethanol evaporation within the droplet was dramatically affected by the addition of different compounds in the precursor solution. Pluronic P123 stabilised the droplets attributed to micelle formation; this was further evidenced by HNO_3 increasing evaporation *via* destabilising the micelle structure as observed in bulk solutions. Additionally, the micelle structure was stabilised through microstructure formation with Al-iPr. The evaporation of ethanol was fully retarded in the HeEPNA droplet, the exact cause was not determined but was ascribed to an encapsulation reaction forming a solid film around the trapped droplet. These observations into the effect that different components have on ethanol evaporation are valuable and can be utilised when designing precursor solutions for aerosol-assisted sol-gel synthesis.

Based upon bulk sol-gel synthesis the EPNA system should form an extended gel network by hydrolysis and poly-condensation reactions with concurrent evaporation of ethanol. However, isothermally trapped EPNA displayed a relative increase in the strength of the Al-NO_3 peak over a four hour trapping period, this Al-NO_3 peak is expected to reduce in size due to the

formation of an extended aluminum gel network. Therefore, no evidence of hydrolysis and condensation observed in bulk sol-gel synthesis was displayed. However, the addition of nickel nitrate in the EPNAN droplet induced reactivity at isothermal conditions and a postulated alternative reaction pathway was suggested as the cause. The addition of heating in HeEPNA whilst hindering evaporation of ethanol displayed evidence of gel formation reactions through the reduction in the Al-NO_3 peak. Indicating that these reactants require enough heat to provide activation energy but do not necessitate evaporation to occur. These novel findings into the formation reactions occurring within a flow tube during AASG synthesis can be used to direct changes in the precursor solutions used to synthesise catalysts.

8.1.4. Conclusions

The presented research covers a large scope and is ambitious at tackling important gaps within the literature. Whilst valuable preliminary experiments have been executed which have developed the research area the effect of alcohol and other solvents during HTC is still a complex and not fully explored research area. In addition, the use of instrumental techniques to understand the molecular environment of the sub-critical solvents system is imperative to fully appreciate and understand the effect that different solvents and processing conditions have on the properties of the hydrochar. The insights gained into AASG synthesis mechanisms and evaporation are both novel and valuable. This demonstrates the potential optical trapping has to develop the understanding of AASG and other aerosol based processes. Thus, based on insights obtained from these initial investigations it is suggested that additional research be executed to construct a well-rounded foundation for future research in these areas. The purpose of this future research should be focussed on understanding these unconventional and emerging synthesis methods and environments so that they can be used to inform the design of more sustainable industrial processes.

8.2. Future Work

8.2.1. Investigation of Alcohol/Water Mixtures at Sub-Critical Conditions

The investigation into the molecular structuring of alcohol/water mixtures using FT-IR provided valuable insight into the relatively unknown effect of sub-critical conditions. Continuing this investigation the analytical systems discussed for analysis of HTW in Section 2.1.2 can be utilised. Raman spectroscopy is the evident next step to provide complementary information to the already obtained FT-IR spectroscopy data. The use of radiolabelled water

(HDO, D_2O) or alcohols (MeOD) verifies the correct assignment of alkyl vibrational bands in addition to isolating the source of interactions between the water and alcohol [466]. Mathematical analysis and data manipulation can be performed on this Raman data using deconvolution and 2D correlation spectroscopy as attempted for FT-IR. In future analysis focussing on a narrower range with the same number of points would allow the crucial transition points to be more precisely determined. In the case of methanol/water mixtures the range between 0 and 40 mol% methanol is recommended at 5 mol% integers. Over this range two of the more significant transitions occur in the structure of methanol/water mixtures at ambient conditions. Following this, either X-ray or neutron scattering could be used to measure the change in intermolecular atomic correlation distances and the co-ordination number of hydrogen bonds to specific groups on both the water and the alcohol. Provided with this combined information the intermolecular and intramolecular dynamics at the lower concentration of alcohol/water mixtures would be more clearly understood. Therefore encouraging their use in separation, purification, and synthesis methods.

8.2.2. Quantifying the Effect of Alcohol as an Additive During HTC

Processing of real biomass waste streams using HTC is the final objective and application for the research area. It is essential to minimise the experimental trials often involved in developing HTC processes. In order to achieve this goal the HTC of the macro components in lignocellulose (lignin, cellulose, and hemicellulose) must be initially characterised [328], [467], [468]. This approach should be utilised to quantify the effect of different alcohol/water mixtures during HTC. Feedstocks of pure lignin, cellulose, and hemicellulose should be separately processed *via* HTC at a small range of temperatures (*e.g.* 180, 200, 220, 240 °C) because temperature has a significant effect on the composition of the hydrochar. Retention time should be a fixed time period of at least 1 hour which is sufficient time to allow for hydrothermal carbonisation reactions to proceed to completion. An inert pressurising gas such as helium should be used so that it does not affect the reactions during HTC. This outlines a total of 12 different reactions which should be completed in duplicate to reduce error.

Following the synthesis of the hydrochar it should be characterised for proximate analysis, ultimate analysis, HHV, surface functionality, and surface area. This will provide a fundamental understanding for the expected properties of hydrochar produced at these processing conditions from lignin, cellulose, and hemicellulose. Once these initial HTC

reactions have been completed, methanol/water mixtures (chosen as the alcohol/water mixture with clear transition in the FT-IR analysis in Chapter 4) should be utilised in the range from 0 mol% at 5 mol% additions (in duplicate) up to 40 mol% methanol. This shorter range of molarities showed the largest changes in the hydrochar properties and requires less alcohol compared to water for processing making it a more sustainable process. The properties of the hydrochar from these reactions can then be compared to the water synthesised hydrochars. Therefore the reactivity of each macro component within lignocellulose along the HTC temperature range and at different methanol/water molar percentage would be heavily characterised. This would provide the groundwork to guide the use of alcohol/water mixtures in HTC of real biomass wastes based on processing temperature, and the biomass composition.

8.2.3. Further Research Utilising Optical Trapping

In future it would be valuable to analyse the catalysts produced by aerosol-assisted sol-gel synthesis using the precursor solutions studied in optical trapping experiments because this would allow the final structure of these catalysts to be related to the observations made during optical trapping. A key finding of the research in Chapter 7 was that the evaporation of ethanol changed when different additives were used and was completely hindered upon external heating in the HeEPNA droplet. This can be expanded upon by analysing different block copolymers and solvents within the optical trapping set-up which would provide further understanding of the physical chemistry during the early stages of aerosol processes utilising these solvent polymer solutions. These solvent interactions can have a significant impact upon the structure of the final catalysts. For example, Long *et al.* demonstrated that the same reactants could produce different metal organic frameworks with high purity by selection of either methanol/water mixtures or acetone/water mixtures which produced MIL-96(Cr) or MIL-100(Cr) respectively [469]. Potential starting points for investigation are other binary alcohol/water mixtures for example methanol or isopropanol and water which are investigated in Chapter 4. Alternatively, polar aprotic solvents such as acetone, N,N-dimethylformamide, and acetonitrile would provide different reaction and evaporation dynamics. The most commonly used block copolymers for investigation instead of pluronic P123 are: pluronic F127 PEG-PEG-PEG (polypropylene glycol), CTAB (cetyltrimethylammonium bromide), and Brij® 58 (polyoxyethylene cetyl ether).

8.2.4. Sustainable Production of Hydrochar from Bread Waste

The favourable combustion properties of hydrochar synthesised from bread waste in Chapter 5 presents a promising area for future industrial research and application. This would involve processing the bread waste in larger batch reactors at a range of conditions based around the established 200 °C, 60 min, and pressurised with carbon dioxide. In this avenue it would be preferable to first perform a thorough techno-economic assessment to estimate the capital and operating costs as well as potential profit from the hydrochar. The hydrochar produced in the larger batch reactors would need to be analysed for combustion properties, HHV, proximate and ultimate analysis. Following this, the production of large amounts of hydrochar would permit testing in coal power plants. If this process was successfully implemented it could work in tandem with food manufacturing companies which produce large amounts of unmixed bread waste, therefore avoiding landfill and producing a source of sustainable energy.

8.2.5. Investigate the Potential Tunability of Hydrothermal Carbonisation Using Carbon Dioxide

In Chapter 5 it was discovered that the use of carbon dioxide instead of helium in the hydrothermal carbonisation of dried bread waste greatly increased energy content of the hydrochar far above what is observed in the literature. This reaction utilised 30 bar of carbon dioxide or helium which was then consequently heated to produce pressures up to 50-60 bar at operation temperature. In comparison industrial hydrothermal carbonisation temperatures often use autogenously generated pressure or very low-pressure systems below 3 bar. This is due to the operational constraints and challenges of processing at higher pressures. Therefore, an investigation into the effect of carbon dioxide at different pressures on hydrothermal carbonisation would be fruitful. It would be important to discover if the effect was directly proportional *i.e.* the more pressure of carbon dioxide you add the higher the HHV of the end hydrochar. Or if the effect contained a critical carbon dioxide pressure whereby a rapid increase in HHV is observed up to a certain pressure then no additional pressure would increase the HHV further. This can be readily investigated by selecting a standard operating time *e.g.* 60 minutes. A range of operating temperatures *e.g.* 180, 200, 220, and 240 °C. Then initial investigations can start at 5, 15, and 30 bar of carbon dioxide, the products analysed, and further initial pressurisation can be investigated to determine any effect. If only a minor carbon dioxide pressure is required, for example 2 bar, to obtain the increase in HHV it would be desirable to redesign industrial reactors around this application for carbon dioxide and thus make it a

valuable area of future research.

References

[1] D. Spratt, I. Dunlop, and A. C. Barrie, “Existential climate-related security risk -- A scenario approach,” no. May, p. 10, 2019, [Online]. Available: https://www.preventionweb.net/publication/existential-climate-related-security-risk-scenario-approach.

[2] D. Töbelmann and T. Wendler, “The impact of environmental innovation on carbon dioxide emissions,” *J. Clean. Prod.*, vol. 244, 2020, doi: 10.1016/j.jclepro.2019.118787.

[3] L. Al-Ghussain, “Global warming: review on driving forces and mitigation,” *Environ. Prog. Sustain. Energy*, vol. 38, no. 1, pp. 13–21, 2019, doi: 10.1002/ep.13041.

[4] S. Suranovic, “Fossil fuel addiction and the implications for climate change policy,” *Glob. Environ. Chang.*, vol. 23, no. 3, pp. 598–608, 2013, doi: 10.1016/j.gloenvcha.2013.02.006.

[5] A. García-Olivares, “Substitutability of electricity and renewable materials for fossil fuels in a post-carbon economy,” *Energies*, vol. 8, no. 12, pp. 13308–13343, 2015, doi: 10.3390/en81212371.

[6] M. Jakob and J. Hilaire, “Unburnable fossil-fuel reserves,” *Nature*, vol. 517, no. 7533, pp. 150–151, 2015, doi: 10.1038/517150a.

[7] S. Shafiee and E. Topal, “When will fossil fuel reserves be diminished?,” *Energy Policy*, vol. 37, no. 1, pp. 181–189, 2009, doi: 10.1016/j.enpol.2008.08.016.

[8] W. Ferdous *et al.*, “Recycling of landfill wastes (tyres, plastics and glass) in construction – A review on global waste generation, performance, application and future opportunities,” *Resour. Conserv. Recycl.*, vol. 173, no. December 2020, p. 105745, 2021, doi: 10.1016/j.resconrec.2021.105745.

[9] S. Das, S. H. Lee, P. Kumar, K. H. Kim, S. S. Lee, and S. S. Bhattacharya, “Solid waste management: Scope and the challenge of sustainability,” *J. Clean. Prod.*, vol. 228, pp. 658–678, 2019, doi: 10.1016/j.jclepro.2019.04.323.

[10] C. SN, “Solid Waste Pollution: A Hazard to Environment,” *Recent Adv. Petrochemical Sci.*, vol. 2, no. 3, pp. 41–43, 2017, doi: 10.19080/rapsci.2017.02.555586.

[11] P. Kjeldsen, M. A. Barlaz, A. P. Rooker, A. Baun, A. Ledin, and T. H. Christensen, “Present and long-term composition of MSW landfill leachate: A review,” *Crit. Rev. Environ. Sci. Technol.*, vol. 32, no. 4, pp. 297–336, 2002, doi: 10.1080/10643380290813462.

[12] F. Obi, B. Ugwuishiwu, and J. Nwakaire, “Agricultural Waste Concept, Generation,

Utilization and Management," *Niger. J. Technol.*, vol. 35, no. 4, p. 957, 2016, doi: 10.4314/njt.v35i4.34.

[13] S. K. Awasthi *et al.*, "Changes in global trends in food waste composting: Research challenges and opportunities," *Bioresour. Technol.*, vol. 299, no. December 2019, p. 122555, 2020, doi: 10.1016/j.biortech.2019.122555.

[14] A. G. Olabi, "Circular economy and renewable energy," *Energy*, vol. 181, pp. 450–454, 2019, doi: 10.1016/j.energy.2019.05.196.

[15] F. Bergius, "The use of high pressure in chemical processes and the formation of the coal formation process," *J. Compress. Liq. Gases*, no. 17, 1915.

[16] Bergius, "Production of hydrogen from water and coal from cellulose at high temperatures and pressures," *J. Soc. Chem. Ind.*, 1913.

[17] J. P. Schuhmacher, F. J. Huntjens, and D. W. Vankrevelen, "Chemical structure and properties of coal. 26. Studies on artificial coalification," *Fuel*, vol. 39, no. 3, pp. 223–234, 1960.

[18] M.-M. Titirici, A. Thomas, and M. Antonietti, "Back in the black: hydrothermal carbonization of plant material as an efficient chemical process to treat the CO2 problem?," *New J. Chem.*, vol. 31, no. 6, pp. 787–789, 2007, doi: 10.1039/B616045J.

[19] M.-M. Titirici and M. Antonietti, *Sustainable Carbon Materials from Hydrothermal Processes*. John Wiley & Sons, Incorporated, 2013.

[20] S. K. Hoekman, A. Broch, and C. Robbins, "Hydrothermal carbonization (HTC) of lignocellulosic biomass," *Energy and Fuels*, vol. 25, no. 4, pp. 1802–1810, 2011, doi: 10.1021/ef101745n.

[21] M. Renz, "Hydrothermal Carbonization and Its Role in Catalysis," *Nanotechnol. Catal.*, pp. 715–752, 2017, doi: 10.1002/9783527699827.ch28.

[22] A. M. Smith, C. Whittaker, I. Shield, and A. B. Ross, "The potential for production of high quality bio-coal from early harvested Miscanthus by hydrothermal carbonisation," *Fuel*, vol. 220, no. January, pp. 546–557, 2018, doi: 10.1016/j.fuel.2018.01.143.

[23] S. Nizamuddin *et al.*, "An overview of effect of process parameters on hydrothermal carbonization of biomass," *Renew. Sustain. Energy Rev.*, vol. 73, no. December 2015, pp. 1289–1299, 2017, doi: 10.1016/j.rser.2016.12.122.

[24] G. Davies, A. El Sheikh, C. Collett, I. Yakub, and J. McGregor, "Chapter 5 - Catalytic carbon materials from biomass," in *Emerging Carbon Materials for Catalysis*, S. B. T.-E. C. M. for C. Sadjadi, Ed. Elsevier, 2021, pp. 161–195.

[25] H. S. Kambo and A. Dutta, "A comparative review of biochar and hydrochar in terms

of production , physico-chemical properties and applications," *Renew. Sustain. Energy Rev.*, vol. 45, pp. 359–378, 2015, doi: 10.1016/j.rser.2015.01.050.

[26] K. Tekin and S. Karagöz, "Non-catalytic and catalytic hydrothermal liquefaction of biomass," *Res. Chem. Intermed.*, vol. 39, no. 2, pp. 485–498, 2013, doi: 10.1007/s11164-012-0572-3.

[27] F. Behrendt, Y. Neubauer, M. Oevermann, B. Wilmes, and N. Zobel, "Direct liquefaction of biomass," *Chem. Eng. Technol.*, vol. 31, no. 5, pp. 667–677, 2008, doi: 10.1002/ceat.200800077.

[28] N. Atiqah Nasir, G. Davies, and J. McGregor, "Tailoring product characteristics in the carbonisation of brewers' spent grain through solvent selection," *Food Bioprod. Process.*, vol. 120, pp. 41–47, 2020, doi: 10.1016/j.fbp.2019.12.010.

[29] Y. T. Yang *et al.*, "Alcohothermal carbonization of biomass to prepare novel solid catalysts for oleic acid esterification," *Fuel*, vol. 219, no. September 2017, pp. 166–175, 2018, doi: 10.1016/j.fuel.2018.01.072.

[30] C. Antonetti *et al.*, "One-pot alcoholysis of the lignocellulosic eucalyptus nitens biomass to n-butyl levulinate, a valuable additive for diesel motor fuel," *Catalysts*, vol. 10, no. 5, pp. 1–22, 2020, doi: 10.3390/catal10050509.

[31] S. H. Feng and G. H. Li, *Chapter 4 - Hydrothermal and Solvothermal Syntheses*. 2017.

[32] S. Liang *et al.*, "One-pot solvothermal synthesis of magnetic biochar from waste biomass: Formation mechanism and efficient adsorption of Cr(VI) in an aqueous solution," *Sci. Total Environ.*, vol. 695, p. 133886, 2019, doi: 10.1016/j.scitotenv.2019.133886.

[33] W. J. J. Huijgen, A. T. Smit, P. J. de Wild, and H. den Uil, "Fractionation of wheat straw by prehydrolysis, organosolv delignification and enzymatic hydrolysis for production of sugars and lignin," *Bioresour. Technol.*, vol. 114, pp. 389–398, 2012, doi: 10.1016/j.biortech.2012.02.143.

[34] J. H. Guo *et al.*, "The molecular structure of alcohol-water mixtures determined by soft-X-ray absorption and emission spectroscopy," *J. Electron Spectros. Relat. Phenomena*, vol. 137–140, no. SPEC. ISS., pp. 425–428, 2004, doi: 10.1016/j.elspec.2004.02.094.

[35] B. Buesser and S. E. Pratsinis, "Design of Nanomaterial Synthesis by Aerosol Processes," *Annu. Rev. Chem. Biomol. Eng.*, vol. 3, no. 1, pp. 103–127, 2012, doi: 10.1146/annurev-chembioeng-062011-080930.

[36] R. Koirala, S. E. Pratsinis, and A. Baiker, "Synthesis of catalytic materials in flames: Opportunities and challenges," *Chem. Soc. Rev.*, vol. 45, no. 11, pp. 3053–3068, 2016,

doi: 10.1039/c5cs00011d.

[37] D. P. Debecker, S. Le Bras, C. Boissière, A. Chaumonnot, and C. Sanchez, “Aerosol processing: A wind of innovation in the field of advanced heterogeneous catalysts,” *Chem. Soc. Rev.*, vol. 47, no. 11, pp. 4112–4155, 2018, doi: 10.1039/c7cs00697g.

[38] N. David G. Grier, “A revolution in optical manipulation,” vol. 424, no. August, pp. 1–7, 2003, [Online]. Available: papers2://publication/uuid/892914CD-D3F6-442E-B5B9-B16C9C78CBF8.

[39] P. Innocenzi, “Understanding sol–gel transition through a picture. A short tutorial,” *J. Sol-Gel Sci. Technol.*, pp. 544–550, 2020, doi: 10.1007/s10971-020-05243-w.

[40] W. Wagner and A. Pruß, “The IAPWS formulation 1995 for the thermodynamic properties of ordinary water substance for general and scientific use,” *J. Phys. Chem. Ref. Data*, vol. 31, no. 2, pp. 387–535, 2002, doi: 10.1063/1.1461829.

[41] N. Akiya and P. E. P. E. Savage, “Roles of water for chemical reactions in high-temperature water,” *Chem. Rev.*, vol. 102, no. 8, pp. 2725–2750, 2002, doi: 10.1021/cr000668w.

[42] V. Vadillo, J. Sánchez-Oneto, J. R. Portela, and E. J. Martínez De La Ossa, “Problems in supercritical water oxidation process and proposed solutions,” *Ind. Eng. Chem. Res.*, vol. 52, no. 23, pp. 7617–7629, 2013, doi: 10.1021/ie400156c.

[43] P. E. Savage, “Organic Chemical Reactions in Supercritical Water,” *Chem. Rev.*, vol. 99, no. 2–3, pp. 603–621, 1999, doi: 10.1021/cr9700989.

[44] G. W. Kauffman and P. C. Jurs, “Prediction of Surface Tension , Viscosity , and Thermal Conductivity for Common Organic Solvents Using Quantitative Structure - Property Relationships,” pp. 408–418, 2001, doi: 10.1021/ci000139t.

[45] M. Zheng, J. Tian, and Á. Mulero, “New correlations between viscosity and surface tension for saturated normal fluids,” *Fluid Phase Equilib.*, vol. 360, pp. 298–304, 2013, doi: 10.1016/j.fluid.2013.09.045.

[46] J. W. Tester and J. A. Cline, “Hydrolysis and Oxidation in Subcritical and Supercritical Water : Connecting Process Engineering Science to Molecular Interactions,” no. November, pp. 1088–1100, 1999, doi: 10.5006/1.3283946.

[47] R. S. Pinheiro, F. M. R. Mesquita, F. X. Feitosa, H. B. De Sant’Ana, and R. S. De Santiago-Aguiar, “Density, viscosity and excess properties of binary mixtures of protic ionic liquid (2-HDeAF, 2-HDEAA) + water at different temperatures,” *Brazilian J. Chem. Eng.*, vol. 35, no. 2, pp. 383–393, 2018, doi: 10.1590/0104-6632.20180352s20160280.

[48] N. A.H, “Molecular dipole moments and electronegativity,” *Chem. Phys. Lett.*, vol. 59, no. 2, pp. 346–350, 1978, doi: 10.1016/0009-2614(78)89109-X.

[49] S. Alavi, R. Susilo, and J. A. Ripmeester, “Linking microscopic guest properties to macroscopic observables in clathrate hydrates: Guest-host hydrogen bonding,” *J. Chem. Phys.*, vol. 130, no. 17, 2009, doi: 10.1063/1.3124187.

[50] R. Notario and J.-L. M. Abboud, “Critical compilation of scales of solvent parameters. Part I. Pure, non-hydrogen bond donor solvents,” *Pure Appl. Chem.*, vol. 71, no. 4, pp. 645–718, 1999, doi: 10.1351/pac199971040645.

[51] T. I. Mizan, P. E. Savage, and R. M. Ziff, “Temperature dependence of hydrogen bonding in supercritical water,” *J. Phys. Chem.*, vol. 100, no. 1, pp. 403–408, 1996, doi: 10.1021/jp951561t.

[52] J. Szala-Bilnik and D. Swiatla-Wojcik, “Hydration of OH radical in high temperature water,” *J. Mol. Liq.*, vol. 164, no. 1–2, pp. 34–38, 2011, doi: 10.1016/j.molliq.2011.04.012.

[53] M. Nakahara, N. Matubayasi, C. Wakai, and Y. Tsujino, “Structure and dynamics of water: From ambient to supercritical,” *J. Mol. Liq.*, vol. 90, no. 1–3, pp. 75–83, 2001, doi: 10.1016/S0167-7322(01)00109-X.

[54] P. Jedlovszky, J. P. Brodholt, F. Bruni, M. A. Ricci, A. K. Soper, and R. Vallauri, “Analysis of the hydrogen-bonded structure of water from ambient to supercritical conditions,” *J. Chem. Phys.*, vol. 108, no. 20, pp. 8528–8540, 1998, doi: 10.1063/1.476282.

[55] K. Maex, M. R. Baklanov, D. Shamiryan, F. Iacopi, S. H. Brongersma, and Z. S. Yanovitskaya, “Low dielectric constant materials for microelectronics,” *J. Appl. Phys.*, vol. 93, no. 11, pp. 8793–8841, 2003, doi: 10.1063/1.1567460.

[56] K. Sakai, R. Sakurai, and N. Hirayama, “Chiral discrimination controlled by the solvent dielectric constant,” *Tetrahedron Asymmetry*, vol. 15, no. 7, pp. 1073–1076, 2004, doi: 10.1016/j.tetasy.2004.02.015.

[57] E. Perlt, M. Von Domaros, B. Kirchner, R. Ludwig, and F. Weinhold, “Predicting the Ionic Product of Water,” *Sci. Rep.*, vol. 7, no. 1, pp. 1–10, 2017, doi: 10.1038/s41598-017-10156-w.

[58] W. L. Marshall and E. U. Franck, “Ion product of water substance, 0-1000 °C, 1-10,000 bars New International Formulation and its background,” *J. Phys. Chem. Ref. Data*, vol. 10, no. 2, pp. 295–304, 1983, doi: 10.1063/1.555643.

[59] H. Ohtaki, T. Radnai, and T. Yamaguchi, “Structure of water under subcritical and

supercritical conditions studied by solution X-ray diffraction," *Chem. Soc. Rev.*, vol. 26, no. 1, pp. 41–51, 1997, doi: 10.1039/cs9972600041.

[60] K. Amann-Winkel *et al.*, "X-ray and Neutron Scattering of Water," *Chem. Rev.*, vol. 116, no. 13, pp. 7570–7589, 2016, doi: 10.1021/acs.chemrev.5b00663.

[61] K. Ichikawa *et al.*, "Neutron-diffraction investigation of the intramolecular structure of a water molecule in the liquid phase at high temperatures," *Mol. Phys.*, no. May 2013, pp. 37–41, 2006, doi: 10.1080/00268979100101071.

[62] F. Lafrad, T. Tassaing, M. Kiselev, and A. Idrissi, "The local structure of sub- and supercritical water as studied by FTIR spectroscopy and molecular dynamics simulations," *J. Mol. Liq.*, vol. 239, pp. 61–67, 2017, doi: 10.1016/j.molliq.2016.07.093.

[63] B. M. Auer and J. L. Skinner, "IR and Raman spectra of liquid water: Theory and interpretation," *J. Chem. Phys.*, vol. 128, no. 22, 2008, doi: 10.1063/1.2925258.

[64] D. M. Carey, "Measurement of the Raman spectrum of liquid water," *J. Chem. Phys.*, vol. 108, no. 7, pp. 2669–2675, 1998, doi: 10.1063/1.475659.

[65] Q. Sun, Q. Wang, and D. Ding, "Hydrogen bonded networks in supercritical water," *J. Phys. Chem. B*, vol. 118, no. 38, pp. 11253–11258, 2014, doi: 10.1021/jp503474s.

[66] Q. Sun, "Local statistical interpretation for water structure," *Chem. Phys. Lett.*, vol. 568–569, pp. 90–94, 2013, doi: 10.1016/j.cplett.2013.03.065.

[67] T. Tassaing, Y. Danten, M. Besnard, and I. Copyright, "Infrared spectroscopic study of hydrogen-bonding in water at high temperature and pressure," *Kaos GL Derg.*, vol. 21, no. 75, pp. 147–173, 2002, doi: 10.1007/978-1-4614-7990-1.

[68] N. Matubayasi, C. Wakai, and M. Nakahara, "NMR study of water structure in super- and subcritical conditions," *Phys. Rev. Lett.*, vol. 78, no. 13, pp. 2573–2576, 1997, doi: 10.1103/PhysRevLett.78.2573.

[69] K. Yoshida, C. Wakai, N. Matubayasi, and M. Nakahara, "A new high-temperature multinuclear-magnetic-resonance probe and the self-diffusion of light and heavy water in sub- and supercritical conditions," *J. Chem. Phys.*, vol. 123, no. 16, 2005, doi: 10.1063/1.2056542.

[70] S. H. Townsend, M. A. Abraham, G. L. Huppert, M. T. Klein, and S. C. Paspek, "Solvent Effects During Reactions in Supercritical Water," *Ind. Eng. Chem. Res.*, vol. 27, no. 1, pp. 143–149, 1988, doi: 10.1021/ie00073a026.

[71] J. M. L. Penninger, R. J. A. Kersten, and H. C. L. Baur, "Reactions of diphenylether in supercritical water - Mechanism and kinetics," *J. Supercrit. Fluids*, vol. 16, no. 2, pp. 119–132, 1999, doi: 10.1016/S0896-8446(99)00024-8.

[72] P. A. Marrone, P. M. Gschwend, K. C. Swallow, W. A. Peters, and J. W. Tester, "Product distribution and reaction pathways for methylene chloride hydrolysis and oxidation under hydrothermal conditions," *J. Supercrit. Fluids*, vol. 12, no. 3, pp. 239–254, 1998, doi: 10.1016/S0896-8446(98)00083-7.

[73] B. Izzo, M. T. Klein, C. LaMarca, and N. C. Scrivner, "Hydrothermal reaction of saturated and unsaturated nitriles: Reactivity and reaction pathway analysis," *Ind. Eng. Chem. Res.*, vol. 38, no. 4, pp. 1183–1191, 1999, doi: 10.1021/ie9803218.

[74] S. D. Iyer, G. R. Nicol, and M. T. Klein, "Hydrothermal reactions of 1-nitrobutane in high-temperature water," *J. Supercrit. Fluids*, vol. 9, no. 1, pp. 26–32, 1996, doi: 10.1016/S0896-8446(96)90041-8.

[75] P. Krammer and H. Vogel, "Hydrolysis of esters in subcritical and supercritical water," *J. Supercrit. Fluids*, vol. 16, no. 3, pp. 189–206, 2000, doi: 10.1016/S0896-8446(99)00032-7.

[76] C. C. Tsao, Y. Zhou, X. Liu, and T. J. Houser, "Reactions of supercritical water with benzaldehyde, benzylidenebenzylamine, benzyl alcohol, and benzoic acid," *J. Supercrit. Fluids*, vol. 5, no. 2, pp. 107–113, 1992, doi: 10.1016/0896-8446(92)90027-H.

[77] H. P. Lesutis, R. Gläser, C. L. Liotta, and C. A. Eckert, "Acid/base-catalyzed ester hydrolysis in near-critical water," *Chem. Commun.*, no. 20, pp. 2063–2064, 1999, doi: 10.1039/a906401j.

[78] Q. Dong, C. Yu, L. Li, L. Nie, D. Li, and H. Zang, "Near-infrared spectroscopic study of molecular interaction in ethanol-water mixtures," *Spectrochim. Acta - Part A Mol. Biomol. Spectrosc.*, vol. 222, p. 117183, 2019, doi: 10.1016/j.saa.2019.117183.

[79] D. R. Palo, R. A. Dagle, and J. D. Holladay, "Methanol Steam Reforming for Hydrogen Production," no. 541, pp. 3992–4021, 2007, doi: 10.1021/cr050198b.

[80] B. S. Akpa *et al.*, "Solvent effects in the hydrogenation of 2-butanone," vol. 289, pp. 30–41, 2012, doi: 10.1016/j.jcat.2012.01.011.

[81] M. Matsugami, R. Yamamoto, T. Kumai, M. Tanaka, T. Umecky, and T. Takamuku, "Hydrogen bonding in ethanol – water and tri fl uoroethanol – water mixtures studied by NMR and molecular dynamics simulation," *J. Mol. Liq.*, vol. 217, no. D, pp. 3–11, 2016, doi: 10.1016/j.molliq.2015.06.050.

[82] T. A. Dolenko *et al.*, "Raman Spectroscopy of Water-Ethanol Solutions: The Estimation of Hydrogen Bonding Energy and the Appearance of Clathrate-like Structures in Solutions," *J. Phys. Chem. A*, vol. 119, no. 44, pp. 10806–10815, 2015, doi: 10.1021/acs.jpca.5b06678.

[83] D. P. Institut and V. Georg-august-uni, “Water - Ethanol Mixtures at Different Compositions and Temperatures. A Dieletric Relaxation Study,” pp. 7420–7428, 2000, doi: 10.1021/jp001393r.

[84] H. Schott, “Hydration of Primary Alcohols,” vol. 14, no. 2, pp. 237–239, 1969, doi: 10.1021/je60041a004.

[85] M. D. Angelo *et al.*, “Self-association of monohydric alcohols in water: Compressibility and infrared absorption measurements,” *J. Chem. Phys.*, vol. 100, no. 4, pp. 3107–3113, 1994, doi: 10.1063/1.466452.

[86] J. A. Larkin, “Thermodynamic properties of aqueous non-electrolyte mixtures I. Excess enthalpy for water + ethanol at 298.15 to 383.15 K,” *J. Chem. Thermodyn.*, vol. 7, no. 2, pp. 137–148, 1975, doi: 10.1016/0021-9614(75)90261-X.

[87] R. F. Lama and B. C. Y. Lu, “Excess Thermodynamic Properties of Aqueous Alcohol Solutions,” *J. Chem. Eng. Data*, vol. 10, no. 3, pp. 216–219, 1965, doi: 10.1021/je60026a003.

[88] H. Yilmaz, “Excess properties of alcohol - Water systems at 298.15 K,” *Turkish J. Phys.*, vol. 26, no. 3, pp. 243–246, 2002, doi: 10.1.1.966.7155&rep=rep1&type=pdf.

[89] Y. Koga, K. Nishikawa, and P. Westh, “‘Icebergs’ or no ‘icebergs’ in aqueous alcohols?: Composition-dependent mixing schemes,” *J. Phys. Chem. A*, vol. 108, no. 17, pp. 3873–3877, 2004, doi: 10.1021/jp0312722.

[90] S. Dixit, J. Crain, W. C. K. Poon, J. L. Finney, and A. K. Soper, “Molecular segregation observed in a concentrated alcohol-water solution,” *Nature*, vol. 416, no. 6883, pp. 829–832, 2002, doi: 10.1038/416829a.

[91] S. P. Benson and J. Pleiss, “Incomplete mixing versus clathrate-like structures: A molecular view on hydrophobicity in methanol-water mixtures,” *J. Mol. Model.*, vol. 19, no. 8, pp. 3427–3436, 2013, doi: 10.1007/s00894-013-1857-1.

[92] R. Li, C. D’Agostino, J. McGregor, M. D. Mantle, J. A. Zeitler, and L. F. Gladden, “Mesoscopic structuring and dynamics of alcohol/water solutions probed by terahertz time-domain spectroscopy and pulsed field gradient nuclear magnetic resonance,” *J. Phys. Chem. B*, vol. 118, no. 34, pp. 10156–10166, 2014, doi: 10.1021/jp502799x.

[93] J. W. Bye, C. L. Freeman, J. D. Howard, G. Herz, J. McGregor, and R. J. Falconer, “Analysis of Mesoscopic Structured 2-Propanol/Water Mixtures Using Pressure Perturbation Calorimetry and Molecular Dynamic Simulation,” *J. Solution Chem.*, vol. 46, no. 1, pp. 175–189, 2017, doi: 10.1007/s10953-016-0554-y.

[94] F. Franks and J. E. Desnoyers, *Alcohol-water mixtures revisited*. 2010.

[95] S. Alavi, S. Takeya, R. Ohmura, T. K. Woo, and J. A. Ripmeester, “Hydrogen-bonding alcohol-water interactions in binary ethanol, 1-propanol, and 2-propanol+methane structure II clathrate hydrates,” *J. Chem. Phys.*, vol. 133, no. 7, 2010, doi: 10.1063/1.3469776.

[96] A. Wakisaka and K. Matsuura, “Microheterogeneity of ethanol-water binary mixtures observed at the cluster level,” *J. Mol. Liq.*, vol. 129, no. 1–2, pp. 25–32, 2006, doi: 10.1016/j.molliq.2006.08.010.

[97] N. Nishi *et al.*, “Hydrogen bonding cluster formation and hydrophobic solute association in aqueous solution of ethanol,” *J. Phys. Chem.*, vol. 99, no. 1, pp. 462–468, 1995, doi: 10.1021/j100001a068.

[98] Y. Marcus, “Extraction by subcritical and supercritical water, methanol, ethanol and their mixtures,” *Separations*, vol. 5, no. 1, 2018, doi: 10.3390/separations5010004.

[99] S. Z. Mikhail and W. R. Kimel, “Densities and Viscosities of Methanol-Water Mixtures,” *J. Chem. Eng. Data*, vol. 6, no. 4, pp. 533–537, 1961, doi: 10.1021/je60011a015.

[100] T. A. Scott, “Refractive index of ethanol-water mixtures and density and refractive index of ethanol-water-ethyl ether mixtures,” *J. Phys. Chem.*, vol. 50, no. 5, pp. 406–412, 1946, doi: 10.1021/j150449a003.

[101] P. McKendry, “Energy production from biomass (part 1): overview of biomass,” *Bioresour. Technol*, vol. 83, no. 1, pp. 37–46, 2002, doi: 10.1016/S0960-8524(01)00118-3.

[102] P. A. Owusu and S. Asumadu-Sarkodie, “A review of renewable energy sources, sustainability issues and climate change mitigation,” *Cogent Eng.*, vol. 3, no. 1, 2016, doi: 10.1080/23311916.2016.1167990.

[103] G. W. Huber, S. Iborra, and A. Corma, “Synthesis of transportation fuels from biomass: Chemistry, catalysts, and engineering,” *Chem. Rev.*, vol. 106, no. 9, pp. 4044–4098, 2006, doi: 10.1021/cr068360d.

[104] K. H. Yeoh, S. A. Shafie, K. A. Al-attab, and Z. A. Zainal, “Upgrading agricultural wastes using three different carbonization methods: Thermal, hydrothermal and vapothermal,” *Bioresour. Technol.*, vol. 265, no. June, pp. 365–371, 2018, doi: 10.1016/j.biortech.2018.06.024.

[105] S. N. Naik, V. V. Goud, P. K. Rout, and A. K. Dalai, “Production of first and second generation biofuels: A comprehensive review,” *Renew. Sustain. Energy Rev.*, vol. 14, no. 2, pp. 578–597, 2010, doi: 10.1016/j.rser.2009.10.003.

[106] J. G. Lambert, C. A. S. Hall, S. Balogh, A. Gupta, and M. Arnold, “Energy, EROI and quality of life,” *Energy Policy*, vol. 64, pp. 153–167, 2014, doi: 10.1016/j.enpol.2013.07.001.

[107] BP, “BP Statistical Review of World Energy 2019,” *Stat. Rev. World Energy 2019*, vol. 68, no. 1, pp. 1–64, 2019, doi: 10.1001/jama.1973.03220300055017.

[108] Y. Jiang, E. van der Werf, E. C. van Ierland, and K. J. Keesman, “The potential role of waste biomass in the future urban electricity system,” *Biomass and Bioenergy*, vol. 107, no. October, pp. 182–190, 2017, doi: 10.1016/j.biombioe.2017.10.001.

[109] V. Johansson, M. Lehtveer, and L. Göransson, “Biomass in the electricity system: A complement to variable renewables or a source of negative emissions?,” *Energy*, vol. 168, pp. 532–541, 2019, doi: 10.1016/j.energy.2018.11.112.

[110] A. Corma Canos, S. Iborra, and A. Velty, “Chemical routes for the transformation of biomass into chemicals,” *Chem. Rev.*, vol. 107, no. 6, pp. 2411–2502, 2007, doi: 10.1021/cr050989d.

[111] A. Demirbaş, “Biomass resource facilities and biomass conversion processing for fuels and chemicals,” *Energy Convers. Manag.*, vol. 42, no. 11, pp. 1357–1378, 2001, doi: 10.1016/S0196-8904(00)00137-0.

[112] P. S. Nigam and A. Singh, “Production of liquid biofuels from renewable resources,” *Prog. Energy Combust. Sci.*, vol. 37, no. 1, pp. 52–68, 2011, doi: 10.1016/j.pecs.2010.01.003.

[113] J. Gressel, “Transgenics are imperative for biofuel crops,” *Plant Sci.*, vol. 174, no. 3, pp. 246–263, 2008, doi: 10.1016/j.plantsci.2007.11.009.

[114] K. A. Gray, L. Zhao, and M. Emptage, “Bioethanol,” *Curr. Opin. Chem. Biol.*, vol. 10, no. 2, pp. 141–146, 2006, doi: 10.1016/j.cbpa.2006.02.035.

[115] A. C. Pinto *et al.*, “Biodiesel: An overview,” *J. Braz. Chem. Soc.*, vol. 16, no. 6 B, pp. 1313–1330, 2005, doi: 10.1590/S0103-50532005000800003.

[116] FAO, IFAD, UNICEF, WFP, and WHO, *Food Security and Nutrition in the World the State of Building Climate Resilience for Food Security and Nutrition*. 2018.

[117] O. Bobleter, “Hydrothermal degradation of polymers derived from plants,” *Prog. Polym. Sci.*, vol. 19, no. 5, pp. 797–841, 1994, doi: 10.1016/0079-6700(94)90033-7.

[118] L. R. Lynd *et al.*, “Cellulosic ethanol: status and innovation,” *Curr. Opin. Biotechnol.*, vol. 45, pp. 202–211, 2017, doi: 10.1016/j.copbio.2017.03.008.

[119] B. Salehi, J. Sharifi-rad, A. M. L. Seca, and D. C. G. A. Pinto, “Current Trends on Seaweeds : Looking at Chemical,” *Molecules*, vol. 24, no. 4182, pp. 1–50, 2019, doi:

10.3390/molecules24224182.

[120] N. S. Mat Aron, K. S. Khoo, K. W. Chew, P. L. Show, W. H. Chen, and T. H. P. Nguyen, "Sustainability of the four generations of biofuels – A review," *Int. J. Energy Res.*, vol. 44, no. 12, pp. 9266–9282, 2020, doi: 10.1002/er.5557.

[121] V. S. Sikarwar, M. Zhao, P. S. Fennell, N. Shah, and E. J. Anthony, "Progress in biofuel production from gasification," *Prog. Energy Combust. Sci.*, vol. 61, pp. 189–248, 2017, doi: 10.1016/j.pecs.2017.04.001.

[122] P. J. Chambers and I. S. Pretorius, "Fermenting knowledge: The history of winemaking, science and yeast research," *EMBO Rep.*, vol. 11, no. 12, pp. 914–920, 2010, doi: 10.1038/embor.2010.179.

[123] P. McKendry, "Energy production from biomass (part 2): conversion technologies," *Bioresour. Technol.*, vol. 83, no. July 2002, pp. 47–54, 2002, doi: 10.1016/j.fuel.2011.10.059.

[124] K. F. Adekunle and J. A. Okolie, "A Review of Biochemical Process of Anaerobic Digestion," *Adv. Biosci. Biotechnol.*, vol. 06, no. 03, pp. 205–212, 2015, doi: 10.4236/abb.2015.63020.

[125] R. Millati, R. Wikandari, T. Ariyanto, R. U. Putri, and M. J. Taherzadeh, "Pretreatment technologies for anaerobic digestion of lignocelluloses and toxic feedstocks," *Bioresour. Technol.*, vol. 304, no. October 2019, p. 122998, 2020, doi: 10.1016/j.biortech.2020.122998.

[126] H. B. Goyal, D. Seal, and R. C. Saxena, "Bio-fuels from thermochemical conversion of renewable resources: A review," *Renew. Sustain. Energy Rev.*, vol. 12, no. 2, pp. 504–517, 2008, doi: 10.1016/j.rser.2006.07.014.

[127] N. Saracoglu and G. Gunduz, "Wood pellets - Tomorrow's fuel for Europe," *Energy Sources, Part A Recover. Util. Environ. Eff.*, vol. 31, no. 19, pp. 1708–1718, 2009, doi: 10.1080/15567030802459677.

[128] S. Sharma, R. Meena, A. Sharma, and P. kumar Goyal, "Biomass Conversion Technologies for Renewable Energy and Fuels: A Review Note.," *IOSR J. Mech. Civ. Eng.*, vol. 11, no. 2, pp. 28–35, 2014, doi: 10.9790/1684-11232835.

[129] F. Ma and M. A. Hanna, "Biodiesel production: a review1Journal Series #12109, Agricultural Research Division, Institute of Agriculture and Natural Resources, University of Nebraska–Lincoln.1," *Bioresour. Technol.*, vol. 70, no. 1, pp. 1–15, 1999, doi: 10.1016/s0960-8524(99)00025-5.

[130] L. C. Meher, D. Vidya Sagar, and S. N. Naik, "Technical aspects of biodiesel production

by transesterification - A review," *Renew. Sustain. Energy Rev.*, vol. 10, no. 3, pp. 248–268, 2006, doi: 10.1016/j.rser.2004.09.002.

[131] B. V. Babu, "Biomass pyrolysis: a state-ofthe- art review," *Biofuels, Bioprod. Biorefining*, vol. 2, no. 1, pp. 393–414, 2008, doi: 10.1002/bbb.92.

[132] G. W. Huber, S. Iborra, and A. Corma, "Synthesis of transportation fuels from biomass: Chemistry, catalysts, and engineering," *Chem. Rev.*, vol. 106, no. 9, pp. 4044–4098, 2006, doi: 10.1021/cr068360d.

[133] M. Kumar, A. O. Oyedun, and A. Kumar, "A review on the current status of various hydrothermal technologies on biomass feedstock," *Renew. Sustain. Energy Rev.*, vol. 81, no. May 2017, pp. 1742–1770, 2018, doi: 10.1016/j.rser.2017.05.270.

[134] A. A. Peterson, F. Vogel, R. P. Lachance, M. Fröling, M. J. Antal, and J. W. Tester, "Thermochemical biofuel production in hydrothermal media: A review of sub- and supercritical water technologies," *Energy Environ. Sci.*, vol. 1, no. 1, pp. 32–65, 2008, doi: 10.1039/b810100k.

[135] K. Tekin, S. Karagöz, and S. Bektaş, "A review of hydrothermal biomass processing," *Renew. Sustain. Energy Rev.*, vol. 40, pp. 673–687, 2014, doi: 10.1016/j.rser.2014.07.216.

[136] J. Lu, S. Guo, Y. Fu, and J. Chang, "Catalytic upgrading of bio-oil by simultaneous esterification and alkylation with azeotropic water removal," *Fuel Process. Technol.*, vol. 161, pp. 193–198, 2017, doi: 10.1016/j.fuproc.2016.10.020.

[137] A. Kruse, "Hydrothermal biomass gasification," *J. Supercrit. Fluids*, vol. 47, no. 3, pp. 391–399, 2009, doi: 10.1016/j.supflu.2008.10.009.

[138] P. Zhao, Y. Shen, S. Ge, Z. Chen, and K. Yoshikawa, "Clean solid biofuel production from high moisture content waste biomass employing hydrothermal treatment," *Appl. Energy*, vol. 131, pp. 345–367, 2014, doi: 10.1016/j.apenergy.2014.06.038.

[139] C. He, A. Giannis, and J. Y. Wang, "Conversion of sewage sludge to clean solid fuel using hydrothermal carbonization: Hydrochar fuel characteristics and combustion behavior," *Appl. Energy*, vol. 111, pp. 257–266, 2013, doi: 10.1016/j.apenergy.2013.04.084.

[140] D. Jung, M. Zimmermann, and A. Kruse, "Hydrothermal Carbonization of Fructose: Growth Mechanism and Kinetic Model," *ACS Sustain. Chem. Eng.*, vol. 6, no. 11, pp. 13877–13887, 2018, doi: 10.1021/acssuschemeng.8b02118.

[141] Y. Feng *et al.*, "Fabrication of hydrochar based on food waste (FWHTC) and its application in aqueous solution rare earth ions adsorptive removal: Process, mechanisms

and disposal methodology," *J. Clean. Prod.*, vol. 212, pp. 1423–1433, 2019, doi: 10.1016/j.jclepro.2018.12.094.

[142] P. Parthasarathy and S. K. Narayanan, "Hydrothermal Carbonization (HTC) of Cow Manure: Carbon and Nitrogen Distributions," *Environ. Prog. Sustain. Energy*, vol. 33, no. 3, pp. 676–680, 2014, doi: 10.1002/ep.

[143] E. Danso-Boateng, G. Shama, A. D. Wheatley, S. J. Martin, and R. G. Holdich, "Hydrothermal carbonisation of sewage sludge: Effect of process conditions on product characteristics and methane production," *Bioresour. Technol.*, vol. 177, pp. 318–327, 2015, doi: 10.1016/j.biortech.2014.11.096.

[144] S. M. Heilmann *et al.*, "Hydrothermal carbonization of microalgae," *Biomass and Bioenergy*, vol. 34, no. 6, pp. 875–882, 2010, doi: 10.1016/j.biombioe.2010.01.032.

[145] Z. Yao and X. Ma, "Characteristics of co-hydrothermal carbonization on polyvinyl chloride wastes with bamboo," *Bioresour. Technol.*, vol. 247, no. 381, pp. 302–309, 2018, doi: 10.1016/j.biortech.2017.09.098.

[146] E. Danso-Boateng, R. G. Holdich, G. Shama, A. D. Wheatley, M. Sohail, and S. J. Martin, "Kinetics of faecal biomass hydrothermal carbonisation for hydrochar production," *Appl. Energy*, vol. 111, pp. 351–357, 2013, doi: 10.1016/j.apenergy.2013.04.090.

[147] A. Y. Krylova and V. M. Zaitchenko, "Hydrothermal Carbonization of Biomass: A Review," *Solid Fuel Chem.*, vol. 52, no. 2, pp. 91–103, 2018, doi: 10.3103/S0361521918020076.

[148] M. M. Titirici *et al.*, "Sustainable carbon materials," *Chem. Soc. Rev.*, vol. 44, no. 1, pp. 250–290, 2015, doi: 10.1039/c4cs00232f.

[149] G. K. Parshetti, S. Kent Hoekman, and R. Balasubramanian, "Chemical, structural and combustion characteristics of carbonaceous products obtained by hydrothermal carbonization of palm empty fruit bunches," *Bioresour. Technol.*, vol. 135, pp. 683–689, 2013, doi: 10.1016/j.biortech.2012.09.042.

[150] H. N. Tran, F. C. Huang, C. K. Lee, and H. P. Chao, "Activated carbon derived from spherical hydrochar functionalized with triethylenetetramine: Synthesis, characterizations, and adsorption application," *Green Process. Synth.*, vol. 6, no. 6, pp. 565–576, 2017, doi: 10.1515/gps-2016-0178.

[151] C. Gai *et al.*, "Hydrochar supported bimetallic Ni-Fe nanocatalysts with tailored composition, size and shape for improved biomass steam reforming performance," *Green Chem.*, vol. 20, no. 12, pp. 2788–2800, 2018, doi: 10.1039/c8gc00433a.

[152] A. Kruse and E. Dinjus, “Hot compressed water as reaction medium and reactant. 2. Degradation reactions,” *J. Supercrit. Fluids*, vol. 41, no. 3, pp. 361–379, 2007, doi: 10.1016/j.supflu.2006.12.006.

[153] H. B. Sharma, A. K. Sarmah, and B. Dubey, “Hydrothermal carbonization of renewable waste biomass for solid biofuel production: A discussion on process mechanism, the influence of process parameters, environmental performance and fuel properties of hydrochar,” *Renew. Sustain. Energy Rev.*, vol. 123, no. May 2019, p. 109761, 2020, doi: 10.1016/j.rser.2020.109761.

[154] Andrea Kruse and Thomas A. Zevaco, “Properties of Hydrochar as Function of Feedstock, Reaction Conditions and Post-Treatment,” *energies*, vol. 1, pp. 1–12, 2018, doi: 10.3390/en11030674.

[155] C. Yao *et al.*, “Hydrothermal dehydration of aqueous fructose solutions in a closed system,” *J. Phys. Chem. C*, vol. 111, no. 42, pp. 15141–15145, 2007, doi: 10.1021/jp074188l.

[156] L. J. R. Higgins, A. P. Brown, J. P. Harrington, A. B. Ross, B. Kaulich, and B. Mishra, “Evidence for a core-shell structure of hydrothermal carbon,” *Carbon*, vol. 161, pp. 423–431, 2020, doi: 10.1016/j.carbon.2020.01.060.

[157] Y. Qi, M. Zhang, L. Qi, and Y. Qi, “Mechanism for the formation and growth of carbonaceous spheres from sucrose by hydrothermal carbonization,” *RSC Adv.*, vol. 6, no. 25, pp. 20814–20823, 2016, doi: 10.1039/c5ra26725k.

[158] A. S. Amarasekara, L. T. D. Williams, and C. C. Ebede, “Mechanism of the dehydration of d-fructose to 5-hydroxymethylfurfural in dimethyl sulfoxide at 150 °C: an NMR study,” *Carbohydr. Res.*, vol. 343, no. 18, pp. 3021–3024, 2008, doi: 10.1016/j.carres.2008.09.008.

[159] T. A. Khan, A. S. Saud, S. S. Jamari, M. H. A. Rahim, J. W. Park, and H. J. Kim, “Hydrothermal carbonization of lignocellulosic biomass for carbon rich material preparation: A review,” *Biomass and Bioenergy*, vol. 130, no. August, p. 105384, 2019, doi: 10.1016/j.biombioe.2019.105384.

[160] A. A. Khan, W. de Jong, P. J. Jansens, and H. Spliethoff, “Biomass combustion in fluidized bed boilers: Potential problems and remedies,” *Fuel Process. Technol.*, vol. 90, no. 1, pp. 21–50, 2009, doi: 10.1016/j.fuproc.2008.07.012.

[161] P. Unrean, B. C. Lai Fui, E. Rianawati, and M. Acda, “Comparative techno-economic assessment and environmental impacts of rice husk-to-fuel conversion technologies,” *Energy*, vol. 151, pp. 581–593, 2018, doi: 10.1016/j.energy.2018.03.112.

[162] W. Yang, H. Wang, M. Zhang, J. Zhu, J. Zhou, and S. Wu, “Fuel properties and combustion kinetics of hydrochar prepared by hydrothermal carbonization of bamboo,” *Bioresour. Technol.*, vol. 205, pp. 199–204, 2016, doi: 10.1016/j.biortech.2016.01.068.

[163] Z. Liu, A. Quek, S. Kent Hoekman, and R. Balasubramanian, “Production of solid biochar fuel from waste biomass by hydrothermal carbonization,” *Fuel*, vol. 103, pp. 943–949, 2013, doi: 10.1016/j.fuel.2012.07.069.

[164] Y. Lin, X. Ma, X. Peng, S. Hu, Z. Yu, and S. Fang, “Effect of hydrothermal carbonization temperature on combustion behavior of hydrochar fuel from paper sludge,” *Appl. Therm. Eng.*, vol. 91, pp. 574–582, 2015, doi: 10.1016/j.applthermaleng.2015.08.064.

[165] Y. Lin *et al.*, “Combustion, pyrolysis and char CO2-gasification characteristics of hydrothermal carbonization solid fuel from municipal solid wastes,” *Fuel*, vol. 181, pp. 905–915, 2016, doi: 10.1016/j.fuel.2016.05.031.

[166] A. Gallifuoco, L. Taglieri, and A. A. Papa, “Hydrothermal carbonization of waste biomass to fuel: A novel technique for analyzing experimental data,” *Renew. Energy*, vol. 149, pp. 1254–1260, 2020, doi: 10.1016/j.renene.2019.10.121.

[167] M. Minami, A. S. Goto, T. Omori, T. Ohta, and T. Nakamura, “Comparison of δ13C and 14C activities of CO2 samples combusted in closed-tube and elemental-analyzer systems,” *Nucl. Instruments Methods Phys. Res. Sect. B Beam Interact. with Mater. Atoms*, vol. 268, no. 7–8, pp. 914–918, 2010, doi: 10.1016/j.nimb.2009.10.063.

[168] J. Posom, P. Sirisomboon, and W. Saechua, “Precision test for spectral characteristic of NIR spectroscopy and bomb calorimeter for measuring higher heating value of Leucaena Leucocephala,” *MATEC Web Conf.*, vol. 192, pp. 8–11, 2018, doi: 10.1051/matecconf/201819203049.

[169] T. J. Buckley, “Calculation of higher heating values of biomass materials and waste components from elemental analyses,” *Resour. Conserv. Recycl.*, vol. 5, no. 4, pp. 329–341, 1991, doi: 10.1016/0921-3449(91)90011-C.

[170] A. Friedl, E. Padouvas, H. Rotter, and K. Varmuza, “Prediction of heating values of biomass fuel from elemental composition,” *Anal. Chim. Acta*, vol. 544, no. 1-2 SPEC. ISS., pp. 191–198, 2005, doi: 10.1016/j.aca.2005.01.041.

[171] G. Zhu *et al.*, “Characterization and pelletization of cotton stalk hydrochar from HTC and combustion kinetics of hydrochar pellets by TGA,” *Fuel*, vol. 244, no. November 2018, pp. 479–491, 2019, doi: 10.1016/j.fuel.2019.02.039.

[172] B. Zhang *et al.*, “Hydrothermal carbonization of fruit wastes: A promising technique for

generating hydrochar," *Energies*, vol. 11, no. 8, pp. 1–14, 2018, doi: 10.3390/en11082022.

[173] M. Śliz and M. Wilk, "A comprehensive investigation of hydrothermal carbonization: Energy potential of hydrochar derived from Virginia mallow," *Renew. Energy*, vol. 156, pp. 942–950, 2020, doi: 10.1016/j.renene.2020.04.124.

[174] M. S. Bhatt, "Effect of ash in coal on the performance of coal fired thermal power plants. Part I: Primary energy effects," *Energy Sources, Part A Recover. Util. Environ. Eff.*, vol. 28, no. 1, pp. 25–41, 2006, doi: 10.1080/009083190523235.

[175] N. Abatzoglou, E. Chornet, K. Belkacemi, and R. P. Overend, "Phenomenological kinetics of complex systems: the development of a generalized severity parameter and its application to lignocellulosics fractionation," *Chem. Eng. Sci.*, vol. 47, no. 5, pp. 1109–1122, 1992, doi: https://doi.org/10.1016/0009-2509(92)80235-5.

[176] J. Cai, B. Li, C. Chen, J. Wang, M. Zhao, and K. Zhang, "Hydrothermal carbonization of tobacco stalk for fuel application," *Bioresour. Technol.*, vol. 220, pp. 305–311, 2016, doi: 10.1016/j.biortech.2016.08.098.

[177] M. Pala, I. C. Kantarli, H. B. Buyukisik, and J. Yanik, "Hydrothermal carbonization and torrefaction of grape pomace: A comparative evaluation," *Bioresour. Technol.*, vol. 161, pp. 255–262, 2014, doi: 10.1016/j.biortech.2014.03.052.

[178] M. Santos Santana, R. Pereira Alves, W. M. da Silva Borges, E. Francisquini, and M. C. Guerreiro, "Hydrochar production from defective coffee beans by hydrothermal carbonization," *Bioresour. Technol.*, vol. 300, no. December 2019, p. 122653, 2020, doi: 10.1016/j.biortech.2019.122653.

[179] N. Tippayawong, P. Kantakanit, and S. Koonaphapdeelert, "Characterization of hydrochar from hydrothermal carbonization of maize residues," *Energy Reports*, vol. 6, pp. 114–118, 2020, doi: 10.1016/j.egyr.2019.11.050.

[180] H. S. Kambo and A. Dutta, "Strength, storage, and combustion characteristics of densified lignocellulosic biomass produced via torrefaction and hydrothermal carbonization," *Appl. Energy*, vol. 135, pp. 182–191, 2014, doi: 10.1016/j.apenergy.2014.08.094.

[181] C. He, A. Giannis, and J. Y. Wang, "Conversion of sewage sludge to clean solid fuel using hydrothermal carbonization: Hydrochar fuel characteristics and combustion behavior," *Appl. Energy*, vol. 111, pp. 257–266, 2013, doi: 10.1016/j.apenergy.2013.04.084.

[182] P. Parthasarathy and S. K. Narayanan, "Effect of Hydrothermal Carbonization Reaction

Parameters on," *Environ. Prog. Sustain. Energy*, vol. 33, no. 3, pp. 676–680, 2014, doi: 10.1002/ep.

[183] N. U. Saqib, S. Baroutian, and A. K. Sarmah, "Physicochemical, structural and combustion characterization of food waste hydrochar obtained by hydrothermal carbonization," *Bioresour. Technol.*, vol. 266, no. June, pp. 357–363, 2018, doi: 10.1016/j.biortech.2018.06.112.

[184] D. Kim, K. Yoshikawa, and K. Y. Park, "Characteristics of biochar obtained by hydrothermal carbonization of cellulose for renewable energy," *Energies*, vol. 8, no. 12, pp. 14040–14048, 2015, doi: 10.3390/en81212412.

[185] S. Román *et al.*, "Hydrothermal carbonization: Modeling, final properties design and applications: A review," *Energies*, vol. 11, no. 1, pp. 1–28, 2018, doi: 10.3390/en11010216.

[186] J. G. Speight, "Handbook of Coal Analysis," *Handb. Coal Anal.*, pp. 1–227, 2005, doi: 10.1002/0471718513.

[187] A. M. Smith, S. Singh, and A. B. Ross, "Fate of inorganic material during hydrothermal carbonisation of biomass : Influence of feedstock on combustion behaviour of hydrochar," *FUEL*, vol. 169, pp. 135–145, 2016, doi: 10.1016/j.fuel.2015.12.006.

[188] J. A. Libra *et al.*, "Hydrothermal carbonization of biomass residuals: A comparative review of the chemistry, processes and applications of wet and dry pyrolysis," *Biofuels*, vol. 2, no. 1, pp. 71–106, 2011, doi: 10.4155/bfs.10.81.

[189] M. Sevilla, A. B. Fuertes, and R. Mokaya, "High density hydrogen storage in superactivated carbons from hydrothermally carbonized renewable organic materials," *Energy Environ. Sci.*, vol. 4, no. 4, pp. 1400–1410, 2011, doi: 10.1039/c0ee00347f.

[190] Z. Heidarinejad, M. H. Dehghani, M. Heidari, G. Javedan, I. Ali, and M. Sillanpää, "Methods for preparation and activation of activated carbon: a review," *Environ. Chem. Lett.*, vol. 18, no. 2, pp. 393–415, 2020, doi: 10.1007/s10311-019-00955-0.

[191] A. Kruse and T. A. Zevaco, "Properties of hydrochar as function of feedstock, reaction conditions and post-treatment," *Energies*, vol. 11, no. 3, pp. 1–12, 2018, doi: 10.3390/en11030674.

[192] C. Bouchelta, M. S. Medjram, O. Bertrand, and J. P. Bellat, "Preparation and characterization of activated carbon from date stones by physical activation with steam," *J. Anal. Appl. Pyrolysis*, vol. 82, no. 1, pp. 70–77, 2008, doi: 10.1016/j.jaap.2007.12.009.

[193] M. Han *et al.*, "Bio-butanol sorption performance on novel porous-carbon adsorbents

from corncob prepared via hydrothermal carbonization and post-pyrolysis method," *Sci. Rep.*, vol. 7, no. 1, pp. 1–12, 2017, doi: 10.1038/s41598-017-12062-7.

[194] L. Li, R. Diederick, J. R. V. Flora, and N. D. Berge, "Hydrothermal carbonization of food waste and associated packaging materials for energy source generation," *Waste Manag.*, vol. 33, no. 11, pp. 2478–2492, 2013, doi: 10.1016/j.wasman.2013.05.025.

[195] A. Jain, R. Balasubramanian, and M. P. Srinivasan, "Tuning hydrochar properties for enhanced mesopore development in activated carbon by hydrothermal carbonization," *Microporous Mesoporous Mater.*, vol. 203, no. C, pp. 178–185, 2015, doi: 10.1016/j.micromeso.2014.10.036.

[196] C. Liang, W. Zhao, Z. Song, and S. Xing, "Influence of precursor pH on the structure and photo-Fenton performance of Fe/hydrochar," *RSC Adv.*, vol. 7, no. 56, pp. 35257–35264, 2017, doi: 10.1039/c7ra06194c.

[197] L. F. Philippe, Serp. José, *Carbon Materials for Catalysis*. 2009.

[198] L. Zhou, J. Ma, H. Zhang, Y. Shao, and Y. Li, "Fabrication of magnetic carbon composites from peanut shells and its application as a heterogeneous Fenton catalyst in removal of methylene blue," *Appl. Surf. Sci.*, vol. 324, pp. 490–498, 2015, doi: 10.1016/j.apsusc.2014.10.152.

[199] C. Gai, F. Zhang, Q. Lang, T. Liu, N. Peng, and Z. Liu, "Facile one-pot synthesis of iron nanoparticles immobilized into the porous hydrochar for catalytic decomposition of phenol," *Appl. Catal. B Environ.*, vol. 204, pp. 566–576, 2017, doi: 10.1016/j.apcatb.2016.12.005.

[200] N. Rattanachueskul, A. Saning, S. Kaowphong, N. Chumha, and L. Chuenchom, "Magnetic carbon composites with a hierarchical structure for adsorption of tetracycline, prepared from sugarcane bagasse via hydrothermal carbonization coupled with simple heat treatment process," *Bioresour. Technol.*, vol. 226, pp. 164–172, 2017, doi: 10.1016/j.biortech.2016.12.024.

[201] J. H. Knox, B. Kaur, and G. R. Millward, "Structure and performance of porous graphitic carbon in liquid chromatography," *J. Chromatogr. A*, vol. 352, no. C, pp. 3–25, 1986, doi: 10.1016/S0021-9673(01)83368-9.

[202] F. Schüth, "Endo- and exotemplating to create high-surface-area inorganic materials," *Angew. Chemie - Int. Ed.*, vol. 42, no. 31, pp. 3604–3622, 2003, doi: 10.1002/anie.200300593.

[203] Y. Meng *et al.*, "Ordered mesoporous polymers and homologous carbon frameworks: Amphiphilic surfactant templating and direct transformation," *Angew. Chemie - Int. Ed.*,

vol. 44, no. 43, pp. 7053–7059, 2005, doi: 10.1002/anie.200501561.

[204] M. M. Titirici and M. Antonietti, “Chemistry and materials options of sustainable carbon materials made by hydrothermal carbonization,” *Chem. Soc. Rev.*, vol. 39, no. 1, pp. 103–116, 2010, doi: 10.1039/b819318p.

[205] M. M. Titirici, A. Thomas, and M. Antonietti, “Replication and coating of silica templates by hydrothermal carbonization,” *Adv. Funct. Mater.*, vol. 17, no. 6, pp. 1010–1018, 2007, doi: 10.1002/adfm.200600501.

[206] R. J. White, K. Tauer, M. Antonietti, and M. M. Titirici, “Functional hollow carbon nanospheres by latex templating,” *J. Am. Chem. Soc.*, vol. 132, no. 49, pp. 17360–17363, 2010, doi: 10.1021/ja107697s.

[207] F. Çeçen and Ö. A, *Activated carbon for water and wastewater treatment: integration of adsorption and biological treatment*, no. July. 2012.

[208] S. Leng *et al.*, “Aqueous phase recirculation during hydrothermal carbonization of microalgae and soybean straw: A comparison study,” *Bioresour. Technol.*, vol. 298, no. November 2019, p. 122502, 2020, doi: 10.1016/j.biortech.2019.122502.

[209] D. D. Do, *Adsorption Analysis: Equilibria and Kinetics*, vol. 2, no. Imperial College Press. 1998.

[210] S. Álvarez-Torrellas, M. Muñoz, J. A. Zazo, J. A. Casas, and J. García, “Synthesis of high surface area carbon adsorbents prepared from pine sawdust-Onopordum acanthium L. for nonsteroidal anti-inflammatory drugs adsorption,” *J. Environ. Manage.*, vol. 183, pp. 294–305, 2016, doi: 10.1016/j.jenvman.2016.08.077.

[211] F. L. Slejko, “Adsorption technology : a step-by-step approach to process evaluation and application,” 1985.

[212] Y. S. Ho, “Review of second-order models for adsorption systems,” *J. Hazard. Mater.*, vol. 136, no. 3, pp. 681–689, 2006, doi: 10.1016/j.jhazmat.2005.12.043.

[213] D. Mohan, A. Sarswat, V. K. Singh, M. Alexandre-Franco, and C. U. Pittman, “Development of magnetic activated carbon from almond shells for trinitrophenol removal from water,” *Chem. Eng. J.*, vol. 172, no. 2–3, pp. 1111–1125, 2011, doi: 10.1016/j.cej.2011.06.054.

[214] D. H. Nguyen, H. N. Tran, H. P. Chao, and C. C. Lin, “Effect of nitric acid oxidation on the surface of hydrochars to sorb methylene blue: An adsorption mechanism comparison,” *Adsorpt. Sci. Technol.*, vol. 37, no. 7–8, pp. 607–622, 2019, doi: 10.1177/0263617419867519.

[215] G. D. R. Nogueira, C. R. Duarte, and M. A. S. Barrozo, “Hydrothermal carbonization of

acerola (Malphigia emarginata D.C.) wastes and its application as an adsorbent," *Waste Manag.*, vol. 95, pp. 466–475, 2019, doi: 10.1016/j.wasman.2019.06.039.

[216] A. Ronix *et al.*, "Hydrothermal carbonization of coffee husk: Optimization of experimental parameters and adsorption of methylene blue dye," *J. Environ. Chem. Eng.*, vol. 5, no. 5, pp. 4841–4849, 2017, doi: 10.1016/j.jece.2017.08.035.

[217] R. Khoshbouy, F. Takahashi, and K. Yoshikawa, "Preparation of high surface area sludge-based activated hydrochar via hydrothermal carbonization and application in the removal of basic dye," *Environ. Res.*, vol. 175, no. March, pp. 457–467, 2019, doi: 10.1016/j.envres.2019.04.002.

[218] Y. Xiong, F. Ye, C. Zhang, S. Shen, L. Su, and S. Zhao, "Synthesis of magnetic porous γ-Fe2O3/C@HKUST-1 composites for efficient removal of dyes and heavy metal ions from aqueous solution," *RSC Adv.*, vol. 5, no. 7, pp. 5164–5172, 2015, doi: 10.1039/c4ra12468e.

[219] X. Duan, W. Hong, C. Srinivasakannan, and X. Wang, "Hydrochar silicate composite sorbent via simple hydrothermal carbonization and its application to methylene blue removal," *Mater. Res. Express*, vol. 6, no. 3, 2019, doi: 10.1088/2053-1591/aaf44f.

[220] P. Ma, S. Wang, T. Wang, J. Wu, X. Xing, and X. Zhang, "Effect of bifunctional acid on the porosity improvement of biomass-derived activated carbon for methylene blue adsorption," *Environ. Sci. Pollut. Res.*, vol. 26, no. 29, pp. 30119–30129, 2019, doi: 10.1007/s11356-019-06177-9.

[221] H. Guo *et al.*, "Camellia oleifera seed shell carbon as an efficient renewable bio-adsorbent for the adsorption removal of hexavalent chromium and methylene blue from aqueous solution," *J. Mol. Liq.*, vol. 249, pp. 629–636, 2018, doi: 10.1016/j.molliq.2017.11.096.

[222] B. Li, J. Q. Lv, J. Z. Guo, S. Y. Fu, M. Guo, and P. Yang, "The polyaminocarboxylated modified hydrochar for efficient capturing methylene blue and Cu(II) from water," *Bioresour. Technol.*, vol. 275, no. October 2018, pp. 360–367, 2019, doi: 10.1016/j.biortech.2018.12.083.

[223] M. Rafatullah, O. Sulaiman, R. Hashim, and A. Ahmad, "Adsorption of methylene blue on low-cost adsorbents: A review," *J. Hazard. Mater.*, vol. 177, no. 1–3, pp. 70–80, 2010, doi: 10.1016/j.jhazmat.2009.12.047.

[224] Y. Wang *et al.*, "Hydrothermal synthesis and applications of advanced carbonaceous materials from biomass: a review," *Adv. Compos. Hybrid Mater.*, vol. 3, no. 3, pp. 267–284, 2020, doi: 10.1007/s42114-020-00158-0.

[225] C. H. Collett and J. McGregor, “Things go better with coke: The beneficial role of carbonaceous deposits in heterogeneous catalysis,” *Catal. Sci. Technol.*, vol. 6, no. 2, pp. 363–378, 2016, doi: 10.1039/c5cy01236h.

[226] K. Qian, A. Kumar, H. Zhang, D. Bellmer, and R. Huhnke, “Recent advances in utilization of biochar,” *Renew. Sustain. Energy Rev.*, vol. 42, pp. 1055–1064, 2015, doi: 10.1016/j.rser.2014.10.074.

[227] J. H. Kim, J. Y. Cheon, T. J. Shin, J. Y. Park, and S. H. Joo, “Effect of surface oxygen functionalization of carbon support on the activity and durability of Pt/C catalysts for the oxygen reduction reaction,” *Carbon*, vol. 101, pp. 449–457, 2016, doi: 10.1016/j.carbon.2016.02.014.

[228] C. Falco *et al.*, “Tailoring the porosity of chemically activated hydrothermal carbons: Influence of the precursor and hydrothermal carbonization temperature,” *Carbon*, vol. 62, pp. 346–355, 2013, doi: 10.1016/j.carbon.2013.06.017.

[229] X. Qi, N. Liu, and Y. Lian, “Carbonaceous microspheres prepared by hydrothermal carbonization of glucose for direct use in catalytic dehydration of fructose,” *RSC Adv.*, vol. 5, no. 23, pp. 17526–17531, 2015, doi: 10.1039/c4ra15296d.

[230] B. Hu, K. Wang, L. Wu, S. H. Yu, M. Antonietti, and M. M. Titirici, “Engineering carbon materials from the hydrothermal carbonization process of biomass,” *Adv. Mater.*, vol. 22, no. 7, pp. 813–828, 2010, doi: 10.1002/adma.200902812.

[231] L. Zhou, M. Cai, X. Zhang, N. Cui, G. Chen, and G. Y. Zou, “Key role of hydrochar in heterogeneous photocatalytic degradation of sulfamethoxazole using Ag3PO4-based photocatalysts,” *RSC Adv.*, vol. 9, no. 61, pp. 35636–35645, 2019, doi: 10.1039/c9ra07843f.

[232] C. Liu, N. Li, L. Peng, W. Zhong, L. Mao, and D. Yin, “Hydrothermal Carbonization of Renewable Natural Plants as Superior Metal-Free Catalysts for Aerobic Oxidative Coupling of Amines to Imines,” *ACS Sustain. Chem. Eng.*, vol. 8, no. 30, pp. 11404–11412, 2020, doi: 10.1021/acssuschemeng.0c03757.

[233] X. Ge, M. Ge, X. Chen, C. Qian, X. Liu, and S. Zhou, “Facile synthesis of hydrochar supported copper nanocatalyst for Ullmann C[sbnd]N coupling reaction in water,” *Mol. Catal.*, vol. 484, no. November 2019, p. 110726, 2019, doi: 10.1016/j.mcat.2019.110726.

[234] M. J. Jiménez Toro *et al.*, “Preparation and Optimization of Macroalgae-Derived Solid Acid Catalysts,” *Waste and Biomass Valorization*, vol. 10, no. 4, pp. 805–816, 2019, doi: 10.1007/s12649-017-0101-0.

[235] P. Wataniyakul, P. Boonnoun, A. T. Quitain, T. Kida, N. Laosiripojana, and A. Shotipruk, “Preparation of hydrothermal carbon acid catalyst from defatted rice bran,” *Ind. Crops Prod.*, vol. 117, no. February, pp. 286–294, 2018, doi: 10.1016/j.indcrop.2018.03.002.

[236] J. Fang, L. Zhan, Y. Sik, and B. Gao, “Journal of Industrial and Engineering Chemistry Minireview of potential applications of hydrochar derived from hydrothermal carbonization of biomass,” *J. Ind. Eng. Chem.*, vol. 57, pp. 15–21, 2018, doi: 10.1016/j.jiec.2017.08.026.

[237] N. Eibisch, R. Schroll, and R. Fuß, “Effect of pyrochar and hydrochar amendments on the mineralization of the herbicide isoproturon in an agricultural soil,” *Chemosphere*, vol. 134, pp. 528–535, 2015, doi: 10.1016/j.chemosphere.2014.11.074.

[238] M. Hussain *et al.*, *Biochar for crop production: potential benefits and risks*, vol. 17, no. 3. Journal of Soils and Sediments, 2017.

[239] S. Schimmelpfennig, C. Müller, L. Grünhage, C. Koch, and C. Kammann, “Biochar, hydrochar and uncarbonized feedstock application to permanent grassland-Effects on greenhouse gas emissions and plant growth,” *Agric. Ecosyst. Environ.*, vol. 191, pp. 39–52, 2014, doi: 10.1016/j.agee.2014.03.027.

[240] I. Bargmann, M. C. Rillig, A. Kruse, J. M. Greef, and M. Kücke, “Effects of hydrochar application on the dynamics of soluble nitrogen in soils and on plant availability,” *J. Plant Nutr. Soil Sci.*, vol. 177, no. 1, pp. 48–58, 2014, doi: 10.1002/jpln.201300069.

[241] M. Härmas, T. Thomberg, T. Romann, A. Jänes, and E. Lust, “Carbon for Energy Storage Derived from Granulated White Sugar by Hydrothermal Carbonization and Subsequent Zinc Chloride Activation,” *J. Electrochem. Soc.*, vol. 164, no. 9, pp. A1866–A1872, 2017, doi: 10.1149/2.0681709jes.

[242] B. E. Conway, “Electrochemical supercapacitors: scientific fundamentals and technological applications,” *Springer, New York*, 1999, doi: 10.1016/0306-4522(88)90044-9.

[243] Y. Wu *et al.*, “Preparation of porous carbons by hydrothermal carbonization and KOH activation of lignite and their performance for electric double layer capacitor,” *Electrochim. Acta*, vol. 252, pp. 397–407, 2017, doi: 10.1016/j.electacta.2017.08.176.

[244] L. Pang *et al.*, “A new route for the fabrication of corn starch-based porous carbon as electrochemical supercapacitor electrode material,” *Colloids Surfaces A Physicochem. Eng. Asp.*, vol. 504, pp. 26–33, 2016, doi: 10.1016/j.colsurfa.2016.05.049.

[245] H. Liu, C. Song, L. Zhang, J. Zhang, H. Wang, and D. P. Wilkinson, “A review of anode

catalysis in the direct methanol fuel cell," *J. Power Sources*, vol. 155, no. 2, pp. 95–110, 2006, doi: 10.1016/j.jpowsour.2006.01.030.

[246] T. Onodera, S. Suzuki, T. Mizukami, and H. Kanzaki, "Enhancement of oxygen reduction activity with addition of carbon support for non-precious metal nitrogen doped carbon catalyst," *J. Power Sources*, vol. 196, no. 19, pp. 7994–7999, 2011, doi: 10.1016/j.jpowsour.2011.05.041.

[247] S. R. Guo, J. Y. Gong, P. Jiang, M. Wu, Y. Lu, and S. H. Yu, "Biocompatible, luminescent Silver@Phenol formaldehyde resin core/shell nanospheres: Large-scale synthesis and application for in vivo bioimaging," *Adv. Funct. Mater.*, vol. 18, no. 6, pp. 872–879, 2008, doi: 10.1002/adfm.200701440.

[248] W. N. Yun Wang, Hui Want, Hongfei Lin, Ying Zheng, Jianshe Zhao, Andre Pelletier, Kecheng Li, "Effects of solvents and catalysts in liquefaction of pinewood sawdust for the production of bio-oils," *Biomass and Bioenergy*, no. 59, pp. 158–167, 2013.

[249] P. Nantnarphirom, W. Kraithong, N. Viriya-Empikul, and A. Eiad-Ua, "Organosolv pretreatment transformation process of bagasse to porous carbon material," *Mater. Today Proc.*, vol. 4, no. 5, pp. 6261–6266, 2017, doi: 10.1016/j.matpr.2017.06.125.

[250] E. E. Xiaomin Yan, Baofeng Wang, Jinjun Zhang, "Liquefaction of cotton seed in sub-critical water/ethanol with modified medical stone for bio-oil," *Bioresour. Technol*, no. 197, pp. 120–127, 2015.

[251] W. Yang, T. Shimanouchi, and Y. Kimura, "Characterization of hydrochar prepared from hydrothermal carbonization of peels of Carya cathayensis sarg," *Desalin. Water Treat.*, vol. 53, no. 10, pp. 2831–2838, 2015, doi: 10.1080/19443994.2014.931537.

[252] X. Z. Yuan, H. Li, G. M. Zeng, J. Y. Tong, and W. Xie, "Sub- and supercritical liquefaction of rice straw in the presence of ethanol-water and 2-propanol-water mixture," *Energy*, vol. 32, no. 11, pp. 2081–2088, 2007, doi: 10.1016/j.energy.2007.04.011.

[253] Y. Li *et al.*, "Facile extraction of cellulose nanocrystals from wood using ethanol and peroxide solvothermal pretreatment followed by ultrasonic nanofibrillation," *Green Chem.*, vol. 18, no. 4, pp. 1010–1018, 2016, doi: 10.1039/c5gc02576a.

[254] S. Feng, R. Wei, M. Leitch, and C. C. Xu, "Comparative study on lignocellulose liquefaction in water, ethanol, and water/ethanol mixture: Roles of ethanol and water," *Energy*, vol. 155, pp. 234–241, 2018, doi: 10.1016/j.energy.2018.05.023.

[255] C.J. Brinker; G. W. Scherer, "Sol-Gel_Science_The_physics_and_chemistry_of_sol-gel_processing_-_Brinker_1990.pdf." p. 462, 1990, doi: 10.1016/S0254-

0584(02)00315-2.

[256] R. Nosrati and U. Berardi, “Long-term performance of aerogel-enhanced materials,” *Energy Procedia*, vol. 132, pp. 303–308, 2017, doi: 10.1016/j.egypro.2017.09.733.

[257] L. L. Hench and J. K. West, “The Sol-Gel Process,” *Chem. Rev.*, vol. 90, no. 1, pp. 33–72, 1990, doi: 10.1021/cr00099a003.

[258] M. Hua, S. Zhang, B. Pan, W. Zhang, L. Lv, and Q. Zhang, “Heavy metal removal from water / wastewater by nanosized metal oxides : A review,” vol. 212, pp. 317–331, 2012, doi: 10.1016/j.jhazmat.2011.10.016.

[259] Q. Liu *et al.*, “One-pot synthesis of ordered mesoporous Ni-V-Al catalysts for CO methanation,” *J. Catal.*, vol. 326, pp. 127–138, 2015, doi: 10.1016/j.jcat.2015.04.003.

[260] N. Pal and A. Bhaumik, “Ordered mesoporous ternary mixed oxide materials as potential adsorbent of biomolecules,” *Chem. Phys. Lett.*, vol. 535, pp. 69–74, 2012, doi: 10.1016/j.cplett.2012.03.037.

[261] M. Peña Alvarez *et al.*, “Ternary oxide nanostructured materials for supercapacitors: a review,” *Faraday Discuss.*, vol. 4, no. 8, pp. 1166–1169, 2014, doi: 10.1039/b000000x.

[262] K. Pielichowski, J. Njuguna, B. Janowski, and J. Pielichowski, “Polyhedral oligomeric silsesquioxanes (POSS)-containing nanohybrid polymers,” *Adv. Polym. Sci.*, vol. 201, no. 1, pp. 225–296, 2006, doi: 10.1007/12_077.

[263] U. Schubert, “Silica-based and transition metal-based inorganic-organic hybrid materials - A comparison,” *J. Sol-Gel Sci. Technol.*, vol. 26, no. 1–3, pp. 47–55, 2003, doi: 10.1023/A:1020729100148.

[264] C. Sanchez, K. J. Shea, S. Kitagawa, and U. Schubert, “Hybrid materials themed issue Cluster-based inorganic – organic hybrid materialsw,” *Chem. Soc. Rev.*, vol. 40, no. 2, pp. 453–1152, 2011, doi: 10.1039/c0cs00009d.

[265] E. J. A. Pope and J. D. Mackenzie, “Sol-gel processing of silica. II. The role of the catalyst,” *J. Non. Cryst. Solids*, vol. 87, no. 1–2, pp. 185–198, 1986, doi: 10.1016/S0022-3093(86)80078-3.

[266] D. P. Debecker, S. Le Bras, C. Boissière, A. Chaumonnot, and C. Sanchez, “Aerosol processing: A wind of innovation in the field of advanced heterogeneous catalysts,” *Chem. Soc. Rev.*, vol. 47, no. 11, pp. 4112–4155, 2018, doi: 10.1039/c7cs00697g.

[267] K. Okuyama, M. Abdullah, I. W. Lenggoro, and F. Iskandar, “Preparation of functional nanostructured particles by spray drying,” *Adv. Powder Technol.*, vol. 17, no. 6, pp. 587–611, 2006, doi: 10.1163/156855206778917733.

[268] F. Iskandar, H. Chang, and K. Okuyama, “Preparation of microencapsulated powders

by an aerosol spray method and their optical properties," *Adv. Powder Technol.*, vol. 14, no. 3, pp. 349–367, 2003, doi: 10.1163/15685520360685983.

[269] D. Grosso, G. J. D. A. A. Soler Illia, E. L. Crepaldi, B. Charleux, and C. Sanchez, "Nanocrystalline transition-metal oxide spheres with controlled multi-scale porosity," *Adv. Funct. Mater.*, vol. 13, no. 1, pp. 37–42, 2003, doi: 10.1002/adfm.200390002.

[270] Y. Lu, H. Fan, A. Stump, T. L. Ward, T. Rieker, and C. J. Brinker, "Aerosol-assisted self-assembly of mesostructured spherical nanoparticles," *Nature*, vol. 398, no. 6724, pp. 223–226, 1999, doi: 10.1038/18410.

[271] S. Pega, C. Boissière, D. Grosso, T. Azaïs, A. Chaumonnot, and C. Sanchez, "Direct Aerosol Synthesis of Large-Pore Amorphous Mesostructured Aluminosilicates with Superior Acid-Catalytic Properties," *Angew. Chemie - Int. Ed.*, vol. 48, no. 15, pp. 2784–2787, 2009, doi: 10.1002/anie.200805217.

[272] V. Smeets *et al.*, "Aerosol Route to TiO 2 -SiO 2 Catalysts with Tailored Pore Architecture and High Epoxidation Activity," *Chem. Mater.*, vol. 31, no. 5, pp. 1610–1619, 2019, doi: 10.1021/acs.chemmater.8b04843.

[273] S. H. Kim, B. Y. H. Liu, and M. R. Zachariah, "Ultrahigh surface area nanoporous silica particles via an aero-sol-gel process," *Langmuir*, vol. 20, no. 7, pp. 2523–2526, 2004, doi: 10.1021/la034864k.

[274] S. Maksasithorn, P. Praserthdam, K. Suriye, and D. P. Debecker, "Preparation of super-microporous WO3-SiO2 olefin metathesis catalysts by the aerosol-assisted sol-gel process," *Microporous Mesoporous Mater.*, vol. 213, pp. 125–133, 2015, doi: 10.1016/j.micromeso.2015.04.020.

[275] D. P. Debecker *et al.*, "Aerosol route to nanostructured WO3-SiO2-Al 2O3 metathesis catalysts: Toward higher propene yield," *Appl. Catal. A Gen.*, vol. 470, pp. 458–466, 2014, doi: 10.1016/j.apcata.2013.06.041.

[276] N. C. Ejiofor, I. E. Ezeagu, M. B. Ayoola, and E. A. Umera, "Determination of the Chemical Composition of Avocado (Persea Americana) Seed," *Adv. Food Technol. Nutr. Sci. - Open J.*, vol. SE, no. 2, pp. S51–S55, 2018, doi: 10.17140/aftnsoj-se-2-107.

[277] W. D. Armstrong, J. C. Rogler, and W. R. Featherston, "Effect of Tannin Extraction on the Performance of Chicks Fed Bird Resistant Sorghum Grain Diets," *Poult. Sci.*, vol. 53, no. 2, pp. 714–720, 1974, doi: 10.3382/ps.0530714.

[278] A. H. Uddin, R. S. Khalid, M. Alaama, A. M. Abdualkader, A. Kasmuri, and S. A. Abbas, "Comparative study of three digestion methods for elemental analysis in traditional medicine products using atomic absorption spectrometry," *J. Anal. Sci.*

Technol., vol. 7, no. 1, 2016, doi: 10.1186/s40543-016-0085-6.

[279] I. Noda, "Techniques of two-dimensional (2D) correlation spectroscopy useful in life," vol. 4, pp. 109–127, 2015, doi: 10.3233/BSI-150105.

[280] I. Noda, "Determination of two-dimensional correlation spectra using the hubert transform," *Appl. Spectrosc.*, vol. 54, no. 7, pp. 994–998, 2000, doi: 10.1366/0003702001950472.

[281] M. A. Farrukh, *Advanced Aspects of Spectroscopy*. 2012.

[282] D. W. MOELLER, "Electromagnetic Radiation," *Environ. Heal.*, vol. 1, pp. 266–294, 2020, doi: 10.2307/j.ctv1cbn3qq.16.

[283] G. M. do Nascimento, *Raman Spectroscopy*. IntechOpen, 2018.

[284] R. Mendelsohn, "Fourier Transform Infrared Spectrometry, 2nd ed By Peter R. Griffiths (University of Idaho, Moscow) and James A. De Haseth (University of Georgia, Athens). J. Wiley & Sons, Inc.: Hoboken, NJ. 2007. xviii + 530 pp. $ 115. ISBN 978-0-471-19404-0.," *J. Am. Chem. Soc.*, vol. 129, no. 43, p. 13358, Oct. 2007, doi: 10.1021/ja076968d.

[285] J. R. Ferraro, K. Nakamoto, and C. W. Brown, *Introductory Raman Spectroscopy: Second Edition*. 2003.

[286] M. Tasumi, P. A. Sakamoto, and S. Ochiai, *Introduction to Experimental Infrared Spectroscopy : Fundamentals and Practical Methods*. New York, UNITED KINGDOM: John Wiley & Sons, Incorporated, 2014.

[287] B. H. Stuart, *Infrared Spectroscopy : Fundamentals and Applications*. Hoboken, UNITED KINGDOM: John Wiley & Sons, Incorporated, 2004.

[288] O. J. Rees, *Fourier Transform Infrared Spectroscopy : Developments, Techniques and Applications*. New York, UNITED STATES: Nova Science Publishers, Incorporated, 2010.

[289] P. Vandenabeele and D. J. Ando, *Practical Raman Spectroscopy : An Introduction*. Hoboken, UNITED KINGDOM: John Wiley & Sons, Incorporated, 2013.

[290] P. Larkin, *Infrared and Raman Spectroscopy : Principles and Spectral Interpretation*. Saint Louis, UNITED STATES: Elsevier, 2017.

[291] E. Vöhringer-Martinez *et al.*, "Hydrogen bond dynamics of superheated water and methanol by ultrafast IR-pump and EUV-photoelectron probe spectroscopy," *Phys. Chem. Chem. Phys.*, vol. 16, no. 36, pp. 19365–19375, 2014, doi: 10.1039/c4cp02063d.

[292] A. A. Kananenka and J. L. Skinner, "Fermi resonance in OH-stretch vibrational spectroscopy of liquid water and the water hexamer," *J. Chem. Phys.*, vol. 148, no. 24,

2018, doi: 10.1063/1.5037113.

[293] P. Laurson, P. Raudsepp, H. Kaldmäe, A. Kikas, and U. Mäeorg, “The deconvolution of FTIR-ATR spectra to five Gaussians for detection of small changes in plant-water clusters,” *AIP Adv.*, vol. 10, no. 8, 2020, doi: 10.1063/5.0011700.

[294] M. Chaplin, “Water Absorption Spectrum,” *Web*, no. Ldl, pp. 1–6, 2013, [Online]. Available: http://www.lsbu.ac.uk/water/vibrat.

[295] Q. Sun, “The Raman OH stretching bands of liquid water,” *Vib. Spectrosc.*, vol. 51, no. 2, pp. 213–217, 2009, doi: 10.1016/j.vibspec.2009.05.002.

[296] S. Burikov, T. Dolenko, S. Patsaeva, Y. Starokurov, and V. Yuzhakov, “Raman and IR spectroscopy research on hydrogen bonding in water-ethanol systems,” *Mol. Phys.*, vol. 108, no. 18, pp. 2427–2436, 2010, doi: 10.1080/00268976.2010.516277.

[297] H. J. Bakker and J. L. Skinner, “Vibrational spectroscopy as a probe of structure and dynamics in liquid water,” *Chem. Rev.*, vol. 110, no. 3, pp. 1498–1517, 2010, doi: 10.1021/cr9001879.

[298] D. N. Glew and N. S. Rath, “ H 2 O, HDO, and CH 3 OH Infrared Spectra and Correlation with Solvent Basicity and Hydrogen Bonding ,” *Can. J. Chem.*, vol. 49, no. 6, pp. 837–856, 1971, doi: 10.1139/v71-142.

[299] C. I. Ratcliffe and D. E. Irish, “Vibrational spectral studies of solutions at elevated temperatures and pressures. 5. Raman studies of liquid water up to 300°C,” *J. Phys. Chem.*, vol. 86, no. 25, pp. 4897–4905, 1982, doi: 10.1021/j100222a013.

[300] H. Inomata, Y. Yagi, M. Saito, and S. Saito, “Density dependence of the molar absorption coefficient-Application of the beer-lambert law to supercritical C02-Naphthalene mixture,” *J. Supercrit. Fluids*, vol. 6, no. 4, pp. 237–240, 1993, doi: 10.1016/0896-8446(93)90033-T.

[301] B. Yang, X. Cao, H. Lang, S. Wang, and C. Sun, “Study on hydrogen bonding network in aqueous methanol solution by Raman spectroscopy,” *Spectrochim. Acta - Part A Mol. Biomol. Spectrosc.*, vol. 225, p. 117488, 2020, doi: 10.1016/j.saa.2019.117488.

[302] T. Pradhan, P. Ghoshal, and R. Biswas, “Structural transition in alcohol-water binary mixtures: A spectroscopic study,” *J. Chem. Sci.*, vol. 120, no. 2, pp. 275–287, 2008, doi: 10.1007/s12039-008-0033-0.

[303] M. K. Ahmed, S. Ali, and E. Wojcik, “The C-O stretching infrared band as a probe of hydrogen bonding in ethanol-water and methanol-water mixtures,” *Spectrosc. Lett.*, vol. 45, no. 6, pp. 420–423, 2012, doi: 10.1080/00387010.2011.627529.

[304] M. Freda, A. Piluso, A. Santucci, and P. Sassi, “Transmittance Fourier transform

infrared spectra of liquid water in the whole mid-infrared region: Temperature dependence and structural analysis," *Appl. Spectrosc.*, vol. 59, no. 9, pp. 1155–1159, 2005, doi: 10.1366/0003702055012591.

[305] A. Brangule and K. A. Gross, "Importance of FTIR spectra deconvolution for the analysis of amorphous calcium phosphates," *IOP Conf. Ser. Mater. Sci. Eng.*, vol. 77, no. 1, 2015, doi: 10.1088/1757-899X/77/1/012027.

[306] D. M. Byler and H. Susi, "Examination of the secondary structure of proteins by deconvolved FTIR spectra," *Biopolymers*, vol. 25, no. 3, pp. 469–487, 1986, doi: 10.1002/bip.360250307.

[307] N. Primeau, C. Vautey, and M. Langlet, "The effect of thermal annealing on aerosol-gel deposited SiO2 films: A FTIR deconvolution study," *Thin Solid Films*, vol. 310, no. 1–2, pp. 47–56, 1997, doi: 10.1016/S0040-6090(97)00340-4.

[308] S. M. Matt and D. Ben-Amotz, "Influence of Intermolecular Coupling on the Vibrational Spectrum of Water," *J. Phys. Chem. B*, vol. 122, no. 21, pp. 5375–5380, 2018, doi: 10.1021/acs.jpcb.7b11063.

[309] S. J. Barlow, G. V. Bondarenko, Y. E. Gorbaty, T. Yamaguchi, and M. Poliakoff, "An IR study of hydrogen bonding in liquid and supercritical alcohols," *J. Phys. Chem. A*, vol. 106, no. 43, pp. 10452–10460, 2002, doi: 10.1021/jp0135095.

[310] A. Dawes, N. J. Mason, and H. J. Fraser, "Using the C-O stretch to unravel the nature of hydrogen bonding in low-temperature solid methanol-water condensates," *Phys. Chem. Chem. Phys.*, vol. 18, no. 2, pp. 1245–1257, 2015, doi: 10.1039/c5cp05299h.

[311] S. Sinha, P. M. Gharat, H. Pal, and S. Dutta Choudhury, "Lumichrome tautomerism in alcohol-water mixtures: Effect of carbon chain length and mole fraction of alcohols," *J. Mol. Liq.*, vol. 314, p. 113621, 2020, doi: 10.1016/j.molliq.2020.113621.

[312] I. Doroshenko, V. Pogorelov, and V. Sablinskas, "Infrared Absorption Spectra of Monohydric Alcohols," *Dataset Pap. Chem.*, vol. 2013, no. November 2015, pp. 1–6, 2013, doi: 10.7167/2013/329406.

[313] P. Giraudeau and L. Frydman, "Ultrafast 2D NMR: An emerging tool in analytical spectroscopy," *Annu. Rev. Anal. Chem.*, vol. 7, pp. 129–161, 2014, doi: 10.1146/annurev-anchem-071213-020208.

[314] I. Noda, "Two-dimensional correlation spectroscopy: Applications in vibrational and optical spectroscopy," *Nova*, vol. 77, pp. 239–244, Jan. 2004.

[315] P. D. B. Harrington, A. Urbas, and P. J. Tandler, "Two-dimensional correlation analysis," pp. 149–174, 2000.

[316] R. Li, C. D'Agostino, J. McGregor, M. D. Mantle, J. A. Zeitler, and L. F. Gladden, "Mesoscopic structuring and dynamics of alcohol/water solutions probed by terahertz time-domain spectroscopy and pulsed field gradient nuclear magnetic resonance," *J. Phys. Chem. B*, vol. 118, no. 34, pp. 10156–10166, 2014, doi: 10.1021/jp502799x.

[317] WRAP, "Reducing household bakery waste," *Final Rep.*, no. December 2010, pp. 1–151, 2011, [Online]. Available: http://www.wrap.org.uk/sites/files/wrap/Research Bakery Report final.pdf.

[318] W. Pietrzak and J. Kawa-Rygielska, "Ethanol fermentation of waste bread using granular starch hydrolyzing enzyme: Effect of raw material pretreatment," *Fuel*, vol. 134, pp. 250–256, 2014, doi: 10.1016/j.fuel.2014.05.081.

[319] C. M. Rosell, *The Science of Doughs and Bread Quality*. Elsevier Inc., 2011.

[320] Y. Meng, Y. Zhou, Y. Shao, D. Zhou, D. Shen, and Y. Long, "Evaluating the potential of the microwave hydrothermal method for valorizing food waste by producing 5-hydroxymethylfurfural," *Fuel*, vol. 306, no. June, p. 121769, 2021, doi: 10.1016/j.fuel.2021.121769.

[321] M. Panahi-Kalamuei, O. Amiri, and M. Salavati-Niasari, "Green hydrothermal synthesis of high quality single and few layers graphene sheets by bread waste as precursor," *J. Mater. Res. Technol.*, vol. 9, no. 3, pp. 2679–2690, 2020, doi: 10.1016/j.jmrt.2020.01.001.

[322] F. Güleç, L. M. G. Riesco, O. Williams, E. T. Kostas, A. Samson, and E. Lester, "Hydrothermal conversion of different lignocellulosic biomass feedstocks – Effect of the process conditions on hydrochar structures," *Fuel*, vol. 302, no. April, p. 121166, 2021, doi: 10.1016/j.fuel.2021.121166.

[323] S. E. Hunter and P. E. Savage, "Acid-catalyzed reactions in carbon dioxide-enriched high-temperature liquid water," *Ind. Eng. Chem. Res.*, vol. 42, no. 2, pp. 290–294, 2003, doi: 10.1021/ie020565z.

[324] Q. V. Bach, K. Q. Tran, and Ø. Skreiberg, "Accelerating wet torrefaction rate and ash removal by carbon dioxide addition," *Fuel Process. Technol.*, vol. 140, pp. 297–303, 2015, doi: 10.1016/j.fuproc.2015.09.013.

[325] K. Saravanan, B. Tyagi, R. S. Shukla, and H. C. Bajaj, "Esterification of palmitic acid with methanol over template-assisted mesoporous sulfated zirconia solid acid catalyst," *Appl. Catal. B Environ.*, vol. 172–173, pp. 108–115, 2015, doi: 10.1016/j.apcatb.2015.02.014.

[326] S. Zhang *et al.*, "Bamboo derived hydrochar microspheres fabricated by acid-assisted

hydrothermal carbonization," *Chemosphere*, vol. 263, p. 128093, 2021, doi: 10.1016/j.chemosphere.2020.128093.

[327] A. Demirbas, "Calculation of higher heating values of fatty acids," *Energy Sources, Part A Recover. Util. Environ. Eff.*, vol. 38, no. 18, pp. 2693–2697, 2016, doi: 10.1080/15567036.2015.1115924.

[328] M. Heidari, O. Norouzi, S. Salaudeen, B. Acharya, and A. Dutta, "Prediction of Hydrothermal Carbonization with Respect to the Biomass Components and Severity Factor," *Energy and Fuels*, vol. 33, no. 10, pp. 9916–9924, 2019, doi: 10.1021/acs.energyfuels.9b02291.

[329] M. Naderi and M. Vesali-Naseh, "Hydrochar-derived fuels from waste walnut shell through hydrothermal carbonization: characterization and effect of processing parameters," *Biomass Convers. Biorefinery*, 2019, doi: 10.1007/s13399-019-00513-2.

[330] F. Gao, G. Shao, J. Qu, S. Lv, Y. Li, and M. Wu, "Tailoring of porous and nitrogen-rich carbons derived from hydrochar for high-performance supercapacitor electrodes," *Electrochim. Acta*, vol. 155, pp. 201–208, 2015, doi: 10.1016/j.electacta.2014.12.069.

[331] Q. Wu, W. Li, S. Liu, and C. Jin, "Hydrothermal synthesis of N-doped spherical carbon from carboxymethylcellulose for CO2capture," *Appl. Surf. Sci.*, vol. 369, pp. 101–107, 2016, doi: 10.1016/j.apsusc.2016.02.022.

[332] E. J. Lynch, F. Dal Bello, E. M. Sheehan, K. D. Cashman, and E. K. Arendt, "Fundamental studies on the reduction of salt on dough and bread characteristics," *Food Res. Int.*, vol. 42, no. 7, pp. 885–891, 2009, doi: 10.1016/j.foodres.2009.03.014.

[333] R. G. O. Araujo, S. M. Macedo, M. D. G. A. Korn, M. F. Pimentel, R. E. Bruns, and S. L. C. Ferreira, "Mineral composition of wheat flour consumed in Brazilian cities," *J. Braz. Chem. Soc.*, vol. 19, no. 5, pp. 935–942, 2008, doi: 10.1590/S0103-50532008000500019.

[334] J. Kalembkiewicz and U. Chmielarz, "Ashes from co-combustion of coal and biomass: New industrial wastes," *Resour. Conserv. Recycl.*, vol. 69, pp. 109–121, 2012, doi: 10.1016/j.resconrec.2012.09.010.

[335] A. Hammer, N. Fedelich, M. Nijman, M. Ag, and C.- Schwerzenbach, "Compositional Analysis of Complex Materials with TGA-GC / MS," vol. 39, no. 2001, p. 8603, [Online]. Available: http://www.stk-online.ch/Basel 2015/talks/10 Hammer.pdf.

[336] M. Heidari, S. Salaudeen, A. Dutta, and B. Acharya, *Effects of Process Water Recycling and Particle Sizes on Hydrothermal Carbonization of Biomass*, vol. 32, no. 11. 2018.

[337] K. K. Chittur, "FTIR/ATR for protein adsorption to biomaterial surfaces," *Biomaterials*,

vol. 19, no. 4–5, pp. 357–369, 1998, doi: 10.1016/S0142-9612(97)00223-8.

[338] M. Al-Mahsaneh, M. Aljarrah, T. Rababah, and M. Alu'Datt, "Using MR-FTIR and Texture Profile to Track the Effect of Storage Time and Temperature on Pita Bread Staling," *J. Food Qual.*, vol. 2018, 2018, doi: 10.1155/2018/8252570.

[339] X. Dong, S. Guo, H. Wang, Z. Wang, and X. Gao, "Physicochemical characteristics and FTIR-derived structural parameters of hydrochar produced by hydrothermal carbonisation of pea pod (Pisum sativum Linn.) waste," *Biomass Convers. Biorefinery*, vol. 9, no. 3, pp. 531–540, 2019, doi: 10.1007/s13399-018-0363-1.

[340] L. F. Silva *et al.*, "Polarized Raman and Infrared Spectroscopy and ab Initio Calculation of Palmitic and Stearic Acids in the Bm and C Forms," *J. Phys. Chem. A*, vol. 121, no. 25, pp. 4830–4842, 2017, doi: 10.1021/acs.jpca.7b04117.

[341] M. E. Fernandez, B. Ledesma, S. Román, P. R. Bonelli, and A. L. Cukierman, "Development and characterization of activated hydrochars from orange peels as potential adsorbents for emerging organic contaminants," *Bioresour. Technol.*, vol. 183, pp. 221–228, 2015, doi: 10.1016/j.biortech.2015.02.035.

[342] S. Kang, X. Li, J. Fan, and J. Chang, "Characterization of hydrochars produced by hydrothermal carbonization of lignin, cellulose, d-xylose, and wood meal," *Ind. Eng. Chem. Res.*, vol. 51, no. 26, pp. 9023–9031, 2012, doi: 10.1021/ie300565d.

[343] N. Saha, A. Saba, and M. T. Reza, "Effect of hydrothermal carbonization temperature on pH, dissociation constants, and acidic functional groups on hydrochar from cellulose and wood," *J. Anal. Appl. Pyrolysis*, vol. 137, no. November 2018, pp. 138–145, 2019, doi: 10.1016/j.jaap.2018.11.018.

[344] T. Wang, Y. Zhai, Y. Zhu, C. Li, and G. Zeng, "A review of the hydrothermal carbonization of biomass waste for hydrochar formation: Process conditions, fundamentals, and physicochemical properties," *Renew. Sustain. Energy Rev.*, vol. 90, no. February, pp. 223–247, 2018, doi: 10.1016/j.rser.2018.03.071.

[345] D. Özçimen and A. Ersoy-Meriçboyu, "Characterization of biochar and bio-oil samples obtained from carbonization of various biomass materials," *Renew. Energy*, vol. 35, no. 6, pp. 1319–1324, 2010, doi: 10.1016/j.renene.2009.11.042.

[346] S. Kannan, Y. Gariepy, and G. S. V. Raghavan, "Optimization and Characterization of Hydrochar Derived from Shrimp Waste," *Energy and Fuels*, vol. 31, no. 4, pp. 4068–4077, 2017, doi: 10.1021/acs.energyfuels.7b00093.

[347] S. Kannan, Y. Gariepy, and G. S. V. Raghavan, "Optimization and characterization of hydrochar produced from microwave hydrothermal carbonization of fish waste," *Waste*

Manag., vol. 65, pp. 159–168, 2017, doi: 10.1016/j.wasman.2017.04.016.

[348] A. Mukherjee, M. J. Dumont, and V. Raghavan, "Review: Sustainable production of hydroxymethylfurfural and levulinic acid: Challenges and opportunities," *Biomass and Bioenergy*, vol. 72, pp. 143–183, 2015, doi: 10.1016/j.biombioe.2014.11.007.

[349] J. B. Ott *et al.*, "Excess enthalpies for (ethanol + water) at 298.15 K and pressures of 0.4, 5, 10, and 15 MPa," *J. Chem. Thermodyn.*, vol. 18, no. 1, pp. 1–12, 1986, doi: 10.1016/0021-9614(86)90036-4.

[350] S. Schimmelpfennig and B. Glaser, "One Step Forward toward Characterization: Some Important Material Properties to Distinguish Biochars," *J. Environ. Qual.*, vol. 41, no. 4, pp. 1001–1013, 2012, doi: 10.2134/jeq2011.0146.

[351] H. J. Huang and X. Z. Yuan, "Recent progress in the direct liquefaction of typical biomass," *Prog. Energy Combust. Sci.*, vol. 49, pp. 59–80, 2015, doi: 10.1016/j.pecs.2015.01.003.

[352] F. Farelo, G. Von Brachel, and H. Offermann, "Solid-liquid equilibria in the ternary system nacl-kcl-h2o," *Can. J. Chem. Eng.*, vol. 71, no. 1, pp. 141–146, 1993, doi: 10.1002/cjce.5450710119.

[353] R. Engineering and F. De Engenharia, "Solubility of NaCl , NaBr , and KCl in Water , Methanol , Ethanol , and their mixed solvents," *J. Chem. Eng. Data*, pp. 29–32, 2005, doi: 10.1021/je049922y.

[354] D. Pasquini, M. T. B. Pimenta, L. H. Ferreira, and A. A. D. S. Curvelo, "Extraction of lignin from sugar cane bagasse and Pinus taeda wood chips using ethanol-water mixtures and carbon dioxide at high pressures," *J. Supercrit. Fluids*, vol. 36, no. 1, pp. 31–39, 2005, doi: 10.1016/j.supflu.2005.03.004.

[355] Z. Yao and X. Ma, "Effects of hydrothermal treatment on the pyrolysis behavior of Chinese fan palm," *Bioresour. Technol.*, vol. 247, no. 381, pp. 504–512, 2018, doi: 10.1016/j.biortech.2017.09.142.

[356] "OECD-FAO Agricultural Outlook 2021-2030 | FAO | Food and Agriculture Organization of the United Nations." .

[357] F. Sánchez, K. Araus, M. P. Domínguez, and G. S. Miguel, "Thermochemical Transformation of Residual Avocado Seeds: Torrefaction and Carbonization," *Waste and Biomass Valorization*, vol. 8, no. 7, pp. 2495–2510, 2017, doi: 10.1007/s12649-016-9699-6.

[358] J. Xue, T. Chellappa, S. Ceylan, and J. L. Goldfarb, "Enhancing biomass + coal Co-firing scenarios via biomass torrefaction and carbonization: Case study of avocado pit

biomass and Illinois No. 6 coal," *Renew. Energy*, vol. 122, pp. 152–162, 2018, doi: 10.1016/j.renene.2018.01.066.

[359] C. Palma, L. Lloret, A. Puen, M. Tobar, and E. Contreras, "Production of carbonaceous material from avocado peel for its application as alternative adsorbent for dyes removal," *Chinese J. Chem. Eng.*, vol. 24, no. 4, pp. 521–528, 2016, doi: 10.1016/j.cjche.2015.11.029.

[360] P. Xu *et al.*, "Use of iron oxide nanomaterials in wastewater treatment: A review," *Sci. Total Environ.*, vol. 424, pp. 1–10, 2012, doi: 10.1016/j.scitotenv.2012.02.023.

[361] L. H. Reddy, J. L. Arias, J. Nicolas, and P. Couvreur, "Magnetic nanoparticles: Design and characterization, toxicity and biocompatibility, pharmaceutical and biomedical applications," *Chem. Rev.*, vol. 112, no. 11, pp. 5818–5878, 2012, doi: 10.1021/cr300068p.

[362] H. Sun, G. Zhou, S. Liu, H. M. Ang, M. O. Tadé, and S. Wang, "Nano-Fe0 encapsulated in microcarbon spheres: Synthesis, characterization, and environmental applications," *ACS Appl. Mater. Interfaces*, vol. 4, no. 11, pp. 6235–6241, 2012, doi: 10.1021/am301829u.

[363] Q. Ma, L. Cui, S. Zhou, Y. Li, W. Shi, and S. Ai, "Iron nanoparticles in situ encapsulated in lignin-derived hydrochar as an effective catalyst for phenol removal," *Environ. Sci. Pollut. Res.*, vol. 25, no. 21, pp. 20833–20840, 2018, doi: 10.1007/s11356-018-2285-7.

[364] X. Zhu *et al.*, "Controllable synthesis of magnetic carbon composites with high porosity and strong acid resistance from hydrochar for efficient removal of organic pollutants: An overlooked influence," *Carbon*, vol. 99, no. 3, pp. 338–347, 2016, doi: 10.1016/j.carbon.2015.12.044.

[365] Y. Liu, X. Zhu, F. Qian, S. Zhang, and J. Chen, "Magnetic activated carbon prepared from rice straw-derived hydrochar for triclosan removal," *RSC Adv.*, vol. 4, no. 109, pp. 63620–63626, 2014, doi: 10.1039/c4ra11815d.

[366] B. N. Altay *et al.*, "Lignin-Derived Carbon-Coated Functional Paper for Printed Electronics," *ACS Appl. Electron. Mater.*, 2021, doi: 10.1021/acsaelm.1c00502.

[367] T. H. Wang, C. C. Yang, K. Qin, C. W. Chen, and C. Di Dong, "Life time enhanced Fenton-like catalyst by dispersing iron oxides in activated carbon: Preparation and reactivation through carbothermal reaction," *J. Hazard. Mater.*, vol. 406, no. September 2020, p. 124791, 2021, doi: 10.1016/j.jhazmat.2020.124791.

[368] S. Pérez-Rodríguez *et al.*, "Biomass waste-derived nitrogen and iron co-doped nanoporous carbons as electrocatalysts for the oxygen reduction reaction," *Electrochim.*

Acta, vol. 387, 2021, doi: 10.1016/j.electacta.2021.138490.

[369] M. I. Khalil, "Co-precipitation in aqueous solution synthesis of magnetite nanoparticles using iron(III) salts as precursors," *Arab. J. Chem.*, vol. 8, no. 2, pp. 279–284, 2015, doi: 10.1016/j.arabjc.2015.02.008.

[370] Z. Li, C. Chanéac, G. Berger, S. Delaunay, A. Graff, and G. Lefèvre, "Mechanism and kinetics of magnetite oxidation under hydrothermal conditions," *RSC Adv.*, vol. 9, no. 58, pp. 33633–33642, 2019, doi: 10.1039/c9ra03234g.

[371] "Magnetite R061111." Database of Raman spectroscopy, X-ray diffraction and chemistry of minerals, pp. 1–11, 2005, [Online]. Available: https://rruff.info/magnetite/display=default/R061111.

[372] "Hematite R110013." Database of Raman spectroscopy, X-ray diffraction and chemistry, [Online]. Available: https://rruff.info/hematite/display=default/R110013.

[373] X. Zhu, Y. Liu, F. Qian, C. Zhou, S. Zhang, and J. Chen, "Role of Hydrochar Properties on the Porosity of Hydrochar-based Porous Carbon for Their Sustainable Application," *ACS Sustain. Chem. Eng.*, vol. 3, no. 5, pp. 833–840, 2015, doi: 10.1021/acssuschemeng.5b00153.

[374] M. Demir *et al.*, "Graphitic Biocarbon from Metal-Catalyzed Hydrothermal Carbonization of Lignin," *Ind. Eng. Chem. Res.*, vol. 54, no. 43, pp. 10731–10739, 2015, doi: 10.1021/acs.iecr.5b02614.

[375] M. Sevilla and A. B. Fuertes, "Catalytic graphitization of templated mesoporous carbons," *Carbon*, vol. 44, no. 3, pp. 468–474, 2006, doi: 10.1016/j.carbon.2005.08.019.

[376] K. V. Kumar *et al.*, "Characterization of the adsorption site energies and heterogeneous surfaces of porous materials," *J. Mater. Chem. A*, vol. 7, no. 17, pp. 10104–10137, 2019, doi: 10.1039/c9ta00287a.

[377] M. Thommes *et al.*, "Physisorption of gases, with special reference to the evaluation of surface area and pore size distribution (IUPAC Technical Report)," *Pure Appl. Chem.*, vol. 87, no. 9–10, pp. 1051–1069, 2015, doi: 10.1515/pac-2014-1117.

[378] M. Asadullah, I. Jahan, M. B. Ahmed, P. Adawiyah, N. H. Malek, and M. S. Rahman, "Preparation of microporous activated carbon and its modification for arsenic removal from water," *J. Ind. Eng. Chem.*, vol. 20, no. 3, pp. 887–896, 2014, doi: 10.1016/j.jiec.2013.06.019.

[379] F. Rodríguez-Reinoso and M. Molina-Sabio, "Textural and chemical characterization of microporous carbons," *Adv. Colloid Interface Sci.*, vol. 76–77, pp. 271–294, 1998, doi: 10.1016/S0001-8686(98)00049-9.

[380] S. B. A. Hamid, S. J. Teh, and Y. S. Lim, “Catalytic hydrothermal upgrading of α-cellulose using iron salts as a lewis acid,” *BioResources*, vol. 10, no. 3, pp. 5974–5986, 2015, doi: 10.15376/biores.10.3.5974-5986.

[381] Y. Liu, Z. He, and M. Uchimiya, “Comparison of Biochar Formation from Various Agricultural By-Products Using FTIR Spectroscopy,” vol. 9, no. 4, pp. 246–253, 2015, doi: 10.5539/mas.v9n4p246.

[382] H. Namduri and S. Nasrazadani, “Quantitative analysis of iron oxides using Fourier transform infrared spectrophotometry,” *Corros. Sci.*, vol. 50, no. 9, pp. 2493–2497, 2008, doi: 10.1016/j.corsci.2008.06.034.

[383] M. Tadic, M. Panjan, B. V. Tadic, M. Kopani, and L. Kopanja, “Magnetic properties of hematite (α − Fe 2 O 3) nanoparticles synthesized by sol-gel synthesis method : The influence of particle size and particle size distribution,” vol. 70, no. 7, pp. 71–76, 2019, doi: 10.2478/jee-2019.

[384] Y. Zhu, P. Kolar, S. B. Shah, J. J. Cheng, and P. K. Lim, “Avocado seed-derived activated carbon for mitigation of aqueous ammonium,” *Ind. Crops Prod.*, vol. 92, pp. 34–41, 2016, doi: 10.1016/j.indcrop.2016.07.016.

[385] M. L. Álvarez, G. Gascó, T. Palacios, J. Paz-Ferreiro, and A. Méndez, “Fe oxides-biochar composites produced by hydrothermal carbonization and pyrolysis of biomass waste,” *J. Anal. Appl. Pyrolysis*, vol. 151, no. May, 2020, doi: 10.1016/j.jaap.2020.104893.

[386] V. K. Gupta, P. J. M. Carrott, M. M. L. Ribeiro Carrott, and Suhas, “Low-Cost adsorbents: Growing approach to wastewater treatmenta review,” *Crit. Rev. Environ. Sci. Technol.*, vol. 39, no. 10, pp. 783–842, 2009, doi: 10.1080/10643380801977610.

[387] N. B. Mc Keown and P. M. Budd, “Polymers of intrinsic microporosity (PIMs): Organic materials for membrane separations, heterogeneous catalysis and hydrogen storage,” *Chem. Soc. Rev.*, vol. 35, no. 8, pp. 675–683, 2006, doi: 10.1039/b600349d.

[388] S. Shinohara, Y. Chiyomaru, F. Sassa, C. Liu, and K. Hayashi, “Molecularly Imprinted Filtering Adsorbents for Odor Sensing,” *Sensors (Basel).*, vol. 16, no. 11, pp. 1–10, 2016, doi: 10.3390/s16111974.

[389] S. Gadipelli and Z. X. Guo, “Graphene-based materials: Synthesis and gas sorption, storage and separation,” *Prog. Mater. Sci.*, vol. 69, pp. 1–60, 2015, doi: 10.1016/j.pmatsci.2014.10.004.

[390] K. V. Kumar, K. Preuss, L. Lu, Z. X. Guo, and M. M. Titirici, “Effect of Nitrogen Doping on the CO2 Adsorption Behavior in Nanoporous Carbon Structures: A

Molecular Simulation Study," *J. Phys. Chem. C*, vol. 119, no. 39, pp. 22310–22321, 2015, doi: 10.1021/acs.jpcc.5b06017.

[391] S. Gadipelli and Z. X. Guo, "Tuning of ZIF-Derived Carbon with High Activity, Nitrogen Functionality, and Yield - A Case for Superior CO2 Capture," *ChemSusChem*, vol. 8, no. 12, pp. 2123–2132, 2015, doi: 10.1002/cssc.201403402.

[392] H. Ma, J. B. Li, W. W. Liu, M. Miao, B. J. Cheng, and S. W. Zhu, "Novel synthesis of a versatile magnetic adsorbent derived from corncob for dye removal," *Bioresour. Technol.*, vol. 190, pp. 13–20, 2015, doi: 10.1016/j.biortech.2015.04.048.

[393] J. M. Thomas and W. J. Thomas, *Principles and Practice of Heterogeneous Catalysis*. Weinheim, GERMANY: John Wiley & Sons, Incorporated, 2015.

[394] L. Ai, C. Zhang, and Z. Chen, "Removal of methylene blue from aqueous solution by a solvothermal-synthesized graphene/magnetite composite," *J. Hazard. Mater.*, vol. 192, no. 3, pp. 1515–1524, 2011, doi: 10.1016/j.jhazmat.2011.06.068.

[395] V. P. Dinh *et al.*, "Insight into the adsorption mechanisms of methylene blue and chromium(III) from aqueous solution onto pomelo fruit peel," *RSC Adv.*, vol. 9, no. 44, pp. 25847–25860, 2019, doi: 10.1039/c9ra04296b.

[396] H. Zhang, F. Zhang, and Q. Huang, "Highly effective removal of malachite green from aqueous solution by hydrochar derived from phycocyanin-extracted algal bloom residues through hydrothermal carbonization," *RSC Adv.*, vol. 7, no. 10, pp. 5790–5799, 2017, doi: 10.1039/c6ra27782a.

[397] T. Selmi *et al.*, "Tetracycline removal with activated carbons produced by hydrothermal carbonisation of Agave americana fibres and mimosa tannin," *Ind. Crops Prod.*, vol. 115, no. February, pp. 146–157, 2018, doi: 10.1016/j.indcrop.2018.02.005.

[398] R. Gomer, "Chemisorption on Metals," *Solid State Phys. - Adv. Res. Appl.*, vol. 30, no. C, pp. 93–225, 1975, doi: 10.1016/S0081-1947(08)60336-7.

[399] J. B. Joo, J. Park, and J. Yi, "Preparation of polyelectrolyte-functionalized mesoporous silicas for the selective adsorption of anionic dye in an aqueous solution," *J. Hazard. Mater.*, vol. 168, no. 1, pp. 102–107, 2009, doi: 10.1016/j.jhazmat.2009.02.015.

[400] J. Li, S. Wang, J. Peng, G. Lin, T. Hu, and L. Zhang, "Selective Adsorption of Anionic Dye from Solutions by Modified Activated Carbon," *Arab. J. Sci. Eng.*, vol. 43, no. 11, pp. 5809–5817, 2018, doi: 10.1007/s13369-017-3006-0.

[401] B. S. Damasceno, A. F. V. Da Silva, and A. C. V. De Araújo, "Dye adsorption onto magnetic and superparamagnetic Fe3O4nanoparticles: A detailed comparative study," *J. Environ. Chem. Eng.*, vol. 8, no. 5, p. 103994, 2020, doi: 10.1016/j.jece.2020.103994.

[402] Z. H. Dastgerdi, S. S. Meshkat, and M. D. Esrafili, “Enhanced adsorptive removal of Indigo carmine dye performance by functionalized carbon nanotubes based adsorbents from aqueous solution: equilibrium, kinetic, and DFT study,” *J. Nanostructure Chem.*, vol. 9, no. 4, pp. 323–334, 2019, doi: 10.1007/s40097-019-00321-0.

[403] M. F. Chowdhury, S. Khandaker, F. Sarker, A. Islam, M. T. Rahman, and M. R. Awual, “Current treatment technologies and mechanisms for removal of indigo carmine dyes from wastewater: A review,” *J. Mol. Liq.*, vol. 318, p. 114061, 2020, doi: 10.1016/j.molliq.2020.114061.

[404] B. A. Messerle and K. Q. Vuong, “Synthesis of spiroketals by iridium-catalyzed double hydroalkoxylation,” *Pure Appl. Chem.*, vol. 78, no. 2, pp. 385–390, 2006, doi: 10.1351/pac200678020385.

[405] D. B. Killian, G. F. Hennion, and J. A. Nieuwland, “The Synthesis of Some Dioxole Derivatives from Alkylacetylenes,” *J. Am. Chem. Soc.*, vol. 58, no. 9, pp. 1658–1659, 1936, doi: 10.1021/ja01300a046.

[406] M. Konkol, H. Schmidt, and D. Steinborn, “Iridium-catalyzed addition of methanol to internal alkynes,” *J. Mol. Catal. A Chem.*, vol. 261, no. 2, pp. 301–305, 2007, doi: 10.1016/j.molcata.2006.10.027.

[407] F. Ke, Z. Li, H. Xiang, and X. Zhou, “Catalytic hydroalkoxylation of alkenes by iron(III) catalyst,” *Tetrahedron Lett.*, vol. 52, no. 2, pp. 318–320, 2011, doi: 10.1016/j.tetlet.2010.11.036.

[408] K. Komeyama, T. Morimoto, Y. Nakayama, and K. Takaki, “Cationic iron-catalyzed intramolecular hydroalkoxylation of unactivated olefins,” *Tetrahedron Lett.*, vol. 48, no. 18, pp. 3259–3261, 2007, doi: 10.1016/j.tetlet.2007.03.004.

[409] B. Alcaide, P. Almendros, and T. M. Del Campo, “Chemodivergence in alkene/allene cycloetherification of enallenols: Iron versus noble metal catalysis,” *Chem. - A Eur. J.*, vol. 14, no. 26, pp. 7756–7759, 2008, doi: 10.1002/chem.200801166.

[410] I. Notar Francesco, B. Cacciuttolo, M. Pucheault, and S. Antoniotti, “Simple metal salts supported on montmorillonite as recyclable catalysts for intramolecular hydroalkoxylation of double bonds in conventional and VOC-exempt solvents,” *Green Chem.*, vol. 17, no. 2, pp. 837–841, 2015, doi: 10.1039/c4gc01990c.

[411] Y. Zhou *et al.*, “Development of highly efficient platinum catalysts for hydroalkoxylation and hydroamination of unactivated alkenes,” *Nat. Commun.*, vol. 12, no. 1, pp. 1–11, 2021, doi: 10.1038/s41467-021-22287-w.

[412] L. L. Santos, V. R. Ruiz, M. J. Sabater, and A. Corma, “Regioselective transformation

of alkynes into cyclic acetals and thioacetals with a gold(I) catalyst: comparison with Brønsted acid catalysts," *Tetrahedron*, vol. 64, no. 34, pp. 7902–7909, 2008, doi: 10.1016/j.tet.2008.06.032.

[413] I. Kondolff, H. Doucet, and M. Santelli, "Direct synthesis of protected arylacetaldehydes by palladium- tetraphosphine-catalyzed arylation of ethyleneglycol vinylether," *Synlett*, no. 9, pp. 1561–1564, 2004, doi: 10.1055/s-2004-829063.

[414] A. E. Haddrell, R. E. H. Miles, B. R. Bzdek, J. P. Reid, R. J. Hopkins, and J. S. Walker, "Coalescence Sampling and Analysis of Aerosols using Aerosol Optical Tweezers," *Anal. Chem.*, vol. 89, no. 4, pp. 2345–2352, 2017, doi: 10.1021/acs.analchem.6b03979.

[415] F. Zhang, X. Tang, A. Tong, B. Wang, and J. Wang, "An automatic baseline correction method based on the penalized least squares method," *Sensors (Switzerland)*, vol. 20, no. 7, 2020, doi: 10.3390/s20072015.

[416] J. H. Christie and D. J. Lockwood, "Electronic Raman spectrum of Co2+ in CoCl2," *Chem. Phys. Lett.*, vol. 8, no. 1, pp. 120–122, 1971, doi: 10.1016/0009-2614(71)80593-6.

[417] B. M. Collins, "New light on an old subject: An FT-Raman study of ion association in aqueous solutions of cobalt(II) nitrate," no. Ii, pp. 695–697, 2010, doi: 10.1063/1.55817.

[418] M. Bouchard and A. Gambardella, "Raman microscopy study of synthetic cobalt blue spinels used in the fieldof art," *J. Raman Spectrosc.*, vol. 41, no. 11, pp. 1477–1485, 2010, doi: 10.1002/jrs.2645.

[419] V. G. Hadjiev, M. N. Iliev, and I. V. Vergilov, "The Raman spectra of Co3O4," *J. Phys. C Solid State Phys.*, vol. 21, no. 7, pp. L199–L201, 1988, doi: 10.1088/0022-3719/21/7/007.

[420] A. Choya, B. de Rivas, J. I. Gutiérrez-Ortiz, and R. López-Fonseca, "Comparative study of strategies for enhancing the performance of Co3o4/Al2o3 catalysts for lean methane combustion," *Catalysts*, vol. 10, no. 7, 2020, doi: 10.3390/catal10070757.

[421] X. Liu and C. T. Prewitt, "High-temperature X-ray diffraction study of Co3O4: Transition from normal to disordered spinel," *Phys. Chem. Miner.*, vol. 17, no. 2, pp. 168–172, 1990, doi: 10.1007/BF00199669.

[422] I. Rutkowska *et al.*, "Chemical and structural characterization of amorphous and crystalline alumina obtained by alternative sol-gel preparation routes," *Materials (Basel).*, vol. 14, no. 7, 2021, doi: 10.3390/ma14071761.

[423] P. D. Moran, G. A. Bowmaker, R. P. Cooney, K. S. Finnie, J. R. Bartlett, and J. L. Woolfrey, "Vibrational Spectra and Molecular Association of Titanium

Tetraisopropoxide," *Inorg. Chem.*, vol. 37, no. 11, pp. 2741–2748, 1998, doi: 10.1021/ic9709436.

[424] S. Degioanni *et al.*, "Surface-enhanced Raman scattering of amorphous silica gel adsorbed on gold substrates for optical fiber sensors," *J. Appl. Phys.*, vol. 118, no. 15, 2015, doi: 10.1063/1.4933280.

[425] M. V. Khedkar, S. B. Somvanshi, A. V. Humbe, and K. M. Jadhav, "Surface modified sodium silicate based superhydrophobic silica aerogels prepared via ambient pressure drying process," *J. Non. Cryst. Solids*, vol. 511, no. January, pp. 140–146, 2019, doi: 10.1016/j.jnoncrysol.2019.02.004.

[426] N. Mironova-Ulmane, A. Kuzmin, I. Steins, J. Grabis, I. Sildos, and M. Pärs, "Raman scattering in nanosized nickel oxide NiO," *J. Phys. Conf. Ser.*, vol. 93, no. 1, pp. 8–13, 2007, doi: 10.1088/1742-6596/93/1/012039.

[427] L. Wu, Y. Wu, H. Wei, Y. Shi, and C. Hu, "Synthesis and characteristics of NiO nanowire by a solution method," *Mater. Lett.*, vol. 58, no. 21, pp. 2700–2703, 2004, doi: 10.1016/j.matlet.2004.03.047.

[428] A. Maleki, A. R. Taherizadeh, H. Issa, B. Niroumand, A. Allafchian, and A. Ghaei, "Development of a new magnetic aluminum matrix nanocomposite," *Ceram. Int.*, vol. 44, May 2018, doi: 10.1016/j.ceramint.2018.05.141.

[429] X. Maeder *et al.*, "Comparison of in-situ oxide formation and post-deposition high temperature oxidation of Ni-aluminides synthesized by cathodic arc evaporation," *Surf. Coatings Technol.*, vol. 309, pp. 516–522, 2017, doi: 10.1016/j.surfcoat.2016.12.013.

[430] M. Shokrollahi Yancheshmeh, O. Alizadeh Sahraei, M. Aissaoui, and M. C. Iliuta, "A novel synthesis of NiAl2O4 spinel from a Ni-Al mixed-metal alkoxide as a highly efficient catalyst for hydrogen production by glycerol steam reforming," *Appl. Catal. B Environ.*, vol. 265, no. December 2019, p. 118535, 2020, doi: 10.1016/j.apcatb.2019.118535.

[431] H. Chen, W. Xu, and N. G. R. Broderick, "An Adaptive and Fully Automated Baseline Correction Method for Raman Spectroscopy Based on Morphological Operations and Mollification," *Appl. Spectrosc.*, vol. 73, no. 3, pp. 284–293, 2019, doi: 10.1177/0003702818811688.

[432] C. Sanchez, J. Livage, and G. Lucazeau, "Infrared and Raman study of amorphous V2O5," *J. Raman Spectrosc.*, vol. 12, no. 1, pp. 68–72, Feb. 1982, doi: https://doi.org/10.1002/jrs.1250120110.

[433] N. Kausar, R. Howe, and M. Skyllas-Kazacos, "Raman spectroscopy studies of

concentrated vanadium redox battery positive electrolytes," *J. Appl. Electrochem.*, vol. 31, no. 12, pp. 1327–1332, 2001, doi: 10.1023/A:1013870624722.

[434] H. Katzke and R. Schlögl, "General structural relationships between rutile-type VO2 and the Magnéli-phases VnO2n-1," *Zeitschrift fur Krist.*, vol. 218, no. 6, pp. 432–439, 2003, doi: 10.1524/zkri.218.6.432.20725.

[435] P. Jing *et al.*, "In-situ XRD study of the structure and electrochemical performance of V2O5 nanosheets in aqueous zinc ion batteries," *Inorg. Chem. Commun.*, vol. 117, no. April, p. 107953, 2020, doi: 10.1016/j.inoche.2020.107953.

[436] G. Mestl and T. K. K. Srinivasan, "Raman spectroscopy of monolayer-type catalysts: Supported molybdenum oxides," *Catal. Rev. - Sci. Eng.*, vol. 40, no. 4, pp. 451–570, 1998, doi: 10.1080/01614949808007114.

[437] J. Song, X. Ni, L. Gao, and H. Zheng, "Synthesis of metastable h-MoO3 by simple chemical precipitation," *Mater. Chem. Phys.*, vol. 102, no. 2–3, pp. 245–248, 2007, doi: 10.1016/j.matchemphys.2006.12.011.

[438] F. Jalilehvand, V. Mah, B. O. Leung, D. Ross, M. Parvez, and R. F. Aroca, "Structural characterization of molybdenum(V) species in aqueous HCl solutions," *Inorg. Chem.*, vol. 46, no. 11, pp. 4430–4445, 2007, doi: 10.1021/ic062047c.

[439] H. Knözinger and H. Jezlorowski, "Raman spectra of molybdenum oxide supported on the surface of aluminas," *J. Phys. Chem.*, vol. 82, no. 18, pp. 2002–2005, 1978, doi: 10.1021/j100507a011.

[440] A. Jannasch *et al.*, *Optical Tweezers Mehtods and Protocols*. 2004.

[441] K. C. Neuman and S. M. Block, "Optical trapping," *Rev. Sci. Instrum.*, vol. 75, no. 9, pp. 2787–2809, 2004, doi: 10.1063/1.1785844.

[442] S. Burikov, T. Dolenko, S. Patsaeva, Y. Starokurov, and V. Yuzhakov, "Raman and IR spectroscopy research on hydrogen bonding in water-ethanol systems," *Mol. Phys.*, vol. 108, no. 18, pp. 2427–2436, 2010, doi: 10.1080/00268976.2010.516277.

[443] V. R. Dantham, P. B. Bisht, and P. S. Dobal, "Whispering gallery modes and effect of coating on Raman spectra of single microspheres," *J. Raman Spectrosc.*, vol. 42, no. 6, pp. 1373–1378, 2011, doi: 10.1002/jrs.2868.

[444] R. J. Hopkins, L. Mitchem, A. D. Ward, and J. P. Reid, "Control and characterisation of a single aerosol droplet in a single-beam gradient-force optical trap," *Phys. Chem. Chem. Phys.*, vol. 6, no. 21, pp. 4924–4927, 2004, doi: 10.1039/b414459g.

[445] Z. He and P. Alexandridis, "Micellization thermodynamics of Pluronic P123 (EO20PO70EO20) amphiphilic block copolymer in aqueous Ethylammonium nitrate

(EAN) solutions," *Polymers (Basel).*, vol. 10, no. 1, 2017, doi: 10.3390/polym10010032.

[446] F. Li, Z. Men, S. Li, S. Wang, Z. Li, and C. Sun, "Study of hydrogen bonding in ethanol-water binary solutions by Raman spectroscopy," *Spectrochim. Acta - Part A Mol. Biomol. Spectrosc.*, vol. 189, pp. 621–624, 2018, doi: 10.1016/j.saa.2017.08.077.

[447] C. Guo, J. Wang, H. Z. Liu, and J. Y. Chen, "Hydration and conformation of temperature-dependent micellization of PEO-PPO-PEO block copolymers in aqueous solutions by FT-Raman," *Langmuir*, vol. 15, no. 8, pp. 2703–2708, 1999, doi: 10.1021/la981036w.

[448] G. A. Ferron and S. C. Soderholm, "Estimation of the times for evaporation of pure water droplets and for stabilization of salt solution particles," *J. Aerosol Sci.*, vol. 21, no. 3, pp. 415–429, 1990, doi: 10.1016/0021-8502(90)90070-E.

[449] B. Yang *et al.*, "Effect of acid on the aggregation of poly(ethylene oxide)-poly(propylene oxide)-poly(ethylene oxide) block copolymers," *J. Phys. Chem. B*, vol. 110, no. 46, pp. 23068–23074, 2006, doi: 10.1021/jp0634149.

[450] J. C. Carter, P. K. Khulbe, J. Gray, J. W. Van Zee, and S. M. Angel, "Raman spectroscopic evidence supporting the existence of Ni 4(OH)44+ in aqueous, Ni(NO3) 2 solutions," *Anal. Chim. Acta*, vol. 514, no. 2, pp. 241–245, 2004, doi: 10.1016/j.aca.2004.03.051.

[451] A. Moatti, J. Javadpour, M. Anbia, and A. Badiei, "The correlation between aging time and pore characteristics in the synthesis of mesoporous Al 2 O 3," *Ceram. Int.*, vol. 40, no. 7, pp. 10231–10236, 2014, doi: 10.1016/j.ceramint.2014.02.111.

[452] P. Singh, P. K. Maiti, and K. Sen, "Pristine and modified-mesoporous alumina : molecular assistance-based drug loading and sustained release activity," *Bull. Mater. Sci.*, vol. 43, no. 1, pp. 1–9, 2020, doi: 10.1007/s12034-019-1991-1.

[453] K. Niesz, P. Yang, and G. A. Somorjai, "Sol-gel synthesis of ordered mesoporous alumina," pp. 1986–1987, 2005, doi: 10.1039/b419249d.

[454] H. Harju, G. Pipitone, and L. Lefferts, "Influence of the Catalyst Particle Size on the Aqueous Phase Reforming of n-Butanol Over Rh/ZrO2," *Front. Chem.*, vol. 8, no. January, pp. 1–13, 2020, doi: 10.3389/fchem.2020.00017.

[455] H. Wang and J. Lu, "A Review on Particle Size Effect in Metal-Catalyzed Heterogeneous Reactions," *Chinese J. Chem.*, vol. 38, no. 11, pp. 1422–1444, 2020, doi: 10.1002/cjoc.202000205.

[456] T. A. Nieminen *et al.*, "Optical tweezers computational toolbox," *J. Opt. A Pure Appl.*

Opt., vol. 9, no. 8, 2007, doi: 10.1088/1464-4258/9/8/S12.

[457] U. Ashraf, O. A. Chat, M. Maswal, S. Jabeen, and A. A. Dar, "An investigation of Pluronic P123-sodium cholate mixed system: Micellization, gelation and encapsulation behavior," *RSC Adv.*, vol. 5, no. 102, pp. 83608–83618, 2015, doi: 10.1039/c5ra13002f.

[458] A. M. Bodratti and P. Alexandridis, "Formulation of poloxamers for drug delivery," *J. Funct. Biomater.*, vol. 9, no. 1, 2018, doi: 10.3390/jfb9010011.

[459] K. Sakai-Kato *et al.*, "General considerations regarding the in vitro and in vivo properties of block copolymer micelle products and their evaluation," *J. Control. Release*, vol. 210, pp. 76–83, 2015, doi: 10.1016/j.jconrel.2015.05.259.

[460] P. Marage, M. Langlet, and J. C. Joubert, "Understanding and improving the deposition conditions of SiO2 thin films obtained by ultrasonic sol-gel procedure - Code: EP30," *J. Sol-Gel Sci. Technol.*, vol. 2, no. 1–3, pp. 615–618, 1994, doi: 10.1007/BF00486320.

[461] M. Langlet, D. Walz, P. Marage, and J. C. Joubert, "Glass and ceramic thin films deposited by an ultrasonically assisted sol-gel technique," *Thin Solid Films*, vol. 221, no. 1–2, pp. 44–54, 1992, doi: 10.1016/0040-6090(92)90794-C.

[462] M. Dietzel and G. Böhme, "The dissolution rates of gibbsite in the presence of chloride, nitrate, silica, sulfate, and citrate in open and closed systems at 20°C," *Geochim. Cosmochim. Acta*, vol. 69, no. 5, pp. 1199–1211, 2005, doi: 10.1016/j.gca.2004.08.027.

[463] R. H. Madon, M. Fawzi, K. I. Sarwani, S. A. Osman, M. A. Razali, and A. W. Mohammad, "Effect of Reaction Temperature on Steam Methane Reforming's yield over Coated Nickel Aluminide (Ni3Al) Catalyst in Micro Reactor," *J. Adv. Res. Fluid Mech. Therm. Sci.*, vol. 50, no. 2, pp. 170–177, 2018.

[464] C. Baerlocher *et al.*, "Structure of the polycrystalline zeolite catalyst IM-5 solved by enhanced charge flipping," *Science (80-.).*, vol. 315, no. 5815, pp. 1113–1116, 2007, doi: 10.1126/science.1137920.

[465] M. Miao *et al.*, "Effects of volatile matter and oxygen concentration on combustion characteristics of coal in an oxygen-enriched fluidized bed," *Energy*, vol. 220, p. 119778, 2021, doi: 10.1016/j.energy.2021.119778.

[466] L. Chen *et al.*, "Identification of Alcohol Conformers by Raman Spectra in the C-H Stretching Region," *J. Phys. Chem. A*, vol. 119, no. 13, pp. 3209–3217, 2015, doi: 10.1021/jp513027r.

[467] E. Atta-Obeng, B. Dawson-Andoh, M. S. Seehra, U. Geddam, J. Poston, and J. Leisen, "Physico-chemical characterization of carbons produced from technical lignin by sub-critical hydrothermal carbonization," *Biomass and Bioenergy*, vol. 107, no. November

2016, pp. 172–181, 2017, doi: 10.1016/j.biombioe.2017.09.023.

[468] M. Volpe *et al.*, "Reactivity of cellulose during hydrothermal carbonization of lignocellulosic biomass," *Fuel Process. Technol.*, vol. 206, no. April, p. 106456, 2020, doi: 10.1016/j.fuproc.2020.106456.

[469] P. Long, H. Wu, Q. Zhao, Y. Wang, J. Dong, and J. Li, "Solvent effect on the synthesis of MIL-96(Cr) and MIL-100(Cr)," *Microporous Mesoporous Mater.*, vol. 142, no. 2–3, pp. 489–493, 2011, doi: 10.1016/j.micromeso.2010.12.036.

[470] and R. C. B. Catherine E. Brewer, Klaus Schmidt-Rohr, Justinus A. Satrio, "Characterization of Biochar from Fast Pyrolysis and Gasification Systems," *Environ. Prog. Sustain. Energy*, vol. 33, no. 3, pp. 676–680, 2014, doi: 10.1002/ep.

[471] V. Bustamante-García, A. Carrillo-Parra, H. González-Rodríguez, R. G. Ramírez-Lozano, J. J. Corral-Rivas, and F. Garza-Ocañas, "Evaluation of a charcoal production process from forest residues of Quercus sideroxyla Humb., & Bonpl. in a Brazilian beehive kiln," *Ind. Crops Prod.*, vol. 42, no. 1, pp. 169–174, 2013, doi: 10.1016/j.indcrop.2012.04.034.

[472] A. J. Baker, "Wood Fuel Properties and Fuel Products from Woods," *Fuelwood Manag. Util. Semin.*, pp. 14–25, 1983.

[473] T. Cordero, F. Marquez, J. Rodriguez-Mirasol, and J. Rodriguez, "Predicting heating values of lignocellulosics and carbonaceous materials from proximate analysis," *Fuel*, vol. 80, no. 11, pp. 1567–1571, 2001, doi: 10.1016/S0016-2361(01)00034-5.

Appendix

Appendix 1 Summary table for different processing conditions on a variety of biomasses and the properties of the hydrochar formed.

Feedstock	Entry	Time (min)	Temp (°C)	VM (%)	FC (%)	Ash (%)	C (%)	H (%)	N (%)	S (%)	O (%)	O/C	H/C	HHV (MJ/Kg)	Reference
Coconut fibres	1	-	-	80.9	11.0	8.10	47.8	5.61	0.90	0.23	45.5	0.71	1.41	18.4	[163]
	1a	30	220	69.8	24.0	6.20	62.5	5.28	0.90	0.26	31.1	0.37	1.01	24.7	
	1a	30	250	67.9	27.1	5.00	67.1	5.20	0.98	0.29	26.4	0.30	0.93	26.7	
	1c	30	300	53.6	42.1	4.30	73.2	5.09	1.13	0.35	20.2	0.47	0.83	29.4	
Eucalyptus leaves	2	-	-	79.2	10.3	10.5	47.0	6.22	1.23	0.77	44.8	0.72	1.59	18.9	[163]
	2a	30	200	72.5	20.2	7.30	61.1	6.13	1.37	0.65	30.7	0.38	1.20	25.3	
	2b	30	250	70.1	23.0	6.90	62.3	5.47	1.44	0.44	30.4	0.37	1.05	25.0	
	2c	30	300	61.2	31.7	7.10	68.9	6.00	1.62	0.72	22.8	0.25	1.05	28.7	
Paper Sludge	3	-	-	47.4	5.18	47.4	22.7	3.22	1.32	1.07	24.3	0.80	1.71	8.20	[164]
	3a	60	180	39.1	6.13	54.8	20.9	2.60	0.78	0.77	20.1	0.72	1.49	9.41	
	3b	60	210	35.3	6.86	57.9	20.3	2.30	0.55	0.70	18.2	0.67	1.36	9.76	
	3c	60	240	32.6	6.91	60.5	19.7	1.96	0.43	0.68	16.7	0.64	1.20	9.43	
	3e	60	270	29.2	6.98	63.8	19.2	1.88	0.42	0.61	14.1	0.55	1.18	9.18	
	3d	60	300	26.8	7.01	66.2	19.1	1.71	0.39	0.63	11.2	0.44	1.07	8.85	
Municipal solid waste	4	-	-	49.0	11.1	39.9	29.9	4.55	2.25	1.46	22.0	0.55	1.83	13.4	[165]
	4a	30	210	43.3	12.8	43.9	33.9	4.63	1.42	1.09	15.1	0.33	1.64	13.5	
	4b	30	230	41.5	13.4	45.1	34.4	4.76	1.04	0.74	14.0	0.30	1.66	14.2	
	4c	30	250	34.4	12.6	53.0	35.0	4.57	1.41	0.67	5.4	0.11	1.57	14.6	
	4d	30	280	33.0	12.1	54.9	35.6	4.19	1.54	0.43	3.3	0.07	1.41	15.2	
	4e	60	210	41.5	12.5	45.9	33.6	4.24	1.13	0.92	14.2	0.32	1.51	13.7	
	4f	60	230	38.1	12.7	49.2	34.8	4.74	1.09	0.57	9.6	0.21	1.63	14.3	
	4g	60	250	34.3	11.8	53.9	34.7	3.45	1.31	0.54	6.1	0.13	1.19	14.7	
	4h	60	280	33.2	12.2	54.7	35.7	3.33	1.54	0.43	4.4	0.09	1.12	15.5	
	4i	90	210	39.7	11.6	48.8	33.2	4.26	0.86	0.83	12.1	0.27	1.54	14.2	

	4j	90	230	36.9	12.2	50.9	36.6	4.32	1.34	0.52	6.4	0.13	1.42	14.4	
	4k	90	250	29.9	9.70	60.4	30.5	3.30	1.38	0.50	4.0	0.10	1.30	14.6	
	4l	90	280	28.6	9.29	62.1	28.9	3.28	1.42	0.33	4.0	0.10	1.36	14.8	
Coffee Beans	5	-	-	81.4	13.4	5.20	46.5	6.98	3.16	0.11	38.4	0.62	1.80	20.3	[178]
	5a	40	150	92.1	7.66	0.25	48.2	6.65	2.19	0.08	42.7	0.66	1.66	20.2	
	5b	40	200	85.5	14.2	0.22	54.8	6.30	2.89	0.09	35.7	0.49	1.38	22.8	
	5c	40	250	63.1	36.8	0.06	68.4	6.40	3.22	0.08	21.9	0.24	1.12	29.1	
Maize residues	6	-	-	73.6	18.8	7.68	45.8	5.60	0.94	0.08	39.9	0.65	1.47	16.4	[179]
	6a	210	180	77.6	17.5	4.95	47.4	5.65	0.14	0.06	41.8	0.66	1.43	15.9	
	6b	120	190	77.9	17.3	4.76	46.7	5.84	0.10	0.05	42.6	0.68	1.50	16.5	
	6c	300	190	76.4	18.0	5.61	46.1	5.80	0.15	0.05	42.3	0.69	1.51	16.3	
	6d	60	215	81.1	17.9	1.02	49.5	5.97	0.00	0.02	43.5	0.66	1.45	18.1	
	6e	210	215	74.2	18.5	7.30	46.4	5.84	0.09	0.05	40.4	0.65	1.51	16.6	
	6f	360	215	80.6	18.2	1.15	49.8	6.24	0.00	0.03	42.8	0.64	1.50	16.8	
	6g	120	240	75.2	18.7	6.19	47.0	5.78	0.11	0.05	40.9	1.14	2.57	16.8	
	6h	300	240	75.6	19.9	4.54	48.6	5.80	0.14	0.06	40.9	0.63	1.43	17.4	
	6i	210	250	75.3	18.5	6.21	47.2	5.13	0.11	0.05	41.3	0.66	1.30	17.5	
Miscanthus	7	-	-	87.5	11.7	0.80	46.7	6.00	0.20	0.00	45.3	0.73	1.54	18.5	[180]
	7a	5	190	83.8	15.7	0.50	48.8	6.00	0.20	0.00	44.7	0.69	1.48	20.2	
	7b	5	225	81.9	17.5	0.70	49.6	6.00	0.30	0.00	41.8	0.63	1.45	21.6	
	7c	5	260	68.9	30.3	0.80	61.2	5.30	0.40	0.00	31.6	0.39	1.04	25.9	
Sewage sludge	8	-	-	70.0	1.42	28.6	36.7	6.40	5.50	9.50	35.9	0.73	2.09	14.7	[139]
	8a	240	200	50.6	5.47	43.9	33.3	4.40	2.10	3.80	18.5	0.42	1.59	15.1	
	8b	360	200	50.3	5.35	44.4	33.2	4.30	2.10	3.80	17.8	0.40	1.55	14.7	
	8c	480	200	48.8	6.56	44.7	32.6	4.20	2.20	3.80	17.6	0.40	1.55	14.4	
	8d	600	200	45.4	8.00	46.6	32.5	4.10	2.20	3.80	17.4	0.40	1.51	14.5	
	8e	720	200	45.0	8.31	46.7	32.5	4.10	2.20	3.90	16.9	0.39	1.51	14.7	
Cow	9	-	-	74.1	9.40	16.4	44.8	5.20	2.30	0.01	34.4	0.58	1.39	19.1	[142]

manure	9a	5	180	74.8	8.46	16.7	46.5	5.20	1.90	0.01	32.3	0.52	1.34	18.8	
	9b	5	220	70.5	9.4	20.1	49.2	5.20	2.00	0.01	29.9	0.46	1.27	20.2	
	9c	5	260	67.7	11.0	21.3	52.1	5.20	2.00	0.01	26.9	0.39	1.20	21.5	
	9d	30	180	70.0	11.3	18.7	46.6	5.20	2.00	0.01	32.0	0.52	1.34	19.6	
	9e	30	220	67.9	9.01	23.1	50.4	5.20	2.10	0.01	28.5	0.42	1.24	21.1	
	9f	30	260	58.5	16.1	25.4	54.0	5.20	2.50	0.01	24.2	0.34	1.16	22.1	
Food waste	10	-	-	79.1	14.5	6.41	39.0	7.32	5.70	0.30	47.7	0.92	2.25	15.0	[183]
	10a	60	200	65.1	30.3	4.52	62.8	7.25	4.35	0.30	24.9	0.30	1.38	20.8	
	10b	60	250	51.8	45.1	3.11	68.1	7.09	4.42	0.30	20.1	0.22	1.25	29.0	
	10c	60	300	50.4	47.4	2.21	73.0	7.01	5.17	0.30	17.1	0.18	1.15	31.0	
Cellulose	11	-	-	93.4	6.1	0.5	43.0	6.4	0.0	0.00	50.1	0.87	1.79	16.5	[184]
	11a	30	150	88.9	9.6	1.5	43.9	6.6	0.0	0.00	48.0	0.82	1.80	16.6	
	11b	30	180	89.3	9.5	1.2	45.6	6	0.0	0.00	47.2	0.78	1.58	18.9	
	11c	30	200	84.0	14.7	1.3	51.2	5.7	0.0	0.00	41.8	0.61	1.34	23	
	11d	30	220	63.6	35.0	1.4	63.5	4.7	0.0	0.00	30.4	0.36	0.89	26.5	
	11e	30	250	56.9	41.2	1.9	69.4	4.6	0.0	0.00	24.1	0.26	0.80	26.8	
	11f	30	280	42.2	55.1	2.7	76.5	4.5	0.0	0.00	16.3	0.16	0.71	27.7	
Grape pomace	12	-	-	72.6	21.9	5.4	49.1	6.3	2.29	0.0	42.3	0.65	1.54	20.0	[177]
	12a	30	175	69.3	1.4	29.2	58.64	6.21	2.19	0.0	33.0	0.42	1.27	24.3	
	12b	30	200	67.7	1.1	31.3	60.16	6.11	1.72	0.0	32.0	0.40	1.22	24.8	
	12c	10	225	67.1	1.9	30.9	61.39	6.4	1.72	0.0	30.5	0.37	1.25	25.8	
	12d	30	225	64.6	1.7	33.7	61.87	6.13	1.79	0.0	30.2	0.37	1.19	25.7	
	12e	60	225	64.6	2.1	33.2	63.05	6.31	1.87	0.0	28.8	0.34	1.20	26.3	
	12f	30	250	58.6	3.4	37.9	65.89	5.8	2.17	0.0	26.1	0.30	1.06	27.0	
	12g	30	275	54.3	2.7	43.0	68.32	5.92	2.32	0.0	23.5	0.26	1.04	28.3	
	12h	30	250	63.9	8.2	27.8	55.92	6.35	2.2	0.0	35.5	0.48	1.36	23.1	
	12i	30	300	51.2	10.5	38.2	62.9	5.41	2.65	0.0	29.0	0.35	1.03	25.3	

Appendix 2 Composition and property ranges for different ranks of coal.

Fuel	VM (%)	FC (%)	Ash (%)	C (%)	H (%)	N (%)	S (%)	O (%)	O/C	H/C	HHV (MJ/Kg)	Reference
Anthracite High	12	85	15	85	3.5	1	2.5	9	0.11	0.041	31.4	[186]
Anthracite Low	2	75	4	75	1.5	0.5	0.5	5.5	0.07	0.020	27.9	
Bituminous High	45	70	15	80	6	2.5	6	10	0.13	0.075	33.7	
Bituminous Low	15	50	4	65	4.5	0.5	0.5	4.5	0.07	0.069	27.9	
Sub-bituminous High	45	57	10	70	6.5	1.5	1.5	30	0.43	0.093	23.3	
Sub-bituminous Low	28	30	3	55	5.5	0.8	0.3	15	0.27	0.100	17.4	
Lignite High	32	30	15	45	7.5	1	2.5	48	1.07	0.167	17.4	
Lignite Low	24	25	3	35	6	0.6	0.3	38	1.09	0.171	14.0	
Switchgrass Slow Pyrolysis	7.1	39.5	52.5	39.4	1.3	0.7	0.00	58.6	1.49	0.033	15.4	[470]
Switchgrass Fast Pyrolysis	16.4	26.4	54.6	38.7	2.5	0.6	0.21	58.0	1.50	0.065	16.3	
Switchgrass Gasification	10.3	34.3	53	42.8	1.6	0.8	0.17	54.6	1.28	0.037	15.86	
Corn Stover Slow Pyrolysis	11.1	54.7	32.4	62.8	2.9	1.3	0.05	33.0	0.52	0.046	21.6	
Corn Stover Fast Pyrolysis	14.9	34.4	49.7	37.8	2.5	0.8	0.06	58.8	1.56	0.066	13.83	
Corn Stover Gasification	5.5	38.5	54	38.5	1.3	0.7	0.09	59.4	1.54	0.034	15.29	
Hardwood High	80	25	3	50	6	0.3	0	44	0.88	0.120	21	[471], [472]
Hardwood Low	75	20	0.6	47	6	0.1	0	44	0.94	0.128	19	
Softwood High	80	25	3	53	6	0.3	0	44	0.83	0.113	22.05	
Softwood Low	75	20	0.6	50	6	0.1	0	44	0.88	0.120	19.95	
Charcoal High	25	75	5	80	3.5	0.4	0	10	0.13	0.044	28	
Charcoal Low	20	70	5	60	2.5	0.2	0	2.5	0.04	0.042	28	

Appendix 3 Pyrolysis conditions for comparison.

Feedstock	Entry	Time (min)	Temp (°C)	VM (%)	FC (%)	Ash (%)	C (%)	H (%)	N (%)	S (%)	O (%)	O/C	H/C	HHV (MJ/Kg)	Reference
Sawdust (Q. Rotundifolia)	1	-	-	83.6	14.1	2.3	50.3	6.1	0.2	0	41.1	0.817	0.121	19.7	[473]
	1a	120	300	65.1	33.4	1.5	58.8	5	0.3	0	34.5	0.587	0.085	23.1	
	1b	120	350	43.4	55.3	1.3	75.7	3.3	0.6	0	19.1	0.252	0.044	27.3	
	1c	120	400	34.5	64.2	1.3	76.9	3.3	0.4	0	18.2	0.237	0.043	28.8	
	1d	120	450	21.8	76.4	1.8	81.2	3	0.4	0	13.6	0.167	0.037	30.7	
	1e	120	500	17.5	79.7	2.8	83.0	2.5	0.6	0	11.2	0.135	0.030	30.2	
	1f	120	550	14.7	82.2	3.1	87.1	2.4	0.5	0	6.9	0.079	0.028	32.7	
	1g	120	600	13.2	83.6	3.2	89.4	2.2	0.4	0	4.8	0.054	0.025	32.6	
Sawdust (P. Halepensis)	1	-	-	82.5	17.0	0.5	48.9	6.0	0.1	0	44.5	0.910	0.123	20.2	
	1a	120	300	68.1	31.3	0.6	57.8	5	0.2	0	36.5	0.631	0.087	22.7	
	1b	120	350	49.5	49.4	1.2	72.1	4.1	0.2	0	22.5	0.312	0.057	26.0	
	1c	120	400	36.5	62.2	1.3	74.7	3.6	0.2	0	20.3	0.272	0.048	28.3	
	1d	120	450	27.4	71.2	1.4	78.3	3.2	0.2	0	16.8	0.215	0.041	29.9	
	1e	120	500	20.2	78.1	1.7	81.8	3	0.2	0	13.4	0.164	0.037	31.2	
	1f	120	550	18.1	80.2	1.7	86.1	2.5	0.2	0	9.6	0.111	0.029	31.6	
	1g	120	600	13.4	84.9	1.7	87.4	2.2	0.3	0	8.5	0.097	0.025	32.4	

Appendix 4 Aggregated Ground Dried Bread Waste combustion analysis, from Bomb Calorimetry, TGA, and CHNS analysis.

Temperature (°C)	Time (Mins)	Environment	VM (%)	FC (%)	Ash (%)	C (%)	H (%)	N (%)	S (%)	O (%)	O/C	H/C	HHV (MJ/Kg)	Yield (g)	Yield (%)
Ground Dried Bread Waste Feedstock			89.8	7.2	3	42.22	6.71	2.55	0.02	48.5	1.15	0.16	17.69	-	-
160	30	CO_2	90.1	6.3	3.6	52.4	7.81	4.53	0.18	35.07	0.67	0.15	29.57	0.92	18.33
160	60	CO_2	85.7	10.4	3.8	50.96	7.46	4.88	0.44	36.27	0.71	0.15	34.50	0.88	17.70
160	90	CO_2	81.4	13.4	5.3	56.85	8.2	5.03	0.57	29.35	0.52	0.14	35.02	0.50	10.05
180	30	CO_2	77.7	16.8	5.6	55.64	6.86	4.76	0.56	32.18	0.58	0.12	35.73	0.71	14.12
180	60	CO_2	80.3	15.4	4.3	58.39	6.44	4.23	0.51	30.44	0.52	0.11	36.02	0.84	16.90
180	90	CO_2	67.3	30.1	2.6	67.69	6.47	4.51	0.34	20.99	0.31	0.10	35.69	1.06	21.20
200	30	CO_2	73.2	23.7	3.1	63.09	5.76	3.95	0.17	27.03	0.43	0.09	37.11	1.21	24.26
200	60	CO_2	58.1	39.6	2.3	64.48	5.47	3.52	0.17	26.36	0.41	0.08	36.46	1.50	30.00
200	90	CO_2	58.8	38.8	2.4	64.54	5.3	3.73	0.13	26.3	0.41	0.08	39.66	1.53	30.60
160	30	He	89.9	7	3.1	48	7.24	4.36	0.16	40.25	0.84	0.15	21.00	0.91	18.10
160	60	He	84	11.5	4.5	50.65	7.55	4.09	0.36	37.35	0.74	0.15	23.52	0.55	10.91
160	90	He	81.2	12.7	6.1	50.77	6.95	4.45	0.49	37.33	0.74	0.14	23.14	0.46	9.11
180	30	He	81.8	12.4	5.8	54.96	7.45	4.52	0.62	32.45	0.59	0.14	23.66	0.35	7.05
180	60	He	69.2	27.8	3	60.36	6.58	4.3	0.41	28.34	0.47	0.11	25.91	1.09	21.86
180	90	He	64.8	32.1	3.1	58.48	5.77	3.79	0.29	31.67	0.54	0.10	34.00	1.08	21.51
200	30	He	67.4	29.8	2.8	62.38	5.98	3.37	0.23	28.04	0.45	0.10	25.85	1.36	27.15
200	60	He	60.5	37.6	1.9	63.63	5.46	3.29	0.16	27.46	0.43	0.09	25.85	1.48	29.56
200	90	He	68.8	28.2	3.1	65.3	5.3	3.23	0.12	26.05	0.40	0.08	26.93	1.38	27.62
180	60	PA	89.5	8.6	1.9	68.01	10	2.59	0.05	19.35	0.28	0.15	31.44	1.40	27.98
180	60	CO_2, 3 mol% EtOH	81.5	13.4	5.2	56.91	6.69	4.59	0	31.81	0.56	0.12	23.60	0.65	12.97
180	60	CO_2, 6.7 mol% EtOH	79.1	14.6	6.2	60.28	7.84	5.33	1.08	25.47	0.42	0.13	35.81	0.60	11.96
180	60	CO_2, 11.1 mol% EtOH	76.6	19.2	4.2	54.33	7.39	4.96	0.77	32.55	0.60	0.14	33.72	0.60	12.05

180	60	CO_2, 16.6 mol% EtOH	81.3	13.6	5.1	52.84	7.34	4.68	0.82	34.32	0.65	0.14	20.09	0.32	6.37
180	60	CO_2, 23.5 mol% EtOH	84.5	6.3	9.3	53.73	7.49	3.65	1.24	33.89	0.63	0.14	18.66	0.26	5.12
180	60	CO_2, 32 mol% EtOH	90.2	5.3	4.6	44.43	7.21	0.56	0.2	47.6	1.07	0.16	17.29	2.74	54.77
180	60	CO_2, 42.9 mol% EtOH	91.6	5.4	3	44.03	7.28	0.45	0.17	48.07	1.09	0.17	17.13	1.41	28.19
180	60	CO_2, 56.9 mol% EtOH	92.1	5.4	2.5	43.09	6.93	0.62	0.06	49.3	1.14	0.16	26.26	2.86	57.24
180	60	CO_2, 75.3 mol% EtOH	81.5	16.3	2.2	44.82	6.88	1.89	0.02	46.39	1.04	0.15	17.58	1.93	38.53
180	60	CO_2, 100 mol% EtOH	84.9	12.9	2.2	42.93	6.73	1.97	0.05	48.32	1.13	0.16	17.43	3.30	66.00

Appendix 5 Pictures of solid sol-gel catalysts synthesised in bulk on a laboratory scale, available for colour verification.

Appendix 6 Pluronic P123 Raman spectra obtained from Sigma Aldrich.

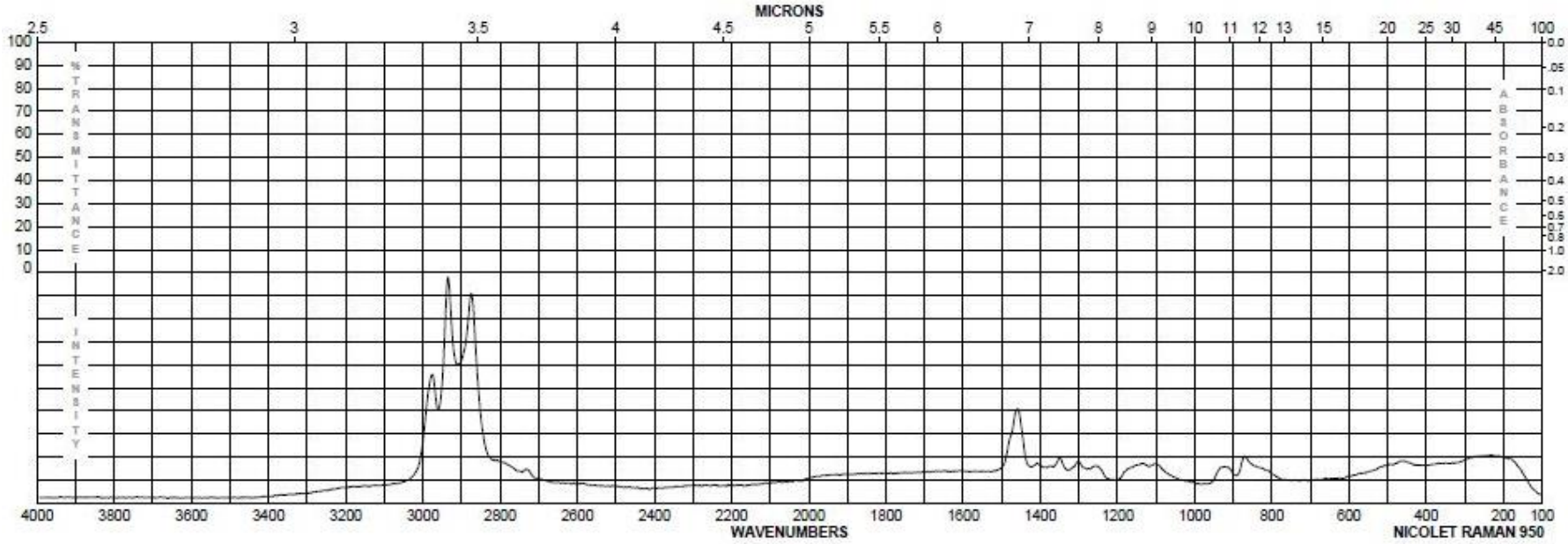

Appendix 7 Collated SEM/EDS Analysis results

Catalyst	Phase 1 type	Phase 1 mass %	Phase 2 type	Phase 2 mass %
CoAl	CuO	7.32	Al_2O_3	90.29
CoSi	CoO*	0.26	SiO_2	99.74
NiAl	NiO	17.97	Al_2O_3	82.03
NiSi	NiO	23.93	SiO_2	76.07
VAl	V_2O_5	21.15	Al_2O_3	78.85
VSi	V_2O_5	4.57	SiO_2	95.43
MoAl	MoO_3	67.54	Al_2O_3	32.46
MoSi	MoO_3	4.03	SiO_2	95.97

Appendix 8 Calibration curve for 5-HMF concentration determination by GC-MS.

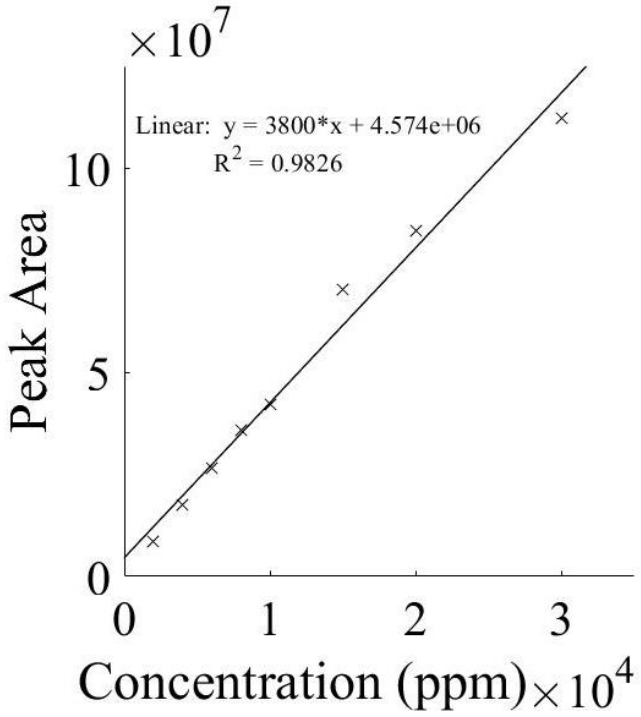

Appendix 9 Synchronous (a) and asynchronous (b) 2D correlation contour plots for ambient ethanol/water mixtures with ethanol concentration as the perturbation.

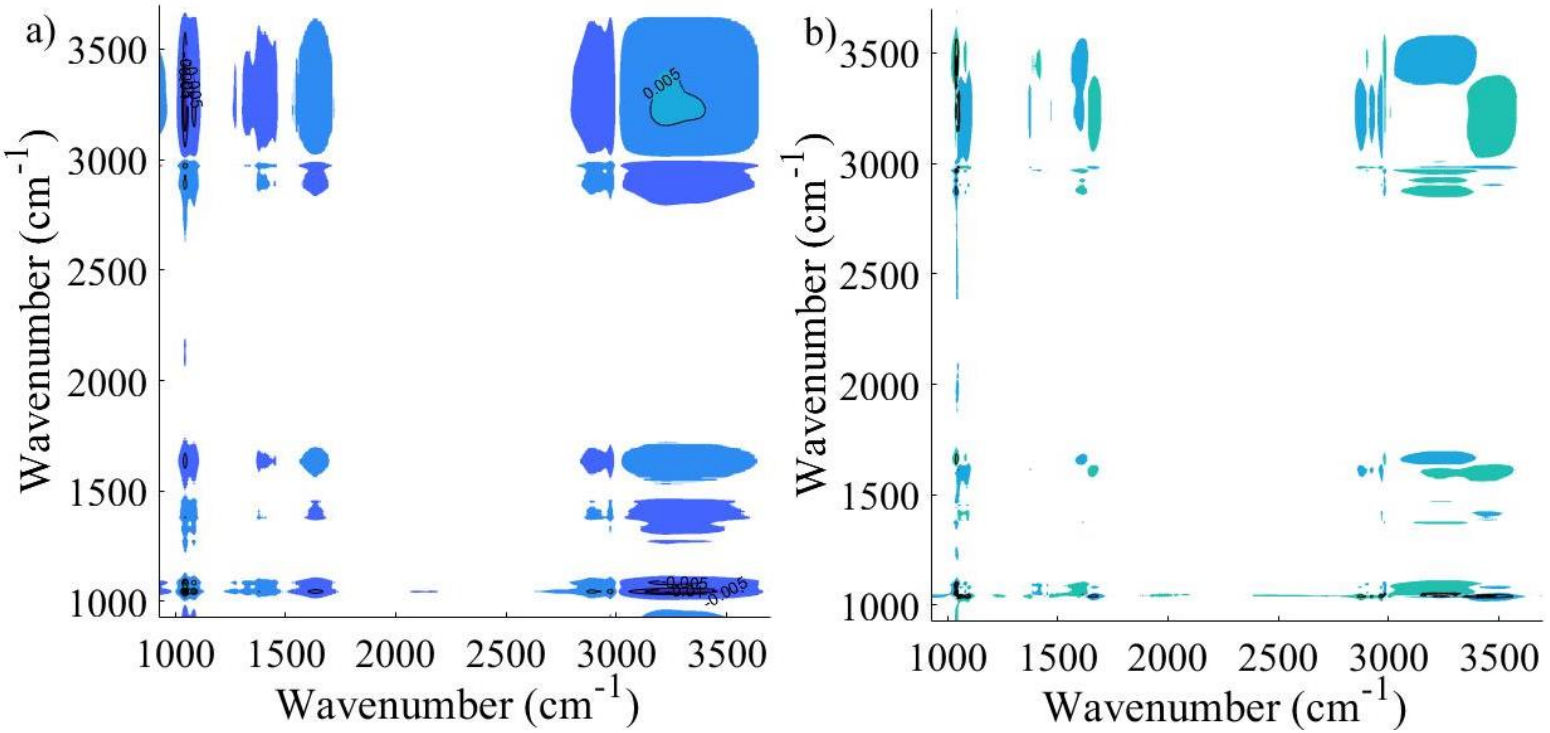

Appendix 10 Synchronous (a) and asynchronous (b) 2D correlation contour plots for ambient isopropanol/water mixtures with isopropanol concentration as the perturbation.

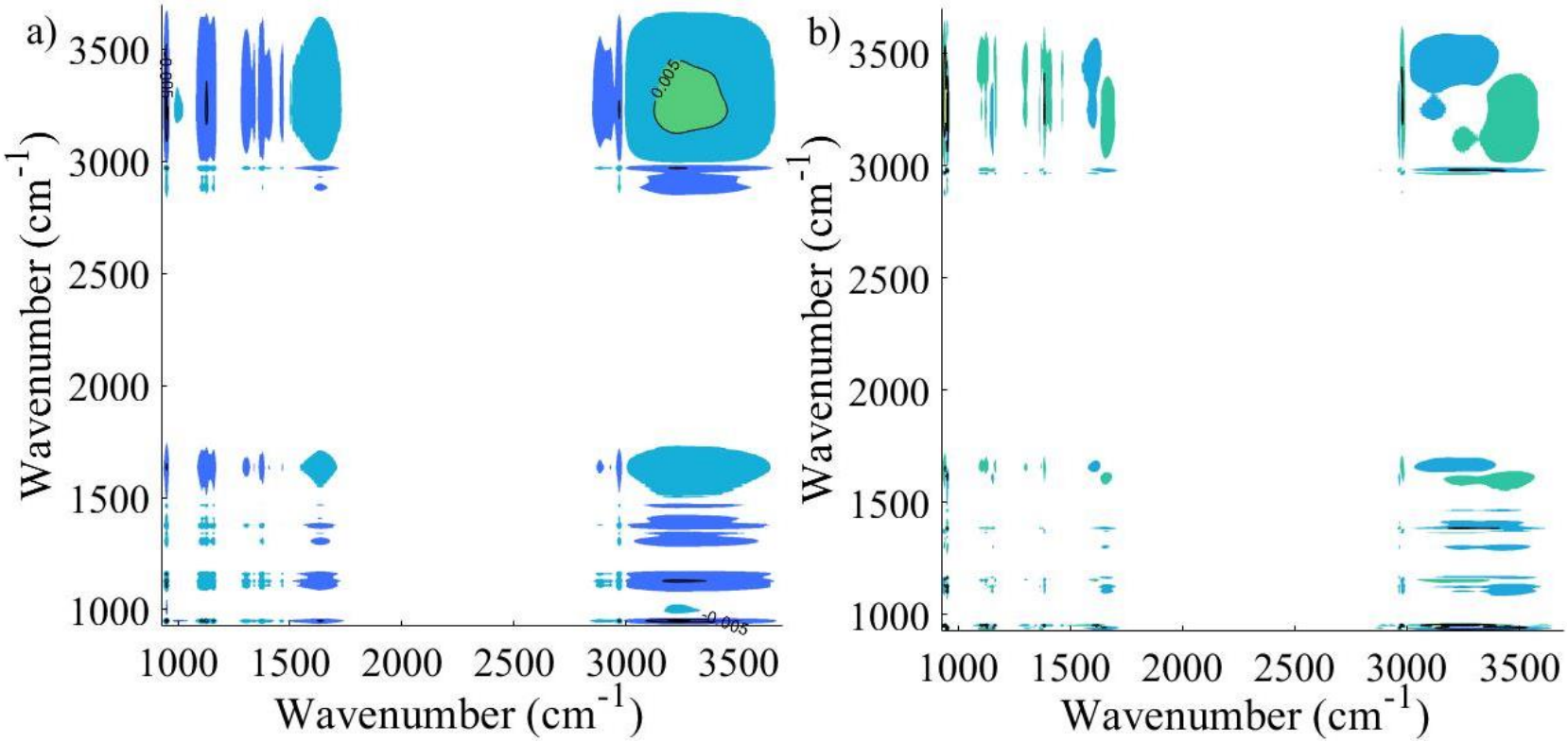

THE JOURNAL OF PHYSICAL CHEMISTRY C
A JOURNAL OF THE AMERICAN CHEMICAL SOCIETY

pubs.acs.org/JPCC

Article

Operando Studies of Aerosol-Assisted Sol−Gel Catalyst Synthesis via Combined Optical Trapping and Raman Spectroscopy

Gareth Davies, Justin Driver, Andrew Ward, Leila Negahdar, and James McGregor*

Cite This: https://doi.org/10.1021/acs.jpcc.1c07517

Read Online

ACCESS | Metrics & More | Article Recommendations | Supporting Information

ABSTRACT: New insights have been gained into chemical transformations occurring in the initial stages of aerosol-assisted sol−gel (AASG) synthesis of catalysts. This has been achieved through the combined application of optical trapping and Raman spectroscopy. AASG is an emerging technology in catalyst manufacturing that presents numerous advantages over conventional approaches, including the ability to access unique catalyst morphologies. However, the processes occurring during synthesis are largely inferred from bulk-phase analyses due to challenges in conducting *in situ* or *operando* measurements on moving aerosols within a flow tube. Herein, these obstacles are overcome through Raman spectroscopic interrogation of a single aerosol droplet constrained within an optical trap, which acts as a direct analogue for a particle moving along a flow tube. These studies represent the first *operando* investigations of AASG synthesis. The synthesis of Ni/Al_2O_3 catalysts has been studied, with spectroscopic interrogation conducted on each component of the precursor synthesis solution, where possible, up to and including a mixture containing all components necessary for catalyst synthesis. Raman spectroscopy confirms the formation of stable self-assembled macrostructures within the aerosol and provides direct insights into the reaction mechanisms. Crucially, evidence was obtained allowing alternative reaction pathways to be postulated within the confined environment of an aerosol droplet in comparison to bulk-phase syntheses. In aerosols where nickel was not present, but contained all other components, isothermal room-temperature studies showed the formation of stable but unreactive droplets of ∼1 μm, which were proposed to contain micelle-type structures. Upon heating, initial gelation transformations were seen to be achieved at temperatures higher than ∼56 °C. Notably, little loss of spectral intensity corresponding to the C−H stretch (ethanol) was observed from the heated aerosol, implying that evaporation is not a prerequisite for the reaction. When nickel is present in the synthesis solution reactive transformations occur at room temperature, proposed to result in a continuous Al−O−Ni−NO_3 structure; a more rapid transformation takes place at elevated temperatures. These results provide the first direct evidence of the processes occurring within aerosols during AASG and shed new light on the mechanistic understanding of this technology. This therefore facilitates the design of new synthetic approaches and hence the production of catalysts and other materials with enhanced properties.

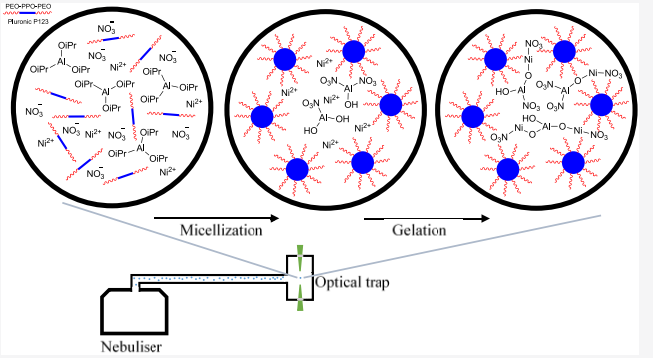

1. INTRODUCTION

Aerosol-assisted sol−gel (AASG) synthesis is a recently established method of synthesizing nanostructured catalysts with controllable porosity and surface functionality using a continuous method, which produces a low volume of waste material.[1] AASG synthesis therefore has advantages over conventional catalyst synthesis methods; however, the transitions that occur during the sol−gel process within the aerosol are complex and still not completely understood. This is in part due to the challenges of conducting *in situ* or *operando* characterization measurements in an aerosol environment.[2] In this work, a novel approach combining optical trapping and Raman spectroscopy is employed to directly probe these processes and hence provide insights into AASG synthesis.

AASG combines aerosol processing with sol−gel synthesis. In conventional sol−gel synthesis, nanostructured materials are produced under acidic or basic conditions using templating agents (e.g., block copolymers) to control the mesophase formation of the material.[3] The chemical precursors react through hydrolysis and condensation reactions to form solid compounds. Sol−gel-synthesized materials have applications in adsorption, catalysis, drug delivery, and energy storage.[4−7] While AASG is a relatively new approach in catalyst manufacturing, a number of promising metallosilicate epoxidation and acetalization catalysts have been synthesized.[8−10]

Received: August 24, 2021
Revised: September 29, 2021

AASG-synthesized titanium silicates were shown to be highly active for cyclohexane epoxidation giving product yields of up to 62%.[11] Additionally, AASG-based processes have no liquid byproducts, offer facile cheap collection processes with no separation, and yield high-purity products with unique morphologies.

Considering the mechanism of AASG, an aerosol is created containing the same component species as in conventional sol−gel synthesis. When the aerosol is heated, it is hypothesized that self-assembled micelles form.[12] Subsequently, multiple hydrolysis and condensation reactions are proposed to proceed concurrently to produce a highly branched agglomerate in the sol, which ultimately becomes sufficiently cross-linked to form a gel. Both steps are either acid- or base-catalyzed (Figure S1). The formation of self-assembled micelles in AASG is referred to as evaporation-induced self-assembly (EISA). After this, thermal or chemical treatment is performed to remove templating agents and expose porosity in the catalyst.

A range of techniques has been applied for the analysis of aerosol-synthesized materials after synthesis, characterizing properties such as particle size, molecular mass, structure, composition, etc.[13] However, it is highly challenging to conduct accurate spectroscopic studies of the aerosol while the synthesis reactions are taking place as the aerosol droplets travel continuously along a flow tube. A single droplet cannot therefore be tracked as a function of time. A further challenge is that chemical concentrations in a given region are typically low due to the low density of droplets. Mechanistic insights are therefore typically inferred from measurements on bulk syntheses. Raman spectroscopy of bulk solutions has been used to identify micelle formation and critical micelle concentration of surfactants, which can be used in AASG.[14,15] The onset of micelle formation and aggregation can be identified by a change in the peak relative intensity, e.g., a change in the ratio of the asymmetric CH_3 stretching vibration to the symmetric CH_3 stretching vibration, or by a shift in the peak position as surfactant concentration increases.

In the present work, these limitations are overcome through conducting Raman spectroscopic interrogation of a single aerosol droplet while it is constrained within an optical trap. Optical tweezers use focused light to hold either liquid or solid particles in place and can be applied to particles ranging in size from 10 nm to 10s of μm.[16] This is achieved by balancing the radiation pressure imparted by two focused laser beams that are vertically (z-axis) opposed in a counter-propagating geometry. Radiation pressure arises through the transfer of momentum as photons are scattered from a surface. Here, the laser beams also have a Gaussian beam profile creating an intensity gradient to assist stability in the horizontal x- and y-axes. The main physical conditions that permit trapping stability are that the levitated droplet has: (i) a refractive index greater than air; (ii) an element of symmetry to evenly scatter light; and (iii) a low enough mass whereby the radiation pressure can offset gravitational force. Optical trapping has previously been used for other applications in conjunction with vibrational spectroscopies to provide information on the nature of multicomponent particles comprising both aqueous and organic phases.[17]

Monitoring a single droplet over time held in a fixed position in space provides a direct analogue for a particle instead of moving through space as happens in a flow tube, with increased time corresponding to increased distance along the tube. A key development is the ability to externally heat the optical trapping cell to induce a reaction. Any influence of the trapping laser on droplet heating is expected to be limited in comparison to the external heating. Boyer et al. have reported minimal heating through his mechanism even at intense laser powers, while Hunt et al. reported only a few degrees of heating at moderate laser powers (<25 mW).[18,19] This approach, applied herein, can therefore be considered an *operando* investigation of the AASG synthesis process. The reaction system of specific focus in this work is organic transformations. which occur in the initial stages of the AASG synthesis of Ni/Al_2O_3, a catalyst with a wide range of current and potential future industrial applications including CO_2 utilization and biomass conversion. This will, for the first time, provide direct measurements of the reactions occurring during AASG synthesis, yielding valuable insights into this process.

2. EXPERIMENTAL SECTION

2.1. Reagents/Chemicals. The catalyst precursors employed were nickel nitrate hexahydrate ($Ni(NO_3)_2{\cdot}6H_2O$, ≥97%) and aluminum isopropoxide (Al-iPr, ≥98%), while the templating agent was pluronic triblock polymer (P123, $M_w \approx$ 5800, poly(ethylene oxide) (PEO)−poly(propylene oxide) (PPO)−PEO). The catalyst synthesis reactions were conducted in acidified solvent solution produced from mixtures of ethanol (C_2H_5OH, ≥98%) and nitric acid (HNO_3, 68%). Prior to use, ethanol was dried using molecular sieves (3 Å, Sigma-Aldrich), whereas all other chemicals were used as received. All chemicals were purchased from Sigma-Aldrich, U.K.

2.2. Sol−Gel Synthesis Procedure. The synthesis procedures were adapted from previous reports describing the bulk preparation of Ni/Al_2O_3 by the EISA method.[3] Under vigorous stirring, a weighed quantity of P123 (1.21 g) was added to ethanol (10 mL), with the mixture then sealed and gently heated (∼40 °C) to assist dissolution. Following the complete dissolution of P123, a weighed quantity of $Ni(NO_3)_2{\cdot}6H_2O$ (0.49 g) was added and the solution (hereafter called "solution A") was then allowed to cool to room temperature. Separately, a measured quantity of Al-iPr (1.72 g) was added to a beaker, prior to the addition of ethanol (10 mL). Under gentle stirring, the dropwise addition of HNO_3 (1 mL) caused a gradual dissolution of Al-iPr without heating, after which the solution (hereafter "solution B") was allowed to cool to room temperature. Following this, solution A was added rapidly to solution B under moderate stirring, consequently affecting final concentrations as follows: P123 (0.01 M); Al-iPr (0.4 M); and $Ni(NO_3)_2{\cdot}6H_2O$ (0.13 M). These quantities corresponded to a theoretical nickel loading of ∼24.5 wt % in the final Ni/Al_2O_3 catalyst. All *operando* investigations were conducted on freshly mixed solutions (∼1−3 days).

2.3. Bulk Analysis (*Ex Situ* Raman). For bulk syntheses, a freshly mixed solution was transferred to an oven and heated (∼70 °C, 16 h) to initiate EISA, which subsequently yielded a powder composed of gel particles. A sample of this gel was retained, with the remainder transferred to a furnace for calcination (600 °C, 3 h) to afford the final Ni/Al_2O_3 catalyst. These samples were then spectroscopically analyzed by *ex situ* Raman spectroscopy. Raman analysis was performed using a Renishaw inVia Raman microscope equipped with a 514 nm (green) Ar laser at a power of 12 mW. Spectra were acquired

https://doi.org/10.1021/acs.jpcc.1c07517
J. Phys. Chem. C XXXX, XXX, XXX−XXX

over the range 4000−50 cm^{-1} employing acquisition parameters of 30 s scans and 20 accumulations.

2.4. Aerosol Analysis (*Operando* Raman). For AASG syntheses, the freshly mixed solution was transferred into a nebulizer (aerosonic, combineb model 3019) that delivered mist of aerosol droplets into a trapping cell, the precise configuration of which is described in Section 2.5. From this aerosol, a single droplet could be trapped and lowered into the center of an annular ceramic heater, with the applied power then increased incrementally (0−14 W) to raise the internal temperature of the cell (≤200 °C). The setup has previously been described in detail by McGrory et al.[20] The heating element in the cell creates convection currents, which apply viscous drag to the trapped aerosol as the flow rate increases. In the present setup, the convective flow was minimized using a baffle system. Direct-temperature measurements were not possible since the positioning of thermocouples sufficiently close to the trapped droplet would disrupt the trapping beams. Instead, the cell temperature was inferred from calibration measurements performed on an empty cell, where a thermocouple could be positioned directly in the center of the annular heater to measure the temperature over a range of powers (Figure S2). The elevated temperature in the cell initiated EISA and the incipient formation of the Ni/Al_2O_3 catalyst, which was spectroscopically analyzed by *operando* Raman spectroscopy. Measurements were typically taken at the onset of trapping and subsequently at intervals of 10 or 30 s over the spectral range 500−3100 cm^{-1} until the droplet was lost from the optical trap. In this way, the catalyst formation could be spectroscopically interrogated under conditions representative of the AASG process.

2.5. Optical Trapping Configuration. Liquid droplets were delivered to a small trapping cell, of aluminum construction, with approximate dimensions 10 × 2 × 1 cm^3. Windows made from borosilicate coverslips allowed the passage of the laser beams through the cell. Droplets were generated using an ultrasonic nebulizer (aerosonic, combineb model 3019) to generate a mist, which flowed into the cell through 1/4″ poly(tetrafluoroethylene) (PTFE) tubing. A right-angle turn in the tubing is achieved using a Portex PVC connector tube.

Droplets were trapped using counter-propagating Nd:YAG laser beams operating at 1064 nm. The typical laser beam powers required for stable trapping were 15 mW through the top objective and 10 mW through the lower objective. The objective lenses were Mitutoyo x50 NA 0.42 long working distance objectives. The asymmetric power balance was required to force the particle into the optical focus plane of the lower objective thereby allowing focused images to be acquired. The Nd:YAG beam is passed through a beam splitter (Oz Optics) to obtain two separate fiber-coupled beams. Both beams are then expanded and collimated so that they slightly overfill the back apertures of the objective lenses. Dichroic mirrors (CVI Melles Griot) reflect the laser beams but allow transmission of illumination light and the Raman signals. The LED illumination (Comar Optics) is filtered to prevent interference with the Raman signal.

Raman spectra were acquired by probing the droplet using a 514.5 nm laser. The laser was directed through the lower objective lens and focused onto the droplet. The backscattered Raman signal was collected using the same lens and focused into a spectrometer (Acton SP2500i and Princeton Instruments Spec 10 CCD). A 600 grove/mm grating was calibrated using spectrophotometric-grade toluene as a reference. The typical laser power was 2 mW, acquisition time was 30 s, and the 514.5 nm laser was shuttered such that the droplet was only illuminated during the collection of spectra.

3. RESULTS AND DISCUSSION

Raman spectroscopic analysis of the bulk solutions and the catalyst obtained via standard sol−gel synthesis are presented in Section 3.1, while Section 3.2 presents, for the first time, the corresponding data for the initial stages of the AASG synthesis at isothermal conditions. The influence of heating is then examined in Section 3.3. Finally, Section 3.4 discusses mechanistic insights gained from these studies.

3.1. Bulk Solutions. Conventional, i.e. nonaerosol, synthesis of Ni/Al_2O_3 via a sol−gel route was initially conducted to compare the bulk solutions to the aerosol. Raman spectroscopic characterization of each stage of the synthesis procedure was conducted, namely: individual components; precursor sol−gel (EISA); and the final solid catalyst. The spectrum obtained for bulk ethanol is shown in Figure 1, and it is compared to the subsequent stages of catalyst synthesis in Figure 2. The assignment of the peaks identified is shown in Table 1.

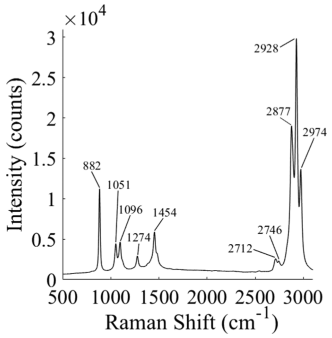

Figure 1. Raman spectra for bulk ethanol (600 groove, centered at 1900 cm^{-1}, 10 s, 2 mW).

When comparing bulk ethanol spectral intensities to the sol precursor under identical conditions, a clear decrease in the peak intensity is observed indicating the reduced concentration of ethanol. There are no additional peaks present, indicating that no reaction has yet taken place. The EISA sample however shows a clear increase in the peak intensity of the 1048 cm^{-1} vibration, indicative of the $-NO_3^-$ symmetric stretch. This increase is ascribed to the increase in the relative concentration of the nitrate component due to evaporation of ethanol during EISA. Raman bands present for the final calcined Ni/Al_2O_3 are of only very low intensity as compared to ethanol, as well as compared to the sol and gel (EISA) phases, consistent with the previous literature.[21]

3.2. Isothermal Aerosols. To determine the influence of each component upon the reactions taking place, spectroscopic interrogation was performed on each component individually, where possible, and on their mixtures up to and including that containing all components required for the AASG synthesis of Ni/Al_2O_3. The composition of the aerosols studied is summarized in Table 2; the aerosols are denoted EP (ethanol, P123), EPN (as EP with the addition of HNO_3), EPNA (as EPN with the addition of Al-iPr), and EPNAN (as EPNA with the addition of $Ni(NO_3)_2{\cdot}6H_2O$). Studies were first conducted

https://doi.org/10.1021/acs.jpcc.1c07517
J. Phys. Chem. C XXXX, XXX, XXX−XXX

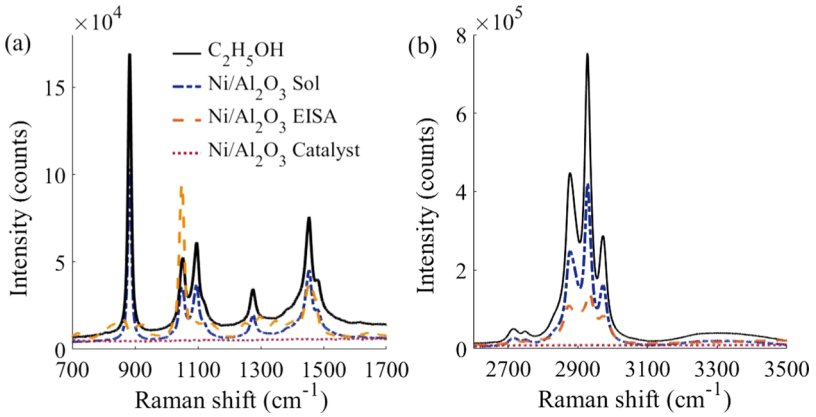

Figure 2. Raman spectra for ethanol and for Ni/Al_2O_3 sol, gel (EISA), and dried catalyst between (a) 700−1700 cm^{-1} and (b) 2600−3500 cm^{-1} acquired using a Renishaw inVia Raman microscope 514 nm (green), Ar laser, 12 mW.

Table 1. Bands Identified in Raman Spectra at Different Stages of Ni/Al_2O_3 Synthesis[a]

$\Delta\nu$ (cm^{-1})	Raman band assignment	$\Delta\nu$ (cm^{-1})	Raman band assignment
1048	$-NO_3^-$ symmetric stretch	∼2705	C_2H_5OH combinational frequencies
1051	C−O symmetric stretch	2744	C_2H_5OH combinational frequencies
1096	C−O asymmetric stretch	2877	CH_2 asymmetric stretch
1274	CH_2 torsion-rotation	2928	CH_3 symmetric stretch
1454	CH_3 and CH_2 bend	2974	CH_3 asymmetric stretch

[a]Band assignment is based on previous studies.[22−25]

at room temperature to provide a stable environment in which to study the stability of the droplets and the initial stages of gelation.

The presence of whispering gallery modes (WGMs) was observed in all Raman spectra for the trapped droplets, indicating sphere formation (Figure S3).[26] WGMs occur in the optical cavity formed by the spherical droplets, as described by the Mie scattering theory.[27] The resonance positions are dependent on the droplet size and refractive index. WGMs were digitally filtered during data processing using Spectragryph (http://spectroscopy.ninja) adaptive baseline removal (25% coarseness) to aid spectral analysis. The presence of WGMs allows for the size and refractive index of the trapped particle to be estimated through Mie scattering analysis; this is explored further in Section 3.2.3.[28]

It is notable that the H_2O content in each system is sufficiently low that Raman spectral bands associated with H_2O are not observed in the Raman spectra of the trapped aerosols over the spectral range investigated. Previous studies have shown that in bulk ethanol/water mixtures the O−H bending vibration (∼1630 cm^{-1}) is of low intensity at water concentrations below ∼60% v/v.[22] In the present work, the water content (v/v%) of EP, EPN, EPNA, and EPNAN are estimated at 2, 3.4, 3.2, and 3.9%, respectively, based on the concentrations of the precursor solutions. Note that the intensity and wavenumber of Raman vibrations associated with water may be influenced by disruptions to the mesoscale hydrogen-bonding network through interaction with other components present in solution.[22,29]

3.2.1. Transformations in Metal-Free Droplets. Raman spectra for EP and EPN are shown in Figure 3. Characteristic Raman peaks for ethanol, i.e., CH_3 and CH_2 bending vibrations at 1454 cm^{-1} and C−H stretching vibrations at 2877, 2928, and 2974 cm^{-1} (cf. Figure 1), are clearly visible and dominate the spectra of both aerosols. The evaporation of ethanol from the droplets is characterized by the reduction in the intensity between the initial and final scans (Figure 3).

Considering the stability of the aerosol in the optical trap, it proved relatively facile to hold EP and monitor changes in the Raman spectra over time (analysis was conducted over a period in excess of 4 h). However, it is notable that an aerosol comprising ethanol alone, in the absence of P123, could only be contained in the trapping environment for less than a few seconds due to rapid evaporation. P123 therefore exerts a stabilizing influence over the aerosol, significantly reducing evaporative losses of ethanol. Different physical mechanisms are discussed to explain this observation. The bulk solution employed has a concentration of P123 40 times larger (10 mM) than the reported critical micellization concentration (CMC) of P123 of 0.25 mM.[30] Therefore, the P123 concentration within the aerosol is expected to be above the

Table 2. Composition of the Droplets Trapped and Investigated with Raman Spectroscopy[a]

	component					
reference	ethanol (C_2H_5OH)	water (H_2O)	triblock pluronic (P123)	nitric acid (HNO_3)	aluminum isopropoxide (Al-iPr)	nickel nitrate ($Ni(NO_3)_2$)
EP	√		√			
EPN	√	√	√	√		
EPNA	√	√	√	√	√	
EPNAN	√	√	√	√	√	√

[a]Water (H_2O) is not added as a separate component but is present in nitric acid (HNO_3) and nickel nitrate hexahydrate ($Ni(NO_3)_2{\cdot}6H_2O$) solutions. H_2O (≤2%) present in ethanol is neglected. EP (ethanol, pluronic P123), EPN (ethanol, pluronic P123, nitric acid), EPNA (ethanol, pluronic P123, nitric acid, aluminum alkoxide), and EPNAN (ethanol, pluronic P123, nitric acid, aluminum alkoxide, nickel nitrate).

https://doi.org/10.1021/acs.jpcc.1c07517
J. Phys. Chem. C XXXX, XXX, XXX−XXX

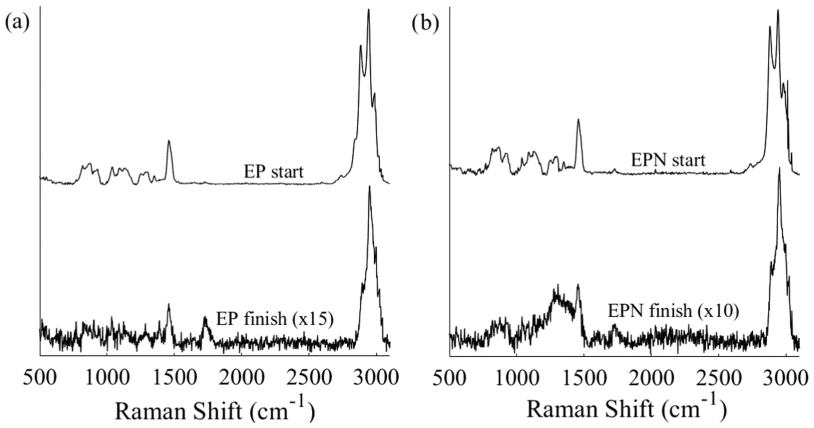

Figure 3. Offset Raman spectra for (a) EP and (b) EPN droplets. Top curves show the averaged first 10 scans and bottom curves show the averaged final 10 scans. The time between initial and final scans was ~250 min for EP and ~50 min for EPN. Note that to ease comparison the intensity of the final scans has been expanded 15-fold for EP and 10-fold for EPN. (600 groove, centered at 1900 cm^{-1}, 30 s, 2 mW).

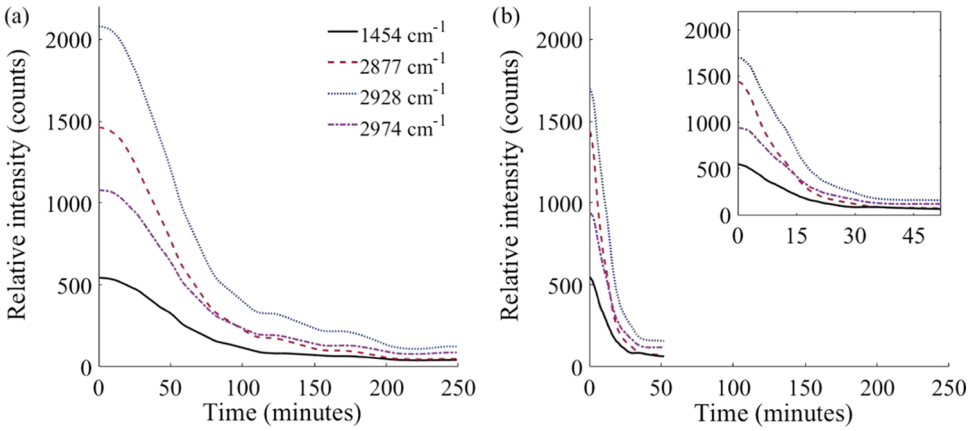

Figure 4. Changes in the Raman spectral intensity of the C−H stretching and $-CH_{2/3}$ bending peak for (a) EP and (b) EPN droplets with time (600 groove, centered at 1900 cm^{-1}, 30 s, 2 mW).

CMC and consequently it is suggested that micelle formation reduces ethanol evaporation. Deconvolution of the C−H stretch region (2800−3025 cm^{-1}) of the Raman spectra provides support for this hypothesis. The Raman band for each C−H stretch is blueshifted as a function time (Table S1). Such behavior has previously been shown to be associated with micelle formation in block copolymers and with the formation of structured networks in ethanol−water binary solutions.[15,31] Further, the intensities of both the CH_3 symmetric and CH_3 asymmetric stretches increase relative to that of the CH_2 asymmetric stretch as a function of time (these ratios are denoted I_2/I_1 and I_3/I_1, respectively, in Table S1). This is indicative of a reduction in the mobility of CH_2 groups as a consequence of the increased structural rigidity of the extended micelle structure.[32] Additionally, as a consequence of high surface/volume ratios with respect to bulk solutions, surface effects may also play a role in stabilizing the aerosol and reducing evaporative losses. For instance, Köhler theory suggests increased stability in water droplets containing salts and other dissolved compounds through a reduction in vapor pressure.[33] A similar process may take place in the aerosols in the present work whereby hygroscopic molecules dissolved in the droplets restrict the evaporation of ethanol through intermolecular interactions. Furthermore, P123 may preferentially segregate to the ethanol−air interface, with the hydrophilic head group on the ethanol side and the hydrophobic tail group on the air side.[34] This could lead to the creation of a surface film, thereby retarding evaporation of ethanol.

The relative stabilities of EP and EPN were investigated by monitoring changes in the relative intensity of the Raman peaks with time. The reduction in the peak height relative to the initial values for the 2928 cm^{-1} C−H stretch and the 1454 cm^{-1} bending vibration over time is shown in Figure 4.

The data show an initial induction period characterized by a relatively stable peak intensity, followed by a decrease in peak intensity, which follows approximately exponential behavior. The time at which the transition to exponential decay occurs has been identified from the derivative of the curves. For all aerosols, peak intensity data beyond this point were fitted to an exponential decay function of the form

$$y = A_1 \times e^{-x/t_1} + y_0 \quad (1)$$

where y_0 is the offset, A_1 is the amplitude, t_1 is the time constant, y is the intensity (counts), and x is the time (minutes). From this, the rates of decay $(1/t_1)$ can be determined, thereby facilitating a comparison of the rate at which the same peaks in different droplets reduce in intensity. All exponential decay data have been tabulated in Table S2, and the fits to the original data are shown in Figures S4−S6.

EPN had a 5 times faster rate of decay relative to EP. Specifically, the CH_3/CH_2 bend at 1454 cm^{-1} has decay rates

https://doi.org/10.1021/acs.jpcc.1c07517
J. Phys. Chem. C XXXX, XXX, XXX−XXX

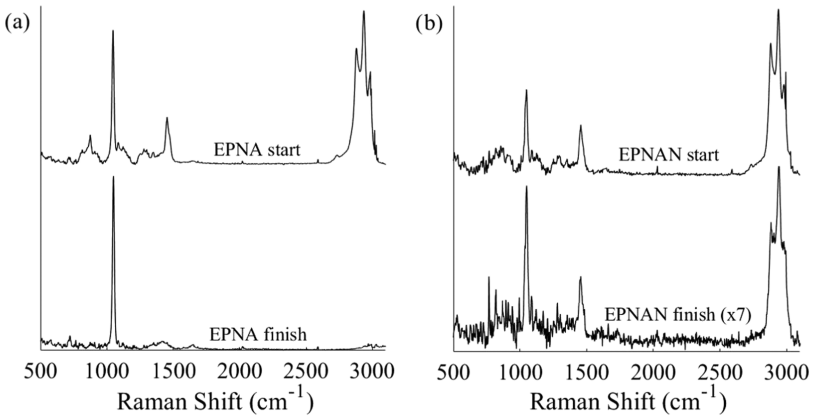

Figure 5. Offset Raman spectra for (a) EPNA and (b) EPNAN. Top curves show the averaged first 10 scans and bottom curves show the averaged final 10 scans. The time between initial and final scans was ∼240 min for EPNA and ∼50 min for EPNAN. Note that to ease comparison the intensity of the final scans for EPNAN (only) has been expanded 7-fold (600 groove, centered at 1900 cm^{-1}, 30 s, 2 mW).

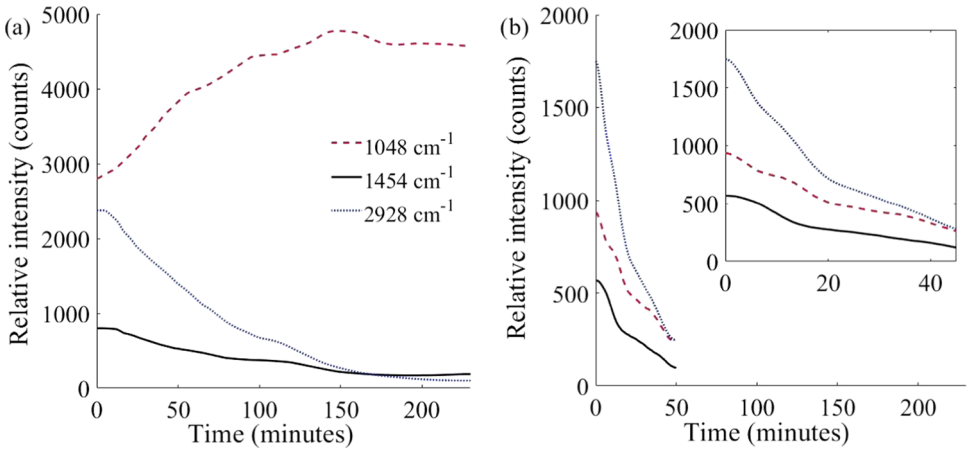

Figure 6. Raman absorbance of peaks at 1048, 1454, and 2928 cm^{-1} for (a) EPNA and (b) EPNAN fitted against time (600 groove, centered at 1900 cm^{-1}, 30 s, 2 mW).

of 0.075 and 0.014 min^{-1} for EPN and EP, respectively. A similar relationship exists for the CH_3 symmetric stretch at 2928 cm^{-1}, which decays at 0.063 and 0.015 min^{-1} for EPN and EP, respectively. This indicates a more rapid loss of ethanol from the aerosol in the case of EPN, which can be directly correlated with the presence of HNO_3. It is proposed that HNO_3 destabilizes the formation of micelles by P123, resulting in a greater proportion of "free" ethanol, which rapidly evaporates. This is consistent with previous observations on the behavior of pure ethanol where Fourier-transform infrared (FT-IR) spectroscopy investigations of bulk solutions showed that the addition of HCl to P123 impeded micellization.[35] The mechanism for this inhibition is attributed to increased hydrogen bonding between the solvent and P123 due to the addition of the acidic proton. This observation supports the assumption that successful micelle formation restricts evaporation and thereby stabilizes the droplet; in contrast, impeding micelle formation accelerates evaporation and lowers the stability of the droplet.

3.2.2. Transformations in Metal-Containing Droplets. The inclusion of Al-iPr in EPNA and $Ni(NO_3)_2{\cdot}6H_2O$ in EPNAN, the latter aerosol comprising all components of the synthesis mixture, has a clear impact on the spectrum of the aerosol (Figure 5). A new peak at 1048 cm^{-1} appears in the spectra of both aerosols and is assigned to symmetric Al−NO_3 and Ni−NO_3 stretching vibrations.[23] The additional components also influence the stability of the aerosol within the optical trap. EPNA demonstrates high stability: an initial period of evaporation took place over the first 200 min, after which no further changes were observed in the spectra. During this initial evaporation period, a reduction in intensity with time of the peaks at 1454, 2877, 2928, and 2974 cm^{-1}—all associated with ethanol (Table 1)—was observed. In contrast, a modest increase in the peak intensity was observed for the band at 1048 cm^{-1} (NO_3^- stretching). That this peak does not decrease in intensity implies that the Al−NO_3 species is not lost and therefore that either hydrolysis and condensation reactions occurred instantaneously or that they do not occur under these conditions in EPNA.

The rates of decay of the bands at 1048, 1454, and 2928 cm^{-1} were calculated for EPNA and EPNAN in the same manner as for EP and EPN (Section 3.2.1). The variation in peak intensity with time for these vibrations is shown in Figure 6 and the exponential decay fits are shown in Figure S5. For EPNA, the rates of decay of the ethanol C−H peaks at 1454 and 2928 cm^{-1} are 0.012 and 0.015 min^{-1}, respectively. This is a much slower rate of decay than observed for EPN where the corresponding values were 0.073 and 0.063 min^{-1}. The enhanced stability of EPNA with respect to EPN is suggestive of the formation of stable micelle-type structures, thereby

https://doi.org/10.1021/acs.jpcc.1c07517
J. Phys. Chem. C XXXX, XXX, XXX−XXX

limiting ethanol evaporation. Al-iPr may interact with the hydrophilic head groups of P123 creating a macrostructure; a similar process has previously been shown whereby micellization is promoted through the addition of a low concentration of ethylammonium nitrate to block copolymers.[30] In the present work, the retardation of the loss of the organic material prevents the aerosol changing in size either significantly or rapidly, thereby contributing to its longevity in the optical trap where it had the potential to be held for a long period of time (hours).

Upon addition of the final component, $Ni(NO_3)_2{\cdot}6H_2O$, no additional peaks were observed when compared to EPNA, although there are some differences when comparing the relative intensity of the peaks (Figure 5). Despite the similarity in the spectra, the behavior of EPNAN differs from that of EPNA. While ethanol evaporates slightly more rapidly than for EPNA (decay rates of 0.035 and 0.044 min^{-1} for 1454 and 2928 cm^{-1} for EPNAN as compared to 0.012 and 0.015 min^{-1} for EPNA), more dramatic differences are observed for the peak associated with Al−NO_3 and Ni−NO_3 stretch (1048 cm^{-1}). In EPNAN, this peak also decreases rapidly over time with a rate of 0.029 min^{-1}. In contrast, in EPNA, the peak at 1048 cm^{-1} increases from its initial intensity, attributed to an increase in Al−NO_3 bonds (Figure 6). The decrease in the peak intensity observed in EPNAN indicates that $Ni(NO_3)_2{\cdot}6H_2O$ induces reactive chemical transformations in the system, either through hydrolysis and condensation reactions that are established to occur in bulk solutions (Section 1) or through an alternative reaction pathway (Section 3.4), with both scenarios ultimately resulting in the formation of cross-linked gel phase. As with EP and EPN (Section 3.2.1), deconvolution of the C−H stretching region (Table S1) supports the conclusion that a more structured phase forms over time, with the intensity of the CH_3 symmetric and CH_3 asymmetric stretches relative to that of the CH_2 asymmetric stretch increasing over the analysis period.

Empirical observations of gelation in bulk solutions were conducted to support the analysis of the changes in Raman spectra with time recorded for the aerosols. Bulk EPNA and EPNAN solutions with the same concentration as that nebulized in the *operando* studies were prepared. When kept in a sealed container over a period of >1 month, neither solution formed a gel, indicating that cross-linking reactions did not occur to a sufficient degree. However, both solutions successfully formed gels through passive evaporation, i.e. when stored in an open container without heating. The EPNAN bulk solution formed a gel after only ∼30 min of evaporation; EPNA in contrast took over a week to form a gel. The EPNA gel formed over this period was notably less viscous than the EPNAN gel and could be poured (Figure S7). This behavior is consistent with previous investigations on solutions of similar composition to EPNA where either time in excess of a week or enhanced evaporation at temperatures above 40 °C were required for gelation to occur.[36−38] These observations confirm that a greater extent of reaction, induced by evaporation, occurs within the EPNAN solution when compared to the EPNA solution. Possible mechanistic pathways are discussed in detail in Section 3.4.

3.2.3. Droplet Size. In AASG synthesis, aerosol droplet size is directly correlated with the particle size of the final solid catalyst. Particle size can influence activity, selectivity, and stability.[39,40] The size of particles constrained by optical tweezers, typically 0.01−10 μm, renders them unsuitable for size determination using imaging optics (for which they are too small) or using Rayleigh scattering calculations (for which they are too large).[41] The presence of WGMs (Section 3.2) however allows the size of the trapped particles to be estimated using the Mie theory. The high stability and strong Raman intensity exhibited by the EPNA droplet presents this as the optimal candidate for calculation of droplet size. The Mie scattering peak positions across the spectral range were compared to a theoretical model for Mie scattering assuming a homogeneous sphere and an initial refractive index approximating to the original components (n = 1.430). The initial radius of the droplet upon trapping was 1.32 μm. It then slowly reduced in size over the trapping period at a rate ∼0.15 μm h^{-1} to a radius of 0.96 ± 0.1 μm, while the refractive index increased slightly to n = 1.437. This radius was maintained until the end of the trapping period beyond 200 min, at which point the aerosol is believed to comprise P123 and Al−NO_3 in a stabilized extended structure (Figure 7). The

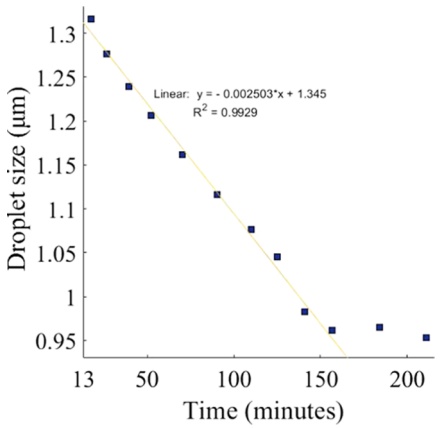

Figure 7. Droplet size in microns for EPNA against time in minutes.

observed reduction in the droplet size and increase in the refractive index are ascribed to the evaporation of ethanol, based on the changes in the Raman spectra presented in Figure 6, where ethanol peaks at 1454 and 2928 cm^{-1} decreased before somewhat stabilizing after 150 min.

3.3. Heated Aerosols. To gain further insights into reactions in the early stages of catalyst synthesis the influence of heating was examined, focusing on EPNA and EPNAN. These are denoted HeEPNA and HeEPNAN, with the He- prefix indicating heating. HeEPNAN contains all chemical components necessary for catalyst synthesis and is an accurate representation of the aerosols applied in AASG synthesis; HeEPNA contains all components except $Ni(NO_3)_2{\cdot}6H_2O$—the absence of which was observed to prevent reactions inducing cross-linking occurring at room temperature (Section 3.2). While some AASG syntheses use temperatures of 100 °C, this study applies lower temperatures as the focus is on the initial reactions leading to formation of the gel. Furthermore, morphological changes in the droplet as it transitions from the liquid precursor to a solid gel intermediate and then to the final solid product mean that it would be experimentally challenging to retain the droplet in the optical trap during the latter stages of catalyst synthesis. The temperature at the droplet position was determined via calibration (Section 2.4).

HeEPNA was heated to 120 °C at 4 °C min^{-1}. Above this temperature, the trapping of the aerosol became unstable. This

https://doi.org/10.1021/acs.jpcc.1c07517
J. Phys. Chem. C XXXX, XXX, XXX−XXX

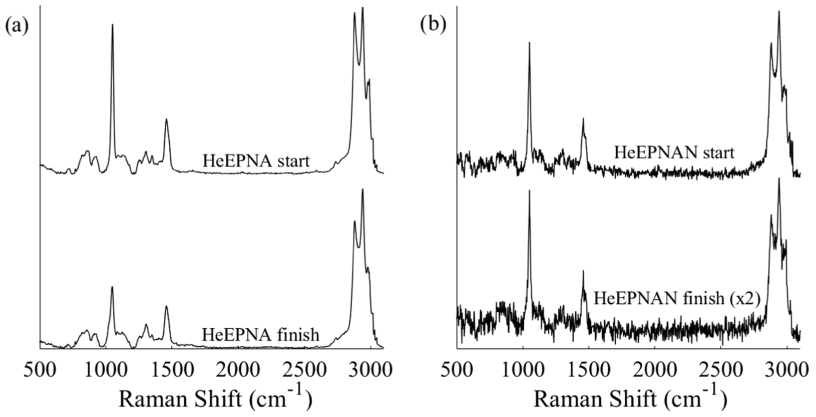

Figure 8. Offset Raman spectra for (a) HeEPNA and (b) HeEPNAN. Top curves show the averaged first 10 scans and bottom curves show the averaged final 10 scans. The time between initial and final scans was ∼30 min for HeEPNA and ∼15 min for HeEPNAN. Note that to ease comparison the intensity of the final scan for HeEPNAN has been expanded 2-fold (600 groove, centered at 1900 cm^{-1}, HeEPNA 30 s, HeEPNAN 10 s, 2 mW).

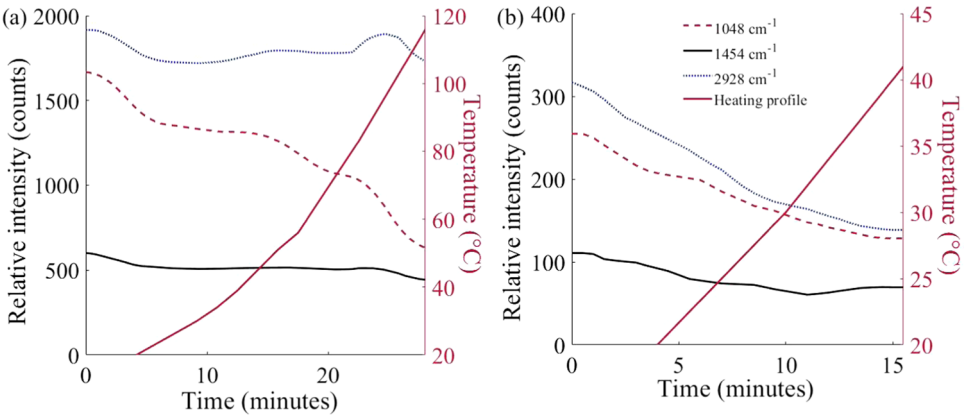

Figure 9. Raman spectral intensity of significant peaks for (a) HeEPNA and (b) HeEPNAN fitted against time with an additional temperature axis to display the temperature of the heated cell at that given point of time (600 groove, centered at 1900 cm^{-1}, HeEPNA 10 s, HeEPNAN 30 s, 2 mW).

instability can be caused by a combination of factors including decreasing aerosol mass and changes in aerosol morphology and physical state. The initial (room temperature) and final (120 °C) Raman spectra for HeEPNA are compared in Figure 8. Despite the elevated temperature, there is relatively little change in the spectra with time, the most significant change being the reduction in the peak intensity of ∼60% between the initial and final scans for the Al−NO_3 peak at 1048 cm^{-1}. This contrasts starkly with the room-temperature behavior of EPNA where (i) the 1048 cm^{-1} stretch increased slightly over the 4 h period and (ii) ethanol evaporation was inferred from the reduction in the 1454 and 2928 cm^{-1} peaks (Section 3.2). The rate of decrease in the intensity of the 1048 cm^{-1} peak increases significantly when the temperature exceeds 56 °C, as shown in Figure 9. After reaching this temperature, the peak intensity falls by ∼46% after 10 min, as compared to a decrease of only ∼13% in the 10 min prior to reaching the temperature. This suggests that reactive transformations are initiated at ∼56 °C or above.

Counterintuitively, heating inhibits the evaporation of ethanol from the droplet as indicated by the stability of the bands arising from ethanol in the Raman spectra (1454 cm^{-1} CH_3 and CH_2 bend, 2877 cm^{-1} CH_2 symmetric stretch, 2928 cm^{-1} CH_3 symmetric stretch, and 2974 cm^{-1} CH_3 asymmetric stretch). A likely contributing factor to this phenomenon is the fact that the CMC of P123 decreases as the temperature is increased. At 25 °C, the CMC of P123 is 0.03 w/v%; this decreases to 0.001 w/v% at 35 °C.[42] Therefore, even a relatively modest increase in temperature increases the strength and interconnectivity of the micelles formed by P123, thereby preventing evaporation of ethanol.[43] A second possible factor that may retard ethanol evaporation is that heating may induce an interaction between the precursors and the block copolymer P123 via an encapsulation-type mechanism.[44] This would inhibit evaporation of ethanol through the formation of a physical barrier around the droplet. The reduction in intensity over time of the peaks arising from components other than ethanol in HeEPNA suggests that the preliminary gelation reactions, which occur in EPNA, (Section 3.4) are initiated through the increase in the concentration of precursors in solution as a consequence of ethanol evaporation.

HeEPNAN showed lower stability in the optical trap as compared to HeEPNA. This is consistent with room-temperature studies (Section 3.2) where the same trend was observed when comparing EPNA and EPNAN. HeEPNAN was heated to 50 °C at 1.5 °C min^{-1}, and above this temperature it became unstable. Raman spectra at room temperature and 40 °C are compared in Figure 8. Exponential decay analysis showed that all peaks decreased at a faster rate for HeEPNAN than EPNAN, although the extent of the

https://doi.org/10.1021/acs.jpcc.1c07517
J. Phys. Chem. C XXXX, XXX, XXX−XXX

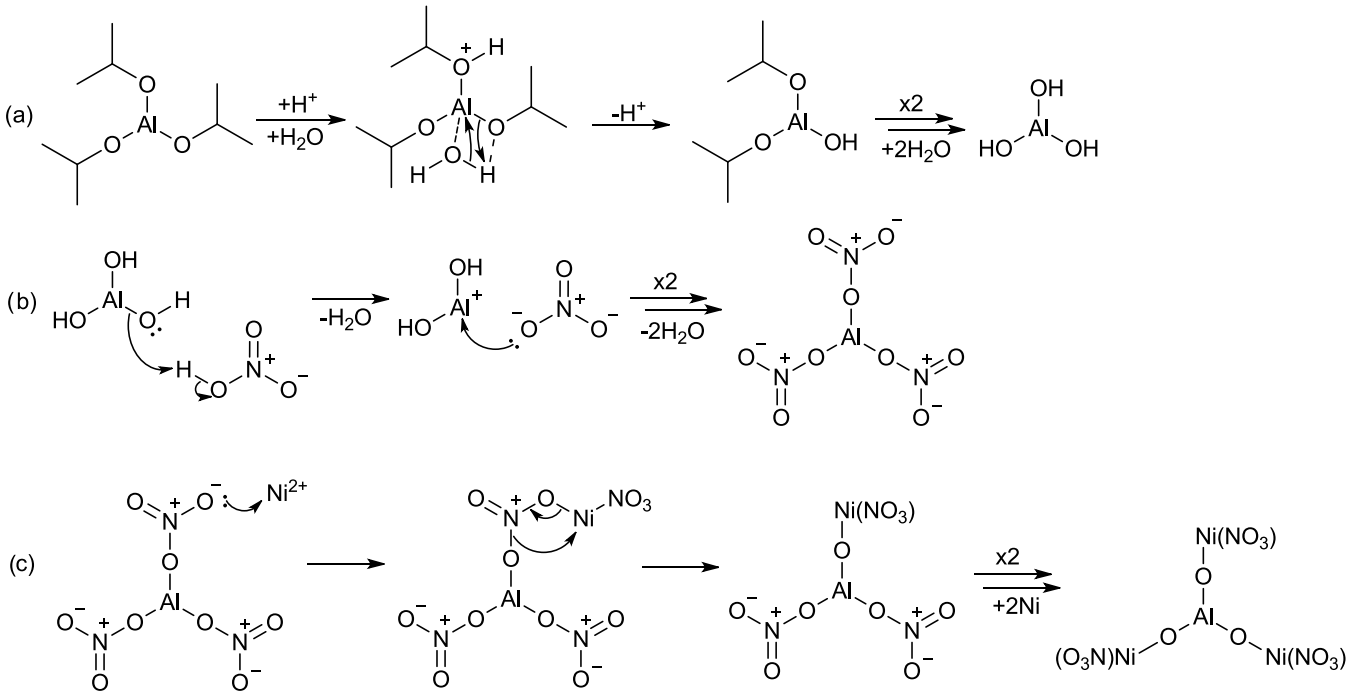

Figure 10. Postulated mechanism for the initial reactions in the AASG synthesis of Ni/Al_2O_3 based upon the Raman spectroscopy observations. Initial hydrolysis reaction of Al-iPr (a), followed by neutralization reaction between HNO_3 and Al−OH (b), and a final proposed cross-linking (gelation) reaction caused by the presence of Ni^{2+} (c).

increase varies for different peaks (Figure S6). The 2928 cm^{-1} CH_3 symmetric stretch exhibits decay rates of 0.074 min^{-1} and 0.044 cm^{-1} for the heated and nonheated aerosols, respectively, a relative increase of ∼50%. The 1454 cm^{-1} CH_3/CH_2 bend, associated with both ethanol and P123, has an even greater proportionate increase in the decay rate, from 0.035 min^{-1} for EPNAN to 0.18 min^{-1} for HeEPNAN (Figure S6). The higher rates of decay for the non-ethanol-derived peaks suggest that the loss of peak intensity is not simply associated with increased evaporation but is instead indicative of increased reactivity and faster gelation upon the application of heating.

3.4. Mechanistic Insights. Previously proposed mechanisms for AASG syntheses involve hydrolysis and condensation reactions, similar to bulk syntheses[45−47] (Figure S1). Chemical equations for these processes are given in eqs 2 and 3. EPNA aerosol, which does not contain Ni, does not show evidence for hydrolysis and condensation reactions (Section 3.2.2). This is consistent with investigations on bulk samples where gelation only occurs at room temperature on long timescales (>1 week). In contrast, HeEPNA aerosol shows a reduction in the intensity of the Al−NO_3 stretch (1048 cm^{-1}) over time during heating. This is indicative of chemical reactivity and suggests that a necessary minimum activation energy is achieved upon heating. As previously stated in Section 3.2, the water content of each droplet is estimated at <4%; this is sufficiently low that no water spectral bands are observed in acquired Raman spectra. However, it has previously been observed that only a minimal amount of water is necessary to effect hydrolysis during bulk synthesis, with reaction occurring at an Al/P123/solvent/water molar ratio of 1:0.015:40.5:0.8.[36] The corresponding ratio in the present work is 0.47:0.012:19:1. It is therefore likely that there is sufficient water for hydrolysis reactions to proceed; however, this only occurs upon the application of external heating. In contrast to aerosol EPNA and to bulk-phase systems, significant retardation of ethanol evaporation is observed for HeEPNA—postulated to be associated with enhanced micelle formation. These data therefore controvert the hypothesis that the reactive hydrolysis−polycondensation transformations that occur during synthesis (Section 1) are contingent on evaporation.

$$Al(OCH(CH_3)_2)_3 + 3H_2O \rightarrow Al(OH)_3 + 3HO - CH(CH_3)_2 \quad (2)$$

$$Al(OH)_3 + Al(OH)_3 \rightarrow (OH)_2AlOAl(OH)_2 + H_2O \rightarrow Al - (OAl(OH)_2)_3 + 2H_2O \quad (3)$$

In contrast to EPNA, and similarly to HeEPNA, EPNAN shows evidence for chemical reactivity from the reduction in the Al−NO_3 and Ni−NO_3 associated stretch (1048 cm^{-1}). The additional component added to EPNA to form EPNAN is $Ni(NO_3)_2{\cdot}6H_2O$. This increases the water content of the precursor mixture by 57%. It is possible that this additional water induces hydrolysis, with the water molecules avoiding rapid evaporation in the aerosol due to their association to the nickel species. In this case, water within the micelles would facilitate the processes shown in Figure S1.

A postulated alternative reaction mechanism is shown in Figure 10. An initial hydrolysis reaction (a) occurs forming aluminum hydroxide (Al−OH) as occurs in bulk solutions. This reaction requires water to proceed. Al−OH then reacts with HNO_3 (b) to form Al−NO_3 in solution. Elsewhere, this process is known from the dissolution of gibbsite ($Al(OH)_3$) in HNO_3.[48] This would therefore regenerate the water previously consumed in the hydrolysis reaction, allowing a cascade whereby further sequential hydrolysis (a) and neutralization (b) reactions could occur. This mechanism is

https://doi.org/10.1021/acs.jpcc.1c07517
J. Phys. Chem. C XXXX, XXX, XXX−XXX

supported by the observation of increasing Al−NO_3 in EPNA over time. It is then proposed that there is insufficient energy available in the isothermal EPNA system to proceed with condensation reactions. When heat is applied, from observations of HeEPNA, sufficient energy is available to induce reactions forming Al−O−Al. For EPNAN, however, the application of heat is not a perquisite to induce reaction. A similar final transition to that occurring in HeEPNA is inferred to occur at room temperature in the presence of Ni, where an alternative pathway (c) of lower activation energy is available. This reaction involves rearrangement of the nickel nitrate aluminum complex to form a continuous Al−O−Ni−NO_3 structure, in contrast to the proposed Al−O−Al structure derived from HeEPNA.

Changes in the stability of the aerosol within the optical trap upon the inclusion of $Ni(NO_3)_2{\cdot}6H_2O$ in the precursor solution are also indicative of chemical and physical transformations. In contrast to the exceptional stability of EPNA, EPNAN is held in the trap for only ∼50 min. This relative instability is assigned to morphological changes induced by chemical reactions, specifically gelation within the aerosol resulting in changes to its size and shape. Figure 10c shows the postulated reaction mechanism leading to the formation of an extended aluminum nickel bonded complex within the aerosol, i.e. gelation (eq 5). Spectroscopic support for this process comes from the reduction in the intensity of aluminum nitrate (1048 cm^{-1}). This proposed reaction mechanism is consistent with previous studies of the bulk-phase sol−gel synthesis of nickel aluminide (Ni_3Al) from Al-iPr, $Ni(NO_3)_2$, and HNO_3 in ethanol by Madon et al.[49] The balanced chemical equation for the proposed reaction pathway is therefore

$$Al(OCH(CH_3)_2)_3 + 3H_2O \rightarrow Al(OH)_3 + 3HO - CH(CH_3)_2 \quad (4)$$

$$Al(OH)_3 + 3HNO_3 \rightarrow Al(NO_3)_3 + 3H_2O \quad (5)$$

$$Al(NO_3)_3 + 3Ni(NO_3)_2 6H_2O \rightarrow Al(ONiNO_3)_3 + 3NO_2 \quad (6)$$

The mechanism, shown schematically in Figures S1 and 10, that is operating could be determined by synthesizing the final Ni/Al_2O_3 catalysts in a flow tube reactor operating at high temperatures using the same precursors described in Section 2.2. Full structural analysis of the final nanostructured catalyst using electron microscopy and X-ray/neutron diffraction would elicit if the catalyst were highly ordered as Ni−Al−N−Al or exhibited structural and compositional heterogeneity, suggesting either the nickel-induced reaction pathway or the condensation reaction observed in bulk solutions, respectively.[50]

4. CONCLUSIONS

Optical trapping combined with Raman spectroscopy has been demonstrated to be a successful approach to facilitate the interrogation of processes occurring during the AASG synthesis of catalysts. Droplets of ∼1 μm in radius, based on analysis of EPNA, have been trapped and held for extended periods of up to 4 h depending on composition. The influence of each component within the Ni/Al_2O_3 precursor solution has been investigated. P123 stabilizes the aerosol against ethanol evaporation, postulated to be a consequence of micelle formation, while HNO_3 acts to destabilize the formed micelles. The latter effect is overcome through the addition of Al-iPr, which is proposed to interact with the hydrophilic head groups of P123, thereby creating a stable macrostructure. No further transitions, such as gelation, are however inferred to occur at room temperature in the absence of nickel. Heating can however affect reactive transformations, seen to be initiated above ∼56 °C. This is not accompanied by evaporation, hence suggesting a different mechanism than that reported from observations of bulk-phase systems. The addition of nickel induces reactivity at room temperature, with the rate of reaction enhanced upon heating. This reaction occurs even in the absence of external heating, suggesting that a lower activation energy pathway exists in this system. Reaction mechanisms have been proposed for both routes that may result in final materials of differing long-range structures. The ability to successfully interrogate AASG syntheses spectroscopically during reaction can therefore bring new understanding to this emerging technology, which can in turn support the design of improved processes and the synthesis of materials with specific targeted properties such as structure or morphology.

■ ASSOCIATED CONTENT

Supporting Information

The Supporting Information is available free of charge at https://pubs.acs.org/doi/10.1021/acs.jpcc.1c07517.

Figure S1: mechanism for acid-catalyzed sol−gel formation. Figure S2: temperature calibration of the heated cell. Figure S3: observed whispering gallery modes. Figure S4: exponential decay fitting for EP and EPN. Figure S5: exponential decay fitting for EPNA and EPNAN. Figure S6: exponential decay fitting for HeEPNA and HeEPNAN. Figure S7: EPNA and EPNAN bulk observation. Table S1: extracted intensity and position of aliphatic (C−H) stretching. Table S2: tabulated exponential decay data (PDF)

■ AUTHOR INFORMATION

Corresponding Author

James McGregor − *Department of Chemical and Biological Engineering, University of Sheffield, Sheffield S1 3JD, U.K.; UK Catalysis Hub, Research Complex at Harwell, Rutherford Appleton Laboratory, Harwell OX11 0FA, U.K.;* orcid.org/0000-0001-6813-306X; Email: james.mcgregor@sheffield.ac.uk

Authors

Gareth Davies − *Department of Chemical and Biological Engineering, University of Sheffield, Sheffield S1 3JD, U.K.*

Justin Driver − *Department of Chemical and Biological Engineering, University of Sheffield, Sheffield S1 3JD, U.K.*

Andrew Ward − *Central Laser Facility, Research Complex at Harwell, Rutherford Appleton Laboratory, Didcot OX11 0FA, U.K.;* orcid.org/0000-0001-6946-2391

Leila Negahdar − *Department of Chemistry, University College London, London WC1H 0AJ, U.K.; UK Catalysis Hub, Research Complex at Harwell, Rutherford Appleton Laboratory, Harwell OX11 0FA, U.K.;* orcid.org/0000-0002-9119-6445

Complete contact information is available at: https://pubs.acs.org/10.1021/acs.jpcc.1c07517

Notes

The authors declare no competing financial interest.

■ ACKNOWLEDGMENTS

EPSRC is acknowledged for its support of the UK Catalysis Hub via Grant EP/R026815/1; EPSRC is also thanked for funding a Ph.D. studentship for G.D. via Award EP/N509735/1. The Central Laser Facility (STFC) is acknowledged for providing access under Grant App19130040. The authors also thank Olivia Ward for collecting the data in Figure S2 during her placement at the CLF. L.N. acknowledges the funding from the European Union's Horizon 2020 Research and Innovation Programme under the Marie Skłodowska−Curie Grant Agreement No. 837794.

■ ABBREVIATIONS AND ACRONYMS

AASG - aerosol-assisted sol−gel
Al-iPr - aluminum isopropoxide
CMC - critical micellization concentration
EISA - evaporation-induced self-assembly
EP - aerosol comprising ethanol and P123
EPN - aerosol comprising ethanol, P123, and nitric acid
EPNA - aerosol comprising ethanol, P123, nitric acid, and aluminum isopropoxide
EPNAN - aerosol comprising ethanol, P123, nitric acid, aluminum isopropoxide, and nickel nitrate hexahydrate
FT-IR - Fourier-transform infrared
HEPNA - heated aerosol comprising ethanol, P123, nitric acid, and aluminum isopropoxide
HEPNAN - heated aerosol comprising ethanol, P123, nitric acid, aluminum isopropoxide, and nickel nitrate hexahydrate
P123 - poly(ethylene glycol)-*block*-poly(propylene glycol)-*block*-poly(ethylene glycol)
PEO - poly(ethylene oxide)
PPO - poly(propylene oxide)
WGM - whispering gallery mode

■ REFERENCES

(1) Debecker, D. P.; Le Bras, S.; Boissière, C.; Chaumonnot, A.; Sanchez, C. Aerosol Processing: A Wind of Innovation in the Field of Advanced Heterogeneous Catalysts. *Chem. Soc. Rev.* **2018**, *47*, 4112−4155.
(2) Innocenzi, P. Understanding Sol−Gel Transition through a Picture. A Short Tutorial. *J. Sol−Gel Sci. Technol.* **2020**, *94*, 544−550.
(3) Gonçalves, A. A. S.; Jaroniec, M. Evaporation-Induced Self-Assembly Synthesis of Nanostructured Alumina-Based Mixed Metal Oxides with Tailored Porosity. *J. Colloid Interface Sci.* **2019**, *537*, 725−735.
(4) Alvarez, M. P.; Burrezo, P. M.; Iwamoto, T.; Qiu, L.; Kertesz, M.; Taravillo, M.; Baonza, V. G.; Navarrete, J. T. L.; Yamago, S.; Casado, J.; et al. Ternary Oxide Nanostructured Materials for Supercapacitors: A Review. *Faraday Discuss.* **2014**, *4*, 1166−1169.
(5) Hua, M.; Zhang, S.; Pan, B.; Zhang, W.; Lv, L.; Zhang, Q. Heavy Metal Removal from Water/Wastewater by Nanosized Metal Oxides: A Review. *J. Hazard. Mater.* **2012**, *212*, 317−331.
(6) Liu, Q.; Gao, J.; Gu, F.; Lu, X.; Liu, Y.; Li, H.; Zhong, Z.; Liu, B.; Xu, G.; Su, F. One-Pot Synthesis of Ordered Mesoporous Ni-V-Al Catalysts for CO Methanation. *J. Catal.* **2015**, *326*, 127−138.
(7) Pal, N.; Bhaumik, A. Ordered Mesoporous Ternary Mixed Oxide Materials as Potential Adsorbent of Biomolecules. *Chem. Phys. Lett.* **2012**, *535*, 69−74.
(8) Vivian, A.; Soumoy, L.; Fusaro, L.; Fiorilli, S.; Debecker, D. P.; Aprile, C. Surface-Functionalized Mesoporous Gallosilicate Catalysts for the Efficient and Sustainable Upgrading of Glycerol to Solketal. *Green Chem.* **2021**, *23*, 354−366.
(9) Manangon-Perugachi, L. E.; Smeets, V.; Vivian, A.; Kainthla, I.; Eloy, P.; Aprile, C.; Debecker, D. P.; Gaigneaux, E. M. Mesoporous Methyl-Functionalized Titanosilicate Produced by Aerosol Process for the Catalytic Epoxidation of Olefins. *Catalysts* **2021**, *11*, No. 196.
(10) Meng, Q.; Liu, J.; Liu, L.; Xiong, G. Aerosol-Assisted Hydrothermal Synthesis of Hierarchical Sn-Beta Nanoaggregates in Fluoride Media. *Microporous Mesoporous Mater.* **2021**, *320*, No. 111090.
(11) Smeets, V.; Boissière, C.; Sanchez, C.; Gaigneaux, E. M.; Peeters, E.; Sels, B. F.; Dusselier, M.; Debecker, D. P. Aerosol Route to TiO 2 -SiO 2 Catalysts with Tailored Pore Architecture and High Epoxidation Activity. *Chem. Mater.* **2019**, *31*, 1610−1619.
(12) Kim, A.; Sanchez, C.; Haye, B.; Boissière, C.; Sassoye, C.; Debecker, D. P. Mesoporous TiO2 Support Materials for Ru-Based CO2 Methanation Catalysts. *ACS Appl. Nano Mater.* **2019**, *2*, 3220−3230.
(13) Haddrell, A. E.; Miles, R. E. H.; Bzdek, B. R.; Reid, J. P.; Hopkins, R. J.; Walker, J. S. Coalescence Sampling and Analysis of Aerosols Using Aerosol Optical Tweezers. *Anal. Chem.* **2017**, *89*, 2345−2352.
(14) Ito, A.; Kamogawa, K.; Sakai, H.; Hamano, K.; Kondo, Y.; Yoshino, N.; Abe, M. Micelle Aggregating Condition of Fluorocarbon-Hydrocarbon Hybrid Surfactants in Aqueous Solution. *Langmuir* **1997**, *13*, 2935−2942.
(15) Guo, C.; Wang, J.; Liu, H. Z.; Chen, J. Y. Hydration and Conformation of Temperature-Dependent Micellization of PEO-PPO-PEO Block Copolymers in Aqueous Solutions by FT-Raman. *Langmuir* **1999**, *15*, 2703−2708.
(16) Grier, D. G. A Revolution in Optical Manipulation. *Nature* **2003**, *424*, 810−816.
(17) Shepherd, R. H.; King, M. D.; Marks, A. A.; Brough, N.; Ward, A. D. Determination of the Refractive Index of Insoluble Organic Extracts from Atmospheric Aerosol over the Visible Wavelength Range Using Optical Tweezers. *Atmos. Chem. Phys.* **2018**, *18*, 5235−5252.
(18) Hunt, O. R.; Ward, A. D.; King, M. D. Laser Heating of Sulfuric Acid Droplets Held in Air by Laser Raman Tweezers. *RSC Adv.* **2013**, *3*, 19448−19454.
(19) Boyer, H. C.; Gorkowski, K.; Sullivan, R. C. In Situ PH Measurements of Individual Levitated Microdroplets Using Aerosol Optical Tweezers. *Anal. Chem.* **2020**, *92*, 1089−1096.
(20) McGrory, M. R.; King, M. D.; Ward, A. D. Using Mie Scattering to Determine the Wavelength-Dependent Refractive Index of Polystyrene Beads with Changing Temperature. *J. Phys. Chem. A* **2020**, *124*, 9617−9625.
(21) Aminzadeh, A.; Sarikhani-fard, H. Raman Spectroscopic Study of Ni/Al2O3 Catalyst. *Spectrochim. Acta, Part A* **1999**, *55*, 1421−1425.
(22) Burikov, S.; Dolenko, T.; Patsaeva, S.; Starokurov, Y.; Yuzhakov, V. Raman and IR Spectroscopy Research on Hydrogen Bonding in Water-Ethanol Systems. *Mol. Phys.* **2010**, *108*, 2427−2436.
(23) Carter, J. C.; Khulbe, P. K.; Gray, J.; Van Zee, J. W.; Angel, S. M. Raman Spectroscopic Evidence Supporting the Existence of Ni 4(OH)44+ in Aqueous, Ni(NO3) 2 Solutions. *Anal. Chim. Acta* **2004**, *514*, 241−245.
(24) McLaughlin, R. P.; Bird, B.; Reid, P. J. Vibrational Analysis of Isopropyl Nitrate and Isobutyl Nitrate. *Spectrochim. Acta, Part A* **2002**, *58*, 2571−2580.
(25) Ruan, H. D.; Frost, R. L.; Kloprogge, J. T. Comparison of Raman Spectra in Characterizing Gibbsite, Bayerite, Diaspore and Boehmite. *J. Raman Spectrosc.* **2001**, *32*, 745−750.
(26) Dantham, V. R.; Bisht, P. B.; Dobal, P. S. Whispering Gallery Modes and Effect of Coating on Raman Spectra of Single Microspheres. *J. Raman Spectrosc.* **2011**, *42*, 1373−1378.
(27) Hopkins, R. J.; Mitchem, L.; Ward, A. D.; Reid, J. P. Control and Characterisation of a Single Aerosol Droplet in a Single-Beam Gradient-Force Optical Trap. *Phys. Chem. Chem. Phys.* **2004**, *6*, 4924−4927.

https://doi.org/10.1021/acs.jpcc.1c07517
J. Phys. Chem. C XXXX, XXX, XXX−XXX

(28) Kolwas, M.; Jakubczyk, D.; Derkachov, G.; Kolwas, K. Interaction of Optical Whispering Gallery Modes with the Surface Layer of Evaporating Droplet of Suspension. *J. Quant. Spectrosc. Radiat. Transfer* **2013**, *131*, 138−145.
(29) Li, R.; D'Agostino, C.; McGregor, J.; Mantle, M. D.; Zeitler, J. A.; Gladden, L. F. Mesoscopic Structuring and Dynamics of Alcohol/Water Solutions Probed by Terahertz Time-Domain Spectroscopy and Pulsed Field Gradient Nuclear Magnetic Resonance. *J. Phys. Chem. B* **2014**, *118*, 10156−10166.
(30) He, Z.; Alexandridis, P. Micellization Thermodynamics of Pluronic P123 (EO20PO70EO20) Amphiphilic Block Copolymer in Aqueous Ethylammonium Nitrate (EAN) Solutions. *Polymers* **2017**, *10*, No. 32.
(31) Li, F.; Men, Z.; Li, S.; Wang, S.; Li, Z.; Sun, C. Study of Hydrogen Bonding in Ethanol-Water Binary Solutions by Raman Spectroscopy. *Spectrochim. Acta, Part A* **2018**, *189*, 621−624.
(32) da Costa, A. M. A.; Geraldes, C. F. G. C.; Teixeira-Dias, J. J. C. Micellar Aggregation of CTAB in Water and Chloroform Solutions-a Study by Laser Raman Spectroscopy. *J. Colloid Interface Sci.* **1982**, *86*, 254−259.
(33) Ferron, G. A.; Soderholm, S. C. Estimation of the Times for Evaporation of Pure Water Droplets and for Stabilization of Salt Solution Particles. *J. Aerosol Sci.* **1990**, *21*, 415−429.
(34) Shao, X.; Duan, F.; Hou, Y.; Zhong, X. Role of Surfactant in Controlling the Deposition Pattern of a Particle-Laden Droplet: Fundamentals and Strategies. *Adv. Colloid Interface Sci.* **2020**, *275*, No. 102049.
(35) Yang, B.; Guo, C.; Chen, S.; Junhe, M.; Wang, J.; Liang, X.; Zheng, L.; Liu, H. Effect of Acid on the Aggregation of Poly(Ethylene Oxide)-Poly(Propylene Oxide)-Poly(Ethylene Oxide) Block Copolymers. *J. Phys. Chem. B* **2006**, *110*, 23068−23074.
(36) Moatti, A.; Javadpour, J.; Anbia, M.; Badiei, A. The Correlation between Aging Time and Pore Characteristics in the Synthesis of Mesoporous Al2O3. *Ceram. Int.* **2014**, *40*, 10231−10236.
(37) Singh, P.; Maiti, P. K.; Sen, K. Pristine and Modified-Mesoporous Alumina: Molecular Assistance-Based Drug Loading and Sustained Release Activity. *Bull. Mater. Sci.* **2020**, *43*, No. 56.
(38) Niesz, K.; Yang, P.; Somorjai, G. A. Sol-Gel Synthesis of Ordered Mesoporous Alumina. *Chem. Commun.* **2005**, 1986−1987.
(39) Harju, H.; Pipitone, G.; Lefferts, L. Influence of the Catalyst Particle Size on the Aqueous Phase Reforming of N-Butanol Over Rh/ZrO2. *Front. Chem.* **2020**, *8*, No. 17.
(40) Wang, H.; Lu, J. A Review on Particle Size Effect in Metal-Catalyzed Heterogeneous Reactions. *Chin. J. Chem.* **2020**, *38*, 1422−1444.
(41) Nieminen, T. A.; Loke, V. L. Y.; Stilgoe, A. B.; Knöner, G.; Brańczyk, A. M.; Heckenberg, N. R.; Rubinsztein-Dunlop, H. Optical Tweezers Computational Toolbox. *J. Opt. A: Pure Appl. Opt.* **2007**, *9*, No. S196.
(42) Bodratti, A. M.; Alexandridis, P. Formulation of Poloxamers for Drug Delivery. *J. Funct. Biomater.* **2018**, *9*, No. 11.
(43) Ashraf, U.; Chat, O. A.; Maswal, M.; Jabeen, S.; Dar, A. A. An Investigation of Pluronic P123-Sodium Cholate Mixed System: Micellization, Gelation and Encapsulation Behavior. *RSC Adv.* **2015**, *5*, 83608−83618.
(44) Sakai-Kato, K.; Nishiyama, N.; Kozaki, M.; Nakanishi, T.; Matsuda, Y.; Hirano, M.; Hanada, H.; Hisada, S.; Onodera, H.; Harashima, H.; et al. General Considerations Regarding the in Vitro and in Vivo Properties of Block Copolymer Micelle Products and Their Evaluation. *J. Controlled Release* **2015**, *210*, 76−83.
(45) Marage, P.; Langlet, M.; Joubert, J. C. Understanding and Improving the Deposition Conditions of SiO2 Thin Films Obtained by Ultrasonic Sol-Gel Procedure - Code: EP30. *J. Sol−Gel Sci. Technol.* **1994**, *2*, 615−618.
(46) Langlet, M.; Walz, D.; Marage, P.; Joubert, J. C. Glass and Ceramic Thin Films Deposited by an Ultrasonically Assisted Sol-Gel Technique. *Thin Solid Films* **1992**, *221*, 44−54.
(47) Primeau, N.; Vautey, C.; Langlet, M. The Effect of Thermal Annealing on Aerosol-Gel Deposited SiO2 Films: A FTIR Deconvolution Study. *Thin Solid Films* **1997**, *310*, 47−56.
(48) Dietzel, M.; Böhme, G. The Dissolution Rates of Gibbsite in the Presence of Chloride, Nitrate, Silica, Sulfate, and Citrate in Open and Closed Systems at 20 °C. *Geochim. Cosmochim. Acta* **2005**, *69*, 1199−1211.
(49) Madon, R. H.; Fawzi, M.; Sarwani, K. I.; Osman, S. A.; Razali, M. A.; Mohammad, A. W. Effect of Reaction Temperature on Steam Methane Reforming's Yield over Coated Nickel Aluminide (Ni3Al) Catalyst in Micro Reactor. *J. Adv. Res. Fluid Mech. Therm. Sci.* **2018**, *50*, 170−177.
(50) Baerlocher, C.; Gramm, F.; Massüger, L.; McCusker, L. B.; He, Z.; Hovmöller, S.; Zou, X. Structure of the Polycrystalline Zeolite Catalyst IM-5 Solved by Enhanced Charge Flipping. *Science* **2007**, *315*, 1113−1116.

https://doi.org/10.1021/acs.jpcc.1c07517
J. Phys. Chem. C XXXX, XXX, XXX−XXX

ACS OMEGA

http://pubs.acs.org/journal/acsodf

Article

Hydrothermal Synthesis of Biomass-Derived Magnetic Carbon Composites for Adsorption and Catalysis

Gareth Davies and James McGregor*

Cite This: https://doi.org/10.1021/acsomega.1c05116

Read Online

ACCESS | Metrics & More | Article Recommendations | Supporting Information

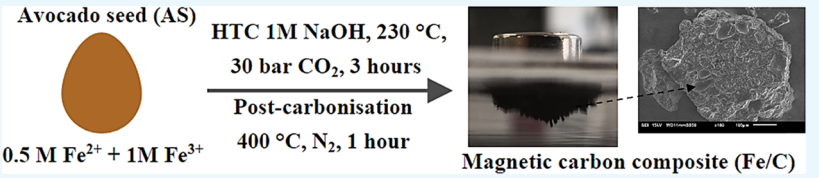

ABSTRACT: The synthesis of magnetic iron−carbon composites (Fe/C) from waste avocado seeds via hydrothermal carbonization (HTC) has been demonstrated for the first time. These materials are shown to be effective in adsorption and catalytic applications, with performances comparable to or higher than materials produced through conventional processing routes. Avocado seeds have been processed in high-temperature water (230 °C) at elevated pressure (30 bar at room temperature) in the presence of iron nitrate and iron sulfate, in a process mimicking natural coalification. Characterization of the synthesized material has been carried out by X-ray diffraction (XRD), atomic absorption spectroscopy (AAS), X-ray fluorescence (XRF), X-ray photoelectron spectroscopy (XPS), inductively coupled plasma-optical emission spectrometry (ICP-OES), Fourier-transform infrared spectroscopy (FT-IR), magnetometry, and through surface area measurements. The supported iron particles are observed to be predominately magnetite, with an oxidized hematite surface region. The presence of iron catalyzes the formation of an extended, ordered polymeric structure in the avocado seed-derived carbon. The magnetic Fe/C has been demonstrated as an adsorbent for environmental wastewater treatment using methylene blue and indigo carmine. Kinetic analysis suggests that the adsorbates are chemisorbed, with the positive surface charge of Fe/C being preferential for indigo carmine adsorption (49 mg g^{-1}). Additionally, Fe/C has been evaluated as a heterogeneous catalyst for the hydroalkoxylation of phenylacetylene with ethylene glycol to 2-benzyl-1,3-dioxolane. Product yields of 45% are obtained, with 100% regioselectivity to the formed isomer. The solid catalyst has the advantages of being prepared from a waste material and of easy removal after reaction via magnetic separation. These developments provide opportunities to produce carbon-based materials for a variety of high-value applications, potentially also including energy storage and biopharmaceuticals, from a wide range of lignocellulosic biomass feedstocks.

1. INTRODUCTION

Climate change, environmental pollution, decreasing fossil fuel reserves, and overpopulation are global grand challenges requiring effective scientific and political solutions.[1] To tackle these challenges, it is imperative that sustainable processes for waste management and valorization are developed and implemented. The majority of the estimated 2 billion tonnes of municipal solid waste (MSW), which is produced globally each year is sent to landfills or incinerated.[2] There are many potential alternative processing methods, which yield value-added products from MSW, such as anaerobic digestion, composting, pyrolysis, fermentation, and hydrothermal processing.[3,4]

Among these, hydrothermal processing and, in particular, hydrothermal carbonization (HTC), present significant opportunities to valorize organic wastes. HTC is a thermochemical conversion technology, which operates at low processing temperatures (180−260 °C) with sufficient pressure to maintain the water in the liquid phase (<50 bar). It has the further advantage of short processing times (30 min to 3 days).[5−8] HTC simulates natural coalification and produces a solid material with increased energy density and carbon content relative to the initial feedstock and with decreased oxygen and volatile content. This solid is usually referred to as hydrochar.[8−11] HTC can be applied to a variety of different waste feedstocks, including biomass, sewage sludge, and waste plastics. There is no need for pretreatment of the feedstock, thereby eliminating the need for costly predrying processes.[8,10,12,13] This facilitates the treatment of high moisture content feedstocks such as MSW or biomass. The latter typically has a moisture content ranging from 0.5 to 1 kg of water per kg after oven-drying. Thermal drying costs of such moisture-rich materials are ∼1.64 MJ/kg_{H_2O}, equivalent to up

Received: September 15, 2021
Accepted: November 16, 2021

to 11% of the energy content of lignite coal.[14] As-synthesized hydrochar has properties approaching the characteristics of low-rank coals, with previous literature focusing on HTC of MSW for solid fuel production.[9,15−17] However, HTC has also more recently been used to synthesize high-value carbon materials for applications in catalysis, surface adsorption, and energy storage.[11,18−21] Additionally, post-synthesis treatments can upgrade hydrochar to yield a material with enhanced physicochemical characteristics for high-value applications.[22−24]

In the present study, avocado seeds (AS) have been investigated as a lignocellulosic feedstock for HTC. AS are a waste product from guacamole production in addition to the manufacture of sauces, oils, and frozen products.[25−27] This is a rapidly growing industry, with the global production of avocados forecast to triple by 2030 as compared to 2010 values.[28] This estimates an annual production of 12 Mt, generating ∼2 Mt of waste seeds. AS are only rarely used as animal feed because of their unpleasant taste and low nutrient content; hence, large amounts are disposed of to landfills. Additionally, AS present an unusual composition for waste biomass, with a high hemicellulose:cellulose ratio; e.g., Lin et al. have previously reported a ratio of ∼9:1 (mass basis).[29] In contrast, more commonly investigated agricultural residues such as sugarcane bagasse present a higher content of cellulose than hemicellulose.[30,31] It is therefore anticipated that in HTC of AS, the dominant conversion route will be carboninzation of soluble hemicelluloses. This therefore serves as an exemplar for the investigation of hemicellulose-rich waste streams and is, to the best knowledge of the authors, the first investigation of AS in hydrothermal processing.[25,32]

Iron oxide nanomaterials have applications in a wide variety of areas, including adsorption, heterogeneous catalysis, photocatalysis, immobilization, and biopharmaceuticals.[33,34] The synthesis conditions employed to produce such materials can give precise control over their surface functionality. Furthermore, they can exhibit ferrimagnetism, high biodegradability, and low toxicity. Iron oxide nanomaterials can be produced using many different procedures, including sol−gel, oxidation, co-precipitation, hydrothermal, aerosol, supercritical, and microbial syntheses. Previous research has shown the potential to produce functional iron oxide materials supported on or encapsulated within hydrochar. For example, carbon-encapsulated nanoparticles have been produced using glucose as the carbon source.[35,36] Other work has focused on post-synthesis modification of hydrochars produced from waste lignocellulosic materials through impregnation with an appropriate iron precursor.[37−39] The latter approach typically requires pyrolysis at temperatures in excess of 600 °C to introduce porosity into carbon. Rattanachueskul et al. have demonstrated the conversion of sugarcane bagasse and an iron precursor into magnetic carbon composites via a one-pot synthesis with a 24 h reaction time.[40] There remains, however, a desire rooted in the principles of green chemistry to develop a process, which can use raw biomass without, e.g., extracting glucose or employing mechanical pretreatment. Further, this should employ as few processing steps as possible and ideally synthesize the material in a one-pot process rather than via post-synthesis modification. The aim of the present work is to produce magnetic carbon composites with desirable properties for applications in adsorption and heterogeneous catalysis from whole AS in a one-pot synthesis process. The adsorption of model dye compounds is investigated as an environmental application, while catalytic studies focus on alkyne hydroalkoxylation—an important C−O bond-forming reaction. This work serves as an exemplar for a range of unprocessed waste lignocellulosic materials.

2. RESULTS AND DISCUSSION

2.1. Physical and Chemical Characteristics of Fe/C.

The powder X-ray diffractogram of the synthesized Fe/C is shown in Figure 1a. The diffractogram is dominated by the

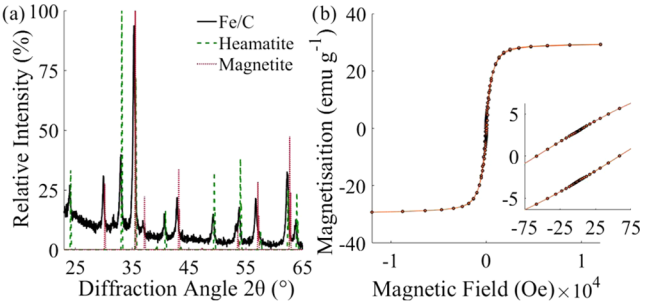

Figure 1. (a) XRD patterns for Fe/C particles compared to RRUFF spectroscopic references[41,42] for magnetite and hematite between 17 and 65° obtained using a Cu tube with 1.54184 Å, scanning for 1 s at increments of 0.02°. (b) Magnetization hysteresis loop for Fe/C particles. The inset shows a small remnant of magnetization at zero field (∼10% of the total moment), measured using a Quantum Design SQUID-VSM Magnetometer MPMS3.

characteristic peaks of magnetite (Fe_3O_4) at 30.2, 35.6, 43.3, 57.2, and 62.8°; additionally, a smaller contribution from hematite (Fe_2O_3) is observed. Quantitative determination of the ratio of the two iron oxide phases was conducted using MATCH! Software (Crystal Impact GbR, Bonn, Germany). Fe/C comprised 73 ± 5.6% magnetite (Index# 96-151-3305[41]) and 27 ± 5.6% hematite (Index# 96-154-6384[42]). The predominance of magnetite is consistent with previous qualitative studies of magnetic iron−carbon composites synthesized from biomass.[40] The sample was strongly attracted to an external magnet. Analysis of the sample employing a superconducting quantum interference device (SQUID) confirmed that the material was weakly ferromagnetic (Figure 1b). Based on previous studies, it is expected that only magnetite is precipitated from the precursor iron salts and sodium hydroxide during initial DAS soaking.[43,44] Therefore, the presence of hematite implies that some oxidation of the formed iron oxide nanoparticles has occurred.[45] The oxidation of magnetite under hydrothermal conditions has previously been observed by Li et al., with 41% of the formed magnetite in that system undergoing further oxidation at 275 °C under autogenous pressure.[46]

Analysis of the Fe/C composition by AAS indicated an iron content of 36.6 ± 5.4 wt %. This is consistent with the results of ICP-OES analysis, which indicate an iron content of 34.5 wt % based on the analysis of a single Fe/C sample. XRF results indicate an iron content of Fe/C of 37.5 ± 9.1 wt %, in agreement with both AAS and ICP-OES measurements.

XPS analysis of the surface composition of Fe/C reveals a surface iron content of 23.9 wt % (Table 1). As this is lower than the total iron content determined via bulk techniques, vide supra, it can be concluded that a significant proportion of the iron content resides within the bulk of the material as opposed to residing entirely in the surface region. Low

https://doi.org/10.1021/acsomega.1c05116
ACS Omega XXXX, XXX, XXX−XXX

Table 1. Surface Composition (wt %) Determined by Quantifying XPS Survey Scans Performed on Kratos Supra Instrument with a Monochromated Aluminum Source

analysis number	Na (wt %)	Fe (wt %)	O (wt %)	In (wt %)	N (wt %)	C (wt %)	S (wt %)
position 1 (20 eV pass)	1.1	22.8	21.9	3.4	2.9	47.1	0.8
position 2 (20 eV pass)	0.9	22.0	22.1	0.7	3.0	50.7	0.6
position 3 indium (20 eV pass)			17.1	67.7	0.5	14.7	
position 3 (10 eV pass)	1.2	27.3	22.6		2.8	45.4	0.8
position 4	1.3	21.0	22.2		2.9	52.1	0.4
position 5 (10 eV pass)	1.1	26.3	22.2		3.1	46.7	0.6

concentrations of sodium, nitrogen, and sulfur were detected, presumably originating from raw AS. C 1s analysis revealed that the majority of the surface carbon is sp^3 hybridized, some of which is oxygen functionalized; however, a smaller component of sp^2 hybridized graphitic carbon is also present. No iron carbide was observed. XPS spectra are shown in Figures S1−S8.

BET analysis reveals surface areas of 546 and 194 m^2g^{-1} for Fe/C and hydrochar, respectively. The surface area of Fe/C is significantly larger than the value of 272 m^2 g^{-1} reported for a carbon-supported iron material prepared from lignin followed by wet impregnation with an iron salt, followed by post carbonization at 1100 °C.[47] That Fe/C has a higher surface area than hydrochar is attributed to the action of iron oxide as a Lewis acid, facilitating the condensation of aromatic groups and the emission of volatile components. This increases the porosity and hence the surface area of this material.[48] Because of this high surface area, it was possible to detect indium through the pores in a pressed sample via XPS (Table 1). Previously, surface areas of up to 1010 m^2 g^{-1} have been obtained for hydrothermally synthesized iron-impregnated carbon.[49] That work, however, employed a templating agent and thus requires additional preparation steps, higher processing temperature (800 °C), and the utilization of more costly and less environmentally friendly reactants. Nitrogen adsorption isotherms for both Fe/C and hydrochar are between Type II and IV (Figure 2). Both materials can

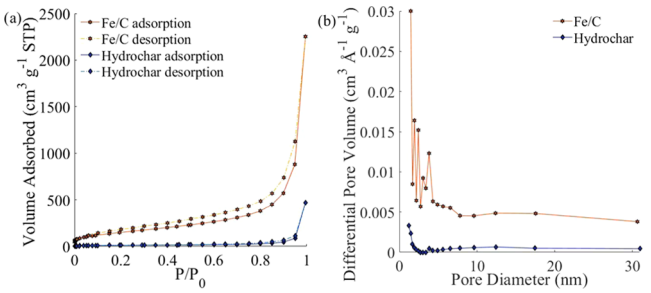

Figure 2. (a) N_2 adsorption−desorption isotherm for F/C and hydrochar. (b) Pore size distribution for Fe/C and hydrochar. Data for both figures were obtained using a quadrasorb surface area analyzer and degasser.

therefore be classified as mesoporous and contain very few micropores.[50] Similar behavior has been observed previously for carbon materials synthesized in hydrothermal environments in the presence of iron catalysts.[47,49] Analysis of the pore size distribution shows that a majority of the pores are below 2 nm in diameter.

The surface functionality of both Fe/C and the hydrochar synthesized in the absence of iron has been characterized by FT-IR spectroscopy (Figure 3). In addition, DAS has also been

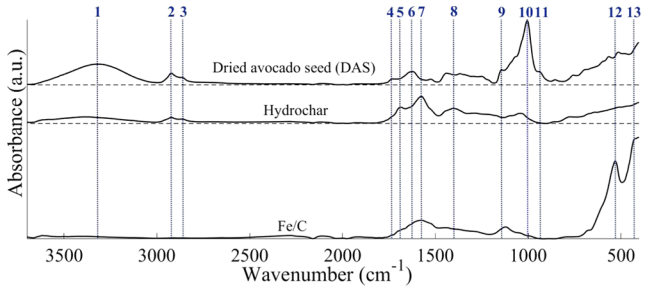

Figure 3. FT-IR spectra obtained for dried avocado seed (DAS), hydrochar, and Fe/C using a Shimadzu IRAffinity-1S spectrometer fitted with a Specac ATR plate. Analysis conditions: scans 4000, resolution 4 cm^{-1}, absorbance mode. The numbered peaks are assigned as follows: 1: νO−H,; 2: ν_{as}C−H; 3: ν_sC−H; 4, 5 and 6: νC═O; 7: νC═C; 8: νC−C; 9: νC−O−C; 10: νC−O; 11: νC−C-O; 12 and 13: νFe−O.

investigated for comparison. DAS exhibits strong absorbance in the O−H stretching region (**1**, 3650−3050 cm^{-1}); however, this is significantly reduced in the hydrochar and fully eliminated in Fe/C. A similar trend is observed in the aliphatic region for asymmetric (**2**, 2919 cm^{-1}) and symmetric (**3**, 2858 cm^{-1}) C−H stretching, which is linked to the presence of methyl and methylene groups. The loss of aliphatic C−H bonds is attributed to condensation reactions occurring during HTC.[51] These aldol polycondensation reactions are the final reactions within HTC that result in the formation of the extended polymeric structure of the synthesized carbonaceous material.[52] That these are further reduced in Fe/C as compared to the hydrochar may indicate that the reaction has proceeded to a greater extent and that it may therefore be catalyzed by the presence of iron. Note also that the presence of iron oxide means that a lower fraction of the surface is hydrocarbonaceous when compared to hydrochar. Carbonyl (C═O) functionalities are also more apparent for DAS, as indicated by the presence of peaks associated with conjugated (**4**, 1737 cm^{-1}) and unconjugated (**6**, 1619 cm^{-1}) stretching. The large C═O stretching band (**5**, 1690 cm^{-1}) present for hydrochar is attributed to conjugated aldehydes formed during HTC. FT-IR also provides evidence for the carbonization of the sample through the appearance of an aromatic C═C stretching band (**7**, 1575 cm^{-1}) in the spectrum of Fe/C and hydrochar, in addition to C−C aromatic stretching (**8**, 1397 cm^{-1}).[53,54] This is supported by the loss of C−O−C (**9**, 1149 cm^{-1}), C−O (**10**, 1005 cm^{-1}), and C−C−O (**11**, 938 cm^{-1}) stretches present in the DAS spectrum. These peaks are associated with ether C−O linkages from cellulose, lignin, and hemicelluloses, and elimination of this is indicative of the loss of this moiety during carbonization.[51] The broad absorbance between 1475 and 1211 cm^{-1} present in the spectrum of DAS is attributed to a mixture of C−C aromatic, C−N, and C−O

https://doi.org/10.1021/acsomega.1c05116
ACS Omega XXXX, XXX, XXX−XXX

stretching vibrations. This is notably reduced in intensity for both hydrochar and Fe/C. Some surface C−O functionality does remain after HTC, as indicated by the peaks between 1050 and 1250 cm^{-1}. Notably, hydrochar has relatively greater absorbance in this region than Fe/C. This is attributed not only to the increased carbonization noted by the reduction in aliphatic C−H vide supra but also to the likely displacement of these functionalities by the supported iron particles.

The FT-IR spectrum of Fe/C is dominated by Fe−O stretching associated with hematite (**12**, 532 cm^{-1}, **13**, 440 cm^{-1}).[55,56] Magnetite typically exhibits a peak at 588 cm^{-1}; if present, this is obscured in this work by the broad hematite peak. Bulk characterization (XRD, vide supra) indicated that magnetite was the dominant iron oxide phase present. ATR is a surface-sensitive technique, and therefore, the identification of hematite is indicative of the oxidation of the outer, air-exposed surface of the iron oxide.

The stability of the synthesized materials against the leaching of either metallic or organic components was qualitatively investigated by placing them in deionized water for 24 h and noting any discoloration. Previously synthesized iron−carbon composites which used sugarcane bagasse as the carbon source had shown discoloration of water after soaking.[40] In the present study, hydrochar visibly discolored the solution to light gray immediately and to dark brown after 24 h. In contrast, the addition of Fe/C to deionized water resulted in no visible discoloration. The material leaching from the hydrochar is most likely unconverted hydrocarbonaceous material, with the brown coloration of the hydrochar indicative of the presence of tannins. Fe/C was obtained as a black powder, consistent with the higher degree of carbonization obtained in the presence of iron inferred from FT-IR spectra. This more carbonized material is, therefore, more resistant to leaching.

To quantify any reduction in iron content, and hence any leaching of iron, Fe/C was collected following soaking using an external magnet and analyzed using AAS, XRF, XRD, and FT-IR spectroscopy. All of the solid material was successfully collected with an external magnet. The recovered Fe/C was shown to have an iron loading of 35.6% by AAS and 36% by XRF, consistent with characterization of the as-synthesized material, indicating that negligible Fe had leached. XRD of Fe/C after leaching tests showed magnetite and hematite contents of 79.2% and 20.8%, respectively, consistent with the as-synthesized materials and therefore indicating that negligible oxidation or reduction of the oxide occurred.

2.2. Adsorption Testing of Fe/C. The efficacy of the synthesized hydrochar and Fe/C have been tested in exemplar adsorption experiments. Synthetic dyes from the textile, paint, and printing industries are a major pollutant in effluent waste streams. Often these dyes are nonbiodegradable, toxic, and carcinogenic.[27,33] These synthetic dyes consequently have adverse effects on the environment and human health. There is, therefore, a necessity to find methods of safe wastewater treatment for their removal. Of the available technologies, magnetic adsorbents have been increasingly proposed as a solution because of their simple operation, high separation, removal efficiency, and wide applicability.[34,57] Methylene blue is widely used as an exemplar organic dye to test the efficiency of adsorbents.[58] Kinetic and isothermal adsorption isotherms of methylene blue adsorption onto Fe/C and hydrochar synthesized in the present work are shown in Figure 4.

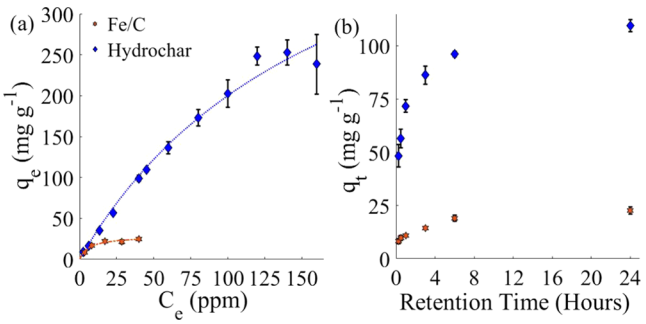

Figure 4. (a) Isothermal adsorption of methylene blue on Fe/C and hydrochar (0.01 g in 25 mL of solution) over 24 h at 30 °C, 180 rpm, fitted to Langmuir adsorption isotherms; (b) kinetic adsorption of methylene blue on Fe/C and hydrochar (0.01 g in 25 mL of solution), for 0.5, 1, 3, 6, and 24 h at 30 °C, 180 rpm. C_e is the concentration of the solution used, and q_e is the concentration of the solution at adsorption equilibrium.

The isothermal adsorption data are fitted to a Langmuir isotherm model.[59] Fe/C showed a maximum adsorption capacity of 24.8 ± 1.3 mg g^{-1}. This adsorption capacity is consistent with previously studied Fe/C materials. For example, a graphene/magnetite material synthesized from high-value activated carbon exhibited a maximum adsorption capacity of 43.82 mg g^{-1}.[58] The results presented herein, therefore, demonstrate that materials produced from a low-value waste materials can exhibit performance competitive with such high-cost materials.

The synthesized hydrochar demonstrated an adsorption capacity of 246 ± 21 mg g^{-1}. Carbonaceous materials (i.e., without iron) can exhibit a wide range of adsorption capacities; however, adsorbents produced from biomass typically have lower capacities than those produced conventionally, e.g., from activated carbon. For instance, adsorbents produced from olive stones, hazelnut shells, apricot stones, and walnut shells have been shown to have adsorption capacities of 22.1, 8.82, 4.11, and 3.53 mg g^{-1}, respectively.[60] The hydrochar obtained from AS herein shows significantly improved adsorption capacity when compared to these.

Hydrochar is clearly observed to be a more effective adsorbent than Fe/C for methylene blue both on a per mass and per surface area basis, having a surface area ∼2.8× smaller than that of Fe/C. This may be ascribed to its higher level of surface functionality, as shown by FT-IR spectroscopy (Section 2.1). Methylene blue binds to surface hydroxide and carbonyl groups on the carbon surface via hydrogen-bond interactions.[61] It is however noteworthy that hydrochar exhibits leaching of organic components such as tannins in aqueous conditions. This may be undesirable where discoloration of the solution cannot be tolerated. Indeed, adsorbents are typically used in the tertiary stage of water treatment to remove any discoloration. The addition of Fe yields a material that is more resistant against leaching and therefore may be better suited to such applications despite its lower adsorption capacity. Furthermore, the removal of Fe/C from the solution after treatment is extremely facile, as this can be accomplished by magnetic separation.

The results of kinetic studies of methylene blue adsorption on both Fe/C and hydrochar are shown in Figure 4b. After 6 h, both materials reach >80% of maximum adsorption. Fe/C shows similar kinetics to previously reported Fe/C materials synthesized by conventional methods, e.g., 54% of maximum

https://doi.org/10.1021/acsomega.1c05116
ACS Omega XXXX, XXX, XXX−XXX

adsorption is achieved after 2.5 h.[40] Kinetic adsorption data were fitted to Lagergren pseudo-first-order and pseudo-second-order rate equations (eqs 1 and 2).[62]

$$\ln(q_e - q_t) = \ln q_e - \frac{k_q t}{2.303} \quad (1)$$

$$\frac{t}{q_t} = \frac{1}{k_2 q_e^2} + \frac{1}{q_e t} \quad (2)$$

The fitted data are shown in Figure 5 and the extracted adsorption capacity at equilibrium and rate constant are shown

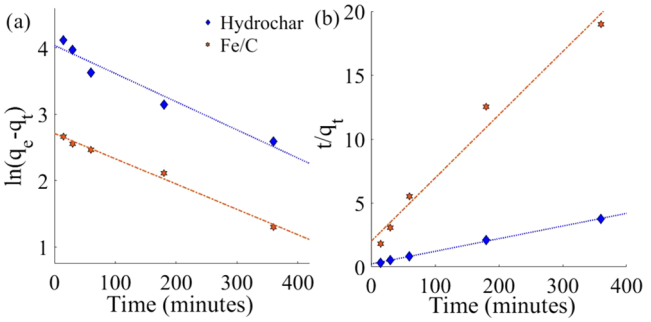

Figure 5. Pseudo-first (a) and -second (b) order fits to kinetic methylene blue adsorption data. Retention times of 0.25−24 h were used, with 16 and 45 ppm methylene blue solutions for Fe/C and hydrochar, respectively.

in Table 2 alongside R^2 values. It is apparent that pseudo-second-order rate equations describe the adsorption process well and significantly better than pseudo-first-order kinetics in the case of hydrochar. Adsorption is therefore inferred to follow second-order kinetics. Mechanistically, this suggests that methylene blue is chemisorbed onto the hydrochar surface (rather than being physisorbed).[63] This results in improved retention and hence better performance in adsorption applications.

Electronic interactions play a key role in adsorption processes: an increase in adsorption is expected if the adsorbate and adsorbent have opposing charges, causing positive interactions.[64] Therefore, it is speculated that the surface charge of Fe/C is positive, thereby lowering its adsorption capacity for the positively charged cationic dye methylene blue relative to that of hydrochar.[65] Adsorption of an alternative adsorbate—indigo carmine, which is an anionic dye (negatively charged)—was therefore investigated (Figure 6).[66] The maximum adsorption capacities of indigo carmine on Fe/C and hydrochar particles were determined to be 49.0 ± 3.7 and 50.9 ± 2.9 mg g^{-1}, respectively. Both the hydrochar and Fe/C therefore show very similar adsorption properties. Fe/C, however, has the advantage of facile magnetic separation from solution. These results support the hypothesis that the comparatively lower maximum adsorption capacity of Fe/C for

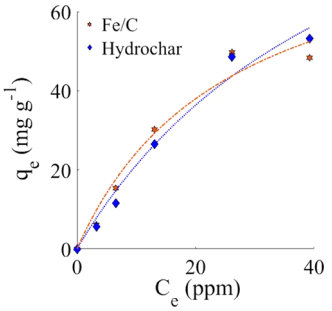

Figure 6. Isothermal adsorption of indigo carmine on Fe/C and hydrochar (0.01 g in 25 mL of solution) over 24 h at 30 °C, 180 rpm. Langmuir adsorption isotherms fits are shown. C_e is the concentration of solution used, and q_e is the concentration of the solution at adsorption equilibrium.

methylene blue is caused by electronic repulsion effects. The affinity of the adsorbents for indigo carmine may be further enhanced by the presence of graphitic carbon on the hydrochar as revealed by XPS (Section 2.1). Interaction between delocalized electrons in the indigo carmine and delocalized electrons in the adsorbate will facilitate adsorption via π-interactions.[67] It should also be noted that, typically, the maximum adsorption capacity for indigo carmine is generally lower than methylene blue, e.g., a commercial activated carbon has exhibited a maximum adsorption capacity 7 times lower for indigo carmine (135 mg g^{-1}) than for methylene blue.[68]

2.3. Catalytic Testing of Fe/C. The catalytic efficiency of Fe/C toward the hydroalkoxylation of phenylacetylene with ethylene glycol was evaluated and compared to both hydrochar and unsupported magnetite nanoparticles. This reaction offers an atom-economical method of creating a carbonyl bond using an alkene or alkyne and an alcohol.[69] The reaction was first demonstrated in 1936 using a mercuric oxide catalyst with boron trifluoride-based co-catalysts.[70] Since then, systems based on Hg, Os, Ru, Pt, Ag, and Au within organic complexes and as oxides have been widely reported.[71] Many of these materials, however, suffer from challenges around high toxicity or high cost. There has therefore been interest in the application of iron salts to overcome these challenges.[72−74] The first studies on heterogeneous iron catalysts were presented in 2015 by Antoniotti et al.[75] These employed montmorillonite-supported iron, achieving yields of up to 86% for the hydroalkoxylation of 5-methyl-2,2-diphenyl-4-hexen-1-ol to 2,2-dimethyl-5,5-diphenyltetrahydro-2H-pyran in dimethyl carbonate (DMC) as a solvent. The further development of low-cost, active, heterogeneous catalysts based on earth-abundant materials remains a desirable objective.

Each catalytic test was performed in triplicate, and results were averaged. Unsupported magnetite nanoparticles were found to successfully yield 2B13D with a yield of 22.7%. This serves as a benchmark against which to compare the catalytic efficiency of the HTC-synthesized materials. Fe/C showed a

Table 2. Extracted Data from Pseudo- First and -Second-Order Fitting of Experimental Kinetic Adsorption Data for Methylene Blue Over Fe/C and Hydrochar

		pseudo-first order			pseudo-second order		
sample	exp q_e (mg g^{-1})	q_e cal (mg g^{-1})	k_1 (min^{-1})	R^2	q_e cal (mg g^{-1})	k_1 (mg g^{-1} min^{-1})	R^2
Fe/C	24.8 ± 1.3	14.9	0.0088	0.9907	20.4	0.0012	0.9777
hydrochar	246 ± 21	54.6	0.0097	0.9553	101	0.00043	0.9985

https://doi.org/10.1021/acsomega.1c05116
ACS Omega XXXX, XXX, XXX−XXX

significantly greater product yield of 45%. The same total quantity of iron oxide is present in reactions involving magnetite nanoparticles and those employing Fe/C. Therefore, this difference is reflective of the higher activity of the HTC-derived material and its differing physicochemical characteristics, including oxidation state, available surface area, *etc.* Previously, the hydroalkoxylation of phenylacetylene with ethylene glycol has been studied utilizing a homogeneous Au(I)/$AgBF_4$ catalyst.[76] In contrast to the present work, Au(I)/$AgBF_4$ demonstrated high selectivity for the alternative regioisomer, producing 2-methyl-2-phenyl-1,3-dioxolane (2P13D) with a yield of 87% (corresponding to a selectivity of 75%). No 2P13D is observed over Fe/C. The exceptional regioselectivity for 2B13D observed over Fe/C is attributed to the conformation adopted by the transition state, with bonding to heterogeneous iron active site taking place via the enol functionality.[77] High selectivity, and the ability to produce exclusively one isomer, is a key objective in catalyst development and one successfully demonstrated by the material synthesized in this work. Hydrochar presented a lower product yield than either iron-based material at 11.2%. While the lower surface area of hydrochar cf. Fe/C contributes to this, the presence of iron in Fe/C enhances catalytic activity via electrophilic bonding to the alkyne.[78] There is then likely a synergistic interaction between iron and carbon, whereby the hydrochar facilitates hydroalkoxylation through stabilizing the hydroxide group, resulting in the formation of the stabilized enol transition state.[78,79] These studies demonstrate the potential to synthesize active and selective catalytic materials from low-value waste and co-product streams via HTC.

3. CONCLUSIONS

A facile, rapid (3 h), and relatively low temperature (230 °C) one-pot HTC synthesis procedure has been demonstrated to synthesize a carbon-supported metal oxide material, with demonstrated applications in adsorption for environmental applications and as a safe and sustainable heterogeneous catalyst. Avocado seeds, a waste material with an expanding production, have been used an exemplar carbon source for the first time. The methodology presented can however be applied to a wide range of lignocellulosic waste streams. The synthesized Fe/C consists predominately of magnetite, allowing easy magnetic separation after application. When employed as a sorbent, Fe/C showed the potential to be used as a selective adsorbent for anionic adsorbates in waste streams with a maximum adsorption capacity for indigo carmine of ∼49 mg g^{-1}. Additionally, Fe/C showed enhanced catalytic efficiency when compared to magnetite nanoparticles, exhibiting a 2-benzyl-1,3-dioxolane yield in the hydroalkoxylation of phenylacetylene of ∼45%, versus ∼23% for the nanoparticles. Additionally, exceptional regioselectivity toward 2-benzyl-1,3-dioxolane was observed. These results suggest a role for HTC in the production of carbon materials for high-value environmental and other applications, rooted in the principles of the circular economy.

4. EXPERIMENTAL SECTION

4.1. Materials. Iron (III) nitrate nonahydrate ($Fe(NO_3)_3 \cdot 9H_2O$), iron (II) sulfate heptahydrate ($FeSO_4 \cdot 7H_2O$), acetone, hexane, nitric acid (64−66%, HNO_3), sodium hydroxide (NaOH), iodobenzene, phenylacetylene, potassium carbonate, indigo carmine, and ethylene glycol were all purchased from Sigma-Aldrich (Dorset, U.K.). Methylene blue trihydrate was purchased from Bio Basic (Cambridgeshire, U.K.). Deionized water was obtained from a Suez L300130 (>1 MΩ cm). Carbon dioxide (N5.0, BOC) and helium (A Grade, 99.996%, BOC) were supplied by BOC. Iron (II, III) oxide (97%, metals basis) was purchased from Alfa Aesar (Lancashire, U.K.). All materials were used as received unless otherwise stated.

4.2. Synthesis Procedure. Magnetic carbon composites (Fe/C) were synthesized by the following procedure. AS were dried in an oven (Memmert, Schwabach, Germany) at 100 °C for 24 h and then subsequently stored in a cold room at 5 °C. Dried avocado seeds (DAS) were pretreated under reflux in sodium hydroxide (0.1 M, 50 mL) at 70 °C for 2 h to remove tannins and dyes prior to separation by filtration and washing with deionized water (3 × 50 mL).[80] The seeds were then dried in an oven (100 °C, 24 h). DAS were soaked in a 1:2 mole ratio Fe^{2+}/Fe^{3+} solution (0.5 M $FeSO_4 \cdot 7H_2O$, 1 M $Fe(NO_3)_3 \cdot 9H_2O$, 50 mL) for ≥3 days. Subsequently, the soaked AS and the iron solution were transferred to a 300 mL autoclave (Series 3050, Parr instrument company, IL) to which NaOH solution (1 M, 50 mL) was added. The vessel was pressurized with CO_2 (30 bar) and transferred to an aluminum block, which had been preheated to 230 °C using a heating mantle (C-MAG HS7, IKA, Oxford, U.K.). The temperature was monitored using a thermocouple. An internal temperature of 230 °C was achieved after 45 min, and this temperature was maintained for 3 h. The reaction was then quenched in a water bath for 30 min. The solid powder was collected by vacuum filtration and soaked in acetone (50 mL) for 24 h. It was then subjected to a further vacuum filtration and then washed with deionized water (3 × 50 mL) and dried in an oven (100 °C, 24 h). The Fe/C was then heated in a tube furnace (Three Zone Horizontal, Elite, Leicestershire, U.K.) to 400 °C (ramp rate 6.5 °C min^{-1}) under constant nitrogen gas flow and held at that temperature for 1 h before cooling to room temperature. The resultant product was ground using a pestle and mortar and sieved to a size fraction of 38−212 μm using mesh steel sieves. Iron-free hydrochar (hereafter referred to as hydrochar) was also synthesized following the same procedure as above but omitting the iron soaking procedure and adding an additional 50 mL of deionized water to the autoclave during carbonization to ensure that the same liquid volume was used in both cases. The overall yield of carbonaceous material, based on the initial mass of AS weight, was 18.2 ± 4.9%. Negligible losses of iron were observed with near-full iron incorporation into the final Fe/C.

Magnetite nanoparticles were synthesized via a conventional route, as described by Liu et al.,[81] to provide a reference against which to measure the catalytic activity of the HTC-derived materials (Section 4.5). $FeCl_3 \cdot 6H_2O$ (6.1 g, 22.6 mmol) and $FeSO_4 \cdot 7H_2O$ (4.2 g, 15.1 mmol) were dissolved in deionized water (100 mL) and heated to 90 °C. NH_4OH (10 mL, 25%) was then added under stirring. After 30 min, the black precipitate was collected by vacuum filtration and dried in an oven (Memmert, Schwabach, Germany) (100 °C, 24 h). The product magnetite nanoparticles were used in the hydroalkoxylation reaction directly.

4.3. Fe/C Characterization. The crystal structure of the synthesized Fe/C was analyzed using powder X-ray diffraction (XRD). XRD was conducted on a D2 Phaser (Bruker, MA) using a Cu tube (λ = 1.54184 Å) with 1 s scanning increments of 0.02° between 24 and 65°. Compositional analysis was conducted by atomic absorption spectroscopy (AAS), X-ray

https://doi.org/10.1021/acsomega.1c05116
ACS Omega XXXX, XXX, XXX−XXX

fluorescence (XRF), and inductively coupled plasma-optical emission spectrometry (ICP-OES). Surface area and pore size analyses were performed using a quadrasorb surface area analyzer and degasser (Micromeritics, Norcross) following Brunauer–Emmett–Teller (BET) theory. For AAS, samples were digested in 1:3 nitric:hydrochloric acid stock solution (aqua regia) and diluted to 1–10 ppm solutions in 1% nitric acid prior to analysis using a AAS AAnalyst 400 (PerkinElmer, MA). The iron powder was digested and analyzed following the same procedure to produce standards for calibration.[82] XRF was conducted on an Olympus Delta DP-2000-C (GP Technical Equipment, Savannah) using a titanium filter, tube voltage of 50 kV and a current of 55 μA. For ICP-OES, Fe/C was dissolved using a 1:1 mixture of nitric and perchloric acid and then analyzed using a Spectro Ciros Vision ICP-OES (AMETEK Materials, Kleve Germany). Further surface composition was examined using X-ray photoelectron spectroscopy (XPS) performed on Kratos Supra (Kratos Analytical Ltd., Manchester, U.K.) instrument with a monochromated aluminum source at two analyses per sample, each of area 700 μm × 300 μm. Survey scans were collected between 1200 and 0 eV binding energy, at 160 eV pass energy, 1 eV intervals, and 300 s/sweep, with one sweep being collected. High-resolution Fe 2p, O 1s, C 1s, N 1s, and In 3d were also collected. The data was analyzed using CasaXPS software. Characterization of surface functionalities was conducted by Fourier-transform infrared (FT-IR) spectroscopy performed on a IRAffinity-1S (Shimadzu, Buckinghamshire, U.K.) at a resolution of 4 cm^{-1} with 4000 scans over the range 400–4000 cm^{-1}. FT-IR data was normalized using an adaptive baseline (25% coarseness) using optical spectroscopy software (Spectragryph, http://spectroscopy.ninja, Germany). Magnetization was measured using a Quantum Design (London, U.K.) superconducting quantum interference device (SQUID)-vibrating sample magnetometer (VSM) MPMS3.

4.4. Adsorption Studies. The isothermal adsorption capacity and the kinetics of adsorption were investigated. All uptake studies were conducted in an Infors HT multitron shaker at 30 °C and 180 rpm. Isothermal experiments were performed over 24 h using 0.01 g of adsorbent and 25 mL of 4–40 ppm methylene blue solution for Fe/C and 25 mL of 4–160 ppm methylene blue solution for hydrochar. Kinetic studies employed retention times of 0.25–24 h with 16 and 45 ppm methylene blue solutions for Fe/C and hydrochar, respectively. After the specified retention time, Fe/C was magnetically separated; alternatively, for nonmagnetic hydrochar, separation was conducted by filtration. The remaining solutions were analyzed using a UV–vis spectrophotometer (Genesys 150, ThermoFisher Scientific, MA) (λ = 634 nm). The quantity of methylene blue adsorbed, q_e (mg/g), and q_t (mg/g) were calculated, as shown in eqs 3 and 4

$$q_e = (C_0 - C_e) \times \frac{V}{W} \quad (3)$$

$$q_t = (C_0 - C_t) \times \frac{V}{W} \quad (4)$$

where C_0 and C_e are initial and equilibrium concentrations of methylene blue ppm (mg L^{-1}), V is the volume of solution (L), and W is the weight of the adsorbent used (g).

Isothermal adsorption studies were also performed on Fe/C and hydrochar using indigo carmine as an alternative adsorbate. This was performed by the same analysis procedure with concentrations between 3 and 36 ppm over a time of 24 h and analyzed using UV–vis spectrophotometry (λ = 610 nm).

4.5. Catalytic Testing. The catalytic performance of Fe/C was evaluated in the hydroalkoxylation of phenylacetylene with ethylene glycol, yielding 2-benzyl-1,3-dioxolane (2B13D) as the desired product (Scheme 1).[69,70] Iodobenzene (1 mmol, 0.20 g/0.11 mL), phenylacetylene (2 mmol, 0.20 g/0.22 mL), potassium carbonate (2 mmol, 0.276 g), and the catalyst (0.058 g magnetite nanoparticles, 0.116 g Fe/C or 0.116 g hydrochar) were dissolved in ethylene glycol (3.34 g/3 mL) and stirred for 48 h under reflux. The quantities of magnetite nanoparticles and Fe/C were selected to give the same quantity of iron oxide (~0.25 mmol) in both cases. After stirring, the solid material was separated using an external magnet or via filtration in the case of hydrochar. Deionized water (5 mL) and hexane (5 mL) were then added to the remaining solution, and the hexane layer was separated. The hexane extract was analyzed by GC-MS (Shimadzu QP2010 SE, Buckinghamshire, U.K.) equipped with a DB5-MS column (24.5 m, 0.25 mm, 0.25 μm). Briefly, 10 μL of hexane was injected at 250 °C with an initial oven temperature of 40 °C, which was raised to 240 °C at 10 °C/min. High purity helium (A Grade, 99.996%, BOC) was used as a carrier gas at a flow rate of 1 mL/min. The product concentration was quantified using external calibration standards with an R^2 value of 0.991. Where possible, all results are reported with 95% confidence intervals from five separately synthesized Fe/C samples and three separately synthesized hydrochar samples.

Scheme 1. Schematic of the Hydroalkoxylation of Phenylacetylene With Ethylene Glycol to Yield 2-Benzyl-1,3-Dioxolane

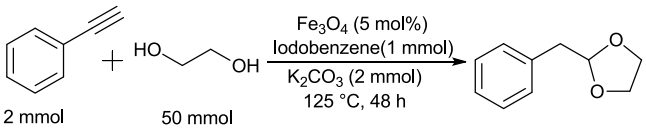

ASSOCIATED CONTENT

Supporting Information

The Supporting Information is available free of charge at https://pubs.acs.org/doi/10.1021/acsomega.1c05116.

Figures S1–S8: high-resolution XPS spectra for Fe/C focused on Fe 2p and C 1s scans in different positions on the sample (PDF)

AUTHOR INFORMATION

Corresponding Author

James McGregor – *Department of Chemical and Biological Engineering, University of Sheffield, Sheffield S1 3JD, U.K.*; orcid.org/0000-0001-6813-306X; Email: james.mcgregor@sheffield.ac.uk

Author

Gareth Davies – *Department of Chemical and Biological Engineering, University of Sheffield, Sheffield S1 3JD, U.K.*

Complete contact information is available at: https://pubs.acs.org/10.1021/acsomega.1c05116

Notes

The authors declare no competing financial interest.

https://doi.org/10.1021/acsomega.1c05116
ACS Omega XXXX, XXX, XXX–XXX

■ ACKNOWLEDGMENTS

EPSRC is acknowledged for funding a Ph.D. studentship for G.D. via Award EP/N509735/1. The authors thank Dr. Debbie Hammond at the Sheffield Surface Analysis Centre for performing the XPS analysis presented in Figures S1−S8 and Table 1. The authors also thank Dr. Tom Hayward and Dr. Richard Rowan-Robinson for providing magnetization analysis presented in Figure 1b.

■ REFERENCES

(1) Arancon, R. A. D.; Lin, C. S. K.; Chan, K. M.; Kwan, T. H.; Luque, R. Advances on Waste Valorization: New Horizons for a More Sustainable Society. *Energy Sci. Eng.* **2013**, *1*, 53−71.
(2) Karak, T.; Bhagat, R. M.; Bhattacharyya, P. Municipal Solid Waste Generation, Composition, and Management: The World Scenario. *Crit. Rev. Environ. Sci. Technol.* **2012**, *42*, 1509−1630.
(3) Nayak, A.; Bhushan, B. An Overview of the Recent Trends on the Waste Valorization Techniques for Food Wastes. *J. Environ. Manage.* **2019**, *233*, 352−370.
(4) Amulya, K.; Dahiya, S.; Venkata Mohan, S. *Building a Bio-Based Economy through Waste Remediation: Innovation towards Sustainable Future*; Elsevier Inc., 2016.
(5) Smith, A. M.; Ross, A. B. Production of Bio-Coal, Bio-Methane and Fertilizer from Seaweed via Hydrothermal Carbonisation. *Algal Res.* **2016**, *16*, 1−11.
(6) Smith, A. M.; Whittaker, C.; Shield, I.; Ross, A. B. The Potential for Production of High Quality Bio-Coal from Early Harvested Miscanthus by Hydrothermal Carbonisation. *Fuel* **2018**, *220*, 546−557.
(7) Mäkelä, M.; Benavente, V.; Fullana, A. Hydrothermal Carbonization of Lignocellulosic Biomass: Effect of Process Conditions on Hydrochar Properties. *Appl. Energy* **2015**, *155*, 576−584.
(8) Funke, A.; Ziegler, F. Hydrothermal Carbonization of Biomass: A Summary and Discussion of Chemical Mechanisms for Process Engineering. *Biofuels, Bioprod. Biorefin.* **2010**, *6*, 160−177.
(9) Hoekman, S. K.; Broch, A.; Robbins, C. Hydrothermal Carbonization (HTC) of Lignocellulosic Biomass. *Energy Fuels* **2011**, *25*, 1802−1810.
(10) Atiqah Nasir, N.; Davies, G.; McGregor, J. Tailoring Product Characteristics in the Carbonisation of Brewers' Spent Grain through Solvent Selection. *Food Bioprod. Process.* **2020**, *120*, 41−47.
(11) Davies, G.; El Sheikh, A.; Collett, C.; Yakub, I.; McGregor, J. In *Catalytic Carbon Materials from Biomass*; Sadjadi, S. B., Ed.; Elsevier, 2021, Chapter 5; pp 161−195.
(12) He, C.; Giannis, A.; Wang, J. Y. Conversion of Sewage Sludge to Clean Solid Fuel Using Hydrothermal Carbonization: Hydrochar Fuel Characteristics and Combustion Behavior. *Appl. Energy* **2013**, *111*, 257−266.
(13) Yao, Z.; Ma, X. Characteristics of Co-Hydrothermal Carbonization on Polyvinyl Chloride Wastes with Bamboo. *Bioresour. Technol.* **2018**, *247*, 302−309.
(14) Haque, N.; Somerville, M. Techno-Economic and Environmental Evaluation of Biomass Dryer. *Procedia Eng.* **2013**, *56*, 650−655.
(15) Reza, M. T.; Yan, W.; Uddin, M. H.; Lynam, J. G.; Hoekman, S. K.; Coronella, C. J.; Vásquez, V. R. Reaction Kinetics of Hydrothermal Carbonization of Loblolly Pine. *Bioresour. Technol.* **2013**, *139*, 161−169.
(16) Cai, J.; Li, B.; Chen, C.; Wang, J.; Zhao, M.; Zhang, K. Hydrothermal Carbonization of Tobacco Stalk for Fuel Application. *Bioresour. Technol.* **2016**, *220*, 305−311.
(17) Zhang, L.; Wang, Q.; Wang, B.; Yang, G.; Lucia, L. A.; Chen, J. Hydrothermal Carbonization of Corncob Residues for Hydrochar Production. *Energy Fuels* **2015**, *29*, 872−876.
(18) Islam, M. A.; Ahmed, M. J.; Khanday, W. A.; Asif, M.; Hameed, B. H. Mesoporous Activated Coconut Shell-Derived Hydrochar Prepared via Hydrothermal. *J. Environ. Manage.* **2017**, *203*, 237−244.
(19) White, R. J.; Yoshizawa, N.; Antonietti, M.; Titirici, M.-M. A Sustainable Synthesis of Nitrogen-Doped Carbon Aerogels. *Green Chem.* **2011**, *13*, 2428.
(20) Wu, Q.; Li, W.; Liu, S.; Jin, C. Hydrothermal Synthesis of N-Doped Spherical Carbon from Carboxymethylcellulose for CO_2 capture. *Appl. Surf. Sci.* **2016**, *369*, 101−107.
(21) Hu, B.; Wang, K.; Wu, L.; Yu, S. H.; Antonietti, M.; Titirici, M. M. Engineering Carbon Materials from the Hydrothermal Carbonization Process of Biomass. *Adv. Mater.* **2010**, *22*, 813−828.
(22) Tran, H. N.; Huang, F. C.; Lee, C. K.; Chao, H. P. Activated Carbon Derived from Spherical Hydrochar Functionalized with Triethylenetetramine: Synthesis, Characterizations, and Adsorption Application. *Green Process. Synth.* **2017**, *6*, 565−576.
(23) Gai, C.; Zhang, F.; Yang, T.; Liu, Z.; Jiao, W.; Peng, N.; Liu, T.; Lang, Q.; Xia, Y. Hydrochar Supported Bimetallic Ni-Fe Nanocatalysts with Tailored Composition, Size and Shape for Improved Biomass Steam Reforming Performance. *Green Chem.* **2018**, *20*, 2788−2800.
(24) Titirici, M. M.; White, R. J.; Brun, N.; Budarin, V. L.; Su, D. S.; Del Monte, F.; Clark, J. H.; MacLachlan, M. J. Sustainable Carbon Materials. *Chem. Soc. Rev.* **2015**, *44*, 250−290.
(25) Sánchez, F.; Araus, K.; Domínguez, M. P.; Miguel, G. S. Thermochemical Transformation of Residual Avocado Seeds: Torrefaction and Carbonization. *Waste Biomass Valoriz.* **2017**, *8*, 2495−2510.
(26) Xue, J.; Chellappa, T.; Ceylan, S.; Goldfarb, J. L. Enhancing Biomass + Coal Co-Firing Scenarios via Biomass Torrefaction and Carbonization: Case Study of Avocado Pit Biomass and Illinois No. 6 Coal. *Renewable Energy* **2018**, *122*, 152−162.
(27) Palma, C.; Lloret, L.; Puen, A.; Tobar, M.; Contreras, E. Production of Carbonaceous Material from Avocado Peel for Its Application as Alternative Adsorbent for Dyes Removal. *Chin. J. Chem. Eng.* **2016**, *24*, 521−528.
(28) OECD-FAO Agricultural Outlook 2021−2030. Food and Agriculture Organization: United Nations, 2020.
(29) Lin, Y.; Ma, X.; Peng, X.; Yu, Z.; Fang, S.; Lin, Y.; Fan, Y. Combustion, Pyrolysis and Char CO2-Gasification Characteristics of Hydrothermal Carbonization Solid Fuel from Municipal Solid Wastes. *Fuel* **2016**, *181*, 905−915.
(30) Durak, H.; Aysu, T. Effect of Pyrolysis Temperature and Catalyst on Production of Bio-Oil and Bio-Char from Avocado Seeds. *Res. Chem. Intermed.* **2015**, *41*, 8067−8097.
(31) Michelin, M.; Ruiz, H. A.; Silva, D. P.; Ruzene, D. S.; Teixeira, J. A.; Polizeli, M. L. T. M. Cellulose from Lignocellulosic Waste BT - Polysaccharides: Bioactivity and Biotechnology, Ramawat, K. G., Mérillon, J.-M., Eds.; Springer International Publishing: Cham, 2025; pp 475−511.
(32) Abiemwense, G. Influence of Hydrothermal Treatment Duration on the Nutritional Quality of Avocado Pear (*Persia americana*) Seed Meal for Livestock Feeding. *Anim. Res. Int.* **2017**, *14*, 2759−2763.
(33) Xu, P.; Zeng, G. M.; Huang, D. L.; Feng, C. L.; Hu, S.; Zhao, M. H.; Lai, C.; Wei, Z.; Huang, C.; Xie, G. X.; et al. Use of Iron Oxide Nanomaterials in Wastewater Treatment: A Review. *Sci. Total Environ.* **2012**, *424*, 1−10.
(34) Reddy, L. H.; Arias, J. L.; Nicolas, J.; Couvreur, P. Magnetic Nanoparticles: Design and Characterization, Toxicity and Biocompatibility, Pharmaceutical and Biomedical Applications. *Chem. Rev.* **2012**, *112*, 5818−5878.
(35) Sun, H.; Zhou, G.; Liu, S.; Ang, H. M.; Tadé, M. O.; Wang, S. Nano-Fe0 Encapsulated in Microcarbon Spheres: Synthesis, Characterization, and Environmental Applications. *ACS Appl. Mater. Interfaces* **2012**, *4*, 6235−6241.
(36) Ma, Q.; Cui, L.; Zhou, S.; Li, Y.; Shi, W.; Ai, S. Iron Nanoparticles in Situ Encapsulated in Lignin-Derived Hydrochar as an Effective Catalyst for Phenol Removal. *Environ. Sci. Pollut. Res.* **2018**, *25*, 20833−20840.
(37) Zhu, X.; Qian, F.; Liu, Y.; Matera, D.; Wu, G.; Zhang, S.; Chen, J. Controllable Synthesis of Magnetic Carbon Composites with High

https://doi.org/10.1021/acsomega.1c05116
ACS Omega XXXX, XXX, XXX−XXX

Porosity and Strong Acid Resistance from Hydrochar for Efficient Removal of Organic Pollutants: An Overlooked Influence. *Carbon* **2016**, *99*, 338−347.
(38) Liu, Y.; Zhu, X.; Qian, F.; Zhang, S.; Chen, J. Magnetic Activated Carbon Prepared from Rice Straw-Derived Hydrochar for Triclosan Removal. *RSC Adv.* **2014**, *4*, 63620−63626.
(39) Altay, B. N.; Aksoy, B.; Banerjee, D.; Maddipatla, D.; Fleming, P. D.; Bolduc, M.; Cloutier, S. G.; Atashbar, M. Z.; Gupta, R. B.; Demir, M. Lignin-Derived Carbon-Coated Functional Paper for Printed Electronics. *ACS Appl. Electron. Mater.* **2021**, *3*, 3904−3914.
(40) Rattanachueskul, N.; Saning, A.; Kaowphong, S.; Chumha, N.; Chuenchom, L. Magnetic Carbon Composites with a Hierarchical Structure for Adsorption of Tetracycline, Prepared from Sugarcane Bagasse via Hydrothermal Carbonization Coupled with Simple Heat Treatment Process. *Bioresour. Technol.* **2017**, *226*, 164−172.
(41) Lafuente, B.; Downs, R. T.; Yang, H.; Stone, N. Software for Identification and Refinement of Cell Parameters from Powder Diffraction Data of Minerals Using the RRUFF Project and American Mineralogist Crystal Structure Databases. Magnetite R061111, https://rruff.info/i/R061111 (accessed Sep 2, 2019).
(42) Lafuente, B.; Downs, R. T.; Yang, H.; Stone, N. Software for Identification and Refinement of Cell Parameters from Powder Diffraction Data of Minerals Using the RRUFF Project and American Mineralogist Crystal Structure Databases. Hematite R110013, https://rruff.info/hematite/R110013 (accessed Sep 2, 2019).
(43) Khalil, M. I. Co-Precipitation in Aqueous Solution Synthesis of Magnetite Nanoparticles Using Iron(III) Salts as Precursors. *Arab. J. Chem.* **2015**, *8*, 279−284.
(44) Yu, W.; Zhang, T.; Zhang, J.; Qiao, X.; Yang, L.; Liu, Y. The Synthesis of Octahedral Nanoparticles of Magnetite. *Mater. Lett.* **2006**, *60*, 2998−3001.
(45) Šutka, A.; Lagzdina, S.; Juhnevica, I.; Jakovlevs, D.; Maiorov, M. Precipitation Synthesis of Magnetite Fe3O4 Nanoflakes. *Ceram. Int.* **2014**, *40*, 11437−11440.
(46) Li, Z.; Chanéac, C.; Berger, G.; Delaunay, S.; Graff, A.; Lefèvre, G. Mechanism and Kinetics of Magnetite Oxidation under Hydrothermal Conditions. *RSC Adv.* **2019**, *9*, 33633−33642.
(47) Demir, M.; Kahveci, Z.; Aksoy, B.; Palapati, N. K. R.; Subramanian, A.; Cullinan, H. T.; El-Kaderi, H. M.; Harris, C. T.; Gupta, R. B. Graphitic Biocarbon from Metal-Catalyzed Hydrothermal Carbonization of Lignin. *Ind. Eng. Chem. Res.* **2015**, *54*, 10731−10739.
(48) Zhu, X.; Liu, Y.; Qian, F.; Zhou, C.; Zhang, S.; Chen, J. Role of Hydrochar Properties on the Porosity of Hydrochar-Based Porous Carbon for Their Sustainable Application. *ACS Sustainable Chem. Eng.* **2015**, *3*, 833−840.
(49) Sevilla, M.; Fuertes, A. B. Catalytic Graphitization of Templated Mesoporous Carbons. *Carbon* **2006**, *44*, 468−474.
(50) Donohue, M. D.; Aranovich, G. L. Classification of Gibbs Adsorption Isotherms. *Adv. Colloid Interface Sci.* **1998**, *76*−*77*, 137−152.
(51) Kang, S.; Li, X.; Fan, J.; Chang, J. Characterization of Hydrochars Produced by Hydrothermal Carbonization of Lignin, Cellulose, d-Xylose, and Wood Meal. *Ind. Eng. Chem. Res.* **2012**, *51*, 9023−9031.
(52) Higgins, L. J. R.; Brown, A. P.; Harrington, J. P.; Ross, A. B.; Kaulich, B.; Mishra, B. Evidence for a Core-Shell Structure of Hydrothermal Carbon. *Carbon* **2020**, *161*, 423−431.
(53) Parshetti, G. K.; Kent Hoekman, S.; Balasubramanian, R. Chemical, Structural and Combustion Characteristics of Carbonaceous Products Obtained by Hydrothermal Carbonization of Palm Empty Fruit Bunches. *Bioresour. Technol.* **2013**, *135*, 683−689.
(54) Liu, Y.; He, Z.; Uchimiya, M. Comparison of Biochar Formation from Various Agricultural By-Products Using FTIR Spectroscopy. *Mod. Appl. Sci.* **2015**, *9*, 246−253.
(55) Namduri, H.; Nasrazadani, S. Quantitative Analysis of Iron Oxides Using Fourier Transform Infrared Spectrophotometry. *Corros. Sci.* **2008**, *50*, 2493−2497.
(56) Tadic, M.; Panjan, M.; Tadic, B. V.; Kopani, M.; Kopanja, L. Magnetic Properties of Hematite (α-Fe2O3) Nanoparticles Synthesized by Sol-Gel Synthesis Method: The Influence of Particle Size and Particle Size Distribution. *J. Electr. Eng.* **2019**, *70*, 71−76.
(57) Ma, H.; Li, J. B.; Liu, W. W.; Miao, M.; Cheng, B. J.; Zhu, S. W. Novel Synthesis of a Versatile Magnetic Adsorbent Derived from Corncob for Dye Removal. *Bioresour. Technol.* **2015**, *190*, 13−20.
(58) Ai, L.; Zhang, C.; Chen, Z. Removal of Methylene Blue from Aqueous Solution by a Solvothermal-Synthesized Graphene/Magnetite Composite. *J. Hazard. Mater.* **2011**, *192*, 1515−1524.
(59) Lafuente, B.; Downs, R. T.; Yang, H.; Stone, N. Stone N Software for Identification and Refinement of Cell Parameters from Powder Diffraction Data of Minerals Using the RRUFF Project and American Mineralogist Crystal Structure Databases. Hematite R110013, https://rruff.info/hematite/R110013 (accessed Sep 2, 2019).
(60) Rafatullah, M.; Sulaiman, O.; Hashim, R.; Ahmad, A. Adsorption of Methylene Blue on Low-Cost Adsorbents: A Review. *J. Hazard. Mater.* **2010**, *177*, 70−80.
(61) Dinh, V. P.; Huynh, T. D. T.; Le, H. M.; Nguyen, V. D.; Dao, V. A.; Hung, N. Q.; Tuyen, L. A.; Lee, S.; Yi, J.; Nguyen, T. D.; et al. Insight into the Adsorption Mechanisms of Methylene Blue and Chromium(III) from Aqueous Solution onto Pomelo Fruit Peel. *RSC Adv.* **2019**, *9*, 25847−25860.
(62) Zhang, H.; Zhang, F.; Huang, Q. Highly Effective Removal of Malachite Green from Aqueous Solution by Hydrochar Derived from Phycocyanin-Extracted Algal Bloom Residues through Hydrothermal Carbonization. *RSC Adv.* **2017**, *7*, 5790−5799.
(63) Gomer, R. Chemisorption on Metals. *Solid State Phys.* **1975**, *30*, 93−225.
(64) Joo, J. B.; Park, J.; Yi, J. Preparation of Polyelectrolyte-Functionalized Mesoporous Silicas for the Selective Adsorption of Anionic Dye in an Aqueous Solution. *J. Hazard. Mater.* **2009**, *168*, 102−107.
(65) Li, J.; Wang, S.; Peng, J.; Lin, G.; Hu, T.; Zhang, L. Selective Adsorption of Anionic Dye from Solutions by Modified Activated Carbon. *Arab. J. Sci. Eng.* **2018**, *43*, 5809−5817.
(66) Damasceno, B. S.; Da Silva, A. F. V.; De Araújo, A. C. V. Dye Adsorption onto Magnetic and Superparamagnetic Fe3O4nanoparticles: A Detailed Comparative Study. *J. Environ. Chem. Eng.* **2020**, *8*, No. 103994.
(67) Dastgerdi, Z. H.; Meshkat, S. S.; Esrafili, M. D. Enhanced Adsorptive Removal of Indigo Carmine Dye Performance by Functionalized Carbon Nanotubes Based Adsorbents from Aqueous Solution: Equilibrium, Kinetic, and DFT Study. *J. Nanostruct. Chem.* **2019**, *9*, 323−334.
(68) Chowdhury, M. F.; Khandaker, S.; Sarker, F.; Islam, A.; Rahman, M. T.; Awual, M. R. Current Treatment Technologies and Mechanisms for Removal of Indigo Carmine Dyes from Wastewater: A Review. *J. Mol. Liq.* **2020**, *318*, No. 114061.
(69) Messerle, B. A.; Vuong, K. Q. Synthesis of Spiroketals by Iridium-Catalyzed Double Hydroalkoxylation. *Pure Appl. Chem.* **2006**, *78*, 385−390.
(70) Killian, D. B.; Hennion, G. F.; Nieuwland, J. A. The Synthesis of Some Dioxole Derivatives from Alkylacetylenes. *J. Am. Chem. Soc.* **1936**, *58*, 1658−1659.
(71) Konkol, M.; Schmidt, H.; Steinborn, D. Iridium-Catalyzed Addition of Methanol to Internal Alkynes. *J. Mol. Catal. A* **2007**, *261*, 301−305.
(72) Ke, F.; Li, Z.; Xiang, H.; Zhou, X. Catalytic Hydroalkoxylation of Alkenes by Iron(III) Catalyst. *Tetrahedron Lett.* **2011**, *52*, 318−320.
(73) Komeyama, K.; Morimoto, T.; Nakayama, Y.; Takaki, K. Cationic Iron-Catalyzed Intramolecular Hydroalkoxylation of Unactivated Olefins. *Tetrahedron Lett.* **2007**, *48*, 3259−3261.
(74) Alcaide, B.; Almendros, P.; Del Campo, T. M. Chemodivergence in Alkene/Allene Cycloetherification of Enallenols: Iron versus Noble Metal Catalysis. *Chem. − Eur. J.* **2008**, *14*, 7756−7759.

https://doi.org/10.1021/acsomega.1c05116
ACS Omega XXXX, XXX, XXX−XXX

(75) Notar Francesco, I.; Cacciuttolo, B.; Pucheault, M.; Antoniotti, S. Simple Metal Salts Supported on Montmorillonite as Recyclable Catalysts for Intramolecular Hydroalkoxylation of Double Bonds in Conventional and VOC-Exempt Solvents. *Green Chem.* **2015**, *17*, 837−841.
(76) Santos, L. L.; Ruiz, V. R.; Sabater, M. J.; Corma, A. Regioselective Transformation of Alkynes into Cyclic Acetals and Thioacetals with a Gold(I) Catalyst: Comparison with Brønsted Acid Catalysts. *Tetrahedron* **2008**, *64*, 7902−7909.
(77) Kondolff, I.; Doucet, H.; Santelli, M. Direct Synthesis of Protected Arylacetaldehydes by Palladium- Tetraphosphine-Catalyzed Arylation of Ethyleneglycol Vinylether. *Synlett* **2004**, *9*, 1561−1564.
(78) Zhou, Y.; Xu, X.; Sun, H.; Tao, G.; Chang, X. Y.; Xing, X.; Chen, B.; Xu, C. Development of Highly Efficient Platinum Catalysts for Hydroalkoxylation and Hydroamination of Unactivated Alkenes. *Nat. Commun.* **2021**, *12*, No. 1953.
(79) Serp, P.; Figueiredo, J. L. *Carbon Materials for Catalysis*; Wiley, 2009.
(80) Armstrong, W. D.; Rogler, J. C.; Featherston, W. R. Effect of Tannin Extraction on the Performance of Chicks Fed Bird Resistant Sorghum Grain Diets. *Poult. Sci.* **1974**, *53*, 714−720.
(81) Liu, J. F.; Zhao, Z. S.; Jiang, G. B. Coating Fe3O4 Magnetic Nanoparticles with Humic Acid for High Efficient Removal of Heavy Metals in Water. *Environ. Sci. Technol.* **2008**, *42*, 6949−6954.
(82) Uddin, A. B. M. H.; Khalid, R. S.; Alaama, M.; Abdualkader, A. M.; Kasmuri, A.; Abbas, S. A. Comparative Study of Three Digestion Methods for Elemental Analysis in Traditional Medicine Products Using Atomic Absorption Spectrometry. *J. Anal. Sci. Technol.* **2016**, *7*, No. 6.

https://doi.org/10.1021/acsomega.1c05116
ACS Omega XXXX, XXX, XXX−XXX